NATO Science for Peace and Security Series - B:
Physics and Biophysics

Biophotonics: Spectroscopy, Imaging, Sensing, and Manipulation

Edited by
Baldassare Di Bartolo
John Collins

Springer

This publication is supported by:

The NATO Science for Peace and Security Programme

Biophotonics: Spectroscopy, Imaging, Sensing, and Manipulation

NATO Science for Peace and Security Series

This Series presents the results of scientific meetings supported under the NATO Programme: Science for Peace and Security (SPS).

The NATO SPS Programme supports meetings in the following Key Priority areas: (1) Defence Against Terrorism; (2) Countering other Threats to Security and (3) NATO, Partner and Mediterranean Dialogue Country Priorities. The types of meeting supported are generally "Advanced Study Institutes" and "Advanced Research Workshops". The NATO SPS Series collects together the results of these meetings. The meetings are co-organized by scientists from NATO countries and scientists from NATO's "Partner" or "Mediterranean Dialogue" countries. The observations and recommendations made at the meetings, as well as the contents of the volumes in the Series, reflect those of parti-cipants and contributors only; they should not necessarily be regarded as reflecting NATO views or policy.

Advanced Study Institutes (ASI) are high-level tutorial courses intended to convey the latest developments in a subject to an advanced-level audience

Advanced Research Workshops (ARW) are expert meetings where an intense but informal exchange of views at the frontiers of a subject aims at identifying directions for future action

Following a transformation of the programme in 2006 the Series has been re-named and re-organised. Recent volumes on topics not related to security, which result from meetings supported under the programme earlier, may be found in the NATO Science Series.

The Series is published by IOS Press, Amsterdam, and Springer, Dordrecht, in conjunction with the NATO Public Diplomacy Division.

Sub-Series

A.	Chemistry and Biology	Springer
B.	Physics and Biophysics	Springer
C.	Environmental Security	Springer
D.	Information and Communication Security	IOS Press
E.	Human and Societal Dynamics	IOS Press

http://www.nato.int/science
http://www.springer.com
http://www.iospress.nl

Series B: Physics and Biophysics

Biophotonics: Spectroscopy, Imaging, Sensing, and Manipulation

edited by

Baldassare Di Bartolo
Boston College, Chestnut Hill, MA
U.S.A.

and

John Collins
Wheaton College, Norton, MA
U.S.A.

Published in cooperation with NATO Public Diplomacy Division

Proceedings of the NATO Advanced Study Institute on
Bio-Photonics: Spectroscopy, Imaging, Sensing, and Manipulation
Erice, Sicily, Italy
2-17 July 2009

Library of Congress Control Number: 2010938914

ISBN 978-94-007-0028-4 (PB)
ISBN 978-90-481-9976-1 (HB)
ISBN 978-90-481-9977-8 (e-book)

Published by Springer,
P.O. Box 17, 3300 AA Dordrecht, The Netherlands.

www.springer.com

Printed on acid-free paper

"*We who preach and write books . . . . write while we make progress. We learn something new every day. We dictate at the same time as we explore. We speak as we are still knocking for understanding.*"

St. Augustine

CONTENTS

POSTER PRESENTATIONS

PREFACE

This volume presents the Proceedings of the NATO Advanced Study Institute on "Bio-Photonics: Spectroscopy, Imaging, Sensing, and Manipulation," held in Erice, Sicily, Italy, from the 2nd to the 17th of July 2009. This meeting was organized by the International School of Atomic and Molecular Spectroscopy of the "Ettore Majorana" Center for Scientific Culture.

Possibly, *bio-optics* started with the work of Dutchman Antoni van Leeuwenhoek who, in the seventeenth century, built optical microscopes for fun and observed bacteria and red blood cells with his homemade instruments. With Albert Einstein's introduction of the photon in 1905, optics turned into photonics, which enabled one of the research tools of modern *bio-photonics* – the laser. Today, it is clear that existing optical technologies can provide many novel opportunities and tools for the life sciences. In turn, biological applications continue to stimulate novel optical technologies: e.g. various emerging approaches for achieving sub-wavelength optical resolution.

The purpose of the Institute was to present a broad overview of the emerging field of bio-photonics including the optical analysis, spectroscopy, sensing and imaging of biological systems as well as their manipulation and modification.

Each lecturer provided a coherent section of the program starting at a somewhat fundamental level and ultimately reaching the frontier of knowledge in a systematic and didactic fashion. The formal lectures were complemented by additional seminars and discussions. The Institute gave the participants an opportunity to present their research work in the form of short seminars or posters.

The participants came from 18 different countries: Belarus, Estonia, France, Germany, Italy, Kazakhstan, the Netherlands, Poland, Romania, Russia, Spain, Sweden, Switzerland, Turkey, Ukraine, United Kingdom, the United States, and Uzbekistan. 21 lecture series and an interdisciplinary lecture were presented. In addition 16 short seminars and 12 posters were contributed by the participants. Two round table discussions were held. The first round-table discussion took place during the first week of the school in order to evaluate the work done and consider suggestions and proposals regarding the organization, format and presentation of the lectures. The second round-table was held at the conclusion of the entire meeting in order to discuss various proposals for the next course of the International School of Atomic and Molecular Spectroscopy.

I would like to thank the co-director of the Course Academician Aleksander Voitovich, the members of the Organizing Committee (Prof. Steve Arnold, Prof. Eric Mazur, and Prof. Martin Wegener), the secretary of the Course, Mr. Ottavio Forte, and Prof. John Collins for his help in organizing and running the Course and for agreeing to be the co-editor of this volume.

I wish to acknowledge the sponsorship of the meeting by the NATO Organization, the Karlsruhe School of Optics, Boston College, the Italian Ministry of Scientific Research and Technology, the Sicilian Regional Government, and the USA National Science Foundation.

I am looking forward to our activities at the Ettore Majorana Center in years to come, including the next 2011 meeting of the International School of Atomic and Molecular Spectroscopy.

Baldassare (Rino) Di Bartolo
Director of the International School of
Atomic and Molecular Spectroscopy of the
“Ettore Majorana” Center


Bio-Photonics Summer School
Erice, July 2-17, 2009
Source of all photos: Ottavio Forte

INTERNATIONAL SCHOOL
OF ATOMIC AND MOLECULAR SPECTROSCOPY

B. Di Bartolo, Director

Advanced Study Institutes Held at the
"Ettore Majorana" Center in Erice, Sicily, Italy

1974 – Optical Properties of Ions in Solids
1975 – The Spectroscopy of the Excited State
1977 – Luminescence of Inorganic Solids
1979 – Radiationless Processes
1981 – Collective Excitations in Solids
1983 – Energy Transfer Processes in Condensed Matter
1985 – Spectroscopy of Solid-State Laser-Type Materials
1987 – Disordered Solids: Structures and Processes
1989 – Advances in Nonradiative Processes
1991 – Optical Properties of Excited States in Solids
1993 – Nonlinear Spectroscopy of Solids: Advances and Applications
1995 – Spectroscopy and Dynamics of Collective Excitations in Solids
1996 – Workshop on Luminescence Spectroscopy
1997 – Ultra-fast Dynamics of Quantum Systems:
Physical Processes and Spectroscopic Techniques
1998 – Workshop on Advances in Solid State Luminescence Spectroscopy
1999 – Advances in Energy Transfer Processes
2000 – Workshop on Advanced Topics in Luminescence Spectroscopy
2001 – Spectroscopy of Systems with Spatially Confined Structures
2002 – Workshop on the Status and Prospects of Luminescence Research
2003 – Frontiers of Optical Spectroscopy
2004 – Workshop on Advances in Luminescence Research
2005 – New Developments in Optics and Related Fields.
Modern Techniques, Materials and Applications
2006 – Workshop on Advances in the Study of Luminescent Materials
2007 – Frontier Developments in Optics and Spectroscopy
2008 – Workshop on Advances in Luminescence Spectroscopy
2009 – Bio-photonics: Spectroscopy, Imaging, Sensing, and Manipulation

LECTURES

BIOPHOTONICS: HARNESSING LIGHT FOR BIOLOGY AND MEDICINE

Nonlinear Optical Imaging and Light Induced Therapy

T.Y. OHULCHANSKYY, A.M. PLISS, P.N. PRASAD*
Institute for Lasers, Photonics and Biophotonics, SUNY at Buffalo, Buffalo, NY, 14260

Abstract Biophotonics is a new multidisciplinary frontier which utilizes light–matter interactions for bioimaging, sensing diagnostics and light activated as well as optically tracked therapies. This article is focused on use of nonlinear optical processes for bioimaging as well as for light induced therapy. Examples illustrating recent achievements in these research fields are provided from our work at the Institute for Lasers, Photonics and Biophotonics. We present our progress in multimodal bioimaging using a combination of nonlinear optical phenomena such as two-photon induced fluorescence, coherent anti-Stokes Raman scattering (CARS), second harmonic generation and sum frequency generation. Synergy of the techniques employing these phenomena in a multimodal imaging approach enables chemically selective imaging and probing of the local macromolecular content in biological specimens. We also provide examples of two-photon induced fluorescence microscopy and two-photon induced therapy using specially designed molecules and nanoparticles.

1. Introduction

Biophotonics, involving interaction of light and biomaterials, is among the most promising and actively developing multidisciplinary approaches which are expected to make a major impact on current and future health care. Biophotonics bridges together several advanced technologies, such as lasers, photonics, nanotechnology and biotechnology, providing a powerful tool in the development of modern life sciences and their applications, including clinical diagnostics and therapy [1].

Optical imaging is one of the most valuable biophotonics techniques used in biomedical applications. Among all the bioimaging modalities, it is the only one which can provide cellular or molecular level information, with almost single molecule sensitivity, allowing probing of cellular structure and dynamics for understanding of the mechanisms of physiological regulation and molecular profiling of diseases [1, 2]. In particular, light transmission and epifluorescence microscopies are among the basic and most common

* P.N. Prasad, Institute for Lasers, Photonics and Biophotonics, SUNY at Buffalo, Buffalo, NY, 14260, e-mail: pnprasad@acsu.buffalo.edu

B. Di Bartolo and J. Collins (eds.), *Biophotonics: Spectroscopy, Imaging, Sensing, and Manipulation*,
DOI 10.1007/978-90-481-9977-8_1,

techniques being used in the study of biological specimens, specifically cells and tissues [1, 3]. The conventional fluorescence microscopy, especially when imaging with objectives of higher magnification and numerical aperture, is significantly limited by the leak of the out-of-focus signal, which deteriorates the sharp image details from the in-focus region of the specimen. First confocal microscopes, designed in the 1960s [4], significantly improved the resolution for fluorescence microscopy, although their sensitivity was, at that time, low. Introduction of lasers as a source of intense monochromatic light resulted in a rapid outburst of all biophotonics applications. In particular, the integration of lasers to confocal systems gave rise to modern confocal laser scanning microscopy (CLSM) and opened a gateway for novel imaging modalities. Further implementation of the femto- and pico-second pulsed near IR lasers provides a basis for development of the non-linear optical microscopic techniques. The nonlinear nature of light-matter interaction (quadratic or higher order dependence of the response on the intensity of light) provides a spatial localization of excitation to provide high 3D spatial resolution and improved signal to noise ratio. The imaging depth is also increased by the use of laser light with near infrared (NIR) wavelengths, which can be selected to be in the biological window of maximum optical transparency (~700–1,000 nm) [5]. A number of nonlinear optical processes such as Two- (or Multi-) Photon Excited Fluorescence (TPEF or MPEF), Second and Third Harmonic Generation (SHG and THG), Sum Frequency Generation (SFG) and Coherent anti-Stokes Raman Scattering (CARS) are the valuable tools for live cells and tissue imaging [6–8].

The most commonly used nonlinear optical process in bioimaging is TPEF [1], which is a resonant process. TPEF microscopy utilizes a broad variety of fluorescence probes; it is increasingly replacing CLSM in the in vivo applications, exploiting advantages of the nonlinear optical imaging. However, TPEF requires efficient two-photon excitation at a specific wavelength, which corresponds to a resonance of the specially chosen two-photon absorbing fluorescent label. In addition, because of its resonant nature, this probe is potentially susceptible to photobleaching. Furthermore, for targeted imaging one has to rely either on the natural targeting abilities of the label, or chemically conjugate it to a targeting moiety. In this regard, non-resonant non-linear processes may offer new advantages such as absence of light absorption in the label, which greatly reduces its photo- and thermal damage or narrow spectral line of the incoming and outgoing emission, allowing for superior discrimination of signal from the background. This article presents examples of application of both resonant (TPEF) and non-resonant (CARS) nonlinear optical processes in the imaging of the biological samples and nonlinear light induced therapy.

2. Nonlinear Optical Imaging

2.1. MULTIMODAL NONLINEAR OPTICAL MICROSCOPY OF CULTURED CELLS

Light–matter interactions produce a small fraction of photons (approximately 1 in 10^5) inelastically or Raman scattered from the specimen [1]. As a result, energies of scattered

photons are shifted by values which are determined by the irradiated molecules; this phenomenon is used in spectroscopic analysis. The Raman spectroscopy has been shown to be a valuable tool for chemical analysis of biological samples [1, 9] and was adopted for chemical imaging. The sensitivity of Raman chemical imaging can be significantly enhanced by its nonlinear optical modification, CARS, which provides signal of five to six orders of magnitude stronger than that of spontaneous Raman process [10].

In biological samples, CARS imaging allows for selective visualization of major types of native biomolecules such as proteins, nucleic acids, lipids and saccharides. Figure 1 shows examples of Raman and corresponding CARS spectra of some biomolecules which can be exploited in CARS imaging. The experimental multimodal microscope setup used for CARS imaging in our group is shown in Fig. 2.

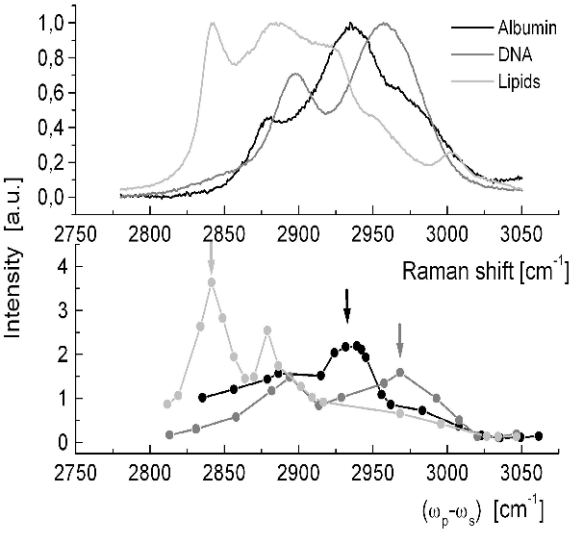

Figure 1. Raman and corresponding CARS spectra (at the top and bottom panels, respectively) of bovine serum albumin, bovine heart lipids extract and DNA purified from the HeLa cells. Resonance peaks for each component are marked by arrows [2,840 cm^{-1} (lipids), 2,930 cm^{-1} (proteins) and 2,970 cm^{-1} (DNA)].

Thus, CARS imaging, which exploits CARS from natural biomolecules, does not require any extrinsic label or probe and can provide submicron 3D resolution and sensitivity sufficient for rapid scanning of samples [11, 12]. Moreover, due to the non-resonant property of Raman scattering process, CARS molecular imaging does not inflict damage on specimens [13]. The advantage of CARS imaging over fluorescence staining is vividly illustrated by the synchronous CARS/TPEF scanning of E. coli bacteria stained with fluorescent YOYO-1 dye (Fig. 3). In these cells, the fluorescence signal is gradually diminished with every scan because of photobleaching, whereas the CARS signal intensity remains constant throughout the whole time of image acquisition, because it is solely determined by the distribution of macromolecules in the sample.

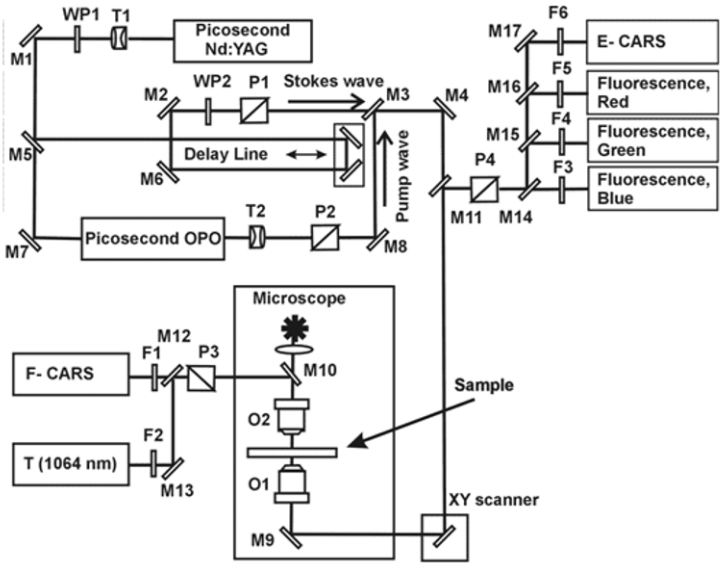

Figure 2. Scheme of a CARS/SHG/SFG/TPEF microscopy setup at ILPB.

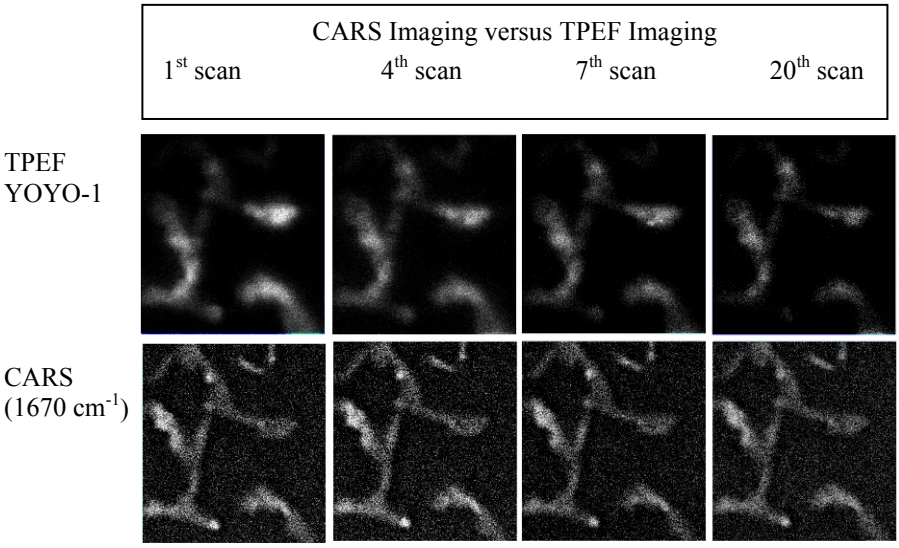

Figure 3. Synchronous CARS/TPEF Scanning of *E. coli* cells. *E. coli* cells stained with YOYO-1 fluorescent dye and simultaneously scanned in CARS and TPEF modes. TPEF images (upper row) reveal diminishing of the TPEF signal because of photobleaching, whereas CARS signal remains constant (lower row). Images obtained at first, fourth, seventh and 20th scans are shown.

Due to the ability of CARS imaging for non-invasive visualization of major types of native macromolecules such as proteins, lipids, nucleic acids and carbohydrates, it has been successfully used for monitoring of lipid metabolism in cells [14], detection of

cancer metastasis [15], histological studies including in vivo observations of tissues [11] and other applications [13, 16, 17]. Moreover, upon introduction of a Raman marker it can be used for visualization of a specific molecular constituent, thus providing a promising alternative for immunofluorescent detection [18]. However the choice of specific Raman markers is still limited.

It is important to note that CARS and fluorescence imaging provide different types of information and can be naturally bridged into a multimodal imaging technique for better understanding of the molecular organization of the specimen. Given that CARS microscopy utilizes high intensity picosecond IR laser pulses for image generation [19], the same laser source can simultaneously excite the fluorescence signal in the TPEF mode, if an appropriate fluorescence probe is introduced. Such a multimodal combination allows for a synchronous visualization of any particular class of biomolecules, e.g. proteins and lipids, by CARS, along with fluorescently labeled specific molecules or subcellular sites in the TPEF mode. Moreover, this dual CARS/TPEF modality is able to improve selectivity of a CARS microscopy towards different types of biomolecules.

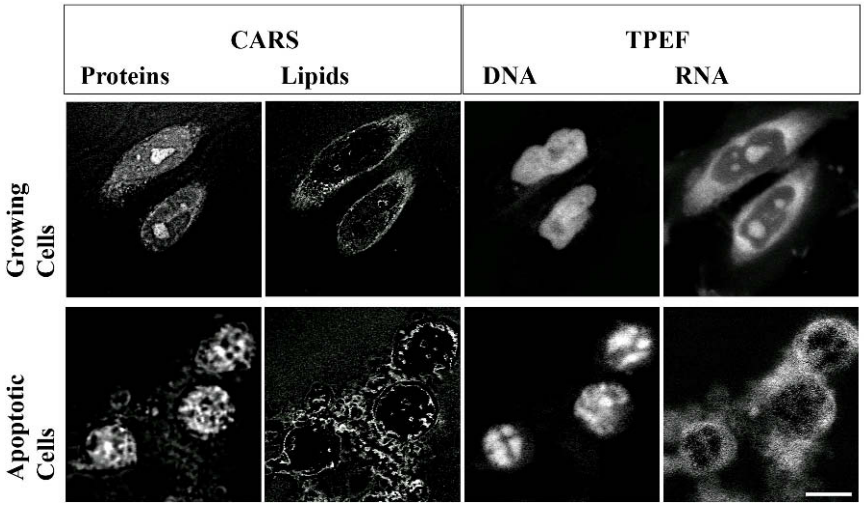

Figure 4. Distribution of proteins, lipids, DNA and RNA in proliferating and apoptotic HeLa cells visualized by multimodal CARS/TPEF imaging. Proteins and lipids were observed in the CARS mode at their characteristic vibrations of 2930 and 2,830 cm^{-1}, respectively. Nucleic acids, stained by acridine orange, were acquired in the red (RNA) and green (DNA) fluorescence channels in the TPEF mode.

We have applied this combinatory approach to perform the pilot observation of the molecular structure in the cultured mammalian cells, through the imaging of the major groups of macromolecules, which are proteins, RNA, DNA and lipids. Imaging of lipids and proteins was performed at 2,830 and 2,928 cm^{-1} respectively (Fig. 4). Obtained CARS images were separated from nonlinear non-resonance background by the use of the standard procedure of digital subtraction of the images of out of the resonance frequency from the one at the resonance frequency. Since the DNA and RNA vibration frequencies are barely distinguishable by the CARS approach, we have also stained the

nucleic acids with a nucleic acid (NA) specific fluorescent stain, acridine orange [20], and selectively visualized NA in a TPEF mode in the red (RNA) and the green (DNA) fluorescent channels. Thus, a combination of the CARS and the TPEF modalities enables visualization of major biomolecules in separate imaging channels as shown in Fig. 4.

This CARS/TPEF combinatory imaging can provide valuable information in the molecular organization of cells and tissues. It appears that the physiological condition of the cell correlates with the intracellular distribution of macromolecules. In response to cell cycle events, transcription inhibition and apoptosis, we observed major redistribution of macromolecules in the cell, using multimodal (CARS/ TPEF) imaging (Fig. 4). Thus, CARS/TPEF multimodal imaging is capable of simultaneous assessment of global macromolecular pattern and molecules specifically labeled by fluorescence markers. Currently, CARS/TPEF applications are in a growing demand for medical imaging as well as for detailed studies of molecular organization of cells and tissues [11, 12, 15, 21, 22].

2.2. TWO-PHOTON EXCITED FLUORESCENCE MICROSCOPY USING FLUORESCENT NANOPARTICLES AS CELLULAR PROBES

To obtain high spatial resolution in fluorescence microscopy, CLSM is being widely employed, providing detailed information on cellular interactions and dynamics [3, 23, 24]. Though confocal microscopy provides high resolution optical sectioning capability, the design of CLSM brings in a few inherent limitations. Since the confocal aperture reduces the detection efficiency for the fluorescence signal, a higher excitation power is required, which, in turn, causes increased photobleaching. Multi-photon induced fluorescence microscopy possesses some advantages over confocal microscopy, such as reduced fluorescence background due to the relatively low two-photon cross-section of most native biomolecules; reduction of photobleaching by selective excitation of the focal volume; and deep penetration into scattering samples, such as tissue, due to the near-IR excitation [25–27]. These advantages are especially valuable for imaging thick samples or for ultra low concentration of analytes (approaching single molecular imaging).

The selection of the appropriate probes for TPEF is limited by the low two-photon absorption cross-section of most of the commonly used fluorophores. In addition, the conjugation of the single molecule-based probe with biomolecules for targeting specific cellular events or sites may be technically challenging if there is a lack of available functional groups on the fluorescent molecule for bioconjugation. Thus, although the TPEF bioimaging provides with significant advantages including a high resolution capability, the production of an efficient single molecule fluorescent probes still lags behind.

Recently, various fluorescent nanoparticle systems have been proposed to replace conventional organic fluorophores in many bioimaging applications. The use of fluorescent nanoparticles in multi-photon microscopy offers a number of advantages over traditional single fluorophore-based probes, such as increased signal/ noise ratio, higher photostability and facile chemistry of conjugation with targeting biomolecules due to availability of numerous reactive groups on the nanoparticle surface.

Although a broad variety of fluorescent nanoparticles can be used as TPEF imaging probes, quantum dots (QDs), which are luminescent semiconductor nanocrystals with

sizes ranging from 2 to 15 nm, occupy a special niche in this group [28]. In addition to the advantage of size-tunable optical properties of QDs, they exhibit high quantum efficiency, high molar extinction coefficients, broad excitation and narrow emission spectra, high resistance to photobleaching, and distinctive emission lifetimes [1, 29–32].

In our group, two types of QDs have been extensively used. They are CdSe/CdS/ZnS core/shell/shell structured and Cd-free QDs, such as InP/ZnS core/shell structured and silicon (Si) QDs. Their shape, size, and surface coating were systematically manipulated for optical bioimaging applications [33]. For instance, we have recently reported the use of bioconjugated CdSe/CdS/ZnS QDs as TPEF imaging contrast agent for pancreatic cancer cells in vitro. In this study transferrin conjugated to the surface of QD was used for targeting the malignant phenotype [34].

It is worth noting the advantages of CdSe-based quantum rods (QRs) that make them potentially better TPEF imaging probes than the spherical quantum dots. In the case of QRs, the Stokes shift is determined by the aspect ratio (length/diameter) of the rod [24]. The unique properties which make QRs advantageous over QDs, are: larger two-photon absorption cross-sections, faster radiative decay rates, and larger surface areas per particle which facilitates functionalization with multiple binding moieties. QRs are shown to be brighter single molecule probes than QDs [7]. Recently our group has demonstrated live cancer cell imaging using CdSe/CdS/ZnS QRs as targeting TPEF imaging probes. Figure 5 shows TPEF (A) and transmission (B) images of HeLa cells targeted with QR-transferrin bioconjugates. The receptor-mediated character of the cellular uptake was confirmed by presaturating the cells with free transferring in order to block the available transferring receptors on the cell surface; this presuturation resulted in a drastic decrease in the cellular uptake of QR-transferrin bioconjugates [34]. The TPEF imaging technique using such efficient (bright and photostable) probes as QRs provides the possibility of long-term imaging of cellular processes with reduced photodamage.

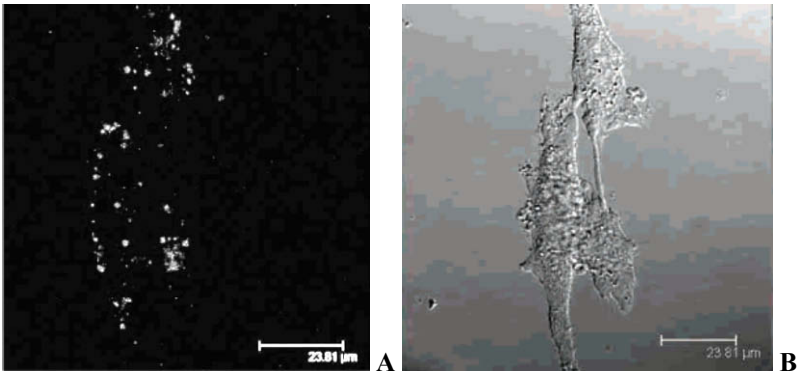

Figure 5. Two-photon excited fluorescence (A) and transmission images of HeLa cells treated with transferrin--conjugated CdSe/CdS/ZnS QRs. Two-photon microscopy images were obtained using excitation at 884 nm [34].

3. Non-linear Light Activated Therapy

The ongoing coupling of photonics and medicine provides new types of light induced clinical applications. It is best demonstrated with photodynamic therapy (PDT), which is the most known and developed type of light activated therapies [35]. It utilizes light-sensitive drugs or photosensitizers (PS) that can be delivered via molecular targeting to malignant tissues. The PDT therapeutic effect arises from photoexcitation of the localized photosensitizer to generate cytotoxic species, i.e. free radicals, peroxides and, most importantly, singlet oxygen ($^1O_2$), the latter being considered the main cytotoxic factor. Generation of the chemically active singlet oxygen leads to localized and irreversible destruction of diseased tissues, without damaging adjacent healthy ones. The scheme of PDT action, involving photophysical processes occurring in the PS molecule, is presented in Fig. 6.

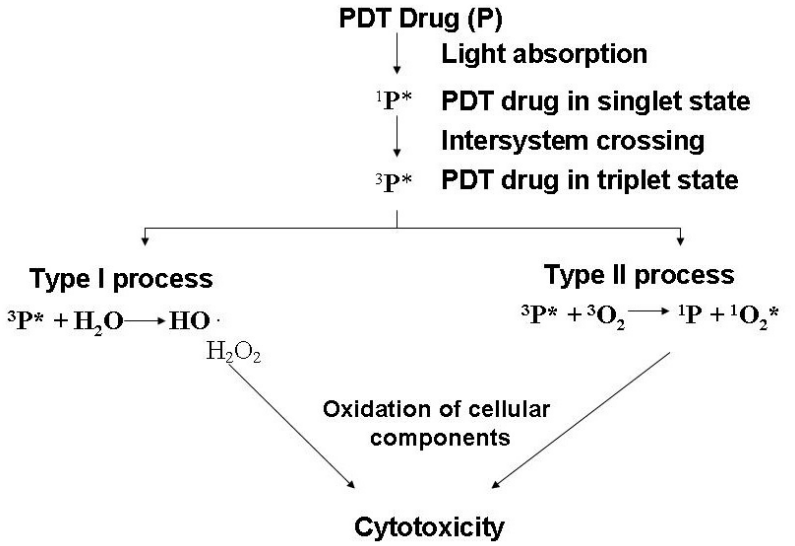

Figure 6. Scheme of PDT action.

Despite some distinctive advantages of PDT over other types of therapy, such as surgery, radiation therapy and chemotherapy, PDT has limited applicability and has yet to gain general clinical acceptance. First, currently approved PDT photosensitizers absorb in the visible spectral region, where light penetration into a tissue is strongly limited by the absorption and scattering of the excitation light, thus clinically restricting PDT to treating topical lesions. Two-photon absorption (TPA) induced excitation of photosensitizers is one of the promising approaches to increase light penetration, as it enables the use of light in the window of tissue transparency. Furthermore, due to the quadratic dependence of TPA on laser intensity, it provides a tool for improving treatment of deeper tumors with enhanced spatial resolution.

Approaches to obtain large intrinsic TPA cross-sections in the near-infrared region, include either design of new photosensitizers or chemical modification of existing ones to produce efficient two-photon sensitization. Another interesting approach is to exploit an energy-transferring combination of existing photosensitizers with TPA dyes. Frechet group in collaboration with our group has designed, synthesized and characterized such type of molecules, were the photosensitizing unit (energy acceptor) is indirectly excited through Forster resonance energy transfer (FRET) from a two-photon absorbing dye unit (energy donor). The molecular structure of the synthesized representative compound and a scheme of the TPA induced generation of singlet oxygen are shown in Fig. 7. The FRET approach was realized by chemically assembling the TPA donors into dendrimer arms with a photosensitizer as the central core. Then, energy harvesting by the TPA donors strongly enhances the efficiency of two-photon excitation of the photosensitizer, while preserving the photophysical properties for PDT due to insignificant chromophore modification [36]. It is important to emphasize that the quadratic dependence on the excitation laser power was observed for fluorescence intensity from the photosensitizing core as well as for the efficacy of singlet oxygen generation, indicating that the excited states of the photosensitizing core do arise from TPA of donor chromophores, followed by an efficient FRET to this core [37]. This means that the therapeutic effect produced by the generated singlet oxygen will be localized similarly to TPEF, providing an enhanced spatial selectivity in the treatment, with only a minimal damage of the adjustment tissues.

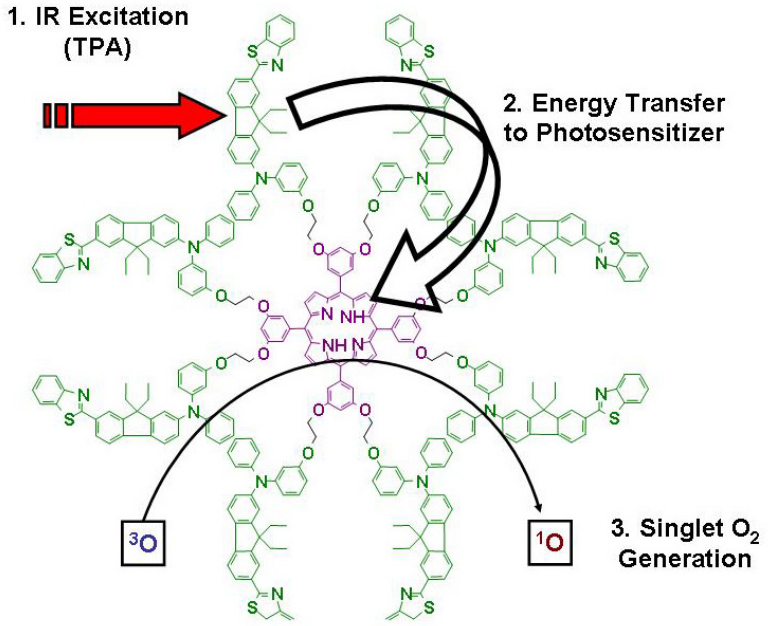

Figure 7. TPA dendrimer-like molecule, harnessing the NIR light and transferring harnessed excitation energy to the core generating singlet oxygen [36].

It should be noted that the synthesis of the compounds with a complexity such as shown in Fig. 7 is challenge on its own, demanding complicated chemistry In addition, to be suitable for even try in physiological medium, the TPA-FRET dendrimer has to be water dispersible, which requires even more complicated synthetic chemistry [38]. It is worth noting that the preparation of pharmaceutical formulations of photosensitizers for parenteral administration is a major challenge in PDT. Most existing photosensitizers are hydrophobic with inherently poor water solubility and, therefore, cannot be simply injected intravenously. Moreover, even with watersoluble photosensitizers, the specificity to diseased tissues is often not sufficient for clinical applications. This limitation, however, can be overcome using colloidal carriers for photosensitizers such as oil-dispersions, liposomes, low-density lipoproteins, polymeric micelles, and nanoparticles which offer benefits of hydrophilicity, appropriate size for passive targeting to tumor tissues by the Enhanced Permeability and Retention (EPR) [39] as well as with the possibility of active targeting by using surface modification. To produce efficient two-photon PDT effect by addressing all the above issues, we introduced a nanophotonics approach, which involved energy-transferring nanoscopic co-assembly of photosensitizers and fluorescent TPA dyes produced by physical entrapment within a single nanocarrier. Our approach provides several advantages: (i) Co-encapsulation eases PDT drug preparation as opposed to chemical conjugation, while offering the flexibility to choose from a wide range of donor-acceptor pairs. (ii) Surface functionalization provides an opportunity to improve biodistribution and to incorporate active targeting. (iii) A nanoscopic volume offers the opportunity for high level of loading of a TPA donor to efficiently harvest IR photons.

To accomplish efficient two-photon excitation using this concept, however, the loading concentration of the energy-donating TPA dye needs to be much higher than that of the energy-accepting photosensitizer. In addition, therapeutic application sets certain requirements on the physical properties of the nanoparticle matrix. In particular, it has to be compatible with the PDT application (e.g. permeable to the molecular oxygen) as well as rigid enough to preserve the initially loaded energy-transferring composition without undesirable release. We have demonstrated [40] the above mentioned approach using organically modified silica nanoparticles (ORMOSIL), which have been previously shown to be biocompatible, colloidally stable in water-based suspensions, not releasing the encapsulated hydrophobic molecules, and suitable for PDT because their porous matrix is permeable to oxygen molecules [41–43].

To explore the ORMOSIL suitability for two-photon induced PDT, we co-encapsulated within the ORMOSIL a photosensitizing anticancer drug, HPPH, and fluorescent aggregates of a two-photon absorbing dye, BDSA. It has been shown that the BDSA aggregates, formed by phase separation from the particle matrix, are efficiently exited with near-IR light through TPA and transfer the absorbed energy to the co-encapsulated HPPH molecules via intrapaticle FRET, which result in the enhanced generation of singlet oxygen. The principle of the two-photon induced PDT action realized in nanoparticles is shown in Fig. 8. These ORMOSIL nanoparticles were shown to be actively uptaken by the cultured tumor cells in vitro and the cytotoxic effect induced by the co-encapsulating nanoparticles under the two-photon irradiation was demonstrated [40]. We believe that our approach of two-photon induced intraparticle FRET, employing two-photon fluorescent aggregates as a donor and a photosensitizing

drug as an acceptor, offers a simple and proper methodology for developing formulations of drug-carrier nanoassemblies applicable in two-photon activated PDT.

Overall, the current practice of PDT is mostly limited to functionalized porphyrins, their derivatives and some other nonporphyrin photosensitizers; all of them generate singlet oxygen. However, another possible approach is the generation of cytotoxic molecules other than singlet oxygen upon light irradiation. Nitric oxide (NO) releasing materials may be another class of promising sensitizers for PDT, and they have already drawn attention because of their utility in PDT of selected types of cancer [44]. Elevated levels of NO may result in a cytotoxic effect [45] thereby promoting apoptosis of tumor cells [46]. We have recently reported the synthesis and photophysical characteristics of a novel NO donor, where NO release can be controlled by IR light, thus having a significant potential for therapeutic application [47].

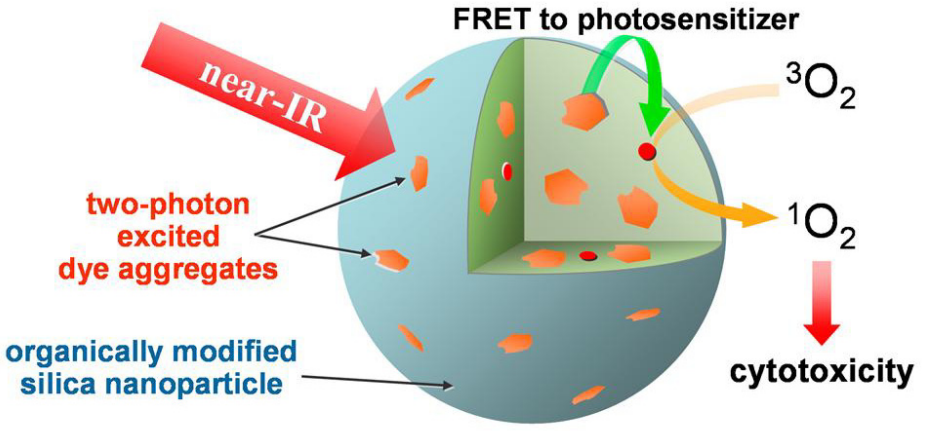

Figure 8. Scheme of the PDT action produced by the ORMOSIL nanoparticles co-encapsulating photosensitizing anticancer drug and fluorescent aggregates of a two-photon absorbing dye [40].

The structure of the synthesized compound, principle of NO release and data on the TPA induced cytotoxicity assay are shown in Fig. 9. The water-soluble metal nitrosyl complex has a fairly large TPA cross-section value as the two-photon chromophores retained their two-photon absorption properties when attached to the metal nitrosyl complex. An increase in TPEF was observed with the time of two-photon light irradiation, as the 2P-M compound decomposes to the monomer species and TPEF quenching caused by the interaction of the adjacent TPA fluorophores does not take place anymore. Simultaneously, the NO release induced by two-photon irradiation was clearly detected using EPR spectroscopy. As the NO release is concomitant with an increase in the fluorescence intensity, it is worth noting that the NO process release can be monitored by the increase in the fluorescence intensity of compound **2P-M**. The NO produced under two-photon irradiation is shown to function as a cytotoxic agent, causing the two-photon induced cytotoxicity of compound **2P-M** in Cos-7 cells. Figure 9 shows the results of the cell viability assay performed with ("Light" columns) and without ("Dark"

columns). As one can see, when the concentration of compound 2P-M loaded in Cos-7 cells increases from 8 to 40 μM, IR light induced cell death increases from 0.4% to 10%. These preliminary results indicate the feasibility of employing two-photon active NO donors for photodynamic therapy application.

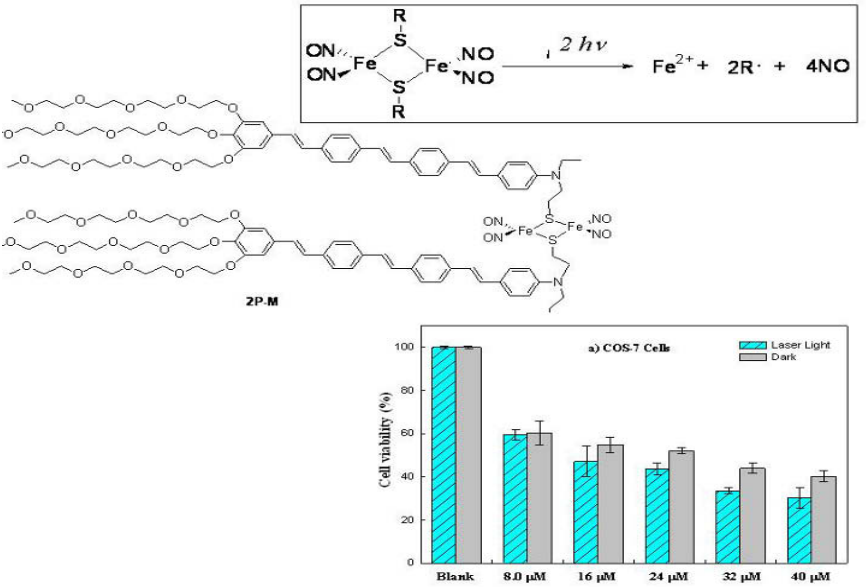

Figure 9. TP induced generation of the nitric oxide resulted in cytotoxic action. Percentage of cell survival of Cos-7 cells, after treatment with 2P-M and subsequent irradiation with 775 nm laser light for 5 min (with reference to untreated cells under dark as having 100% survival). Cell viability was assayed by the Cell Titer-Glo method (values: mean ± standard deviation) [47].

4. Conclusion

Modern biophotonics dealing with broad aspects of light–matter interactions represents a synergy between optical physics, lasers, chemistry, material science and others scientific areas. Rapid development in these disciplines has been beneficial for the non-linear optical imaging applications in biomedical disciplines. In our article we have described the ongoing research activities in our research group in the field of nonlinear optics applications including CARS and two-photon PDT. We show that a combination of different modalities in imaging or synergy of such photophysical phenomena as FRET and TPE allows achieving a breakthrough in biological research and biomedical applications.

Acknowledgements The authors are grateful to Drs A.V. Kachynski and A.N. Kuzmin for their collaboration on CARS/TPEF imaging and valuable discussion. The authors would like to acknowledge funding from the NIH grants (R01CA119397 and RO1CA119358) and the John R. Oishei Foundation.

References

1. Prasad, P.N., *Introduction to biophotonics*. 2003, Hoboken, NJ: Wiley-Interscience. 593 p.
2. Michaelis, J., et al., Optical microscopy using a single-molecule light source. *Nature*, 2000. 405(6784): p. 325–8.
3. Lichtman, J.W. and J.A. Conchello, Fluorescence microscopy. *Nat Methods*, 2005. 2(12): p. 910–9.
4. Egger, M.D. and M. Petran, New reflected-light microscope for viewing unstained brain and ganglion cells. *Science*, 1967. 157(786): p. 305–7.
5. Sevick-Muraca, E.M., J.P. Houston, and M. Gurfinkel, Fluorescence-enhanced, near infrared diagnostic imaging with contrast agents. *Curr Opin Chem Biol*, 2002. 6(5): p. 642–50.
6. Campagnola, P.J., et al., High-resolution nonlinear optical imaging of live cells by second harmonic generation. *Biophys J*, 1999. 77(6): p. 3341–49.
7. Fu, A.H., et al., *Semiconductor* quantum rods as single molecule fluorescent biological labels. *Nano Lett*, 2007. 7(1): p. 179–82.
8. Kachynski, A.V., et al., Zinc oxide nanocrystals for nonresonant nonlinear optical microscopy in biology and medicine. *J Phys Chem C*, 2008. 112(29): p. 10721–24.
9. Hanlon, E.B., et al., Prospects for in vivo Raman spectroscopy. *Phys Med Biol*, 2000. 45(2): p. R1–59.
10. Maker, P.D. and R.W. Terhune, study of optical effects due to an induced polarization third order in electric field strength. *Phys Rev*, 1965. 137(3A): p. A801–&.
11. Evans, C.L., et al., Chemical imaging of tissue in vivo with video-rate coherent anti-Stokes Raman scattering microscopy. *Proc Natl Acad Sci USA*, 2005. 102(46): p. 16807–12.
12. Xie, X.S., J. Yu, and W.Y. Yang, Living cells as test tubes. *Science*, 2006. 312(5771): p. 228–30.
13. Cheng, J.X., et al., Laser-scanning coherent anti-stokes Raman scattering microscopy and applications to cell biology. *Biophys J*, 2002. 83(1): p. 502–09.
14. Nan, X., J.X. Cheng, and X.S. Xie, Vibrational imaging of lipid droplets in live fibroblast cells with coherent anti-Stokes Raman scattering microscopy. *J Lipid Res*, 2003. 44(11): p. 2202–8.
15. Le, T.T., T.B. Huff, and J.X. Cheng, Coherent anti-Stokes Raman scattering imaging of lipids in cancer metastasis. *BMC Cancer*, 2009. 9: p. 42.
16. Cheng, J.X. and X.S. Xie, Coherent anti-Stokes Raman scattering microscopy: Instrumentation, theory, and applications. *J Phys Chem B*, 2004. 108(3): p. 827–40.
17. Cheng, J.X., et al., Ordering of water molecules between phospholipid bilayers visualized by coherent anti-Stokes Raman scattering microscopy. *Proc Natl Acad Sci USA*, 2003. 100(17): p. 9826–30.
18. Evans, C.L. and X.S. Xie, Coherent anti-Stokes Raman scattering microscopy: chemical imaging for biology and medicine. *Annu Rev Anal Chem*, 2008. 1: p. 883–909.
19. Volkmer, A., Vibrational imaging and microspectroscopies based on coherent anti-Stokes Raman scattering microscopy. *J Phys D-Appl Phys*, 2005. 38(5): p. R59–81.
20. Kornfield, H.J. and A.A. Werder, A differential nucleic acid fluorescent stain applied to cell culture systems. *Cancer*, 1960. 13: p. 458–61.

21. Huff, T.B. and J.X. Cheng, In vivo coherent anti-Stokes Raman scattering imaging of sciatic nerve tissue. *J Microsc*, 2007. 225(Pt 2): p. 175–82.
22. Krafft, C., B. Dietzek, and J. Popp, Raman and CARS microspectroscopy of cells and tissues. *Analyst*, 2009. 134(6): p. 1046–57.
23. Brakenhoff, G.J., P. Blom, and P. Barends, Confocal scanning light-microscopy with high aperture immersion lenses. *J Microsc-Oxford*, 1979. 117(Nov): p. 219–32.
24. Conchello, J.A. and J.W. Lichtman, Optical sectioning microscopy. *Nat Methods*, 2005. 2(12): p. 920–31.
25. Denk, W., J.H. Strickler, and W.W. Webb, Two-photon laser scanning fluorescence microscopy. *Science*, 1990. 248(4951): p. 73–6.
26. Konig, K., Multiphoton microscopy in life sciences. *J Microsc*, 2000. 200(Pt 2): p. 83–104.
27. Zipfel, W.R., R.M. Williams, and W.W. Webb, Nonlinear magic: multiphoton microscopy in the biosciences. *Nat Biotechnol*, 2003. 21(11): p. 1369–77.
28. Prasad, P.N., *Nanophotonics*. 2004, Hoboken, NJ: Wiley-Interscience. xv, 415 p.
29. Alivisatos, P., The use of nanocrystals in biological detection. *Nat Biotechnol*, 2004. 22(1): p. 47–52.
30. Gao, X., et al., In vivo cancer targeting and imaging with semiconductor quantum dots. *Nat Biotechnol*, 2004. 22(8): p. 969–76.
31. Kim, S., et al., Near-infrared fluorescent type II quantum dots for sentinel lymph node mapping. *Nat Biotechnol*, 2004. 22(1): p. 93–7.
32. Chan, W.C., et al., Luminescent quantum dots for multiplexed biological detection and imaging. *Curr Opin Biotechnol*, 2002. 13(1): p. 40–6.
33. Yong, K.T., et al., Multifunctional nanoparticles as biocompatible targeted probes for human cancer diagnosis and therapy. *J Mater Chem*, 2009. 19(27): p. 4655–72.
34. Yong, K.T., et al., Quantum rod bioconjugates as targeted probes for confocal and two-photon fluorescence imaging of cancer cells. *Nano Lett*, 2007. 7(3): p. 761–5.
35. Castano, A.P., P. Mroz, and M.R. Hamblin, Photodynamic therapy and anti-tumour immunity. *Nat Rev Cancer*, 2006. 6(7): p. 535–45.
36. Dichtel, W.R., et al., Singlet oxygen generation via two-photon excited FRET. *J Am Chem Soc*, 2004. 126(17): p. 5380–81.
37. Oar, M.A., et al., Light-harvesting chromophores with metalated porphyrin cores for tuned photosensitization of singlet oxygen via two-photon excited FRET. *Chem Mater*, 2006. 18(16): p. 3682–92.
38. Oar, M.A., et al., Photosensitization of singlet oxygen via two-photon-excited fluorescence resonance energy transfer in a water-soluble dendrimer. *Chem Mater*, 2005, 17(9): p. 2267–75.
39. Maeda, H., The enhanced permeability and retention (EPR) effect in tumor vasculature: The key role of tumor-selective macromolecular drug targeting. *Adv Enz Regul*, 2001, 41: p. 189–207.
40. Kim, S., et al., Organically modified silica nanoparticles co-encapsulating photosensitizing drug and aggregation-enhanced two-photon absorbing fluorescent dye aggregates for two-photon photodynamic therapy. *J Am Chem Soc*, 2007. 129(9): p. 2669–75.
41. Roy, I., et al., Ceramic-based nanoparticles entrapping water-insoluble photosensitizing anticancer drugs: A novel drug-carrier system for photodynamic therapy. *J Am Chem Soc*, 2003. 125(26): p. 7860–65.
42. Ohulchanskyy, T.Y., et al., Organically modified silica nanoparticles with covalently incorporated photosensitizer for photodynamic therapy of cancer. *Nano Lett*, 2007. 7(9): p. 2835–42.
43. Kim, S., et al., Organically modified silica nanoparticles with intraparticle heavy-atom effect on the encapsulated photosensitizer for enhanced efficacy of photodynamic therapy. *J Phys Chem C*, 2009. 113(29): p. 12641–44.
44. Reeves, K.J., M.W.R. Reed, and N.J. Brown, Is nitric oxide important in photodynamic therapy? *J Photochem Photobiol B-Biol*, 2009. 95(3): p. 141–7.

45. Tozer, G.M. and S.A. Everett, Nitric oxide in tumour biology and cancer therapy. Part 1: Physiological aspects. *Clin Oncol (R Coll Radiol)*, 1997. 9(5): p. 282–93.
46. Cui, S., et al., Activated murine macrophages induce apoptosis in tumor cells through nitric oxide-dependent or -independent mechanisms. *Cancer Res*, 1994. 54(9): p. 2462–7.
47. Zheng, Q.D., et al., Water-soluble two-photon absorbing-nitrosyl complex for light-activated therapy through nitric oxide release. *Mole Pharma*, 2008. 5(3): p. 389–98.

NANO-PLASMONICS FOR BIO-PHOTONICS

An Introduction

M. WEGENER*
Institut für Angewandte Physik
Karlsruhe Institute of Technology (KIT)
Wolfgang-Gaede-Strasse 1
D-76131 Karlsruhe, Germany

1. Introduction

One of the major aims in the emerging field of nano-plasmonics is to obtain complete control over electromagnetic light waves by means of tailoring optical materials on the nanometer scale – for example aiming at squeezing light into very tight spaces for the purpose of microscopy or lithography. Yet, isn't the wavelength of light hundreds of nanometers in size or, talking about the important telecom regime, even exceeding 1 μm? What's "nano" here? Clearly, one carefully has to distinguish between the vacuum wavelength and the effective material wavelength of light. While the frequency and the photon energy of light are generally conserved quantities in linear optics, the wavelength of light is not. For example, the special type of light waves that propagates on metal surfaces and that is commonly referred to as surface plasmons (or, more precisely, as surface plasmon polaritons) can have wavelengths that are two orders of magnitude smaller than the vacuum wavelength due to the special dispersion relation of surface plasmons. This possibility of having X-ray wavelengths at visible or telecom frequencies is one of the keys to the entire field of plasmonics. The usual diffraction limit of visible light remains to be a valid and important concept, but it has to be applied to wavelengths of just a few nanometers. As a result, metals are suddenly becoming a key ingredient in nanophotonics, whereas they have previously often been quite unwanted in optics as they do not transmit light in their bulk form.

Bio-photonics is all about inspecting or manipulating biological systems by means of light. In this regard, the small length scales of nano-plasmonics help by increasing the interaction of light with, e.g., biomolecules.

The set of lectures given at Erice 2009 aimed at providing a broad introduction into the field of nano-plasmonics with particular emphasis on existing products or emerging applications in the field of bio-photonics. Extensive corresponding literature and reviews are available [1–3]. Hence, this contribution provides only a very much shortened version of these lectures with some selected entry points into the vast literature.

* M. Wegener, Institut für Angewandte Physik, Karlsruhe Institute of Technology (KIT), Wolfgang-Gaede-Strasse 1, D-76131 Karlsruhe, Germany, e-mail: wegener@physik.uni-karlsruhe.de

B. Di Bartolo and J. Collins (eds.), *Biophotonics: Spectroscopy, Imaging, Sensing, and Manipulation*,
DOI 10.1007/978-90-481-9977-8_2,

2. Nano-plasmonics

The optical resonances of individual metal spheres with radii of few tens of nanometers have already been described theoretically by Gustav Mie in 1907. Under these conditions, the wavelength of light is much larger than the diameter of the spheres. Thus, one can apply the limit of infinitely large wavelength. Combined with the vacuum dispersion relation of light, this limit is equivalent to that of infinitely small frequency. This means that the electrostatic approximation can be used – at optical frequencies. In other words: The problem of a metal nanosphere exposed to a plane wave of light is strictly equivalent to that of a macroscopic bulk metallic sphere between the plates of an electrostatic plate capacitor in air or vacuum.

However, the latter problem is not so simple after all. Due to charges accumulating at the metal sphere's surface, the local electric field, E, inside of the sphere is different from the external light field E_{ext} by the so-called depolarization field. This leads to the expression for the polarization P of the sphere

$$P = 3\varepsilon_0 \frac{\varepsilon - 1}{\varepsilon + 2} E_{ext} . \tag{1}$$

Obviously, a resonance occurs if the metal permittivity equals $\varepsilon(\omega) = -2$. More generally, the resonance occurs if the permittivity equals twice the permittivity of the surrounding medium (one for air or vacuum as above). Within the free-electron Drude model and neglecting damping, the metal permittivity follows the well known frequency dependence

$$\varepsilon(\omega) = 1 - \frac{\omega_{pl}^2}{\omega^2} . \tag{2}$$

Here, ω_{pl} is the plasma frequency, which is typically located within the UV region of the electromagnetic spectrum. This leads to a resonance, the good old Mie resonance, at angular frequency

$$\omega = \sqrt{\frac{1}{3}} \omega_{pl} . \tag{3}$$

For silver and gold, the Mie resonance lies in the visible part of the spectrum. The British Museum exposes the colorful roman Lycurgus cup containing gold and silver nanoparticles. The optical effects are immediately visible, even for small concentrations of nanoparticles. This highlights an extremely important point: The cross section of the Mie resonance is much larger than that of typical molecules, making metal nanoparticles extremely attractive for nano-biology.

Shapes other than spheres "just" correspond to different electrostatic depolarization factors, leading to spectral shifts of the resonances with respect to a sphere. Such shifts, however, can be extremely important for biological applications. We will come back to examples below.

3. Bio-photonics Using Nano-plasmonics

The large cross sections of Mie resonances are, for example, commonly used in commercially available pregnancy tests. Human chorionic gonadotropin (hCG) is a pregnancy hormone also present in the urine. In a popular pregnancy test, the urine sample flows over a capture stripe functionalized with nitrocellulose-bound anti-hCG. If hCG is present, it binds to the stripe. Next, 40-nm diameter gold particles also functionalized with anti-hCG are introduced. In the presence of hCG, they also bind to hCG, hence to the stripe, leading to a clearly visible pink color (partly due to gold-particle agglomeration).

Dimers of gold nanoparticles can be used as molecular rulers [4]. The physics is roughly analogous to that of Förster resonant energy transfer (FRET): The coupling of the two individual Mie resonances leads to two effective modes, a symmetric and an anti-symmetric one. The latter is optically forbidden within the dipole approximation. The symmetric one is shifted towards lower frequencies compared to that of an individual nanoparticle – just like for the binding of two molecules. By measuring the spectral position of the combined resonance, the distance can be inferred. This approach allows for measuring distances of up to 70 nm, while usual molecule FRET is restricted to distances below 10 nm. Furthermore, blinking of molecules is often a nuisance in molecule spectroscopy. Metal nanoparticles do not blink. Finally, molecule experiments can suffer from finite dye-molecule lifetimes, whereas metal nanoparticles essentially live forever.

Gold nanoparticle dimers can also be used as "plasmonic tweezers" [5]. Here, one utilizes the enhanced and strongly localized electric field between the two metal nanospheres. This hot spot can be viewed as a tiny focus of light, which can be very much smaller than a diffraction-limited focus of light using a conventional microscope lens. The gradient force in the focus can be used to trap nanoscopic particles. Using plasmonic tweezers, one can trap smaller particles and/or trap particles at a lower incident optical power. However, one looses the ability to freely move the focus in three dimensions as the field enhancement is obviously restricted to the immediate vicinity of the metal nanostructure surface.

Hybridization of individual Mie-type resonances also occurs in so-called "metal nanoshells" [6] – hollow (rather than bulk) metal spheres. For a thick shell, one gets two independent resonances. One is the Mie resonance that we have already discussed above, i.e., a gold sphere embedded in air or vacuum. The other one is the Mie resonance of the inner air sphere surrounded by metal. Following the reasoning outlined in the previous section, the latter resonance occurs at angular frequency

$$\omega = \sqrt{\frac{2}{3}}\omega_{pl} . \tag{4}$$

The hybridization of these two modes with frequencies different by a factor of $\sqrt{2}$ again leads to an avoided crossing, i.e., the symmetric low-frequency mode is red-shifted with respect to the Mie frequency according to (3). The anti-symmetric mode of the combined system is again dipole forbidden. The red-shift of the symmetric mode brings one from the visible towards the near-infrared, a spectral region for which human tissue is much less opaque than in the visible. This allows for using gold nanoshells in photo-thermal cancer therapy (see, e.g., www.nanospectra. com). Clinical test are ongoing – potentially contributing to "health", one of the current grand challenges of research.

Trimers of metal nanoparticles offer yet further interesting possibilities [3, 7, 8]. For example, consider a metal–particle dimer made from metal A nearby a single metal nanoparticle composed of metal B. This situation can lead to so-called Szigeti-Fano resonances. The anti-symmetric mode of the dimer alone does not couple to the light field within the dipole approximation. It is "dark". As a result, it cannot radiate light into the far-field either. In general, the damping of metal nanoparticle resonances has two contributions, namely Ohmic losses and radiation losses. Provided that Ohmic losses are small, the small radiation loss of the anti-symmetric dimer mode corresponds to a very sharp resonance. Even minute changes in the dielectric surrounding can shift this sharp resonance by frequencies comparable to its linewidth. This situation would be ideal for biological sensing applications. Unfortunately, the anti-symmetric mode is dark. However, the presence of the third nanoparticle – which should be resonant with the dark mode of the dimer – can further change the combined modes. The magic of the situation is that one can achieve modes that couple quite strongly to the light field, and, at the same time, have a very small linewidth. In contrast, for a single metal nanoshere, strong coupling to the light field goes hand in hand with large damping. The mathematics of Szigeti-Fano resonances can rather easily be understood by considering two coupled harmonic oscillators, see, e.g. [3].

Finally, we note that a (circular) hole in a planar metal film can be viewed as the complementary structure of a (circular) metal nanoparticle in the sense that, in the plane, metal is exchanged by air and vice versa. The generalized version of Babinet's principle [3, 9] connects these two situations. When going from the original to the complementary structure, transmittance and reflectance have to be exchanged as well as electric and magnetic fields have to be exchanged. Thus, even a single hole in a real metal film also reveals a Mie-type resonance behavior. Thus, metal apertures and combinations thereof are potentially also well suited for, e.g., bio-sensing applications.

References

1. Prasad, P.N. (2003) *Biophotonics*, Wiley, Hoboken, NJ.
2. Novotny, L. and Hecht, B. (2006) *Nano-Optics*, Cambridge University Press, Cambridge.
3. Busch, K., von Freymann, G., Linden, S., Mingaleev, S., Tkeshelashvili, L., and Wegener, M. (2007) Periodic nanostructures for photonics, *Phys. Rep.* **444**, 101–202.
4. Sonnichsen, C., Reinhard, B.M., Liphardt, J., and Alivisatos, A.P. (2005) A molecular ruler based on plasmon coupling of single gold and silver nanoparticles, *Nat Biotechnol.* **23**, 741–745.

5. Grigorenko, A.N., Roberts, N.W., Dickinson, M.R., and Zhang, Y. (2008) Nanometric optical tweezers based on nanostructured substrates, *Nat Photon* **2**, 365–370.
6. Prodan, E., Radloff, C., Halas, N.J. and Nordlander, P. (2003) A Hybridization Model for the Plasmon Response of Complex Nanostructures, *Science* **302**, 419–422.
7. Liu, N. Kaiser, S., and Giessen, H. (2008) Magnetoinductive and Electroinductive Coupling in Plasmonic Metamaterial Molecules, *Adv. Mater.* **20**, 4521–4525.
8. Verellen, N., Sonnefraud, Y., Sobhani, H., Hao, F., Moshchalkov, V.V., Van Dorpe, P., Nordlander, P., and Maier, S.A. (2009) Fano resonances in individual coherent plasmonic nanocavities, *Nano Lett.* **9**, 1663–1667.
9. Falcone, F., Lopetegi, T., Laso, M.A.G., Baena, J.D., Bonache, J., Beruete, M., Marques, R., Martin, F., and Sorolla, M. (2004) Babinet Principle applied to the design of metasurfaces and metamaterials, *Phys. Rev. Lett.* **93**, 197401:1–4.

PHOTONS AND PHOTON CORRELATION SPECTROSCOPY

RALPH VON BALTZ*
Institut für Theorie der Kondensierten Materie
Universität Karlsruhe, D–76128 Karlsruhe, Germany

1. Introduction

The majority of optical phenomena and even most of photonics can be well understood on the basis of *Classical Electrodynamics*. The *Maxwell-Theory* is perfectly adequate for understanding diffraction, interference, image formation, photonic-band-gap and negative-index materials, and even most nonlinear phenomena such as frequency doubling, mixing or short pulse physics. However, spontaneous emission or intensity correlations are not (or incorrectly) captured. For example, photons in a single-mode laser well above the threshold are (counter-intuitively) completely uncorrelated whereas thermal photons have a tendency to "come" in pairs (within the coherence time).

This contribution addresses the following questions:

– Basic properties of photons
– Quantum description of the Electromagnetic Field (EMF)
– Special photon states
– Selected optical devices
– Examples of photon correlations

To "step into" the field the Paul's easy readable introduction [1], Loudon's classic text [2] and Kidd's [3] historical survey and critical discussion on the evolution of the modern photon will be especially helpful. There are many very good modern textbooks on Quantum Optics available now, e.g. Gerry and Knight [4] or Scully and Zubairy [5]. Bachor [6] discusses basic experiments in Quantum Optics and Haroche and Raimond [7] describe fascinating thought experiments and new concepts of quantum mechanics which now became feasable. In addition there are many proceedings of summer schools and conferences, e.g. Refs. [8–11] which may serve as a resource which almost never runs dry. Perhaps the article of this author in a previous Erice School [12] may be useful, too.

* Ralph Von Baltz, Institut für Theorie der Kondensierten Materie, Universität Karlsruhe, D–76128 Karlsruhe, Germany, e-mail: http://www-tkm.uni-karlsruhe.de

B. Di Bartolo and J. Collins (eds.), *Biophotonics: Spectroscopy, Imaging, Sensing, and Manipulation*, 25
DOI 10.1007/978-90-481-9977-8_3, © Springer Science+Business Media B.V. 2011

2. Basic Properties of Photons

2.1. PARTICLES AND CORPUSCLES

A *particle* is, by definition, a lossless transport of energy and momentum through free space with a universal *energy–momentum relation*

$$E(\mathbf{p}) = \sqrt{(m_0c^2) + (c\mathbf{p})^2}, \qquad v(\mathbf{p}) = \frac{\partial E(\mathbf{p})}{\partial \mathbf{p}} = \frac{c^2\mathbf{p}}{E}. \tag{1}$$

m_0 is the rest mass of the particle and **v(p)** defines the transport velocity of energy and momentum. In addition, a particle may also have charge, spin, angular momentum etc. Examples are electrons, protons or photons.

Bodies (*Corpuscles*) are distinguishable, localizable particles with energy–momentum relation (1). In addition they behave as individuums and have a size, shape, elasticity etc. Examples are bullets, golf balls or planets.

2.2. EXPERIMENTAL FACTS

Basic facts of photons are listed in Table 1. Based on Lenard's [13] observations on the photo-electric effect and guided by an ingenious thermodynamic approach to describe the black body radiation, Einstein [14] got the vision that the transport of energy of light occurs in form of *light-quanta* "$\hbar\omega$" rather than in a continuous fashion. However, he formulated his idea very reserved:

> *Mit den von Herrn Lenard beobachteten Eigenschaften der lichtelek-trischen Wirkung steht unsere Auffassung, soweit ich sehe, nicht im Widerspruch*.
>
> Literal translation:
>
> *Mr. Lenard's observed characteristics of the photoelectric effect is, in our opinion, not inconsistent to our interpretation*.

In a series of intricate experiments, Millikan [15] provided the first experimental verification of the Einstein-hypothesis $E_{\text{kin}} = \hbar\omega - W$ and photoelectric determination of the Planck's constant (as well as the contact potential = difference of work–functions W of cathode and anode).

Further evidence for these "light-quanta", later termed *photons*, arose from the *Compton effect* [16] and the absence of an energy–accumulation time during photo-emission as discovered by Lawrence and Beams [17] and refined later by Forrester et al. [18].

The concept of light-quanta as small corpuscles is in apparent contradiction with typical wave properties like interference fringes and it was expected that such fringes fade out if the intensity of the incident light becomes smaller and smaller so that the

TABLE 1. Basic properties of photons

Property	Phenomenon	Quantity	Discoverer (year)
Quantization of energy	Photo-electric effect	$E = \hbar\omega$	Einstein (1905) Millikan (1914)
Interference of a photon with itself	Persistence of interf. Patterns at low intens.		Taylor (1909)
Particle-like transport of energy + momentum	Compton-effect	$E(\mathrm{p}) = c\,\lvert\,\mathrm{p}\rvert$	Compton (1923)
Quantum theory of light	Unification of wave and particle properties	EMF	Dirac (1927)
Absence of a delay-time for photoelectrons	Prompt photoelectrons	$\tau < 3\,\mathrm{ns}$ $\tau < 0.1\,\mathrm{ns}$	Lawrence (1928) Forrester (1955)
Photon correlations (thermal light)	Hanbury Brown and Twiss effect	photon coincidences	Hanbury Brown & Twiss (1956)

probability of having more than a single photon in the spectrometer becomes negligible. Interference experiments at very low intensity were carried out in 1909 by Taylor [19] and later, by Dempster and Batho [20] and Janossy et al. [21]. Yet the interference fringes persisted – a photon interferes (only) with itself, as Dirac [23] said.

In contrast to widespread belief neither the photo-electric effect (cf. Clauser [25]) nor the Compton-effect (cf. Dodd [26]) provide watertight proofs of the photon, yet the wholeness of phenomena is only consistently described within quantum theory. This holds, in particular, for the absence of an energy accumulation time and the angular dependence of the Compton scattering cross section ("Klein–Nishina formula"). For a discussion of alternative theories see, e.g., the Rochester Proceedings from 1972 [11].

2.3. WHAT IS A PHOTON NOT?

Many contradictory uses exist for the photon [3]. Elementary survey course textbooks usually leave the impression that the photon is a small spherical object which flies on a straight trajectory. A figure like Fig. 1 is dangerous as it pretends that photons in a light beam are tiny corpuscles which have well defined positions. However, as early as in 1909, Lorentz raised the objection that, despite of some striking success of the corpuscular model, one cannot speak of propagating light-quanta concentrated in small regions of space that at the same time remain undivided. He pointed out that the coherence length in interference experiments required a longitudinal extension up to one meter for the photon, while ordinary optical properties demanded a lateral extension on the order of the diameter of the telescope for light from distant stars. Moreover, a photon cannot be just a scalar "bundle of energy" but has rather definite "vector properties" [22].

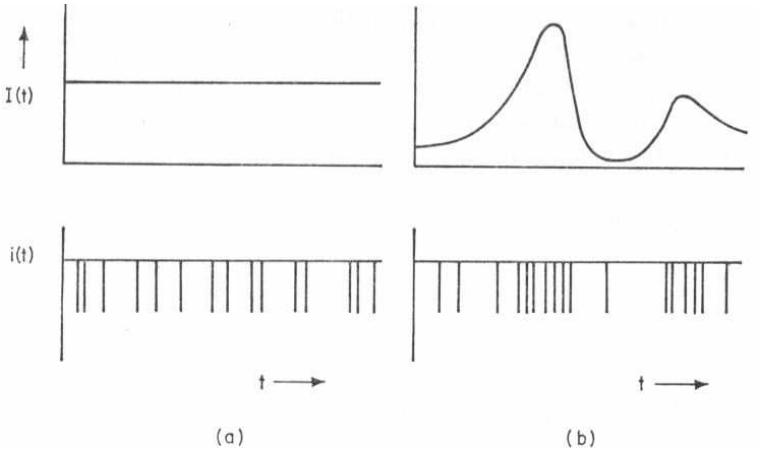

Figure 1. Photoelectric detection. (a) Constant current, (b) fluctuating current. The "combs" refer to the response of a photodetector with high time resolution rather than to "incoming" photons (According to Pike [10]).

In 1921 Einstein complained to Ehrenfest that the problem of quanta was enough to drive him to the madhouse.[1] It was left to Dirac [23] to combine the wave- and particle-like aspects of light so that this description is capable of explaining all interference and particle phenomena of the EMF. We shall follow his traces in Chapter 4. The answer to the question "What is a photon?" will be left for section 4.5.

3. Basics of Quantum Theory

3.1. CANONICAL QUANTIZATION

Quantum theory provides a very general frame for the description of nature on the microscopic as well as on the macroscopic level. In some cases the extension of a classical theory such as mechanics or electrodynamics to a quantum theory can be found along a *correspondence principle*.

First, from the classical theory we have to find (within the Lagrangian formulation, see e.g. Landau and Lifshitz [27] (Vol. I)):

– *Canonical variables* p_i, q_k *with Poisson-brackets* $\{p_i, q_k\} = \delta_{i,k}$, where

$$\{F,G\} = \frac{\partial F}{\partial p}\frac{\partial G}{\partial q} - \frac{\partial G}{\partial p}\frac{\partial F}{\partial q}, \quad \frac{dG}{dt} = \frac{\partial G}{\partial t} + \{H,G\}.$$

– Observables (=physical quantities) $G = G(p, q, t)$, in particular the *Hamiltonian* (=energy) $H = H(p, q, t)$.

[1] Nobel Prize 1921 for "his services to theoretical physics, and especially for his discovery of the law of the photoelectric effect"!

Then, the corresponding quantum theory is constructed:

– States are described by (normalized) *ket-vectors* $|\psi\rangle$ which are elements of a Hilbert space $\mathcal{H}$ with a scalar product $\langle\psi_1|\psi_2\rangle=(\langle\psi_2|\psi_1\rangle)^*$.

– Canonical (unconstrained) variables $p\to\hat{p}\,q\to\hat{q}$ and observables $G\to\hat{G}$ are represented by linear, hermitian operators in $\mathcal{H}$

$$\{F,G\}\to\frac{i}{\hbar}\left[\hat{F},\hat{G}\right],\qquad\text{where}\quad\left[\hat{F},\hat{G}\right]=\hat{F}\hat{G}-\hat{G}\hat{F},\tag{2}$$

$$\hat{G}\to G(p\to\hat{p},q\to\hat{q},t),\quad[\hat{p}_j,\hat{q}_k]=-i\hbar\delta_{j,k}.\tag{3}$$

Commutators between the *p*'s or the *q*'s themselves vanish.
(Products of noncommuting operators may be ambiguous).

– The (expectation) value of an observable $\hat{G}$ in state $|\psi\rangle$ is obtained by

$$\langle G\rangle=\langle\psi|\hat{G}|\psi\rangle:=\langle\psi|\left(\hat{G}|\psi\rangle\right).\tag{4}$$

$\langle\psi|\hat{G}|\psi\rangle$ can be cast in the form of an *expectation value*

$$\langle\psi|\hat{G}|\psi\rangle=\sum_g gP(g),\quad P(g)=\left|\langle g|\psi\rangle\right|^2.\tag{5}$$

$|g\rangle$ denotes an eigenstate of $\hat{G}$ with eigenvalue $g:\ \hat{G}|g\rangle=g|g\rangle$ and $P(g)>0,\sum_g P(g)=1$ is the probability to find *g* in a measurement.

– Dynamics: Initially, the system is supposed to be in state $|\psi_0\rangle=|\psi(t_0)\rangle$. Then, the sequence of states $|\Psi(t)\rangle$ which the system runs through as a function of time is governed by the

$$\text{Schrödinger}-\text{Equation}\quad\boxed{i\hbar\frac{\partial|\Psi(t)\rangle}{\partial t}=\hat{H}|\Psi(t)\rangle.}\tag{6}$$

$\hat{H}$ denotes the *Hamiltonian* (=energy) of the system.[2]

– Steady states: In a *steady state* values of all observables (which don't explicitly depend on time) are time-independent. Such states exist if $\hat{H}$ is time-independent

[2] Equation (6) holds not only for non-relativistic particles but also for photons.

$$|\Psi(t)\rangle = e^{-iEt/\hbar}|\psi\rangle, \qquad \hat{H}|\psi\rangle = E|\psi\rangle. \tag{7}$$

Different stationary states will be labelled by n, i.e. $E = E_n$, $\psi = \psi_n$.

Pure and mixed states:

Ket-vectors $|\psi\rangle$ describe so-called *pure states* which have zero entropy. They are – loosely speaking – analogs of the mechanical states with fixed q, p or the states of the classical EMF with fixed electrical and magnetic fields ("signals").

Classical statistical states, e.g. particles in thermal equilibrium or thermal radiation ("noise"), are described by a *probability distribution P(p, q)*. Such states have nonzero entropy and are called *mixed states*. In quantum theory they are described by a *state-operator* (density operator) $\hat{\rho}$ and (4) is replaced by

$$\langle G\rangle = \text{trace } (\hat{\rho}\hat{G}). \tag{8}$$

For a pure state $\hat{\rho} = |\psi\rangle\langle\psi|$ is a projector onto $|\psi\rangle$.

3.2. HARMONIC OSCILLATOR

As a "warm-up" we consider the (one-dimensional) harmonic oscillator.

Classical Oscillator:

– States are described by x, v (or) x, p. $v = \dot{x}$, $p = mv$.

– The Newtonian equation of motion reads

$$m\ddot{x} + Dx = F_{ext}(t), \tag{9}$$

where m, D, F_{ext} denote the mass, spring constant and external force on the particle. The frequency of free oscillations is $\omega_0 = \sqrt{D/m}$.

– Lagrangian: $L = \frac{1}{2}m\dot{x}^2 - \frac{1}{2}Dx^2 + xF_{ext}$, ,

– Canonical momentum: $p = \partial L/\partial\dot{x} = m\dot{x}, \{p, x\} = 1$..

– Hamiltonian: $H = p\dot{x} - L = \frac{p^2}{2m} + \frac{D}{2}x^2 - xF_{ext}(t)$.

Instead of using real p, x we may also use a complex (dimensionless) amplitude a which turns out to be very useful for quantum mechanics.

$$a = \frac{1}{\sqrt{2}}\left(\frac{x}{\ell} + i\frac{p}{m\omega_0\ell}\right), \qquad \{a, a^*\} = \frac{i}{m\omega_0\ell^2} \to i/\hbar, \tag{10}$$

$$H = \frac{1}{2} m\omega_0 \ell^2 (a^* a + a a^*) - (a + a^*) f(t), \tag{11}$$

$$\rightarrow \hbar\omega_0 \frac{1}{2} (a^* a + a a^*) - (a + a^*) f(t), \quad f(t) = \frac{\ell}{\sqrt{2}} F_{ext}(t). \tag{12}$$

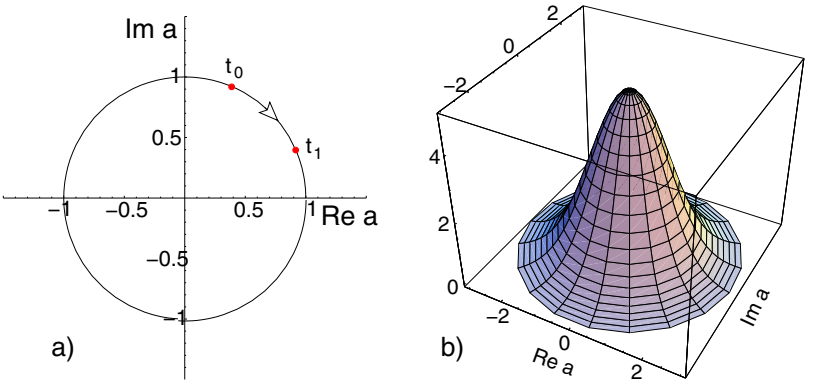

Figure 2. Classical harmonic oscillator. (a) Trajectory in phase space, (b) thermal probability distribution. *(F_{ext} = 0).*

With respect to quantum theory the "natural unit of length" $\ell = \sqrt{\hbar / (m\omega_0)}$ has been used. In contrast to (9) *a(t)* fulfills a first order differential equation

$$\frac{d}{dt} a(t) + \mathrm{i}\omega_0 a(t) = \mathrm{i} f(t) / \hbar. \tag{13}$$

For a free oscillator in thermal contact with a heat bath at temperature *T, x* and *p* fluctuate with a *Gaussian* probability distribution, see Fig. 2b,

$$P_{th}(a) = \frac{1}{Z} e^{-H(p,q)/k_B T} = \frac{1}{\pi I_{av}} e^{-|a|^2 / I_{av}}. \tag{14}$$

Z is the statistical sum (normalization factor), $I_{av} = <|a|^2> = \hbar\omega_0 / k_B T$.

Quantum oscillator:

With canonical operators $p \rightarrow \hat{p}$, $x \rightarrow \hat{x}$, $[\hat{p}, \hat{x}] = -\mathrm{i}\hbar$ and $a \rightarrow \hat{a}$, $[\hat{a}, \hat{a}^\dagger] = 1$, we have

$$\hat{H} = \frac{\hat{p}^2}{2m} + \frac{m\omega_0^2}{2} \hat{x}^2 - x F_{ext}(t), \tag{15}$$

$$\rightarrow \hbar\omega_0\left(\hat{N}+\frac{1}{2}\right)-\mathrm{i}(\hat{a}+\hat{a}^\dagger)f(t), \tag{16}$$

$$\hat{N}=\hat{a}^\dagger\hat{a}, \qquad \hat{N}\,|\,n\rangle = n\,|\,n\rangle, \qquad n=0,\,1,\,2,\,\ldots \tag{17}$$

$\hat{N}$ denotes the *number-operator*. The action of $\hat{a},\hat{a}^\dagger$ on the number-states is

$$\hat{a}\,|\,n\rangle=\sqrt{n}\,|\,n-1\rangle, \qquad \hat{a}^\dagger\,|\,n\rangle=\sqrt{n+1}\,|\,n+1\rangle. \tag{18}$$

These operators are called *ladder operators* because repeated operation with *on* $|\,n\rangle$ creates the "ladder" of all other states: $\hat{a}^\dagger$ "climbs-up", whereas $\hat{a}$ "steps down", see Fig. 3.

$$\hat{a}\,|\,0\rangle=0, \qquad |\,n\rangle=\frac{1}{\sqrt{n!}}(\hat{a}^\dagger)^n\,|\,0\rangle. \tag{19}$$

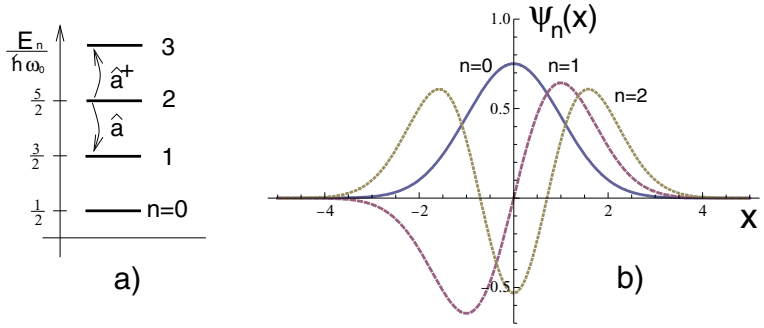

Figure 3. Harmonic oscillator. (a) Energies and (b) stationary wave functions.

Stationary states:

Stationary states are identical with the number-eigenstates $|\,n\rangle$ and belong to energies $E_n=\hbar\omega_0(n+1/2)$. In position representation $\hat{x}=x, \hat{p}=-\mathrm{i}\hbar\dfrac{\partial}{\partial x}$, $\psi(x)=\langle x\,|\,\psi\rangle$ where $|\,x\rangle$ is an eigenstate of the position operator $\hat{x}$,

$$\psi_n(x) = \frac{1}{\sqrt{\sqrt{\pi}\,2^n n!}} e^{-x^2/2} H_n(x), \qquad E_n = \hbar\omega_0\left(n + \frac{1}{2}\right). \tag{20}$$

$H_n(x)$ denote *Hermite-polynomials,* $H_0(x) = 1$, $H_1(x) = 2x$, $H_2(x) = 4x^2 - 2$, ... and $n = 0, 1, 2, \ldots$ (x in units of $\ell = \sqrt{\hbar/(m\omega_0)}$.

Note: The classical oscillator has only a single steady state, $x_0 = 0$, $p_0 = 0$, whereas a quantum oscillator has infinitely many steady states labelled by $n = 0, 1, 2, \ldots$. In contrast to widespread belief, a single steady quantum state does not correspond to classical motion.

Almost classical states (α-states):

We are looking for states where the expectation values of $\hat{x}$ and $\hat{p}$ vary sinusoidally in time. In addition we require both Δx, Δp to be time-independent and as small as possible. These states were already found by Schrödinger and correspond to a displaced Gaussian ground state wavefunction multiplied by a momentum eigenfunction, see Fig 4. In dimensionless quantities, we have

$$\psi_\alpha(x,t) = \frac{1}{\sqrt[4]{\pi}} \exp\left[-\frac{[x - x_c(t)]^2}{2}\right] e^{\mathrm{i}xp_c(t)} e^{\mathrm{i}\varphi(t)}. \tag{21}$$

$x_c(t)$ and $p_c(t)$ are the solutions of the classical equations of motion of the oscillator (9,13) (even for $f(t) \neq 0$). $\vartheta(t)$ is a (irrelevant) time-dependent phase which, however, is needed to solve (6).

In number-representation, these states are given by ($\vartheta(t)$ omitted)

$$|\alpha\rangle = e^{-\frac{1}{2}|\alpha|^2} \sum_{n=0}^{\infty} \frac{\alpha^n}{\sqrt{n!}} |n\rangle, \qquad \alpha \to \alpha(t) = x_c(t) = x_c(t) + \mathrm{i}p_c(t) = \sqrt{2}a(t). \tag{22}$$

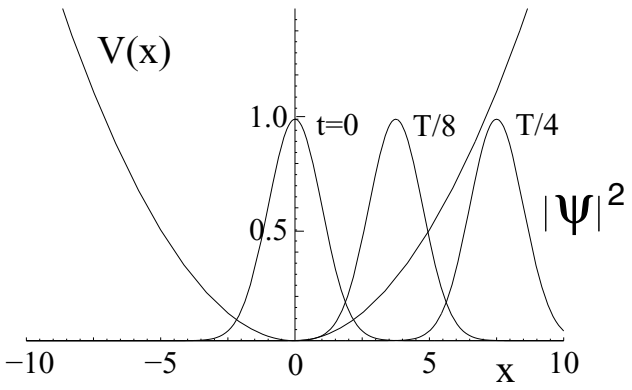

Figure 4. Time development of the coherent state wave function *($\omega_0 T = 2\pi$).*

Nowadays, these states are called *coherent states*, *Glauber states*, or just *α-states*. Roy J. Glauber [28] was the first who recognized their fundamental role for the description of laser radiation.[3] Some further details will be discussed in Sect. 5.3.

We shall show in the next section that the EMF is dynamically equivalent to a system of harmonic oscillators, yet for photons wave functions like (20,21) are neither needed nor useful. Instead, only the algebraic properties of $\hat{a},\hat{a}^\dagger$ will be used.

4. Quantum Theory of Light

4.1. MAXWELL-EQUATIONS

The state of the EMF is described by two (mathematical) vector fields $\boldsymbol{\mathcal{E}},\boldsymbol{\mathcal{B}}$ which are coupled to the charge and current density of matter ρ, $\mathbf{j}$ by the *Maxwell-Equations*[4]

$$\begin{aligned} &\frac{\partial \boldsymbol{\mathcal{E}}}{\partial t} - c^2 \operatorname{curl} \boldsymbol{\mathcal{B}} = -\frac{1}{\varepsilon_0}\mathbf{j}(\mathbf{r},t), \quad \text{(a)} \quad \operatorname{div} \boldsymbol{\mathcal{E}} = \frac{1}{\varepsilon_0}\rho(\mathbf{r},t), \quad (c) \\ &\frac{\partial \boldsymbol{\mathcal{B}}}{\partial t} + \operatorname{curl} \boldsymbol{\mathcal{E}} = 0, \qquad\qquad \text{(b)} \quad \operatorname{div} \boldsymbol{\mathcal{B}} = 0. \qquad (d) \end{aligned} \tag{23}$$

For our purposes a detailed knowledge how to calculate field configurations for specific systems is not required. However, we have to know the relevant dynamical variables of the EMF. Analogous to the interpretation of Classical Mechanics one may view the two differential equations (a,b) with respect to time as equations of motion of the Maxwell field, whereas (c,d) represent "constraints". Hence, from the six components of $\boldsymbol{\mathcal{E}},\boldsymbol{\mathcal{B}}$ at most 6 − 2 = 4 components are independent dynamical variables at each space point. Therefore, potentials Φ, $\boldsymbol{\mathcal{A}}$ are more appropriate than $\boldsymbol{\mathcal{E}},\boldsymbol{\mathcal{B}}$,

$$\boldsymbol{\mathcal{E}} = -\frac{\partial}{\partial t}\boldsymbol{\mathcal{A}}(\mathbf{r},t) - \operatorname{grad}\Phi(\mathbf{r},t), \qquad \boldsymbol{\mathcal{B}} = \operatorname{curl}\boldsymbol{\mathcal{A}}(\mathbf{r},t). \tag{24}$$

However, $\boldsymbol{\mathcal{A}}$, Φ are not uniquely determined, rather $\boldsymbol{\mathcal{A}} \to \boldsymbol{\mathcal{A}}' = \boldsymbol{\mathcal{A}} + \operatorname{grad}\Lambda(\mathbf{r},t), \Phi \to \Phi' = \Phi - \dot{\Lambda}(\mathbf{r}\,t)$, lead to the same $\boldsymbol{\mathcal{E}},\boldsymbol{\mathcal{B}}$-fields and, hence, contain the "same physics". $\Lambda(\mathbf{r},t)$ is an arbitrary gauge function. This property is called *gauge invariance* and it is considered as a fundamental principle of nature.

In Quantum Optics (and in solid state physics as well), the *Coulomb gauge,* $\operatorname{div}\boldsymbol{\mathcal{A}} = 0$, is particularly convenient where

[3] Nobel Prize (1/2) 2005 for "his contribution to the quantum theory of optical coherence", other half of the prize was given to J. L. Hall and Th. W. Hänsch.

[4] Vectors are set in boldface, electromagnetic fields in calligraphic style.

$$\begin{aligned} \Delta\Phi(\mathbf{r},t) &= -\frac{1}{\epsilon_0}\rho(\mathbf{r},t), \\ \Delta\mathcal{A}(\mathbf{r},t) - \frac{1}{c^2}\frac{\partial^2\mathcal{A}(\mathbf{r},t)}{\partial t^2} &= -\mu_0 \mathbf{j}_{tr}(\mathbf{r},t). \end{aligned} \tag{25}$$

$\mathbf{j}_{tr}$ denotes the "transverse" component of the current,

$$\mathbf{j}_{tr}(\mathbf{r},t) = \mathbf{j}(\mathbf{r},t) - \epsilon_0 \frac{\partial}{\partial t}\,\mathrm{grad}\,\Phi(\mathbf{r},t), \quad \mathrm{div}\mathbf{j}_{tr} = 0. \tag{26}$$

Some advantages of the Coulomb gauge are:

- The equations for Φ and $\mathcal{A}$ decouple.
- Φ is not a dynamical system, i.e. Φ is not governed by a differential equation with respect to time. (i.e. Φ will not be quantized and there are no "scalar photons").
- As div $\mathcal{A} = 0$ only two of the three components of $\mathcal{A}$ are independent variables of the EMF (i.e. there are no "longitudinal photons").

Hence, the EMF has two independent "internal" degrees of freedom at each space point corresponding to two polarization states.

4.2. MODES AND DYNAMICAL VARIABLES

In order to extract the dynamical variables of the EMF from Eq. (25) we decompose the vector potential in terms of *modes* $\mathbf{u}_\ell(\mathbf{r})$

$$\mathcal{A}(\mathbf{r},t) = \sum_\ell A_\ell(t)\,\mathbf{u}_\ell(\mathbf{r}), \tag{27}$$

$$\Delta\mathbf{u}_\ell(\mathbf{r}) + \left(\frac{\omega_\ell}{c}\right)^2 \mathbf{u}_\ell(\mathbf{r}) = 0, \quad \mathrm{div}\,\mathbf{u}_\ell(\mathbf{r}) = 0, \tag{28}$$

$$\int \mathbf{u}_\ell^*(\mathbf{r})\,\mathbf{u}_{\ell'}(\mathbf{r})\,d^3\mathbf{r} = \delta_{\ell,\ell'}. \tag{29}$$

In addition, there will be boundary conditions for $\mathcal{E}, \mathcal{B}$ which fix the eigenfrequencies ω_ℓ of the modes labelled by ℓ. (To lighten the notation we omit the index "tr" from now on). The set of $A_\ell(t)$ can be obtained by using the orthogonality relations (29) of the mode-functions and they represent the generalized coordinates or *dynamical variables* of the EMF which obey the equation of motion

$$\ddot{A}_\ell(t) + \omega_\ell^2\, A_\ell(t) = \frac{1}{\epsilon_0} j_\ell(t). \tag{30}$$

$j_\ell(t)$ is defined in the same way as $A_\ell(t)$.

From (30) we guess the Lagrangian

$$\begin{aligned} L &= \sum_\ell \frac{1}{2}\dot{A}_\ell^2 - \frac{\omega_\ell^2}{2}A_\ell^2 + \frac{1}{\varepsilon_0} j_\ell(t)\, A_\ell, \\ &= \int\left(\frac{\varepsilon_0}{2}\boldsymbol{\mathcal{E}}_{tr}^2(\mathbf{r},t) - \frac{1}{2\mu_0}\boldsymbol{\mathcal{B}}^2(\mathbf{r},t) + \mathbf{j}_{tr}(\mathbf{r},t)\,\boldsymbol{\mathcal{A}}(\mathbf{r},t)\right) d^3\mathbf{r}. \end{aligned} \tag{31}$$

The canonical variables are, obviously, $Q_\ell = A_\ell$, $P_\ell = \dot{A}_\ell$ and the Hamiltonian becomes

$$\begin{aligned} H &= P\dot{Q} - L, \\ &= \int\left(\frac{\varepsilon_0}{2}\boldsymbol{\mathcal{E}}_{tr}^2(\mathbf{r},t) + \frac{1}{2\mu_0}\boldsymbol{\mathcal{B}}^2(\mathbf{r},t) - \mathbf{j}_{tr}(\mathbf{r},t)\,\boldsymbol{\mathcal{A}}(\mathbf{r},t)\right) d^3\mathbf{r}. \end{aligned} \tag{32}$$

In conclusion, each mode of the EMF is equivalent to a driven harmonic oscillator. The state of the EMF is, thus, specified by the set of mode amplitudes A_ℓ and their velocities $\dot{A}_\ell$ at a given instant of time.

$\boldsymbol{\mathcal{A}}(\mathbf{r},t)$ is a real field so that $\mathbf{u}_\ell(\mathbf{r})$ as well as $A_\ell(t)$ ought to be real as well. Nevertheless, the choice of complex modes may be convenient. In particular, in free space we will use "running plane waves" (wave vector $\boldsymbol{k}$)

$$\mathbf{u}_{\mathrm{k},\sigma}(\mathbf{r}) = \frac{1}{\sqrt{V}}\boldsymbol{\varepsilon}_{\mathrm{k},\sigma}\, e^{\mathrm{ikr}}, \qquad \boldsymbol{\varepsilon}^*_{\mathrm{k},\sigma'}\cdot\boldsymbol{\varepsilon}_{\mathrm{k},\sigma} = \delta_{\sigma,\sigma'}. \tag{33}$$

$\boldsymbol{\varepsilon}_{\mathrm{k},\sigma}$ denotes the polarization vector which, by $\operatorname{div}\mathbf{u} = \mathrm{i}\mathbf{k}\cdot\boldsymbol{\varepsilon}_{\mathrm{k},\sigma} = 0$, is orthogonal to the wave vector $\boldsymbol{k}$ (here the notation "transversal" becomes manifest). The two independent polarization vectors will be labelled by σ = 1, 2. V denotes the normalization volume and, as usual, periodic boundary conditions are implied.

To follow the scheme outlined in the previous section we have to bring the Maxwell-Theory into Hamiltonian form. This is, however, almost trivial because the EMF is dynamically equivalent to a system of uncoupled harmonic oscillators with generalized "coordinates" A_ℓ, see (30).

$$\boldsymbol{\mathcal{A}}(\mathbf{r},t) = \sum_{\mathrm{k},\sigma}\sqrt{\frac{\hbar}{2\varepsilon_0\omega_\mathrm{k}V}}\left(a_{\mathrm{k},\sigma}(t)\,\boldsymbol{\varepsilon}_{\mathrm{k},\sigma}\, e^{\mathrm{ikr}} + a^*_{\mathrm{k},\sigma}(t)\,\boldsymbol{\varepsilon}^*_{\mathrm{k},\sigma}\, e^{-\mathrm{ikr}}\right), \tag{34}$$

$$\begin{aligned}\boldsymbol{\mathcal{E}}(\mathbf{r},t) &= -\frac{\partial \boldsymbol{\mathcal{A}}(\mathbf{r},t)}{\partial t} \\ &= \sum_{\mathrm{k},\sigma}\sqrt{\frac{\hbar}{2\mathsf{e}_0\omega_\mathrm{k}V}}\left(i\omega_\mathrm{k}\; a_{\mathrm{k},\sigma}(t)\,\mathsf{e}_{\mathrm{k},\sigma}\,e^{\mathrm{ikr}}+cc\right), \qquad (35)\end{aligned}$$

$$\begin{aligned}\boldsymbol{\mathcal{B}}(\mathbf{r},t) &= \mathrm{curl}\;\boldsymbol{\mathcal{A}}(\mathbf{r},t) \\ &= \sum_{\mathrm{k},\sigma}\sqrt{\frac{\hbar}{2\mathsf{e}_0\omega_\mathrm{k}V}}\left(\mathrm{i}(\mathbf{k}\times\mathsf{e}_{\mathrm{k},\sigma})\,a_{\mathrm{k},\sigma}(t)\,e^{\mathrm{ikr}}+cc\right), \qquad (36)\end{aligned}$$

$$H=\sum_{\mathrm{k},\sigma}\hbar\omega_\mathrm{k}\;a^*_{\mathrm{k},\sigma}a_{\mathrm{k},\sigma}-\sqrt{\frac{\hbar}{2\mathsf{e}_0\omega_\mathrm{k}}}\left(j^*_{\mathrm{k},\sigma}(t)\,a_{\mathrm{k},\sigma}+cc\right), \qquad (37)$$

$$P=\int\left(\frac{1}{\mu_0}\boldsymbol{\mathcal{E}}_{tr}(\mathbf{r},t)\times\boldsymbol{\mathcal{B}}(\mathbf{r},\,t)\right)d^3\mathbf{r}=\sum_{\mathrm{k},\sigma}\hbar\mathbf{k}a^*_{\mathrm{k},\sigma}a_{\mathrm{k},\sigma}. \qquad (38)$$

P denotes the momentum of the EMF. The complex amplitudes obey the Poisson bracket relations and equation of motion analogous to (10,13)

$$\left\{a_{\mathrm{k},\sigma},a^*_{\mathrm{k}',\sigma'}\right\}=\frac{\mathrm{i}}{\hbar}\delta_{\mathrm{k},\mathrm{k}'}\,\delta_{\sigma,\sigma'}, \qquad (39)$$

$$\frac{da_{\mathrm{k},\sigma}(t)}{dt}+\mathrm{i}\omega_\mathrm{k}\;a_{\mathrm{k},\sigma}(t)=\mathrm{i}\sqrt{\frac{1}{2\mathsf{e}_0\hbar\omega_\mathrm{k}}}j_{\mathrm{k},\sigma}(t). \qquad (40)$$

Equation (40) has been already used performing the time-derivative of $\boldsymbol{\mathcal{A}}(\mathbf{r},t)$ in (35).[5]

The complex amplitudes $a_{\mathbf{k},\,\sigma}$ represent the dynamical variables of the EMF. Its real and imaginary parts are called *quadrature amplitudes*

$$a_{\mathrm{k},\sigma}=X^{(1)}_{\mathrm{k},\sigma}+\mathrm{i}X^{(2)}_{\mathrm{k},\sigma},$$

which (apart from numerical factors) are the analogues of position and momentum of a mechanical oscillator, see section 3.2.

---

[5] The contribution from $\mathbf{j}_{tr}$ drops out in the final result; beware of $a^*_{\mathrm{k},\sigma}\neq a_{-\mathrm{k},\sigma}$ although $j^*_{\mathrm{k},\sigma}=j_{-\mathrm{k},\sigma}$! In contrast to most treatments of the subject no efforts have been made to preserve the "natural sequence" of the amplitudes $a_{\mathrm{k},\sigma}, a^*_{\mathrm{k},\sigma}$. Potential energy/momentum contributions from the scalar potential to Eqs. (37–38) have been omitted. For technical details see Kroll's article in Ref. [8].

4.3. QUANTUM OPTICS

The quantum version of the EMF together with a (nonrelativistic) theory of matter is called *Quantum Optics*. As the EMF is dynamically equivalent to a system of uncoupled harmonic oscillators this task is almost trivial when using ladder operators $a_{\mathrm{k},\sigma} \to \hat{a}_{\mathrm{k},\sigma}$. In the following we shall use the Schrödinger picture, where operators are time-independent.

$$\left[\hat{a}_{\mathrm{k},\sigma}, \hat{a}^{\dagger}_{\mathrm{k}',\sigma'}\right] = \delta_{\mathrm{k},\mathrm{k}'}\, \delta_{\sigma,\sigma'}. \tag{41}$$

The (infinite) zero point energy which arises from the noncommutativity of the $\hat{a}_{\mathrm{k},\sigma}, \hat{a}^{\dagger}_{\mathrm{k},\sigma}$ operators has been omitted in the Hamiltonian as this has no influence on the dynamics of the EMF. The zero point fluctuations of the EMF, however, are still present in the fields, as we shall see later.

The steady states of the infinite set of mode oscillators of the EMF is, thus, labelled by the (infinite set of) quantum numbers $\{n_{\mathbf{k},\sigma}\}$, which individually can take on different nonnegative integers. In free space, the time dependence of $|\{n_{\mathbf{k},\sigma}\}\rangle$ is, as usual, determined by an exponential factor $\exp(-in\omega_{\mathrm{k},\sigma}t)$ for each mode. Arbitrary states can be represented as a superposition of these *number-states*, which, therefore, represent a natural basis for the description of the quantum states of the EMF. But, where are the photons?

4.4. OSCILLATORS AND BOSONS

Dirac [23] has made the important discovery that

> *... a system of noninteracting bosons with single particle energies* e_ℓ *is dynamically equivalent to a system of uncoupled oscillators with frequencies* ω_ℓ *and vice versa. The two systems are just the same looked at from two different points of view ...*

Here, *dynamic equivalence* means that all states of an N-boson system which are conventionally described by a symmetric wave function are equally well described in the "oscillator picture", where each single particle state with energy e_ℓ corresponds to an oscillator with frequency $\omega_\ell = \mathsf{e}_\ell / \hbar$. Remarkably, the commutation relations $\left[\hat{a}_\ell, \hat{a}^{\dagger}_{\ell'}\right] = \delta_{\ell,\ell'}$ between the ladder operators are fully equivalent to the permutation symmetry of the boson wavefunction, and, fortunately, a great deal of notational redundancy in the description of a many-body system is removed. All operators in the "particle picture" (lhs of Fig. 5) can be translated into operators acting on the oscillator states. These operators are conveniently expressed in terms of ladder operators which

are now named *creation and destruction operators* for particles because they change the particle number by one. Particle conservation implies that all observables contain products of operators with an equal number of $\hat{a}_{\mathrm{k},\sigma}$ and $a^{\dagger}_{\mathrm{k}',\sigma'}$. In contrast to massive particles (in nonrelativistic quantum theory) detection of photons mostly enforces annihilation of them.

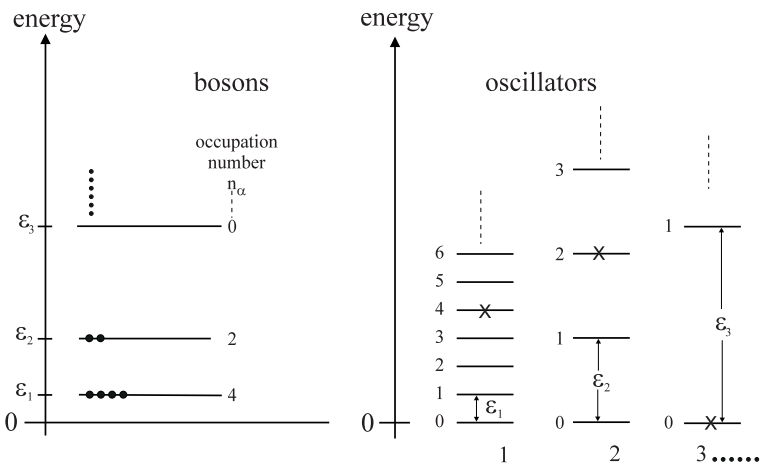

Figure 5. Equivalence of a system of N (noninteracting) bosons with single-particle energies ε_ℓ and occupation numbers n_ℓ and an infinite (uncoupled) set of harmonic oscillators with frequencies $\omega_\ell = \varepsilon_\ell / \hbar$. Note that the zero-point energies of the oscillators are omitted. Dots symbolize particles, crosses excited states, respectively. ($N = 6$).

The union of all sets of N = 1,2 ... particle subspaces plus the N = 0 "no particle" state (vacuum)

$$|0\rangle = |0,0,0,\doteq\rangle$$

is called *Fock space*. The number states $|\{n_\ell\}\rangle$ are the eigenstates of the *particle number operator*

$$\hat{N} = \sum_{\ell} \hat{a}^{\dagger}_{\ell}\, \hat{a}_{\ell}. \tag{42}$$

Now, the particle number itself becomes a dynamical variable and we can even describe states which are not particle number eigenstates of the system. The Fock representation is also called *occupation number representation* or "second quantization". It is much more flexible than the original formulation with a fixed particle number.

4.5. WHAT IS A PHOTON?

The bosons corresponding to the quantized oscillators of the EMF are called *photons*.

- Photons are the eigenstates of the number operator $\hat{N}$. In particular, there are photon number-eigenstates belonging to each mode, $|\{n_{\mathbf{k},\sigma}\}\rangle$ with integer $n_{\mathbf{k},\sigma} = 0,1,2 \ldots$
- A single photon belonging to a fixed mode ($\mathbf{k}$, σ) is also eigenstate of the Hamiltonian with energy $E = \hbar\omega_{\mathrm{k},\sigma}$ and momentum $\mathbf{p} = \hbar\mathbf{k}$ with $E(\mathbf{p}) = c|\mathbf{p}|$.
- Photons have two polarization degrees of freedom, e.g. there are two orthogonal linear polarizations $\sigma = 1, 2$ or left/right circular polarization base states

$$|1_{\pm}\rangle = \frac{1}{\sqrt{2}}\left(|1_{\mathrm{k},1}\rangle \pm \mathrm{i}\,|1_{\mathrm{k},2}\rangle\right).$$

According to the prevailing belief, the spin of the photon[6] or some other particle is a mysterious internal angular momentum for which no concrete physical picture is available, and for which there is no classical analog. However, it can be shown that the spin of the photon may be regarded as an angular momentum generated by a circulating flow of energy in the wave field, see the nice article by Ohanian [29].

- All types of classical interference phenomena are automatically captured by the mode structure of (34).
- Localization of energy arises as the outcome of a measurement which causes the state of the EMF to "collapse" into an eigenstate of the measuring device as a result of a position measurement, e.g. the absorption of a photon by an atom or in a pixel of a CCD-camera.

Today our interpretation of photons differs substantially from the original idea of small energy "bullets" or "darts" [22]. Although photons (in free space) have a definite energy–momentum relation, photons are not "objects" in the sense of individual, localizable classical corpuscles. By contrast, they are nonlocalizable, indistinguishable, obey Bose-statistics, and they can be created and annihilated easily. Moreover, in most cases the relevant photon states are not states with a fixed photon number. This will become obvious when discussing various examples in the next sections.

5. Special Photon States

In the following we shall discuss some special states of the EMF and their expectation values of the $\mathcal{E}$, $\mathcal{B}$, energy, and momentum. The physically relevant states cannot be eigenstates of the electrical field operator $\hat{\mathcal{E}}$ as these have infinite energy. ($\hat{\mathcal{E}}$ corresponds to the position or momentum of a mechanical oscillator).

[6] Although photons are spin-1 particles there are only but two spin projections (parallel and antiparallel to momentum), i.e. photons are characterized by helicity. For massless particles there is no rest frame.

The "quantum unit" of the electrical field strength is $\mathcal{E}_0 = \sqrt{\hbar\omega / 2\varepsilon_0 V}$. For green light, λ = 500 nm, and a quantization volume of V = 1 cm^3, $\mathcal{E}_0 \approx 0.075\,\mathrm{V/m}$, whereas, in a microresonator of linear dimension 1μm, $\mathcal{E}_0 \approx 7.5 \times 10^4\,\mathrm{V/m}$!

5.1. N-PHOTONS IN A SINGLE MODE

We consider n photons in a single mode with $\mathbf{k} = (k, 0,0)$ and linear polarization along y-direction $\mathbf{e}_{\mathrm{k},\sigma} = (0, 1, 0) \cdot |n\rangle$ is, of course, an eigenstate of the photon number operator (42). (Mode indices $\mathbf{k}$, σ are omitted, for brevity).

Without a driving current source this state is an eigenstate of the Hamiltonian with energy $n\hbar\omega$ and it evolves in time according to

$$|n; t\rangle = |n\rangle\, e^{-in\omega t}. \tag{43}$$

In addition, this state is also a momentum eigenstate with eigenvalue $n\hbar\mathbf{k}$, see (38). However, $|n\rangle$ is not an eigenstate of the electrical field operator, Eq. (35), because $\hat{a}_{\mathrm{k},\sigma}, \hat{a}^{\dagger}_{\mathrm{k},\sigma}$ changes the number of photons by ±1. In particular, we have

$$\langle n; t\,|\,\hat{\mathcal{E}}(\mathbf{r})\,|\,n; t\rangle = 0, \tag{44}$$

$$\langle n; t\,|\,\hat{\mathcal{E}}^2(\mathbf{r})\,|\,n; t\rangle = \mathcal{E}_0^2(2n+1). \tag{45}$$

Certainly, such a state does not correspond to a classical sinusoidal wave, instead it is pure "quantum noise". Note, even in the vacuum state $|0\rangle$, *zero point fluctuations* of $\mathcal{E}, \mathcal{B}$ are present.

5.2. SINGLE PHOTON WAVE PACKET

We consider a superposition of one-photon states with are composed of different modes (but with the same polarization).

$$|\phi_\sigma(\mathbf{k}); t\rangle = \sum_{\mathrm{k}} \phi_\sigma(\mathbf{k}) e^{-\mathrm{i}\omega_{\mathrm{k}} t}\,|1_{\mathrm{k},\sigma}\rangle. \tag{46}$$

$\phi_\sigma(\mathbf{k})$ is an arbitrary, normalized function which, with some care, may be interpreted as a wave function of a photon (–wave packet) in momentum space. However, there is no well defined photon position representation, see, e.g. Landau–Lifshitz [27] (Vol. 4a). The question of localization of photons is discussed, e.g., by Clauser in Ref. [11].

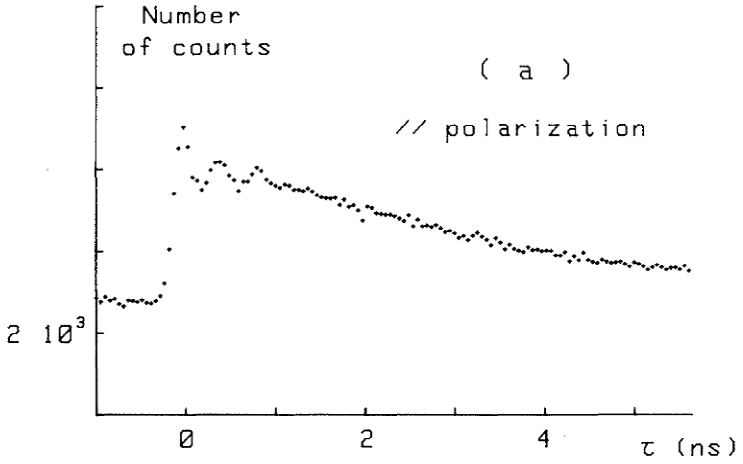

Figure 6. Two Ca-atoms radiate a single photon. Number of detected fluorescent photons (same polarization as the laser light) as function of time delay τ (50 ps per channel) (According to Grangier et al. [30]).

Grangier et al. [30] reported an interesting phenomenon where two Ca atoms shared a single photon similar to a two-slit diffraction experiment. Photodissociation of a diatomic homonuclear molecule A_2 (Ca_2) yielding two atoms recoiling in opposite directions, one in excited state (A*) and the other in the ground state (A). Either atom can actually be excited, and subsequently reemit a photon at the atomic frequency ω_0, so one must consider two undishinguishable paths for the whole process

$$\hbar\omega_L + A_2 \rightarrow \left\{ \begin{matrix} A + A^* \\ A^* + A \end{matrix} \right\} \rightarrow 2A + \hbar\omega_0 .$$

$\hbar\omega_L$ refers to the photodissociating light. Interference oscillations in Fig. 6 originate from two recoiling atomic dipoles at distance $d = 2v\tau$, where $v \approx 1{,}100$ m/s is the velocity and τ time of observation. By using a tunable laser, one could thus obtain interesting information about the "energy–landscape" of the dissociating molecular state.

5.3. COHERENT STATES (IDEAL SINGLE MODE LASER)

We are looking for a state, in which the $\mathcal{E}, \mathcal{B}$ fields vary sinusoidally in space and time with $\mathcal{E}$-uncertaincy as small as possible, i.e., have time independent uncertaincies in the quadrature amplitudes with $\Delta X_1 = \Delta X_2 = 1/2$ and $\Delta X_1 \Delta X_2 = 1/4$. We have already discussed these states in section 3.2

$$|\alpha\rangle = e^{-\frac{1}{2}|\alpha|^2} \sum_{n=0}^{\infty} \frac{\alpha^n}{\sqrt{n!}} |n\rangle. \tag{47}$$

α-states, also termed *Glauber states* or *coherent states* have a number of interesting properties [5]:

– $|\alpha\rangle$ is an eigenstate of the destruction operator

$$\hat{a}|\alpha\rangle = \alpha|\alpha\rangle, \tag{48}$$

where α is an arbitrary complex number.

– α-states can be generated by the unitary "displacement" operator $\hat{D}$

$$|\alpha\rangle = \hat{D}(\alpha)|0\rangle, \tag{49}$$

$$\hat{D}(\alpha) = e^{\alpha\hat{a}^\dagger - \alpha^*\hat{a}} = e^{-\frac{1}{2}|\alpha^2|} e^{\alpha\hat{a}^\dagger} e^{-\alpha\hat{a}}, \tag{50}$$

$$\hat{D}^\dagger \hat{a} \hat{D} = \hat{a} + \alpha. \tag{51}$$

– The time dependence of an α-state (even with a classical external current source) is obtained just by replacing $\alpha \rightarrow \alpha(t)$,

$$|\alpha, t\rangle = |\alpha(t)\rangle, \tag{52}$$

where $\alpha(t) = x_c(t) + \mathrm{i}p_c(t) = \sqrt{2}a(t)$ correspond to the position and momentum of a classical oscillator. For a free oscillator $\alpha(t) = \alpha e^{-\mathrm{i}\omega t}$.

– Although the α-eigenvalues form a continuous spectrum, they are normalizable and (over-) complete but not orthogonal. These states form a convenient basis for the description of "almost classical states" of the EMF for which the state-operator can be solely represented by its diagonal elements

$$\hat{\rho} = \int P(\alpha)|\alpha\rangle\langle\alpha| d^2\alpha. \tag{53}$$

For example, for thermal states the Glauber P-function is $P(\alpha) = \frac{1}{\pi\bar{n}} \exp(-|\alpha|^2/\bar{n})$, where $\bar{n}$ is the mean photon number in the mode, see also (14) and Fig. 2b.

Expectation values and uncertainties of the electrical field and photon number and the probability to measure n photons are [$\alpha = |\alpha| \exp(\mathrm{i}\phi)$, polarization index omitted]:

$$\mathcal{E}(\mathbf{r}, t) = \langle\alpha(t)|\hat{\mathcal{E}}(\mathbf{r})|\alpha(t)\rangle = -2\mathcal{E}_0(|\boldsymbol{\alpha}| \sin \mathbf{kr} - \omega_k t + \phi), \tag{54}$$

$$(\Delta\mathcal{E})^2 = \mathcal{E}_0^2, \tag{55}$$

$$\langle \hat{N} \rangle = |\alpha|^2 = \bar{n}, \qquad (\Delta\hat{N})^2 = \langle \hat{N} \rangle, \tag{56}$$

$$p_n = |\langle n \,|\, \alpha \rangle|^2 = e^{-\bar{n}} \frac{\bar{n}^n}{n!}. \tag{57}$$

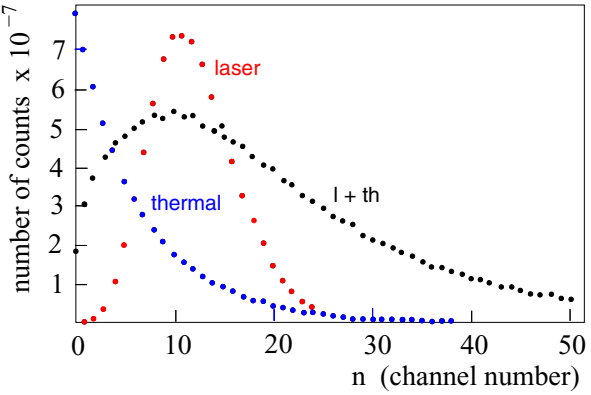

Figure 7. Photon count distribution for a single mode laser, thermal light, and mixing of both (According to Arecchi, in Ref. [9]).

- α is not an eigenstate of the photon number operator.
- The photon distribution function p_n is a *Poissonian* with mean photon number $\bar{n} = |\alpha|^2$ and uncertainty $(\Delta N)^2 = \bar{n}$.
- The relative amount of fluctuations in the electrical field decreases with increasing amplitude, $\Delta N / \langle N \rangle = 1/\sqrt{\langle \bar{n} \rangle}$.
- Thus, in a coherent state photons behave like uncorrelated classical objects! In contrast to naive expectations, the photons in a (single mode) laser (and well above the threshold) "arrive" in a random fashion, in particular they do not "ride" on the electrical field maxima. See also Fig. 1.

How to generate α-states? As α-states are eigenstates of the (non-Hermitian) destruction operator $\hat{a}$, there is no observable with a corresponding "apparatus" to create these states just by doing a measurement! However, α-states can be simply generated from the vacuum by a classical current source (e.g. antenna of a radio transmitter)

$$\hat{H} = \hbar\omega \hat{a}^\dagger \hat{a} - \left[f(t)\hat{a}^\dagger + f^*(t)\,\hat{a} \right], \tag{58}$$

where $f(t) \propto j(t)$. Nevertheless, it was a great surprise that the light–matter interaction in a laser (well above the threshold) could be modelled in such a simple way.

The amplitude of the electrical field of a laser may be well stabilized by saturation effects, but there is no possibility to control the phase, i.e., a more realistic laser state would be described by the density operator

$$\hat{\rho} = \int \frac{d\phi}{2\pi} |\alpha\rangle \langle\alpha| = \sum_n p_n |n\rangle \langle n| . \tag{59}$$

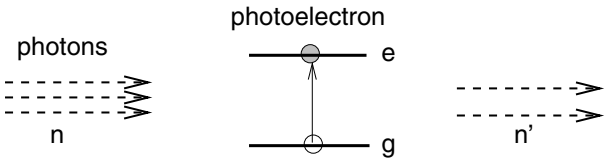

Figure 8. Principle of a photodetector. Absorption of a photon induces a transition from a bound electron state to an excited "free" state which leads to a current (–impulse).

This state is made up of an (incoherent) superposition of n-photon states with a *Poissonian distribution*. [A simple model to describe laser light with a finite linewidth which is caused by phase diffusion has been given by Jacobs [31].]

5.4. THERMAL (CHAOTIC) PHOTON STATES

A single mode of thermal (black body) radiation is described by the statistical operator

$$\hat{\rho} = \frac{1}{Z} e^{-\beta \hat{H}} = \sum_{n=0}^{\infty} b_n |n\rangle \langle n| , \tag{60}$$

$$b_n = \frac{\bar{n}^n}{(\bar{n}+1)^{n+1}} = \frac{1}{1+\bar{n}} \left(1 + \frac{1}{\bar{n}}\right)^{-n} = \frac{1}{Z} e^{-\beta\hbar\omega}, \tag{61}$$

$$\langle \hat{N} \rangle = \mathrm{tr}(\hat{\rho}\hat{N}) = \frac{1}{e^{\beta\hbar\omega} - 1} = \bar{n}, \qquad (\Delta\hat{N})^2 = \bar{n}(\bar{n}+1). \tag{62}$$

$\beta = 1/(k_B T)$, $Z = 1/(1 - \exp(-\beta\hbar\omega))$ is the partition function, b_n is the *Bose–Einstein* photon distribution (geometric sequence), and $\bar{n}$ is the mean photon number in the mode, see Fig. 7. In contrast to coherent states, $\Delta\hat{N}/\bar{n} \to 1$ for $\bar{n} \to \infty$.

Problem P1: A provoking question:
"Are there photons in static electric and magnetic fields?"
(The answer will be given at the end of the article.)

6. Detectors and Optical Devices

Passive optical components like phase shifters, lenses, mirrors, polarizers etc., are used in Quantum Optics to change modes (base transformation) whereas a photodetector gives a "click" by absorbing a photon.

6.1. PHOTODETECTORS

In a classical description the electrical current of a photodetector is proportional to the light intensity (energy density) averaged over a cycle of oscillation [2]

$$J_{\mathrm{PD}} \propto \langle \mathcal{E}(t)^2 \rangle_{\mathrm{cycl}} \propto \mathcal{E}^{(-)}(t)\, \mathcal{E}^{(+)}(t). \tag{63}$$

$\mathcal{E}^{(\pm)}$ denote the positive(negative) frequency parts of the electric field, e.g. $\boldsymbol{\mathcal{E}}^{(+)} \propto \exp(-\mathrm{i}\omega t)$ (polarization properties and space variables have been omitted for simplicity). For a stochastic field, the product $\mathcal{E}^{(-)}\mathcal{E}^{(+)}$ has to be additionally averaged on the different realizations of the ensemble.

In a quantum treatment $\boldsymbol{\mathcal{E}}^{(+)}$ becomes a destruction operator (in the Heisenberg picture) and the response of the detector arises from transitions from the ground state of the atoms $|g\rangle$ in the photocathode to highly excited quasi-free states $|e\rangle$ by absorption of photons, see Fig. 8. Initially, we have for the combined system "atom plus EMF" $|i\rangle = |g,\ \{n\}\rangle$. The electrical dipole interaction $\hat{H}_{dip} = -e\hat{\boldsymbol{\mathcal{E}}}\,\mathbf{r}_{\mathrm{atom}}$ induces transitions to final states $|f\rangle = |e,\ \{n'\}\rangle$. With the golden rule and summing over all possible final states, we have for the total transition rate (for single photon absorption), see Refs. [8–10],

$$\begin{aligned} \Gamma(t) &= \frac{2\pi}{\hbar^2} \sum_f \left| \langle f \,|\, \hat{H}_{dip} \,|\, i \rangle \right|^2 \delta(E_e + n'\hbar\omega - E_g - n\hbar\omega), \\ &= \zeta \langle \hat{\mathcal{E}}^{(-)}(\mathbf{r}, t) \hat{\mathcal{E}}^{(+)}(\mathbf{r}, t) \rangle. \end{aligned} \tag{64}$$

Implicitly, we shall assume a perfect photocathode (ζ = const.) with unit quantum efficiency so that each absorbed photon causes an atom in the phototube to emit an

electron and register a single count during times t, $t + dt$. In first order dipole approximation absorption of more than one photon (per transition) does not occur. The number of photons which a counter records in a finite interval of time is described by a photon count distribution function $P_m(T)$, where m is the number of recorded photons. For details see, e.g. Loudon [2].

6.2. BEAM SPLITTERS

A beam-splitter (BS) is an optical device that splits a beam of light into two. It is the key element of most optical interferometers. In a quantum mechanical description one has to take into account two incoming "wave beams" with fields $\mathcal{E}_1, \mathcal{E}_2$ even if one of them is the vacuum [32, 33]. These beams are transformed into a transmitted and a reflected output beam with fields $\mathcal{E}_3, \mathcal{E}_4$, respectively. For a symmetric dielectric beam splitter (and equal polarizations) the complex amplitudes transform according to

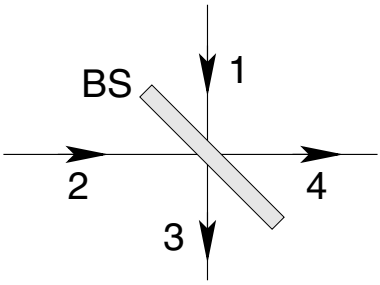

Figure 9. Sketch of a beam splitter. Modes (1, 2) are transformed into (3, 4).

$$\begin{pmatrix} a_3 \\ a_4 \end{pmatrix} = \begin{pmatrix} \sqrt{1-R} & \mathrm{i}\sqrt{R} \\ \mathrm{i}\sqrt{R} & \sqrt{1-R} \end{pmatrix} \begin{pmatrix} a_1 \\ a_2 \end{pmatrix}. \tag{65}$$

R is the (intensity) reflection coefficent.

In quantum optics amplitudes a_j become operators $\hat{a}_j$ and (65) represents a unitary base transformation. The counterpart of "no incident wave" refers to the vacuum state of that mode rather than to "nothing". A beam splitter does not "split" photons, rather it conserves the number of photons and acts as a random selector which divides the incident flow of photons in a reflected and a transmitted one. As a consequence, the photon statistics of the reflected/transmitted beams correspond to that of the input beam after a random selection process has taken place.

In particular, we discuss the case of a dielectric 50:50 beam splitter [4]

$$\hat{a}_3 = \frac{1}{\sqrt{2}}\left(\hat{a}_1 + \mathrm{i}a_2\right), \qquad \hat{a}_4 = \frac{1}{\sqrt{2}}\left(\hat{a}_2 + \mathrm{i}a_1\right). \tag{66}$$

6.2.1. *Single photon input in port 2, (vacuum in 1)*

$$|\,0_1, 1_2\rangle = \hat{a}_2^\dagger\,|\,0\rangle \to \frac{1}{\sqrt{2}}\left(|\,0_3, 1_4\rangle + \mathrm{i}\,|\,1_3, 0_4\rangle\right).$$

Indices label different modes. Note, the output state is *entangled*, although the input was not.

6.2.2. *N photons in port 2, (vacuum in 1)*

$$|\,0_1, N_2\rangle = \frac{1}{\sqrt{N!}}\left(\hat{a}_2^\dagger\right)^N |\,0\rangle \to \sum_{k=0}^{N} \mathrm{i}^k \sqrt{\frac{1}{2^N}\binom{N}{k}}\,|\,k\rangle_3\,|\,(N-n)\rangle_4.$$

The photon count statistics is binominal.

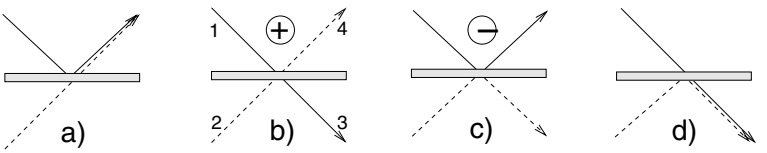

Figure 10. The four amplitudes of reflection and transmission of two photons at a 50:50 beam-splitter. Note the destructive interference of (b) and (c).

Special case $N = 2$:

$$|\,0_1, 1_2\rangle \to \frac{1}{2}\,|\,2_3, 0_4\rangle + \frac{1}{\sqrt{2}}\,|\,1_3, 1_4\rangle - \frac{1}{2}\,|\,0_3, 2_4\rangle.$$

The probability that both photons "go together" after passing the beam splitter is $(1/2)^2 + (1/2)^2 = 1/2$.

6.2.3. *Single photons in ports 1 and 2*

$$|1_1, 1_2\rangle = \hat{a}_1^\dagger \hat{a}_2^\dagger |0\rangle \rightarrow \frac{\mathrm{i}}{\sqrt{2}}\left(|2_3, 0_4\rangle + |0_3, 2_4\rangle\right).$$

The output state is entangled and both photons "go together", see also Fig. 10. [N.B.: Entanglement is not a base invariant property.]

6.2.4. *α-state in port 2 (vacuum in 1)*

$$|\alpha\rangle_1 |0\rangle_2 \rightarrow \left|\frac{\mathrm{i}\alpha}{\sqrt{2}}\right\rangle_3 \left|\frac{\alpha}{\sqrt{2}}\right\rangle_4 .$$

As expected from classical electrodynamics the incident beam is splitted in two beams of half of the input intensity and there is a phase shift of $\pi/2$. For a coherent state (with a Poissonian photon distribution), a random selection yields again a Poissonian, hence, a coherent state remains a coherent state after reflection or transmission by a beam splitter, yet with a reduced value of α. Moreover, the output state is not entangled (product of states in ports 3 and 4), i.e. the outputs are statistically independent.

6.2.5. *Thermal state in port 2 (vacuum in 1)*

A thermal state transforms under a beam splitter also in thermal states at the output ports. This nontrivial result may be conveniently obtained from the Glauber P-representation (53) and the result of Sect. 6.2.4.

$$\hat{\rho}_{in} = \left(|0\rangle\langle 0|\right)_1 \otimes \frac{1}{\pi\bar{n}} \int e^{-|\alpha|^2/\bar{n}} \left(|\alpha\rangle\langle\alpha|\right)_2 d^2\alpha \rightarrow \hat{\rho}_{out} .$$

$\bar{n}$ denotes the mean input photon number. The reduced density operator for port 4

$$\hat{\rho}_4 = \mathrm{tr}_3 \hat{\rho}_{out} = \sum_n {}_3\langle n | \hat{\rho}_{out} | n\rangle_3$$

is also a thermal state (60), but with half of the mean photon number $\bar{n}_4 = \bar{n}/2$. The same holds for $\hat{\rho}_3$. Although the output state of the whole system is entangled, $\hat{\rho}_{out} \neq \hat{\rho}_3\, \hat{\rho}_4$,

the (intensity) correlations between the photons in ports 3,4 are not affected. We leave this as problem P2.

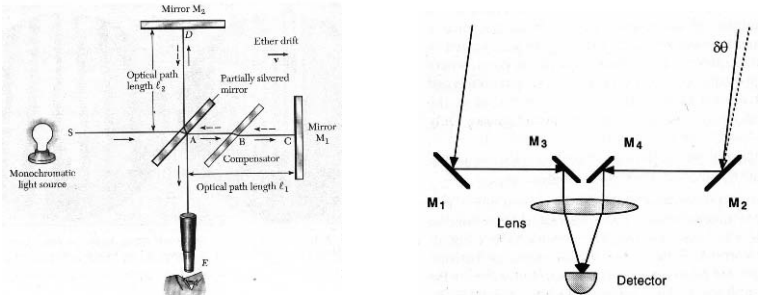

Figure 11. Sketch of the Michelson interferometer (left) and Michelson stellar interferometer (right). With these instruments the temporal and spatial correlation of the EMF can be measured independently (According to Bachor [6]).

6.3. INTERFEROMETERS

Interferometers are devices to measure the correlation of the EMF between different space–time points ($\mathbf{r}_1$, t_1) and ($\mathbf{r}_2$, t_2) by superposition of the (electrical) fields "on a screen" ($\mathbf{r}_s$, t_s) by using pinholes/slits, mirrors, beam splitters and delay lines.

$$\mathcal{E}_{int}(\mathbf{r}_s, t_s) \propto \mathcal{E}(\mathbf{r}_1, t_1) + \mathcal{E}(\mathbf{r}_2, t_2).$$

The Michelson interferometers – as depicted in Figs. 11 – are particularily well suited to investigate coherence properties as these instruments separately measure the temporal and spatial dependencies of G_1 (2,1).

The (cycle averaged) intensity of light at position of the interferometer screen can be expressed in terms of the (first order) correlation function $G_1(\mathbf{r}_2, t_2; \mathbf{r}_1, t_1)$

$$I(t) \propto G_1(1, 1) + G_1(2, 2) + 2\mathrm{Re}G_1(2, 1), \tag{67}$$

$$G_1(\mathbf{r}_2, t_2; \mathbf{r}_1, t_1) = \langle \hat{\boldsymbol{\mathcal{E}}}^{(-)}(\mathbf{r}_2, t_2)\hat{\boldsymbol{\mathcal{E}}}^{(+)}(\mathbf{r}_1, t_1)\rangle, \tag{68}$$

where G_1 (2, 1) is short for $G_1(\mathbf{r}_2, t_2; \mathbf{r}_1, t_1)$ etc. It is seen from (67) that the intensity on the screen consists of three contributions: The first two terms represent the intensities caused by each of the two path (or "slits") in the absence of the other, whereas the third term gives rise to interference effects. For a symmetric configuration (equal slit width,

homogeneous illumination, $G_1(1, 1) = G_1(2,2)$)) the visibility of the fringes is given by the magnitude of the normalized correlation function $g_1(1, 2)$

$$\mathcal{V} = \frac{I_{max} - I_{min}}{I_{max} + I_{min}} = \left| g(2, 1) \right|^2, \tag{69}$$

$$g_1(\mathbf{r}_2, t_2; \mathbf{r}_1, t_1) = \frac{G_1(\mathbf{r}_2, t_2; \mathbf{r}_1, t_1)}{\sqrt{G_1(1,1) G_1(2,2)}}. \tag{70}$$

Hence, coherence, i.e. the possibility of interference, of light is a measure of correlations in the EMF.

6.3.1. *Examples for* G_1

We study two examples for the (first order) classical coherence functions.
(a) Single mode (deterministic/stochastic) field.

$$G_1(\mathbf{r}_2, t_2; \mathbf{r}_1, t_1) = \left\langle | a_{\mathbf{k},\sigma} |^2 \right\rangle \exp(-\mathrm{i}[\mathbf{k}(\mathbf{r}_2 - \mathbf{r}_1) - \omega_{\mathbf{k}}(t_2 - t_1)]) \tag{71}$$

Obviously, this correlation function is (apart from the numerical value of $\left\langle | a_{\mathbf{k},\sigma} |^2 \right\rangle$) the same for a deterministic and a stochastic single mode field and displays maximum contrast for arbitrary space–time separations (unlimited spatial and temporal coherence).
(b) Many statistically independent modes (of equal polarization) and intensity profile:

$$I(\omega_{\mathbf{k}}) = \left| \mathcal{E}(\omega) \right|^2, \left\langle \hat{a}^*_{\mathbf{k}',\sigma'} a_{\mathbf{k},\sigma} \right\rangle = I(\omega_{\mathbf{k}}) \delta_{\mathbf{k},\mathbf{k}'} \delta_{\sigma,\sigma'}.$$

$$\mathcal{E}^{(+)}(\mathbf{r}, t) = \sum_{\mathbf{k}} a_{\mathbf{k},\sigma} e^{\mathrm{i}(\mathbf{k}\mathbf{r} - \omega_{\mathbf{k}} t)}, \tag{72}$$

$$G_1(\mathbf{r}_2, t_2; \mathbf{r}_1, t_1) = \sum_{\mathbf{k}} I(\omega_{\mathbf{k}}) \, e^{-\mathrm{i}[\mathbf{k}(\mathbf{r}_2 - \mathbf{r}_1) - \omega_{\mathbf{k}}(t_2 - t_1)]}. \tag{73}$$

In particular, we have at the same space point, $\mathbf{r}_2 = \mathbf{r}_1 = \mathbf{r}$, (as measured by a Michelson interferometer)

$$G_1(t_2 - t_1) = G_1(\mathbf{r}, t_2; \mathbf{r}, t_1) = \int_0^\infty I(\omega) \, e^{\mathrm{i}\omega(t_2 - t_1)} \frac{d\omega}{2\pi} \tag{74}$$

For examples see Fig. 12.

For Gaussian and Lorentzian line-sources centered at $\omega_0 > 0$, we have

$$I(\omega) = \begin{cases} I_0 e^{-\frac{(\omega - \omega_0)^2}{2(\Delta\omega)^2}}, \\ I_0 \dfrac{(\Delta\omega)^2}{(\omega - \omega_0)^2 + (\Delta\omega)^2}, \end{cases} \qquad g_1(t) = \begin{cases} e^{-\frac{(\Delta\omega t)^2}{2}} e^{\mathrm{i}\omega_0 t}, & \text{(a)} \\ e^{-\Delta\omega|t|} \, e^{\mathrm{i}\omega_0 t}. & \text{(b)} \end{cases} \tag{75}$$

Wiener–Khinchine theorem:

- $G_1(\mathbf{r}, t)$ is the Fourier-transform of the intensity spectrum $I(\omega)$.
- Concerning temporal coherence, the filtered many mode field is virtually indistinguishable from the single mode field provided the time difference is less than the coherence time, $t < t_{coh}$. The same reasoning holds for filtering within various directions in **k**-space by apertures (spatial coherence).

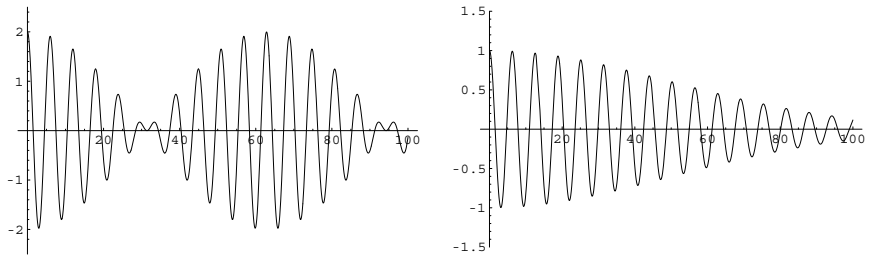

Figure 12. Real part of the coherence functions G_1 as a function of time delay. Left: two modes with $\omega_j = (1 \pm 0.05)\omega_0$ ("Na-D doublett"), right: many uncorrelated modes with a Gaussian spectrum.

Prior to the invention of the laser, coherent light was made out of "chaotic" radiation by (wave length) filters and apertures. Here, the visibility in the Michelson interferometers vanishes (and remains zero!) if the distance between the arms becomes larger than the (longitudinal) coherence length $l_{coh} = ct_{coh}$ (point like source of spectral width $\Delta\lambda$) or larger than the (transversal) coherence diameter d_{coh} (monochromatic source of angular diameter $\Delta\theta$)

Coherence time: $t_{coh} = \dfrac{2\pi}{\Delta\omega} = \dfrac{\lambda_0^2}{c\Delta\lambda}$

Coherence diameter: $d_{coh} = \dfrac{2\pi}{\Delta k} = 1.22\dfrac{\lambda}{\Delta\theta}$

The numerical factor of 1.22 holds for a circular light source. Note, the vanishing of the interference pattern is not the result of interference but of the shift of individual patterns which are produced independently by each frequency component or each volume element of an extended source.

Examples:

red Cd-line: $\lambda_0 = 643.8\text{nm}$, $\Delta\lambda = 0.0013\text{nm}$, $l_{coh} = 32\text{cm}$.

sun: $\lambda_0 = 500\text{nm}$, $\Delta\theta = 32'$, $d_{coh} = 66\,\mu\text{m}$.

Since 1985, coherence experiments with genuine single photon states are possible, see Fig. 13. A Ca-atom is excited by a two-photon transition which, subsequently, decays by two emitting two photons consecutively in opposite directions. One photon is used as a trigger, the second photon enters the Mach-Zehnder interferometer (MZI). Although beam splitters may change the photon correlations, first order coherence properties are not affected.

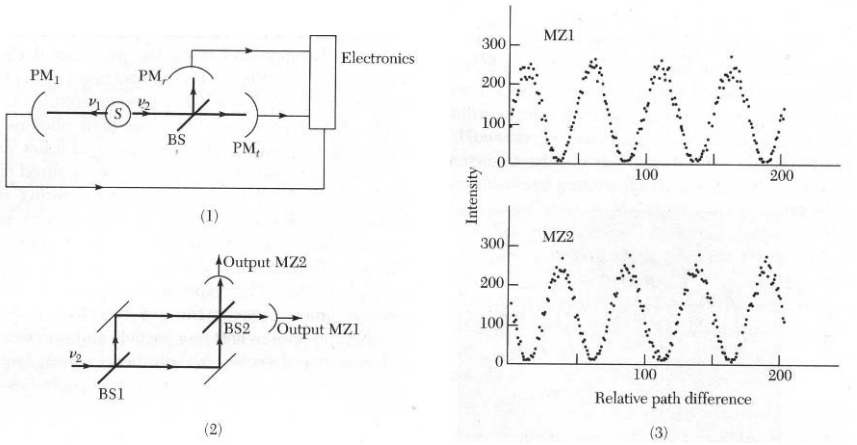

Figure 13. (1) Triggered photon cascade experiment to produce single photon states. (2) Mach-Zehnder Interferometer. (3) Number counts in the outputs of the photodetector MZ1 and MZ2 as a function of the path difference between the arms of the interferometer. (One channel corresponds to a variation of $\delta = \lambda/50$) (According to Grangier et al. [34]).

7. Photon Correlations

7.1. THE HANBURY BROWN AND TWISS EFFECT

The idea to use intensity correlations (in thermal radiation) instead of field correlations [e.g. using a Michelson interferometer] dates back to 1949 where Hanbury Brown and Twiss, two radio astronomers at Jodrell Bank (Great Britain), were trying to design a radio interferometer which would solve the intriguing problem of measuring the angular size of the most prominent radio sources at this time: Cygnus A and Cassiopeia A. If, as some people thought their angular size is as small as the largest visible stars, then a global base line would be needed and a coherent superposition of the radio signals have been impossible in praxis those days.

First, a pilot model was built in 1950 and was tested by measuring the angular diameter of the sun at 2.4 m wavelength, and, subsequently, the radio sources Cygnus A and Cassiopeia A. The intermediate-frequency outputs of the two independent superheterodyne receivers were rectified in square law detectors and bandpass filtered (1...2.5 kHz). Then, the low frequency (LF) outputs were brought together (by cable, radio link or telephone) and after analogue multiplication and integration the correlator output was investigated as a function of antenna separation $|\mathbf{r}_2 - \mathbf{r}_1|$.

$$G_2^{cl}(\mathbf{r}_2,t_2;\mathbf{r}_1,t_1)=\left\langle I(\mathbf{r}_2,t_2)\ I(\mathbf{r}_1,t_1)\right\rangle \tag{76}$$

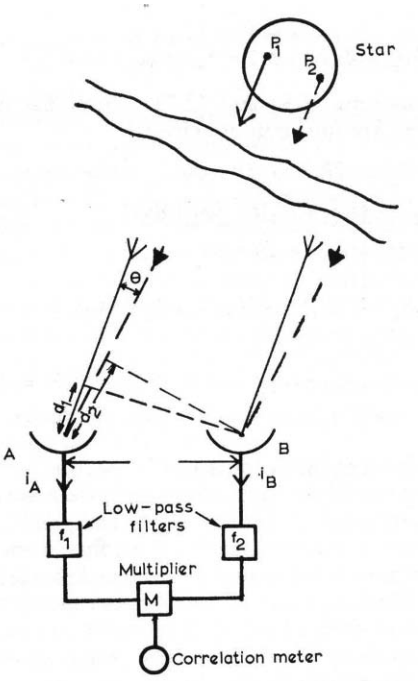

Figure 14. Optical intensity interferometer proposed and built in Australia by Hanbury Brown [35] to measure the angular diameter of stars. (Today there are much better methods/instruments available!).

For many independent modes, Eq. (76) can be evaluated in the same way as for G_1. As a result, we have

$$G_2^{cl}(\mathbf{r}_2,t_2;\mathbf{r}_1,t_1)=\sum_{\mathbf{k}}\left(\left\langle|a_{\mathbf{k}}|^4\right\rangle-2\left\langle|a_{\mathbf{k}}|^2\right\rangle^2\right)$$

$$+|G_1(0,0;)|^2+|G_1(\mathbf{r}_2,t_2;\mathbf{r}_1,t_1)|^2\,. \tag{77}$$

Moreover, for thermal radiation (Gaussian statistics) $\left\langle|a_{\mathbf{k}}|^4\right\rangle=2\left\langle|a_{\mathbf{k}}|^2\right\rangle^2$, so that the first term of Eq. (77) drops out. In all other cases this contribution is negative so that the "contrast" in $G_2(2,\ 1)$ between adjacent $(\mathbf{r}_2,\ t_2)$, $(\mathbf{r}_1,\ t_1)$ and distant arguments is reduced. For thermal radiation, intensity correlation measurements yield the same information as conventional first order coherence experiments, e.g. using the Michelson interferometers. This was directly confirmed by experiment [35].

The optical analogue of the intensity interferometer seemed to be straight-forward. Instead of two RF receivers, one uses two photodetectors and a correlator (or coincidence counter) measures the combined absorption of photons at different space time points $(\mathbf{r}_2,\ t_2)$ and $(\mathbf{r}_1,\ t_1)$, see Fig. 14. If one thinks in terms of photons one must

accept that thermal photons at two well separated detectors are correlated – they tend to "arrive" in pairs ("photon bunching"). But how, if the photons are emitted at random in a thermal source, can they appear in pairs at two well separated detectors? First, there was a strong opposition from theory but eventually, this problem was settled by experiment which clearly showed photon bunching in thermal radiation [24, 36]. However, due to the low bandwidth of the electronics and low efficiency of the photocathodes the magnitude of the effect was only about 2% of the theoretical limit.

7.2. QUANTUM THEORY OF INTENSITY CORRELATIONS

In quantum theory, the classical result (77) is replaced by

$$G_2(\mathbf{r}_2,t_2;\mathbf{r}_1,t_1)=\left\langle \hat{\mathcal{E}}^{(-)}(\mathbf{r}_2,t_2)\,\hat{\mathcal{E}}^{(-)}(\mathbf{r}_1,t_1)\,\hat{\mathcal{E}}^{(+)}(\mathbf{r}_2,t_2)\,\hat{\mathcal{E}}^{(+)}(\mathbf{r}_1,t_1)\right\rangle. \tag{78}$$

Here, operators are in the *Heisenberg-picture* and $\hat{\mathcal{E}}^{(+)}(\mathbf{r},t)\propto \hat{a}\exp(-\mathrm{i}\omega t)$ denotes the positive frequency part of the electrical field. In contrast to the classical formulation, the sequence of operators is different from (77), where $I\propto \hat{\mathcal{E}}^{(-)}\hat{\mathcal{E}}^{(+)}$ – creation and destruction operators are in "normal order" (creation operators left to the destruction operators). Nevertheless, for thermal radiation, the classical result (77) remains valid.

Today, the photon bunching effect can be simply demonstrated with an artificial "chaotic" source which synthesizes pseudothermal light by passing laser radiation through a rotating ground glass disk (speed v) with long adjustable coherence times ("Martienssen lamp") [38], see Fig. 15.

It is instructive to define a coincidence ratio

$$R=\frac{C-C_{rand}}{C_{rand}}=\frac{(\Delta N)^2-<\hat{N}>}{(<\hat{N}>)^2},$$

where $C=G_2(1,1)=<\hat{N}(\hat{N}-1)>$. The number of random coincidences is proportional to $C_{rand}=G_2(2,1)=<\hat{N}>^2$ when the separation of $\mathbf{r}_2$, t_2, $\mathbf{r}_1$, t_1 is much larger than the coherence area/time.

$\alpha-$states:	$(\Delta N)^2=\bar{n},$	$R=0,$
thermal states:	$(\Delta N)^2=\bar{n}(\bar{n}+1),$	$R=0,$
number states:	$(\Delta N)^2=0.$	$R=-\frac{1}{n}.$

Classical states have photon number distributions which are always broader than a Poissonian, i.e., $(\Delta N)^2\geq\bar{n}$, hence, the correlation ratio is always positive, $R\geq 0$, ("photon bunching"). α states (as generated by an amplitude stabilized laser) represent the optimum with respect to low photon fluctuations.

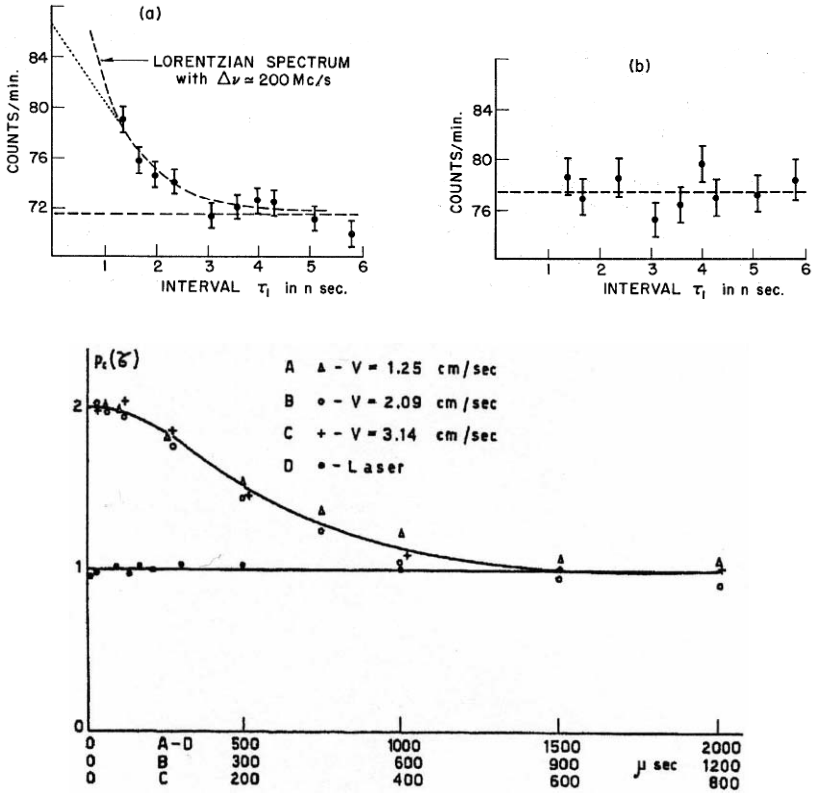

Figure 15. Measured photon coincidences in thermal and laser light. Upper panel: (a) mercury arc (Hg-198) and (b) tungsten lamp [37]. Lower panel: single mode laser light and chaotic light with adjustable coherence time (According to Arecchi et al. [39]).

On the other hand, states which have less photon number fluctuations than a Poissonian, e.g., the number states, show "antibunching", i.e., the photons prefer to "come" not too close. In particular, the single photon state $|n=1\rangle$ is the most nonclassical state one can think of! Obviously, photon bunching is not "a typical Bose property".

The generation of nonclassical light (which still showed "photon bunching") was first demonstrated in 1977 by Mandel's group [40] whereas the first clear evidence for anti-bunching was presented by Diedrich and Walther [41] in 1987, using a single Mg–ion in a Paul-trap.

As an application of photon correlations we mention the determination of the diffusion coefficient of protein molecules in aqueous solution, see Fig. 16. The diffusion constant controls the Brownian motion which is characterized by the density-fluctuation autocorrelation function

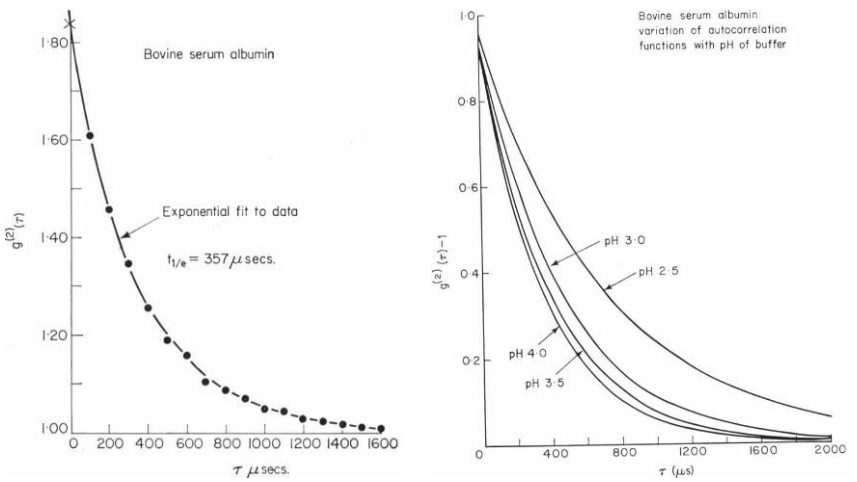

Figure 16. Left: Second order correlation function of laser light scattered from the protein bovine serum albumin. Right: effect of changing ph on the diffusion constant (and hence size of the protein) (According to Pike, in Ref. [10]).

$$\langle \delta C(\mathbf{r}_2, t_2)\, \delta C(\mathbf{r}_1, t_1)\rangle = \langle C\rangle \frac{1}{(4\pi D t)^{3/2}} \exp\left(-\frac{r^2}{4Dt}\right).$$

$\langle C \rangle$ is the mean concentration, D is the diffusion coefficient, and $r = |\mathbf{r}_2 - \mathbf{r}_1|$, $t = |t_2 - t_1|$. In Born-approximation, the light scattered at a fixed scattering angle picks out the spatial Fourier component with $\mathbf{k} = \mathbf{k}_{in} - \mathbf{k}_{out}$ so that the first and second order coherence functions of the scattered light become

$$G_1(\mathbf{r}=0,t) \propto \int e^{-\mathrm{ikr}}\, C(\mathbf{r},t)\, d^3\mathbf{r}, \quad g_1(\mathbf{r}=0,t) = e^{-Dk^2 t},$$

$$g_2(\mathbf{r}=0,t) = 1 + f\,|\,g_1(\mathbf{r}=0,t)\,|^2 = 1 + f\, e^{-2Dk^2 t}.$$

f is a "fudge factor" ($0 < f \leq 1$) which depends on the finite area of the photocathode, finite counting time, etc.

Today, photon correlation spectroscopy has become a versatile tool for investigating the spectral dynamics of single molecules which was treated in more detail in lectures by Prof. Schwille during this school.

Ultraweak correlated photon emission phenomena originating from biological organisms have been reported from time to time, e.g. see the recent article by Kobayashi and Inaba [42]. However, these phenomena resemble the pathological "mitogenic rays" reported by Gurwitsch in 1923 [43].

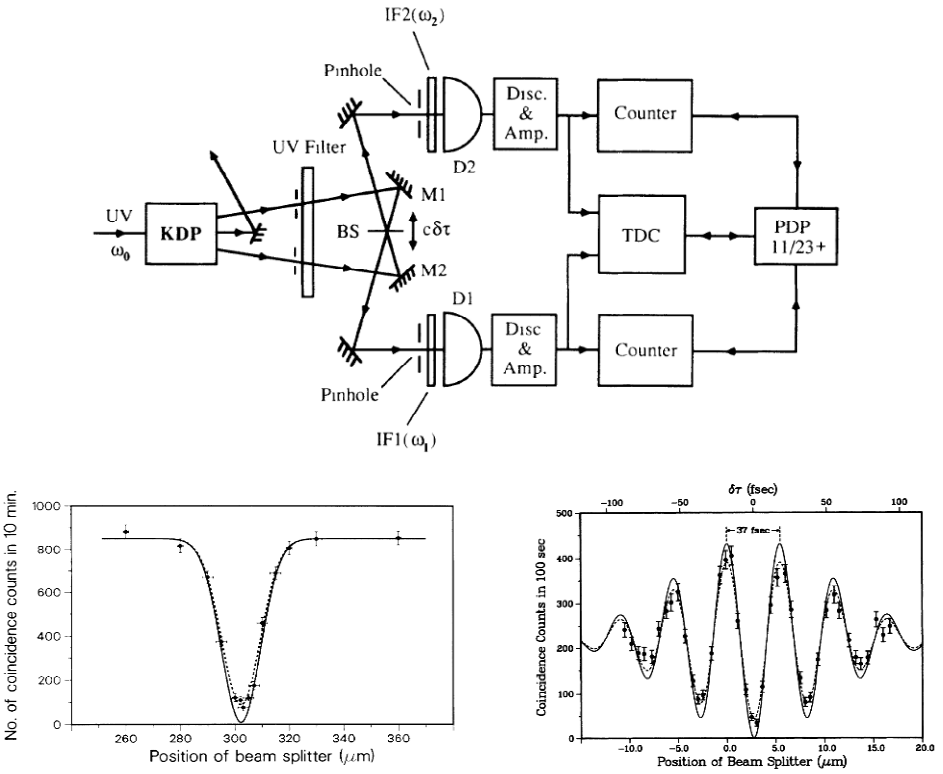

Figure 17. Interference of two photons as a function beam splitter displacement (time delay). Upper panel: Sketch of experimental set up; Lower panel: (left) both photons have the same frequency; (right): different frequencies (According to Mandel et al. [44, 45])

7.3. TWO PHOTON INTERFERENCE

How to measure the time interval between two photons? Do two different photons interfere? For intense laser pulses containing many photons this problem can be experimentally investigated using nonlinear optics. For single photons, this question was raised and answered by Mandel and coworkers more than 20 years ago [44, 45]. An outline of their experiment is shown in Fig. 17. A coherent beam of UV light with frequency ω_0 is parametrically down converted in a KDP crystal to a "signal" and "idler" photon with $\omega_1 + \omega_2 = \omega_0$. Then, the two photons are directed by mirrors M_1, M_2 to pass a beam splitter BS, and the supposed beams interfere and are directed to detectors D_1, D_2. Neglecting the band-width of filters IF_1 and IF_2, the fields at detectors D_1, D_1 are (in the notation of section 6.2.3 – $1' = 3$, $2' = 4$)

$$\hat{\mathcal{E}}_{1'}^{(+)}(t) = \frac{1}{\sqrt{2}}\hat{a}_1 e^{-i\omega_1(t-\tau_1)} + \frac{i}{\sqrt{2}}\hat{a}_2 e^{-i\omega_1(t-\tau_1+\delta\tau)},$$

$$\hat{\mathcal{E}}_{2'}^{(+)}(t) = \frac{1}{\sqrt{2}}\hat{a}_2 e^{-i\omega_2(t-\tau_1)} + \frac{i}{\sqrt{2}}\hat{a}_1 e^{-i\omega_2(t-\tau_1+\delta\tau)}.$$

τ_1 is the propagation time between mirror M_1 and detector D_1 (or M_2, D_2). According to (78) the joint probability of photodetection by D_1 at time t and D_2 at $t + \tau$ is

$$P_{12}^{(0)}(\tau) \propto \langle \hat{\mathcal{E}}_{1'}^{(-)}(t)\hat{\mathcal{E}}_{2'}^{(-)}(t+\tau)\hat{\mathcal{E}}_{2'}^{(+)}(t+\tau)\hat{\mathcal{E}}_{1'}^{(+)}(t)\rangle,$$

$$\propto 1-\cos[(\omega_2-\omega_1)\delta\tau] \propto \sin^2\left[\frac{(\omega_2-\omega_1)\delta\tau}{2}\right].$$

(Beware of $\tau \neq \tau_1$). The rate at which photons are detected in coincidence, when BS is displaced from its symmetry position by $\pm c\delta\tau$ displays a typical interference pattern, see Fig. 17. Nevertheless, signal and idler photons have no definite phase, and are therefore mutually incoherent, in the sense that the individual signals from D_1 and D_2 exhibit no oscillatory structure. In praxis, the spectral distributions of signal and idler photons, band-widths of filters IF_1 and IF_2 as well as the resolving time of the detectors (i.e. integration on τ) must be taken into account which can be lumped into a coherence factor f_c.

$$P_{12} \propto 1 - f_c \cos[(\omega_1-\omega_2)\delta\tau], \quad f_c = e^{-(\sigma\delta\tau)^2/2}.$$

Parameters:

(a) $\omega_1 = \omega_2 = 2.77\times10^{15}\mathrm{s}^{-1}$: $\lambda = 680\mathrm{nm}$, $\Delta\omega = 3\times10^{13}\mathrm{s}^{-1}$, $\sigma = \sqrt{2}\Delta\omega$

(b) $\omega_1 \neq \omega_2$: mean wave length $\bar{\lambda} = 680\mathrm{nm}$, $(\bar{\omega} = 2.77\times10^{15}\mathrm{s}^{-1})$. $\omega_1 = \omega_2 = 1.70\times10^{14}s^{-1}, \sigma = 1.85\times10^{13}s^{-1}$. (No spectral overlap of IF_1 and IF_2. Coherence time ≈ 100 fs.)

It is noteworthy that this interference technique, in principle, allows beating at optical frequencies $|\omega_2 - \omega_1|$ to be detected with photodetectors whose response times are thousands of times slower. In addition, both photons may even originate from different sources [46].

Problem P3:

Finally, one may ask the question: is the Hong-Ou-Mandel-effect a quantum effect or can it be understood classically?, i.e. will a "classical" state $|in\rangle = |\alpha\rangle_1 |\alpha\rangle_2$ lead to the same result as for a two single photons, $|1\rangle_1 = |1\rangle_2$?

8. Outlook

Probably many of you are disappointed with the rather formal definition of photons given in section 4.5. However, even Haroche and Raimond's superb book [7] *Exploring the Quantum* is less definitive. Therefore, let the master himself have the last words:

Die ganzen Jahre bewusster Grübelei haben mich der Antwort der Frage "Was sind Lichtquanten" nicht näher gebracht. Heute glaubt zwar jeder Lump, er wisse es, aber er täuscht sich...

Literal translation:

All the years of willful pondering have not brought me any closer to the answer to the question "what are light-quanta". Today every good-for-nothing believes he should know it, but he is mistaken...

Albert Einstein
In a letter to M. Besso, 1951.

Acknowledgement Due to unexpected circumstances, this contribution could not be presented at the summer school. The author thanks Prof. Di Bartolo for the possibility to include this article in the proceedings nevertheless.

References

1. H. Paul, *Photonen. Eine Einführung in die Quantenoptik*, B. G. Teubner Stuttgart, Leipzig (1999).
2. R. Loudon, *The Quantum Theory of Light*, Clarendon Press, Oxford (1973).
3. R. Kidd et al. *The evolution of the modern photon*, Am. J. Phys. **57**, 27 (1988).
4. Ch. C. Gerry and P. L. Knight, *Introductory Quantum Optics*, Cambridge University Press, Cambridge (2005).
5. M. O. Scully and S. S. Zubairy, *Quantum Optics*, Cambridge University Press, Cambridge (1999).
6. H. A. Bachor, *A Guide to Experiments in Quantum Optics*, Wiley-VCH, New York (1998).
7. S. Haroche and J-M. Raimond, *Exploring the Quantum*, Oxford University Press, Oxford (2006).
8. C. de Witt, A. Blandin, and C. Cohen-Tannoudji (eds), *Quantum Optics and Quantum Electronics*, Gordon & Breach, New York (1965).
9. R. J. Glauber (ed.), *Quantum Optics*, Academic, New York (1969).
10. *Quantum Optics*, S. M. Kay and A. Maitland (eds). Academic (1970).
11. L. Mandel and E. Wolf, (eds.), *Coherence and Quantum Optics*, Plenum, New York (1973).
12. R. v. Baltz, *Photons and Photon Statistics: From Incandescent Light to Lasers*, in: Frontiers of Optical Spectroscopy, B. Di Bartolo (ed.), Kluwer, New York (2004).
13. Ph. Lenard, *Über die lichtelektrische Wirkung*, Annalen der Physik (Leipzig), **8**, 149 (1902).
14. A. Einstein, *Über einen die Erzeugung und Verwandlung des Lichts betreffenden heuristischen Gesichtspunkt*, Annalen der Physik (Leipzig), **17**, 132 (1905).
15. R. A. Millikan, *A direct photoelectric determination of Planck's h*, Phys. Rev. **7**, 355 (1914).
16. A. H. Compton, *The spectrum of scattered X-rays*, Phys. Rev. **22**, 409 (1923).
17. E. O. Lawrence and J. W. Beams, *The element of time in the photoelectric effect*, Phys. Rev. **32**, 478 (1928).
18. A. T. Forrester, R. A. Gudmundsen, and P. O. Johnson, *Photoelectric mixing of incoherent light*, Phys. Rev. **99**, 1691 (1955).
19. G. I. Taylor, *Interference fringes with feeble light*, Proc. Cambr. Phil. Soc. **15**, 114 (1909).

20. A. J. Dempster and H. F. Batho, *Light Quanta and Interference*, Phys. Rev. **30**, 644 (1927).
21. L. Janossy, *Experiments and Theoretical Considerations Concerning The Dual Nature of Light*, in H. Haken and M. Wagner (eds.), Cooperative Phenomena, Springer-Verlag, Berlin (1973).
22. G. Breit, *Are quanta unidirectional?*, Phys. Rev. **22**, 313 (1923).
23. P. A. M. Dirac, *The Quantum Theory of the Emission and Absorption of Radiation*, Proc. R. Soc. A **114**, 243 (1927), see also *The Principles of Quantum Mechanics*, fourth edition, Oxford University Press, Oxford (1958).
24. R. Hanbury Brown and R. Q. Twiss, *Correlations between photons in two coherent beams of light*, Nature **177**, 27 (1956).
25. J. F. Clauser, *Experimental distinction between the quantum and classical field theoretic predictions for the photoelectric effect*, Phys. Rev. D **9**, 853 (1974).
26. J. N. Dodd, *The Compton effect – a classical treatment*, Eur. J. Phys. **4**, 205 (1983).
27. L. D. Landau and E. M. Lifshitz, *Theoretische Physik*, Akademie Verlag, Berlin (1970).
28. R. J. Glauber, *The Quantum Theory of Optical Coherence*, Phys. Rev. **130**, 2529 (1963), *Coherent and Incoherent States of the Radiation Field*, Phys. Rev. **131**, 2766 (1964), and in Refs.[8, 9].
29. H. C. Ohanian, *What is spin?*, Am. J. Phys. **54**, 500 (1986).
30. Ph. Grangier, A. Aspect and J. Vigue, *Quantum interference effect for two atoms radiating a single photon*, Phys. Rev. Lett. **54**, 418 (1985).
31. S. F. Jacobs, *How monocromatic is laser light?*, Am. J. Phys. **47**, 597 (1979).
32. C. H. Holbrow, E. Galvez, and M. E. Parks, *Photon quantum mechanics and beam splitters*, Am. J. Phys. **70**, 260 (2002).
33. S. Prasad, M. O. Scully, and W. Martienssen, *A quantum description of the beam splitter*, Opt. Commun. **62**, 139 (1987).
34. P. Grangier, G. Roger, and A. Aspect, *Experimental evidence for photon anticorrelation effects on a beam splitter: a new light on single-photon interferences*. Eur. Phys. Lett. **1**, 173 (1986). See also Physics World, Feb. (2003).
35. R. Hanbury Brown, *The Intensity Interferometer*, Taylor & Francis (1974); see also http://www.science.org.au/academy/memoirs/brown.htm
36. G. A. Rebka and R. V. Pound, *Time-correlated photons*, Nature **180**, 1035 (1957).
37. B. L. Morgan and L. Mandel, *Measurement of photon bunching in thermal light*, Phys. Rev. Lett. **16**, 1012 (1966); H. J. Kimble, M. Dagenais, and L. Mandel, *Photon antibunching in resonance fluorescence*, Phys. Rev. Lett **39**, 691 (1977).
38. W. Martiensen and E. Spiller, *Coherence and fluctuations in light beams*, Am. J. Phys. **32**, 919 (1964).
39. F. T. Arecchi, E. Gatti, and A. Sona, *Time distribution of photons from coherent and Gaussian sources*, Phys. Lett. **20**, 27 (1966).
40. M. Dagenais and L. Mandel, *Investigations of two-time correlations in photon emissions from a single atom*, Phys. Rev. A**18**, 2217 (1978).
41. F. Diedrich and H. Walther, *Nonclassical radiation of a single stored ion*, Phys. Rev. Lett. **58**, 203 (1987).
42. M. Kobayashi and H. Inaba, *Photon statistics and correlation analysis of ultraweak light originating from living organisms for extraction of biological information*, Appl. Opt. **39**, 183 (2000).
43. I. Langmuir, *Pathological Science*, Phys. Today, Oct. 1989, p. 36.
44. C. H. Hong, Z. Y. Ou, and L. Mandel, *Measurement of subpicosecond time intervals between two photons by interference*, Phys. Rev. Lett. **59**, 2044 (1987).
45. Z. Y. Ou and L. Mandel, *Observation of spatial quantum beating with separated photodetectors*, Phys. Rev. Lett. **61**, 54 (1988).
46. J. Beugnon et al. (Grangier's group), *Quantum interference between two single photons emitted by independently trapped atoms*, Lett Nat **440**, 779 (2006).

Solutions to Problems

1. (a $\mathcal{E} = -\text{grad}\Phi$, $\mathcal{A} = 0$. The scalar potential is not quantized, hence, there are no photons in a static electric field.
(b A static $\mathcal{B}$ field originates from a time independent current source, i.e. $f(t) = f_0 =$ const in (37) for a single mode. Eigenstates of (58) can be found by the canonical transformation

$$\hat{a} = \hat{b} + f_0/\hbar\omega_0, \quad [\hat{b},\hat{b}^\dagger] = 1,$$

$$\hat{H} = \hbar\omega_0\hat{a}^\dagger\hat{a} - \left(f_0\hat{a}^\dagger + f_0^*\hat{a}\right) = \hbar\omega_0\hat{b}^\dagger\hat{b} + \frac{|f_0|^2}{\hbar\omega_0},$$

$$\hat{N} = \hat{a}^\dagger\hat{a} = \hat{b}^\dagger\hat{b} + \left(\frac{f_0^*}{\hbar\omega_0}\hat{b} + hc\right) + \left|\frac{f_0}{\hbar\omega_0}\right|^2.$$

The expectation value of $\hat{N}$ in the ground state, $\hat{b}\,|\,g\rangle = 0$, is nonzero:

$$<\hat{N}> = \left|\frac{f_0}{\hbar\omega_0}\right|^2 > 0.$$

Hence, there are photons in a static magnetic field – but they are "virtual" and cannot "fly away"! [Result should be summed over all contributing modes].
2. Use the number representation of $|\,a\rangle$ and polar "coordinates", $d^2\alpha = |\alpha|d|\alpha|d\varphi$.
3. $\hat{\mathcal{E}}_{2'}^{(+)}(t+\tau)\hat{\mathcal{E}}_{1'}^{(+)}(t)$ leads to operator products $\hat{a}_1\hat{a}_2, \hat{a}_1^2, \hat{a}_2^2$ which, upon operation on $|\,a\rangle$, can be replaced by α^2, see (48). Analogous for $\langle\alpha\,|\,\mathcal{E}_{1'}^{(-)}\hat{\mathcal{E}}_{2'}^{(-)}$. Fast oscillating terms, e.g. $\cos^2[(\omega_1 + \omega_2)\delta\tau]$, can be replaced by their averages. This leads to an additional contribution of 1/2 to $P_{12}^{(0)}(\tau)$. Hence, the visibility contrast (69) is reduced to $\mathcal{V} = 1/2$, whereas $\mathcal{V} = 1$ for two photons.

PRINCIPLES AND APPLICATIONS OF FLUORESCENCE CORRELATION SPECTROSCOPY (FCS)

PETRA SCHWILLE*, JONAS RIES
Biophysics Group, BIOTEC TU Dresden
Tatzberg 47-51, D-01307 Dresden

1. Introduction

Fluorescence correlation spectroscopy (FCS) is one of the various modern optical techniques that allow access to single fluorescently labeled biomolecules in aqueous solution. In contrast to other fluorescence measurements, however, the parameter of primary interest is not the emission intensity itself, but rather spontaneous intensity fluctuations caused by the minute deviations of a small ensemble of molecules from thermal equilibrium. In general, all physical parameters that give rise to fluctuations in the fluorescence signal are accessible by FCS. It is, for example, rather straightforward to determine local concentrations, mobility coefficients or characteristic rate constants of inter- or intramolecular reactions of fluorescently labeled biomolecules at nanomolar to micromolar concentrations.

Fluorescence correlation spectroscopy has been developed in the early 1970s as a special case of relaxation analysis. Classical relaxation methods induce external perturbations such as temperature or pressure jumps to a reaction system, and gain information about involved kinetic parameters from the way the system returns back to equilibrium. The novel concept of FCS with respect to these classical techniques is to take advantage of the minute spontaneous fluctuations of physical parameters that are characteristic for any system at ambient temperature. If the sensitivity of the detection system allows for their observation, this is a much more benign method of study. Such fluctuations are generally represented as (usually unwanted) noise patterns of the measured signal, in our case, fluorescence. The fluctuations can be quantified in their strength and duration by temporally autocorrelating the recorded intensity signal, a mathematical procedure well known in information processing. Autocorrelation analysis provides a measure for the self-similarity of a signal in time, and therefore describes the persistence of information carried by it. Essential information about processes governing molecular dynamics can thus be derived from the temporal pattern by which fluorescence fluctuations arise and decay.

At its first introduction by Madge, Elson and Webb in 1972 [1], FCS was applied to measure diffusion and chemical dynamics of DNA-drug intercalation. This pioneering study was then followed by a number of other publications by many different groups

* Petra Schwille, Biophysics Group, BIOTEC TU Dresden, Tatzberg 47-51, D-01307 Dresden, e-mail: schwille@biotec.tu-dresden.de

B. Di Bartolo and J. Collins (eds.), *Biophotonics: Spectroscopy, Imaging, Sensing, and Manipulation*, 63
DOI 10.1007/978-90-481-9977-8_4, © Springer Science+Business Media B.V. 2011

describing, e.g., attempts to determine particle concentration, translational and rotational mobility in two or three dimensions, even in the cellular environment or in flow systems. These early measurements suffered from poor signal-to-noise ratios, mainly because of low detection efficiency, large ensemble numbers and insufficient background suppression. It is obvious that techniques based on spontaneous thermal fluctuations only function properly if one somehow manages to reduce the concentrations and observation volumes, such that only few molecules are simultaneously detected. To gain proper signal-to-noise levels, the fluorescence photon yield per single molecule needs to be maximized at the same time.

Taking the above into account, FCS is crucially dependent on strong and stable light sources like lasers, ultrasensitive detectors, e.g. avalanche photodiodes with single-photon sensitivity, and efficient fluorescence labels with high extinction coefficient and a quantum yield close to 100%. Experimentally, the breakthrough for FCS applications was achieved by Rigler and his coworkers by employing confocal detection geometries [2]. Here, the excitation laser is strongly focused by a high numerical aperture objective to a diffraction-limited spot. Only the fluorescently labeled molecules within the illuminated region, of the order of one at low concentrations, are addressed. In order to limit the detection volume in axial direction, a pinhole is introduced in the image plane, which blocks all light from out-of-focus areas.

To date, most FCS measurements are performed on fluorescently labeled biomolecules diffusing in aqueous environments. Because of the most elegant way of limiting the detection volume to less than 1 fl, i.e. approximately the volume of an *E. coli* bacterial cell, concentrations in the nanomolar range are optimal for FCS measurements. Under these circumstances, the signal fluctuations induced by molecules diffusing into or out of the focal volume are large enough to yield good signal-to-noise ratios. During the time a particle spends in the focus, chemical or photochemical reactions, or conformational changes may alter the emission characteristics of the fluorophore and give rise to additional fluctuations in the detected signal.

2. Principle of FCS

The principle of FCS can no longer be called a recent invention. It is a versatile method that already has demonstrated its vast possibilities for many different problems. Nowadays, it is – together with other confocal fluorescence readout techniques – one of the standard tools used for biochemistry or biotechnology, combining short data acquisition times of several seconds to minutes with straightforward analysis.

Recently, an increasing number of cellular applications has been reported. Local concentrations and mobilities of proteins and DNA- or RNA-fragments within the cytosol or other cell organelles belong to the most easily accessible measurement parameters. An increasing number of studies is now devoted to the analysis of molecular (e.g. protein–protein) interactions or translocation processes. One reason this has not been done earlier is certainly the poor signal quality due to autofluorescence and light absorption or scattering. Another problem consists in the limited supply of dye molecules within the cell, which may lead to irreversible photobleaching.

The confocal FCS setup, which has already been mentioned briefly above, is illustrated schematically in Fig. 1. The excitation light provided by a laser beam is

directed into a microscope objective via a dichroic mirror and focused onto the sample. As the sample molecules are usually dissolved in aqueous solution, water immersion objectives with a high numerical aperture (ideally >0.9) are used. The fluorescence light from the sample is collected by the same objective and passes through the dichroic and the emission filter. The pinhole in the image plane blocks any fluorescence light not originating from the focal region, thus providing axial resolution. Afterwards, the light is focused onto the detector, preferably an avalanche photodiode or a photomultiplier with single photon sensitivity.

The fluorescence signal is either directly autocorrelated by a hardware correlator card, or collected in photon-counting mode and then software-correlated, which usually takes more effort and data storage capacities. Data recording times usually vary between 10 and 120 s. Longer data recording renders the autocorrelation curve smoother, but bears the risk of collecting artifacts like bright diffusing aggregates or mechanical instabilities of the setup. For better control of the adjustment, the fluorescence signal and the calculated autocorrelation function are displayed simultaneously on the monitor. After data recording, it can be imported in any math program for further analysis. Fitting routines using the Levenberg–Marquardt non-linear least-square routine have proved very efficiently.

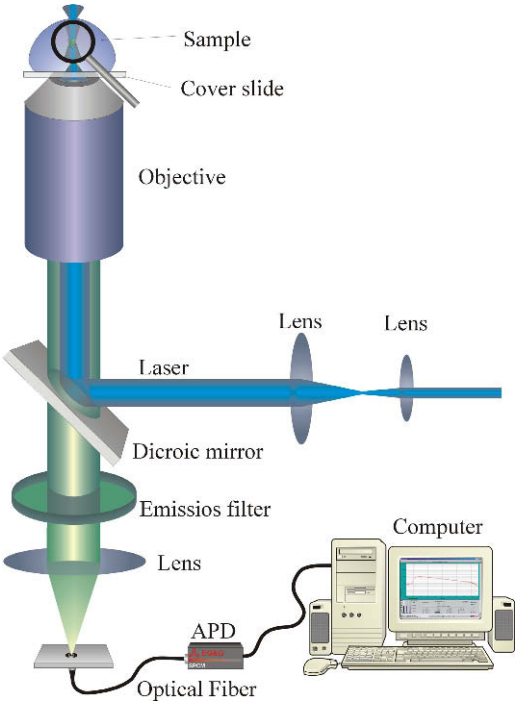

Figure 1. Schematic drawing of a confocal FCS setup. The sample is illuminated by a focused laser beam, the fluorescence light is collected through the same objective, projected to a very sensitive detector (APD) through a pinhole or optical fiber, and autocorrelated in time.

3. Applications

3.1. FCS MOBILITY ANALYSIS

*Auto*correlation analysis is performed by focusing on one particular species of fluorescent particles. Fluctuations in the fluorescence signal are quantified by temporally autocorrelating the recorded intensity signal. This routine provides a measure for the self-similarity of a time signal and highlights characteristic time constants of underlying processes.

The number of molecules contained within the focal volume at any time is governed by Poissonian distribution. Therefore, the root mean square fluctuation of the particle number N is given by

$$\frac{\sqrt{\langle (\delta N)^2 \rangle}}{\langle N \rangle} = \frac{\sqrt{\langle (N - \langle N \rangle)^2 \rangle}}{\langle N \rangle} = \frac{1}{\sqrt{\langle N \rangle}} \tag{1}$$

Since the relative fluctuations become smaller with increasing numbers of measured particles, it is important to minimize the number of molecules in the focal volume. However, the fluorescence signal must still be higher than the residual background signal. If there are too few molecules in the solution, there may be times with no molecule at all in the focus. Roughly, the temporal average of the particle number should be between 0.1 and 1,000. The focal volume being about 1 fl, this corresponds to concentrations between sub-nanomolar ($<10^{-9}$ M) and micromolar (10^{-6} M).

The fluorescence emitted by the molecules in the focal spot is recorded photon by photon. Assuming constant excitation power, the fluctuations of the fluorescence signal are defined as the deviations from the temporal average of the signal:

$$\begin{aligned} \delta F(t) &= F(t) - \langle F(t) \rangle \\ \langle F(t) \rangle &= \tfrac{1}{T} \int_0^T F(t) dt \end{aligned} \tag{2}$$

If all fluctuations arise only from changes in the local concentration δC within the effective volume V_{eff} of the focal spot, the variations may be written as

$$\delta F(t) = \kappa \int_V I_{ex}(\underline{r}) \cdot S\ (\underline{r}) \cdot \delta\big(\sigma \cdot q \cdot C(\underline{r}, t)\big) \cdot dV \tag{3}$$

The individual parameters listed above are mainly describing the probability of exciting a fluorophore within the focal volume and detecting the emitted photon afterwards due to the final detection efficiency of the setup:

κ:	overall detection efficiency
$I_{ex}(r)$:	spatial distribution of the excitation energy with the maximum amplitude I_0
$S(\underline{r})$:	optical transfer function of the objective-pinhole combination. This determines the spatial collection efficiency of the setup and is dimensionless
$\delta(\sigma \cdot q \cdot C(\underline{r},t))$:	dynamics of the fluorophore on the single-particle level
$\delta\sigma$:	fluctuations in the molecular absorption cross-section
δq:	fluctuations in the quantum yield
$\delta C(\underline{r},t)$:	fluctuations in the local particle concentration at time t, e.g. because of Brownian motion

Determining all these parameters is extremely difficult or even impossible. In order to simplify Eq. (3), the convolution factor of the two dimensionless spatial optical transfer functions $I_{ex}(\underline{r})/I_0$ * $S(\underline{r})$ can be combined into a single function $W(\underline{r})$, which describes the spatial distribution of the emitted light. Often, this is approximated by a three-dimensional Gaussian, which is decayed to $1/e^2$ at r_0 in lateral direction and for $z = z_0$ in axial direction:

$$W(\underline{r}) = e^{-2\frac{x^2+y^2}{r_0^2}} \cdot e^{-2\frac{z^2}{z_0^2}} \tag{4}$$

The remaining parameters κ, σ and q can be combined with the excitation intensity amplitude I_0 to give a parameter that determines the photon count rate per detected molecule per second: $\eta_0 = I_0 \cdot \kappa \cdot \sigma \cdot q$. This parameter can be a measure for the signal-to-noise ratio of the measurement and therefore often used for a quick comparison regarding the quality of different adjustments or setups.

Taking this into account, Eq. (3) now reads

$$\delta F(t) = \int_V W(\underline{r}) \delta(\eta C(\underline{r},t)) \cdot dV \tag{5}$$

The normalized autocorrelation function is defined as:

$$G(\tau) = \frac{\langle \delta F(t) \cdot \delta F(t+\tau) \rangle}{\langle F(t) \rangle^2} \tag{6}$$

The signal is analyzed with respect to its self-similarity after the lag time τ. The autocorrelation amplitude G(0) is therefore merely the normalized variance of the fluctuating fluorescence signal $\delta F(t)$.

Substituting Eq. (5) into Eq. (6) yields:

$$G(\tau) = \frac{\int\int W(\underline{r})W(\underline{r}')\left\langle \delta(\eta \cdot C(\underline{r},t))\delta(\eta \cdot C\ (\underline{r}',t+\tau))\right\rangle dVdV'}{\left(\int W\ (\underline{r})\left\langle (\eta \cdot C(\underline{r},t))\right\rangle dV\right)^2} \tag{7}$$

We can now separate the fluctuation term

$$\delta(\eta \cdot C(\underline{r},t)) = C\delta\eta\ + \eta\delta C\,.$$

Obviously, Eq. (7) will be simplified to a large extent, if either the concentration or the parameter η are constant for a given system. Assuming first that the chromophore's fluorescence properties are not changing within the observation time, i.e. $\delta\eta\ = 0$, Eq. (7) can be rewritten as

$$G(\tau) = \frac{\int\int W(\underline{r})W(\underline{r}')\left\langle \delta C(\underline{r},0)\delta C(\underline{r}',\tau)\right\rangle dVdV'}{\left(\left\langle C\right\rangle \int W(\underline{r})dV\right)^2}$$

Considering only particles that are freely diffusing in three dimensions with the diffusion coefficient D, the so-called number density autocorrelation term $\left\langle \delta C(\underline{r},0)\delta C(\underline{r}',\tau)\right\rangle$ can be calculated:

$$\left\langle \delta C(\underline{r},0)\delta C\ (\underline{r}',\tau)\right\rangle = \left\langle C\right\rangle^{-1} \cdot (4\pi D\tau)^{-\frac{3}{2}} \cdot e^{-\frac{(\underline{r}-\underline{r}')^2}{4D\tau}}$$

$$G(\tau) = \frac{\int\int W(\underline{r})W(\underline{r}')\left\langle C\right\rangle \frac{1}{(4\pi D\tau)^{\frac{3}{2}}} \cdot e^{-\frac{(\underline{r}-\underline{r}')^2}{4D\tau}} dVdV'}{\left(\left\langle C\right\rangle \int W(\underline{r})dV\right)^2}$$

$$= \frac{1}{\left\langle C\right\rangle (4\pi D\tau)^{\frac{3}{2}}} \frac{\int\int W(\underline{r})W(\underline{r}') \cdot e^{-\frac{(\underline{r}-\underline{r}')^2}{4D\tau}} dVdV'}{\left(\int W(\underline{r})dV\right)^2}$$

With two more conventions, this finally leads to the expression for the normalized three-dimensional diffusion autocorrelation function for one species of molecules. First, there is the following relationship between the lateral diffusion time τ_D that a molecule stays in the focal volume, and the diffusion coefficient D, which is independent of the particular setup used:

$$\tau_D = \frac{r_0^2}{4 \cdot D} \tag{8}$$

Using this and the following definition of the effective focal volume V_{eff},

$$V_{eff} = \frac{\left(\int W(\underline{r})dV\right)^2}{\int W^2(r)dV} \underset{equation\ 4}{=} \frac{\left(\int e^{-2\frac{x^2+y^2}{r_0^2}} \cdot e^{-2\frac{z^2}{z_0^2}} dV\right)^2}{\int e^{-4\frac{x^2+y^2}{r_0^2}} \cdot e^{-4\frac{z^2}{z_0^2}} dV} \underset{\substack{integration \\ over\ space}}{=} \pi^{\frac{3}{2}} \cdot r_0^2 \cdot z_0 \tag{9}$$

one can finally calculate the autocorrelation function for one freely diffusing species of molecules:

$$G(\tau) = \frac{1}{V_{eff}\langle C\rangle} \cdot \frac{1}{\left(1+\frac{\tau}{\tau_D}\right)} \cdot \frac{1}{\sqrt{1+\left(\frac{r_0}{z_0}\right)^2 \cdot \frac{\tau}{\tau_D}}} \tag{10}$$

The first factor of Eq. (8) is exactly the inverse of the average particle number in the focal volume. Therefore, by knowing the dimensions r_0 and z_0 from calibration measurements, the local concentration of fluorescent molecules can be determined very exactly from the amplitude G(0) of the autocorrelation curve:

$$G(0) = \frac{1}{\langle N\rangle} = \frac{1}{V_{eff} \cdot \langle C\rangle} \quad \Leftrightarrow \quad \langle C\rangle = \frac{1}{V_{eff} \cdot G(0)} \tag{11}$$

The diffusion coefficient can be easily derived from the characteristic decay time of the correlation function τ_D as mentioned above.

The determination of mobility-related parameters of biologically relevant molecules is one of the primary goals of FCS analysis in aqueous solution, and one it is especially suitable for. The sub-micrometer spatial resolution also makes it a useful technique for intracellular measurements. When trying to figure out how biological processes work in detail, it is essential to distinguish between diffusion or active transport, anomalous subdiffusion or even convection. Signal transduction or metabolic regulatory pathways can only be understood once the underlying transport mechanisms are revealed and well characterized. Because supporters of the FCS technique initially had to struggle with background suppression and unwanted photobleaching, the FRAP (fluorescence recovery after photobleaching) method has long been preferred for in vivo motility studies. The latter requires much higher dye concentrations and is thus less liable to suffer from the autofluorescence background (for detailed discussion of FCS vs FPR, see (3)). However, the temporal resolution is mainly limited to the millisecond time scale, so that FCS offers both higher dynamic performance and increased sensitivity. Low chromophore concentrations and laser power suffice for this equilibrium measurement, which is definitely less stressful for the cells under investigation.

However, because of this inherent sensitivity, the proper selection of dyes is crucial. Dyes might interfere with the monitored mechanism or introduce their own dynamics to the system. Many standard dyes, such as Rhodamines and Cyanines, are highly lipophilic and tend to associate to intracellular membranes, inducing severe deviations from free diffusion in the cytosol.

3.2. INTERNAL FLUCTUATIONS (FLICKERING)

Hitherto, it was assumed that the chromophore's fluorescence properties are not changing while it is traversing the laser focus, i.e. $\delta\eta = 0$. Unfortunately, this assumption does not hold for real dyes and higher excitation powers. The most common cause for such a "flickering" in the fluorescence intensity is the transition of the dye to the first excited triplet state. As this transition is a forbidden one by quantum mechanics, the chromophore needs a comparably long time to relax back to the ground state. During these intervals, the dye cannot emit any fluorescence photons and appears dark. Indeed, one can imagine the intersystem crossing as a series of dark intervals interrupting the otherwise continuous fluorescence emission of the molecule on its path through the illuminated region.

Instead of recalculating the correct autocorrelation function for these slightly altered conditions, a much simpler and more general form that can be used. If intra- or intermolecular reactions give rise to fluorescence fluctuations on time-scales much faster than those caused by the mere movement of the particles, a separation of the dynamics is possible:

$$G_{total}(\tau) = G_{motion}(\tau) \cdot X_{kinetics}(\tau) \tag{12}$$

Of course, this assumption holds only for situations in which the diffusion coefficient is unaltered by the reaction (4). The triplet blinking mentioned above can be described by a simple exponential decay $X_{triplet}(\tau)$

$$X_{triplet}(\tau) = 1 - T + T \cdot e^{-\frac{\tau}{\tau_{triplett}}}, \tag{13}$$

which shows as an additional shoulder in the measured curves for short time scales. It is also possible to normalize this expression by dividing by (1 − T) [5, 6]. Inserting Eqs. (8) and (10) into Eq. (9), the overall autocorrelation function for a freely diffusing dye can be written as:

$$\begin{aligned} G_{total}(\tau) &= X_{kinetics}(\tau) \cdot G_{motion}(\tau) \\ &= (1 - T + T \cdot e^{-\frac{\tau}{\tau_{triplett}}}) \cdot \frac{1}{V_{eff}\langle C \rangle} \cdot \frac{1}{\left(1 + \frac{\tau}{\tau_D}\right)} \cdot \frac{1}{\sqrt{1 + \left(\frac{r_0}{z_0}\right)^2 \cdot \frac{\tau}{\tau_D}}} \end{aligned}$$

The triplet blinking can be generalized to any fast photophysical phenomenon that results in reversible transitions between a bright – fluorescent – state B, and a dark state D in which no photons are emitted:

$$B \underset{k_B}{\overset{k_D}{\rightleftarrows}} D$$

In analogy to Eq. (11), one can write:

$$X_{flickering}(\tau) = 1 - F + F \cdot e^{-\frac{\tau}{\tau_F}} \tag{14}$$

with $\tau_F = \dfrac{1}{k_D + k_B}$: relaxation time

$F = \dfrac{k_D}{k_D + k_B}$: average fraction of dark molecules

$\hat{=}$ average fraction of time a molecule spends in the dark state

If the dark state D is not completely dark, the molecular emission yields η_i of the two states have to be taken into account to get the correct expression for F:

$$F = \frac{k_D k_B (\eta_B - \eta_D)^2}{(k_D + k_B)(k_B \eta_B^2 + k_D \eta_D^2)}$$

There may also be reactions, however, that do influence the mobility of the particle in some way. In this case, Eq. (9) must be generalized to take into account all different kinds of possible motion, weighted with the relative emission rate:

$$G_{motion}(\tau) = \frac{1}{V_{eff}} \frac{\sum_{\substack{all\ different \\ species\ \ i}} \eta_i^2 \langle C_i \rangle M_i(\tau)}{\left(\sum_i \eta_i \langle C_i \rangle \right)^2} \tag{15}$$

The motility-term $M_i(\tau)$ must be adapted to the particular case. Besides the free three-dimensional diffusion discussed above, there are numerous other possibilities:

Free 3D diffusion: $$M_i(\tau) = \frac{1}{\left(1 + \frac{\tau}{\tau_{d,i}}\right) \cdot \sqrt{1 + \left(\frac{r_0}{z_0}\right)^2 \cdot \frac{\tau}{\tau_{d,i}}}} \tag{16a}$$

Free 2D membrane diffusion $$M_i(\tau) = \frac{1}{\left(1 + \frac{\tau}{\tau_{d,i}}\right)} \tag{16b}$$

Active transport with velocity v_i $$M_i(\tau) = e^{-\left(\frac{\tau \cdot v_i}{r_0}\right)^2} \tag{16c}$$

The triplet state parameters depend mainly on the excitation intensity, but also the environment of the dye may have some influence. Molecular oxygen is one of the most common triplet state quenchers, but also some heavy metal ions have been shown to alter the triplet state kinetics [4]. This sensitivity to ion concentrations could potentially be useful for probing the intracellular environment.

Among other mechanisms leading to fast reversible changes in the fluorescence emission yield are intramolecular reversible quenching due to electron transfer [6, 7], light-induced blinking due to a protonation reaction in several GFP mutants [9] and photoisomerization as observed for Cyanine dyes [10]. Also, dynamic FRET (fluorescence resonance energy transfer) on a single molecule level may be considered, although the underlying mechanism is different.

3.3. ANOMOLOUS DIFFUSION

In natural membranes and inside living cells, the ideal case of Brownian diffusion does often not apply, because the movement of the particles is restricted or the mobility shows strong local changes [11, 12]. These deviations may be due to the confinement of the particles within cellular compartments or lipid domains in membranes, but also to nonspecific interaction of the diffusing molecules with other molecules or cellular structures. Regarding diffusion within membranes, the complex composition might also lead to an altered topology and thus to a changed mobility. Up to now, this phenomenon of anomalous diffusion is not completely understood. For various reasons, the mean square displacement is no longer directly proportional to time, but rather depends on t^{α}, so that in above equations $\tau/\tau_{d,i}$ has to be replaced by $(\tau/\tau_{anom,i})^{\alpha}$ [13]:

$$\left\langle r^2 \right\rangle \propto t^{\alpha} \quad \Leftrightarrow \quad \frac{\tau}{\tau_{d,i}} \rightarrow \left(\frac{\tau}{\tau_{anom,i}} \right)^{\alpha} \quad with \quad \alpha < 1$$

No conventional diffusion constant can be defined in this case, and $\tau_{anom,i}{}^{\alpha} = r_0^2/\Gamma_i$ with Γ_i being a transport coefficient of fractional time dimension.

Local confinement of the diffusion to organelles of a size comparable to that of the focal volume element requires even more sophisticated models. For example, trying to describe the particle motion within neuronal dendrites by the models mentioned above will fail completely. In such cases, complex non-analytic solutions of the correlation function have to be considered to appropriately model the biological situation [14].

It is to some extent possible to distinguish the different molecular processes by the characteristic shape of the autocorrelation function. As a rule of thumb, the curves for anomalous subdiffusion decay more gradually than those for free diffusion, whereas active transport leads to a steeper, more abrupt decay. The latter may also apply for attractive or repulsive interactions between the particles under study.

3.4. FLUORESCENCE CROSS-CORRELATION SPECTROSCOPY (FCCS)

A very important feature of FCS is its ability to probe molecular interactions between different species *in situ*. This can be done by the spectral cross-correlation mode (FCCS). Two spectrally different dyes are excited within the same detection element using two overlapping laser beams and separate detection pathways [15, 16]. A vast number of experiments have been carried out applying this technique to different kinds of reactions, also in the cellular environment.

The theoretical formalism can be briefly described in analogy to the autocorrelation theory. Generalizing Eq. (5), the fluctuating signals recorded in the two detection channels are given as

$$\begin{aligned} \delta F_1(t) &= \int W_1(\underline{r})\eta_1 \delta\left(C_1(\underline{r},t) + C_{12}(\underline{r},t)\right)dV \\ \delta F_2(t) &= \int W_2(\underline{r})\eta_2 \delta\left(C_2(\underline{r},t) + C_{12}(\underline{r},t)\right)dV \end{aligned} \tag{17}$$

with

$W_i(\underline{r})$	spatial intensity distribution of the fluorescence emission for species i (i = 1,2)
$C_i(\underline{r},t)$	concentrations for the single labeled species i (i = 1,2)
$C_{12}(\underline{r},t)$	concentration of the double-labeled species

The motion of the different components is supposed to be described by the term $M_i(\tau)$ (cf. Eq. (12)). Assuming ideal conditions, where both channels have identical $W_i(\underline{r})$ (and thus the same effective volume element V_{eff}), fully separable emission spectra and a negligible emission-absorption overlap integral, the following correlation curves can be derived [16]:

Autocorrelation: $$G_i(\tau) = \frac{\left(\langle C_i\rangle M_i(\tau) + \langle C_{12}\rangle M_{12}(\tau)\right)}{V_{eff}\left(\langle C_i\rangle + \langle C_{12}\rangle\right)^2} \quad with \quad i = 1,2$$

Crosscorrelation: $$G_{\times}(\tau) = \frac{\langle C_{12}\rangle M_{12}(\tau)}{V_{eff}\left(\langle C_1\rangle + \langle C_{12}\rangle\right)\left(\langle C_2\rangle + \langle C_{12}\rangle\right)} \tag{18}$$

There is, however, one additional advantage of this technique in comparison to the autocorrelation mode: If there is no reaction-induced quenching or fluorescence enhancement, and no particle exchange in the sample, the amplitude of the cross-correlation function is directly proportional to the concentration of double labeled particles. Knowing the amplitudes of the autocorrelation curves and thus, the concentrations of both single-labeled species, the concentration $\langle C_{12}\rangle$ can be determined from Eq. (18) as follows:

$$\langle C_{12} \rangle = \frac{G_{\times}(0)}{G_1(0) \cdot G_2(0) \cdot V_{eff}} \tag{19}$$

A correct evaluation of concentrations measured by cross-correlation requires good prior knowledge of the system or a careful calibration procedure of the two basic parameters resulting from FCS analysis, the effective volume element and the lateral characteristic residence time.

The beauty of FCCS is that it allows to also quantify the stoichiometry of molecular interactions, through the parameter of molecular brightness. We successfully demonstrated that by studying the complex calcium-dependent binding of calmodulin (CaM) to Ca21/CaM-dependent protein kinase II (CaMKII) where up to 12 red-labeled CaMs can bind to a single green-labeled dodecameric CaMKII holoenzyme [17, 18].

3.5. FCS WITH TWO-PHOTON EXCITATION

The experimental realization of a dual-color cross-correlation setup is very demanding, because it also requires exact spatial superposition of the two laser beams, such that the focal volumes overlap. Checking and optimizing the alignment either directly by measuring the illumination profiles with a specifically designed focus scanner or indirectly by FCS calibration measurements can be quite tedious. Using two-photon excitation, it is possible to excite two carefully selected spectrally different dyes with only one IR laser line.

Two-photon excitation requires the absorption of two photons of theoretically double the wavelength usually required for the excitation, within the tiny time interval of about 1 fs (10^{-15} s). In order to get a reasonable probability of such three-particle events, the photon flux must be extremely high. This means, that not only a high output power is required, but usually also pulsed excitation is used, to get an even higher photon density per pulse relative to the average output power. The joint probability of absorbing two photons per excitation process is proportional to the mean square of the intensity. This results in inherent depth discrimination such that only the immediate vicinity of the objective's focal spot receives sufficient intensity for significant fluorescence excitation.

Intracellular measurements primarily benefit from this inherent axial resolution, because under two-photon excitation, bleaching really occurs only in the focal region [19]. In contrast to this, under one-photon excitation, all fluorophores residing in the double cone above and below the focal spot are excited and bleached, the depth discrimination by the pinhole is quasi an artificial effect, restricted to the detection signal. As cells and tissue also tend to be more tolerant to near infrared radiation and there is less autofluorescence and scattering, multi-photon excitation is a very attractive alternative for FCS applications in living cells and tissues [20].

Unfortunately, determining the two-photon excitation spectra of different dyes turns out quite difficult. As two-photon excitation is a quantum mechanically forbidden process, the selection rules differ greatly from those valid for one-photon processes. The idea of simply taking photons with half the energy required for the transition to the excited state often gives very unsatisfactory results. The experimentally determined

two-photon excitation spectrum very often exhibits a significant blue shift relative to the one-photon spectrum, indicating a first transition to a higher excited state. After internal relaxation, the system finally returns to the same excited state as for the one-photon process, and the emission spectra are the same. Maybe because of this complicated, symmetry forbidden absorption process in addition to the pulsed excitation, the maximum number of photons that a dye molecule emits before undergoing photodestruction is significantly lower than for the quantum mechanically allowed processes. Moreover, due to the quadratic intensity dependence, the range of applicable powers is much narrower [20].

As mentioned above, this dye-specific blue-shift can be used to simultaneously excite two dyes with different emission characteristics to perform two-photon dual color cross-correlation experiments. Only one laser line is required for excitation, and the inherent axial resolution renders pinholes redundant, so that adjustment is greatly simplified [21].

4. Scanning the FCS Probe Volume

Due to commercial availability, confocal FCS has become a standard tool in life-sciences. However, its application to systems more complex than freely diffusing molecules in buffer solution, such as cells or biological membranes, is challenged by several limitations of this technique.

First, there are optical artifacts [22] such as varying cover slide thickness, refractive index mismatch, optical saturation or aberrations which change the size of the detection volume. This precludes a precise calibration, necessary for quantitative concentration or diffusion measurements. Second, the slow diffusion in biological samples demands long measurement times and the long residence times of the molecules in the detection volume promote photobleaching. Measurements in biological membranes bear the additional complication that even tiny membrane movements or instabilities lead to severe artifacts [23].

These limitations can be greatly reduced, if not overcome, if the detection volume is scanned during the measurement. This approach is called scanning FCS [24–31]. The advantages are as follows: sampling of a larger volume increases the statistical accuracy for slowly moving molecules and leads to shorter measurement times; short residence times in the detection volume reduce the effect of photobleaching; and the scan speed can be determined with a high accuracy, eliminating the need of calibrating the detection volume.

On biological membranes, where diffusion is usually very slow, the application of scanning FCS is especially beneficial. Here, an alternative implementation of a moving detection volume has proven very useful: Choosing a scan path that is perpendicular to the membrane plane eliminates the effect of membrane movements and instabilities [31].

Scanning FCS has been implemented with a variety of scanpaths, such as small circles [24, 30] for exact and absolute diffusion measurements or large circles or single lines [32, 33] to reduce photobleaching and increase the statistics for slow moving molecules. By scanning a whole image instead of just a line, raster image correlation

spectroscopy (RICS) [34] allows constructing diffusion and concentration maps of whole cells and bridges the gap between FCS and image correlation spectroscopy (ICS).

In the following we will introduce as examples three implementations of scanning FCS: small-circle scanning FCS in solution, line-scan FCS on membranes and scanning FCS with a scanpath perpendicular to a membrane to reduce the influence of instabilities.

4.1. SMALL-CIRCLE SCANNING

In small-circle canning FCS [24] (Fig. 2) the radius of the circle is of the order of the size of the detection volume and the scanning frequency is as high as possible, preferably faster than 1 kHz. The autocorrelation curves show oscillations which reflect the periodic movement of the detection volume. The peaks of this correlation curve lie on an autocorrelation curve corresponding to a fixed detection volume that the beam is covering during its revolution. The minima lie on a cross-correlation curve between two detection volumes on opposite positions of the circle (compare section 5.1). The radius R of the circle can be determined with a high precision by scanning over a grid with a fixed line-spacing. The determination of this spatial parameter replaces the calibration of the size of the detection volume in static confocal FCS. Fitting the experimental correlation curve with the proper model therefore allows precise determination of diffusion coefficients, not corrupted by optical artifacts and without calibration of the detection volume. In this way, small-circle scanning FCS is a technique similar to dual-focus FCS (see section 5.1). With this technique, diffusion coefficients for various common dyes were characterized [24].

4.2. LINE-SCAN FCS

A scanning FCS scheme, ready to be used with a commercial laser scanning microscope, is line-scan FCS [33]. The detection volume is scanned repeatedly in the membrane. Each line can be used to calculate a correlation curve. Since the detection volume is a different positions at different times, this corresponds to a spatial correlation of the signal. In addition, the cross-correlation of each line with every other line can be calculated. In this way the complete spatio-temporal correlation can be determined (Fig. 3). Since the length of the scanpath, and therefore the scan-velocity, can be easily determined, also in line-scan FCS the detection volume needs not be calibrated, which greatly increases the accuracy. Line-scan FCS measures diffusion coefficients and concentrations within minimal measurement times due to the acquisition along the whole line, which would correspond to a simultaneous measurement with many confocal detection volumes. An application of line-scan FCS was the determination of the temperature dependence of diffusion coefficients in membranes [33]; a task not accomplishable by static confocal FCS due to temperature induced aberrations and therefore changes in the size of the detection volume.

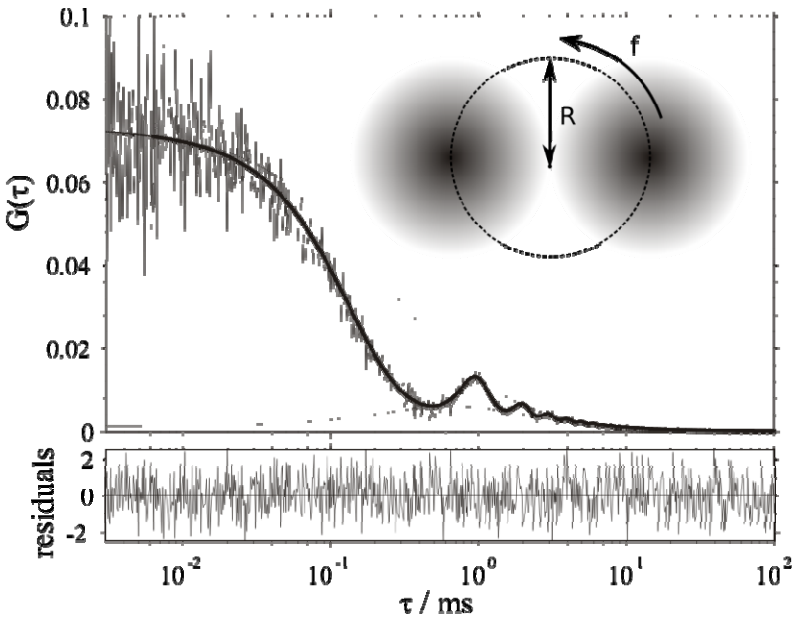

Figure 2. Small-circle scanning FCS for robust and precise determination of diffusion coefficients. (Inset) The laser beam is scanned in a circle with frequency f and radius R which is comparable to the measurement volume size r_0. (Graph) The auto-correlation of the fluorescence signal (sample: eGFP in buffer solution) is modulated as a result of scanning. The upper and lower envelopes correspond to the auto-correlation at a fixed position and the spatial cross-correlation at a distance equal to the diameter 2R of the scanned circle, respectively. From a fit of the data the diffusion coefficient D = 92.8 m²/s and the volume size r_0 = 0.29 μm were determined. Scanning parameters: f = 1 kHz and R = 0.3 μm.

4.3. SCANNING FCS PERPENDICULAR TO THE MEMBERANE PLANE

If accurate positioning of the detection volume with respect to the membrane is difficult to achieve or stability cannot be guaranteed, scanning FCS through a vertical membrane is a valuable alternative. This approach was used by Ruan [26] to measure membrane diffusion in presence of an excess of free dye in solution which almost concealed the membrane bound fluorophores. Correlation of corresponding time windows of a circular scan resulted in a series of correlation curves. Due to the scanning, the membrane cannot be missed and some correlation curves in the series displayed membrane diffusion.

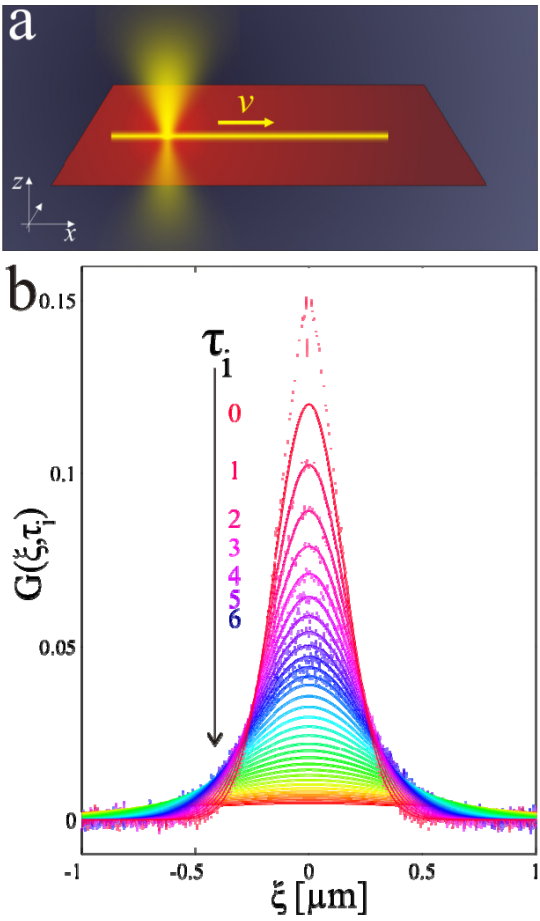

Figure 3. Line-scan FCS on horizontal membranes. (a) In line-scan FCS the detection volume is scanned repeatedly in a linear fashion in the membrane with a scan velocity v. (b) Spatio-temporal correlation curves and fit. Diffusion of the molecules in the membrane results in a decreasing amplitude of the correlation curves and a broadening with increasing τ (time difference between cross-correlated scans).

An extension of this approach, where the membrane contributions from each scan are added up, allows correcting for membrane movements (Fig. 4) [31]. Very long measurement times are therefore feasible, allowing the measurement of very slow diffusion as found for proteins in yeast cell membranes. In addition, correlation curves are not influenced by membrane undulations any more.

The simple implementation of scanning FCS with a commercial laser scanning microscope with its selection of multiple laser lines permits the use of fluorophores spanning the whole visible range. Scanning dual-color cross-correlation enables quantitative binding measurements on membranes. Alternating excitation to avoid spectral cross talk is easily achieved by scanning every other line with a different laser. Note that the risk

of false positive cross-correlation due to membrane movements is also greatly reduced since they are corrected for.

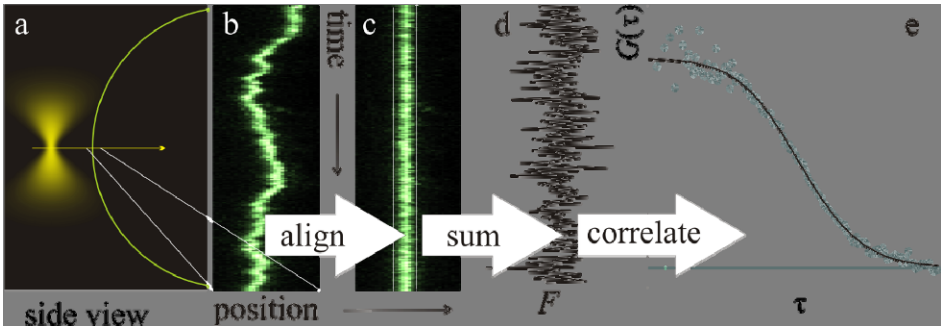

Figure 4. Scanning FCS perpendicular to the membrane plane. The detection volume is scanned repeatedly through the vertical membrane (a). Line scans are arranged beneath each other (b), the membrane is clearly visible. Membrane movements are corrected for (c). For each line scan, the photons detected during the transient of the membrane are counted to result in one point of the intensity trace (d). The fluctuations in the intensity trace are due to the diffusion of the fluorophores through the detection area, which is defined by the intersection of the scanned line with the membrane. The intensity trace can be correlated to result in the auto-correlation curve (e)

5. New Developments in FCS

Several limitations of FCS have been overcome by the various implementations of scanning FCS. But also other novel implementations of FCS bear great potential to reduce artifacts, improve the accuracy and to extend the use FCS to systems previously not accessible. An important extension of FCS, nowadays realized with several different detection schemes, is dual-focus FCS. Here, the use of two detection volumes in a known distance overcomes the need of calibrating the size of the detection volume. Excitation or detection schemes alternative to the usual confocal configuration create detection volumes of different shapes. FCS with Stimulated Emission Depletion (STED-FCS), and FCS using sub wavelength apertures (FCS using zero-mode waveguides and FCS using probes for near-field scanning optical microscopy (NSOM)) lead to tiny detection volumes necessary to probe highly concentrated molecules or to detect spatial heterogeneities below the diffraction limit cite. FCS using total internal reflection excitation (TIR-FCS) or supercritical angle detection (SA-FCS) only probe the close vicinity of the cover slide and can be used to study biological membranes even with an excess of fluorescent molecules in the solution above.

5.1. DUAL-FOCUS FCS

The idea of dual-focus FCS is to use two detection volumes in a well known distance d (Fig. 5). From the intensities $F_1(t)$ and $F_2(t)$, measured in the two detection volumes, two similar auto-correlation curves $G_{AC}(\tau)$ can be calculated. In addition, the spatial cross-correlation curve, defined as

$$G_{CC}(\tau) = \frac{\langle \delta F_1(t) \cdot \delta F_2(t+\tau) \rangle}{\langle F_1(t) \rangle \langle F_2(t) \rangle} \tag{20}$$

can be inferred. Its shape is determined by the distance d. For Gaussian detection areas, $G_{CC}(\tau)$ is found to be:

$$G_{CC}(\tau) = G_{AC}(\tau) \cdot \exp\left(- \frac{d^2}{4D\tau + r_0^2} \right) \tag{21}$$

Therefore by analyzing auto- and cross-correlation curves together, the size of the detection volume r_0 and the diffusion coefficient D can be determined directly from the fit, once d is known. This is not possible with one-focus measurements, since in the fitting function (Eq. (10)) only the ratio of D and r_0^2 appear in form of the diffusion time τ_D.

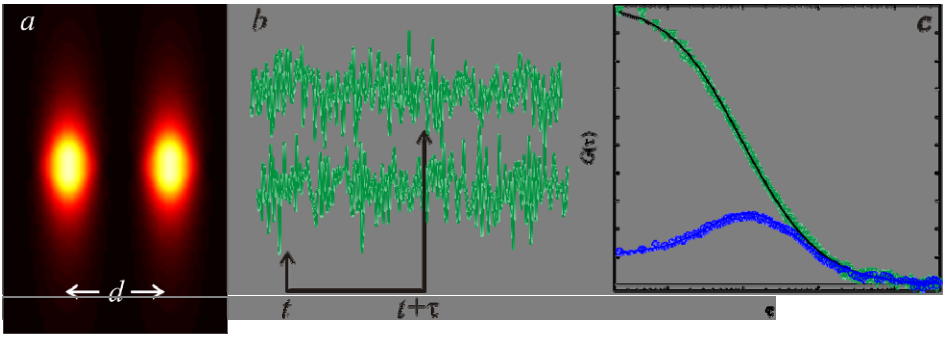

Figure 5. Dual-focus FCS. (a) From two detection volumes in a distance d two intensity traces $F_1(t)$ and $F_2(t)$ are measured (b). (c) The spatial cross-correlation curve (o) exhibits a maximum at a lagtime τ corresponding to the average time a molecule needs to diffuse from one into the other detection volume. A combined fit of the auto- and cross-correlation curve allows determination of diffusion coefficients, concentrations and also the size of the detection volume, rendering a previous calibration measurement obsolete.

Spatial cross talk from one detection area into the other would seriously complicate the data analysis and should be avoided. This is usually achieved by alternating excitation. Repeatedly, the excitation in the foci is switched on in an alternating fashion. The photons can then be associated with their corresponding detection area depending on their arrival times.

If the distance between the detection areas is well known, dual-focus FCS is a very accurate method for calibration-free diffusion and concentration measurements. E.g. it allows monitoring conformational changes of proteins upon calcium binding via a change in the diffusion coefficient [35]. Two detection volumes can be generated in different ways. The straight forward approach is to use two incident laser beams at slightly different angles. However, their distance might vary due to instabilities of the setup. This is avoided by using a Normanski-prism (usually used for differential interference contrast microscopy), which causes a similar, but fixed angle between two

co-propagating beams with orthogonal polarizations [36]. An alternative, very flexible approach is to just use different areas of a CCD-chip under homogeneous (e.g. TIRF) illumination.

Dual-focus FCS does not only measure diffusion coefficients with a high accuracy, it also can quantify flow rates much better than single-focus FCS. In case of flow, the forward cross-correlation curve and the backward cross-correlation curve (Eq. (20) with indices 1 and 2 exchanged) are not the same any longer but split up, even for comparatively slow flow rates [37].

5.2. STED-FCS

Stimulated Emission Depletion (STED) microscopy uses a confocal detection volume and a second laser with a beam profile in the shape of a doughnut [38]. This second light pattern suppresses fluorescence emission due to depopulation of the excited state via stimulated emission. Since it features zero intensity in the center, fluorescence is only emitted from a central region of the detection volume of 20–50 nm in diameter. This approach has been used to realize far-field FCS with a subdiffraction detection volume [39].

Due to the small size of the detection volume in STED-FCS, it is optimally suited to study small spatial heterogeneities, such as lipid rafts [40]. Eggeling et al. [41] could show that certain raft-associated lipids, such as the ganglioside GM1, are transiently trapped in domains of <20 nm, whereas non-raft lipids show free diffusion even on these length scales. Using confocal microscopy, this spatial range is more difficult to probe, since only average diffusion coefficients can be measured. However, also the use of confocal detection volumes of different sizes [42] allows investigation of transient trapping of molecules.

5.3. FCS USING SUB-WAVELENGTH APERATURES

An approach alternative to STED to create detection volumes below the diffraction barrier is to physically confine the light field. Although light cannot propagate through sub-wavelength apertures, it leaves the opening as an evanescent wave.

This principle is the basis for near field scanning optical microscopy (NSOM), which usually uses optical fibers coated with a metallic film with a sub wavelength aperture. For NSOM-FCS the tip is not scanned but positioned at the target, e.g. at biological membranes. The resulting detection volume is significantly smaller than that of confocal FCS [43].

Even more impressive reduction in the detection volume can be achieved with so called zero mode waveguides which are sub wavelength optical nanostructures. Small holes (diameter 35–200 nm) are fabricated in an opaque aluminum layer on fused silica and are illuminated from below. Characteristic decay lengths of the evanescent field depend on the diameter and range from 15 to 35 nm, creating detection volumes three orders of magnitude below those in confocal FCS [44]. Such small detection volumes are of special use in dual-color FCS, since they allow binding studies under high concentration as necessary to investigate weak binding [45]. Zero-mode waveguides

have also been used to study heterogeneities in cell membranes as described in the paragraph 'STED-FCS' [46].

5.4. SURFACE-CONFINED FCS

A flat detection volume is very useful for the study of biological membranes in presence of fluorescence from the surrounding medium. In cellular membranes this can be cytosolic fluorescent proteins or bright fluorescent vesicles such as endocytotic vesicles. Also to study membrane interactions of molecules with a low membrane affinity requires an excess of free molecules above the membrane. With a confocal detection volume the free fluorophores tend to mask the contributions from the membrane.

Close to a glass/water interface, an evanescent field can be used to excite only a small slice above the interface (total internal reflection (TIR) excitation, reviewed e.g. in [26]). The exclusive detection of surface generated fluorescence leads to a similar surface selectivity (supercritical angle fluorescence (SAF) detection [48]).

In FCS using total inter reflection excitation (TIR-FCS), the excitation light incides on the glass/water interface with an angle larger than the critical angle, given by

$$\theta_C = \arcsin(n_1 / n_2), \tag{22}$$

with n_1 and n_2 being the refractive index of the liquid and the substrate, respectively. The light is then reflected totally, creating an exponentially decaying evanescent wave above the substrate with a decay length of

$$d = \frac{\lambda}{4\pi}\left(n_2^2 \sin^2\theta - n_1^2\right)^{-1/2} \tag{23}$$

d can be significantly below 100 nm and depends on the vacuum wavelength λ, the refractive indices and, most importantly, the angle of incidence θ. Since only fluorophores in the evanescent field are excited, an excellent surface selectivity is achieved.

There are two different approaches for the practical realization of a TIR-FCS setup: a prism- and an objective-based setup [47]. In the first case a prism is used to generate high enough incidence angles and fluorescence is collected by a microscope objective opposite to the prism [49]. In the second case the laser is focused through the periphery of a high numerical aperture objective, which is directly coupled to the surface of interest, to generate internal reflection. Emission is collected with the same objective [50].

Since the TIR-excitation profile is rather large (several μm), a pinhole in the image plane is usually used for lateral confinement [47]. For diffusion measurements in membranes, a tight lateral confinement is especially important to obtain reasonable diffusion times [51, 52]. Instead of a physical pinhole, pixels of a CCD-camera can be used for confining the detection volume [53]. The drawback of using pinholes is significant out-of-focus photobleaching. Many fluorophores will get bleached in the large excitation spot before they can enter the detection area. As this can be a serious

limitation in the study of membrane diffusion, TIR-FCS is well suited to study binding kinetics [54, 55].

In supercritical angle FCS (SA-FCS) [48] only surface generated fluorescence is detected. This is achieved by blocking all light collected in angles below the critical angle θ_C (Eq. (22)). Since only fluorophores in close vicinity to the substrate emit into supercritical angles, a high surface selectivity is achieved.

Supercritical angle detection is efficiently realized with a parabolic mirror element. The combination with an aspheric lens allows excitation with a focused laser beam. The vertical confinement in supercritical detection is similar to TIRF, but much better lateral confinement of the excitation profile is achieved, facilitating diffusion measurements in membranes. The excellent surface selectivity combined with the flexibility in excitation renders supercritical angle FCS a promising technique for membrane measurements. However, a supercritical angle objective is not yet commercially available, and experiments performed so far [48] have used a prototype.

6. FCS in Complex Specimen

FCS has only recently been applied to living multicellular organisms [56, 57], a real challenge for this technique: living organisms are intrinsically mobile and unstable and thick tissue distorts the FCS detection volume which results in poor signal and errors in the measurement parameters. However, by using FCS techniques less sensitive to instabilities and by restricting the measurement to the first few layers of cells, meaningful measurements in whole organisms are possible.

Recently, we applied FCS to quantitatively study the formation of morphogen Fgf8 in living zebrafish embryos [56]. Using confocal FCS, the diffusion coefficient of GFP-labeled Fgf8 in the extracellular space in between the cells was measured. Comparing this value to control measurements on GFP, it could be shown that Fgf8 diffuses freely as single molecules and is not part of a larger complex, or, as suggested before, is associated to vesicles. A significant contribution of directed motion could be excluded. Concentration measurements at different distances from the source of Fgf8-GFP revealed that Fgf8 indeed forms a stable concentration gradient. A rather simple model for morphogen movement can explain the experimental results: Fgf8 is produced locally, diffuses through the extracellular space in form of single molecules and binds to its receptors. Via endocytosis, the Fgf8 is cleared from the extracellular space. In addition, via interactions with the receptors the concentration is read out and the signaling cascade is started. Predictions of this model, such as the degradation rate of the Fgf8 or the dependence of the shape of the gradient on modifications of the rate of endocytosis were tested in control experiments.

In a related work [57], dual color scanning FCS with alternating excitation was combined with dual-focus scanning FCS and static confocal FCS to directly measure the binding affinity of Fgf8 to its receptors in the living embryos (Nature methods paper). Static confocal FCS alone would have failed in this task, since measurements on membranes are especially sensitive with respect to instabilities, they are not very accurate due to distortions in deeper tissue and the fluorescent proteins eGFP and mRFP, which were used to label the two binding partners, exhibit strong spectral cross talk. On the other hand, the use of dual-color scanning FCS avoids a calibration of the

detection volume and therefore is accurate even in case of distortions. Dual-color scanning FCS with alternating excitation can then be used to quantify the concentrations of the receptor and the receptor–ligand complex in the membranes of the cells, not influenced by membrane movements or spectral cross-talk. Finally, static FCS in the extracellular space measures the free ligand concentration, the last parameter necessary to calculate dissociation constants. These measurements could show that the two receptors Fgfr1 and Fgfr4 have similar binding affinities to Fgf8 in vivo. This is in contrast to previous in vitro measurements which apparently cannot capture the full complexity of a living organism.

References

1. Madge, et al., Phys. Rev. Lett. 29, 705 (1972)
2. Rigler, R and Mets, Ü., Proc. SPIE 1921, 239 (1993)
3. Petersen, N.O. and Elson, E.L., Meth. Enzymol. 130, 454 (1986)
4. Widengren, J. and Rigler, R.J., Fluoresc. 4, 255 (1994)
5. Widengren, J. et al., J Phys. Chem. 99, 13368 (1995)
6. Schwille, P.; et al., PNAS 97, 151 (2000)
7. Widengren, J. and Rigler, R., J Fluoresc. 7, 211 (1997)
8. Edman, L. et al., PNAS 93, 6710 (1996)
9. Haupts, U.et al., PNAS 95, 13573 (1998)
10. Widengren, J. and Schwille, P., J. Phys. Chem. A 104 (27) 6416 (2000)
11. Schwille, P et al., Cytometry 36, 176 (1999)
12. Wachsmuth, M. et al., J. Mol. Biol. 298, 677 (2000)
13. Feder, T.J. et al., Biophys. J. 70, 2767 (1996)
14. Gennerich, A. and Schild, D., Biophys. J. 79, 3294 (2000)
15. Schwille, P. et al., Biophys. J. 72, 1878 (1997)
16. Schwille P., Cell Biochem. Biophys. 34, 383 (2001)
17. Kim, S. et al., PNAS 101, 105 (2004)
18. Kim, S. et al., Biophys. J. 88, 4319 (2005)
19. Denk,W. et al., Science 248, 73 (1990)
20. Schwille, P. et al., Biophys. J. 77, 2251 (1999)
21. Heinze, K.G. et al., PNAS 97, 10377 (2000)
22. Enderlein, J. et al., Chem. Phys. Chem. 6, 2324 (2005)
23. Ries, J. and Schwille, P., PCCP 10, 3487 (2008)
24. Petrasek, Z. and Schwille, P., Biophys. J. 94, 1437 (2008)
25. Petrasek, Z. et al., Methods Enzymol. 472, 317 (2010)
26. Ruan, Q.Q. et al., Biophys. J. 87, 1260 (2004)
27. Petersen, N.O., Biophys. J. 49, 809 (1986)
28. Petersen, N.O. et al., Biophys. J. 49, 817 (1986)
29. Berland, K.M. et al., Biophys. J. 71, 410 (1996)
30. Skinner, J.P. et al., Biophys. J. 89, 1288 (2005)
31. Ries, J. and Schwille, P., Biophys. J. 91, 1915 (2006)
32. Petrasek, Z. et al., Biophys. J. 95, 5476 (2008)
33. Ries J. et al., Biophys. J. 96, 1999 (2009)
34. Digman, M.A. et al., Biophys. J. 89, 1317 (2005)

35. Dertinger, T. et al., Ultrasensitive and single-molecule detection technologies II, San Jose, California, USA, 6444, 64440H (2007)
36. Dertinger, T. et al., Chem. Phys. Chem. 8, 433 (2007)
37. Brinkmeier, M. et al., Anal. Chem. 71, 609 (1999)
38. Klar, T.A. et al., PNAS 97, 8206 (2000)
39. Kastrup, L. et al., Phys. Rev. Lett. 94, 178104 (2005)
40. Rajendran, L. and Simons, K. , J. Cell Sci. 118, 1099 (2005)
41. Eggeling, C. et al., Nature 457, 1159 (2009)
42. Lenne, P.F. et al., EMBO J. 25, 3245 (2006)
43. Vobornik, D. et al., Appl. Phys. Lett. 93, 163904 (2008)
44. Levene, M.J. et al., Science. 299, 682 (2003)
45. Wenger, J. et al., Opt. Expr. 14, 12206 (2006)
46. Wenger, J. et al., Biophys. J. 92, 913 (2007)
47. Thompson, N.L. and Steele, B.L., Nat. Prot. 2, 1754 (2007)
48. Ries, J. et al., Biophys. J. 95, 390 (2008)
49. Thompson, N.L. and Axelrod, D., Biophys. J. 43, 103 (1983)
50. Hassler, K., et al., Biophys. J. 88, L01 (2005)
51. Ohsugi, Yu., et al., Biophys. J. 91, 3456 (2006)
52. Ries, J. et al., Biophys. J. 94, 221 (2008)
53. Kannan, B. et al., Anal. Chem. 79, 4463 (2007)
54. Lieto, A.M. et al., Biophys J. 85, 3294 (2003)
55. Hansen, R.L. and Harris, J.M., Anal. Chem. 70, 4247 (1998)
56. Yu, S.R., et al. Nature 461, 533 (2009)
57. Ries, J., et al., Nat. Methods 6, 643 (2009)

NANOSCOPY USING LOCALIZATION AND TEMPORAL SEPARATION OF FLUORESCENCE FROM SINGLE MOLECULES

C. STEINHAUER[1], C. FORTHMANN[1], R. JUNGMANN[2], J. VOGELSANG[1], F.C. SIMMEL[2], P. TINNEFELD* [1]
[1]*Angewandte Physik – Biophysik & Center for Nanoscience, Ludwig-Maximilians-Universität München, Amalienstrasse 54, 80799 München, Germany*
[2]*Physics Department E14 & Center for Nanoscience, Technische Universität München, James-Franck-Straße 1, D-85748 Garching, Germany*

1. Introduction

Since the development of the first techniques [1, 2] that bypass the diffraction limit postulated by Ernst Abbe in 1873, so called superresolution microscopies have spread rapidly diverging into different variants that are capable of resolving details smaller than 200 nm. This article focuses on those based on the subsequent localization of single molecules. Therein, most molecules are prepared in a non-fluorescent dark state, leaving only a few single molecules fluorescing, which can be localized by fitting a two dimensional Gaussian function to their respective point spread functions (PSF).

To allow resolution enhancement, two criteria must be met: (i) Sufficient temporal separation of ON-states and (ii) high precision of the localization of the single molecules influenced mainly by photophysical parameters but also by mechanical stability.

In this article, we discuss the effect of different parameters on the obtainable resolution for one recently developed superresolution technique termed Blink-Microscopy [3]. Many of these parameters, i.e. the ON/OFF-time ratio, label density, photon numbers, noise and frame rate are, however, also crucial for other superresolution techniques based on the subsequent localization of single moleucles. We provide a guide to achieve the best possible resolution depending on the parameters immanent to certain experimental conditions which can be very helpful when planning a superresolution experiment.

The improvement of optical microscopy towards higher resolution has been subject to extensive research over the past years. The diffraction limit of light prohibits resolving details smaller than half its wavelength, resulting in a fundamental resolution limit of 250–300 nm. It is the goal, however, to reach a resolution that enables imaging of much smaller structures by optical microscopy. Recent developments in fluorescence microscopy have enabled far-field imaging beyond this diffraction limit. In 1994, Hell and Wichmann suggested stimulated emission depletion (STED) microscopy that was

* P. Tinnefeld, Angewandte Physik – Biophysik & Center for Nanoscience, Ludwig-Maximilians-Universität München, Amalienstrasse 54, 80799 München, Germany, e-mail: Philip.Tinnefeld@lmu.de

B. Di Bartolo and J. Collins (eds.), *Biophotonics: Spectroscopy, Imaging, Sensing, and Manipulation*, DOI 10.1007/978-90-481-9977-8_5, © Springer Science+Business Media B.V. 2011

realized at the end of the century, starting a new era of far-field fluorescence microscopy [1, 2]. Overcoming the diffraction limit is achieved by switching OFF the molecules in the outer parts of the focus of a confocal microscope using an additional STED beam and has, since its first application, led to fluorescence images of unprecedented resolution and to the commercialisation of the technique. In 2006, the work of several labs disclosed an alternative wide-field approach to superresolution which employs stochastic switching of molecules between an ON- and an OFF-state [4–6]. This switching is used to separate the overlapping fluorescence of fluorophores whose point-spread functions overlap in a conventional fluorescence image.

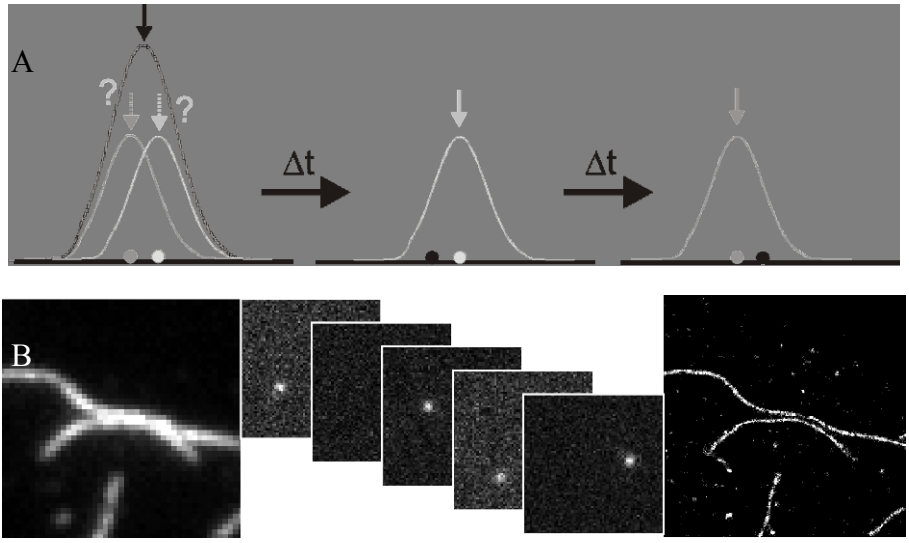

Figure 1. (a) Scheme of fluorescence nanoscopy using localization and temporal separation of single-molecule fluorescence. (b) Example of resolution enhancement with Blink Microscopy: Diffraction limited image of actin filaments immobilized on a glass slide (left), some frames from a time series that show single molecule emission (center) and the resulting superresolution image (right).

The principle of fluorescence nanoscopy using localization and temporal separation of single molecule fluorescence is shown in Fig. 1. Commonly, the fluorescence of two single emitters that are too close to be resolved as described by the Rayleigh criterion sums up and yields a blurred fluorescence image. The underlying structure cannot be resolved since the number of molecules contributing to the fluorescence and their intensities are not known (see Fig. 1 for scheme and data obtained with immobilized actin filaments). If however, the fluorescence of most emitters is switched OFF so that it can safely be assumed that the fluorescence from single fluorescent spots originates from single emitters, the emitters can be localized with a precision only limited by the FWHM of the spot and the number of detected photons. After all emitters in the sample are subsequently localized by stochastically switching emitters ON and OFF over time, a superresolved fluorescence image can be reconstructed from all emitters' positions.

Meanwhile, many techniques based on this approach have been implemented which distinguish themselves in the way the stochastic switching is achieved. While some exploit photoactivatable fluorescent proteins [4, 6], also switchable fluorescent molecules have been applied [5, 7, 8]. Recently, it was demonstrated that essentially any single-molecule compatible fluorophore could be used for this kind of superresolution microscopy by cleverly exploiting generic dark states of the fluorophores [3, 9–11]. It turned out that especially radical anion states often have a lifetime sufficient for switching the largest fraction of fluorophores in a sample OFF while localizing the remaining subpopulation [11, 12]. For some fluorophores, this approach just exploiting controlled blinking (→Blink-Microscopy) could also be applied in the presence of oxygen under physiologically relevant conditions [11, 13].

Fluorescence nanoscopy using localization and temporal separation of single-molecule fluorescence is especially simple and only requires wide-field (or total internal reflection (TIR) illumination. Excitation is carried out with a laser of moderate power (20–500 mW). An image sequence is recorded with a highly sensitive emCCD camera. Each of the images is analyzed for the presence of single-molecule fluorescence and each such event is fitted with a two-dimensional Gaussian function to obtain the exact position of each single fluorophore. Every position is then visualized in a two - dimensional histogram which is the high resolution image (Fig. 1b).

In this book article, we discuss factors that influence the resolution of the nanoscopic image. We consider the specific characteristics of Blink-Microscopy and develop a model that quantitatively describes the achievable resolution and how measurement parameters have to be optimized. In Blink-Microscopy, fluorescence emission is mainly characterized by the time a single fluorophore spends in its bright and dark state, i.e. its ON-time (τ_{on}) and OFF-time (τ_{off}), as well as the number of emitted photons per ON-state (N_{on}). While resolution is fundamentally limited by the detected photon number ($d = FWHM*(N)^{-0.5}$, where d is the localization precision, and *N* represents the number of photons detected from one single molecule in one image frame), other factors also contribute to the practically achievable resolution. It is, for example, interesting to note that some of the superresolution techniques employ photoactivatable fluorescent molecules, i.e. fluorophores can only be localized once, whereas others such as Blink-Microscopy offer the possibility to repeatedly localize the same molecules. Obviously the latter is advantageous for studying dynamic processes that require several superresolution images to be recorded. Here, we will discuss that multiple localizations of the same molecule also is advantageous for the resolution since a better signal-to-noise is achieved in the reconstructed image. The repeated measurement of the same molecule, however, brings about the disadvantage, e.g. in Blink-Microscopy, that the OFF-state lifetime is not arbitrarily long, limiting the number of fluorophores that can be colocalized and albeit the achievable resolution is compromised. This risk that several fluorophores are ON simultaneously is, however, not only a problem for Blink-Microscopy but other techniques also suffer from uncontrolled photophysics such as spontaneous activation and undefined blinking. Taking into account that the data acquisition time is not infinite and measurements should be as fast as possible, the problem of two ON-molecules in one spot is universal for all stochastic superresolution approaches. It is discussed in this article how multiple localizations minimize this problem and how the optimal measurement speed is achieved. In particular, we discuss

this trade-off of acquisition speed and spatial resolution and evaluate quantitatively the role of the ratio of ON-time to OFF-time.

We further discuss other practical issues such as the localization precision in the presence of noise and elaborate a method to optimally adapt the camera frame rate to the ON-time of the fluorophores. This is not straightforward since localizations are carried out frame by frame and the ON-counts do all have to be detected within one camera frame. This poses the question about the optimal integration time since ON-times are expected to obey an exponential distribution while the camera integration time per frame is a constant. So far, the camera frame rate has been approximately adapted to the average ON-time of the molecules often determined separately. Here, we deduce a formula that indicates how to optimally adapt the integration time of the camera at given ON-time and signal-to-noise ratio.

In the last section of this article, we address the problem of practically evaluating and calibrating superresolution microscopes. To date, inhomogenous filamentous structures such as actin filaments or microtubules have been used to demonstrate optical resolution. Short double stranded DNA has also served as a nanoscale ruler [5, 14–16], but is disadvantageous because of its non-negligible flexibility which becomes noticeable already at short distances [17]. A defined standard is desired to quantify and demonstrate the obtainable resolution, to verify optical magnification, to correct for aberrations, and to study and calibrate the photophysical and photochemical properties of the fluorescent probes under defined conditions [3, 8]. Such a structure dubbed “nanoscopic ruler” should also be robust so that it can be used as calibration standard for superresolution microscopes all over the world. We introduce folded DNA structures, also called DNA-origami, as robust nanoscopic ruler. Folded DNAs are prepared from a long single-stranded DNA scaffold that is interconnected by short DNA staple strand. These staple strands only bind at particular points along the long scaffold thus organizing the DNA into the desired shape [18]. With this technique, large numbers of identical structures can be assembled simultaneously in a single experiment. In addition, the technique offers a facile route to assemble other molecules such as fluorophores by simply using modified staple strands. We present the potential of this approach using rectangular DNA origami with a designed distance between the fluorophores of 81 and 54 nm. Resolving these distances using Blink-Microscopy demonstrates the potential of both the DNA origami as calibration ruler and the resolving power of nanoscopies using stochastic single-molecule localizations.

In Blink-Microscopy, redox blinking of molecules is exploited for superresolution. Fluorophores are first emitting brightly until they undergo a photoinduced electron transfer through reaction with a reductant such as ascorbic acid. The formed reduced state has a lifetime that can be adapted between 1 and 10^4 ms by choosing the concentration of oxidants such as oxygen. The oxygen accept the electron in a second a second photoinduced electron transfer reaction yielding the fluorophore back in the ground state ready to go through bright fluorescent cycles again. This process can be repeated up to 3,000 times and was used to switch most molecules in the sample OFF and localize the remaining subfraction. In the following we examine the parameters influencing resolution starting with the role of ON- and OFF- state lifetimes.

2. Temporal Separation of ON-States

While the localization precision based on photon statistics will be discussed later, this chapter is dedicated purely to the *temporal separation* of ON-states. The important parameter in this context is the ratio of ON- and OFF-times resulting in an ON-probability p_{on} (Eq. (1)). To simplify formulations, the ON-time is considered to be 1 frame for the moment as this can be easily achieved by adjusting the camera integration time and laser power. Furthermore, the OFF-time is normalized to the ON-time, yielding a factor named τ, which is the ratio of τ_{off} devided by τ_{on}. In simple terms, the larger τ, the more molecules could be localized within one diffraction limited spot and the higher the resolution of Blink-Microscopy can be.

First, we introduce some equations derived from probability theory to calculate the probability of zero, one and more than one fluorophores being in their ON-state.

$$p_{on} = \frac{\tau_{on}}{\tau_{on} + \tau_{off}} \tag{1}$$

where τ_{on} and τ_{off} are average ON- and OFF-times derived from single-molecule blinking experiments under the same conditions as the superresolution experiment.

$$p_0 = (1 - p_{on})^n \tag{2}$$

where *n* is the number of molecules within the area of the diffraction limited PSF.

$$p_1 = n \cdot p_{on} \cdot (1 - p_{on})^{n-1} \tag{3}$$

The probability that exactly one fluorophore is in its on state (p_1) can be calculated as a binomial distribution (Eq. (3)).

$$p_x = \sum_{k=2}^{n} \binom{n}{k} \cdot {p_{on}}^k \cdot (1 - p_{on})^{n-k} = 1 - p_0 - p_1 \tag{4}$$

For the case of multiple fluorophores emitting simultaneously (p_x), the binomial distributions for any number of fluorophores >1 have to be summed up.

These considerations are only valid when assuming that the fluorophore is synchronized with the camera frame rate, meaning that the ON-time begins with the start of a frame and lasts exactly one frame. In reality, the emission of a fluorophore most likely stretches over multiple frames. With an exponential distribution of the ON-times, ~90% of the molecules switch to the dark state within two frames. To avoid temporally overlapping emission, it is reasonable to exclude fluorescent spots when there are two molecules emitting within two successive frames as this most likely biases

the localization of both molecules. To correct for temporal overlapping, each ON-state must be followed by a frame where no molecule emits.

$$p_{1corr} = p_1 \cdot p_0 \tag{5}$$

This equation provides a value for the probability to obtain a correct localization. At this point, it is important to also distinguish photoswitching and photoactivation based microscopies. With photoactivation [4], every molecule can only be localized once and then bleaches irreversibly, while photoswitching approaches like (d)STORM and Blink Microscopy [3, 5, 8] cycle the fluorophore between a bright and a dark state repeatedly. This way each molecule is localized several times, so the information about its precise position is not lost in case of a wrong localization due to temporal overlapping emission of multiple fluorophores.

With Eq. (5) it is now possible to calculate the minimum number of frames that need to be recorded in order to acquire a fully detailed image:

$$n_{frames} \geq a \cdot n \cdot p_{1corr}^{-1} \tag{6}$$

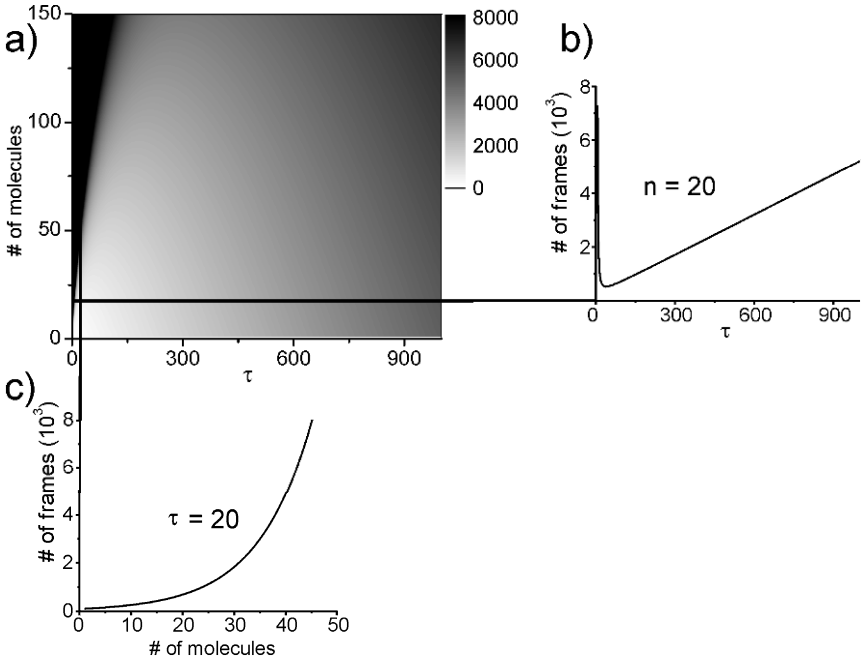

Figure 2. (a) Number of frames to record to obtain five localizations from each molecule for different OFF-times and numbers of molecules. The z scale is capped at 8000 frames for better graphical representation. (b) crossection through (a) for a constant n = 20 and (c) for constant τ = 20.

where a is the desired number of localizations per molecule while neglecting the effects of photobleaching. For a = 5, the number of frames is plotted for different values of τ_{off} and different numbers of molecules n (Fig. 2). Two cross-sections, one parallel to the x-axis (constant n) and one parallel to the y-axis (constant τ), are plotted to better visualize the curve progression for these two dimensions (Fig. 2b, c).

According to Fig. 2, any number of molecules can be resolved if the recording time is sufficiently extended. However, as the number of frames grows exponentially, the experimental limitation of data acquisition is quickly reached. In addition, this graph only shows how many frames are needed to get a sufficient number of correct localizations. To obtain a meaningful image, the number of "wrong" pixels, resulting from multiple molecules emitting within one frame and within one PSF (p_x) must be lower than the number of correct localizations.

We define, that the number of localizations resulting from single molecule events must be at least 1.5 times higher than those where multiple simultaneously emitting fluorophores lead to a wrong determination of the position. This ratio can be expressed as a ratio of probabilities $p_{1corr}/p_x = \rho$ to be at least 1.5. When plotting this ratio into Fig. 2c), it can be determined at which number of molecules the fraction of biased localizations exceeds our threshold. Figure 3 exemplarily depicts this for an OFF-time of 20 frames (τ = 20).

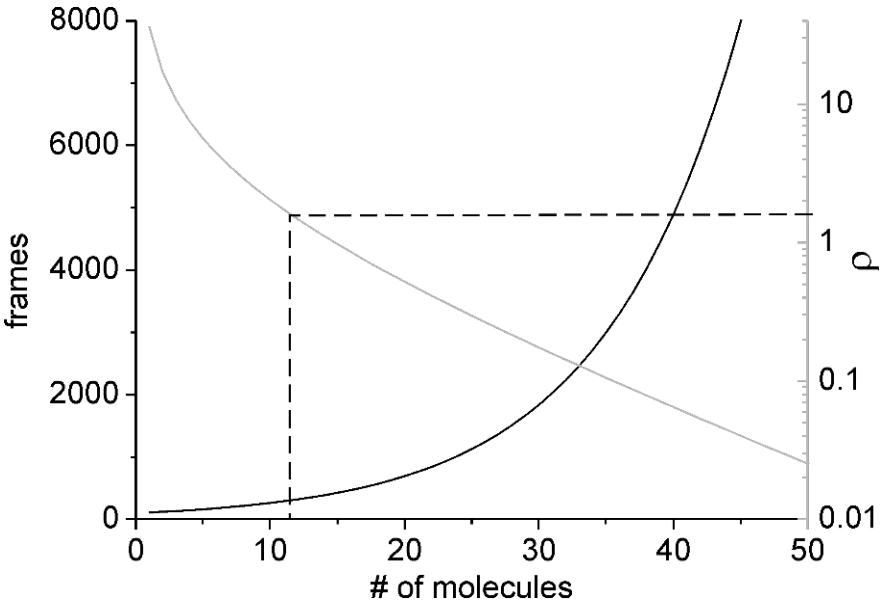

Figure 3. The gray line shows the ratio ρ for τ = 20. The position ρ ~ 1.5 is indicated by the dashed line.

As can be read from Fig. 3, the maximum number of resolvable molecules is 11 it looks more like 12? es sind auch fast 12, aber es ist eher sinnvoll abzurunden. This value is independent of the number of frames recorded but can be used to limit the recording time to a reasonable level.

For different OFF-times this cut-off value shows a surprising behaviour. It follows a straight line with a slope of 0.6 (see Fig. 4). We hence tried to find an analytical approximation to explain this behaviour. Therefore, we used Eqs. (1–4) to calculate ρ and converted this equation to calculate n. For reasonable blinking parameters (e.g. $\tau > 5$) we can estimate

$$n_{\max} \approx \frac{\tau}{\rho} \tag{7}$$

which is in reasonable agreement with graph 3 for $\rho = 1.5$.

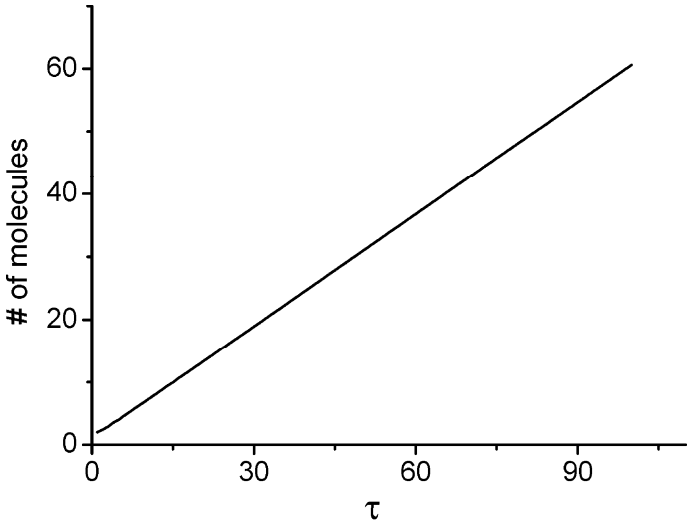

Figure 4. Maximum number of temporally separable molecules for $\rho = 1.5$.

When Figs. 3 and 4 are combined, the exponential increase of frames towards the y-axis can be excluded as the values for ρ are too low in this regime. What remains is a linear dependence on the OFF-time (see also Fig. 2b for $\tau > 50$).

In order to calculate the resolution that can be achieved at a given number of temporally separable molecules (n), we regard the limiting case where these molecules are arranged in a regular grid structure with a lattice constant of d. This way, we obtain a resolution of

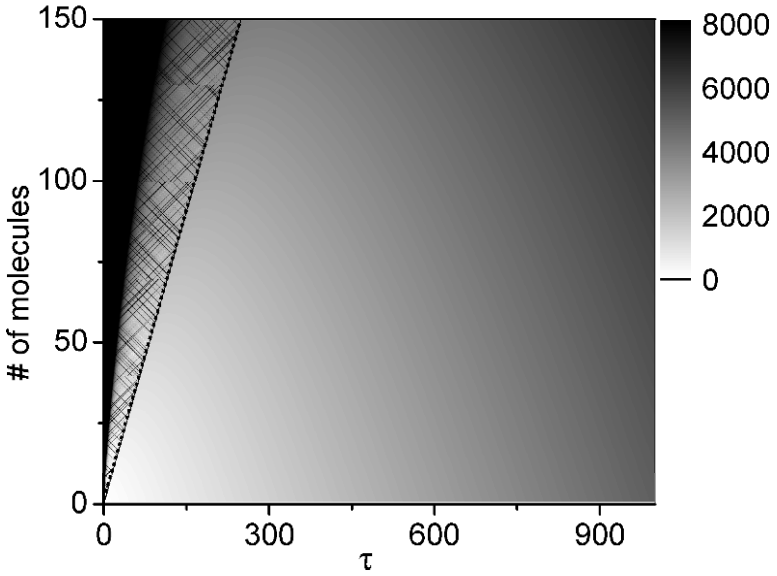

Figure 5. Combination of Figs. 3 and 4. The shaded area indicates the regime where no superresolution imaging is possible due to $\rho < 1.5$.

$$d = \frac{FWHM \cdot \pi}{\sqrt{n} \cdot 4} \tag{8}$$

The factor of $\pi/4$ accounts for the circular shape of the PSF. However, experimentally, with a pixel size of 140 nm, the PSF is better approximated as a square. This resolution is plotted, together with previously performed Monte Carlo Simulations (red dots) of regular grids, versus τ in Fig. 6 [3].

For a regular diffraction limited square grid of point emitters a stochastic blinking behaviour was simulated. The simulated movies then underwent the same analysis procedure as the real data. Varied parameters were the distance of the molecules in the regular two-dimensional grid formed by the molecules (30–180 nm), and the ratio of OFF-time to ON-time. The size of the grids was always of the order of the size of the PSF, so that it was effectively infinite. Such a grid was defined as resolvable, if two specific points in the center were clearly separated (in analogy to Rayleigh's criterion). Every condition was simulated 20 times and the fraction of resolvable grids was determined. If at least 50% of the grids could be resolved at any condition, that condition is considered resolvable. The best obtainable resolution is plotted for each τ in Fig. 6 (squares).

Figure 6 shows that our simplified theoretical model nicely describes the achievable resolution simulated using Monte–Carlo simulations. Therefore the model will be valuable to adapt ON- and OFF-times to the specific experimental conditions such as labelling density and desired resolution.

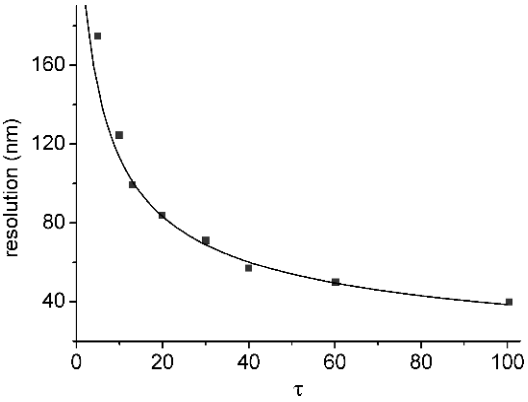

Figure 6. τ- limited resolution. Theory (solid line) and simulations (squares).

From the results presented in Figs. 5 and 6 one can draw further conclusion for the experimental design. If there is the possibility to adjust τ as described by Vogelsang et al. [11], one can choose between high resolution or high data acquisition speed [19]. For low values of τ, the required acquisition time (Fig. 5) can be kept low to observe nanoscale dynamics, however the label density or the expected resolution must not be too high. With longer OFF-times, many molecules' emission can be separated in time, resulting in better resolution, but this requires longer acquisition times.

Of course, higher resolution can also be achieved when the emitters are not evenly distributed within the PSF as in the grid structure described above. If there is only a few dye molecules at very short distances, also exhibiting relatively long OFF-times, resolution is no longer limited by temporal separation of the ON-states, but by the precision with which they can be localized.

3. Localization Precision

The second crucial parameter to localization based superresolution microscopy is independent of the temporal separation of the bright states discussed above. To localize a single molecule with high precision it must emit a high number of photons. First, we consider the shot-noise limited case, assuming that all photons of an ON-state are collected in exactly one camera frame and without any background noise. In this case, a single molecule can be localized with a standard deviation σ, depending on the standard deviation of its diffraction limited PSF σ_{PSF}

$$\sigma \approx \frac{\sigma_{PSF}}{\sqrt{\langle N_{on} \rangle}} \tag{9}$$

where N_{on} is the number of photons detected from a single molecule. In practice, this value is usually higher than expected from the calculated number of photons. There can be several reasons for this phenomenon:

1. Equation (8) must be corrected for an increase in noise present in high-end emCCD cameras commonly used for superresolution microscopy. According to Bossi et al. [20], Eq. (9) requires the following modification

$$\sigma \approx \frac{\sigma_{PSF}}{\sqrt{\langle N_{on} \rangle / 2}} \tag{10}$$

2. Mechanical instability of the microscope also worsens the obtainable resolution. This influence, however, is hard to quantify in general as it can change strongly between experiments. We definitely recommend to check the setup for drift effects right before the experiment on the expected timescale, e.g. with fluorescent beads.

The resolution can again be improved by only selecting a subset of photon bursts. In case of photoswitching microscopy, each molecule emits multiple times with an exponential distribution of photon numbers. When only taking into account those events where the molecule emits more photons than it does on average, the effective number of photons is increased, directly resulting in a better localization precision. With photoactivation methods, this can only be done at a loss of detail as fluorescent labels that emit less photons cannot contribute to the high resolution image.

4. Integration Time and Noise

Closely linked to chapter 3, experimental parameters like camera integration time and background noise are introduced in this chapter and their effect on the localization precision is discussed.

The localization precision is strongly dependent on the number of photons used for fitting the PSF, i.e. the photon number detected within one frame N_{frame}. For a fixed integration time t and ON-time τ_{on} the average number of detected photons can be calculated as follows, where γ is the photon emission rate of a molecule during an ON-state:

1. Case ($t < \tau_{on}$):

$$\left\langle N_{frame} \right\rangle_{t<\tau_{on}} = \frac{t \cdot \frac{1}{2}\gamma t + (\tau_{on} - t) \cdot \gamma t + t \cdot \frac{1}{2}\gamma t}{\tau_{on} + t} = \gamma \frac{\tau_{on} \cdot t}{\tau_{on} + t} \tag{11}$$

2. Case ($t > \tau_{on}$):

$$\left\langle N_{frame} \right\rangle_{t>\tau_{on}} = \frac{\tau_{on} \cdot \frac{1}{2}\gamma\tau_{on} + (t-\tau_{on}) \cdot \gamma\tau_{on} + \tau_{on} \cdot \frac{1}{2}\gamma\tau_{on}}{t+\tau_{on}} = \gamma \frac{\tau_{on} \cdot t}{\tau_{on}+t} \tag{12}$$

Equations (11) and (12) are derived by considering different possibilities of the temporal overlap of ON-time and integration time. For each case, there are three terms representing the three possibilities of initial overlap, complete overlap and terminal overlap. Both cases yield the same equation, so the average number of detected photons for a fixed τ_{on} is given by

$$\left\langle N \right\rangle_{\tau_{on}} = \gamma \frac{\tau_{on} \cdot t}{\tau_{on}+t} \tag{13}$$

The ON-time is exponentially distributed with the following density function

$$\nu(\tau_{on}) = \frac{1}{\left\langle \tau_{on} \right\rangle} e^{-\frac{\tau_{on}}{\left\langle \tau_{on} \right\rangle}}) \tag{14}$$

So the average number of detected photons can be calculated by integration over all possible values for the ON-time:

$$\left\langle N_{frame} \right\rangle = \int_0^\infty \left\langle N \right\rangle_{\tau_{on}} \nu(\tau_{on}) d\tau_{on} = \int_0^\infty \gamma \frac{\tau_{on} \cdot t}{\tau_{on}+t} \frac{1}{\left\langle \tau_{on} \right\rangle} e^{-\frac{\tau_{on}}{\left\langle \tau_{on} \right\rangle}} d\tau_{on}$$

$$= \frac{\gamma t}{\left\langle \tau_{on} \right\rangle} \int_0^\infty \frac{\tau_{on}}{\tau_{on}+t} e^{-\frac{\tau_{on}}{\left\langle \tau_{on} \right\rangle}} d\tau_{on} \tag{15}$$

This integral can be divided into two parts by substitution with $x = \tau + t$, whereby the first part can be easily solved:

$$\left\langle N_{frame} \right\rangle = \frac{\gamma t}{\left\langle \tau_{on} \right\rangle} \int_t^\infty \frac{x-t}{x} e^{-\frac{x-t}{\left\langle \tau_{on} \right\rangle}} dx = \frac{\gamma t}{\left\langle \tau_{on} \right\rangle} \left(\int_t^\infty e^{-\frac{x-t}{\left\langle \tau_{on} \right\rangle}} dx - \int_t^\infty \frac{t}{x} e^{-\frac{x-t}{\left\langle \tau_{on} \right\rangle}} dx \right)$$

$$= \frac{\gamma t}{\left\langle \tau_{on} \right\rangle} \left(\left\langle \tau_{on} \right\rangle - e^{\frac{t}{\left\langle \tau_{on} \right\rangle}} t \int_t^\infty \frac{1}{x} e^{-\frac{x}{\left\langle \tau_{on} \right\rangle}} dx \right)$$

For simplifying the second integral a substitution with $\xi = x/\langle\tau_{on}\rangle$ is done:

$$\langle N_{frame}\rangle = \frac{\gamma t}{\langle\tau_{on}\rangle}\left(\langle\tau_{on}\rangle - e^{\frac{t}{\langle\tau_{on}\rangle}} t \int_{t/\langle\tau_{on}\rangle}^{\infty} \frac{1}{\xi\langle\tau_{on}\rangle} e^{-\xi}\langle\tau_{on}\rangle d\xi\right)$$

$$= \gamma t\left(1 - e^{\frac{t}{\langle\tau_{on}\rangle}} \frac{t}{\langle\tau_{on}\rangle} \int_{t/\langle\tau_{on}\rangle}^{\infty} \frac{1}{\xi} e^{-\xi} d\xi\right)$$

This simplified integral is solved by the exponential integral function $E_1(\xi)$.

$$\langle N_{frame}\rangle = \gamma t\left(1 - e^{\frac{t}{\langle\tau_{on}\rangle}} \frac{t}{\langle\tau_{on}\rangle} E_1\left(\frac{t}{\langle\tau_{on}\rangle}\right)\right)$$

With $N_{on} = \gamma\langle\tau_{on}\rangle$ and $\varepsilon = t/\langle\tau_{on}\rangle$ the number of detected photons is given by the equation:

$$\langle N_{frame}\rangle = N_{on}\varepsilon\left(1 - \varepsilon e^{\varepsilon} E_1(\varepsilon)\right) \tag{16}$$

In Fig. 7 the average number of detected photons divided by the average number of emitted photons is plotted against ε:

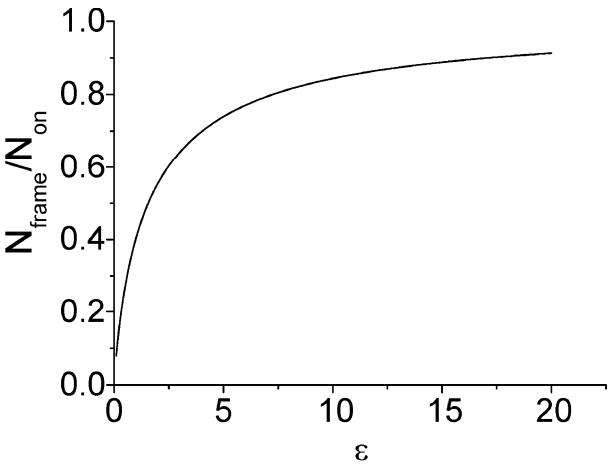

Figure 7. Average number of photons detected in one frame divided by the average number of photons emitted during one ON-time depending on the ratio of integration time to the average ON-time. The graph shows a linear increase for small values of ε and an asymptotic convergence against 1 for big numbers of ε.

Another important factor for the localization precision is the background noise. The background signal per pixel is given by

$$B = \beta \cdot t$$

Thereby β is the background photon emission rate per pixel. The shot-noise limited background noise is given by

$$b = \sqrt{B} = \sqrt{\beta t}$$

As β is proportional to the excitation intensity just like γ, it can be written as

$$\beta = c \cdot \gamma$$

with the proportionality constant c. So the background noise can be calculated as a function of ε:

$$b = \sqrt{\beta t} = \sqrt{c\gamma t} = \sqrt{c\frac{N_{on}}{\langle \tau_{on} \rangle} t} = \sqrt{cN_{on}\varepsilon} \tag{17}$$

The localization precision can be calculated according to Thompson et al. [21]:

$$\begin{aligned} \left\langle (\Delta x)^2 \right\rangle &= \frac{s^2 + \frac{a^2}{12}}{N} + \frac{8\pi s^4 b^2}{a^2 N^2} \\ &= \frac{s^2 + \frac{a^2}{12}}{N_{on}\varepsilon\left(1 - \varepsilon e^{\varepsilon} E_1(\varepsilon)\right)} + \frac{8\pi s^4 c}{a^2 N_{on}\varepsilon\left(1 - \varepsilon e^{\varepsilon} E_1(\varepsilon)\right)^2} \end{aligned} \tag{18}$$

For s = 250 nm, a = 140 nm, c = 0.01 and N_{on} = 500 following dependence of the localization precision on the ratio of the acquisition time to the average ON-time:

This curve provides an optimum at ε = 1.75. This optimum is independent of the total number of photons the molecule emits during an ON-time. Also the pixel size a does not significantly influence the result as c is proportional to a^2 in Eq. (18). The parameter c can be extracted from experiments by solving Eq. (17) for c.

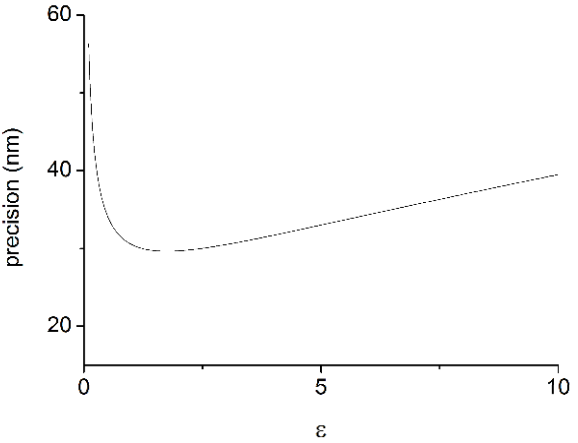

Figure 8. Localization precision depending on the ratio of integration time to the average ON-time. This graph shows an optimum between an asymptotic divergence to infinity for ε close to 0 and a linear increase for bigger values of ε.

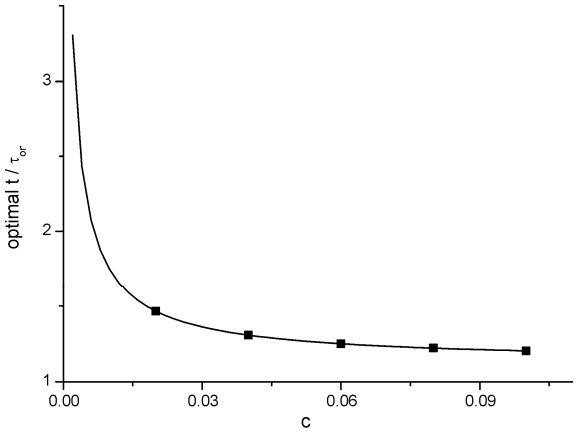

Figure 9. Position of the optimum of the graph in Fig. 8 against the noise parameter c. The black squares indicate the c values selected for Fig. 10.

The resolution obtained at the optimal integration time depends on the number of photons a molecule emits during an ON-time. For some values of realistic *c* (indicated by black boxes in Fig. 9), the precision is plotted in Fig. 10.

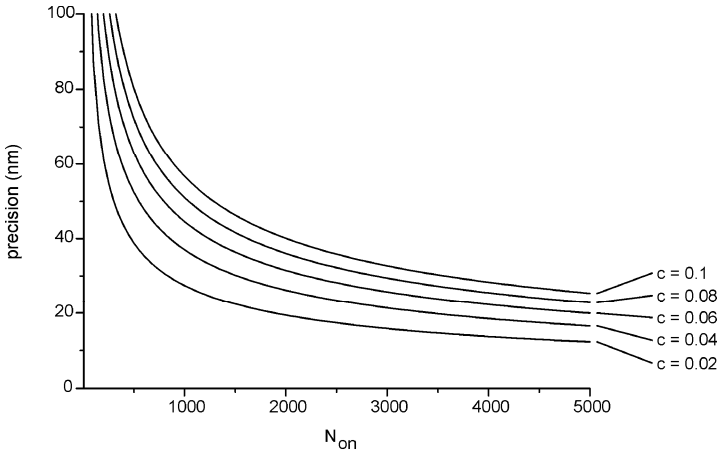

Figure 10. Localization precision at optimized integration time against the average number of photons emitted during one ON-time for the values of c selected in Fig. 9.

These considerations indicate that the integration time should be selected somewhat larger than the average ON time (about a factor of 1.5 depending on the noise present in the system) of the molecules to optimize the number of photons per frame. On the other hand, it has to be kept in mind that the integration time should not be selected too long because this would increase the probability that another molecule within the diffraction limited area starts emitting as discussed in chapter 2.

5. How to Calibrate a Superresolution Microscope

While the localization precision can easily be quantified by investigating a single molecule, it is substantially more difficult to measure the influence of τ experimentally. To do so, a well defined nanometer sized pattern of fluorescent molecules is required that needs to be immobilized on a glass surface. Randomly occurring distances from biological contexts (e.g. actin filaments) have often been used to test new microscopy techniques. In this context, a nano-scale ruler would be very much appreciated. Such a structure could not only be used to evaluate and compare different superresolution approaches, it could also be used to quantitatively study the photophysics of fluorophores used, e.g. the fraction of molecules that can actually be photoactivated, and to calibrate every single superresolution microscope if robustness allows good reproducibility, and easy sample distribution.

We have developed a nanoscopic ruler employing DNA nanostructures labeled with fluorophores at defined positions. In the so-called “DNA origami technique”, single stranded DNA molecules are made to self-assemble into well-defined two-dimensional macromolecular structures [18, 22, 23]. The name “origami” comes from the fact that a long single stranded DNA molecule is “folded” into a particular shape. With a diameter of typically 100 nm and a fully addressable breadboard-like structure, rectangular DNA origami are used to arrange nanoscale objects with nanometer precision. This very

feature makes DNA origami the desired ruler. The concept of DNA origami used as molecular ruler for superresolution microscopy is shown in Fig. 11.

To fold DNA into the desired shape, a 7.2 kilobase long single stranded viral DNA scaffold is taken. Along this scaffold, many short staple strands (~200) bind specifically. As fractions of the sequence of staple strands are designed to be complementary to several specific regions, each of them interconnects different regions of the long scaffold strand. As any of the staple strands can be purchased with a fluorescent label covalently attached, these labels can be placed anywhere on the final origami structure. For our experiments, we chose a rectangular structure with dimensions of 70 × 100 nm.

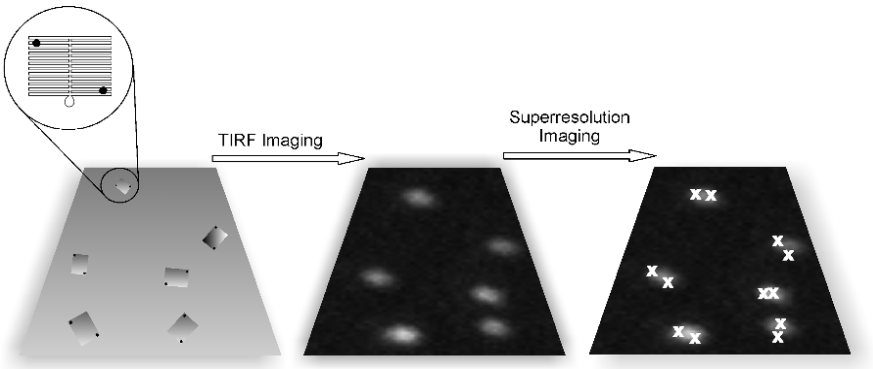

Figure 11. DNA origami with two fluorophores at a specific distance (top) are applied to a glass surface (bottom left) where they stick due to electrostatic interactions in the presence of magnesium ions. Fluorescence imaging in TIRF mode (bottom middle) shows diffraction limited PSFs of the Origami. Single fluorophores on the origami sample are identified by using superresolution fluorescence microscopy (bottom right).

If one wants to verify Fig. 6 experimentally, calibration standards for different distances are required. However, for the multitude of different labeling patterns, many labeled DNA strands need to be synthesized. It can therefore be more cost-efficient not to use labeled staple strands as was done before [24], but to extend staple strands with a region that remains single-stranded in the origami. These single-stranded regions at the end of certain staple strand stick out of the origami on a defined side and are subsequently available for binding to a DNA oligo labeled with a fluorophore. If the single-stranded regions are chosen to be identical only one modified DNA staple strand has to be used to incorporate several fluorescent labels. This also offers the option for different labeling geometries using different cheap unlabeled DNA staple strands. Fluorophores are again incorporated by hybridization with a single, labeled DNA strand. To test this procedure for the design of a nanoscopic origami ruler, we designed single stranded overhangs at 81 and 54 nm distance on the origami and hybridized an ATTO655-labeled DNA to these strands. Immobilization on surfaces is easily done by integrating biotin linkers or simply using electrostatic interactions between DNA and a positively charged surface [24]. Blink-Microscopy images on those probes are shown in Fig. 12. The average distances measured with Blink Microscopy are 83 ± 3.0 nm and 52 ± 2.6 nm. The standard deviation of the Gaussian fits is 18 and 16 nm, respectively. While the

data in Fig. 12 show that the design principle works, we found significantly lower yields of doubly-labeled origami compared to direct incorporation of fluorophores via labeled staple strands. The theoretically designed distance was measured experimentally with a deviation of only one nanometer for direct staple labeling [24] optically resolving 90% of the structures. The major drawback of the labeling strategy by hybridizing a single labeled strand thus is the relatively low efficiency of hybridization. At 12.5 μM $MgCl_2$ concentration for hybridization, the ratio of resolvable to unresolvable structures was usually <25% which corresponds to a labeling efficiency of ~50%. For experiments with only two fluorophores per DNA origami, it is still possible to determine the distance; however for more complex structures like a grid, this method needs optimization.

We showed that different superresolution techniques can be used to resolve the distance between two fluorophores grafted into the DNA origami structure [24]. The theoretically designed distance was measured experimentally with a deviation of only a few nanometers. This demonstrates the robustness of both DNA origami as nanoscopic ruler as well as Blink-Microscopy, thus offering the required calibration structures for superresolution microscopies.

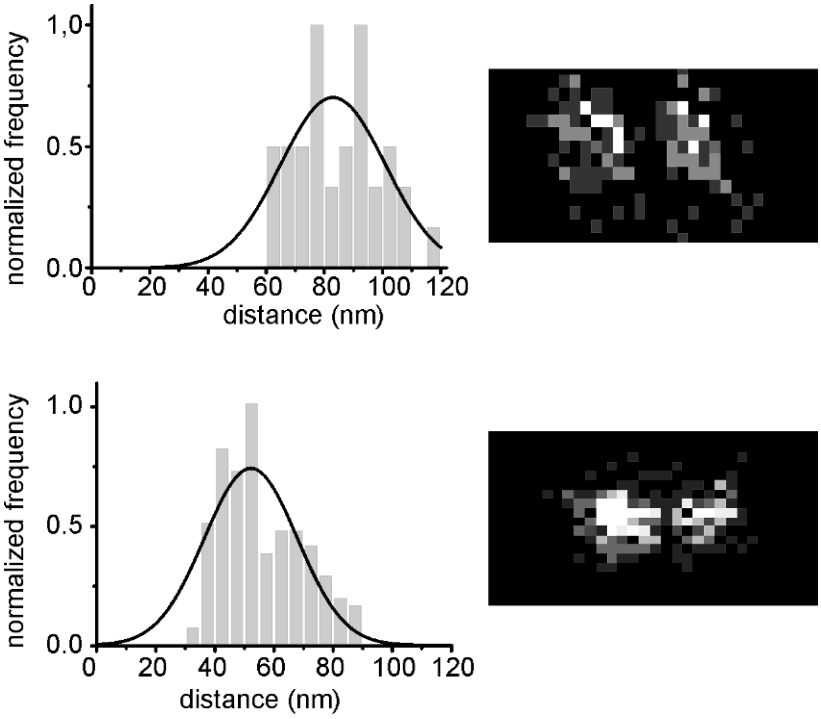

Figure 12. Distance distributions and Gaussian fit of 40 and 100 DNA origami at a theoretical distance of 81 and 54 nm respectively (left). Typical superresolution images of the respective samples (right).

6. Summary

In this article, we developed a simple theory for the resolution enhancement in superresolution microscopy on the basis of stochastic single-molecule localization. The model was used to estimate the obtainable resolution of Blink-Microscopy depending on the ratio of ON-times to OFF-times. The model nicely predicts the achievable resolution achieved by Monte-Carlo simulations of Blink-Microscopy measurements. We further studied the influence of the localization precision on resolution and deduced a formula to optimally adapt the integration time to the average ON-time of the fluorophores. In order to experimentally study the achievable resolution, model structures with defined number of fluorophores that are arranged in a nanometer precise pattern are required. We introduced DNA origami that can principally accomplish the task to serve as models for the evaluation of superresolution microscopies and have the robustness to be used as calibration standard for every microscope. For the preparation of labeled origami, we found much better yield if the fluorophores were directly incorporated with the staple strands while significantly lower yields were obtained if a single labeled DNA strand was hybridized to single stranded parts of the origami staple strands. In order to successfully use this latter and cheaper method, the yields have to be improved.

References

1. Klar, T. A., Jakobs, S., Dyba, M., Egner, A. & Hell, S. W. (2000). Fluorescence microscopy with diffraction resolution barrier broken by stimulated emission. *Proc Natl Acad Sci U S A* **97**, 8206–8210.
2. Hell, S. W. & Wichmann, J. (1994). Breaking the diffraction resolution limit by stimulated emission: stimulated-emission-depletion fluorescence microscopy. *Opt. Lett.* **19**, 780–782.
3. Steinhauer, C., Forthmann, C., Vogelsang, J. & Tinnefeld, P. (2008). Superresolution microscopy on the basis of engineered dark states. *J Am Chem Soc* **130**, 16840–16841.
4. Betzig, E., Patterson, G. H., Sougrat, R., Lindwasser, O. W., Olenych, S., Bonifacino, J. S., Davidson, M. W., Lippincott-Schwartz, J. & Hess, H. F. (2006). Imaging intracellular fluorescent proteins at nanometer resolution. *Science* **313**, 1642–1645.
5. Rust, M. J., Bates, M. & Zhuang, X. (2006). Sub-diffraction-limit imaging by stochastic optical reconstruction microscopy (STORM). *Nat Methods* **3**, 793–795.
6. Hess, S. T., Girirajan, T. P. & Mason, M. D. (2006). Ultra-high resolution imaging by fluorescence photoactivation localization microscopy. *Biophys J* **91**, 4258–4272.
7. Heilemann, M., Margeat, E., Kasper, R., Sauer, M. & Tinnefeld, P. (2005). Carbocyanine Dyes as Efficient Reversible Single-Molecule Optical Switch. *Journal of the American Chemical Society* **127**, 3801–3806.
8. Heilemann, M., van de Linde, S., Schuttpelz, M., Kasper, R., Seefeldt, B., Mukherjee, A., Tinnefeld, P. & Sauer, M. (2008). Subdiffraction-Resolution Fluorescence Imaging with Conventional Fluorescent Probes. *Angew Chem Int Ed Engl* **47**, 6172–6176.
9. Folling, J., Bossi, M., Bock, H., Medda, R., Wurm, C. A., Hein, B., Jakobs, S., Eggeling, C. & Hell, S. W. (2008). Fluorescence nanoscopy by ground-state depletion and single-molecule return. *Nat Methods* **5**, 943–945.
10. van de Linde, S., Kasper, R., Heilemann, M. & Sauer, M. (2008). Photoswitching microscopy with standard fluorophores. *Appl Phys B* **93**, 725–731.

11. Vogelsang, J., Cordes, T., Forthmann, C., Steinhauer, C. & Tinnefeld, P. (2009). Controlling the fluorescence of ordinary oxazine dyes for single-molecule switching and superresolution microscopy. *Proc Natl Acad Sci U S A* **106**, 8107–8112.
12. Vogelsang, J., Kasper, R., Steinhauer, C., Person, B., Heilemann, M., Sauer, M. & Tinnefeld, P. (2008). A reducing and oxidizing system minimizes photobleaching and blinking of fluorescent dyes. *Angew Chem Int Ed* **47**, 5465–5469.
13. Heilemann, M., van de Linde, S., Mukherjee, A. & Sauer, M. (2009). Super-resolution imaging with small organic fluorophores. *Angew Chem Int Ed Engl* **48**, 6903–6908.
14. Qu, X., Wu, D., Mets, L. & Scherer, N. F. (2004). Nanometer-localized multiple single-molecule fluorescence microscopy. *Proc Natl Acad Sci U S A* **101**, 11298–11303.
15. Gordon, M. P., Ha, T. & Selvin, P. R. (2004). Single-molecule high-resolution imaging with photobleaching. *Proc Natl Acad Sci U S A* **101**, 6462–6465.
16. Heinlein, T., Biebricher, A., Schlueter, P., Roth, C. m., Herten, D.-P., Wolfrum, J., Heilemann, M., Mueller, C., Tinnefeld, P. & Sauer, M. (2005). High-resolution colocalization of single molecules within the resolution gap of far-field microscopy. *Chemphyschem* **6**, 949–955.
17. Wiggins, P. A., van der Heijden, T., Moreno-Herrero, F., Spakowitz, A., Phillips, R., Widom, J., Dekker, C. & Nelson, P. C. (2006). High flexibility of DNA on short length scales probed by atomic force microscopy. *Nat Nanotechnol* **1**, 137–141.
18. Rothemund, P. W. (2006). Folding DNA to create nanoscale shapes and patterns. *Nature* **440**, 297–302.
19. Shroff, H., Galbraith, C. G., Galbraith, J. A. & Betzig, E. (2008). Live-cell photoactivated localization microscopy of nanoscale adhesion dynamics. *Nat Methods* **5**, 417–423.
20. Bossi, M., Folling, J., Belov, V. N., Boyarskiy, V. P., Medda, R., Egner, A., Eggeling, C., Schonle, A. & Hell, S. W. (2008). Multicolor far-field fluorescence nanoscopy through isolated detection of distinct molecular species. *Nano Lett* **8**, 2463–2468.
21. Thompson, R. E., Larson, D. R. & Webb, W. W. (2002). Precise nanometer localization analysis for individual fluorescent probes. *Biophys Jl* **82**, 2775–2783.
22. Jungmann, R., Liedl, T., Sobey, T. L., Shih, W. & Simmel, F. C. (2008). Isothermal assembly of DNA origami structures using denaturing agents. *J Am Chem Soc* **130**, 10062–10063.
23. Douglas, S. M., Dietz, H., Liedl, T., Hogberg, B., Graf, F. & Shih, W. M. (2009). Self-assembly of DNA into nanoscale three-dimensional shapes. *Nature* **459**, 414–418.
24. Steinhauer, C., Jungmann, R., Sobey, T. L., Simmel, F. C. & Tinnefeld, P. (2009). DNA Origami as Nanoscopic Ruler for Superresolution Microscopy. *Angew Chem Int Ed* **48**, 8870–8873.

FLUORESCENCE SPECTROSCOPY AND ENERGY TRANSFER PROCESSES IN BIOLOGICAL SYSTEMS

BALDASSARE DI BARTOLO*
Department of Physics
Boston College
Chestnut Hill, MA 02467

Abstract This article is divided into three parts. In the first part we review the fundamental principles of fluorescence spectroscopy, starting with the consideration of fluorophores and of the characteristics of fluorescence spectroscopy. The processes of fluorescence quenching, fluorescence anisotropy, and resonance energy transfer are presented, together with the information they can provide. The techniques that produce absorption spectra, excitation spectra, fluorescence under continuous excitation and response to pulsed excitation are also examined.

In the second part the basic interactions between atoms are introduced by considering first the static and then the dynamic effects of these interactions in a two-atom system ad in a linear chain of atoms. Subsequently the different types of interactions (multipolar electric and magnetic, and exchange) are examined. After a review of the different modes of excitation of a system containing both donors and acceptors, a statistical treatment of energy transfer is presented by considering first the case of energy transfer without migration among donors, and then the case when such migration occurs.

In the third part the concepts presented in the second part are applied to distance-distribution analysis and FRET (Fluorescence Resonance Energy Transfer) in biological systems.

1. Introduction to Fluorescence

1.1. FLUORESCENCE AND PHOSPHORESCENCE

Luminescence is the spontaneous emission of light from excited electronic states of physical systems.

The emission is preceded by the process of excitation that may be produced by a variety of agents. If it is achieved by the absorption of light it is called *photoluminescence*, if by the action of an electric field *electroluminescence*, if by a chemical reaction *chemiluminescence*, and so on. Following the excitation, if the system is left alone, without any additional influence from the exciting agent, it will emit spontaneously.

* Baldassare Di Bartolo, Department of Physics, Boston College, Chestnut Hill, MA 02467, e-mail: dibartob@bc.edu

B. Di Bartolo and J. Collins (eds.), *Biophotonics: Spectroscopy, Imaging, Sensing, and Manipulation*, 107
DOI 10.1007/978-90-481-9977-8_6, © Springer Science+Business Media B.V. 2011

Even in absolute vacuum an excited atom, devoid of any external influence, will emit a photon and return to its ground state. The spontaneity of the emission presents a conceptual problem. A tenet of physical science, expressed by the so-called *fluctuation–dissipation theorem* sets forth the fact that any dissipation of energy from a system, is the effect of its interaction with some external entity that provides the perturbation necessary for the onset of the process. Such an entity seems to be missing in the case of an isolated excited atom. If we hold a classical view of natural phenomena, we cannot explain the presence of spontaneous emission.

In the quantum world things are very different. The harmonic radiative oscillators that populate the vacuum and that classically hold no energy when in their ground state, have each in this state the energy ½ hν and may produce a fluctuating electric field at the site of the atom, setting the perturbation necessary for the onset of spontaneous emission.

Luminescence is divided into two categories: *fluorescence* and *phosphorescence*, depending on the nature of the excited state. For most organic molecules in their ground state, the highest occupied molecular orbital is a singlet and is the seat of two electrons. The spins of these electrons are antiparallel resulting in a singlet for the ground state.

The excitation of an electron from the ground state orbital to an upper orbital results in the formation of two states,

- A singlet, in which the electron in the excited orbital is paired by opposite sign to the electron in the ground state orbital.
- A triplet, lower in energy than the singlet, in which the electron in the excited orbital and the electron in the ground state orbital have parallel spin.

The decay of an excited state singlet to the ground state singlet is spin allowed and occurs by the rapid emission of a photon. Such an emission is called *fluorescence*; it has typical rates of 10^8 s^{-1}. The average time between excitation and return to the ground state is then 10^{-8} s = 10 ns (in 1 ns light travels 30 cm).

The systems that exhibit fluorescence are called *fluorophores.* [1.1]. Several fluorophores have lifetimes shorter than 10 ns.

Two types of measurements are generally used, the *steady-state fluorescence* and the *time-resolved fluorescence*. Due the short lifetimes, time-resolved measurements require sophisticated optics and electronics; they provide, however, additional important information.

The emission of light from triplet excited states is called *phosphorescence*. It is related to forbidden transitions, because of the difference in the spins of the electron in the excited orbital and of the electron in the ground state orbital; its rates are typically 10^3–1 s^{-1}, so that phosphorescence lifetimes are typically milliseconds to seconds. On account of this long radiative lifetime phosphorescence is not usually seen in fluid solutions at room temperature: various deactivation processes such as non-radiative decay and quenching processes compete successfully with the radiative decay of the triplet state.

Aromatic molecules, the stable molecules with rings of atoms, are typically fuorophores. Among them *quinine*, a substance present in quinine water, when exposed to ultraviolet light from the sun, emits light with wavelength close to 450 nm. *John*

Frederick William Herschel first reported this process in 1845 in an article titled "on a case of superficial colour presented by a homogeneous liquid internally colourless" [1.2].

1.2. FLUOROPHORES

Many fluorophores are part of our daily life. Antifreeze, due to trace quantity of fluoroscein or rhodamine, glows with a green or red-orange color. Anthracene and perylene, two polynuclear aromatic hydrocarbons are also fluorescent, and their emission is used to monitor oil pollution.

Unlike the aromatic organic molecules, atoms do not generally fluoresce in the condensed phases. Notable exceptions are the rare earth and some of the transition metal elements.

Fluorophores can be divided into two main classes:

1. *Intrinsic fuorophores*. In these systems fluorescence occurs naturally. They include aromatic amino acids, NADH, flavins, derivatives of pyridoxyl and chlorophyll.
2. *Extrinsic fluorophores*. In these systems fluorophores are added to provide fluorescence when none exists or to change the spectral output of the sample, when the fluorescence is not adequate for an experiment. Fluorophores that provide extrinsic fluorescence include dansyl, fluorescein, rhodamine and many other substances. Useful information can be found in the Molecular Probes catalogue [1.3].

1.3. THE JABLONSKI DIAGRAM

A typical *Jablonski diagram* [1.4] is shown in Fig. 1.1. The ground state singlet and the singlet excited states are called S_0, S_1, S_2, …. At each of these electronic levels the system can occupy a number of vibrational energy levels that are designated 0, I, 2, …. The radiative transitions both in absorption and in emission are depicted by vertical lines, according to the *Franck–Condon Principle*, that expresses the fact that *they occur in a time much shorter than a period of molecular vibration and therefore without a change in the positions of the nuclei*.

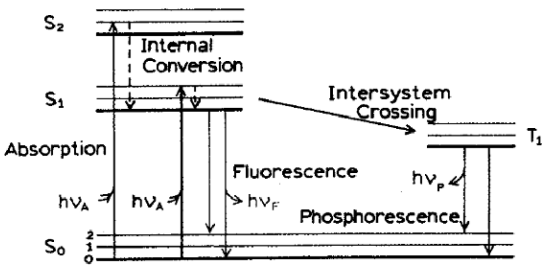

Figure 1.1. The Jablonski diagram (reproduced from [1.1] by permission granted by Springer Science and Business Media and Professor Lakowicz).

We can use the Jablonski diagram to follow the steps that a molecule excited by the absorption of a photon to a vibrational state of a singlet S_n can take:

1. The molecule transitions to the lowest vibrational state of S_1 by converting its vibrational and electronic energy into heat. This process is called *internal conversion* (rate $\approx 10^{12}$ s^{-1}).
2. The molecule will reach the ground state S_0 via different competitive processes:
   (a) *Emission of a photon* with a rate constant w_r. This process constitutes the fluorescence ($w_r \approx 10^8$ s^{-1}). The molecule will generally end up in a higher excited vibrational level, which then quickly reaches thermal equilibrium in $\approx 10^{-12}$ s.
   (b) *Non-radiative decay to the ground state S_0* with a rate constant w_{nr}.
   (c) *Transfer of energy to molecules located nearby* (collisional quenching rate constant w_q) *or to molecules at a distance* (energy transfer rate w_T).
   (d) *Passage from S_1 to the lower triplet state T_1* (*intersystem crossing*; rate constant w_{isc}). For each singlet state S_n there is an excited triplet state T_n of lower energy.

The de-excitation of molecules in the triplet state proceeds by processes similar to those acting in the de-excitation of S_1:

(a) *Emission of a photon with a rate constant w_p*. This process constitutes the p phosphorescence ($w_p \approx 10^3$ to 1 s^{-1}).
(b) *Non-radiative decay to the ground state S_0* with a rate constant w_{nr}'.
(c) *Transfer of energy to molecules located nearby* (collisional quenching rate constant w_q') *or to molecules at a distance* (energy transfer rate w_T').

1.4. FLUORESCENCE PROPERTIES

1.4.1. *The Stokes Shift*

An examination of the Jablonski diagram reveals the fact that the energy of the emitted photon is generally smaller than the energy of the absorbed photon. This phenomenon was first observed by *G. G. Stokes* in 1852 [1.5].

Energy losses between absorption and emission are always observed in fluorescent molecules in solution. They are mainly due to the rapid decay of the singlet S_1 to its lowest vibrational level. Also fluorescence transitions generally end up in higher vibrational levels of S_0, reducing further the absorption energy.

Further *Stokes shifts* may be due to solvent effects, excited state reactions and energy transfer.

1.4.2. *Kasha's Rule*

The radiationless processes $S_n \rightarrow S_1$ or $T_n \rightarrow T_1$ are usually so fast that lifetimes of higher levels are very short and *quantum yields* are very small. *In the vast majority of cases luminescence is observed from the lowest excited states*. This expresses the so-called *Kasha's rule* [1.6].

According to this rule *the same fluorescence spectrum is generally observed independently of the excitation wavelength.* Actually already in 1926 Vavilov had

reported that quantum yields were generally independent of the excitation wavelength [1.7].

Exceptions to Kasha's rule exist: they are represented by molecules that emit from the S_2 level, but such cases are generally not observed in biological molecules. Molecules that emit fluorescence from S_2 are azulene and its derivatives.

1.4.3. *Mirror Image Rule*

The emission spectrum of a fluorophore is the mirror image of its absorption spectrum if this spectrum is due only to the $S_0 \rightarrow S_1$ transition. The *generally symmetric aspect of the absorption and emission spectrum* is due to the fact that the same transitions are involved in the two processes and that S_0 and S_1 have similar vibrational energy levels.

The following two points should be kept in mind:

1. In most fluorophores the vibrational energy levels are not altered by the electronic excitation.
2. If the absorption reaches singlet states higher than S_1 the mirror image rule is not respected (see Fig. 1.2).

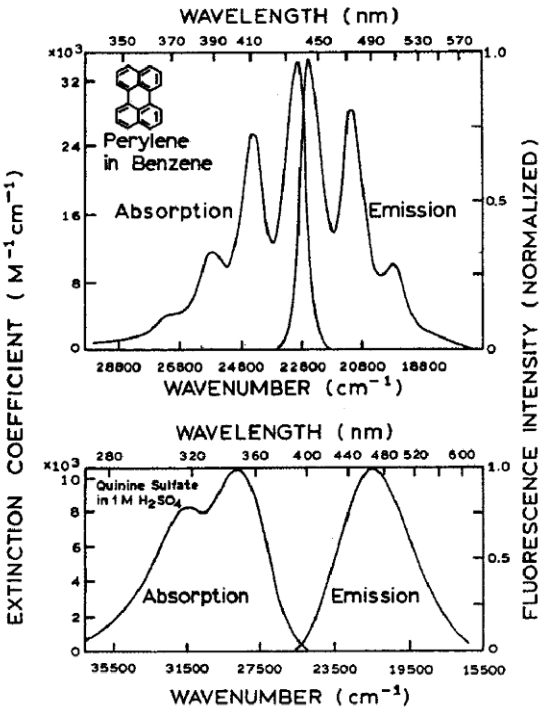

Figure 1.2. Absorption and fluorescence emission spectra of perylene and quinine (Reproduced from [1.1] by permission granted by Springer Science and Business Media and Professor Lakowicz).

1.4.4. *Fluorescence Lifetime and Quantum Yield*

The *fluorescence lifetime* is the *average value of the time that a fluorophore spends in its excited state*. If the decay is exponential the intensity will decrease as

$$I(t) = I_0 \exp(-t/\tau) \tag{1.1}$$

In this case 63% of the molecules decay before the time $t = \tau$ and 37% at times longer than τ.

The *quantum yield* Y is the *ratio of the number of emitted photons to the number of absorbed photons*. Looking at the Jablonski diagram we can derive for the quantum yield the formula

$$Y = w_r / (w_r + w_{nr}) \tag{1.2}$$

where now w_{nr} includes all processes other than the radiative one. The fluorescence lifetime is given by

$$\tau = 1/(w_r + w_{nr}) \tag{1.3}$$

The lifetime of the fluorophore in the absence of nonradiative processes is $\tau_r = 1/w_r$. Therefore we can express the quantum yield as follows:

$$Y = \tau / \tau_r \tag{1.4}$$

1.4.5. *Fluorescence Excitation Spectrum*

The *fluorescence excitation spectrum* is obtained by fixing the wavelength of the emission and changing the wavelength of the exciting light by means of a monochromator.

This measurement presents two problems: one is due to the variation of the intensity of the exciting lamp with wavelength and the other to the variation with wavelength of the sensitivity of the apparatus (monochromator plus detecting system).

Corrections to these problems may be achieved by running first the spectrum of a black-body emitter through the apparatus and then comparing it with the known black-body spectrum. This comparison will produce the sensitivity curve of the apparatus.

The real excitation spectrum is then obtained by dividing the recorded spectrum by the sensitivity curve of the apparatus.

1.4.6. *Fluorescence Quenching*

The fluorescence intensity may be *quenched* by various processes:

(a) *Collisional quenching* takes place when an excited fluorophore is de-excited by contact with a quencher molecule in solution. During the diffusive encounter with the quencher the fluorophore is returned to the ground state.

The *velocity of the fluorophore de-excitation* can be described as follows:

$$v = w_q [F] [Q] \tag{1.5}$$

where w_q = molecular quenching constant [$M^{-1}s^{-1}$],
[F] = fluorophore concentration, and
[Q] = quencher concentration.

If [Q] >> [F] the system can be considered pseudo-first order with a constant w_q [Q]:

$$v = \{w_q [Q]\} [F] \tag{1.6}$$

The quantum yield in the absence of the quencher is given by

$$Y_F = w_r / (w_r + w_{nr} + w_{is} \tag{1.7}$$

where w_r = radiative constant, w_{nr} = constant representing non-radiative processes and w_{isc}= intersystem crossing constant.

In the presence of the quencher the quantum yield becomes:

$$Y_{F(Q)} = w_r / (w_r + w_{nr} + w_{isc} + w_q [Q]) \tag{1.8}$$

Then

$$Y_F / Y_{F(Q)} = (w_r + w_{nr} + w_{isc} + w_q [Q]) / (w_r + w_{nr} + w_{isc}) =$$

$$= 1 + \{w_q [Q] / (w_r + w_{nr} + w_{isc})\} = 1 + \tau_0 w_q [Q]) \tag{1.9}$$

where τ_0 = unquenched lifetime. We can then write:

$$Y_F / Y_{F(Q)} = 1 + \tau_0 w_q [Q] = 1 + w_{SV} [Q] \tag{1.10}$$

where $w_{SV} = \tau_0 w_q$ is the *Stern–Volmer constant*. The above equation is called the *Stern–Volmer equation* [1.8].

Since the fluorescence intensity is proportional to the quantum yield, we can rewrite the Stern–Volmer equation as follows

$$I_0/I = 1 + \tau_0 w_q [Q] = 1 + w_{SV} [Q] \tag{1.11}$$

where I_0 = fluorescence intensity in the absence of the quencher and I = fluorescence intensity in the presence of the quencher.

We can also write:

$$\tau_0 = 1/ (w_r + w_{nr} + w_{isc}) \tag{1.12}$$

$$\tau_Q = 1/ (w_r + w_{nr} + w_{isc} + w_q [Q]) \tag{1.13}$$

and

$$\tau_0 / \tau_Q = 1 + \tau_0 w_q [Q] = 1 + w_{SV} [Q] \quad (1.14)$$

The constant w_{SV} is a measure of the sensitivity of a fuorophore to the presence of a quencher; the constant w_q indicates the importance of the diffusion of the quencher within the medium.

The mechanism of quenching varies with the fluorophore-quencher pair. If a fluorophore is well inside a macromolecule it is inaccessible to water-soluble quenching molecules and its w_{SV} will be low. On the contrary for a fluorophore free in solution or on the surface of a biomolecule w_{SV} will be large.

(b) Fluorescence quenching can also take place by a process that is called *static quenching*. Fluorophores can form nonfluorescent complexes; when one of these complexes absorbs light, it returns to its fundamental state without emitting photons.

We can describe this process as follows

$$F + Q \Leftrightarrow FQ \quad (1.15)$$

The association constant K_a is given by [1.9]

$$K_a = [FQ] / \{ [F]_f [Q]_f \} \quad (1.16)$$

where [FQ] = concentration of complex, $[F]_f$ = concentration of free fluorophores and $[Q]_f$ = concentration of free quenchers

The total concentration of fluorophores is given by

$$[F]_0 = [F]_f + [FQ] \quad (1.17)$$

Then

$$K_a = \{ [F]_0 - [F]_f \} / \{[F]_f [Q]_f \quad (1.18)$$

$$K_a [Q]_f = \{ [F]_0 - [F]_f \} / \{[F]_f \} = \{ [F]_0 / [F]_f \} - 1 \quad (1.19)$$

and

$$[F]_0/[F]_f = 1 + K_a [Q]_f = I_0 / I \quad (1.20)$$

If the concentration of bound quenchers is very small compared to the concentration of free quenchers we can write

$$[F]_0/[F]_f = I_0 / I = 1 + K_a [Q] \quad (1.21)$$

(c) Aside from the two processes presented above, *fluorescence quenching can take place by a variety of processes*, such as attenuation of incident light by the fluorphore itself or other absorbing species.

1.4.7. *Resonance Energy Transfer*

The process of *resonance energy transfer* (RET) takes place in the excited state of a fluorophore. It occurs whenever the emission spectrum of a fluorphore called the *donor* overlaps with the absorption spectrum of another molecule called the *acceptor*.

Energy transfer takes place via dipole–dipole interaction and without the intervention of photons. For this process the expression *fluorescence resonance energy transfer* (FRET) is also commonly used.

The rate of energy transfer is determined by the distance between donor and acceptor and by the extent of the spectral overlap. This overlap is described in terms of the so-called *Förster distance* (R_0). The rate of energy transfer is given by

$$w_T(R) = 1/\tau_D \, (R_0^6/R^6) \tag{1.22}$$

where R = distance between donor (D) and acceptor (A), and τ_D = lifetime of the donor in the absence of the acceptor.

The efficiency of the energy transfer process is given by the fraction of photons absorbed by the donor whose energy is transferred to the acceptor:

$$E = w_T(R) / [\tau_D^{-1} + w_T(R)] \tag{1.23}$$

This expression represents the ratio of the transfer rate to the total decay rate of the donor in the presence of the acceptor. Taking into account the formula for $w_T(R)$ the expression for E becomes

$$E = R_0^6/ [R_0^6 + R^6] \tag{1.24}$$

For a certain R_0, the extent of the energy transfer depends on the distance R. Conveniently the Förster distances are of the same size of biological molecules: 30–60 A. Therefore in principle energy transfer can be used as a *ruler* for measurements of distances between sites in proteins [10].

We note at this point that the diffusion of donors can increase the magnitude of energy transfer beyond that predicted by the above equation.

1.5. TIMESCALE OF MOLECULAR PROCESSES IN SOLUTION

Once an excited system decides to undergo a transition, the ensuing process is instantaneous. This is the reason why in the Jablonski diagram the transitions are indicated as vertical lines. Transitions actually occur in $\sim 10^{-15}$ s and during this time the nuclei do not undergo significant displacements: this statement expresses the Franck–Condon Principle.

The difference between fluorescence and absorption is that the latter is an induced process and the former is a spontaneous process. Even if the actual transition, once started, takes place instantaneously, molecules in an excited state remain in such a state in a time whose average length is the *fluorescence lifetime*.

The lifetime provides an expansion of time and distance that allows the excited molecule to interact with other molecules in solution. For this reason, while the absorption measurements are sensitive only to the immediate and instantaneously averaged environment of the fluorophore, fluorescence measurements may provide information about such dynamical processes as collisional quenching, and vibrational or solution relaxation.

1.6. FLUORESCENCE ANISOTROPY

Measurements of anisotropy of light emitted by fluorescent molecules are used in biochemical applications and provide information on the size and shape of proteins or the rigidity of the molecular environment.

The basic idea of fluorescence anisotropy is that a fluorescent molecule excited by polarized light will emit polarized fluorescence. However, if the molecule is moving, it will tend to scramble the polarization of light depending on the *rotational diffusion* (see Fig. 1.3).

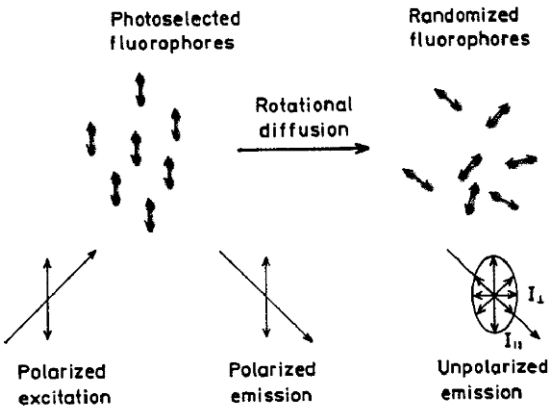

Figure 1.3. Effects of polarized excitation and rotational diffusion on the polarization or anisotropy of the emission (Reproduced from [1.1] by permission granted by Springer Science and Business Media and Professor Lakowicz).

Rotational diffusion is a process by which the overall orientation of molecules is maintained or restored. It represents the counterpart of translational diffusion, which maintains or restores the equilibrium statistical distribution of particles position in space.

In the random re-orientation process, because of the *equipartition theorem*, larger molecules re-orient more slowly than do small molecules, and, for this reason, measurements of the re-orientation times can provide information regarding the mass and distribution of mass within a molecular complex.

The scrambling effect is greatest with fluorophores freely tumbling in solution. Protein interactions can be detected when one interacting protein is fused to a fluorophore: upon binding of this protein to another protein, a larger, more stable complex is formed, which will *tumble* more slowly and will increase the polarization of the emitted light.

The technique of fluorescence anisotropy works best if the fluorophore is fused to a small molecule and binds to a large partner, thus maximizing the difference in polarization between bound and unbound states.

1.7. FLUORESCENCE UNDER CONTINUOUS AND PULSED EXCITATION

Under *continuous excitation* a sample is illuminated by a continuous beam of light and the intensity of the emitted light is recorded versus the wavelength. Because of the nanosecond time scale of fluorescence, steady state is reached almost immediately after the sample has been exposed to light.

Under *pulsed excitation* the sample is exposed to a light pulse whose width is typically shorter than the decay time. The decaying fluorescence intensity is recorded with a high-speed detection system that may measure the intensity or anisotropy on a time scale.

We shall now consider the relation between steady state and time-resolved measurements. The steady-state observation is an average of a time-resolved parameter over the intensity decay of the signal.

The intensity and anisotropy decay are given by the two relations:

$$I(t) = I_0 \, e^{-t/\tau} \tag{1.25}$$

$$r(t) = r_0 \, e^{-t/\theta} \tag{1.26}$$

where I_0 and r_0 are the intensity and anisotropy at time $t = 0$, following immediately the exciting pulse, respectively.

τ is the *lifetime* of the fluorescent state and θ is the *rotational correlation time* of the fluorophore, a parameter that describes how fast a molecule tumbles in solution and is given by

$$\theta = \eta V / RT \tag{1.27}$$

where η = viscosity, V = volume of the rotating unit, R = gas constant and T = temperature in K.

The steady state anisotropy is given by the time average of r(t) weighed by I(t):

$$r = \int_0^\infty r(t) \, I(t) \, dt \, / \int_0^\infty I(t) \, dt = r_0 / (1 + \tau/\theta) \tag{1.28}$$

The above formula is known as *Perrin equation* [1.11].

If the correlation time is much shorter than the lifetime ($\theta << \tau$) the anisotropy is zero and the molecules will randomize in solution during the emission and, as a result, the emitted light of the fluorophore will be depolarized.

If the correlation time is much larger than the lifetime ($\theta >> \tau$), then the measured anisotropy is equal to the fundamental anisotropy r_0 and the excited molecules will stay aligned during the process of emission and, as a result, the emission will be polarized.

We note also the simpler relation for the steady state intensity to the decay time:

$$I_{SS} = \int_0^{\infty} I_0 \, e^{-t/\tau} \, dt = I_0 \, \tau \tag{1.29}$$

I_0 is a parameter that depends on the fluorophore concentration and on a number of instrumental parameters.

It is appropriate to note that, despite the above relations tying the steady state to time-resolved parameters, much of the molecular information available from fluorescence is lost during the time averaging process. For this reason pulse-excited fluorescence ends up providing additional data.

The precise shape of the anisotropy decay, lost during the averaging process over the decay time, may contain information about the shape of the molecule and its flexibility.

The precise shape of the intensity decay contains also information lost during the averaging process. Macromolecules may exist in more than one conformation and the decay pattern of a probe bound to such a molecule could depend on the conformation.

The shape of excited donor decay may provide information regarding the distribution of acceptors around the donor. Time-resolved measurements may also provide information regarding the quenching processes.

1.8. A SUMMARY OF FLUORESCENCE SPECTROSCOPY

It is appropriate at this point to recount the basic rules of fluorescence [1.12]:

1. *The Franck–Condon Principle*: the nuclei are stationary during electronic transitions, and, for this reason, excitation occurs to vibrationally excited levels of the excited electronic state.
2. *Kasha's rule*: fluorescence emission occurs generally from the lowest excited singlet state.
3. *The Stokes shift*: emission is always of lower energy than absorption due to the nuclear relaxation in the excited state.
4. *The mirror image rule*: emission spectra are mirror images of the lowest absorption band.

The basic measurements related to fluorescence are:

1. *Absorption*: these measurements are mainly used to set the energy level scheme.
2. *Steady state fluorescence*: the steady state spectra are used to identify the fluorescent state(s).
3. *Excitation spectra*: these spectra tell us in what spectral region we have to ***pump*** the system in order to obtain the emission that is being monitored.
4. *Response to pulsed excitation*: the decay constant τ of an exponentially decaying fluorescence signal is the lifetime of the state from which the transition originates. Deviation of the decay pattern from exponentiality may indicate the presence of other processes such as energy transfer.

In addition to the above, we want to point out some of the relevant information that can be derived from particular techniques:

1. *Emission spectra and Stokes shift*: the shifts between absorption and fluorescence wavelengths are most effective for measuring the interaction of a fluorophore with its immediate surroundings. An important property of many fluorophores is their sensitivity to their immediate environment.
2. *Quenching of fluorescence*: a number of molecular interactions can result in the quenching of fluorescence: excited state reactions, molecular rearrangements, energy transfer, ground state complex formation, and collisional quenching.
   Fluorescence quenching is studied both as fundamental phenomenon and as a source of information regarding biochemical systems. These biochemical applications are due to the molecular interactions that produce the quenching.
   Quenching studies can be used to reveal the localization of fluorophores in proteins and membranes, and their permeability to quenchers. Also, the rate of collisional quenching can be used to measure the diffusion coefficient of the quencher.
3. *Fluorescence anisotropy*: fluorophores absorb light along a particular direction with respect to the molecular axes. The extent to which a fluorophore rotates during its excited state lifetime determines its polarization and anisotropy.
   Fluorescence polarization can be used to measure the apparent volume or molecular weight of proteins. Larger proteins rotate more slowly; then, if a protein binds to another protein, the rotational rate decreases, and the anisotropy increases.
4. *Fluorescence resonance energy transfer (FRET)*: FRET provides a means to measure the distance between sites on macromolecules. *The distance between donor and acceptor can be calculated from the transfer efficiency.*

2. Theory of Resonance Energy Transfer

2.1. QUANTUM-MECHANICAL TREATMENT OF THE INTERACTIONS AMONG ATOMS

2.1.1. *Two-Atom System*

Let us consider for simplicity two atoms of hydrogen with the two nuclei located at positions a and b and the two electrons at positions (x_1, y_1, z_1) and (x_2, y_2, z_2) as in Fig. 2.1. Let the internuclear distance R be such that

$$R >> x_1, y_1, z_1, x_2, y_2, z_2 \tag{2.1}$$

so that the overlap between the wavefunctions of the two atoms may

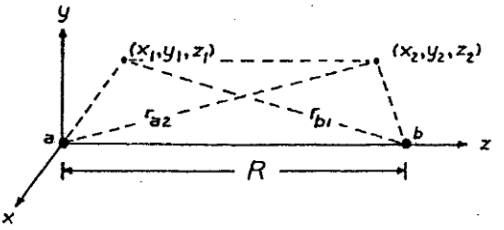

Figure 2.1. System consisting of two hydrogen atoms.

be neglected. The wavefunction of the system, neglecting the interatomic interaction is given by [2.1]

$$\Psi(1,2) = \psi_a(1)\,\psi_b(2) \tag{2.2}$$

where $\psi_a(1)$ and $\psi_b(2)$ are the wavefunctions of the individual atoms; 1 and 2 stand for the coordinates of the two electrons. The interaction Hamiltonian is given by

$$H' = e^2 \left(\frac{1}{r_{ab}} + \frac{1}{r_{12}} - \frac{1}{r_{a2}} - \frac{1}{r_{b1}} \right) \tag{2.3}$$

where

$$\begin{cases} r_{ab} = R \\ r_{12} = \sqrt{(x_1 - x_2)^2 + (y_1 - y_2)^2 + (z_1 - z_2 - R)^2} \\ r_{a2} = \sqrt{x_2^2 + y_2^2 + (R + z_2)^2} \\ r_{b1} = \sqrt{x_1^2 + y_1^2 + (z_1 + R)^2} \end{cases} \tag{2.4}$$

The correction to the energy eigenvalue to first order in H' is

$$E' = \langle \psi_a(1)\,\psi_b(2)\,|H'|\psi_a(1)\,\psi_b(2) \rangle \tag{2.5}$$

We use the expansion

$$\frac{1}{1+\varepsilon} = 1 - \frac{\varepsilon}{2} + \frac{3}{8}\varepsilon^2 - \frac{15}{48}\varepsilon^3 + \ldots \tag{2.6}$$

and retain only the first two powers of the electrons' coordinates. The result is

$$H' = \frac{e^2}{R^3}(x_1x_2 + y_1y_2 - 2z_1z_2) \tag{2.7}$$

and

$$E' = \langle \psi_a(1)\ \psi_b(2)|H'|\psi_a(1)\ \psi_b(2)\rangle$$

$$= \frac{e^2}{R^3}\langle \psi_a(1)\,\psi_b(2)\,|(x_1x_2 + y_1y_2 - 2z_1z_2)|\psi_a(1)\,\psi_b(2)\rangle = 0 \tag{2.8}$$

because H' is an odd operator and Ψ_a *and* Ψ_b have definite parity. The correction to the ground state energy to first order in H' is zero. But to second order where

$$E'' = \sum_{k\neq 0} \frac{\langle 0|H'|k\rangle\langle k|H'|0\rangle}{E_o - E_k} \tag{2.9}$$

$|0\rangle$ and $|k\rangle$ are the ground and excited states of the two - atom system, respectively.

The energy levels of the hydrogen atom are given by

$$E_n = -\frac{e^2}{2n^2 a_o} \tag{2.10}$$

where $a_o = \hbar^2/me^2$. The ground state energy E_o is equal to $-(e^2/a_o)$. The states that $|k\rangle$ contribute to the sum in (2.9) are made up of products of odd wavefunctions of the two atoms; the energy of the lowest such state is $-(e^2/4a_o)$ and the energy of the highest such state is zero. Therefore $(E_o - E_k)$ lies in the interval

$$\left(-\frac{3}{4}\frac{e^2}{a_o}, -\frac{e^2}{a_o}\right);$$

we shall approximate this quantity with the value $-(e^2/a_o)$ for all k's.

Going back to (2.9) we find

$$E'' = -\frac{1}{e^2/a_o}\sum_{k\neq 0}\langle 0|H'|k\rangle\langle k|H'|0\rangle$$

$$= -\frac{1}{e^2/a_o}\left[\sum_{k\neq 0}\langle 0|H'|k\rangle\langle k|H'|0\rangle + \langle 0|H'|0\rangle\langle 0|H'|0\rangle\right]$$

$$= - \frac{1}{e^2/a_o} \sum_k < 0|H'|k >< k|H'|0 > = - \frac{1}{e^2/a_o} < 0|(H')^2|0 > \qquad (2.11)$$

where we have used the relation (2.8) reexpressed as

$$< 0|H'|0 > = 0 \qquad (2.12)$$

and also

$$\sum_k < 0|H'|k >< k|H'|0 > = < 0|(H')^2|0 > \qquad (2.13)$$

We have

$$< 0|(H')^2|0 > = \frac{e^4}{R^6} < \psi_a(1)\,\psi_b(2)\,|x_1^2 x_2^2 + y_1^2 y_2^2 + 4z_1^2 z_2^2|\,\psi_a(1)\,\psi_b(2) >$$

$$= \frac{e^4}{R^6} (\overline{x_1^2}\,\overline{x_2^2} + \overline{y_1^2}\,\overline{y_2^2} + \overline{4z_1^2}\,\overline{z_2^2}) \qquad (2.14)$$

In the ground state of the hydrogen atom

$$\overline{x^2} = \overline{y^2} = \overline{z^2} = \frac{1}{3}\,\overline{r^2} \qquad (2.15)$$

and

$$\overline{r^2} = 3a_o^2 \qquad (2.16)$$

Then

$$< 0|(H')^2|0 > = \frac{e^4}{R^6} \left(\frac{1}{9}\overline{r_1^2}\,\overline{r_2^2} + \frac{1}{9}\overline{r_1^2}\,\overline{r_2^2} + \frac{4}{9}\overline{r_1^2}\,\overline{r_2^2} \right)$$

$$= \frac{2}{3} \frac{e^4}{R^6} \overline{r_1^2}\,\overline{r_2^2} = \frac{6e^4}{R^6} a_o^4 \,, \qquad (2.17)$$

and

$$E'' = - \frac{1}{e^2/a_o} < 0|(H')^2|0 > = - \frac{6e^2 a_o^5}{R^6} \qquad (2.18)$$

If we extend the expansion of H' and include higher power of the electrons' coordinates the result is [2.2].

$$E'' = -\frac{6e^2 a_o^5}{R^6} - \frac{135e^2 a_o^7}{R^8} - \frac{1416e^2 a_o^9}{R^{10}} \tag{2.19}$$

This energy, intrinsically negative, is called *the van der Waals' energy*. Note that this energy goes to zero as $h \to 0$.

For many electron atoms the perturbation Hamiltonian is represented by a sum of terms of type (2.7) with one term for each pair of electrons [2.3].

2.1.2. *Static Effects of the Interaction*

The van der Waals interaction is responsible for one type of chemical bond, called *van der Waals bond*.

The forces that produce this bond are the weakest, but probably the most universal. They are usually associated with energies of 1–10 kcal/mol (~0.04–0.4 eV), and are generally masked by the stronger covalent forces which are present in molecules and are associated with stronger energies of about 100 kcal/mol (~4 eV). The role of van der Waals forces is important in explaining the bond between molecules and atoms with saturated orbitals, where no covalent bonding is possible.

In addition, we shall see that the van der Waals interaction is responsible for the time evolution of a two-atom excited system, in that it may lead to the transfer of excitation energy from one atom to another.

2.1.3. *Dynamical Effects of the Interaction*

Consider a system with a time – independent Hamiltonian H_o. The time-dependent Schrödinger equation is

$$H_o \Psi = i\hbar \frac{\partial \Psi}{\partial t} \tag{2.20}$$

If the system is in a stationary state labeled i

$$\Psi(t) = \Psi_i(t) = e^{-i(E_i/\hbar)t} \Psi_i(0) \tag{2.21}$$

where the energy values are given by

$$H_o \Psi_i(0) = E_i \Psi_i(0) \tag{2.22}$$

We shall assume that the wavefunctions $\Psi_i(t)$ are orthonormal.

Let us now suppose that the system is subjected to a time-dependent perturbation represented by H'(t). The system will be represented by a wavefunction $\Psi(t)$ such that

$$H\Psi(t) = (H_o + H')\,\Psi(t) = i\hbar \frac{\partial \Psi(t)}{\partial t} \tag{2.23}$$

We can expand $\Psi(t)$ in terms of the complete set $\Psi_i(t)$

$$\Psi(t) = \sum_i c_i(t)\ \Psi_i(t) \tag{2.24}$$

If $H' = 0$, the coefficients c_i's are time - independent. Replacing Eq. (2.24) in Eq (2.23).

$$(H_o + H') \sum_i c_i(t)\ \Psi_i(t) = i\hbar \left[\sum_i c_i(t) \frac{\partial \Psi_i(t)}{\partial (t)} + \sum_i \frac{\partial c_i(t)}{\partial (t)}\ \Psi_i(t) \right] \tag{2.25}$$

Then

$$\sum_i c_i(t)\, H'\ \Psi_i(t) = i\hbar \sum_i \frac{\partial c_i(t)}{\partial t}\ \Psi_i(t) \tag{2.26}$$

where we have taken advantage of Eqs. (2.21) and (2.22). Multiplying by $\Psi_k^*(t)$ and and integrating over all space we obtain

$$i\hbar \frac{\partial c_k(t)}{\partial t} = \sum_i c_i(t)\ < \Psi_k(t) | H' | \Psi_i(t) >$$

$$= \sum_i c_i(t)\ < \Psi_k(0) | H' | \Psi_i(0) >\ e^{i\omega_{ki} t} \tag{2.27}$$

where

$$\omega_{ki} = \frac{E_k - E_i}{\hbar} \tag{2.28}$$

1. Coherent Energy Transfer in a Two-Atom System. We shall now make the following assumptions:

   (a) The system has only two energy states, say 1 and 2.
   (b) The perturbation H' is constant, but is turned on at time t = 0.

In a two-atom A and B system, state 1(2) consists of atom A(B) excited and B(A) deexcited.

The coupled equations (2.27) becomes

$$\begin{cases} i\hbar\,\dot{c}_1(t) = c_1(t) < \Psi_1(0)|H'|\Psi_1(0) > \\ \qquad\qquad + c_2(t) < \Psi_1(0)|H'|\Psi_2(0) > e^{i\omega_{12}t} \\ i\hbar\,\dot{c}_2(t) = c_1(t) < \Psi_2(0)|H'|\Psi_1(0) > e^{i\omega_{21}t} \\ \qquad\qquad + c_2(t) < \Psi_2(0)|H'|\Psi_2(0) > \end{cases} \tag{2.29}$$

Set

$$\begin{cases} < \Psi_i(0)|H'|\Psi_i(0) > \;=\; V_i \\ < \Psi_i(0)|H'|\Psi_k(0) > \;=\; M_{ik} \end{cases} \tag{2.30}$$

Then

$$\begin{cases} i\hbar\,\dot{c}_1(t) = c_1(t)\,V_1 + c_2(t)\,M_{21}^{*}\,e^{-i\omega_{21}t} \\ i\hbar\,\dot{c}_2(t) = c_2(t)\,M_{21}\,e^{-i\omega_{21}t} + c_2(t)\,V_2 \end{cases} \tag{2.31}$$

If at time t = 0, the system is in state 1:

$$c_1(0) \;=\; 1, \quad c_2(0) \;=\; 0 \tag{2.32}$$

and the time evolution of the system is given by the equations

$$\begin{cases} c_1(t) = \cos at + \dfrac{i}{2a\hbar}[(E_2 + V_2) - (E_1 + V_1)]\sin at \\ \qquad\qquad \cdot e^{-i\left(\frac{V_1 + V_2}{2\hbar}\right)t}\; e^{-i\frac{\omega_{21}}{2}t} \\ c_2(t) = \dfrac{M_{21}}{i\hbar a}\sin at\; e^{-i\left(\frac{V_1 + V_2}{2\hbar}\right)t}\; e^{i\frac{\omega_{21}}{2}t} \end{cases} \tag{2.33}$$

where

$$a = \left\{ \frac{|M_{21}|^2}{\hbar^2} + \frac{[(E_2 + V_2) - (E_1 + V_1)]^2}{4} \right\}^{1/2} \text{sec}^{-1} \tag{2.34}$$

We note that

$$|c_1(t)|^2 + |c_2(t)|^2 = 1 \tag{2.35}$$

at all times. Assume now

$$E_1 = E_2, \quad V_1 = V_2 \tag{2.36}$$

In this case

$$\begin{cases} |c_1(t)|^2 \cos^2 at \\ |c_2(t)|^2 \sin^2 at \end{cases} \tag{2.37}$$

where

$$a = \frac{|M_{12}|}{\hbar} \tag{2.38}$$

and at the time evolution of the system is represented in Fig. 2.2

At time t = 0

$$|c_1(0)| = 1, \quad |c_2(0)|^2 = 0 \tag{2.39}$$

At time $t = \frac{\pi}{2a} = \frac{\pi\hbar}{2|M_{12}|}$

$$|c_1(\frac{\pi}{2a})|^2 = 0 \quad , \quad |c_2(\frac{\pi}{2a})^2 = 1 \tag{2.40}$$

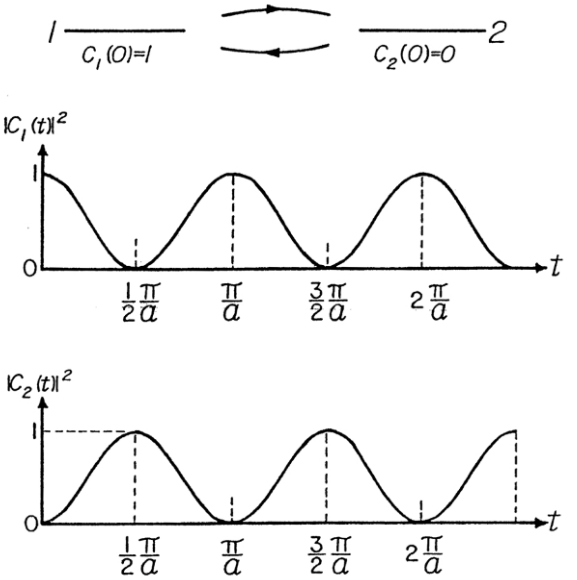

Figure 2.2. Coherent time evolution of a two-atom system.

This time evolution is called *coherent*.

2. Incoherent Energy Transfer in a Two-Atom System. If at time t = T (small) the phase of the wavefunction is interrupted, the change in $|c_2(t)|^2$ in time T is

$$\Delta|c_2(t)|^2 \approx a^2 T^2 \tag{2.41}$$

and in time t >> T

$$|c_2^2(t)|^2 \approx \frac{t}{T}\Delta|c_2(t)|^2 = \frac{t}{T}a^2 T^2 = a^2 Tt \tag{2.42}$$

The probability $|c_2(t)|^2$ is now proportional to t and a probability per unit time can be defined

$$w_{12} = \frac{|c_2(t)|^2}{t} = a^2 T = \frac{|M_{21}|^2}{\hbar^2} T \tag{2.43}$$

But

$$T = \frac{h}{\Delta E} \tag{2.44}$$

where ΔE = width of the transition. Then

$$w_{12} = \frac{|M_{21}|^2}{h^2} \frac{h}{\Delta E} = \frac{2\pi}{\hbar} |< \Psi_2(0) |H'| \Psi_1(0) >|^2 \, g(E) \tag{2.45}$$

where g(E) = density of final states. If both state 1 and state 2 are smeared

$g_1(E_1)\, dE_1$ = probability that state 1 has energy in $(E_1, E_1 + dE_1)$

$g_2(E_2)\, dE_2$ = probability that state 2 has energy in $(E_2, E_2 + dE_2)$

and g(E) in (2.45) is replaced by

$$\int g_1(E_1)[\int g_2(E_2)\, \delta(E_2 - E_1)\, dE_2]\, dE_1 = \int g_1(E_1)\, g_2(E_1)\, dE_1$$

$$= \int g_1(E)\, g_2(E)\, dE \tag{2.46}$$

The question now is: If at time t = 0, the system is in state 1, how will it evolve? And the answer is: Since probabilities per unit time are appropriate, a *master equation* treatment must be used. Let

$$\begin{aligned} P_1(t) &= |c_1(t)|^2 \\ P_2(t) &= |c_2(t)|^2 \end{aligned} \tag{2.47}$$

Then, since $w_{12} = w_{21} = w$

$$\begin{cases} \dfrac{dP_1(t)}{dt} = w[P_2(t) - P_1(t)] \\ \dfrac{dP_2(t)}{dt} = w[P_1(t) - P_2(t)] \end{cases} \tag{2.48}$$

Given the initial conditions

$$P_1(0) = 1, \quad P_2(0) = 0 \tag{2.49}$$

the solutions of (2.48) are

$$\begin{cases} P_1(t) = \frac{1}{2}\,(1 + e^{-2wt}) \\ P_2(t) = \frac{1}{2}\,(1 - e^{-2wt}) \end{cases} \tag{2.50}$$

and are represented in Fig. 2.3.

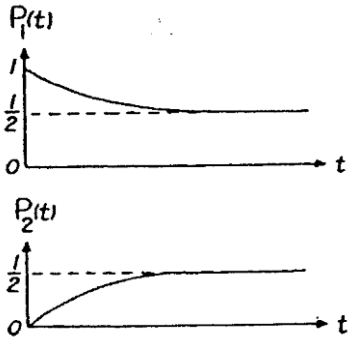

Figure 2.3. Incoherent time evolution of a two-atom system.

This time evolution is called *incoherent*.

We want at this point to associate some key words and expressions to coherent and incoherent evolutions.

Coherent evolution

Reversibility
Oscillations
Characteristic time $\propto \frac{1}{M}$
Transfer rate $\propto M$

Incoherent evolution

Irreversibility
Approach to equilibrium
Characteristic time $\propto \frac{1}{M^2}$
Transfer rate $\propto M^2$

2.1.4. *The Relevant Energy Transfer Hamiltonian*

Let us now consider again a two-atom system as in Fig. 2.4. Let H_A and H_B be the Hamiltonian of atom A and B, respectively. The Hamiltonian of the two-atom system is then given by

$$H = H_A + H_B + H_{AB} \tag{2.51}$$

where

$$H_{AB} = \frac{Z_a Z_b e^2}{R} + \frac{e^2}{r_{12}} - \frac{Z_a e^2}{r_{a2}} - \frac{Z_b e^2}{r_{b1}}$$

$$= \frac{Z_a Z_b e^2}{R} + \frac{e^2}{r_{12}} - \frac{Z_a e^2}{|\vec{R} + \vec{r}_{b2}|} - \frac{Z_b e^2}{|-\vec{R} + \vec{r}_{a1}|} \tag{2.52}$$

Let |a> and |a'>| be the ground state and excited state wavefunctions of atom A, respectively and |b> and |b' the ground state and excited state wavefunctions of atom B, respectively. We shall consider a transition from and initial *state* |1> to a final state |2> of the two-atom system, where

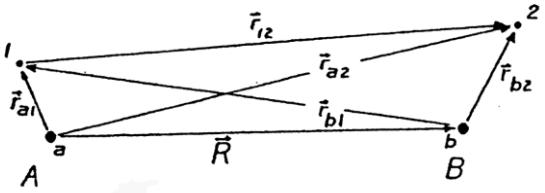

Figure 2.4. Two-atom system

$$|1> = |a'b>, \quad |2> = |ab'> \tag{2.53}$$

The relevant matrix element is given by

$$< a'(1)\ b(2)|H_{AB}|a(1)\ b'(2) >$$

$$= Z_a Z_b \frac{e^2}{R} < a'(1)|a(1) >< b(2)|b'(2) >$$

$$+ < a'(1)\ b(2)\left|\frac{e^2}{r_{12}}\right|a(1)\ b'(2) >$$

$$-Z_a\, e^2 \;<a'(1)\;|a(1)><b(2)\left|\frac{1}{|\vec{R}+\vec{r}_{b2}|}\right|b'(2)>$$

$$-Z_b\, e^2 \;<a'(1)\left|\frac{1}{|-\vec{R}+\vec{r}_{a1}|}\right|a(1)><b(2)|b'(2)>$$

$$=\; <a'(1)\;\; b(2)\left|\frac{e^2}{r_{12}}\right|a(1)\;\; b'(2)> \tag{2.54}$$

Taking into account the overlap of the wavefunctions we replace the relevant product wavefunctions as follows:

$$\begin{cases} |a'(1)\; b(2)> \;\rightarrow \dfrac{1}{\sqrt{2}}\Big|\, a'(1)\; b(2) \;-\; b(1)\; a'(2)> \\ |a(1)\;\; b'(2)> \;\rightarrow \dfrac{1}{\sqrt{2}}|a(1)\;\; b'(2) \;-b'(1)\; a(2)> \end{cases} \tag{2.55}$$

Then

$$\begin{aligned} <a'(1)\;\; b(2)|H_{AB}|a(1)\;\; b'(2)> \quad \rightarrow & \frac{1}{2}<a'(1)\;\; b(2)|H_{AB}|a(1)\;\; b'(2)> \\ & +\frac{1}{2}<b(1)\;\; a'(2)|H_{AB}|b'(1)\;\; a(2)> \\ & -\frac{1}{2}<b(1)\; a'(2)|H_{AB}|a(1)\; b'(2)> \\ & -\frac{1}{2}<a'(1)\;\; b(2)|H_{AB}|b'(1)\;\; a(2)> \\ =\; & <a'(1)\;\; b(2)|H_{AB}|a(1)\;\; b'(2)> \\ - \; & <a'(1)\;\; b(2)|H_{AB}|b'(1)\;\; a(2)> \end{aligned} \tag{2.56}$$

and

$$<a'(1)\;\; b(2)|H_{AB}|b'(1)\;\; a(2)> = Z_a\;\; Z_b\;\; \frac{e^2}{R}<a'(1)|b'(1)><b(2)|a(2)>$$

$$+ \ < a'(1) \ b(2) \left| \frac{e^2}{r_{12}} \right| b'(1) \ a(2) >$$

$$- Z_a \, e^2 < a'(1) \ |b'(1)>< b(2) \left| \frac{1}{|\vec{R} + \vec{r}_{b2}|} \right| a(2) >$$

$$- Z_b \, e^2 < b(2) \ |a(2)>< a'(1) \left| \frac{1}{|\vec{R} + \vec{r}_{a1}|} \right| b'(1) >$$

$$\approx \ < a'(1) \ b(2) \left| \frac{e^2}{r_{12}} \right| b'(1) \ a(2) > \qquad (2.57)$$

The relevant matrix element is then given by

$$< |H_{AB}| > \ = \ < a'(1) \ b(2) \left| \frac{e^2}{r_{12}} \right| a(1) \ b'(2) >$$
$$- \ < a'(1) \ b(2) \left| \frac{e^2}{r_{12}} \right| b'(1) \ a(2) > \qquad (2.58)$$

where the first term is called the *direct term* and the second term the *exchange term*.

2.1.5. *Interaction Between Two Atoms at Fixed Distance*

Let A and B be two atoms in fixed position; Fig. 2.5 reports the relevant coordinates. In this system

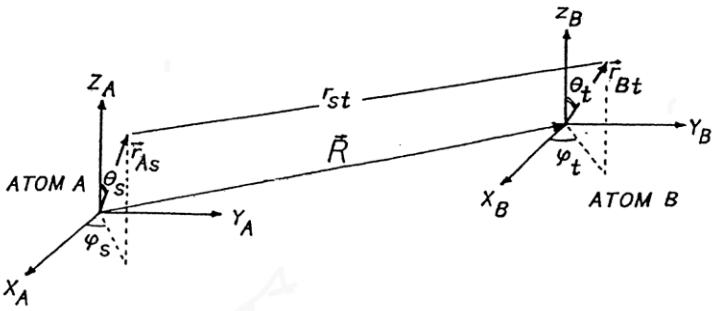

Figure 2.5. Two-atom system.

$$\vec{R} \equiv (R, \theta, \phi) \quad , \quad R >> r_{As}, r_{Bt}$$

$$\vec{r}_{st} = \vec{R} + \vec{r}_{Bt} - \vec{r}_{As}$$

The relevant energy transfer Hamiltonian is

$$H_{AB} = \sum_{s,t} \frac{e^2}{r_{st}} = \sum_{s,t} \frac{e^2}{\left|\vec{R} + \vec{r}_{Bt} - \vec{r}_{As}\right|} \tag{2.59}$$

where the sum is over the electrons of the two atoms.

Carlson and Rushbrooke [2.4] have carried out the expansion of H_{AB} in spherical harmonics taking into account the fact that $R >> r_{As}, r_{Bt}$. The result of their calculations is

$$H_{AB} = e^2 \sum_{\ell=0}^{\infty} \sum_{\ell_2=0}^{\infty} \sum_{m_1=-\ell}^{\ell} \sum_{m_2=-\ell}^{\ell} \frac{1}{R^{\ell_1+\ell_2+1}}$$

$$\cdot G_{12}\ C^{\ell_1+\ell_2}_{m_1+m_2}(\theta, \phi)^*\ D^{\ell_1}_{m_1}(A)\ D^{\ell_2}_{m_2}(B) \tag{2.60}$$

where

$$G_{12} = (-1)^{\ell_1} \sqrt{\frac{(2\ell_1 + 2\ell_2 + 1)!}{(2\ell_1)!(2\ell_2)!}} \begin{pmatrix} \ell_1 & \ell_2 & \ell_1+\ell_2 \\ m_1 & m_2 & -m_1-m_2 \end{pmatrix} \tag{2.61}$$

$$D^{\ell}_{m}(A) = \sum_{s} r_s^{\ell}\ C^{\ell}_{m}(0_s, \phi_s) \tag{2.62}$$

$$C^{\ell}_{m}(\Omega) = \sqrt{\frac{4\pi}{2\ell + 1}}\ Y_{\ell m}(\Omega) \tag{2.63}$$

$$\underbrace{\begin{pmatrix} j_1 & j_2 & j_3 \\ m_1 & m_2 & m_3 \end{pmatrix}}_{\text{3j symbols}} = (-1)^{j_1 - j_2 - m_3} \sqrt{2j_3 + 1}$$

$$\underbrace{\cdot < j_1\ m_1\ j_2\ m_2 \mid j_1\ j_2\ j_3\ -m_3 >}_{\text{Clebsch-Gordan coefficients}}$$

3j symbols = 0 unless

$$\Delta(j_1\ j_2\ j_3);\quad m_1 + m_2 + m_3 = 0$$

Example

$$Y_{10} = \sqrt{\frac{3}{4\pi}\cos\theta} = \sqrt{\frac{3}{4\pi}}\,\frac{z}{r}$$

$$Y_{1,\pm1} = m\sqrt{\frac{3}{8\pi}}\,e^{\pm i\phi}\sin\theta = m\sqrt{\frac{3}{8\pi}}\,\frac{x \pm iy}{r}$$

Then

$$C^1_0 = \sqrt{\frac{4\pi}{3}}\,Y_{10} = \sqrt{\frac{4\pi}{3}}\sqrt{\frac{3}{4\pi}}\,\frac{z}{r} = \frac{z}{r}$$

$$C^1_{\pm1} = \sqrt{\frac{4\pi}{3}}\,Y_{1\pm1} = \sqrt{\frac{4\pi}{3}}\left[\mp\sqrt{\frac{3}{8\pi}}\,\frac{x \pm iy}{r}\right] = \mp\,\frac{1}{\sqrt{2}}\,\frac{x \pm iy}{r}$$

and

$$D^1_0 = rC^1_0 = z$$

$$D^1_1 = rC^1_1 = -\,\frac{1}{\sqrt{2}}\,(x + iy)$$

$$D^1_{-1} = rC^1_{-1} = \frac{1}{\sqrt{2}}\,(x - iy)$$

Then the direct term of $<|H_{AB}|>$ is

$$<a'b|H_{AB}|ab'> = \sum_{\substack{\ell_1\ell_2\\ m_1m_2}} \frac{e^2}{R^{\ell_1+\ell_2+1}}\,G_{12}\;C^{\ell_1+\ell_2\,*}_{m_1+m_2}$$

$$\cdot\,<a'\left|D^{\ell_1}_{m_1}\right|a>\cdot<b\left|D^{\ell_2}_{m_2}\right|b'> \qquad (2.64)$$

The relevant quantity that enters the transition probability is

$$|< a'b|H_{AB}|ab'>|^2 = \sum_{\substack{\ell_1\ell_2 \\ m_1 m_2}} \sum_{\substack{\ell_3\ell_4 \\ m_3 m_4}} \frac{e^4}{R^{\ell_1+\ell_2+\ell_3+\ell_4+2}} G_{12}\ G_{34}$$

$$\cdot C^{\ell_1+\ell_2 *}_{m_1+m_2}\ C^{\ell_3+\ell_4}_{m_3+m_4}$$

$$\cdot\ < a'\left|D^{\ell_1}_{m_1}\right|a >< a'\left|D^{\ell_3}_{m_3}\right|a >^*$$

$$\cdot\ < b\left|D^{\ell_2}_{m_2}\right|b' >< b\left|D^{\ell_4}_{m_4}\right|b' >^* \qquad (2.65)$$

We average over θ, ϕ :

$$\frac{1}{4\pi} \int\int \sin\theta\, d\theta\, d\phi\, C^{\ell_1+\ell_2 *}_{m_1+m_2}\ C^{\ell_3+\ell_4}_{m_3+m_4}$$

$$\frac{1}{\sqrt{(2\ell_1 + 2\ell_2 + 1)(2\ell_3 + 2\ell_4 + 1)}}$$

$$\cdot \delta_{\ell_1+\ell_2,\ell_3+\ell_4}\ \delta_{m_1+m_2,m_3+m_4}$$

and use the following approximations

(1) Neglect cross terms : $\ell_1 \neq \ell_3, \ell_2 \neq \ell_4, m_1 \neq m_3, m_2 \neq m_4$

$$\left|< \left|H_{AB}\right| >\right|^2 \approx \sum_{\substack{\ell_1\ell_2 \\ m_1 m_2}} \left[\frac{e^2}{\ell_1 + \ell_2 + 1}\right]^2 G^2_{12}\ \frac{1}{2\ell_1 + 2\ell_2 + 1}$$

$$\cdot\ |< a'|D^{\ell_1}_{m_1}|a >|^2 |< b|D^{\ell_2}_{m_2}|b' >|^2$$

where

$$G^2_{12} = \frac{(2\ell_1 + 2\ell_2 + 1)!}{(2\ell_1)!(2\ell_2)!} \begin{pmatrix} \ell_1 & \ell_2 & \ell_1+\ell_2 \\ m_1 & m_2 - m_1 - m_2 & \end{pmatrix}^2$$

(2) Take the average of G^2_{12} :

$$< G^2_{12} > = \frac{1}{(2\ell_1 + 1)(2\ell_2 + 1)} \sum_{m_1, m_2} G^2_{12}$$

$$= \frac{1}{(2\ell_1\ 1)(2\ell_2\ +\ 1)} \sum_{m_1,m_2} \frac{(2\ell_1\ +\ 2\ell_2\ +\ 1)!}{(2\ell_1)!(2\ell_2)!}$$

$$\cdot \begin{pmatrix} \ell_1 & \ell_2 & \ell_1 + \ell_2 \\ m_1 & m_2 & -m_1 - m_2 \end{pmatrix}^2$$

$$= \frac{(2\ell_1 + 2\ell_2 + 1)!}{(2\ell_1 + 1)!(2\ell_2 + 1)!} \underbrace{\sum_{m_1 m_2} \begin{pmatrix} \ell_1 & \ell_2 & \ell_1 + \ell_2 \\ m_1 & m_2 & -m_1 - m_2 \end{pmatrix}^2}_{1}$$

$$= \frac{(2\ell_1\ +\ 2\ell_2\ +\ 1)!}{2\ell_1\ +\ 1)!\,(2\ell_2\ +\ 1)!}$$

Therefore

$$\left|<\left|H_{AB}\right|>\right|^2 = \sum_{\substack{\ell_1 \ell_2 \\ m_1 m_2}} \left[\frac{e^2}{{}_R\,\ell_1 + \ell_2 + 1}\right]^2$$

$$\cdot \frac{(2\ell_1\ +\ 2\ell_2\ +\ 1)!}{(2\ell_1\ +\ 1)!(2\ell_2\ +\ 1)!} \quad \frac{1}{2\ell_1\ +\ 2\ell_2\ +\ 1}$$

$$\cdot \left|< a'|D^{\ell_1}_{m_1}|a >\right|^2 \left|< b|D^{\ell_2}_{m_2}|b' >\right|^2$$

$$\cdot \sum_{\ell_1 \ell_2} \left(\frac{e^2}{\ell_1 + \ell_2 + 1}\right)^2 \frac{(2\ell_1 + 2\ell_2)!}{(2\ell_1 + 1)!(2\ell_2 + 1)!}$$

$$\cdot \left[\sum_{m_1} \left|< a'|D^{\ell_1}_{m_1}|a >\right|^2\right]\left[\sum_{m_2} \left|< b|D^{\ell_2}_{m_2}|b' >\right|^2\right] \tag{2.66}$$

2.2. DIFFERENT TYPES OF INTERACTIONS

2.2.1. *Multipolar Electric Interactions*

An electric multipole of a charge distribution $\rho(\vec{x})$ with $\vec{x} \equiv (r, \theta, \phi)$ is defined as follows:

$$D_{\ell,m} = \sqrt{\frac{4\pi}{2l\ +\ 1}} \int d\tau\, \rho(\vec{x})\, r^{\ell}\, Y_{\ell m}(\theta, \phi) \tag{2.67}$$

If we set

$$\rho(\vec{x}) = \sum_s e\delta(\vec{x} - \vec{x}_s) \tag{2.68}$$

we obtain

$$D_{\ell,m} = \sqrt{\frac{4\pi}{2\ell+1}} \int d\tau \sum_s e\delta(\vec{x} - \vec{x}_s)\ r^{\ell}\ Y_{\ell m}(\theta,\phi)$$

$$= e\sum_s \sqrt{\frac{4\pi}{2\ell+1}}\ r_s^{\ell}\ Y_{\ell m}(\theta_s,\phi_s) \tag{2.69}$$

These multipoles are, apart e, the same quantities D_m^{ℓ} defined in Eq. (2.62).

The square of the matrix element of the multipolar interaction can be written as

$$|\langle|H_{AB}|\rangle|^2 = \frac{C^{(6)}}{R^6} + \frac{C^{(8)}}{R^8} + \frac{C^{(10)}}{R^{10}} + \ldots \tag{2.70}$$

where

$C^{(6)}$ is a dipole - dipole term

$$= \frac{e^4}{R^6}\ \frac{4!}{3!3!}\left[\sum_{m=-1}^{1} |\langle a'|D_m^1|a\rangle|^2\right]\quad\left[\sum_{m=-1}^{1} |\langle b|D_m^1|b'\rangle|^2\right] \tag{2.71}$$

$C^{(8)}$ is a dipole - dipole term $= \frac{e^4}{R^8}\ \frac{6!}{3!5!}$

$$\cdot\left\{\left[\sum_{m=-1}^{1} |\langle a'|D_m^1|a\rangle|^2\right]\left[\sum_{m=-2}^{2} |\langle b|D_m^2|b'\rangle|^2\right]\right.$$

$$\left.+\left[\sum_{m=-2}^{2} |\langle a'|D_m^2|a\rangle|^2\right]\left[\sum_{m=-1}^{1} |\langle b|D_m^1|b'\rangle|^2\right]\right\} \tag{2.72}$$

and $C^{(10)}$ is a quadrupole- quadrupole term $= \frac{e^4}{R^{10}}\ \frac{8!}{5!5!}$

$$\cdot \left[\sum_{m=-2}^{2} |< a'|D_m^2|a >|^2 \right] \left[\sum_{m=-2}^{2} |< b|D_m^2|b' >|^2 \right] \tag{2.73}$$

The quantities $|< a'|D_m^1|a >|^2$, $|< b'|D_m^1|b >|^2$ can in principle be derived from spectroscopic data.

Example: dipole–dipole term

In classical electrodynamics the power irradiated by an oscillating electric dipole M cos ωt is given by

$$P = \frac{\omega^4}{3c^3} M^2 \tag{2.74}$$

A classical oscillator of amplitude M has two Fourier components

$$M \cos \omega t = \frac{1}{2} Me^{i\omega t} + \frac{1}{2} Me^{i\omega t} \tag{2.75}$$

with frequency ω and −ω. Classically we do not distinguish the frequency ω from the frequency −ω, namely photons absorbed from photons emitted. Quantum mechanics, however, allows only one of the two components to enter the relevant matrix element

$$M_{classical} \rightarrow 2|M_{QM}| \tag{2.76}$$

and

$$P_{QM} = \frac{\omega^4}{3c^3} |2M|^2 = \frac{4\omega^4}{3c^3} |M|^2 \tag{2.77}$$

Therefore

$$A = \text{rate of decay} = \frac{\text{energy emitted per unit time}}{\text{energy of a photon}}$$

$$= \frac{1}{\tau_o} = \frac{4\omega^4 |M|^2}{3c^3 \hbar\omega} = \frac{8\pi\omega^3}{3hc^3} |M|^2 \tag{2.78}$$

where τ_o = radiative lifetime. Then

$$e^2 \sum_m |< a'|D_m^1|a >|^2 = |M|^2 = \frac{3hc^3}{8\pi\omega^3} \frac{1}{\tau_o} \tag{2.79}$$

The *f* number, a quantity usually derived from absorption data, is defined as follows:

$$f = \frac{2m\omega}{3\hbar e^2} |M|^2 \tag{2.80}$$

We can then write

$$e^2 \sum_m |< b|D'_m|b' >|^2 = |M|^2 = \frac{3\hbar e^2}{2m\omega} f \tag{2.81}$$

If we use (2.79) and (2.81) in (2.71) we obtain

$$C^{(6)} = |<|H_{AB}|>|dd = \frac{1}{R^6} \frac{4!}{3!3!} \left(\frac{3hc^3}{8\pi\omega^3} \frac{1}{\tau_{oA}} \right) \left(\frac{3\hbar e^2}{2m\omega} f_B \right)$$

$$= \frac{1}{R^6} \frac{3e^2c^3\hbar^6}{4mE^4} \frac{f_B}{\tau_A} \varepsilon \tag{2.82}$$

where $E = \hbar\omega$ and

$$\varepsilon = \frac{\text{probability of radiative decay}}{\text{probability of radiative decay} + \text{probability of nonradiative decay}}$$

$$= \frac{1/\tau_{oA}}{1/\tau_A} = \text{quantum efficiency} \tag{2.83}$$

Here τ_o = radiative lifetime of atom A and τ_A = effective lifetime of atom A.

The transfer rate is then given by

$$w_{AB} = \frac{2\pi}{\hbar} |<|H_{AB}|>|^2 \int g_A(E)\, g_B(E)\, dE$$

$$= \frac{2\pi}{\hbar} \frac{1}{R^6} \frac{3e^2c^3\hbar^6}{4m} \frac{f_B}{\tau_A} \varepsilon \int \frac{g_A(E)\, g_B(E)}{E^4} dE$$

$$= \frac{3e^2c^3\hbar^5\pi}{2mR^6} \frac{f_B}{\tau_A} \varepsilon \int \frac{g_A(E)\, g_B(E)}{E^4} dE = \frac{1}{\tau_A} \left(\frac{R_o}{R} \right)^6 \tag{2.84}$$

where

$$R_o = \varepsilon f_B \left(\frac{3e^2c^3\hbar^5\pi}{2m} \right) \int \frac{g_A^{(A)}\ g_B^{(E)}}{E^4}\, dE \qquad (2.85)$$

= radius at which the transfer rate is equal to the decay rate.

Let w_{AB}^{dd}, w_{AB}^{dq} and w_{AB}^{qq} be the energy transfer rates by dipole-dipole, dipole-quadrupole and quadrupole- quadrupole mechanisms, respectively. We can compare the magnitudes of w_{AB}^{dd} and w_{AB}^{dq}:

$$w_{AB}^{dd} = \frac{e^4}{R^6}\ \frac{2}{3} \left| < D^1 > \right|^2 \left| < D^1 > \right|^2 \qquad (2.86)$$

$$w_{AB}^{dq} = \frac{e^4}{R^8} \left| < D^1 > \right|^2 \left| < D^2 > \right|^2 \qquad (2.87)$$

$$\frac{w_{AB}^{dq}}{w_{AB}^{dd}} = \frac{1}{R^2}\ \frac{3}{2}\ \frac{\left| < D^2 > \right|^2}{\left| < D^1 > \right|^2} \approx \frac{1}{R^2}\ \frac{a_o^4}{a_o^2} = \left(\frac{a_o}{R} \right)^2 \qquad (2.88)$$

If the electric dipole transition in atom B is not allowed, then $\left| < D^1 > \right|^2 < a_o$ and it is possible that

$$w_{AB}^{dq} > w_{AB}^{dd} \qquad (2.89)$$

Note that

$$\frac{w_{AB}^{qq}}{w_{AB}^{dd}} \approx \frac{1}{R^4}\ \frac{\left| < D^2 > \right|^2 \left| < D^2 > \right|^2}{\left| < D^1 > \right|^2 \left| < D^1 > \right|^2} \approx \left(\frac{a_o}{R} \right)^4 \qquad (2.90)$$

2.2.2. *Multipolar Magnetic Interactions*

Magnetic multipoles can be defined similarly to electric multipoles. The magnetic field due to a magnetic dipole $\vec{m}$ placed at position $\vec{x}$, as in Fig. 2.6, is given by

$$B(\vec{x}) = -\vec{\nabla}\phi(\vec{x}) \qquad (2.91)$$

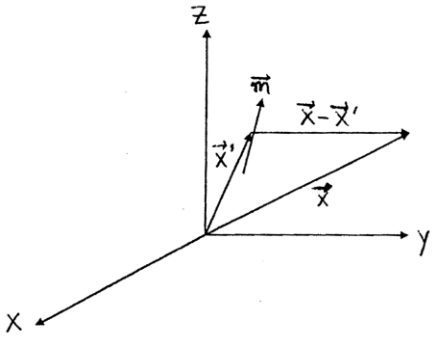

Figure 2.6. Positioning of a magnetic dipole.

where

$$\phi(\vec{x}) = -\vec{m} \cdot \vec{\nabla}_x \frac{1}{|\vec{x} - \vec{x}'|} \tag{2.92}$$

If we have a distribution of magnetic dipoles represented by the function $\vec{M}(\vec{x})$ = magnetic dipole per unit volume, then the potential $\phi(\vec{x})$ is given by

$$\phi(\vec{x}) = -\int \vec{M}(x) \cdot \vec{\nabla}_x \frac{1}{|\vec{x} - \vec{x}'|} d\tau'$$

$$= \int \vec{M}(\vec{x}') \cdot \vec{\nabla}_{x'} \frac{1}{|\vec{x} - \vec{x}'|} d\tau' \quad ^{IP}$$

$$= \int d\tau' \frac{-\vec{\nabla}_{x'} \cdot \vec{M}(\vec{x}')}{|\vec{x} - \vec{x}'|} \tag{2.93}$$

where the notation IP indicates an integration by parts. Then

$$\vec{B}(\vec{x}) = -\vec{\nabla}_x \int d\tau' \frac{-\vec{\nabla}_{x'} \cdot \vec{M}(\vec{x}')}{|\vec{x} - \vec{x}'|} \tag{2.94}$$

If in the two formulae above we replace the quantity $[-\vec{\nabla} \cdot \vec{M}(\vec{x})]$ with the electric charge density $\rho(\vec{x})$, then Eqs. (2.93) and (2.94) give us the electric potential and the electric field of a charge distribution, respectively.

We may then use for the magnetic multipoles the formulae related to the electric multipoles by replacing in them the quantity $\rho(\vec{x})$ with the quantity $\left[-\vec{\nabla}_x \cdot \vec{M}(\vec{x})\right]$ which for this reason is sometimes called *magnetic charge distribution*.

A magnetic multipole of a magnetic dipole distribution $\vec{M}(\vec{x})$ with $\vec{x} \equiv (r, \theta, \phi)$ is then defined, in accordance with Eq. (2.67), as

$$D_{\ell,m}^{magn} = \sqrt{\frac{4\pi}{2\ell+1}} \int dt \left[-\vec{\nabla}_x \cdot \vec{M}(\vec{x})\right] r^{\ell} Y_{lm}(\theta,\phi) \tag{2.95}$$

It is clear that

$$D_{00}^{magn} = \int \left[-\vec{\nabla} \cdot \vec{M}\right] dt = 0$$

and

$$D_{l,0}^{magn} = \int \left[-\vec{\nabla} \cdot \vec{M}(\vec{x})\right] z\, dt = -\int \left(\frac{\partial M_x}{\partial x} + \frac{\partial M_y}{\partial y} + \frac{\partial M_z}{\partial z}\right) z\, dt$$

$$= -\int \frac{\partial M_x}{\partial x} z\, dt - \int \frac{\partial M_y}{\partial y} z\, dt - \int \frac{\partial M_z}{\partial z} z\, dt$$

$$-\int M_z d\tau = M_z$$

where M_z = z-component of total magnetic dipole. Similarly

$$D_{l,\pm 1}^{magn} = \mp \frac{1}{\sqrt{2}} (M_x \pm i M_y)$$

We shall now consider the static and dynamic effects of the magnetic interactions. Consider the dipole–dipole interaction between atoms in solids. The magnetic field due to a dipole μ_B at distance $R = 2.2 \times 10^{-8}$ cm is given by

$$H \approx \frac{\mu_B}{R^3} = \frac{10^{-20}}{10^{-23}} = 10^3 \text{ gauss}$$

On the other hand, the energy of a dipole in the internal field a ferromagnet is on the order of $kT_c = \mu_B H_{eff}$, where T_c = Curie temperature ≈ 1,000 K. We find for H_{eff} the order of magnitude

$$H_{eff} = \frac{kT_c}{\mu_B} = \frac{10^{-16} \cdot 10^3}{10^{-20}} \approx 10^7 \text{ gauss},$$

a much larger value than the one provided by the magnetic interactions. This proves the fact that magnetic ordering cannot be due to magnetic interactions of this type.

We know from other sources that the magnetic ordering in ferromagnets is due to *exchange interactions*.

As for the dynamical effects, we may calculate the approximate ratio of the probability per unit time of energy transfer via dipole–dipole electric interaction to the probability per unit time that the transfer takes place via dipole–dipole magnetic interaction:

$$w_{AB}^{dd}(el) \propto \left|\left\langle D_{el}^{1}\right\rangle\right|^2 \left|\left\langle D_{el}^{1}\right\rangle\right|^2 \approx (ea_o)^4 \tag{2.96}$$

$$w_{AB}^{dd}(magn) \propto \left|\left\langle D_{magn}^{1}\right\rangle\right|^2 \left|\left\langle D_{magn}^{1}\right\rangle\right|^2 \approx \mu_B^4 \tag{2.97}$$

where μ_B = Bohr's magneton. We find

$$\frac{w_{AB}^{dd}(el)}{w_{AB}^{dd}(magn)} = \left[\frac{(ea_o)^2}{\mu_B^2}\right]^2 = (6.7 \times 10^4)^2 = 4.5 \times 10^9 \tag{2.98}$$

The coefficient 10^9 makes us aware of the fact that magnetic interactions play a negligible role in energy transfer processes.

2.2.3. *Exchange Interactions*

We shall now examine more closely the matrix element (2.58). The direct term can be written as follows:

$$< a'(1)\, b(2) \left|\frac{e^2}{r_{12}}\right| a(1)\, b'(2) > = \int\int a'(\vec{r}_1)^* a(\vec{r}_1) \frac{e^2}{r_{12}} \cdot b(\vec{r}_2)^*\, b'(\vec{r}_2)\, d\tau_1\, d\tau_2 \tag{2.99}$$

and represents the Coulomb interaction between the charge distributions $ea'(r_1)^* a(r_1)$ and $eb(\vec{r}_2) * b'(\vec{r}_2)$ at a distance $\vec{R}$ from each other. The exchange term can be written

$$- < a'(1)\, b(2) \left|\frac{e^2}{r_{12}}\right| b'(1)\ a(2) > = \int\int a'(\vec{r}_1)^*\, b'(\vec{r}_1) \frac{e^2}{r_{12}} \cdot a(\vec{r}_2)\ b(\vec{r}_2)^*\, d\tau_1\ d\tau_2 \tag{2.100}$$

and represents the Coulomb interaction between the charge distributions $ea'(\vec{r}_1)^*\, b'(\vec{r}_1)$ and $ea(\vec{r}_2)\ b(\vec{r}_2)^*$ at distance $\vec{R}$ from each other; these two charge distributions are very small if $\vec{R}$ is large. Therefore the exchange term is small if $\vec{R}$ is

not small. For the donor–acceptor distances in biological systems these interactions can be neglected.

2.3. MODES OF EXCITATION AND TRANSFER

2.3.1. *Setting of the Problem*

A typical sequence of events that includes the transfer of energy from one atom or ion called *sensitizer* or *energy donor (D)*, to an atom or ion called *activator* or *energy acceptor (A)* consists of:

(i) Absorption of a photon by *D*
(ii) Energy transfer from *D* to *A*
(iii) Emission of a photon by *A*

In the present treatment we shall assume that D and A are weakly interacting, so that the energy level shifts due to the interaction are smaller than the width of the D and A levels. This means that the absorption bands of D and A are identifiable.

Also, the present treatment will not consider the process of *radiative transfer* which consists of the emission of a photon by D and the absorption of the same photon by A. When such a process occurs the lifetime of D is in general not affected by the presence of A. If only one ion, say D, is present in the sample and if its concentration is high, the $D \rightarrow D$ radiative transfer may lead to trapping of the radiation and to an increase of the measured lifetime. In such case this lifetime may depend on the size and shape of the sample.

The process we will be considering consists of the *nonradiative transfer* of energy from D to A (step ii above).

2.3.2. *Pulsed Excitation*

Assume that we have a number of N_D of donors and N_A of acceptors and call w_{DA} the probability of $D \rightarrow A$ energy transfer per unit of time. Assume also that w_{DD} the probability of $D \rightarrow D$ energy transfer is negligible.

The question we shall try to answer is the following: If we excite a number of donors with a light pulse, how will the system respond? Let the pulse of light begin at time $t = -T$ and end at time $T = 0$, and let T be much smaller than w_{DA}^{-1} :

$$T << w_{DA}^{-1} \tag{2.101}$$

Let

$N_{d'}(0)$ = number of excited donors at time $t = 0$
$N_{a'}(0)$ = number of excited acceptors at time $t = 0$

We shall put

$$N_{a'}(0) = 0 \tag{2.102}$$

because during the short interval of time $(-T, 0)$ no relevant $D \rightarrow A$ transfer takes place. If

$N_d(0)$ = number of donors in the ground state at time $t = 0$
$N_a(0)$ = number of acceptors in the ground state at time $t = 0$

then

$$N_d(0) = N_D - N_{d'}(0) \tag{2.103}$$

$$N_a(0) = N_A \tag{2.104}$$

We shall also call τ the lifetime of the donor, in the absence of the activator:

$$\tau^{-1} = P + w_{nr} \tag{2.105}$$

where

P = probability of spontaneous emission per unit time
w_{nr} = probability of nonradiative decay per unit time

We shall define

$\rho_i(t)$ = probability that the donor at position $\vec{R}_i$ is excited at time t

and

$\overline{\rho}(t)$ = statistical average of $\rho_i(t)$

The number of excited donors at time t is given by $N_{d'}(0)\,\overline{\rho}(t)$ and the probability of finding a donor excited at time t by

$$\overline{\rho}(t)\frac{N_{d'}(0)}{N_D} \xrightarrow[t\to 0]{} \frac{N_{d'}(0)}{N_D} \tag{2.106}$$

The number of quanta emitted as luminescence by the donors per unit time is

$$P\,N_{d'}(0)\,\overline{\rho}(t) \tag{2.107}$$

The total number of quanta emitted as luminescence by the donors is

$$N = P\,N_{d'}(0)\int_0^\infty \overline{\rho}(t)\,dt \tag{2.108}$$

The total number of quanta emitted by the donors, in the absence of activators, is

$$N_o = P\,N_{d'}(0)\int_0^\infty e^{-(t/\tau)}\,dt = P\,N_{d'}(0)\,\tau \tag{2.109}$$

The *quantum yield of luminescence* is

$$\frac{N}{N_o} = \frac{1}{\tau} \int_o^\infty \bar{\rho}(t)\, dt \tag{2.110}$$

2.3.3. *Continuous Excitation*

If we excite the donors with a light pulse beginning at $t_o - T$ and ending at t_o, $\bar{\rho}(t - t_o)$ is the response of the donor system. The response of this system to N short pulses of equal amplitude will be

$$\phi(t) = \sum_{k=1}^{N} \bar{\rho}(t - t_k) \tag{2.111}$$

The luminescence signal due to this excitation is

$$S(t) = \text{const} \sum_{k=1}^{N} \bar{\rho}(t - t_k) \xrightarrow[(t_{k+1} - t_k) \to 0]{} \text{const} \int_{-\infty}^{+\infty} \bar{\rho}(t - t')\, dt' \tag{2.112}$$

where the constant depends on the intensity of light and the donor absorption transition probability. By making the interval between pulses go to zero we are essentially exciting the donor system continuously. If we replace $+\infty$ with zero in the integral we get

$$S(t) = \text{const} \int_{-\infty}^{o} \bar{\rho}(t - t')\, dt' = \text{const} \int_t^\infty \bar{\rho}(t')\, dt' \tag{2.113}$$

and

$$S(0) = \text{const} \int_o^\infty \bar{\rho}(t)\, dt \tag{2.114}$$

The quantity S(0) is proportional to the number of excited donors at the time of observation under continuous excitation.

In order to find the value of the constant let us consider the donor system with the same type of excitation, in the absence of acceptors, as in Fig. 2.7. w is the absorption transition probability per unit time; it depends on the intensity of light and on the $d \to d'$ absorption cross section. In steady state

$$w N_d - \frac{1}{\tau} N_{d'} = 0 \tag{2.115}$$

But

$$N_{d'} = N_D - N_d \tag{2.116}$$

Therefore

$$N_{d'} = \frac{w N_d}{w + \frac{1}{\tau}} = \frac{w \tau N_d}{1 + w\tau} \xrightarrow[w \ll \tau^{-1}]{} w \tau N_D \tag{2.117}$$

On the other hand, using the result (2.114)

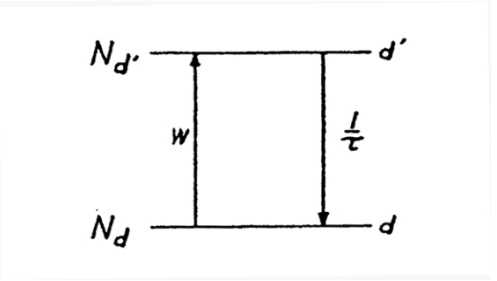

Figure. 2.7. Donor system in the absence of activators.

$$N_{d'} = \text{const} \int_o^\infty \bar{\rho}(t)\, dt = \text{const} \int_o^\infty e^{-(t/\tau)}\, dt = \text{const}\, \tau \tag{2.118}$$

Therefore the value of the constant is wN_D and in general

$$N_{d'} = w N_D \int_o^\infty \bar{\rho}(t)\, dt \tag{2.119}$$

The quantum yield of the luminescence is given by

$$\frac{N_{d'} \text{ in presence of activators}}{N_{d'} \text{ in absence of activators}} = \frac{wN_D \int_o^\infty \bar{\rho}(t)\, dt}{wN_D\, \tau} = \frac{1}{\tau} \int_o^\infty \bar{\rho}(t)\, dt \tag{2.120}$$

Comparing this result with (2.110) we can conclude that quantum yields of the donors can be measured by either the pulsed excitation method or the continuous excitation method.

2.4. ENERGY TRANSFER WITH NO MIGRATION AMONG DONORS

2.4.1. *Basic Equation*

Following the pulsed excitation of the donor system, the probability that the donor at position $\vec{R}_i$ is excited at time t is given by the function $\rho_i(t)$ whose time evolution is described by the equation [2.5]

$$\frac{d}{dt}\,\rho_i(t) = \left[-\frac{1}{\tau} - \sum_{j=1}^{N_A} w_{DA}\left(\left|\vec{R}_i - \vec{R}_j\right|\right)\right]\rho_i(t) \tag{2.121}$$

where $\vec{R}_j$ = position of acceptor j. In the equation above we assume that only a small number of acceptors is excited at all times, so that it is always $N_a(t) \approx N_A$.

The solution of the equation above, if the initial condition is

$$\rho_i(0) = 1 \tag{2.122}$$

is given by

$$\rho_i(t) = \exp\left[-\frac{t}{\tau} - t\sum_{j=1}^{N_A} w_{DA}\left(\left|\vec{R}_i - \vec{R}_j\right|\right)\right] \tag{2.123}$$

$$= e^{-(t/\tau)} \prod_{j=1}^{N_A} \exp\left[-t\, w_{DA}\left(\left|\vec{R}_i - \vec{R}_j\right|\right)\right]$$

The mode of decay described by $\rho_i(t)$ depends on the particular environment of donor i. Let $\overline{\rho}(t)$ be the average of $\rho_i(t)$ over a large number of donors. Let also w(R) be the probability of D – A distances R in the volume of the solid V; if this probability is uniform within the solid, as we assume, w will be given by 1/V:

$$\begin{aligned}\overline{\rho}(t) &= e^{-(t/\tau)} \lim_{\substack{N_A\to\infty \\ V_A\to\infty}} \left[\int_V e^{-t w_{DA}(R)}\, w(R)\, d^3\vec{R}\right]^{N_A} \\ &= e^{-(t/\rho)} \lim_{\substack{N_A\to\infty \\ V_A\to\infty}} \left[\frac{4\pi}{V}\int_0^{R_V} e^{-t w_{DA}(R)}\, R^2\, dR\right]^{N_A} \\ &= e^{-(t/\tau)} \lim_{\substack{N_A\to\infty \\ V_A\to\infty}} [I(t)]^{N_A}\end{aligned} \tag{2.124}$$

where $V = (4/3)\pi R_V^3$ and R_V = radius of the largest spherical volume, and

$$I(t) \frac{4\pi}{V}\int_0^{R_V} e^{-t w_{DA}(R)}\, R^2\, dR \tag{2.125}$$

Note that the limit in (2.124) is taken for a large system, but in such a way that the concentration of activators N_A/V remains constant.

In order to evaluate I(t) and then $\overline{\rho}(t)$ we need to know the function $w_{DA}(\vec{R})$.

2.4.2. *Simple Models*

1. Perrin Model. In this model [2.6]

Then

$$w_{DA}(R) = \begin{cases} \infty & R < R_o \\ 0 & R > R_o \end{cases} \tag{2.126}$$

$$I(t) = \frac{4\pi}{V} \int_0^{R_V} e^{-t w_{DA}(R)} R^2 \, dR = \frac{4}{3} \frac{R_V^3 - R_o^3}{V} = 1 - \frac{R_o^3}{R_V^3}$$

$$= 1 - \frac{c_A}{c_o N_A} \tag{2.127}$$

where

$$c_A = \text{concentration of acceptors} = \frac{N_A}{V} = \frac{N_A}{4\pi R_V^3/3} \tag{2.128}$$

$$c_o^{-1} = \frac{4\pi}{3} R_o^3 = \text{volume of donor's "sphere of influence"} \tag{2.129}$$

$$\frac{c_A}{c_o} = \text{number of acceptors in the sphere of influence of donor} \tag{2.130}$$

We have then

$$\overline{\rho}(t) = e^{-(t/\tau)} \lim_{\substack{N_A \to \infty \\ V \to \infty}} [I(t)]^{N_A} = \lim_{\substack{N_A \to \infty \\ V \to \infty}} e^{-(t/\tau)} (1 - c_A/c_o N_A)^{N_A}$$

$$= e^{-(t/\tau)} \, e^{-(c_A/c_o)} \tag{2.131}$$

Note that if $R_o = \infty$, $c_o = 0$ and $\overline{\rho}(t) = 0$ (immediate transfer). If $R_o = 0$, $c_o = \infty$ and $\overline{\rho}(t) = e^{-(t/\tau)}$ (no transfer).

The quantum yield of the donor luminescence is given by

$$\frac{N}{N_o} = \frac{1}{\tau} \int_o^\infty \overline{\rho}(t) \, dt = \frac{1}{\tau} \int_o^\infty e^{-(t/\tau) - (c_A/c_o)} \, dt = e^{-(c_A/c_o)} \tag{2.132}$$

The *transfer yield* is

$$1 - \frac{N}{N_o} = 1 - e^{-(c_A/c_o)} \tag{2.133}$$

2. Stern–Volmer Model. In this model [2.7] w_{DA} has the form

$$w_{DA}(R) = w = \text{const} \tag{2.134}$$

Then

$$I(t) = \frac{4\pi}{V} \int_0^{R_V} e^{-tw_{DA}(R)} R^2 \, dR = \frac{4\pi}{V} e^{-tw} \frac{R_V^3}{3} = e^{-tw} \tag{2.135}$$

and

$$\bar{\rho}(t) = e^{-(t/\tau)} e^{-N_A wt} = e^{-(1+N_A w\tau)(t/\tau)} \tag{2.136}$$

where purposely we have not taken the limit $N_A \to \infty$.

The quantum yield of the donor luminescence is

$$\frac{N}{N_o} = \frac{1}{\tau} \int_o^\infty \bar{\rho}(t) \, dt = \frac{1}{1 + N_A w} \tag{2.137}$$

The transfer yield is

$$1 - \frac{N}{N_o} = \frac{N_A w\tau}{1 + N_A w\tau} \tag{2.138}$$

2.4.3. *Multipolar Interactions*

For multipolar interactions

$$w_{DA}(R) = \frac{C^{(6)}}{R^6} + \frac{C^{(8)}}{R^8} + \frac{C^{(10)}}{R^{10}} + \ldots \tag{2.139}$$

Assume a prevalent multipolar interaction

$$w_{DA}(R) = \frac{C^{(n)}}{R^n} \tag{2.140}$$

We define a radius R_o as follows

$$w_{DA}(R) = \frac{C^{(n)}}{R^n} = \frac{1}{\tau} \left(\frac{R_o}{R} \right)^n \tag{2.141}$$

R_o is the distance at which the energy transfer rate is equal to the decay rate of the donor.

We set

$$I_n(t) = \frac{4\pi}{V} \int_{R_m}^{R_V} R^2 e^{-(t/\tau)(R_o/R)^n} dR \tag{2.142}$$

where

R_m = smallest possible D–A distance
R_V = radius of largest spherical volume

Also

$$x = \left(\frac{R_o}{R}\right)^n \frac{t}{\tau} \tag{2.143}$$

$$x_m = \left(\frac{R_o}{R_m}\right)^n \frac{t}{\tau} \tag{2.144}$$

$$x_V = \left(\frac{R_o}{R_V}\right)^n \frac{t}{\tau} \tag{2.145}$$

Then

$$I_n(t) = \frac{3}{n} x_V^{3/n} \int_{x_V}^{x_m} x^{-1-(3/n)} e^x dx \tag{2.146}$$

But

$$\int_{x_V}^{x_m} x^{-1-(3/n)} e^{-x} dx = \int_{x_V}^{x_m} e^{-x} d\left(-\frac{n}{3} x^{-3/n}\right)$$

$$\overset{IP}{=} \left[e^{-x}\left(-\frac{n}{3} x^{-3/n}\right)\right]_{x_V}^{x_m} - \frac{n}{3} \int_{x_V}^{x_m} (x^{-3/n} e^{-x}) dx$$

$$= -\frac{n}{3} x_m^{-3/n} e^{-x_m} + \frac{n}{3} x_V^{-3/n} e^{-x_V} - \frac{n}{3} \int_o^\infty x^{-3/n} e^{-x} dx + \frac{n}{3} \int_o^{x_V} x^{-3/n} e^{-x} dx + \frac{n}{3} \int_o^\infty x^{-3/n} e^{-x} dx \tag{2.147}$$

where IP indicates integration by parts. Note that

$$\int_o^\infty x^{3/n} e^{-x} dx = \Gamma\left(1 - \frac{3}{n}\right) \tag{2.148}$$

We shall consider the limiting situation where

$$x_m = \left(\frac{R_o}{R_m}\right)^n \frac{t}{\tau} \xrightarrow[t\to\infty]{} \infty \tag{2.149}$$

$$x_V = \left(\frac{R_o}{R_V}\right)^n \frac{t}{\tau} \xrightarrow[V\to\infty]{} 0 \tag{2.150}$$

Note the following asymptotic expansions of incomplete Γ functions

$$\int_{x_m}^{\infty} x^{-3/n} e^{-x}\, dx \xrightarrow[x_m\to\infty]{} x_m^{-3/n} e^{-x_m}\left(1-\frac{3}{n} x_m^{-1} + \ldots\right)$$

$$= x_m^{-3/n} e^{-x_m} - \frac{3}{n} x_m^{-(3/n)-1} e^{-x_m} + \ldots \tag{2.151}$$

$$\int_o^{x_V} x^{-3/n} e^{-x}\, dx \xrightarrow[x_V\to 0]{} x_V^{1-(3/n)}\left[1-\left(\frac{n}{2n-3}\right) x_V + \ldots\right]$$

$$= x_V^{1-(3/n)} - \frac{n}{2n-3} x_V^{2-(3/n)} + \ldots \tag{2.152}$$

Then we can write

$$I_n(t) = \frac{3}{n} x_V^{3/n} \int_{x_V}^{x_m} x^{-1-(3/n)} e^{-x}\, dx$$

$$= \frac{3}{n} x_V^{3/n}\left[-\frac{n}{3} e^{-x_m} x_m^{-(3/n)} + \frac{n}{3} x_V^{-(3/n)} e^{-x_V} - \frac{n}{3}\Gamma\left(1-\frac{3}{n}\right)\right.$$

$$+ \frac{n}{3} x_m^{-(3/n)} e^{x_m} - x_m^{-(3/n)-1} e^{-x_m} + \frac{n}{3} x_V^{1-(3/n)}$$

$$\left. - \frac{n}{3}\frac{n}{2n-3} x_V^{2-(3/n)}\right]$$

$$= e^{-x_V} - x_V^{3/n}\Gamma\left(1-\frac{3}{n}\right) - \frac{3}{n} x_V^{3/n} x_m^{-(3/n)-1} e^{-x_m}$$

$$+ x_V - \frac{2}{2n-3} x_V^2 \xrightarrow[\substack{x_V\to 0\\ x_m\to\infty}]{} 1 - x_V^{3/n}\Gamma\left(1-\frac{3}{n}\right) \tag{2.153}$$

Then

$$I_n(t) = 1 - x_V^{3/n}\,\Gamma(1-\frac{3}{n}) = 1-\left[(\frac{R_o}{R_V})^n\ \frac{t}{\tau}\right]^{3/n}\Gamma(1-\frac{3}{n})$$

$$= 1 - \frac{R_o^3}{R_V^3}\,(\frac{t}{\tau})^{3/n}\,\Gamma(1-\frac{3}{n}) \tag{2.154}$$

But

$$c_A = \frac{N_A}{V} = \frac{^{N}A}{(4\pi/3)\,R_V^3} \tag{2.155}$$

$$c_o^{-1} = \frac{4\pi R_o^3}{3} \tag{2.156}$$

$$\frac{R_o^3}{R_V^3} = \frac{c_A}{c_o\ N_A} \tag{2.157}$$

Then

$$I_n(t) = 1 - \frac{c_A}{c_o\,N_A}\,(\frac{t}{\tau})^{3/n}\,\Gamma(1-\frac{3}{n}) \tag{2.158}$$

Also

$$\lim_{\substack{N_A\to\infty\\ V\to\infty}} I_n(t) = \exp\left[-\frac{c_A}{c_o\,N_A}\,(\frac{t}{\tau})^{3/n}\,\Gamma(1-\frac{3}{n})\right] \tag{2.159}$$

and finally

$$\bar{\rho}(t) = e^{-(t/\tau)}\left[I_n(t)\right]^{N_A} = \exp\left[-\frac{t}{\tau} - \frac{c_A}{c_o}\,\Gamma(1-\frac{3}{n})(\frac{t}{\tau})^{3/n}\right] \tag{2.160}$$
$$(x_m \to \infty\ ;\ x_V \to 0)$$

This result was first derived by Förster [2.8]. We want to discuss the conditions under which this formula has been derived. $x_m >> 1$ means

$$(\frac{R_o}{R_m})^n\ \frac{t}{\tau} >> 1$$

and

$$\frac{t}{\tau} >> (\frac{R_m}{R_o})^n$$

Take $R_m = 3A$, $R_o = 10A$ and $n = 6$

$$\frac{t}{\tau} >> (\frac{3}{10})^6 = 7 \times 10^{-4}$$

$$t >> 7 \times 10^{-4}\tau$$

This shows that the approximation $x_m >> 1$ may be good even for very short times.

$x_V << 1$ means

$$\left(\frac{R_o}{R_V}\right)^n \frac{t}{\tau} << 1$$

$$\frac{t}{\tau} << \left(\frac{R_V}{R_o}\right)^n$$

Take $R_V = 1\text{cm}$, $R_o = 10\text{A}$ and $n = 6$

$$\frac{t}{\tau} << \left(\frac{10^8}{10}\right)^6 = 10^{42}$$

$$t << 10^{42}\tau$$

which is indeed always the case.

Figure 2.8 reports a plot of the function $\bar{p}(t)$ given in (2.160) for the case n = 6 (dipole–dipole interaction).

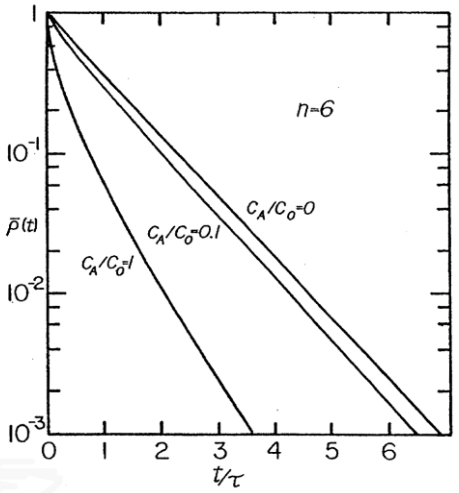

Figure 2.8. The average probability of donor excitation in the case of dipole–dipole interaction.

The following observations can be made regarding Fig. 2.8.

1. At the beginning the decay is faster, because the donors close to the acceptors decay first.
2. After a while other donors, which are farther away from acceptors, and remained excited, start transferring energy.

3. At very long times donors that are very far from acceptors will finally decay with their own lifetime.
4. The greater is c_A/c_o = number of acceptors in donor's sphere of influence, the longer one has to wait for the $\bar{p}(t)$ curve to become parallel to the one for $c_A/c_o = 0$.

In Fig. 2.9 a comparison is made of the $\bar{\rho}(t)$ curves for the various processes: n = 6 (dipole–dipole), n = 8 (dipole–quadrupole) and n = 10 (quadrupole–quadrupole).

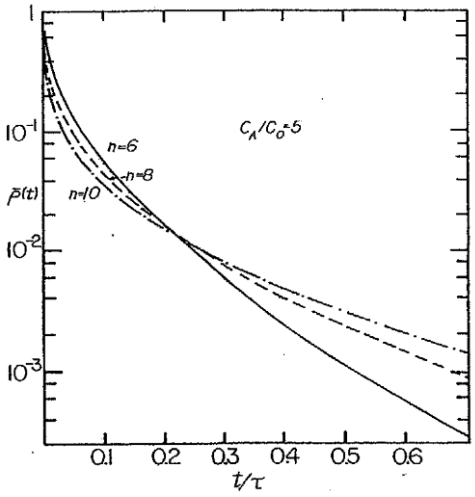

Figure 2.9. The average probability of donor excitation for n = 6 (dipole–dipole interaction), n = 8 (dipole–quadrupole interaction), and n = 10 (quadrupole–quadrupole interaction).

We wish now to consider the quantum yield of donor luminescence. If n = 6 (dipole–dipole interaction)

$$\bar{\rho}(t) = \exp\left[-\frac{t}{\tau} - \frac{c_A}{c_o}\Gamma\left(\frac{1}{2}\right)\left(\frac{t}{\tau}\right)^{1/2}\right] = \exp\left[-\frac{t}{\tau} - \frac{c_A}{c_o}\sqrt{\pi}\left(\frac{t}{\tau}\right)^{1/2}\right] \qquad (2.161)$$

Then

$$\frac{N}{N_o} = \frac{1}{\tau}\int_o^\infty exp\left[-\frac{t}{\tau} - \frac{c_A}{c_o}\sqrt{\pi}\left(\frac{t}{\tau}\right)^{1/2}\right]dt = \int_o^\infty e^{-t-2qt^{1/2}}\,dt$$

$$= e^{q^2}\int_o^\infty e^{-(q+t^{1/2})^2}dt = 1 - 2qe^{q^2}\int_q^\infty e^{-x^2}\,dx \qquad (2.162)$$

where

$$2q = \sqrt{\pi}\,\frac{c_A}{c_o}$$

But

$$\operatorname{erf} q = 1 - \frac{2}{\sqrt{\pi}}\int_q^\infty e^{-x^2}\,dx = \frac{2}{\sqrt{\pi}}\int_o^q e^{-x^2}\,dx \tag{2.163}$$

Then [2.8-2.10]

$$\frac{N}{N_o} = 1 - q\,e^{q^2}\sqrt{\pi}\,(1 - \operatorname{erf} q) \tag{2.164}$$

We shall examine the following two limiting cases:

$$q \to 0: \quad c_A \to 0, \quad \operatorname{erf} q \to 0$$

$$\frac{N}{N_o} \to 1 - \frac{\pi}{2}\,\frac{c_A}{c_o} \to 1$$

$$q \to \infty: \quad c_A \to \infty \text{ or } c_o^{-1} \to \infty, \quad \operatorname{erf} q \to 1$$

$$\frac{N}{N_o} \to 0$$

2.5. ENERGY TRANSFER WITH MIGRATION OF EXCITATION AMONG DONORS

2.5.1. *Migration as Diffusion Process*

The case treated in the previous section 2.4 deals with direct transfer from donor to acceptor, with no migration among donors and is exemplified in Fig. 2.11a. We shall now consider the case in which $w_{DD} \neq 0$, and energy transfer processes can take place among donors, so that the energy of excitation may reach an acceptor after hopping resonantly among donors as in Fig. 2.10b.

Since migration among donors can be viewed as a diffusion process we shall review some elementary considerations regarding the phenomenon of diffusion.

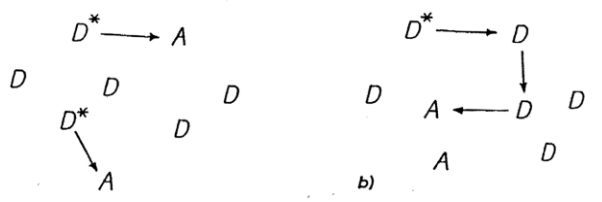

Figure 2.10. (a) Direct transfer; (b) Transfer with migration.

Consider a system consisting of N similar molecules in a volume V, and let n be the density N/V. Let n_1 be the density of especially labeled molecules, for example, of radioactive molecules. Assume $n_1 = n_1(x)$, i.e. a non-equilibrium situation, but assume also n = const, so that no net motion of whole substance occurs during diffusion.

The mean number of molecules of type 1 crossing the unit area of a plane perpendicular to the x direction in the x direction in the unit time is given by

$$J_x = -D\frac{\partial n_1}{\partial x} \qquad [\mathrm{cm}^{-2}\ \mathrm{sec}^{-1}] \tag{2.165}$$

where

$$D = \text{coefficient of self diffusion} \qquad [\mathrm{cm}^{-2}\ \mathrm{sec}^{-1}]$$

The above formula (2.165) is valid for gases, liquids and isotropic solids [2.11]. If $\partial n_1/\partial x > 0$, $J_x < 0$ and the flow takes place in the –x direction.

Let us consider now the crossing by molecules of type 1 of an area A perpendicular to the x direction, as in Fig. 2.11. We have

$$\frac{\partial}{\partial t}(n_1 A\, dx) = A J_x(x) - A J_x(x + dx) \tag{2.166}$$

and

$$\frac{\partial n_1}{\partial t} dx = J_x(x) - [J_x(x) + \frac{\partial J_x(x)}{\partial x} dx] = -\frac{\partial J_x(x)}{\partial x}$$

or, because of (2.165)

$$\frac{\partial n_1(x,t)}{\partial t} = D\frac{\partial^2 n_1(x,t)}{\partial x^2} \tag{2.167}$$

The above equation is called *diffusion equation*.

We shall consider the initial condition of N_1 molecules introduced at the

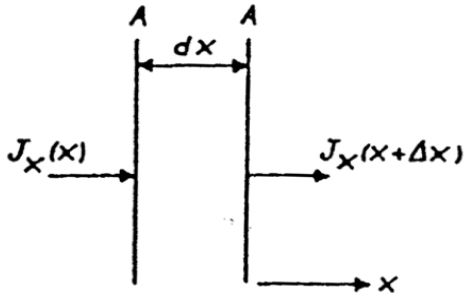

Figure 2.11. Crossing of plane by especially labeled molecules.

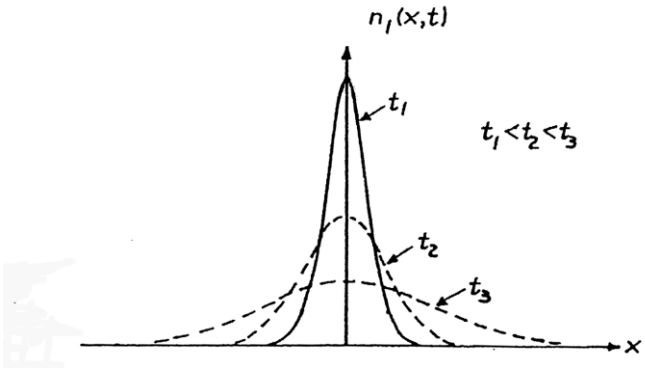

Figure 2.12. Evolution of the density function of especially labeled molecules.

time $t = 0$ near the plane $x = 0$:

$$n_1(x,0) = N_1\,\delta(x) \tag{2.168}$$

The solution of the diffusion equation under this condition is

$$n_1(x,t) = \frac{N_1}{\sigma\sqrt{2\pi}}\,e^{-(x^2/2\sigma^2)} = \frac{N_1}{\sqrt{4\pi\,Dt}}\,e^{-(x^2/4Dt)} \tag{2.169}$$

The shape of the $n_1(x,t)$ curve is always Gaussian (see Fig. 2.12) with the standard deviation

$$\sigma = \sqrt{2Dt} \tag{2.170}$$

Also

$$\langle x^2 \rangle = \frac{1}{N_1}\int_{-\infty}^{+\infty} x^2\, n_1(x,t)\, dx = \sigma^2 = 2Dt \tag{2.171}$$

In three dimensions the diffusion equation is

$$\frac{\partial}{\partial t}\, n_1(\vec{r},t) = D\,\nabla^2\, n_1(\vec{r},t) \tag{2.172}$$

If the initial condition is

$$n_1(\vec{r},t) = N_1\,\delta(\vec{r}) \tag{2.173}$$

the solution is given by

$$n_1(\vec{r},t) = \frac{N}{(4\pi\ Dt)^{3/2}}\, e^{-(r^2/4Dt)} \tag{2.174}$$

Also

$$< r^2 > = \frac{1}{N} \int r^2\, n_1(\vec{r},t)\, d^3\vec{r} = 6Dt \tag{2.175}$$

We shall now relate these notions to the case of donor to acceptor energy transfer. We define a function $\rho(\vec{R},t)$ by stating that $\rho(\vec{R},t)d^3\vec{R}$ is the probability that the donor with coordinate in $(\vec{R}, \vec{R} + d\vec{R})$ is excited at time t. We shall now consider the following cases.

1. Diffusion Only. In this simplest case the diffusion equation gives us

$$\frac{\partial}{\partial t}\, \rho(\vec{R},t) \ = \ D\, \nabla^2\, \rho(\vec{R},t) \tag{2.176}$$

If the excitation is initially localized at $\vec{R} \ = \ 0,$ then

$$\rho(\vec{R},t) = \frac{1}{\sqrt{4\pi\, Dt}}\, e^{-(R^2/4Dt)} \tag{2.177}$$

with

$$< R^2 > \ = \ 6Dt \tag{2.178}$$

2. Diffusion and Relaxation. In this case a term has to be added to the relevant equation

$$\frac{\partial}{\partial t}\, \rho(\vec{R},t) = D\, \nabla^2\, \rho(\vec{R},t) - \frac{1}{\tau}\, \rho(\vec{R},t) \tag{2.179}$$

If we set

$$\rho(\vec{R},t) = \psi(\vec{R},t)\, e^{-(t/\tau)} \tag{2.180}$$

we obtain for $\psi(\vec{R},t)$

$$\frac{\partial}{\partial t}\, \psi(\vec{R},t) = D\, \nabla^2\, \psi(\vec{R},t) \tag{2.181}$$

If, again, the excitation is initially localized at $\vec{R} \ = \ 0,$ we obtain

$$\vec{\rho}(\vec{R},t) = e^{-(t/\tau)} \frac{1}{(4\pi\ Dt)^{3/2}} e^{-(R^2/4Dt)} \tag{2.182}$$

and

$$\int \vec{\rho}(\vec{R},t)\, d^3\vec{R} = e^{-(t/\tau)} \tag{2.183}$$

3. Diffusion, Relaxation and Transfer. In this case the relevant equation is

$$\frac{\partial}{\partial t}\rho(\vec{R},t) = \left[D\nabla^2 - \frac{1}{\tau} - \sum_{j=1}^{N_A} w_{DA}(|\vec{R} - \vec{R}_j|) \right] \rho(\vec{R},t) \tag{2.184}$$

where the first term in the [ ] parentheses deals with diffusion among donor, the second with the self-decay of donors, and the third with donor-acceptor energy transfer.

Equation (2.184) is analogous to (2.121), but differs from it in two respects. First, the diffusion term is included in (2.184) and, also, the equivalent of $\rho_j(t)$ is $\rho(\vec{R},t)\ d^3\vec{R}$. The form of $\rho_j(t)$, given the initial condition $\rho_j(0) = 1$, is given by (2.123); the average of $\rho_j(t)$ over a large number of donors is given by (2.124) and finally by

$$\overline{\rho}(t) = \exp\left[\frac{t}{\tau} - \frac{c_A}{c_o} \Gamma\left(1 - \frac{3}{n}\right)\left(\frac{t}{\tau}\right)^{3/n} \right] \tag{2.185}$$

In the present case the analogous of $\overline{\rho}(t)$ is the function $\phi(t)$

$$\phi(t) = \frac{1}{N_D} \int \rho(\vec{R},t)\ d^3\vec{R}\ . \tag{2.186}$$

$\phi(t)$ reduces to the $\overline{\rho}(t)$ in (2.185) in the limit $D \to 0$.

No general expression for $\phi(t)$ has been found. However, Yokota and Tanimoto [2.12] have obtained an expression for $\phi(t)$ in the case of dipole–dipole interaction when

$$w_{DA} = \frac{C_{DA}}{R^6} = \frac{1}{\tau}\left(\frac{R_o}{R}\right)^6 \tag{2.187}$$

They obtained the following expression by using the method of the Padé approximants

$$\phi(t) = \exp\left[-\frac{t}{\tau} - \frac{c_A}{c_o} \Gamma\left(\frac{1}{2}\right)\left(\frac{t}{\tau}\right)^{1/2} \left(\frac{1 + 10.87x + 15.5x^2}{1 + 8.743x} \right)^{3/4} \right. \tag{2.188}$$

where

$$x = \frac{D\tau}{R_o^2}\left(\frac{t}{\tau}\right)^{2/3} = DC_{DA}^{-1/3}\,t^{2/3} \tag{2.189}$$

For $x << 1$ $\phi(t)$ reduces to

$$\phi(t) = \exp\left[-\frac{t}{\tau} - \frac{c_A}{c_o}\,\Gamma\left(\frac{1}{2}\right)\left(\frac{t}{\tau}\right)^{1/2}\right] \tag{2.190}$$

At early times diffusion is not important. Only donors with nearby acceptors are decaying; the time is not sufficient for the excitation to diffuse among the donors before being transferred to the acceptors.

$$DC_{DA}^{-1/3}\,t^{2/3} << 1$$

or

$$t << t^* = \frac{C_{DA}^{1/2}}{D^{3/2}} \tag{2.191}$$

Note that if C_{DA} is large (D – A interaction strong) t^* is large, and if D is large (fast diffusion among donors) t^* is small. Before the characteristic time t^* diffusion is negligible. During the time t^* the excitation, if initially localized in one place, would diffuse a distance R^* given by

$$R^{*2} = 6Dt^*$$

then

$$R^* = \sqrt{6Dt^*} = \sqrt{6D\frac{C_{DA}^{1/2}}{D^{3/2}}} \approx \left(\frac{C_{DA}}{D}\right)^{1/4} \tag{2.192}$$

The asymptotic behavior of $\phi(t)$ can be found by letting $t \to \infty$, namely $x \to \infty$. In this case,

$$\phi(t) \xrightarrow[x\to\infty]{} \exp\left[-\frac{t}{\tau} - \frac{c_A}{c_o}\,\Gamma\left(\frac{1}{2}\right)\left(\frac{t}{\tau}\right)^{1/2}\left(\frac{15.5x}{8.743}\right)^{3/4}\right]$$

$$= \exp\left[-\frac{t}{\tau} - \frac{c_A}{c_o}\,\sqrt{\pi}\left(\frac{t}{\tau}\right)^{1/2}(1.733x)^{3/4}\right] \tag{2.193}$$

Now

$$(1.733x)^{3/4} = 1.536\left[\frac{D\tau}{R_o^2}\left(\frac{t}{\tau}\right)^{2/3}\right]^{3/4} = 1.536\,\frac{D^{3/4}\,\tau^{3/4}}{R_o^{3/2}}\left(\frac{t}{\tau}\right)^{1/2} \qquad (2.194)$$

and

$$\frac{c_A}{c_o}\sqrt{\pi}\left(\frac{t}{\tau}\right)^{1/2}(1.733x)^{3/4} = 4\pi\, c_A\,\frac{D^{3/4}\,R_o^{3/2}}{\tau^{1/4}}\,0.907t$$

$$= 4\pi\, c_A\,\frac{D^{3/4}}{\tau^{1/4}}\,\tau^{1/4}\,C_{DA}^{1/4}\,0.907t$$

$$\approx 4\pi\, Dc_A\, 0.91\left(\frac{C_{DA}}{D}\right)^{1/4} t = 4\pi\, Dc_A\, R_D\, t$$

where

$$R_D = 0.91\left(\frac{C_{DA}}{D}\right)^{1/4} \approx R^* \qquad (2.195)$$

Then

$$\phi(t) \xrightarrow[t\to\infty]{} \exp\left(-\frac{t}{\tau} - 4\pi\, D\, c_A\, R_D\, t\right)$$

$$= \exp\left(-\frac{t}{\tau} - K_D\, t\right) = e^{-(t/\tau_{eff})} \qquad (2.196)$$

where

$$K_D = 4\pi\, D\, c_A\, R_D \qquad \left[R_D \approx \left(\frac{C_{DA}}{D}\right)^{1/4}\right] \qquad (2.197)$$

$$\tau_{eff}^{-1} = \tau^{-1} + K_D \qquad (2.198)$$

At these later times the only donors that are still excited are those far away from any acceptor. They now transfer their energy by first diffusing it, i.e., by sending it to a donor near an acceptor.

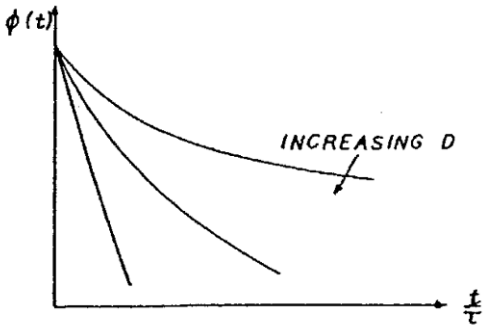

Figure 2.13. Behavior of the average probability of donor excitation in the case of migration among donors.

The behavior of the function $\phi(t)$ is sketchily presented in Fig. 2.13.

Summarizing the results just obtained:

1. $\phi(t)$ is non-exponential for t small enough that migration is not important. In this limit $\phi(t)$ has the previous form found for the no-migration case.
2. $\phi(t)$ is exponential for large t; it decays at a rate determined by migration.
3. As migration becomes more rapid, the boundary between these two regions shift,

$$t^* \approx \frac{C_{DA}^{1/2}}{D^{3/2}}$$

shifts to shorter times, until, for sufficiently fast migration, the decay appears to be entirely exponential.

2.5.2. *Regimes of Migration Among Donors*

There are three regimes of migration among donors:

1. No Diffusion. c_D is small. The decay of donor excitation is given by $\overline{\rho}(t)$. $\overline{\rho}(t)$ is the average of exponentials corresponding to the various transfer rates $w_{DA}(R)$. An extreme case is that of a donor which is far away from all acceptors; the donor decay function is

$$\rho(t) = e^{-(t/\tau)} \tag{2.199}$$

where τ = intrinsic lifetime of donor. The other extreme case is that of a donor which has an acceptor as nearest neighbor; in this case

$$\rho(t) = \exp\left[- \frac{t}{\tau} - t\, w_{DA}(R_m) \right] \tag{2.200}$$

where R_m = minimum D – A distance.

2. Diffusion-Limited Decay. c_D is higher. For $t << C_{DA}^{1/2} / D^{3/2}$, $\overline{\rho}(t)$ is the same as for the case of no migration. For $t >> C_{DA}^{1/2} / D^{3/2}$

$$\overline{\rho}(t) \sim e^{-(t/\tau) - K_D t} \tag{2.201}$$

$t^* = C_{DA}^{1/2} / D^{3/2}$ represents a boundary between the "transfer without migration" region and the "transfer with migration" region.

3. Fast Diffusion. c_D is still higher. An increase in the concentration of donors produces a faster migration of energy, i.e. a larger D, and a larger K_D. The characteristic time t^* becomes shorter and shorter until it reaches the value $w_{DA}^{-1}(R_m)$, R_m being the shortest D–A distance. Any additional increase of c_D has effect on D, but no effect on K_D which takes a saturated value [2.13]. In these conditions the decay of the donor luminescence is purely exponential, since the fast diffusion averages out all the different donor environments.

   In this case we set

$$K_D = K c_A \tag{2.202}$$

where K = const, independent of c_D, or, taking into account the possibility that a large fraction of acceptors are excited

$$K_D = K n_A \tag{2.203}$$

where n_A = concentration of ground state acceptors. In this case the evolution of the excited donor population follows the *rate equation*

$$\frac{d}{dt} n_{d'}(t) = - \frac{n_{d'}(t)}{\tau} - K\, n_A(t)\, n_{d'}(t) \tag{2.204}$$

Rate equations have been used for explaining energy transfer in rare-earth doped systems [2.14].

3. Applications of Fluorescence Energy Transfer (FRET) to Biological Systems

3.1. THE USES OF FRET IN BIOLOGY [3.1, 3.2]

The usage of FRET provides a rather unique chance to observe previously inaccessible physical phenomena related to the arrangement and separation of molecules in solution and in solids on a molecular scale.

Particularly useful is found the possibility of measuring directly the molecular separation between two molecules Donor (D) and Acceptor (A), counting on the strong dependence of the rate and efficiency of energy transfer on the sixth power of the D–A distance.

The usage of FRET has expanded considerably since the early fifties, with its applications to such various fields as physics, chemistry, biology and polymer science. However its greatest usage has been with biological macromolecules.

Biological systems are complex molecular entities involving macromolecules (e.g. proteins, nucleic acid polymers, fatty acids, lipids, and poly-carbohydrates) that associate to form supramolecular structures e.g. multi-protein assemblies, membranes, chromosomes), that, in turn, comprise living cells and their respective parts.

All biological systems in general present intricate and interdependent organization in their various structures. In order to understand and manipulate the functions of biological systems, it is necessary to study the structures of their components and to determine how these components are associated into larger molecular organizations.

FRET is unique in its capacity to supply accurate spatial information about molecular structures at distances ranging from ~10 to ~100 Å. In many cases geometrical information can also be obtained.

FRET is observed only if D and A are in proximity ($\sim R < 2R_0$). This possibility of detecting and quantifying molecular proximities has led to numerous applications of FRET to biology over the past 30 years and continues to generate much of the present interest in the subject.

3.2. A SUMMARY OF FLUORESCENCE RESONANCE ENERGY TRANSFER

3.2.1. *General Characteristics*

1. The distance at which FRET is 50% efficient is called the Förster distance, and is typically in the range 2060 Å.
2. The *rate of energy transfer from a D to an A* in the case of dipole–dipole interaction is given by

$$w_{DA}(R) = 1/\tau_D \, (R_0/R)^6 \tag{3.1}$$

when $R = R_0$, $w_{DA}(R) = 1/\tau_D$.

3. The value of R_0 can be reliably predicted from the knowledge of the spectral properties of donors and acceptors and of the orientation factor.
4. FRET is a through-space interaction that is mostly independent of intervening solvent and/or micromolecules.
5. FRET does not involve emission and re-absorption of photons.
6. FRET contains molecular information that is different from that revealed by solvent relaxation, excited state reactions, fluorescence quenching or fluorescence anisotropy. These fluorescence phenomena depend on interactions of the fluorophore with other molecules in the surrounding solvent shell.

FRET is effective over much longer distances, and the intervening solvent or macromolecule has little effect on the efficiency of the process that depends primarily on R.

3.2.2. *The Orientation Factor*

Biological systems encountered in fluorescence spectroscopy are usually complex objects consisting of supramolecular structures and large organizations of molecular components.

Spectroscopic probes that interact with biological material are often oriented and undergo less rotational motion than they do in less organized surroundings.

The proximity of immobilized molecular species leads to directional interactions between neighboring molecules, and the mutual orientation of closed spaced D and A molecules affects the effect of FRET through the variations of an *orientation factor*, called K^2.

One must be careful in quantitatively interpreting FRET measurements made on highly structured samples on highly structured biological samples. The orientation factor K^2 is often considered the limiting factor for estimating accurate D–A distances from FRET data. K^2 can vary from 0 to 4 although its actual values rarely, if ever, extend over this total range.

In general we do not have sufficient information (often none at all) regarding D-A orientations and approximations must be made. The D and A fluorescence anisotropy values, and consequently the range of K^2 values, depend on the extent to which D and A rotate while D is in its excited state.

3.2.3. *Calculation of the Orientation Factor*

The magnitude of the time-dependent field strength of an oscillating dipole in the near-field zone is identical to that of a static dipole.

The electric interaction between two static electric dipoles is a dot product between the dipole moment of one dipole with the electric field of the other, and K is the factor describing the relative orientation.

No generality is lost by discussing K in terms of classical static dipoles. The rate of energy transfer w_{DA} is proportional to K^2 because w_{DA} is proportional to the square of the interaction energy between D and A.

Considering the angles that define the orientation factor K in Fig. 3.1, K^2 is given by

$$K^2 = (\cos\theta_{DA} - 3\cos\theta_D \cos\theta_A)^2 \tag{3.2}$$

θ_{DA} is the angle between the emission transition dipole of the donor $\mathbf{M}_D$ and the absorption transition dipole of the acceptor $\mathbf{M}_A$.

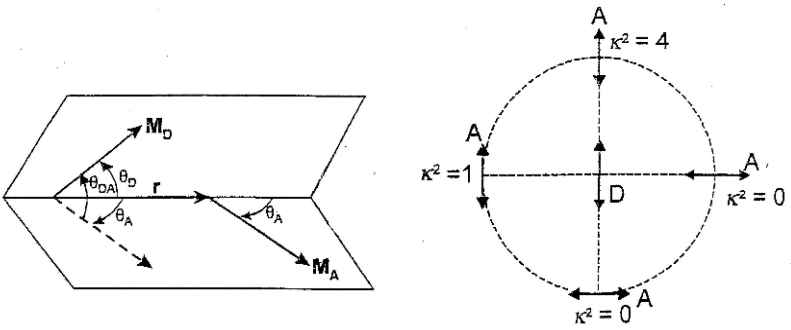

Figure 3.1. (Left) angles that define the orientation factor K^2 and (right) examples of various situations and related values of K^2.

Experimental results show that the value of K^2 affects the rate of energy transfer. The following figure shows the chemical structure of two D–A pairs.

When sufficient orientation information is lacking, the assumption is made that $\langle K^2 \rangle = 2/3$, a value corresponding to an average made when both D and A are randomly oriented.

3.3. ENERGY TRANSFER IN SOLUTION

Energy transfer may take place for donors and acceptors randomly distributed in three-dimensional solutions.

For this case we can rely on the treatment in section 2.4. The rate of transfer in the case of dipole–dipole interaction is given by:

$$w_{DA}(R) = 1/\tau_D \, (R_0/R)^6 \tag{3.3}$$

R_0 is now related not only to the overlap integral and to the quantum efficiency of the donor, but also to the orientation factor: it is proportional to $(K^2)^{1/6}$.

The response of the donor to pulsed excitation will be given by the formula (2.161)

$$\overline{\rho}(t) = \exp\left(-t/\tau_D - c_A/c_0 \sqrt{\pi}\, t/\tau_D\right)^{1/2} \tag{3.4}$$

where c_A = concentration of acceptors and $c_0^{-1} = 4\pi/3\, R_0^3$

3.4. DISTANCE DISTRIBUTIONS

Up to this point we have considered two situations:

1. The donor and the acceptor are at a fixed distance R.
In this case the pattern of donor's decay is exponential with a time constant given by

$$\tau_{DA} = 1/\tau_D + w_{DA}(R) \tag{3.5}$$

with $w_{DA}(R) = 1/\tau_D \, (R_0/R)^6$

The assumption of a single D–A distance R allows the calculation of R from the quantum yield of the donor in the presence of the acceptor.

2. The distribution of D-A distances is uniform in a volume V of a solution:

$$w_{DA}(R) = 1/V \tag{3.6}$$

We shall now consider the case of flexible D–A pairs, i.e. the case where the range of D–A distances can be expressed by a probability distribution. Some of the D–A pairs are closely spaced and display shorter decay times, and other D-A pairs are further apart and display longer decay times.

The range of distances results in a range of decay times, so that the decay pattern becomes more complex than a single exponential.

The goal of most distance distribution studies is to recover the D–A probability distribution from the non-exponential pattern of the donor. This pattern is the summation of the intensity decays for all accessible distances:

$$I_{DA}(t) = \int_o^\infty w(R) \exp[-t/\tau_D - 1/\tau_D \, (R_o/R)^6] \, dR \tag{3.7}$$

The response of the donors to a pulsed excitation is given in the form of an integral that represented the weighted average of the decays for all D–A distances.

The task of the researcher is to try to recover the probability distribution w(R) from the decay pattern of the donor system.

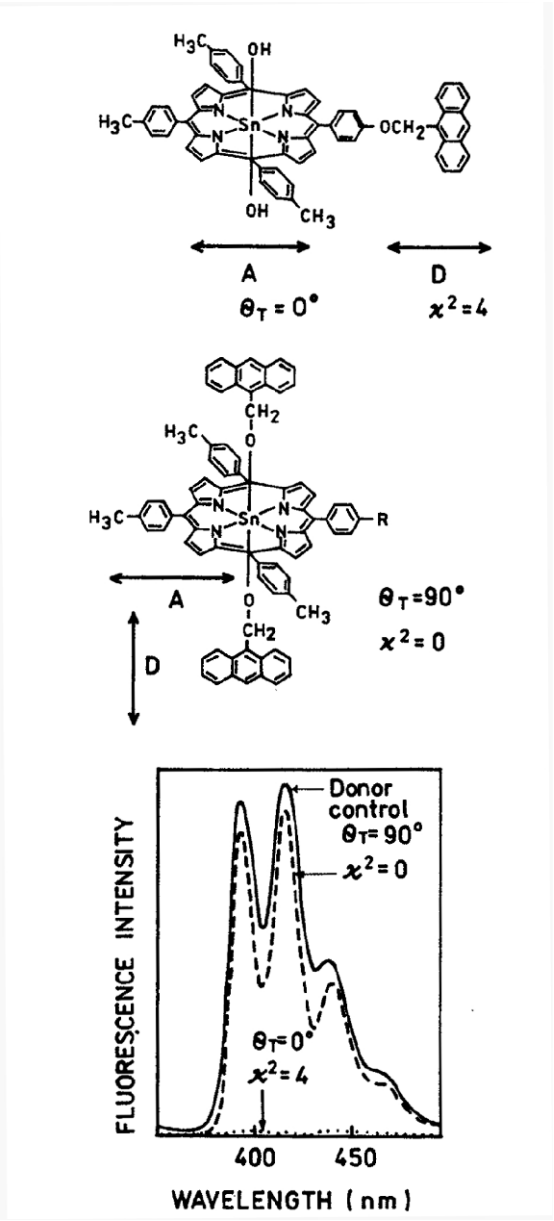

Figure 3.2. Chemical structures an emission spectra of covalently linked D-A pairs used to study the effect of K^2 on RET (reproduced from [3.1] by permission granted by Springer Science and Business Media and Professor Lakowicz).

3.5. EFFECT OF DIFFUSION ON LINKED D–A PAIRS

In the preceding sections we have considered donors and acceptors to be static in space and to remain at the same distance during the donor lifetime. However, depending on the donor lifetime and the mutual diffusion coefficient

$$D = D_D + D_A \tag{3.8}$$

there can be changes in the linked D–A distances during the donor lifetime. It is found that, as diffusion increases, the patterns of donors' decay become more rapid, indicating a more rapid energy transfer.

This seems surprising, since one would think that diffusion is just as likely to move donors and acceptors apart, as it is likely to bring them closely together.

A deeper understanding of diffusion and FRET can be obtained by pondering the following considerations:

1. The distance dependence of $w_{DA}(R)$ causes the more closely spaced D–A pairs to transfer more rapidly.
2. For rapid D–A diffusion the population of D–A at shorter distance is replenished by diffusion and the closely spaced D–A pairs by diffusion result in increased energy transfer with increased rates of diffusion.

3.6. EFFECT OF DIFFUSION ON UNLINKED D–A PAIRS

The theory of energy transfer for unlinked D–A pairs in the presence of diffusion is very complex. No general expression for the decay pattern of the donor system in this situation has been found. However, an expression for this pattern has been obtained by Yokota and Tanimoto [3.3] for the case, of interest here, of dipole–dipole interaction:

We report the formula already cited as (2.188):

$$\phi(t) = \exp\left\{(-t/\tau_D - C_A/C_o\sqrt{\pi}\ t/\tau_D)^{1/2}\ [(1+10.86x+15.5x^2)/(1+8.743x)]^{3/4}\right\} \tag{3.9}$$

For D = 0 this formula becomes equivalent to the formula (3.4).

Acknowledgement I want to acknowledge the kind permission granted by Springer Science and Business Media and by Professor Joseph R. Lakowicz to reproduce in this paper some figures that appear in the book "Principles of Fluorescence Spectroscopy" by J. R. Lakowicz (third ed.), published by Springer in 2006.

References

1.1. Lakowicz J. R. (2006), *Principles of Fluorescence Spectroscopy*, 3rd ed., Springer, New York.
1.2. Herschel J. F. W. (1845), Phil. Trans. Roy. Soc. (London) **135**, 143
1.3. Gregory J. (ed.) (1966) *Handbook of fluorescent probes and research products*, 9th ed., Molecular Probes Inc., Eugene, OR
1.4. Jablonski A. (1935), Z. Phys. **94**, 38
1.5. Stokes G. G. (1852), Phil. Trans. R. Soc. (London) **142**, 463
1.6. Kasha M. (1950), Disc. Faraday Soc. **9**, 14
1.7. Berlman I. B. (1971), *Handbook of aromatic molecules*, 2nd ed., Academic, New York
1.8. Stern O. and Volmer M. (1919), Phys. Z. **20**, 183
1.9. Albani J. R. (2007), *Principles and Applications of Fluorescence Spectroscopy*, Blackwell Publishing, New York
1.10. Stryer L. (1978), Annu. Rev. Biochem. **47**, 819
1.11. Berberan-Santos M. N. (2001), in *New Trends in Fluorescence Spectroscopy: Applications to Chemical and Life Sciences*, **18**, 733, B. Valeur and J.C. Brochon eds, Springer, New York
1.12. Royer C. A. (1966), Biophys. J. **68**, 1191
2.1. Eyring H., Walter J and Kimball G. F. (1944), *Quantum Chemistry*, Wiley, New York, p. 351
2.2. Morgenau H. (1931), Phys. Rev. **38**, 747
2.3. Morgenau H. (1939), Rev. Mod. Phys. **11**, 1
2.4. Carlson B. C. and Rushbrooke G. S. (1950), Proc. Camb. Phil. Soc. **46**, 626
2.5. Watts R. K. (1975), in *Optical Properties of Ions in Solids*, B. Di Bartolo ed., Plenum Press, New York and London, p. 307
2.6. Perrin F. (1928), Compt. Rend. **178**, 1978
2.7. Stern O. and Volmer M. (1919), Physik Z. **20**, 183
2.8. Förster Th. (1949), Z. Naturforsch **4a**, 321
2.9. Förster Th. (1959), Discussions Faraday Soc. **27**, 7
2.10. Galanin M. D, (1955), Sov. Phys. JETP **1**, 317
2.11. Reif F. (1965), *Fundamentals of Statistical and Thermal Physics*, McGraw Hill, New York, p.483
2.12. Yokota M. and Tanimoto O. (1967), J. Phys. Soc. Japan **22**, 779
2.13. Watts R. K. and Richter H. J. (1972), Phys. Rev. **B6**, 1584
2.14. Karpick J. T. and Di Bartolo B. (1971), J. of Luminescence **4**, 309
3.1. Lakowicz J. R. (2006), *Principles of Fluorescence Spectroscopy*, 3rd ed., Springer, New York
3.2. Clegg R. M. (1966), in *Fluorescence Imaging Spectroscopy*, X. F. Wang and B. Herman, eds., p. 179, Wiley, New York
3.3. Yokota M. and Tanimoto O. (1967), J. Phys. Soc. Japan **22(3)**, 779

FLUORESCENCE OF STRONGLY ABSORBING MULTICOMPONENT MEDIA

A.P. VOITOVICH*, V.S. KALINOV, A.P. STUPAK
Institute of Physics
National Academy of Sciences
68 Nezalezhnosci Ave., Minsk, 220072, Belarus

1. Introduction

Fluorescence is widely used for examinations of biological objects and for the diagnostic purposes in medicine [1]. New fluorescent methods of research such as Stimulated Emission Depletion (STED), Fluorescence Correlation Spectroscopy (FCS) and Fluorescence Lifetime Imaging Microscopy (FLIM) are developed. For a long time Fluorescence Resonance Energy Transfer (FRET) method is successfully applied to study of donor–acceptor interactions in biological systems. Use of fluorescence markers becomes routine procedure in medical practice. All characteristics of fluorescence – intensity, spectrum, polarization, lifetime and quantum yield – are used now for research and diagnostics in biology and medicine.

All biological systems are multicomponent. Very often in this situation: (a) absorption bands of various components are overlapped, (b) bands of fluorescence and absorption of the system are overlapped, (c) the optical density of absorption appears to be not small I n comparison with unity. Under such conditions fluorescence intensity measurements of one of components or system as a whole and measurements of fluorescence excitation spectra (FES) of each component are distorted. For example, the measured dependence of fluorescence intensity of one component on an exciting radiation wavelength characterizes system as a whole and not just absorption of the given component. That is such dependence is not FES of the given component and does not correspond to its absorption spectrum. The possibility of identification of a component on its FES is thus lost. Distortions can be brought also by radiation scattering in the investigated medium. All these circumstances demand development of the methods of the account of specified factors influence on measurement data of fluorescence intensities, spectra and FES in multicomponent absorbing and scattering media.

The overlapping of fluorescence spectrum of an investigated component with absorption spectra of other medium components does not influence on lifetime measurements of this fluorescence if FRET and quenching of fluorescence do not take place. The electromagnetic scattering does not influence on lifetime of fluorescence too. Lifetime changing denotes that fluorescent molecules interact substantially with their surroundings. Therefore in many cases fluorescence lifetime measurements give very

* A.P. Voitovich, Institute of Physics, National Academy of Sciences, 68 Nezalezhnosci Ave., Minsk, 220072, Belarus, e-mail: voitovich@imaph.bas-net.by

B. Di Bartolo and J. Collins (eds.), *Biophotonics: Spectroscopy, Imaging, Sensing, and Manipulation*, 173
DOI 10.1007/978-90-481-9977-8_7, © Springer Science+Business Media B.V. 2011

important information about positions and interactions of molecules. This circumstance promoted a wide spread occurrence of FLIM method for investigations in biology and medicine [2, 3].

In the present paper the method of FES determination for components with the overlapped absorption bands, being in the medium under study with optical density not small in comparison with unity, is stated. The proposed method allows determining of FES, which is characteristic for each component, on the base of two measured functions: (a) dependence of fluorescence intensity of the component on an exciting radiation wavelength, (b) an absorption spectrum of the medium.

The method application is illustrated by several examples. In one of them FES of coumarin-7 dissolved in ethanol together with tetrachloride 5,10,15,20-tetrakis – (4-*N*-methylpyridyl) porphyrin is determined. Coumarin compounds are anticoagulants of indirect activity**.** Porphyrins play the important role in biological processes, and also are successfully used as sensitizers in photodynamic therapy [4]. In all cases of FES determination the experimental peculiarities of fluorescence measurement are taken into consideration.

2. The Equation for FES of Components with Overlapping Absorption Bands

In [5] the equation which describes excitation wavelength dependence of fluorescence intensity is given. This equation is suitable for each of components which are characterized the overlapped absorption bands and located in a multicomponent medium. It looks like:

$$I_i(\nu) = \frac{F \cdot \beta_i \cdot J_0 \cdot \nu_{i,fl} \cdot k_i(\nu) \cdot \left\{1 - \exp\left[-(l \cdot \sum_i k_i(\nu))\right]\right\}}{\nu \cdot \sum_i k_i(\nu)}. \qquad (1)$$

In Eq. (1) the following designations are used: I_i (ν) – integrated on spectrum intensity of fluorescence for ith component at excitation by radiation with frequency ν, F – the geometrical factor taking account of a fluorescence fraction collected by recording system, β_i – a quantum yield, J_0 – magnitude of an excitation flux at the entrance into the investigated medium, $\nu_{i,fl}$ – frequency of a maximum at the symmetrical contour or a centre of gravity at the nonsymmetrical contour of a fluorescence band, k_i (ν) – an absorption coefficient of ith component on an excitation frequency ν, l – a thickness of the sample under study along a direction of propagation of an excitation flux. Summation is conducted on all components absorbing on frequency ν.

In many cases at measuring of excitation wavelength dependence the fluorescence intensity I_i ($\nu_{i,\,reg}$, ν) on certain frequency $\nu_{i,\,reg}$, instead of integral on spectrum intensity, is experimentally recorded. The Eq. (1) remains valid, if in it to interchange integrated intensity I_i (ν) on spectral intensity I_i ($\nu_{i,\,reg}$, ν) in an unit interval of frequencies, frequencies $\nu_{i,\,fl}$ on $\nu_{i,\,reg}$ and in expressions for intensities to input coefficients A_i ($\nu_{i,\,reg}$). For determination of the coefficients it is necessary to know the normalized on a maximum function $\varphi_{i,\,fl}$ (ν) which describes a contour of fluorescence band. Coefficient

$A_i(\nu_{i,\,reg})$ is defined as the ratio of value of this function on frequency $\nu_{i,\,reg}$ to value of a definite integral of this function within full contour. The function can be set analytically or in a digital form.

It is necessary to point out, that the relation (1) is derived without the account of the stimulated emission and absorption saturation, i.e. in linear approach on an exciting electromagnetic field. It is assumed also, that in integrated intensity (or in intensity on registration frequency ν_{reg}) of fluorescence of i^{th} component there is no contribution of other components, the emission of which is excited because of the overlapping of absorption spectra. At use (1) in case when the last requirement is not fulfilled, it is necessary to extract the part of i^{th} component intensity from the total intensity. It should be emphasized that the equation (1) is valid for arbitrary value of the $lk_i(\nu)$ and $l\sum k_i(\nu)$ quantities.

If the condition $(l \sum k_i(\nu)) << 1$ is satisfied, the exponent in (1) is expanded into a series. Being restricted to two first terms of the series, we derive

$$I_i(\nu) \approx F\, \beta_i\, J_0\, \nu_{i,fl}\, \nu^{-1}\, k_i(\nu)\, l. \tag{2}$$

For spectral intensity $I_i(\nu_{i,\,reg}, \nu)$ taking into account the mentioned replacements it is possible to write an analogous relation. It is obvious from (2), that experimentally measured fluorescence excitation contour (to be more precise – quantity $\nu \cdot I_i(\nu)$) of any i^{th} component from total ensemble of luminescence centres in multicomponent medium coincides with its absorption contour (in the relative units).

Very often in the process of measurements the number of quanta at excitation of fluorescence by radiation with various frequencies is kept constant. In such cases in relations (1) and (2) it is necessary to omit a factor ν^{-1}. Then fluorescence intensity of each component, as it is evident from (2), is proportional to its optical density, i.e. concentration. Thus, in this case FES of each component of medium separately is measured directly without additional calculations. It allows directly from such measurements to determine absorption spectra and, hence, to identify these components if their absorption spectra are known. Proportionality between quantities $I_i(\nu)$ and $k_i(\nu)$ ensures tracing of concentration variations of a components on a variation of their fluorescence intensity.

Using equation (1), it is possible to determine FES of any of fluorescent components which are located in strongly absorbing multicomponent medium. Such spectrum in the relative units is defined as:

$$k_i(\nu)\cdot l = \frac{B_i \cdot J_i(\nu_{i,reg}, \nu) \cdot \sum_i k_i(\nu)\cdot l}{\left\{1 - \exp\left[-(l \cdot \sum_i k_i(\nu))\right]\right\}}, \tag{3}$$

where $B_i = [F \cdot A_i(\nu_{i,\,reg}) \cdot \beta_i \cdot J_0 \cdot \nu_{i,\,reg}]^{-1}$ – a constant factor. Here, as well as in the following relations, the factor ν is omitted. The normalized spectral contour of quantity $k_i(\nu)l$ in the Eq. (3) coincides with a contour $\varphi_{i,abs}(\nu_i)$ of the absorption band of i^{th} component. For its determination it is necessary to measure two functions: a) $I_i(\nu_{i\,reg}, \nu)$

- dependence of fluorescence intensity of i^{th} component of medium on a wavelength of an exciting radiation and b) $l\sum k_i(\nu)$ – absorption spectrum of medium. The spectrum of quantity $k_i(\nu)\cdot l$, which is determined in accordance with a developed procedure, allows to identify the components, which are located in multicomponent medium. If as a result of such definition the unknown spectrum is received, then it is possible to determine correctly central frequency, width and a contour of the received absorption band.

The Eqs. (1)–(3) are derived under assumption, that the contributions of each part of the medium illuminated by an exciting radiation to detected (registered) signal $I_i(\nu)$ with equal coefficients are proportional to the intensity of the fluorescence emitted by this part. Because of limitation of the aperture of the radiation detector or the registering system as a whole this condition is usually valid only at small thickness l of investigated medium. Therefore in practice very often the indicated requirement is not fulfilled. In Fig. 1 the normalized on a maximum function $f(x)$ is shown, representing the measured dependence of efficiency of the fluorescence collection from very thin (l <1 mm) material layer upon the layer position in cuvette compartment of the spectrofluorimeter used by us. (In a spectrofluorimeter a standard cuvette with thickness of 10 mm is usually applied.)

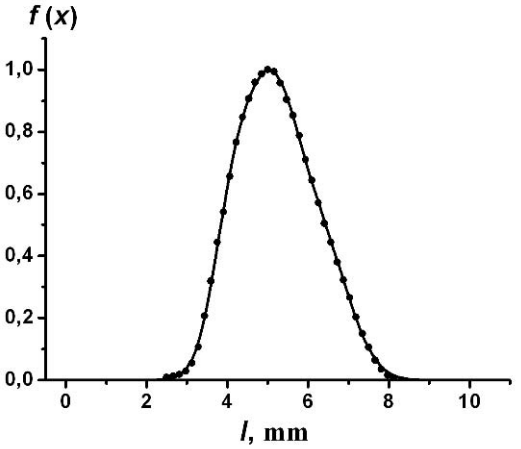

Figure 1. Function $f(x)$ for a used spectrofluorimeter, solid circles – data of measurements.

Measurements of function $f(x)$ are made at perpendicular orientation of directions of excitation and fluorescence registration. The fast decrease of efficiency at displacement of the cuvette with material from the centre of cuvette compartment is evident. To satisfy a requirement of an efficiency constancy a thickness of investigated material layer at use of our spectrofluorimeter should be approximately equal or less than 1 mm.

In the case when $f(x) \neq$ const the differential equation given in [5] can be used for calculation of fluorescence intensity. With the account function $f(x)$ it can be written as

$$I_i(\nu) = \int_0^l dI_i(\nu) = F\,\beta_i\,k_i(\nu)\,\nu_{i,fl}\,J_0 \int_0^l \{\exp[-(\sum_i k_i(\nu)\,x)]\}\,f(x)\,dx. \qquad (4)$$

The integral in the ratio (4) can be found by a numerical method and so the dependence (4) is possible to present in the form:

$$I_i(\nu) = \frac{F \cdot \beta_i \cdot J_0 \cdot \nu_{i,fl} \cdot k_i(\nu) \cdot G[f(\mathrm{x}), \sum_i k_i(\nu)]}{\sum_i k_i(\nu)}, \tag{5}$$

where function G for perpendicular orientation of directions of excitation and fluorescence recording is defined as follows:

$$G = \sum_{m=0}^{n} f(l_m) \{\exp[-l_m \sum_i k_i(\nu)] - \exp[-(l_m + \Delta l) \sum_i k_i(\nu)]\}. \tag{6}$$

In the sum (6) $l_0 = 0$, $l_1 = \Delta l$, $l_2 = 2\Delta l$, … $l_n = n\Delta l = l - \Delta l$, $f(l_m) = 0.5[f(l_m) + f(l_{m+1})]$. It is assumed, that within a summation step Δl function $f(x)$ can be approximated, as linear, and quantity of a step is small and does not bring an essential error to the result of summation. A relation (5) is similar on structure to a relation (1).

Equation (5) can be used for definition of FES of medium components. For such a definition it is necessary to know three functions: (a) intensity of fluorescence $I_i(\nu)$, (b) absorption $l \sum k_i(\nu)$ or optical density D of medium ($l \sum k_i(\nu) = D \cdot \ln 10$) and (c) function $f(x)$, describing efficiency of the fluorescence collecting depending on a position of an investigated material layer in cuvette compartment. From the Eq. (5) FES of a fluorescent component is defined as:

$$k_i(\nu) \cdot l = \frac{B_i \cdot J_i(\nu_{i,reg}, \nu) \cdot l \sum_i k_i(\nu)}{G[f(\mathrm{x}), \sum_i k_i(\nu)]}. \tag{7}$$

In the presence of absorption on frequencies of fluorescence the measured intensity will not match to the true intensity emitted by exited ensemble. In [6] this situation is examined and for various experiment arrangements mathematical relations are given, defining distortions of true intensity quantities, originating at measuring. When directions of propagation of recorded and exciting beams are perpendicular, a reduction coefficient of recorded intensity on a wavelength $\lambda_{i,reg}$, originating as a result of a fluorescence reabsorption, does not depend on quantity $l \sum k_i(\nu)$. Therefore relations (3) and (7) remain valid for any wavelengths of excitation and in the presence of absorption on frequencies of fluorescence. In the cases when directions of propagation of recorded and exciting fluxes coincide or are opposite, there is a dependence of the reduction coefficient on magnitude $l \sum k_i(\nu)$. Thus using of relations (3) and (7) in the last two cases is possible only under condition of absence of absorption on a fluorescence recording wavelength $\lambda_{i\,reg}$.

In experiment options at which directions of propagation of exciting and recorded fluxes coincide or are opposite, the relation (3) can be applied independently of a

function $f(x)$ form, if density J_0 of an exciting flux is constant in range of values where $f(x) \neq 0$.

3. Examples of FES Determination of Medium Components

The Eq. (1) and the relations derived in [6] have allowed to calculate fluorescence quantum yields [5]; to define correctly contours, central frequencies and widths of fluorescence bands in media, where absorption and fluorescence bands are overlapped [6]; to develop methods of the quantitative fluorescence analysis of the materials, not demanding using of standard samples with known contents of detected components [7]. In the given section use of the Eqs. (3) and (7), defined from the relation (1), for determination of FES of separate components with the overlapped absorption bands in multicomponent medium will be shown.

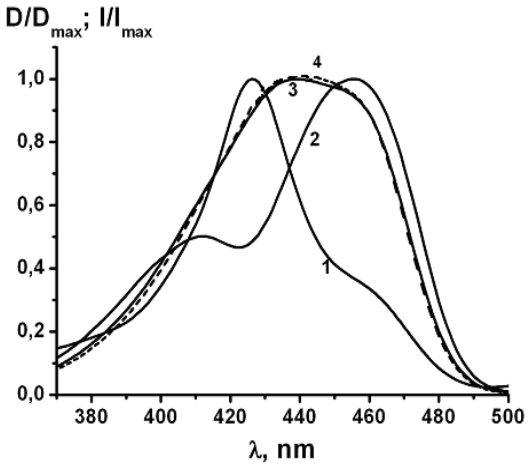

Figure 2. The normalized to the maximum value: a spectrum of optical density D of the investigated medium (1); dependence of fluorescence intensity I of this medium upon a wavelength of an exciting radiation (2); absorption spectrum of coumarin-7 (3) and FES (4) of luminescent component, calculated with use of the Eq. (3).

Figure 2 demonstrates measured and the normalized on the maximum values spectrum of optical density D of the investigated medium (curve 1) and dependence of intensity I of its fluorescence upon excitation wavelength λ_{exc} (curve 2). The medium is formed of coumarin-7 and tetrachloride 5,10,15,20-tetrakis - (4-*N*-methylpyridyl) porphyrin dissolved in ethanol. The optical density of the medium in a spectrum maximum was 1.43 and a fluorescence registration wavelength λ_{reg} = 530 nm. Data are received at a thickness of investigated material l < 1 mm. At such thickness of a cuvette it is possible to assume $f(x)$ = const. Directions of propagation of recorded and exciting fluxes are perpendicular at all measurements which results are demonstrated in the present section.

The dependence, introduced by a curve 2 (Fig. 2), strongly differs from an absorption spectrum of the medium under study. It is also distinct from coumarin and porphyrin absorption spectra. We will calculate FES of a fluorescent component with using the Eq. (3) and measured dependences D (λ), I/I_{max} (λ). Data of such calculation, which are normalized on the maximum value, are presented by a dashed curve 4 in Fig. 2. They coincide well with coumarin-7 absorption spectrum (curve 3). Thus, the used procedure allows retrieving true FES of the fluorescent component which is located in multicomponent medium.

Let's give two examples of FES definition in a case, when for fluorescence measuring the standard cuvette of 10 mm thickness is used. Function $f(x)$ for this case is demonstrated by the curve shown in Fig. 1. It is necessary to mention, that in a spectrofluorimeter used by us the cuvette holder screens fluorescence from two medium layers, from which one is in a front part and other in a rear part of a cuvette. A thickness of each of these layers is 1 mm. For these layers function $f(x)$ and the appropriate summands in the sum (6) are equal to zero.

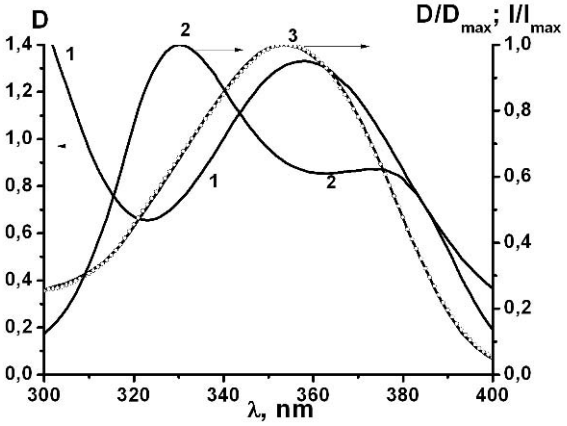

Figure 3. Spectrum of an optical density of the analyzed medium (1); dependence of fluorescence intensity on an excitation wavelength λ_{exc} (2); an absorption spectrum of coumarin-102 (3) and FES of coumarin-102 (open circles) calculated under the formula (7).

In Fig. 3 the measured absorption spectrum of iodine and coumarin-102 dissolved in ethanol (a curve 1) is shown. For this medium a dependence of fluorescence intensity I at a wavelength λ_{reg} = 440 nm upon a wavelength λ_{exc} of exciting radiation is measured. This dependence, which is normalized to the maximum value of intensity, is given by a curve 2 in Fig. 3. It differs from the coumarin-102 absorption spectrum (curve 3, Fig. 3) very much. Calculation of an absorption spectrum of a fluorescent component by formula (7) with use of measured dependences D (λ), I/I_{max} (λ) and function $f(x)$, given in Fig. 1, is carried out. Calculation data are shown with open circles in Fig. 3. They coincide very well with the coumarin-102 absorption spectrum measured independently on a standard procedure.

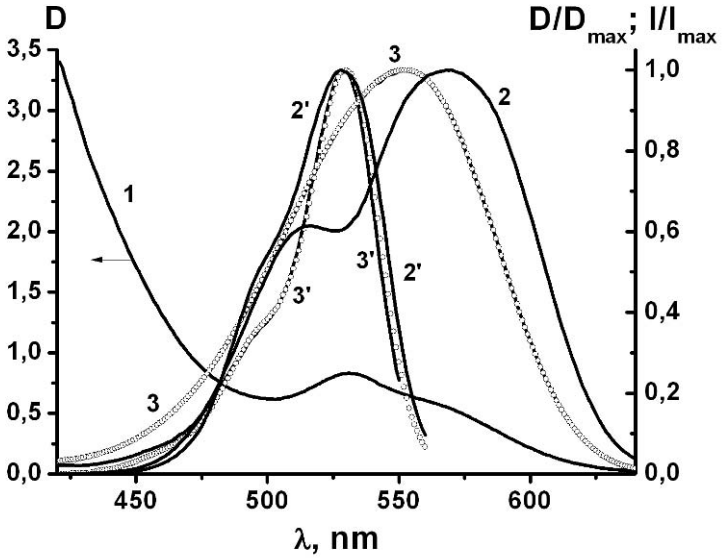

Figure 4. Spectrum of an optical density of the analyzed medium (1); dependences of fluorescence intensities upon an excitation wavelength λ_{exc} at λ_{reg} = 670 (2) и 580 nm (2′); an absorption spectra of oxazine 17 (3) and rhodamine 6G (3′) and FES (open circles) calculated under the formula (7).

In Fig. 4 the measured and calculated data for the medium consisting of iodine, rhodamine 6G and oxazine 17 dissolved in ethanol are shown. Dependences of fluorescence intensities of medium on a wavelength λ_{exc} are measured at two wavelengths of fluorescence recording: 670 and 580 nm. These dependences normalized to the peak values of intensities are presented in Fig. 4 by curves 2 and 2′ accordingly. They differ from absorption spectra of oxazine 17 and rhodamine 6G (curves 3 and 3′ accordingly). As well as in the previous case absorption spectra of oxazine 17 and rhodamine 6G, which are shown by open circles in Fig. 4, are calculated under the formula (7). The calculated spectra well coincide with the spectra measured on a standard procedure. Small differences of the calculated and measured spectra of rhodamine 6G on the long wavelength side of its absorption band are explained by the small contribution of oxazine 17 to the rhodamine 6G fluorescence intensity measured at λ_{reg} = 580 nm. This contribution increases at fluorescence excitation by radiation with wavelengths near to an absorption band maximum of oxazine 17.

On a registration wavelength λ_{reg} = 580 nm appreciable absorption takes place. However it, as was already mentioned, will not lead to distortion of measured dependence $I(\lambda_{exc})$.

Thus, definition of FES of components with the overlapped absorption bands, with no restrictions on the optical densities. It allows studying multicomponent media, including biological, for which it is impossible to satisfy requirement $D << 1$.

Acknowledgments One of the authors (V.A.P.) thanks to Prof. Baldassare Di Bartolo, the staff of the Majorana Center and all the participants for providing a wonderful stimulating atmosphere of the school.

This work is partly supported by the Belarusian Republic Foundation for Fundamental Research.

References

1. Lacowicz, J.R. (2006) *Principles of Fluorescent Spectroscopy*. Springer, New York.
2. Wouters, F.S., Bastiaens, P.I. (1999) Fluorescence lifetime imaging of receptor tyrosine kinase activity in cells, *Curr. Biol.* **9**, 1127–1130.
3. Yasuda, R. (2006) Imaging spatiotemporal dynamics of neuronal signaling using fluorescence resonance energy transfer and fluorescence lifetime imaging microscopy, *Curr. Opin. Neurobiol.* **16**, 551–561.
4. Bonnett, R. (2000) *Chemical Aspects of Photodynamic Therapy*. Gordon & Breach Science Publishers, Amsterdam.
5. Voitovich, A.P., Kalinov, V.S., Stupak, A.P. (2009) The photoluminescence excitation spectra of multicomponent media, *Opt. Spectrosc.* **106**, 255–261.
6. Voitovich, A.P., Harbachova, A.N., Kalinov, V.S., Stupak, A.P. (2008) Analytical relations for luminescence intensities accounting for reabsorption, *J. Appl. Spectr.* **75**, 791–797.
7. Voitovich, A.P., Kalinov, V.S., Runets, L.P., Stupak, A.P. (2009) Methods for quantitative luminescent analysis, *J. Appl. Spectr.* **76**, N 5.

COHERENT QUANTUM CONTROL IN BIOLOGICAL SYSTEMS

J.P. WOLF*
GAP-Biophotonics, University of Geneva
20, rue de l'Ecole de Médecine
1211 Geneva 4 (Switzerland)

1. Introduction

Coherent quantum control has recently induced a revolution in photochemistry. Not only can the atomic motion be *observed* within molecules by snapshots of a few femtoseconds duration, it can now also be *controlled*. The basic idea of this revolution is the use of quantum interference between different states that are in coherent superposition so that a target state is reached with maximum probability. The mechanism reminds interference in optics, where some optical paths are favored (constructive interference) while others are discarded (destructive interference), as in Young's double slit experiment. A key element for achieving this control is the transfer of coherence from the exciting light field to the atomic or molecular system via the electric dipole operator. A tailored coherent laser pulse is used to excite a molecule in a superposition of states, which drives the molecule along a specific path to obtain a targeted result.

A famous example of coherent control is the Tannor, Koslov and Rice [1, 2] "pump-dump" method (Fig. 1), in which many vibrational states of a molecule ABC are coherently excited for generating a vibrational wavepacket. This wavepacket explores, as a function of time, a large fraction of the electronically excited hypersurface. By firing a second laser at convenient times t1 or t2, the molecule is brought back to its ground state but onto different dissociation paths, resulting in different species AB + C or A + BC. The system can thus be driven to a specific fragment by using the quantum control of the photodissociation process.

In 1992, H. Rabitz at Princeton introduced [3, 4] the concept of "optimal control", in which a feedback loop optimizes the laser pulse characteristics to reach most efficiently the desired target. For this, a large number of parameters (corresponding to the amplitude and phase of each spectral component within the exciting laser spectrum) have to be controlled. This "pulse shaping" technique is usually performed by introducing a liquid crystal array in the Fourier plane between two gratings (4f arrangement) [5]. Excellent results in terms of efficiency have been obtained using genetic-type optimization algorithms [6–8].

Besides the above mentioned "pump-dump" scheme, other successful control methods have been extensively applied, including stimulated Raman scattering (STIRAP), Four Wave Mixing like CARS (Coherent AntiStokes Raman Scattering), multiphoton absorption and multiphoton ionization. For more information about general quantum control aspects,

* J.P. Wolf, GAP-Biophotonics, University of Geneva, 20, rue de l'Ecole de Médecine, 1211 Geneva 4 (Switzerland), e-mail: Jean-pierre.wolf@physics.unige.ch

B. Di Bartolo and J. Collins (eds.), *Biophotonics: Spectroscopy, Imaging, Sensing, and Manipulation*, 183
DOI 10.1007/978-90-481-9977-8_8, © Springer Science+Business Media B.V. 2011

a detailed review article has recently been published by M. Dantus et al. [6]. The controlled targets can be, for instance, specific fragments, specific isomers or specific isotopes, but also the enhancement or reduction of the fluorescence of a specific molecule (by driving it preferentially into other relaxation pathways). In this respect, a pioneering work has been performed by the group of G. Gerber [9, 10], in which the capability of distinguishing two different dyes using 2-photon absorption control was demonstrated, although the dyes had similar linear absorption and fluorescence spectra.

Experiments based on quantum control in biology have also been performed. Some striking examples are the control of the relaxation pathways in rhodopsin complexes [11, 12], the vibrational CO ladder climbing in hemoglobin [13] and pH-sensitive measurements in multi-photon microscopy [14].

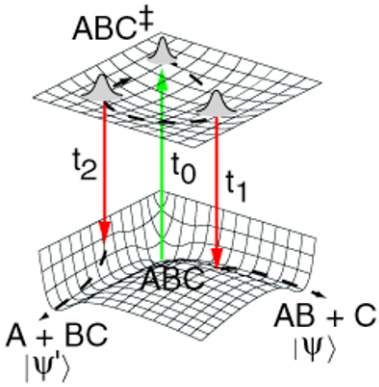

Figure 1. Coherent control of the dissociation pathways of the molecule "ABC" [1, 2].

An attractive application is the ability of discriminating different biological systems that are usually undistinguishable with standard linear spectroscopic approaches. One can think for instance to the early detection of cancer using the detection of specific proteins, the label-free monitoring of the cell metabolism, or the detection and identification of harmful bacteria. The aim of this chapter is to discuss these potential applications of quantum control.

Rapid detection and identification of pathogenic aerosols such as *Bacillus anthracis* (anthrax) from potential bioterrorism release, or infectious epidemic agents are urgent safety issues. However, in order to efficiently protect populations bioaerosol analyzers need to be both very fast (typ. minutes) and very selective (in order to discriminate pathogen from non-pathogen particles and thus minimize false alarm rates).

Two development directions were followed these latter years in order to reach this important but difficult objective: (1) biochemical identification procedures, which are selective but slow, and (2) optical devices, which are fast but not specific enough.

Currently available biochemical techniques, such as polymerase chain reaction (PCR), fluorescence in situ hybridization (FISH) or chip matrix of biochemical microsensors

(biochips), can identify the genus and species of a bacteria or a virus. However, these bio-chemical assay procedures require time (many hours or even days).

On the other hand, several groups have developed sophisticated optical systems to distinguish bio-aerosols from nonbio-aerosols based on fluorescence [15–18] and/or elastic scattering [19, 20]. Most advanced experiments have been realized by the group of Prof. R. Chang at Yale University, in which each individual aerosol particle is spectrally analyzed [15, 21–23]. These instruments can run continuously, in-situ, and in real-time in order to provide rapid warning/alarm for the existence of a few potentially life threatening bio-aerosols in the midst of a vast number of nonbio-aerosols. The major flaw inherent in these instruments is frequent false alarms because UV-Visible fluorescence is incapable of distinguishing different molecules with similar fluorescence spectra (such as tryptophan and diesel vapor or cigarette smoke) [21, 24], or of identifying different kinds of bacteria. In this latter case, extensive studies based on principle components analysis of the excitation versus fluorescence spectral matrix have been performed to distinguish the spectrum from one type of bacteria from another, without success [25].

A very attractive capability of optical techniques is remote sensing, and especially Lidar (Light Detection and Ranging). The Lidar technique [26–28] allows to map aerosols in 3D over several kilometers, similar to an optical Radar. It is therefore possible to detect the release and spread of potentially harmful plumes (such as bioterrorism release or legionella from industrial cooling towers) at large distance and then provide time to take the necessary measures to protect populations or identify sources. So far, Lidar detection of aerosols has concentrated on the measurement of size distribution and concentrations [29–34], but little work was reported on the determination of the aerosol composition. In particular, the distinction between bioaerosols and nonbio-aerosols was either impossible (elastic scattering only) or very unsatisfactory for LIF-Lidars (interference with pollens and organic particles like traffic related soot or PAHs) [35].

A further requirement imposed by biochemical assays and spectroscopic techniques is that the few target bio-aerosols should not be overwhelmed by the presence of nonbio-aerosols. A point sensor should be able to analyze a few hundred liters of sample air within 1 min at different environmental conditions and locations (e.g. subway stops, hospitals, and airports). In the early phase of a bio-aerosol release situation, the potentially harmful aerosols detected by the sensor are generally the minority entrained within a majority of innocuous background aerosols (e.g. one bio-aerosol in 1,000 background aerosols per liter of air). The large quantity of background aerosols could contaminate the reactions, and disable the biochemical assays within minutes.

Conventional biochemical and optical methods have shown limits, and novel approaches involving basic research aspects are required. We present in this chapter the potential of femtosecond non-linear spectroscopy, and in particular of “coherent control”, to address, as a first example, the primary issue of fast detection and identification of bacteria in air.

2. Non-linear Interactions with Aerosols

2.1. MULTI-PHOTON-EXCITED FLUORESCENCE (MPEF) FROM AEROSOL MICROPARTICLES

A possible way of overcoming the limits of conventional linear spectroscopy is to excite the fluorescence with ultrashort laser pulses in order to access specific molecular dynamics features in the *time domain*. Recent experiments using coherent control and multiphoton ultrafast spectroscopy have shown the ability of discriminating between molecular species (organic dyes) that have similar one-photon absorption and emission spectra [9, 10]. Sophisticated pulse shaping techniques should allow for even more selective enhancement of the fluorescence of one molecule versus an almost identical other, which moreover exhibit almost identical spectra. This approach, called "Optimal Dynamic Discrimination (ODD)" [36] provides the basis for generating optimal signals in order to identify similar molecular agents.

We recently demonstrated that femtosecond pump-probe spectroscopy allows for distinguishing biological microparticles from nonbiological PAH (Polycyclic Aromatic Hydrocarbons)-containing ones. More precisely, we could distinguish amino acids (Tryptophan, Trp) and flavins (riboflavin RBF, FMN and FAD) from PAHs (naphthalene) and diesel fuel in the liquid phase using a "Pump-Probe Deletion" (PPD) technique. We also showed that the non-linear properties of aerosols and droplets produce a strong backward enhancement of the emitted light, which is most favorable for remote sensing applications.

The most prominent feature of non-linear processes in aerosol particles using femtosecond laser pulses is a strong localization of the emitting molecules within the particle, and subsequent backward enhancement of the emitted light [37–40]. This unexpected behavior is very attractive for remote detection schemes, such as Lidar applications.

Localization is achieved by non-linear processes, which typically involve the n-th power of the internal intensity $I^n(\boldsymbol{r})$ ($\boldsymbol{r}$ for position inside the particle, Fig. 2). Backward enhancement can be illustrated by the reciprocity (or "time reversal") principle: Re-emission from regions with high $I^n(\boldsymbol{r})$ tends to return toward the illuminating source by essentially retracing the direction of the incident beam that gave rise to the high intensity points.

More precisely, we investigated, both theoretically and experimentally, multiphoton processes involving n = 1–5 photons [38]. For n = 1, 2, 3, MPEF occurs in bioaerosols because of natural fluorophors such as amino acids (tryptophan, tyrosin), NADH, and flavins. The strongly anisotropic MPEF emission was demonstrated on individual microdroplets containing tryptophan, riboflavin, or other synthetic fluorophors. Fig. 2 (right column) shows the angular distribution of the MPEF emission and the comparison between experimental and theoretical (Lorentz–Mie calculations) results for the one- (400 nm) (upper), two- (800 nm) (center) and three-photon (1,2 μm) (lower) excitation cases. They show that fluorescence emission is maximum in the direction towards the

exciting source. The directionality is dependent on the increase of n, because the excitation process involves the nth power of the intensity $I^n(r)$. The ratio $R_f = P(180°)/P(90°)$ increases from 1.8 to 9 when n is changes from 1 to 3 (P is the emitted light power). For 3-PEF, fluorescence from aerosol microparticles is therefore mainly backwards emitted, which is ideal for Lidar experiments, as demonstrated in the field using the Teramobile system (section 2.2).

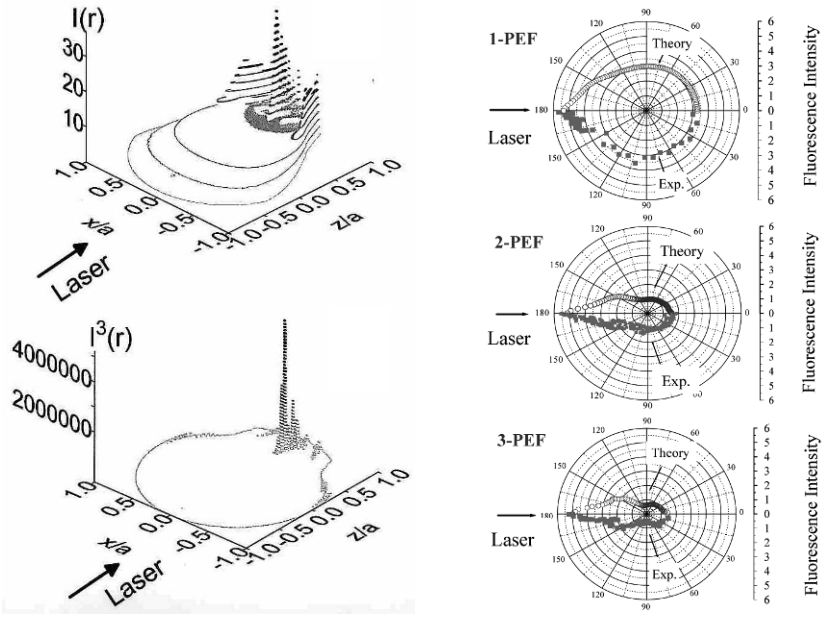

Figure 2. Backward enhanced MPEF from spherical microparticles [37]. *Left column*: Molecular excitation within droplets, proportional to $I^n(r)$ with n=1 and 3. *Right column*: Angular distribution of MPEF emission for 1, 2 and 3 photon excitation.

This backward enhancement has been observed for both spherical and non spherical [39] microparticles, such as 2-PEF from dye doped spheroids [43]. Within aspect ratios ranging from 0.8 to 1.2, backward enhancements of similar values as for spheres are obtained, although the round shape of the backward fluorescence image (Fig. 3) is somewhat affected by the shape of the particle. In particular, multi foci are produced within the spheroid. Due to the large aspect ratios considered, exact Lorentz-Mie calculations could not be achieved. Novel ray tracing approaches were therefore developed in order to determine both the intensity distribution (and its square $I^2(r)$) and the re-emission efficiencies. Although limited to rather large droplets (50 μm in our case), the ray tracing approach satisfactorily reproduced the experimental data, as shown in Fig. 3.

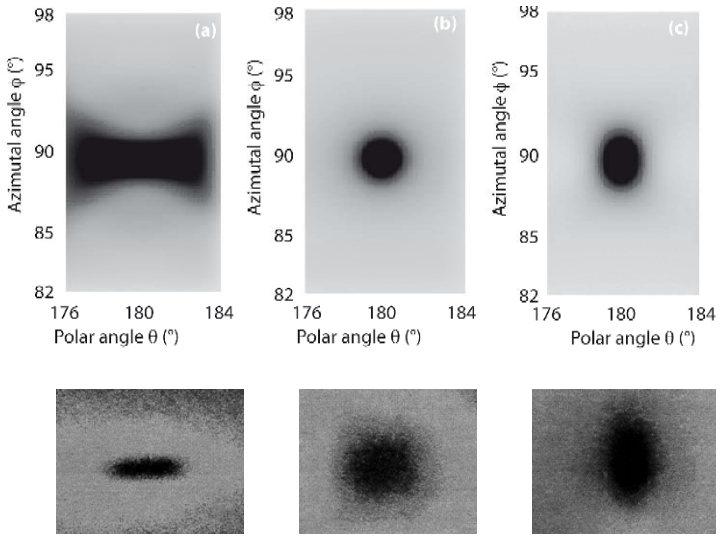

Figure 3. Backward enhanced 2PEF in spheroidal microdroplets [43]. *Upper*: simulations using ray-tracing *Lower*: Experimental measurements using a CCD camera capturing 2-PEF in the backward direction (a) oblate (b) spherical (c) prolate.

Similar experiments were conducted on clusters of spheres and solid tryptophan microparticles. Backward enhancement was observed in any of the studied cases, demonstrating that the effect understood as an illustration of the time reversal principle is generic [39].

The very small spatial extension of femtosecond pulses (15 fs corresponds to 3.4 μm in water, i.e. the equator of a 0.6 μm droplet) can be used for measuring the size of microparticles [44, 45]. An experimental scheme for this consists in creating an optical correlator between two wavepackets, centered at wavelengths λ_1 = 1,200 nm, and λ_2 = 600 nm, which circulate on ballistic orbits (see Fig. 4). 2-PEF is then recorded as a function of the time delay between the two wavepackets in order to quantify the path length traveled within the particle. With this method, the size of droplets up to 670 μm could be precisely measured [44].

The time delay between the two pulses gives access to ballistic pathlengths, so that lengths different from a multiple of the orbital roundtrip evidences the contribution of other trajectories than MDRs (Morphology Dependent Resonance). In order to better understand this behavior, the impact parameter (*a* in Fig. 5) of the laser onto the droplet was modified, so that evanescent coupling in surface modes could be distinguished from refractive penetration onto inner ballistic trajectories.

Detailed analysis of the results showed that for large impact parameters, only surface modes contributed, while for smaller ones, light bullets traveled on rainbow trajectories.

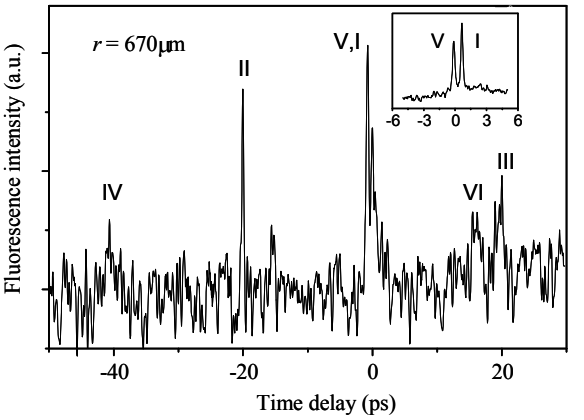

Figure 4. Ballistic trajectories of femtosecond pulses within microdroplets using 2PEF pump-probe technique. Each peak of the series I, II, III, IV corresponds to a roundtrip of the travelling pulse [44].

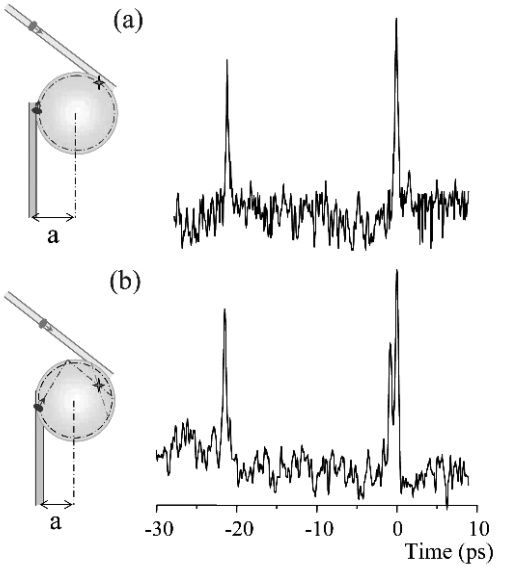

Figure 5. Control of the ballistic trajectories used by the travelling pulse by modifying the impact parameter [44]: (a) evanescent coupling (b) evanescent + refractive coupling.

The sizing capability of this method was applied for a wide range of sizes, but could not be performed experimentally for droplets smaller than 100 μm, due to experimental limitations.

In order to address Lidar applications of the pump-probe approach for measuring remotely both size and composition of atmospheric aerosols, time resolved Lorentz-Mie

calculations have been carried out (50 fs pulses) [45]. In a pump-probe 2-PEF Lidar experiment, the composition would be addressed by the excitation/fluorescence signatures and the size by the time delay between the two exciting pulses. The high peak contrast obtained by the numerical simulations shows that measurements should be feasible for microparticles even of sub-micronic size.

2.2. MPEF-FEMTOSECOND LIDAR DETECTION OF BIOAEROSOLS

The first multiphoton excited fluorescence Lidar detection of biological aerosols was performed using the "Teramobile" system. The Teramobile (www.teramobile.org) is the first femtosecond-terawatt laser based Lidar [41, 42], and was developed by a French–Swiss–German consortium.

The bioaerosol particles, consisting of 1 μm size water droplets containing 0.03 g/l Riboflavin (typical for bacteria), were generated at a distance of 50 m from the Teramobile system. Riboflavin was excited by two photons at 800 nm and emitted a broad fluorescence around 540 nm. This experiment [41, 42] is the first demonstration of the remote detection of bioaerosols using a 2-PEF-femtosecond Lidar. The broad fluorescence signature is clearly observed from the particle cloud (typ. 10^4 p/cm^3), with a range resolution of a few meters (Fig. 6). As a comparison, droplets of pure water do not exhibit any parasitic fluorescence in this spectral range. However, a background is observed for both types of particles, arising from the scattering of white light generated by filaments in air.

Primarily, MPEF might be advantageous as compared to linear LIF for the following reasons: (1) MPEF is enhanced in the backward direction as seen above and (2) the transmission of the atmosphere is much higher for longer wavelengths. For example, if we consider the detection of tryptophan (which can be excited with three photons of 810 nm), the transmission of the atmosphere is typically 0.6 km^{-1} at 270 nm, whereas it is 3×10^{-3} km^{-1} at 810 nm (for a clear atmosphere, depending on the background ozone concentration). This compensates the lower 3-PEF cross-section compared to the 1-PEF cross-section at distances larger than a couple of kilometers [42]. The most attractive feature of MPEF is, however, the possibility of using pump-probe techniques, as described hereafter in order to discriminate bioaerosols from background interferents such as traffic related soot and PAHs.

2.3. MULTI-PHOTON-IONIZATION (MPI) AND LIBS

For $n = 5$ photons, laser induced breakdown (LIBS) in water microdroplets occurs, initiated by multiphoton ionization. The ionization potential of water molecules is 6.5 eV, so that five photons are required at a laser wavelength of 800 nm to initiate the process of plasma formation. Both localization and backward enhancement strongly increase with the order n of the multiphoton process, exceeding $R_f = 35$ for $n = 5$ [38]. As for MPEF, LIBS has the potential of providing information about the aerosols composition, as was demonstrated for bacteria.

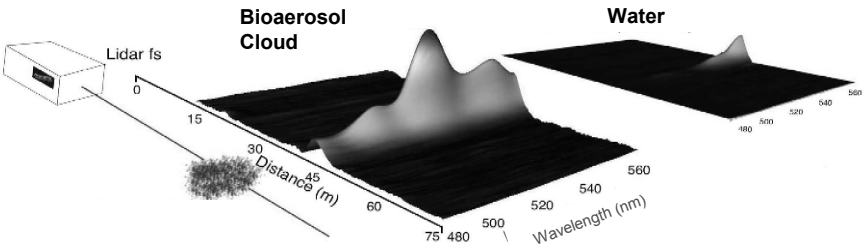

Figure 6. Two-photon Excited Fluorescence Lidar detection of bioaerosols [42].

Although nanosecond-laser LIBS (nano-LIBS) has already been applied to the study of bacteria [46, 47], femtosecond lasers open new perspectives in this respect. The plasma temperature is indeed, much lower in the case of femtosecond excitation, which strongly reduces the blackbody radiation background and interfering lines from excited N_2 and O_2. This allows performing time gated detection with very short delays, and thus observing much richer and cleaner spectra from biological samples. This crucial advantage is shown in Fig. 7, where the potassium (K) line emitted by a sample of *Escherichia coli* is clearly detected in femto-LIBS and almost unobservable under ns-laser excitation [48].

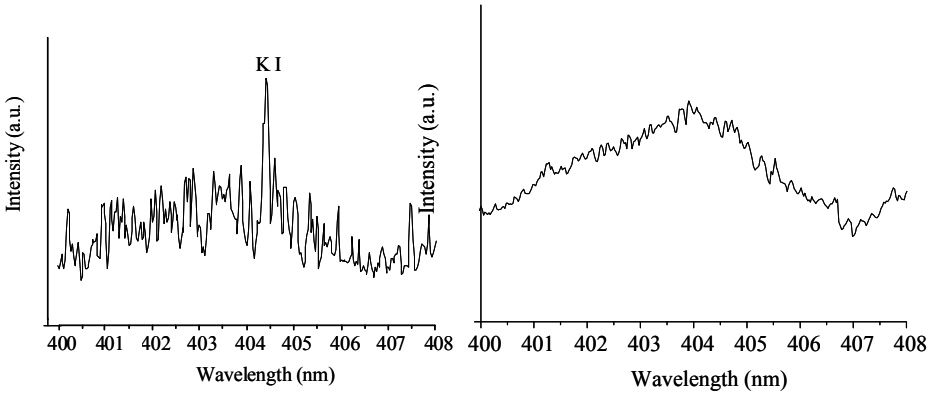

Figure 7. Comparison of fs-LIBS (left) and ns-LIBS results on the K line of *Escherichia coli* [48].

The low thermal background in fs-LIBS allowed the recording of 20–50 lines for each bacterial sample considered in the study (*Acinetobacter*, *Escherichia coli, Erwinia*, *Shewanella* and *Bacillus subtilis*). A systematic sorting with sophisticated algorithms is in progress in order to evaluate whether the spectra are sufficiently different for univoquely identifying each species [49]. Some first results are promising, where significant difference between *Escherichia coli* and *Bacillus subtilis* are observed for the Li line intensity (also observed for the Ca line). This difference can be understood by the typical difference of the cell wall structure between a Gram+ and a Gram– bacterium.

Low temperature plasma is not the only advantage of fs-LIBS: the ablation process itself seems different. fs-LIBS acts more as a direct bond-braking and evaporation process than as a thermal evaporation. This particular ablation process could be put into evidence since not only atomic and ionic lines were observed but also molecular signatures such as CN or C_2 [50]. It was shown in particular that these molecular species are directly ablated from the sample, and not created by recombination of C atoms or ions with Nitrogen from the air (which occurs for ns excitation). Obtaining molecular signatures in addition to trace elements is a significant improvement of the method. The presence of CN molecules is, for instance, a good indicator for a biological material.

3. Pump-Probe Femtosecond Spectroscopy for Identifying Bacteria and Biomolecules

As already mentioned, a major drawback inherent in LIF instruments is the lack of selectivity because UV-Vis fluorescence is incapable of discriminating different molecules with similar absorption and fluorescence signatures. While mineral and carbon black particles do not fluoresce significantly, aromatics and polycyclic aromatic hydrocarbons from organic particles and diesel soot strongly interfere with biological fluorophors such as amino acids. The similarity between the spectral signatures of PAHs and biological molecules under UV excitation lies in the fact that similar π-electrons from carbonic rings are involved. Therefore, PAHs (from Diesel soot for instance) exhibit absorption and emission bands similar to those of amino acids like Tryptophan (Fig. 8). Some shifts are present because of differences in specific bonds and the number of aromatic rings, but the broad featureless nature of the bands renders them almost indistinguishable.

In order to discriminate these fluorescing molecules we applied a novel femtosecond pump-probe depletion (PPD) concept (Fig. 9). It is based on the time-resolved observation of the competition between excited state absorption (ESA) into higher lying excited states and fluorescence into the ground state. This approach makes use of two physical processes beyond that available in the usual linear fluorescence spectroscopy: (1) the dynamics in the intermediate pumped state (S_1) and (2) the coupling efficiency to higher lying excited states (Sn).

As sketched in Fig. 9, a first femtosecond pump pulse (at 270 nm for Trp and PAHs, 405 nm for flavins), resonant with the first absorption band of the fluorophores, coherently excites them from the ground state S_0 to a set of vibronic levels $S_1\{v'\}$. The vibronic excitation relaxes by internal energy redistribution to lower {v} modes. Fluorescence relaxation to the ground state occurs within a lifetime of several nanoseconds. Meanwhile, a second 810 nm femtosecond probe pulse is used to transfer part of the $S_1\{v\}$ population to higher lying electronic states S_n.

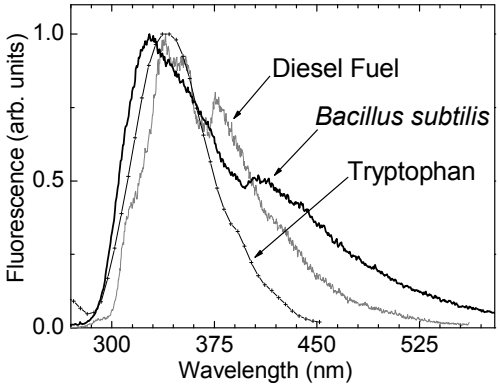

Figure 8. Comparison of the fluorescence spectra of Tryptophan, *B. Subtilis* and Diesel fuel.

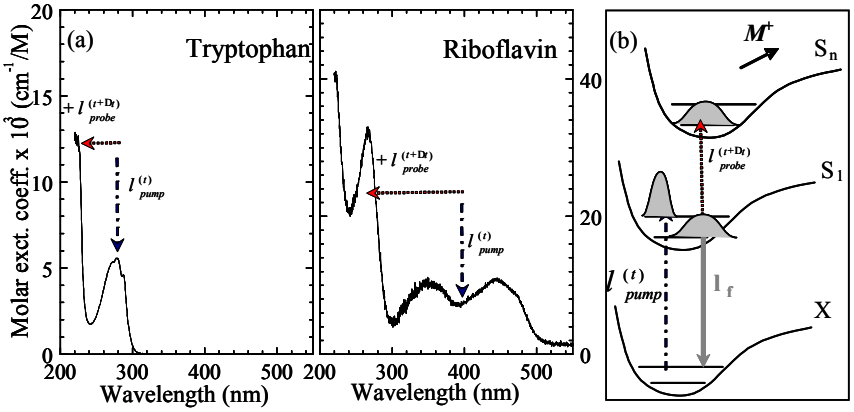

Figure 9. Absorption spectra of Tryptophan (a) and Riboflavin (b). (c) PPD scheme in Trp, flavins and polycyclic aromatics. The pump pulse brings the molecules in their first excited state S_1. The S_1 population (and therefore the fluorescence) is depleted by the second probe pulse [51].

The depletion of the S_1 population under investigation depends on both the molecular dynamics in this intermediate state and the transition probability to S_n. The relaxation from the intermediate excited state may be associated with different processes, including charge transfer, conformational relaxation [52, 53] and intersystem crossing with repulsive πσ* states [54].

Sn states are both autoionizing and relaxing radiationless into S_0. By varying the temporal delay Δt between the UV-Vis and the IR pulses, the dynamics of the internal energy redistribution within the intermediate excited potential hypersurface S_1 is explored. The S_1 population and the fluorescence signal are therefore depleted as a function of Δt. As different species have distinct S_1 hypersurfaces, discriminating signals can be obtained [55, 56].

Figure 10 (left) shows the PPD dynamics of S_1 in Trp as compared to diesel fuel and naphtalene in cyclohexane, one of the most abundant fluorescing PAHs in diesel. While depletion reaches as much as 50% in Trp, diesel fuel and naphtalene appear almost unaffected (within a few percent), at least on these timescales [55, 56].

The depletion factor δ is defined as $\delta = (P_{undepleted} - P_{depleted})/P_{undepleted}$. (where P is the fluorescence power). This remarkable difference allows for efficient discrimination between Trp and organic species, although they exhibit very similar linear excitation/fluorescence spectra.

Two reasons might be invoked to understand this difference: (1) the intermediate state dynamics are predominantly influenced by the NH- and CO- groups of the amino acid backbone and (2) the ionization efficiency is lower for the PAHs. Further electronic structure calculations are required to better understand the process, especially on the higher lying *Sn* potential surfaces.

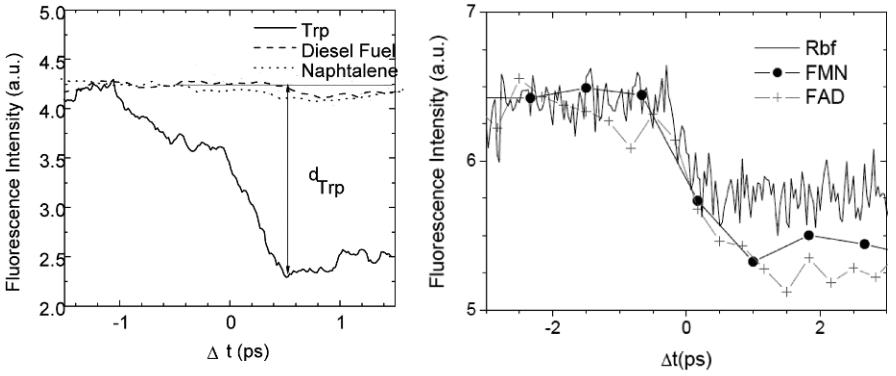

Figure 10. Left: PPD experiment on Trp and PAHs, demonstrating discrimination capability between the amino acid and other aromatic molecules. *Right:* Similar results obtained in flavins [55, 56]

Fluorescence depletion has been obtained as well for RBF, FMN, and FAD (Fig. 10, right). However, the depletion in this case is only about 15% (with a maximum intensity of 5×10^{11} W/cm^2 at 810 nm).

In order to more closely approach the application of detecting and discriminating bioagents from organic particles, we applied PPD spectroscopy to live bacteria (λ_1 = 270 nm and λ_2 = 810 nm), such as *Escherichia coli*, *Enterococcus* and *Bacillus subtilis*. Artifacts due to preparation methods have been discarded by using a variety of samples, i.e. lyophilized cells and spores, suspended either in pure or in biologically buffered water (i.e. typically 10^7–10^9 bacteria per cc). The bacteria containing solutions replaced the Trp or flavin containing solutions of the formerly described experiment. The observed pump-probe depletion results are remarkably robust (Fig. 11), with similar depletion values for all the considered bacteria (results for *Enterococcus*, not shown in the figure, are identical), although the Trp microenvironment within the bacteria proteins is very different from water.

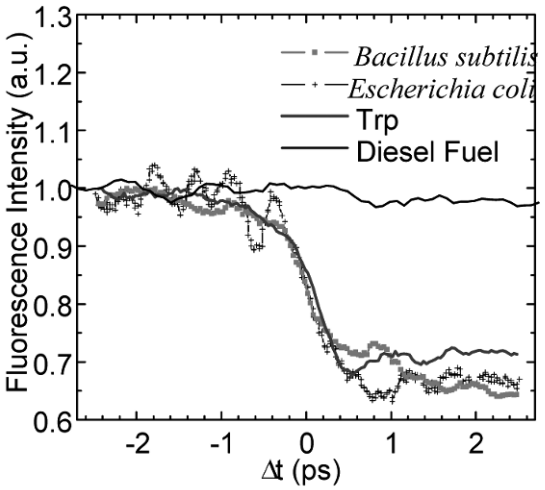

Figure 11. Discrimination between bacteria and diesel fuel using PPD ultrafast spectroscopy [55].

On the other hand the very similar depletion behaviour for all bacteria and Trp also shows the limitations of PPD spectroscopy in the present configuration. Biomolecules can be distinguished from other aromatics but PPD is unable to discriminate two different bacteria in solution.

We finally investigated bacteria embedded in microdroplets, as it usually occurs in nature. Saliva drops (coughing, breathing, speaking, etc.) are indeed the most current infectious vectors.

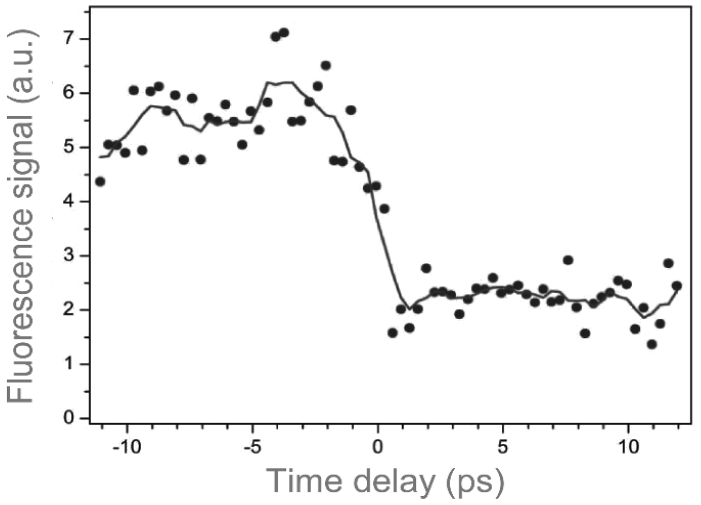

Figure 12. PPD in 20 μm droplets containing about 100 *E. coli* bacteria.

The most impressive result of these experiments is the very high PPD efficiency as compared to depletion ratios in liquids. In particular, we used PPD on 20 μm water droplets containing typically 100 live bacteria (*Escherichia coli*). As shown in Fig. 12, the depletion factor δ is enhanced as compared to bacteria in bulk water: 60% depletion in the microdroplet and 20% in solution ($\lambda_1 = 270$ nm, $\lambda_2 = 810$ nm).

Some tentative explanations could be (1) The spatial overlap between pump and probe pulses might be enhanced by the shape of the droplet, or (2) The spherical shape induces hot spots inside the droplet where intensities are up to 100 times higher than the incident one, but the total hot spot volume is rather small.

4. Coherent Control for Discriminating Almost Identical Biomolecules

The identification or discrimination of molecules and quantum systems that are nearly identical (proteins, bacteria, etc.) is normally an exceedingly difficult task. The conventional means of addressing this common need is through various *static* spectroscopic techniques, which can be especially difficult in complex remote environments. However, recent theoretical work showed that two or more quantum systems, even if they differ only infinitesimally, may be drawn apart to have distinct signatures through tailored control of their *dynamics*. Ultrafast broad bandwidth lasers with adaptive pulse shaping provide a means to implement this theoretical concept through controlled quantum optimal dynamic discrimination (ODD) [36]. In collaboration with the group of H. Rabitz at Princeton University, we demonstrated the capabilities of ODD by discriminating between two almost identical molecules of riboflavin (RBF) and flavin mononucleotide (FMN) in water solution, which have virtually identical linear absorption and fluorescence spectra (see Fig. 13a and b) [57]. The successful implementation of ODD opens up numerous applications including in fluorescence microscopy, protein identification, as well as possible remote discrimination of different bacteria. A key component of ODD is operation with shaped laser pulses, which can nonlinearly interact with the molecules to fully exploit their dynamical capabilities and create discriminating signatures. The similar optical spectra of RBF and FMN arise from the common isoalloxazine ring with the only distinguishing feature being changes at the end of the side chain tail (Fig. 13a).

The present application of ODD utilizes a control field consisting of a shaped ultraviolet (UV) portion at 400 nm and a near infrared (IR) component at 800 nm, which is Fourier transform limited. The unshaped IR pulse follows the shaped UV pulse by a time delay τ , and the structure of the shaped UV pulse is deduced optimally under adaptive control to achieve ODD in the fluorescence signals from RBF and FMN. The primary operation of ODD relies on the shaped UV pulse coherently transferring the ground state population into the flavin S_1 or S_2 excited states with the IR component likely creating further excitation of the molecules to higher lying S_n states. The IR field disrupts the vibronic excitation in S_1 or S_2 created by the UV pulse in order to make a discriminating difference in the fluorescence spectra of RBF and FMN from S_1 recorded in the window 525–535nm after a relaxation period of ~5ns (see Fig. 1c). Fluorescence is therefore depleted, and this fluorescence depletion value is used as measure of the molecular response to the field. The overall mechanism also may take advantage of any beneficial intra- and inter-molecular dynamical processes, and the ODD discrimination can draw on suitable coherent and incoherent aspects of the molecular dynamics.

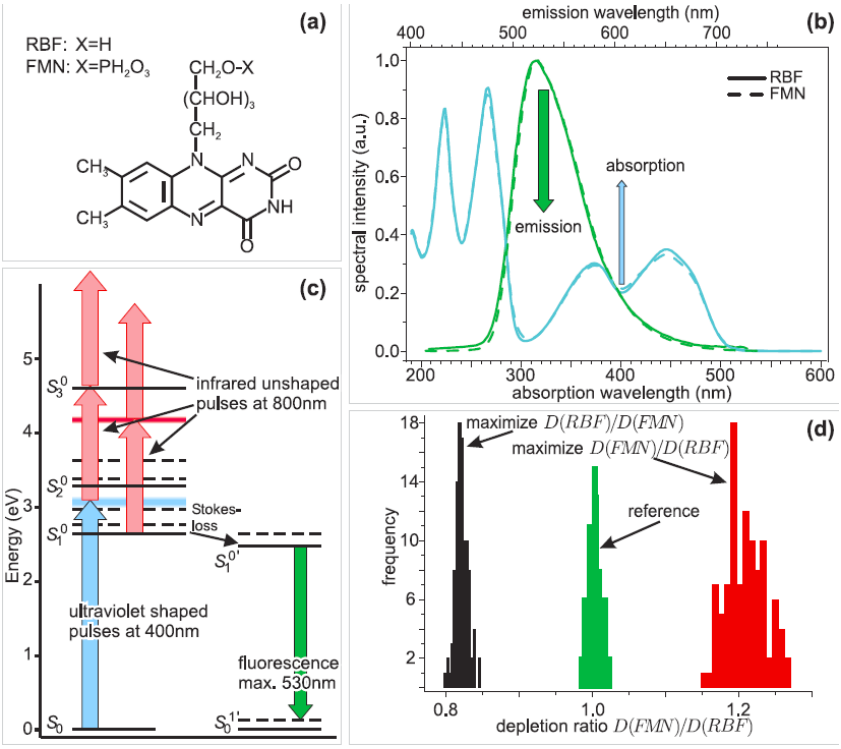

Figure 13. The RBF and FMN molecules in (a) are very similar exhibiting nearly identical linear absorption and emission spectra in (b). The shaped UV control is centred at 400 nm and the flavin fluorescence signals are recorded over a window around 530 nm indicated by the respective arrows. The controlled optimal dynamic discrimination (ODD) of the flavins operates as indicated in (c) with a shaped UV pulse coordinated with a time delayed unshaped IR pulse to draw apart the vibronic dynamics of the flavins in the S_1 or S_2 excited states. The unshaped IR pulse serves to selectively disrupt the subsequent fluorescence signals from the two flavins and the red arrows indicate various possible means of action for the IR pulses. A typical outcome is shown in (d) where the ratio of flavin depletion signals, either *D(RBF)/D(FMN)* or *D(FMN)/D(RBF)*, is maximized. The reference case corresponds to the application of transform limited pulses [57].

In the first series of experiments the RBF and FMN solutions are in separate identical flow cells exposed to the same trial shaped UV pulse and time delayed unshaped IR pulse. An acousto-optic modulator is used to shape the UV pulses. A sequence of experiments $n = 1, 2, \ldots$ was performed to record the relative depletion signal D_n

$$D_n(RBF) = [F_n^{und}(RBF) - F_n^{d}(RBF)] / F_n^{und}(RBF),$$

where $F_n^{und}(RBF)$ is the undepleted fluorescence signal from the RBF cell (i.e., without application of the time delayed IR pulse) and $F_n^{d}(RBF)$ is the depleted signal in the presence of the IR pulse. An analogous expression applies to $D_n(FMN)$ for data collected from the FMN cell exposed to the same laser pulses.

The pulse shaper operated through phase modulation with 50 pixels, each on the range $0–2\pi$, over the bandwidth of the UV pulse (only 3–4 nm). A genetic algorithm of 30 individuals was used to optimize the UV pulse phases with convergence typically occurring in 100–300 generations.

Figure 13d demonstrates the ability of ODD to significantly draw apart the RBF and FMN fluorescence signatures in spite of their nearly identical linear optical spectra in Fig. 13b [57]. For a given time delay τ, a specific optimal UV pulse is determined in the adaptive control experiment. The best discrimination was found for τ ~250–500 fs and the procedure was not able to find significant discrimination for $\tau \geq 1\text{ps}$ indicating a loss of coherence and/or insufficient overlap between the UV and IR pulses.

With a delay time τ typically around 250–500 fs, optimal pulse shapes found in different runs were very complex and showed considerable difference. They however produced exactly the same discrimination ratio when applying them, even weeks after the initial experiment. The underlying mechanisms are currently investigated, in order to identify whether this behaviour is generic or particular to this RBF/FMN system.

The assembled set of optimally discriminating laser pulses and their long-term stable performance permits exploiting ODD as a novel means for detection of nearly identical molecules when they are simultaneously present in a sample. In this work the recorded fluorescence depletion signals F_n^{d} are utilized, as they are proportional to their respective flavin concentrations. Thus, the fluorescence signal $F_n(mix)$ from a mixture of flavins generated with the *n*-th control UV-IR pulse pair is related to its individual counterparts by

$$F_n(mix) = c(RBF)\,F_n^{d}(RBF) + c(FMN)\,F_n^{d}(FMN),$$

where $c(RBF)$ is the fraction of RBF present and $c(RBF)+c(FMN)=1$. The reference signals $F_n^{d}(RBF)$ and $F_n^{d}(FMN)$ are normalized to their respective concentrations deduced in learning the n-th control field, and similarly F_n is normalized to the total sum of the two flavins present. Two distinct ODD laser pulses could successfully determine the fractional content of the two flavins (the constrained relation between the fractions was not used in order to test the capabilities of ODD). Increasing the number of interrogating optimal pulses improves the standard deviation of the extracted component concentration fractions and a typical result using six pulses was $c(RBF)$ =0.35 ± 0.04 and $c(FMN)$ =0.68 ± 0.05 where the exact values were 0.33 and 0.66, respectively [57].

5. Conclusion

Quantum control and femtosecond spectroscopy shine a new light onto the detection and identification of biological systems, such as biochromophores but also highly complex systems like cells or bacteria. These applications are only at their beginning, and there is a reasonable hope for widely spread applications in the future, such as label-free microscopy or discrimination of pathogen from non-pathogen bacteria in air. Major technical improvements required for reaching these goals lie in the spectral range and the spectral bandwidth accessible by future femtosecond coherent sources. For instance the access to the deep UV (230–300 nm) will open up applications to proteins and DNA, which constitute major biological targets. Recent developments showed the way in this respect, with first deep-UV pulse shaping devices [58, 59]. The other aspect, namely broad spectral bandwidth, will provide a better controllability, as more states within the excited potential sheets will be coherently superposed. It is remarkable, that even with a very limited bandwidth (4 nm), ODD was able to draw apart the fluorescence signatures of quasi identical molecules such as RBF and its phosphated counterpart. This might constitute an example of the capability of molecular complexity helping discrimination rather than preventing it. Complexity indeed increases the local density of states, which is favorable in the case of relatively narrowband pumping. However, broadband UV pulses would allow a far more efficient discrimination capability. A novel and very attractive approach for producing UV supercontinuua is filamentation in rare gases, as reported recently [60–65].

Acknowledgements The author gratefully acknowledges his collaborators at the Universities of Geneva and Lyon, in particular F. Courvoisier, L. Guyon, V. Boutou, E. Salmon, J. Yu, G. Mejean, J. Kasparian, A. Rondi, B. Bejot, L. Bonacina, S. Weber, D. Kiselev, and M. Moret, as well as H. Rabitz and his group at Princeton, particularly M. Roth and J. Roslund.

We also acknowledge the support of the Swiss National Science Foundation (contracts No. 2000021-111688 and No 200020-124689), the Swiss SER through the COST P18 and MP0603 projects and the Swiss NCCR Quantum Photonics program.

References

1. D. A. Tannor, R. Kosloff, S. A. Rice, J. Chem. Phys. 85, 5805 (1986)
2. D. A. Tannor, S. A. Rice, J. Chem. Phys. 83, 5013 (1985)
3. R. Judson, H. Rabitz, Phys. Rev. Lett. 68, 1500 (1992)
4. S. Warren, H. Rabitz, M. Daleh, Science 259, 1581 (1993)
5. A. M. Weiner, Rev. Sci. Inst. 71, 1929 (2000)
6. M. Dantus, V. Lozovoy, Chem. Rev 104, 1813–1859 (2004)
7. R. J. Levis, G. Menkir, H. Rabitz, Science 292, 709–713 (2001)
8. L. Bonacina, J. Extermann, A. Rondi, V. Boutou, J. P. Wolf, Phys. Rev. A 76(2), 023408 (2007)
9. T. Brixner, N. H. Damrauer, P. Niklaus, G. Gerber, Nature 414, 57 (2001)
10. T. Brixner, N. H. Damrauer, B. Kiefer, G. Gerber, J. Chem. Phys. 118(8) (2003)

11. J. L. Herek, W. Wohlleben, R. J. Cogdell, D. Zeidler, M. Motzkus, Nature 417, 533 (2002)
12. V. I. Prokhorenko, A. M. Nagy, S. A. Waschuk, L. S. Brown, R. R. Birge, R. J. D. Miller, Science 313, 1257 (2006)
13. C. Ventalon, J. M. Fraser, M. H. Vos, A. Alexandrou, J. L. Martin, M. Joffre, PNAS 101, 13216–13220 (2004)
14. I. Pastirk, J. M. Dela Cruz, K. A. Walowicz, V. V. Lozovoy, M. Dantus, Opt. Express 11, 1695 (2003)
15. Y. L. Pan, J. Hartings, R. G. Pinnick, S. C. Hill, J. Halverson, R. K. Chang, Aerosol Sci. Tech. 37, 627–638 (2003)
16. F. L. Reyes, T. H. Jeys, N. R. Newbury, C. A. Primmerman, G. S. Rowe, A. Sanchez, 3, 240–248 (1999)
17. J. D. Eversole, W. K. Cary, C. S. Scotto, R. Pierson, M. Spence, A. J. Campillo, Field Anal. Chem. Tech. 5, 205–212 (2001)
18. G. A. Luoma, P. P. Cherrier, L. A. Retfalvi, Field Anal. Chem. Tech. 3, 260–273 (1999)
19. Y. L. Pan, K. B. Aptowicz, R. K. Chang, M. Hart, J. D. Eversole, Opt. Lett. 28, 589–591 (2003)
20. P. Kaye, E. Hirst, T. J. Wang. Appl. Opt. 36, 6149–6156 (1997)
21. S. C. Hill, R. P. Pinnick, S. Niles, Y. L. Pan, S. Holler, R. K. Chang, J. Bottiger, B. T. Chen, C. S. Orr, G. Feather, Field Anal. Chem. Tech. 5, 221–229 (1999)
22. Y. L. Pan, P. Cobler, S. Rhodes, A. Potter, T. Chou, S. Holler, R. K. Chang, R. G. Pinnick, J. P. Wolf, Rev. Sci. Inst. 72, 1831–1835 (2001)
23. Y. L. Pan, V. Boutou, J. R. Bottiger, S. Zhang, J. P. Wolf, R. K. Chang, Aero. Sci. Tech. 38, 598–602 (2004)
24. R. G. Pinnick, S. C. Hill, Y. L. Pan, R. K. Chang, Atmos. Environ. 38, 1657–1672 (2004)
25. Y. S. Cheng, E. B. Barr, B. J. Fan, P. J. Hargis, D. J. Rader, T. J. OHern, T. R. Torczynski, G. C. Tisone, B. L. Preppernau, S. A. Young, R. J. Radloff, Aero. Sci. Tech. 31, 409–421 (1999)
26. C. Weitkamp, *LIDAR*, Springer Verlag, New York (2005)
27. J. Kasparian, E. Fréjafon, P. Rambaldi, J. Yu, P. Ritter, P. Viscardi, J. P. Wolf, Atmos. Environ. 32(17), 2957–2967 (1998)
28. M. Beniston, M. Beniston-Rebetez, H. J. Kölsch, P. Rairoux, J. P. Wolf, L. Wöste, J. Geophys. Res. 95 (D7), 13 (1990)
29. L. Stefanutti, F. Castagnoli, M. Del Guasta, M. Morandi, V. M. Sacco, V. Venturi, L. Zuccagnoli, J. Kolenda, H. Kneipp, P. Rairoux, B. Stein, D. Weidauer, J. P. Wolf, Appl. Phys. B 55, 13–17 (1992)
30. B. Stein, M. del Guasta, J. Kolenda, M. Morandi, P. Rairoux, L. Stefanutti, J. P. Wolf, L. Wöste, Geophys. Res. Lett. 21(13), 1311 (1994)
31. M. del Guasta, M. Morandi, L. Stefanutti, B. Stein, J. Kolenda, P. Rairoux, J. P. Wolf, R. Matthey, E. Kyrö, Geophys. Res. Lett. 21(13), 1339 (1994)
32. M. del Guasta, M. Morandi, L. Stefanutti, B. Stein, J. P. Wolf, Appl. Optics 33(24), 5690 (1994)
33. V. Rizi, G. Redaelli, M. Verdecchia, G. Visconti, L. Stefanutti, J. P. Wolf, Geophys. Res. Lett. 21(13), 1435 (1994)
34. E. Fréjafon, J. Kasparian, P. Rambaldi, J. Yu, B. Vezin, J. P. Wolf, Appl. Optics 37(12), 2231–2237 (1998)
35. F. Immler, D. Engelbart, O. Schrems, Atmos. Chem. Phys. Disc. 4, 5831–5854 (2004)
36. B. Li, H. Rabitz, J. P. Wolf, J. Chem. Phys. 122 154103-1-8 (2005)
37. S. C. Hill, V. Boutou, J. Yu, S. Ramstein, J. P. Wolf, Y. Pan, S. Holler, R. K. Chang, Phys. Rev. Lett. 85(1), 54 (2000)
38. V. Boutou, C. Favre, S. C. Hill, Y. Pan, R. K. Chang, J. P. Wolf, App. Phys. B 75, 145–153 (2002)

39. Y. Pan, S. C. Hill, J. P. Wolf, S. Holler, R. K. Chang, J. R. Bottiger, Appl. Optics 41(15), 2994–2999 (2002)
40. C. Favre, V. Boutou, S. C. Hill, W. Zimmer, M. Krenz, H. Lambrecht, J. Yu, R. K. Chang, L. Woeste, J. P. Wolf, Phys. Rev. Lett. 89(3), 035002 (2002)
41. J. Kasparian, M. Rodriguez, G. Méjean, J. Yu, E. Salmon, H. Wille, R. Bourayou, S. Frey, Y. B. Andre, A. Mysyrowicz, R. Sauerbrey, J. P. Wolf, L. Woeste, Science 301(5629), 61–64 (2003)
42. G. Méjean, J. Kasparian, J. Yu, S. Frey, E. Salmon, J. P. Wolf, Appl. Phys. B 78(5), 535–537 (2004)
43. J. Kasparian, V. Boutou, J. P. Wolf, Y. Pan, R. K. Chang, Appl. Phys. B 91, 167–171 (2008)
44. J. P. Wolf, Y. Pan, S. Holler, G. M. Turner, M. C. Beard, R. K. Chang, C. Schmuttenmaer, Phys. Rev. A 64, 023808-1-5 (2001)
45. L. Méès, J. P. Wolf, G. Gouesbet, G. Gréhan, Optics Comm. 208, 371–375 (2002)
46. P. B. Dixon and D. W. Hahn, Anal. Chem. 77, 631 (2005)
47. S. Morel, N. Leone, P. Adam, and J. Amouroux, Appl. Optics 42, 6184 (2003)
48. M. Baudelet, L. Guyon, J. Yu, J. P. Wolf, T. Amodeo, E. Frejafon, and P. Laloi, J. Appl. Phys. 99 (2006)
49. M. Baudelet, J. Yu, M. Bossu, J. Jovelet, J. P. Wolf, T. Amodeo, E. Frejafon, and P. Laloi, Appl. Phys. Lett. 89 (2006)
50. M. Baudelet, L. Guyon, J. Yu, J. P. Wolf, T. Amodeo, E. Frejafon, and P. Laloi, Appl. Phys. Lett. 88 (2006)
51. F. Courvoisier, et al. Faraday Discussions 137, 37 (2008)
52. H. B. Steen, J. Chem. Phys. 61, 3997 (1974)
53. J. T. Vivian and P. R. Callis, Biophys. J. 80, 2093 (2001)
54. Y. Iketaki, T. Watanabe, S. Ishiuchi, M. Sakai, T. Omatsu, K. Yamamoto, M. Fujii, and T. Watanabe, Chem. Phys. Lett. 372, 773 (2003)
55. F. Courvoisier, V. Boutou, L. Guyon, M. Roth, H. Rabitz, and J. P. Wolf, J. Photochem. Photobiol. A-Chem. 180, 300 (2006)
56. F. Courvoisier, V. Boutou, V. Wood, A. Bartelt, M. Roth, H. Rabitz, and J. P. Wolf, Appl. Phys. Lett. 87 (2005)
57. M. Roth, L. Guyon, J. Roslund, V. Boutou, F. Courvoisier, J. P. Wolf, H. Rabitz, Phys. Rev. Lett. 102, 253001 (2009)
58. A. Rondi, J. Extermann, L. Bonacina, S. Weber, J.-P. Wolf, Appl. Phys. B 96 757–761 (2009)
59. S. Weber, M. Barthélemy, B. Chatel, Appl. Phys. B (2009) DOI 10.1007/s00340-009-3745-z
60. G. Méjean, J. Kasparian, J. Yu, E. Salmon, R. Ackermann, J.-P. Wolf, L. Bergé, S. Skupin, Appl. Phys. B 82 341-345 (2006)
61. L. Bergé, S. Skupin, U. Peschel, F. Lederer, G. Méjean, J. Kasparian, J. Yu, S. Frey, E. Salmon, J.-P. Wolf, Phys. Rev. E 71 016602 (2005)
62. A. Couairon, A. Mysyrowicz, Phys. Rep. 441, 47–189 (2007)
63. J. Kasparian, J.-P. Wolf, Opt. Express 16, 466–493 (2007)
64. L. Bergé, S. Skupin, R. Nuter, J. Kasparian, J.-P. Wolf, Rep. Prog. Phys. 70, 1633–1713 (2007)
65. S. L. Chin, S. A. Hosseini, W. Liu, Q. Luo, F. Théberge, N. Aközbek, A. Becker, V. P. Kandidov, O. G. Kosareva, H. Schroeder, Can. J. Phys. 83, 863–905 (2005)

SUBCELLULAR SURGERY AND NANONEUROSURGERY USING FEMTOSECOND LASER PULSES

VALERIA NUZZO[1], IVA MAXWELL[1], SAMUEL CHUNG[1], ERIC MAZUR*[1], ALEXANDER HEISTERKAMP[2]
Harvard University, School of Engineering and Applied Sciences,
[1]*Cambridge, MA 02138, USA*
[2]*Laser Zentrum Hannover, Hollerithallee 8, 30419 Hannover, Germany*

Abstract Femtosecond lasers provide a powerful means to address biological questions. The nonlinearity of the interaction of ultrashort laser pulses with matter opens the door to a wide range of applications. In this review, we discuss the submicrometer precision of femtosecond laser ablation and its application in severing individual cytoskeleton actin fibers and *Caenorhabditis elegans* sensory dendrites without causing collateral damage. Laser severing provides insight into the molecular mechanisms of the viscoelastic recoil of individual stress fibers and the regenerative capability of neuronal fibers, respectively. Additionally, we discuss the poration of cell membranes for delivery of molecular factors by nanoparticle-mediated femtosecond laser field amplification.

1. Introduction

In the last 2 decades, the femtosecond (fs) laser has emerged as an exquisite tool to perform non-invasive, submicrometer-sized surgeries in the bulk of biological matter [1–5] There are certain advantages in using a near-infrared femtosecond laser: it can be strongly confined, as it interacts with the material only at the focal volume; due to the shortness of the pulse, undesired mechanical and thermal effects are reduced; biological samples with a high content of water are transparent at that wavelength. In addition, advances in laser technology [6–8] have made ultrashort pulsed systems more accessible in terms of cost and maintenance, leading to an increased number of settings for research and clinical applications.

Laser-matter interaction in the femtosecond regime is governed by laser-induced-plasma-mediated ablation or laser-induced optical breakdown and results in micromachining of transparent material and disruption of tissues or cellular structures. For simplicity, it is often referred to as femtosecond laser ablation, even though ablation technically describes material removal (such as that associated with nanosecond laser-matter interactions). Below the threshold irradiance for optical breakdown of the material, nonlinear processes, such as multiphoton absorption and second harmonic

* Eric Mazur, Cambridge, MA 02138, USA, e-mail: mazur@physics.harvard.edu

B. Di Bartolo and J. Collins (eds.), *Biophotonics: Spectroscopy, Imaging, Sensing, and Manipulation*, 203
DOI 10.1007/978-90-481-9977-8_9, © Springer Science+Business Media B.V. 2011

generation (SHG), can occur, and these have mostly been exploited for imaging and understanding tissue structures and functions [9–14].

Several review articles discuss plasma-mediated laser ablation and its applications [15–19]. The underlying mechanism is nonlinear absorption in the target, which is achieved when a material-specific radiant exposure is exceeded. The threshold irradiance can be as high as 10^{15} W/cm^2, which generates an electric field comparable to that of the atomic Coulomb electric field. The absorption of infrared irradiation in a material typically transparent at that wavelength is nonlinear because there are no allowed electronic transitions to permit single near-infrared photon absorption. Two competing mechanisms are believed to contribute to the generation of seed electrons: multiphoton ionization, corresponding to a simultaneous absorption of several photons by an electron to be promoted to the conduction band, and tunnel ionization, which occurs when the potential barrier is sufficiently decreased to allow an electron to escape from the atom [15, 18, 20]. The nonlinearly excited electrons undergo further phonon-mediated linear absorption until they acquire enough kinetic energy to excite other bound electrons — a process called avalanche ionization. When the density of excited electrons reaches about 10^{21} cm^{-3}, the electrons behave as a plasma whose natural frequency is resonant with the laser — leading to reflection and absorption of the remaining pulse energy [21, 22]. For a transparent biological specimen, this process causes chemical bond breaking and cutting [18].

Understanding the different time scales involved in converting the laser pulse energy to structural change provides insight into why ultrashort laser pulses are well suited for cutting applications. For pulses of subpicosecond duration, the time scale over which the electrons are excited is smaller than the electron-phonon scattering time (about 1 ps). Thus, a femtosecond laser pulse ends before the electrons thermally excite any ions. Heat diffusion outside the focal area is minimized, improving the submicrometer localization of the energy deposition [23, 24].

Our group has used femtosecond lasers for addressing a range of biological questions. In this paper we review (1) the mechanical properties of cell cytoskeleton; [4, 25–27] (2) cell transfection [28] by field amplification; and (3) the neuronal origins of behavior in Caenorhabditis elegans. [5, 29]

2. Experimental Methods

Laser nanoscissor set-up. Figure 1 shows the femtosecond laser ablation setup, which consists of a femtosecond laser composed of a mode-locked oscillator (pulse width 100-fs, repetition rate 80 MHz, central wavelength 790 nm), followed by a chirped pulse amplifier. The output pulses are delivered at a repetition rate of 5 to 10 kHz and have energy up to 12 μJ. The pulses are too energetic for cellular surgery and are attenuated to the nanojoule range by neutral density filters inserted into the beam path. The laser beam is focused on the sample by singlet lens with a 140-mm focal length. Alternatively, the beam is coupled into a microscope and tightly focused by a 1.4-NA oil-immersion objective. The sample is mounted on a 3-D positioning stage. Light from a mercury-arc lamp illuminates the sample and a CCD camera captures the emitted fluorescence.

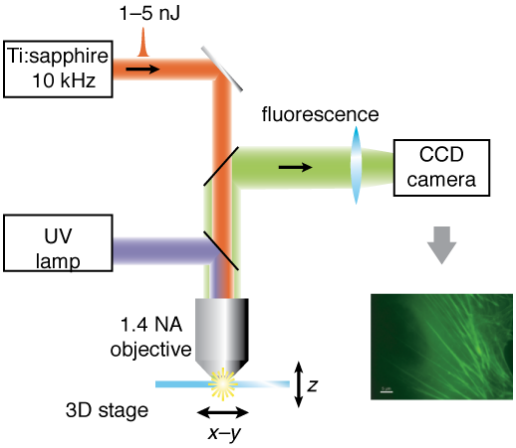

Figure 1. Schematic diagram of experimental setup for nanosurgery.

Cell preparation. Bovine capillary endothelial cells were maintained at 37°C in 10% CO_2 on tissue culture dishes in low-glucose Dulbecco's modified Eagle's medium (DMEM; Gibco-BRL). The cells were supplemented with 10% fetal calf serum (Hyclone), 10-mM HEPES (JRH-Biosciences), and glutamine (0.292 mg/ml)/penicillin (100 U/ml)/ streptomycin (100 g/ml). For living experiments, cells were transfected for 48 h with an adenoviral vector encoding either enhanced yellow fluorescent protein (YFP)-tagged G-actin or green fluorescent protein (YFP)-tagged G-tubulin. For some of the experiments, the cells were fixed in 4% formaldehyde (electron microscopy grade), permeabilized in 0.1% Triton X-100, blocked in 1% bovine serum albumin, and stained for either actin (Alexa Fluor488 phalloidin, Molecular Probes) or nuclear DNA (Hoechst 33348, Molecular Probes). Afterwards the cells were stored and treated in phosphate buffered saline (PBS). Following laser treatment, the cells were fixed in 2.5% glutaraldehyde in 0.1-M cacodylate buffer, then washed and stored in this buffer at 4°C until processing. Prior to TEM imaging with a Philips CM-10 microscope, cells were fixed in 1% osmium tetroxide in 0.1-M cacodylate buffer, washed in the same buffer, dehydrated in graded ethanol solutions, critical point dried, and carbon coated.

Cells used in the perforation experiments were cultivated in glass-bottom-dishes (MatTek). Besides a canine cell line (ZMTH3), which was cultivated in RPMI-1640 medium, we used primary cells from 12 weeks old albino mice (DRG neurons) and different human stem cells (embryonic and iPS cells).

For nanoparticle mediated cell perforation, spherical gold particles from 80 to 250 nm in diameter (Kisker GmbH) were added to the surrounding cell medium and incubated for several hours. During laser treatment Lucifer yellow (LY) was added to the medium to label successfully perforated cells. After laser exposure the cells were washed with PBS. The viability of the cells was evaluated by adding propidium iodide to the medium. To prove successful transfection a non-recombinant pEGFP-C1 vector plasmid was added to the medium at a concentration of 50 µg/ml. The non-recombinant vector labels the whole cell in case of transfection.

C. elegans preparation. During the early stages of larval development, imaging and ablation can occur anywhere in the worm; however, increasing turbidity and pigmentation limit the imaging depth in the body of the worm to about 50 μm by the young adult stage. Because the adult worm diameter is about 100 μm, much of the worm is beyond the imaging depth. However, imaging and ablation is still possible on any target within adult worms by rotating worms so the target is closest to the coverslip. Unfortunately, when a coverslip is placed onto adult worms on a flat agarose pad the protruding vulva is pushed to the side, consistently forcing worms into a lateral imaging orientation.

We developed a method to hold worms in any flat-lying orientation. We polymerize polydimethylsiloxane (PDMS) against the grooves of a 12-in. long-playing (LP) vinyl record to create a negative replica mold. Agarose fabricated against the ridges of the PDMS mold has channels, which hold worms in a fixed orientation even when the coverslip is added.

3. Cytoskeleton Surgery

Cells actively control their shape through diverse networks of cytoskeletal stress fibers, which transmit forces to the extracellular environment and within the cell. An understanding of the molecular and biophysical mechanisms behind the transmission of these forces provides insight into cell motility, differentiation, and apoptosis [25]. Femtosecond laser ablation can sever fiber bundles without disrupting the rest of the cell, allowing *in situ* perturbation and simultaneous monitoring of cytoskeleton dynamics.

A proof-of-principle set of experiments determined the optimal laser parameters and submicrometer surgical precision of femtosecond laser ablation of cytoskeletal stress fibers [4–26]. Actin fibers within bovine endothelial cells stained with a green fluorescent F-actin binding dye (Alexa Fluor 488-phalloidin) were irradiated at different pulse energies. Figure 2 shows the dependence of fluorescence intensity on pulse energy. At 1.8 nJ the effect of irradiation is barely visible in the fluorescence image. Increasing the pulse energy to 2.2 nJ produces a clear dip in fluorescence with a width of 240 nm at FWHM. At higher energy the FWHM-width of the dip in fluorescence scales with pulse energy, from 360 nm at 2.8 nJ, to 500 nm at 3.5 nJ and 600 nm at 4.4 nJ. A comparison of fluorescence and transmission electron microscopy (TEM) images of a nucleus irradiated at various energies [26] reveals that, at low pulse energies, the loss of fluorescence is due to photobleaching as no material removal is observed. Therefore, three regimes of irradiation can be identified: no damage visible in either image, photobleaching without material loss (fluorescence decreases at point of interaction with the laser), and removal of material at higher energy (TEM images also show material removal).

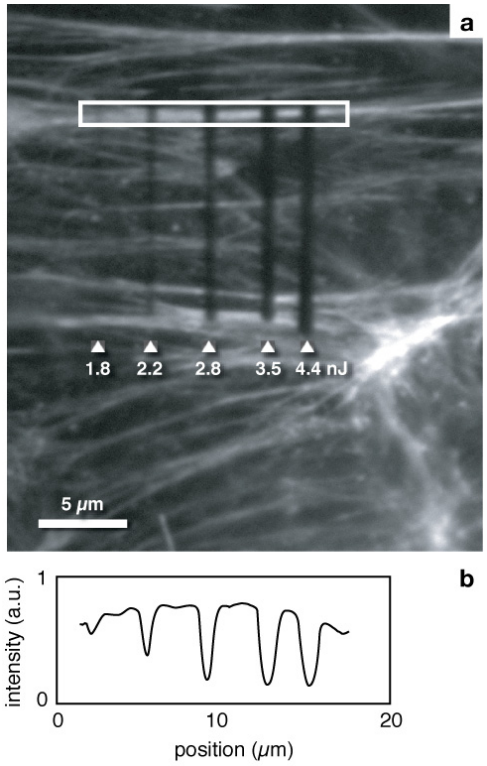

Figure 2. (a) Cuts through fluorescently-labeled actin fibers in a fixed endothelial cell obtained by irradiation with femtosecond laser pulses of energies between 1.8 and 4.4 nJ. (b) Fluorescence intensity profile along the actin bundle outlined in the image.

Pulses corresponding to the threshold energy for plasma-mediated ablation were subsequently applied to the central region of a single stress fiber within living endothelial cells cultured on fibronectin-coated glass coverslips. The severed ends immediately (<1 s) retract and progressively pull farther apart over a time-period of approximately 15 s, reflecting a release of isometric tension (Fig. 3). The newly severed ends also "fray" while the cut widens, as expected for a stretched elastic element that is suddenly unloaded [30]

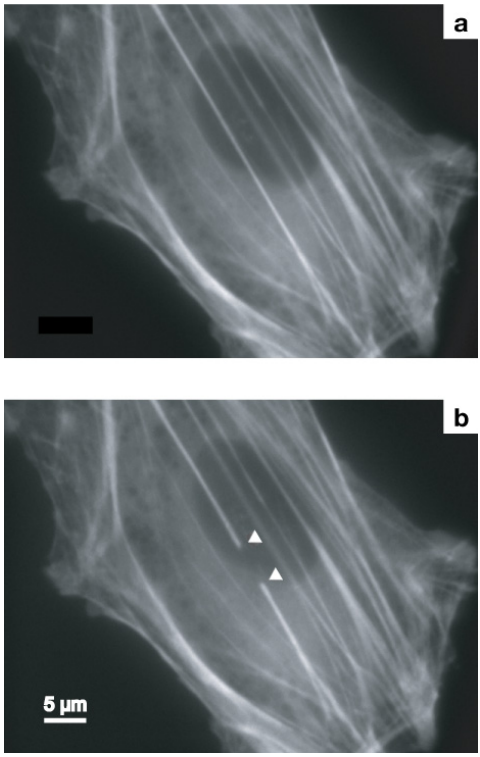

Figure 3. (a) Stress fiber bundle in an endothelial cell expressing EYFP-actin. (b) Retraction of a severed stress fiber.

Because previous efforts to sever cytoskeletal elements with picosecond laser pulses produced rapid filament depolymerization [31], we needed to ensure that the shortening of the severed ends is due to physical retraction, rather than progressive material loss. To distinguish between these possibilities, we severed stress fiber bundles immediately adjacent to bifurcation points. If the stress fibers physically retract rather than depolymerize on the time scale of the experiment, then the branched end should retract as an intact structure. Conversely, in the case of rapid depolymerization, the branch point should be lost as the severed ends depolymerize (Fig. 4a). When we irradiated stress fiber bundles at these locations, we observed that the branched end retracted and deformed as an intact structure and remained so for more than 3 min following incision (Fig. 4b). This observation confirms that stress fiber irradiation does not induce substantial depolymerization on the time scale of this experiment.

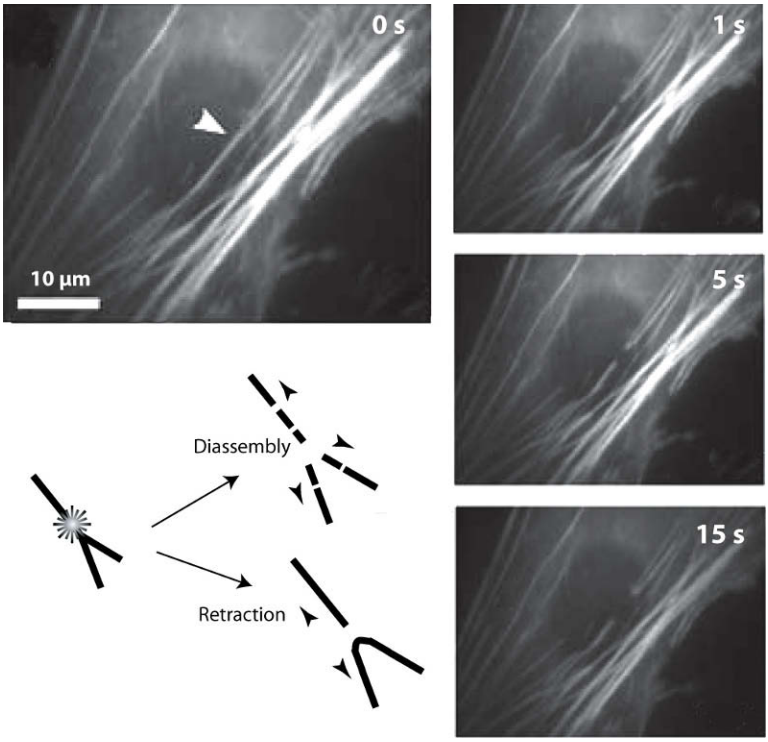

Figure 4. Stress fibers retract rather than disassemble following incision. Schematic of predicted observations in the case of stress fiber retraction versus disassembly in response to laser incision. In the case of actin depolymerization or bundle disassembly, both severed ends should fall apart, including the branch point. In the case of physical retraction, the branched portion of the bifurcation should remain whole following irradiation and physically retract as an intact structure. The fluorescence images show the result of laser irradiation of a stress fiber bundle near a bifurcation and subsequent retraction of an intact stress fiber bundle fork in a living cell. The white arrowhead shows the point of laser irradiation.

From the measurement of the retraction as a function of time, it is possible to model the dynamics of the fiber as that of a viscoelastic rope. The length of the gap between the severed ends grows at a rate described by a time constant and it asymptotically approaches the resting (unstressed) severed ends. Figure 5 shows a plot of the distance a single end moves from the cutting site versus time. The solid line is a fit, based on the predicted retraction of a viscoleastic cable, which can be represented as a spring and a dashpot in parallel, in essence modeling the stress relaxation of the biopolymer [32, 33].

$$L = L_o(1 - e^{-t/\tau}) + D_a \tag{1}$$

In this model, L is the distance retracted (one-half the distance between the severed ends), L_o is the asymptotic value of that distance, t is time following severing, t is a characteristic time constant equal to the ratio of the Young's modulus of the material to its damping coefficient, and D_a is the length of the stress fiber destroyed by the laser irradiation. The damping coefficient arises from a combination of the intrinsic viscoelasticity of the stress fiber and that of the surrounding medium.

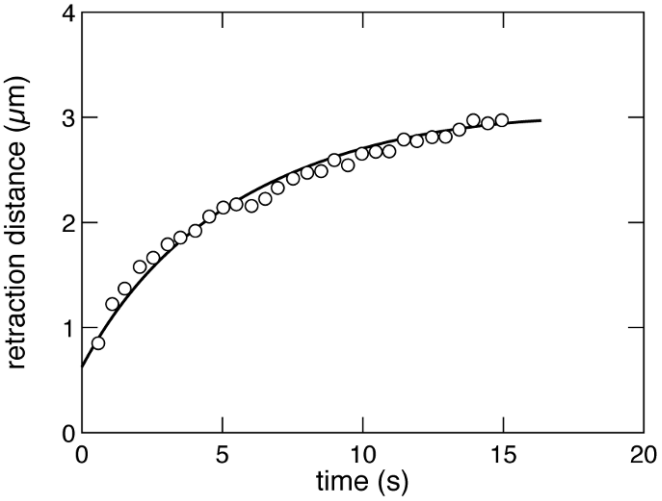

Figure 5. Fiber retraction, defined as half the distance between the severed ends, as function of the time after laser severing.

The viscoelastic behavior of actin fibers has been widely assumed but never experimentally demonstrated in living cells. Previous *in vitro* studies with single actin filaments [34–37], reconstituted actin gels [38], and isolated myofibrils [39, 40] have produced equivocal descriptions of stress fiber mechanics. For example, stress fibers have been widely described as either tensile [41] elastic [42], or viscoelastic [43]. This study represents the first unequivocal demonstration that stress fiber bundles retract viscoelastically within the complex cytoplasm of living cells.

4. Optical Perforation of Cells

The efficient introduction of genetic vectors into mammalian cells is the first step toward studying and optimizing the modification of gene expression. Although a variety of tools for transfection exist for the molecular biologist, these techniques often hold significant drawbacks. Lipid-based DNA-complexing agents need to be tailored to

specific cell types and have only moderate efficiencies. Viral-mediated gene transfers, while efficient, tend to be cell-specific, integrate irreversibly into a host's genome, and are often countered by the host's immune response. On the other hand, electroporation is very general but suffers from cell mortality. A recent technique, optotransfection, employs lasers to porate cell membranes [44] and has shown promise for being highly efficient and non-toxic, but the process is slow given that each cell must be porated individually. To achieve high throughput, a new method has been recently introduced for facilitating the diffusion of genetic vectors into a large number of cells by means of localized, transient cell membrane poration [45] Ultrafast laser excitation of plasmons on nanoparticles diluted in cell medium can generate submicrometer points of high local electric field enhancement on the cell membrane. In our experiments, after incubation of gold nanoparticles of different sizes (80, 150, 200 and 250 nm) for 3 h, cells were irradiated with femtosecond laser pulses while scanning an area of 3 mm^2, as shown in Fig. 6. A membrane-impermeable fluorescent dye, Lucifer yellow (LY), was used as an indicator for successfully perforated cells. The viability of the cells was checked with propidium iodide.

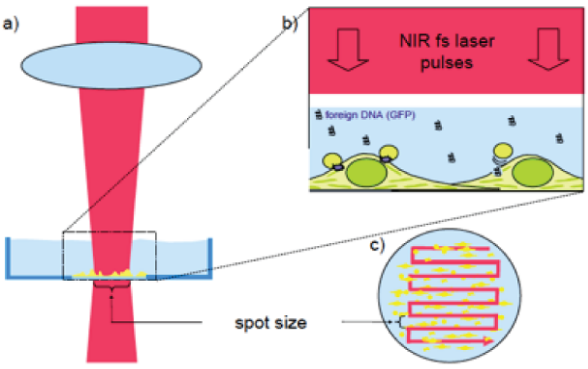

Figure 6. (a) Experimental setup for femtosecond optoporation: using a 140-mm lens, the laser beam is focused onto the bottom of a petri dish. By moving the sample relatively to the laser beam, a field of 3 mm^2 is treated. (b) Gold nanoparticles are located close to the cell membrane and irradiated by femtosecond laser pulses. Due to plasmon resonances and subsequent effects the cell membrane is disrupted. (c) Top view, showing scanning path.

Perforation experiments were performed with different cell lines and different sizes of gold nanoparticles. The results show a successful perforation for all sizes between 80 and 250 nm (Fig. 7). The highest perforation rate of nearly 80% was achieved using ZMTH3 cells, 200-nm GNP with a cell viability of 83.3%, meaning nearly every vital cell was perforated (at a nanoparticle concentration of 11.33 μg/ml, a laser fluence of 0.1 J/cm^2 and a scanning velocity of 15 mm/s).

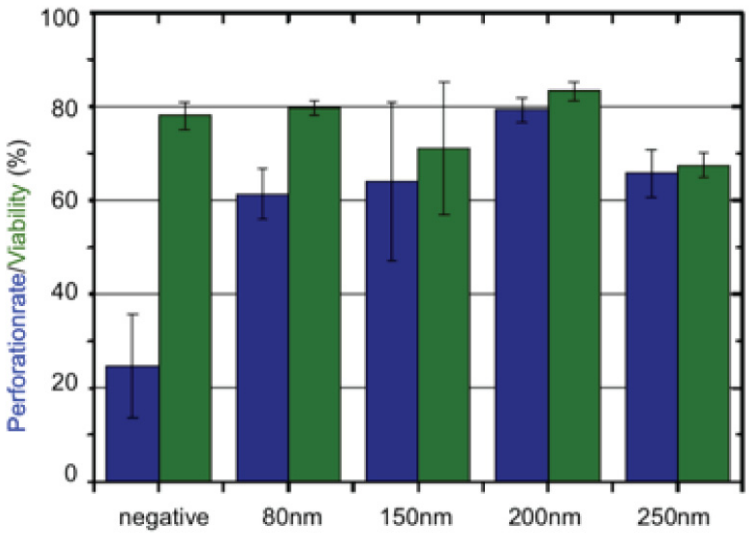

Figure 7. Dependence of viability and optoporation efficiency of ZMTH3 cells on nanoparticle size (11.33-µg/ml particle concentration, laser fluence of 0.1 J/cm^2 and scanning velocity of 15 mm/s.)

Using nanoparticles of 200-nm size and the parameters given above, we performed transfection experiments with pEGFP-C1 vectors. These plasmid vectors have a size of 4.7 kbp, which is much larger than the LY molecules, which readily diffuses into the cells. Nevertheless, pEGFP-C1 vector plasmid diffuses into the cells after laser treatment, although with a lower efficiency than the LY molecule. Cells were imaged by fluorescent microscopy 48 h after laser treatment. In case of successful GFP expression the whole cell becomes fluorescent, proving successful transfection (Fig. 8). These preliminary experiments show that nanoparticles-mediated cell transfection is a promising alternative to current techniques, in terms of efficiency, cell viability and throughput. However, further investigation is necessary to verify the long-term low toxicity of the method.

5. *C. elegans* Surgery

Severing neuronal fibers with femtosecond laser pulses has the advantage of eliminating specific neuronal connections along with its behavioral contribution, while sparing the rest of the neuron and its function. After neuron cell body irradiation, plasma membrane typically remains intact, confirming localization of damage, and the cell loses fluorescence and function over a time period of 24 h. Irradiating the cell body with 10-nJ pulses eliminates cell function within a few hours of surgery but increases the chance of collateral damage. In particular, pulse energies above 10 nJ lead to cell rupture and puncture of the cuticle if the cell is superficial.

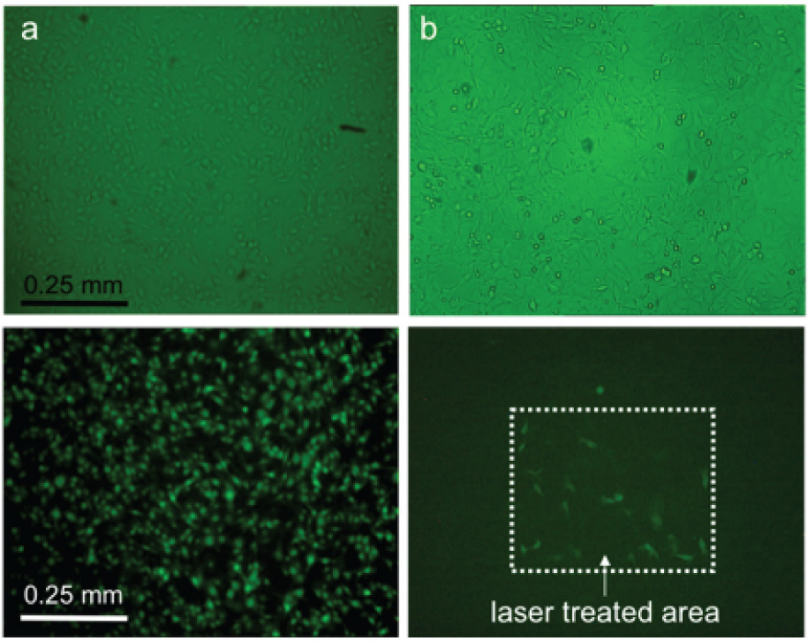

Figure 8. (a) Laser optoporation and (b) transfection of ZMTH3 cells with DNA. The higher delivery efficiency for small molecules can be seen clearly from the fluorescence images (lower images). In (a) the whole area was scanned, whereas in (b) only the outlined square was scanned.

One interesting recent discovery in *C. elegans* is the regrowth of neuronal fibers after femtosecond laser ablation [44]. In principle, regrowth can restore neuronal functions previously eliminated by surgery. If the regrown fiber is functional, the post-surgery assay will not detect a behavioral deficit and therefore not identify the contribution of the fiber. Although many neuronal fibers regrow after ablation, thus far, only one publication in *C. elegans* has presented evidence of functional regeneration [44]. In agreement with several publications on *C. elegans* regeneration [48, 49], we find that neurites regrow to varying degrees depending on neuronal type, fiber type (*i.e.*, dendrite or axon), age of the worm, and ablation location.

After hatching from the egg, worms develop through four larval stages (L1–L4) before molting to the adult stage. Imaging and behavioral assays confirm that amphid dendrites do not regenerate after severing during the L1, dauer, L4, or adult life stages [29]. Figure 9 shows amphid dendrite cuts made in L1 (top) and L4 (bottom) persisting into the adult life stage. In contrast, amphid axons regenerate after severing in the L1, L2, and L4, but not the dauer or the adult stage [50]. The morphology of the regrown axon is significantly different from that of the original axon. Amphid axons typically run ventrally from the cell body to the nerve ring (thick red line) and then proceed anterodorsally up the ring (see Fig. 9b, top). New axons can grow anterodorsally from the cell body to the nerve ring and then reverse to proceed down the ring posteroventrally (see Fig. 9b, middle). New axons can also sprout from a section of the dendrite close to the ring and follow the ring posteroventrally (see Fig. 9b, bottom).

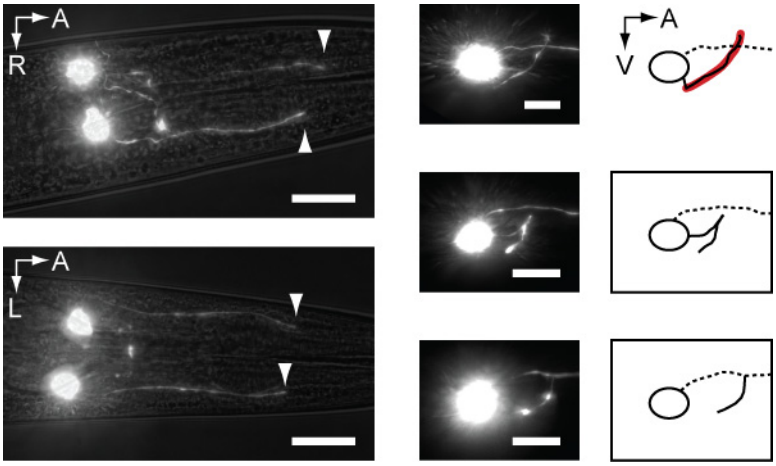

Figure 9. Regeneration of amphid fibers. Surgery locations marked by arrowheads. Corner arrows show directions (ventral, right, left, anterior) in images. (a) Amphid dendrites do not regrow after surgery in L1 (top) or L4 (bottom). Images taken in adult stage. Maximum projection of GFP fluorescence *z*-stack overlaid with bright field image. Scale bars are 20 μm. (b) Amphid axons regrow after surgery in L1. Line drawings show dendrite (dotted line), axon (solid line), and nerve ring (red), which appears flat because it is viewed along edge. Top: normal axon in control worm runs ventrally to ring and then anterodorsally up ring. Middle: regrown axon extends from cell body to nerve ring, turns, and then follows ring posteroventrally. Original axon cut near cell body and not visible. Bottom: regrown axon sprouts from dendrite and follows ring posteroventrally. Images taken 16 h after surgery. Maximum projection of GFP fluorescence *z*-stack. Scale bars are 10 μm.

Motor axons demonstrate the most regeneration capability and diversity; they even regenerate in the adult stage [49, 50]. The HSN motor neuron, which controls egg laying, is an instructive example. The line drawings in Fig. 9 show lateral and dorsal-ventral views of the left and right HSNs. The neuron sends an axon ventrally to synapse with muscles that open the vulva for egg laying [51]. The axon continues anteriorly along the ventral nerve cord (VNC) to the nerve ring (thick red line), where it synapses to other neurons that increase the worm's locomotion velocity prior to egg laying [52]. Cutting the axon eliminates the neuron's contribution to different behaviors depending on the location of the cut. The location of the cut also determines whether the HSN regrows a new axon from the cell body or from the severed end. As shown in the fluorescence image in Fig. 10a, if the original axon is severed proximal to the vulva (surgery at arrowhead), the cell body extends a new axon, which generally does not follow the path of the original axon (dotted line). In fact, some clearly non-functional axons improperly extend dorsally or posteriorly. If the original axon is severed distal to the vulva within the VNC, both the proximal section and the distal section can sprout new axons (see fluorescence image in Fig. 10b), but ablating the distal section into smaller segments prevents it from sprouting.

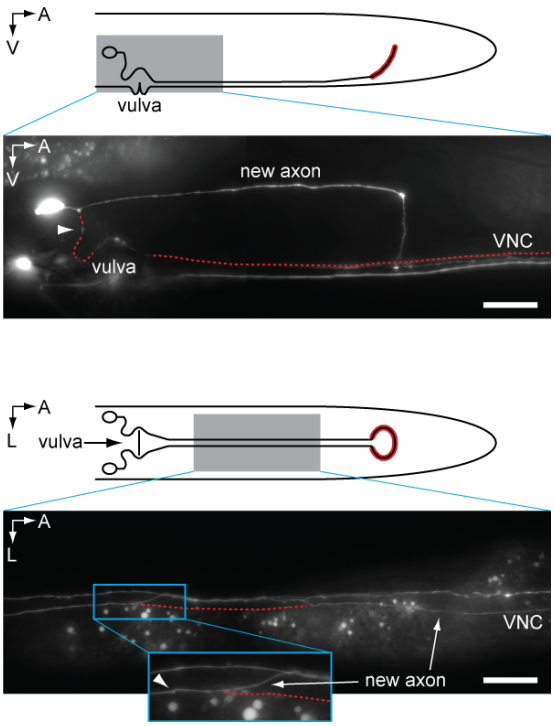

Figure 10. HSN motor axon regenerates after surgery in young adult stage. Surgery locations marked by arrowheads. Decayed original axon marked with white dotted line in fluorescence images. Corner arrows show directions (ventral, left, anterior) in images. Scale bars are 20 μm. (a) Line drawing: lateral view of HSN neuron. Fluorescence image: after severing axon proximal to vulva, new axon extends anteriorly from cell body, turns ventrally, and then reaches the VNC. Image taken 42 h after surgery. (b) Line drawing: dorsal-ventral view of HSN neuron. Fluorescence image: after severing axon distal to vulva, new axon sprouts from severed tip (see inset) and travels along VNC. Image taken 19 h after surgery.

The submicrometer precision of femtosecond laser ablation in the bulk and the relatively simple and invariant neuronal circuit of *C. elegans* made it possible to investigate the neuronal origins of behavior at a subcellular level.

6. Conclusion

The femtosecond laser is a powerful tool for performing submicrometer ablation of biological samples without causing any collateral damage. We reviewed two applications of this technique: severing individual cytoskeleton actin fibers and *Caenorhabditis elegans* sensory dendrites. These experiments provide insight into the molecular mechanisms of the viscoelastic recoil of individual stress fibers and the regenerative capability of neuronal fibers, respectively. We also present data on the poration of cell membranes for delivery of molecular factors by nanoparticle-mediated femtosecond laser field amplification.

Acknowledgments The work reviewed in this paper was carried out by several people. The contributions of each of these people to the experiments can be found in the references cited. V.N. wrote the first draft of this review; A.H. contributed the section on optical perforation of cells. All authors subsequently took part in the revision process and approved the final copy of the manuscript. Paul Peng, Jonathan Bradley, and Yu-Ting Lin provided feedback on the manuscript throughout its development. The research described in this review was supported by the National Science Foundation under contracts DMR-0820484, PHY-0555583 and CBET-0854288 and the DFG through the cluster REBIRTH (work of A.H.)

References

1. Konig, K., Riemann, I., Fischer, P. and Halbhuber, K.-J. (1999) Intracellular nanosurgery with near infrared femtosecond laser pulses. *Cell. Mol. Biol.* **45**, 195–201.
2. Juhasz, T., Loesel, F. H., Horvath, C., Kurtz, R. M. and Mourou G. (1999) Corneal refractive surgery with femtosecond lasers, *IEEE J. Sel. Top. Quant. Electron.* 5, 902–910.
3. Watanabe, W., Arakawa, N., Matsunaga, S., Higashi, T., Fukui, K., Isobe, K. and Itoh, K. (2004) Femtosecond laser disruption of subcellular organelles in a living cell. *Optics Express* **12**, 4203–4213.
4. Shen, N., Datta, D., Schaffer, C. B., LeDuc, P., Ingber, D. E. and Mazur E. (2005) Ablation of cytoskeletal filaments and mitochondria in live cells using a femtosecond laser nanoscissor. *Mech Chem Biosyst* **2**, 17.
5. Chung, S. H. and Mazur E. (2009) Femtosecond laser ablation of neurons in C. elegans for behavioral studies. *Appl. Phys. A* **96**, 335.
6. Strickland, D. and Mourou, G. (1985) Compression of amplified chirped optical pulses, *Opt. Commun.* **55**, 447–49.
7. Moulton, P. F. (1986) Spectroscopic and laser characteristics of Ti:Al2O3, *J. Opt. Soc. Am. B* **3**, 125–33.
8. Kopf, D., Kartner, F. X., Keller, U. and Weingarten, K. J. (1995) Diode-pumped mode-locked Nd:glass lasers with an antiresonant Fabry-Perot saturable absorber, *Opt. Lett.* **20**, 1169–71.
9. Denk, W., Strickler, J.H. and Webb, W.W. (1990) Two-photon laser scanning fluorescence microscopy, *Science* **248**, 73–76.
10. Zoumi, A., Yeh, A. T. and Tromberg, B.J. (2002) Imaging cells and extracellular matrix in vivo by using second-harmonic generation and two-photon excited fluorescence, *PNAS* **99**, 11014–11019.
11. Campagnola, P.J. and Loew L.M. (2003) Second-harmonic imaging microscopy for visualizing biomolecular arrays in cells, tissues and organisms. *Nat Biotechnol.* **21**, 1356–1360.
12. Cox, G., Kable, E., Jones, A., Fraser, I.K., Manconi, F. and Gorrell, M.D. (2003) Three-dimensional imaging of collagen using second harmonic generation, *Journal of Structural Biology* **141**, 53–62.
13. Nuzzo, V., Plamann, K., Savoldelli, M., Merano, M., Donate, D., Albert, O., Gardeazabal Rodriguez, P.F., Mourou, G. and Legeais, J.M. (2007) In situ monitoring of second-harmonic generation in human corneas to compensate for femtosecond laser pulse attenuation in keratoplasty, *J. Biomed. Opt.* **12**, 064032.

14. Strupler, M., Pena, A.M., Hernest, M., Tharaux, P.L., Martin, J.L., Beaurepaire, E. and Schanne-Klein, M.C. (2007) Second harmonic imaging and scoring of collagen in fibrotic tissues, *Opt. Expr.* **145**, 4054–4065.
15. Schaffer, C.B., Brodeur, A. and Mazur, E. (2001) Laser-induced breakdown and damage in bulk transparent materials induced by tightly-focused femtosecond laser pulses, *Meas. Sci. Technol.* **12**, 1784–1794.
16. Vogel A. and Venugopalan V. (2003) Mechanisms of pulsed laser ablation of biological tissues, *Chem. Rev.* **103**, 577–644.
17. Boyd, R.W. (2003) *Nonlinear optics*, 2nd ed. Academic, Amsterdam.
18. Vogel, A., Noack, J., Hüttman G. and Paltauf G. (2005) Mechanisms of femtosecond laser nanosurgery of cells and tissues, *Appl. Phys. B* **81**, 1015–1047.
19. Gattass, R.F. and Mazur E. (2008) Femtosecond laser micromachining in transparent materials, *Nat. Phot.* **2**, 219–225.
20. Keldysh, L.V. (1965) Ionization in field of a strong electromagnetic wave, *Sov. Phys. JETP* **20**, 1307–1314.
21. Stuart, B.C., Feit, M.D., Herman, S., Rubenchik, A.M., Shore, B.W. and Perry, M.D. (1996) Nanosecond-to-femtosecond laser-induced breakdown in dielectrics, *Phys. Rev. B* **53**, 1749–1761.
22. Bloembergen, N. (1974) Laser-induced electric breakdown in solids. *IEEE J. Sel. Top. Quant. Electron.* **QE10**, 375–386.
23. Liu, X., Du, D. and Mourou, G. (1997) Laser ablation and micromachining with ultrashort laser pulses. *IEEE J. Sel. Top. Quant. Electron.* **33**, 1706–1716.
24. Loesel, F.H., Niemz, M.H., Bille, J.F. and Juhasz T. (1996) Laser-induced optical breakdown on hard and soft tissues and its dependence on the pulse duration: Experiment and model *IEEE J. Quant. Electron.* **32**, 1717–1722.
25. Kumar, S., Maxwell, I. Z., Heisterkamp, A., Polte, T. R., Lele, T. P., Salanga, M., Mazur, E. and Ingber, D. E. (2006) Viscoelastic retraction of single living stress fibers and its impact on cell shape, cytoskeletal organization, and extracellular matrix mechanics. *Biophys. J.* **90**, 3762–3773.
26. Heisterkamp, A., Maxwell, I. Z., Mazur, E., Underwood, J. M., Nickerson, J. A. Kumar, S. and Ingber, D. E. (2005) Pulse energy dependence of subcellular dissection by femtosecond laser pulses. *Opt. Expr.* **13**, 3690–3696.
27. Maxwell, I., Chung, S. and Mazur E. (2005) Nanoprocessing of subcellular targets using femtosecond laser pulses *Med. Laser Appl*. **20**, 193–200.
28. Baumgart J., Bintig, W., Ngezahayo, A., Willenbrock, S., Murua Escobar, H., Ertmer, W., Lubatschowski, H. and Heisterkamp, A., (2008), *Opt. Express* **16**, 3021–3031.
29. Chung, S.H., Clark, D.A., Gabel, C.V., Mazur, E. and Samuel A.D. (2006) The role of the AFD neuron in C. elegans thermotaxis analyzed using femtosecond laser ablation. *BMC Neurosci*. **7**, 30.
30. Landau, L.D. and Lifshitz, E.M. (1986) *Theory of elasticity*. Pergammon, Oxford. 187 pp.
31. Botvinick, E.L., Venugopalan, V., Shah, J.V., Liaw, L.H. and Berns, M.W. (2004) Controlled ablation of microtubules using a picosecond laser. *Biophys. J.* **87**, 4203–4212.
32. Osswald, T.A. and Menges, G. (1995) *Materials science of polymers for engineers*. Hanser/Gardner, Munich. 475 pp.
33. Canadas, P., Laurent, V.M., Oddou, C., Isabey, D. and Wendling, S. (2002) A cellular tensegrity model to analyse the structural viscoelasticity of the cytoskeleton. *J. Theor. Biol.* **218**,155–173.
34. Finer, J.T., Simmons, R.M. and Spudich, J.A. (1994) Single Myosin Molecule Mechanics - Piconewton Forces and Nanometer Steps. *Nature*. **368**, 113–119.
35. Kojima, H., Ishijima, A. and Yanagida, T. (1994) Direct Measurement of Stiffness of Single Actin-Filaments with and without Tropomyosin by in-Vitro Nanomanipulation. *Proc. Natl. Acad. Sci.* **91**, 12962–12966.

36. Ishii, Y., Ishijima, A. and Yanagida, T. (2001) Single molecule nanomanipulation of biomolecules. *Trends Biotech.* **19**, 211–216.
37. Liu, X.M. and Pollack, G.H. (2002) Mechanics of F-actin characterized with microfabricated cantilevers. *Biophys. J.* **83**, 2705–2715.
38. Gardel, M.L., Shin, J.H., MacKintosh, F.C., Mahadevan, L., Matsudaira, P. and Weitz, D.A. (2004) Elastic Behavior of cross-linked and bundled actin networks. *Science*. **304**, 1301–1305.
39. Opitz, C.A., Kulke, M., Leake, M.C., Neagoe, C., Hinssen, H., Hajjar, R.J. and Linke, W.A. (2003) Damped elastic recoil of the titin spring in myofibrils of human myocardium. *Proc. Natl. Acad. Sci.* **100**, 12688–12693.
40. Linke, W.A. and Leake, M.C. (2004) Multiple sources of passive stress relaxation in muscle fibres. *Phys. Med. Biol.* **49**, 3613–3627.
41. Cortes, P., Mendez, M., Riser, B.L., Guerin, C.J., Rodriguez-Barbero, A., Hassett, C. and Yee, J. (2000) F-actin fiber distribution in glomerular cells: Structural and functional implications. *Kidney Int.* **58**, 2452–2461.
42. Satcher, R.L. and Dewey C.F. (1996) Theoretical estimates of mechanical properties of the endothelial cell cytoskeleton. *Biophys. J.* **71**, 109–118.
43. Kruse, K. and Julicher, F. (2003) Self-organization and mechanical properties of active filament bundles. *Phys. Rev. E*. **67**, 051913.
44. Stevenson, D., Agate, B., Tsampoula, X., Fischer, B., Brown, C.T.A., Sibbett, W., Riches, A., Gunn-Moore, F. and Dholakia K., (2006) *Opt. Expr.* **14**, 7125–7133.
45. Yao, C., Rahmanzadeh, R., Endl, E., Zhang, Z., Gerdes, J., Huettmann, G., (2005), *J. Biomed. Opt.* **10**, 064012
46. Yao, C., QU, X. and Zhang, Z., (2009) *Chin. Opt. Lett*. **7**, 10.
47. Yanik, M.F., Cinar, H., Cinar, H.N., Chisholm, A.D., Jin, Y.S. and Ben-Yakar, A. (2004) Neurosurgery – Functional regeneration after laser axotomy. *Nature* **432**, 822.
48. Bourgeois, F. and Ben-Yakar, A. (2007) Femtosecond laser nanoaxotomy properties and their effect on axonal recovery in C-elegans. *Opt. Expr.* **15**, 8521–8531.
49. Wu, Z., Ghosh-Roy, A., Yanik, M.F., Zhang, J.Z., Jin, Y. and Chisholm, A.D. (2007) Caenorhabditis elegans neuronal regeneration is influenced by life stage, ephrin signaling, and synaptic branching. *Proc. Natl. Acad. Sci.* **104**, 15132–15137.
50. Gabel, C.V., Antonie, F., Chuang, C.F., Samuel, A.D. and Chang, C. (2008) Distinct cellular and molecular mechanisms mediate initial axon development and adult-stage axon regeneration in C. elegans. *Development* **135**, 1129–1136.
51. Trent, C., Tsung, N. and Horvitz, H.R. (1983) A Novel Dominant Transformer Allele of the Sex-Determining Gene Her-1 of Caenorhabditis Elegans. *Genetics* **104**, 619–647.
52. Hardaker, L.A., Singer, E., Kerr, R., Zhou, G. and Schafer, W.R. (2001) *J. Neurobiol.* **49**, 303–313.

SOLAR ENERGY CONVERSION – NATURAL TO ARTIFICIAL

VILLY SUNDSTROM*
Department of Chemical Physics
Lund University, Box 124
22100 Lund, Sweden

Abstract Photosynthesis is the process by which energy of light is converted into chemical energy by plants, algae and photosynthetic bacteria. For this, highly specialized pigment–proteins have evolved that capture the light and transform the short-lived excited states of pigment molecules into a stable transmembrane potential. By close scrutiny of organization and processes of the photosynthetic pigment systems a number of "design principles" can be recognized. By combining knowledge about structure and light converting energy and electron transfer processes, we can identify the most important features for efficient photosynthetic solar energy conversion. We will also consider two types of nanostructured materials used for solar cell applications and identify conceptual similarities and differences compared to the natural systems.

1. Nature's Way

1.1. CONSTRUCTION OF LIGHT HARVESTING AND ENERGY CONVERTING PIGMENT SYSTEMS OF PHOTOSYNTHESIS

There is a large variety of photosynthetic organisms, ranging from very old photosynthetic bacteria containing only one photosystem to more recently evolved cyanobacteria, algae and green plants having two photosystems operating in series and capable of water oxidation and oxygen production. Despite large differences in composition and architecture of the pigment–protein systems of various organisms, the overall function of most photosynthetic light energy converting systems is surprisingly similar. Thus, it is generally seen that light is very efficiently collected by a light-harvesting antenna and within ~100 ps transferred to the photochemical reaction center (RC) where the light-energy is converted to a stable charge separated state with almost 100% quantum efficiency creating a transmembrane potential, which is the source of energy for all subsequent processes in the organisms [1–4]. This general pattern of overall time scale of the primary photosynthetic processes can easily be understood as a combined result of the high (~95%) overall quantum efficiency of light-to-charge conversion and the known nanosecond fluorescence lifetimes of many photosynthetic pigments (chlorophyll,

* Villy Sundstrom, Department of Chemical Physics, Lund University, Box 124, 22100 Lund, Sweden, e-mail: Villy.sundstrom@chemphys.lu.se

B. Di Bartolo and J. Collins (eds.), *Biophotonics: Spectroscopy, Imaging, Sensing, and Manipulation*,
DOI 10.1007/978-90-481-9977-8_10,

bacteriochlorophyll, phycocyanin, etc.) – to efficiently compete with fluorescence deactivation of the excited states the functional energy and charge transfer processes have to be at least 10–100 times faster. These requirements for efficient conversion of light into chemical energy in pigment systems that are robust against changes in environmental factors, variation in light intensity, presence of reactive species, variation in pigmentation and structure, have through the eons of evolution lead to a number of "design principles" that can be recognized in most photosynthetic systems. In what follows we will identify the most important concepts and discuss how they contribute to achieve an efficient light harvesting and converting process. In the search for efficient man-made devices for solar energy conversion the principles of Nature are very interesting to pursue.

1.2. NEED FOR A LIGHT HARVESTING ANTENNA

Natural photosynthesis utilizes two coupled pigment systems, a light-harvesting antenna and a photochemical reaction center (RC), for efficient conversion of light-energy into stabilized charges, eventually used to synthesize chemically stable high-energy products. This is nicely illustrated by the photosynthetic unit (PSU) of purple bacteria (Fig. 1a), where two different antenna systems, the LH2 peripheral antenna (smaller circles) and the core LH1 antenna (bigger circle), are surrounding the photosynthetic reaction center inside of LH1. Both pigment systems are absolutely essential for the operation of photosynthesis. The light-harvesting antenna is composed of a large number (~100) of pigment molecules, whose task is to collect sunlight over a broad spectral range and efficiently deliver it to the RC. The RC consists of a few highly specialized pigment molecules, whose organization and interactions are fine tuned to optimize unidirectional electron transfer across the photosynthetic membrane, achieving a long lived charge separated state with high efficiency. In oxygenic photosynthesis the oxidizing power of this charge-separated state is used to extract electrons from water, with the help of a catalytic manganese cluster.

The need for a coupled antenna-RC system is easily realized by considering the fact that the photochemical reaction in photosynthesis, splitting of water and formation of molecular oxygen, requires that four photochemical cycles of the RC occur in quite short time (typically milliseconds). On longer time scales all charge-separated states undergo recombination reactions to the ground state, causing loss of the acquired photon energy. Due to this constraint, without an antenna system coupled to the RC the conversion efficiency of a photosynthetic system would be very low at the ambient light fluxes delivered by the sun. Thus, an antenna coupled to a photochemical RC unit is a necessary feature for efficient photocatalytic operation at ambient solar light intensities. This is also an important lesson to learn from Nature for the construction of an artificial solar energy conversion system. Figure 1a–d shows a few examples of photosynthetic antenna-reaction center pigment systems from different types of organisms. Their function is discussed below.

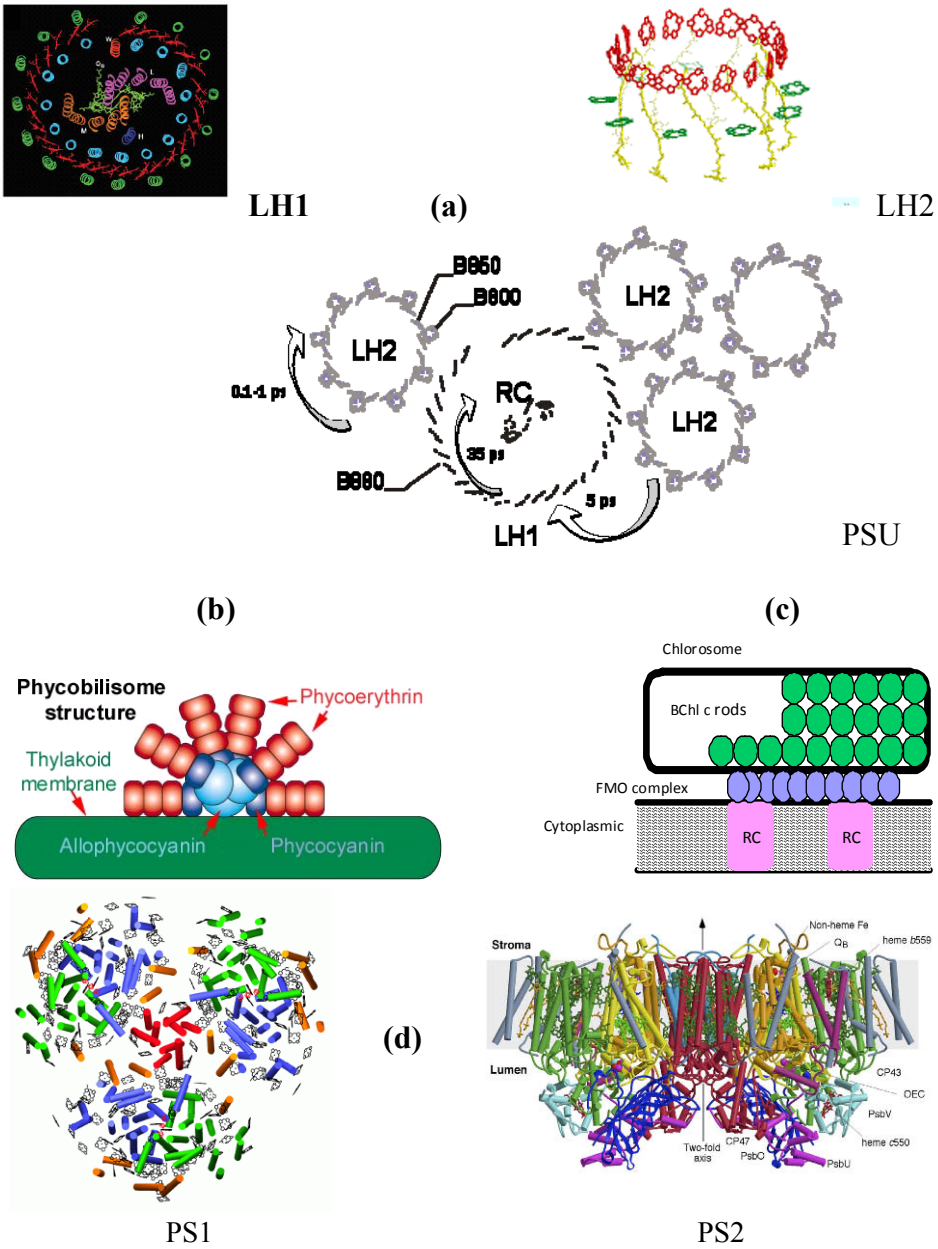

Figure 1. A few examples of photosynthetic pigment systems. (a) LH1, LH2 and full photosynthetic unit (PSU) of purple bacteria. (b) Phycobilisome antenna attached to the photosynthetic membrane of cyanobacteria. (c) Chlorosome and FMO antenna complexes attached to the photosynthetic membrane of green sulfur bacteria. (d) The PS1 (left) and PS2 (right) photosystems of green plants.

1.3. SPECTRAL COVERAGE

Photosynthetic organisms live in habitats with greatly varying conditions of light intensity and spectral distribution. Land based plants are exposed to the full solar spectrum, whereas organisms living in water or in the soil all see a more or less heavily filtered solar spectrum. This implies that species have developed their pigment composition to optimize light collection in each specific location. This fact is illustrated in Fig. 2 where the solar spectrum is reproduced along with characteristic regions of light absorption of different organisms and pigments. Thus, we can see that the useful parts of the solar spectrum from the blue (~400 nm) to the near-infrared (~1,100 nm) is completely covered by various pigments without any gaps; Nature has devised pigment systems and organisms have evolved to efficiently harvest all colors of the sunlight impinging on the Earth.

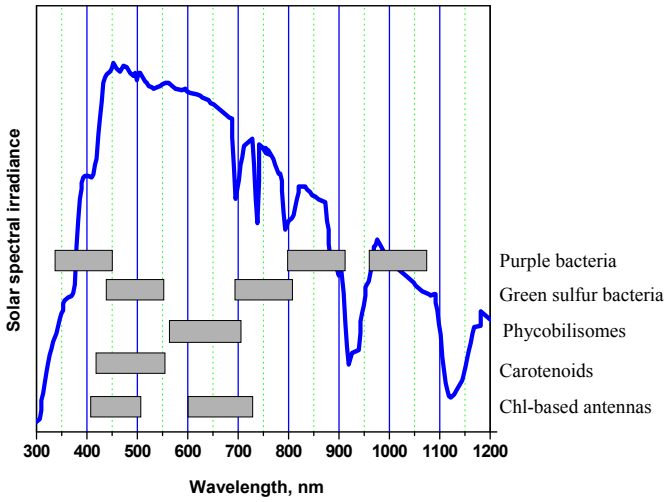

Figure 2. Spectrum of the solar radiation that reaches the surface of the earth. Wavelength ranges of absorption for different pigments and a few types of photosynthetic organisms.

This large variety of pigmentation is integrated into a range of functional pigment–protein structures. In Fig. 1 we show just a few examples to illustrate the great structural diversity of the photosynthetic pigment apparatus construction. In photosynthetic purple bacteria, both antenna and reaction centers are trans-membrane proteins fully integrated into the photosynthetic membrane (Fig 1a). The antenna consists of a circular core antenna LH1 surrounding the reaction center and a peripheral LH2 complex also of circular shape. High-resolution crystal structures have been obtained for both LH1 [5] and LH2 [6]. The pigments of these antennas have well separated absorption and fluorescence spectra and the high symmetry of the complexes makes them amenable for quantum chemistry calculations and computer simulations of energy and electron transfer processes. It also turns out that the antennas of purple bacteria constitute a representation of various energy transfer mechanisms. Antennas and reaction centers of

purple bacteria have therefore served as test grounds for studies of energy and electron transfer in photosynthesis; much of our knowledge today about these processes stems from studies of purple bacterial pigment–protein complexes. In cyanobacteria (Fig. 1b) there is an extramembrane antenna, the phycobilisome [7], attached to the thylakoid membrane holding the core antenna and the photochemical reaction center. The chromophores of phycobilisomes are open chain tetrapyrolles (phycoerythrin, phycocyanin and allophycocyanin) arranged in such a way that downhill energy transfer (from high to low-energy pigments) occurs towards the membrane and chlorophyll containing core antenna and reaction center [2]. The overall construction of the photosynthetic pigment apparatus of green sulfur bacteria (Fig. 1c) is reminiscent of that of cyanobacteria. Here, a large antenna containing thousands of bacteriochlorophyll molecules arranged in rod-like structures and encapsulated in cigar-shaped structures (chlorosomes) [8] are attached via a baseplate and a linking pigment–protein complex (the so-called Fenna–Mathews–Olsen, FMO [9], complex) to the membrane. One chlorosome can funnel energy to 10–15 reaction centers. To conclude this survey of different photosynthetic units, we consider that of green plants consisting of the two photosystems PS1 [10] and PS2 [11, 12] (Fig. 1d), operating in series. Here, chlorophyll *a* and chlorophyll *b* are the main chromophores of both antenna and reaction centers, and despite the presence of many different pigment-protein complexes the spectral properties are quite similar. This difficulty to spectroscopically distinguish different parts of the photosynthetic apparatus has delayed a detailed understanding of energy and electron transfer pathways and mechanisms. However, using the most powerful spectroscopic methods combined with theoretical modeling important progress has been made.

1.4. EFFICIENT ENERGY FLOW THROUGH THE LIGHT HARVESTING ANTENNA SYSTEMS

Examination of different photosynthetic antennas reveal one of Nature's remarkable achievements – despite often very large antennas of hundreds or sometimes even thousands of pigment molecules, all of them are coupled to each other such that energy flows through the system and is channelled into the reaction center with a total quantum conversion efficiency approaching unity. How remarkable this design is, is maybe best appreciated when one tries to build an artificial pigment system for light harvesting – it is very difficult to make a large system containing many pigment molecules that are all well-coupled and at the same time avoid excited state quenching. The distance dependence to the sixth power of Förster energy transfer [13], generally active in photosynthetic systems, imply that molecules have to be within ~1–3 nm for efficient energy transfer. If the distance is shorter, excited state quenching often occurs and efficiency decreases. Nature has solved this problem by using proteins that holds the pigment molecules in well defined and fixed positions that optimise energy transport and minimize quenching processes. In the PS1 and PS2 antennas (Fig. 1d) more than half the mass is pigment and in chlorosomes (Fig. 1c) there is no protein in the interior of the chlorosome; the bacteriochlorophyll-*c* molecules are self-assembled into a very ordered aggregate. Nevertheless, the excited state lifetimes of the pigments in antennas are generally ~1 ns and there is plenty of time for energy transfer over quite long distances. Typical energy transfer times between two pigment molecules are sub-picosecond to

few picoseconds [2–4, 14]. We will use the photosynthetic apparatus of purple bacteria (Fig. 1a) to illustrate the concepts just discussed, since it contains spectrally and structurally distinct pigment systems, implying that using the tools of time resolved spectroscopy we can in detail monitor the flow of energy through the antenna and relate observed dynamics to structural features.

Figure 3a illustrates the absorption spectrum of the purple bacterial photosynthetic unit (Fig. 1a), demonstrating the two infrared absorption bands of LH2 characteristic of the B800 and B850 pigments, as well as a red wing due to the LH1 core antenna. The reaction center absorption is overwhelmed by the absorption of many more LH1 antenna molecules. Energy flow through the pigment system can be monitored with time resolved fluorescence or transient absorption spectroscopy. The nicely separated spectral bands of the different pigments facilitate the resolution of the various transfer steps. This is illustrated by the time resolved transient absorption spectrum of a purple bacterial PSU in Fig. 3b. The peripheral LH2 antenna was excited with an ultrashort femtosecond laser pulse. At the earliest times after photoexcitation the B800 and B850 bands are bleached due to the direct optical excitation. On the tens of picosecond time scale the low energy bands of LH1 and the RC grow in intensity at the expense of the higher energy LH2 bands, showing that the energy has reached the RC within this time [2, 4, 14].

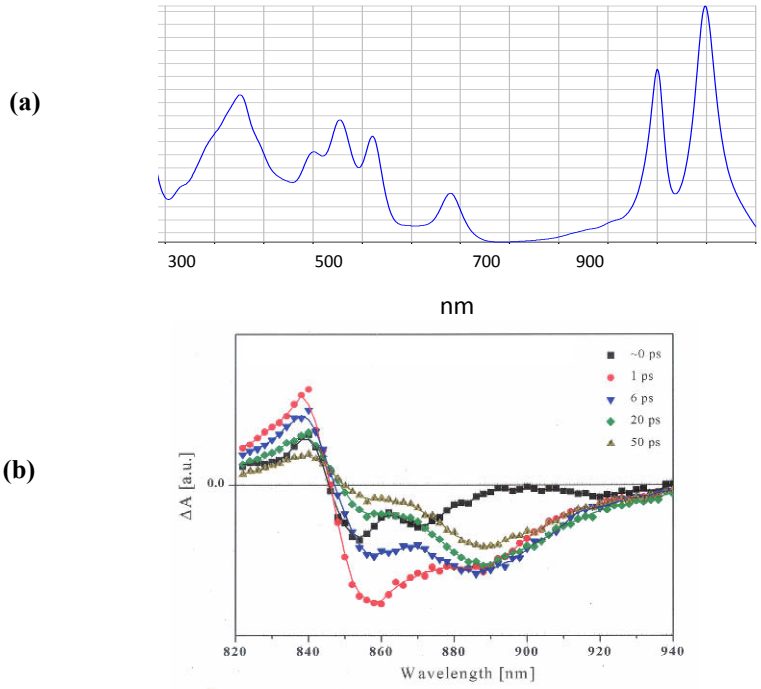

Figure 3. (a) Absorption spectrum of the purple bacterial PSU. (b) Time evolution of the transient absorption spectrum of the purple bacterial photosynthetic unit, following excitation of the LH2 antenna with an ultrashort optical pulse.

Energy transfer from an LH2 to an LH1 ring was studied in a membrane preparation of *Rb. sphaeroides* and concluded to be characterized by a ~5 ps transfer time, consistent with the estimated inter-ring distance. Transfer between aggregated B850 rings was studied using time resolved excitation annihilation combined with a Monte Carlo simulation, together with transmisson electron microscopy [15]. The random-walk Monte Carlo calculation showed that the ring-to-ring hopping time is ~30 ps and the number of B850 rings in an aggregate is ~15, in good agreement with the spot size observed in the TEM images [15]. The ring-to-ring hopping time of ~30 ps implies that for a B850 ring surrounded by six neighboring rings the excitation residence time is ~5 ps. This time is in good agreement with the 3–8 ps LH2–LH1 transfer time obtained for native membranes [16–18].

Upon inspecting the structures of for instance the purple bacterial (Fig. 1a) and PS1 (Fig. 1d) photosynthetic units the concept of multiple energy transfer pathways becomes obvious, i.e. from a given point in the antenna system there are many possible paths to reach the reaction center. This is a design principle that renders high efficiency and robustness to the antenna system. In the purple bacterial PSU, LH2 rings are connected to other LH2s as well as to LH1, implying that if an excitation in a LH2 ring for some reason is disconnected from the LH1 core antenna, it can always find an alternative path through other LH2s. Once in LH1, the excitation can enter the RC from any point on the LH1 circle. The multiple pathways of energy transfer in combination with the very fast (hundreds of femtosecond time scale) energy transfer within B850 of LH2 and LH1, result in a very fast and efficient percolation of excitation energy over the photosynthetic pigment system. The energy gradient of the light harvesting pigments towards the core antenna and reaction center results in the observed very fast and efficient (~50 ps and close to 100% quantum efficiency) overall transfer of excitations from antenna to reaction center.

1.5. INTRA-COMPLEX ENERGY TRANSFER

Using biochemical methods individual pigment-protein complexes can be isolated from the photosynthetic membrane. Spectroscopic studies of such preparations offer additional detail about the photosynthetic processes. We give one example, B800 to B850 energy transfer in the LH2 complex (Fig. 1a). The BChls of B800 are well separated from each other and from the B850s and thereby have mainly monomeric spectroscopic properties. Excitation absorbed in the B800 ring is first transferred among B800 BChls [4]. Calculations based on the Förster theory [13] agree remarkably well with the measured pair-wise transfer time of 300 fs, suggesting that for the B800 ring the point-dipole approximation is applicable. Also low temperature transient absorption anisotropy kinetics measured at different wavelengths inside the B800 band were successfully simulated by a model of Förster hopping in a spectrally inhomogeneous ring of BChl molecules. B800 to B850 transfer occurs with a time-constant of 0.7 ps at room temperature [4] and it slows down upon lowering the temperature to 1.2 ps at 77 K and to 1.5 ps at 4 K (Fig. 4). Both B800 and B850 can be spectrally tuned by selective mutations of key amino acids and the B800 BChls can be exchanged to other similar BChl and Chl pigments [4, 19]. A series of pigment-protein complexes where either the B800 or B850 band was spectrally shifted were studied and significant changes of the

transfer time was observed [4, 20]. The complex with the most blue-shifted B800 pigment, Chl at 670 nm, gave the transfer time of 8.3 ps, as compared to 0.7 ps for the wild-type complex. All the observed trends of the transfer time are in qualitative agreement with what one would expect based on Förster spectral overlap. However, quantitative Förster theory calculations of the transfer time based on the dipole–dipole interaction between B800 and nearby B850s failed to reproduce the observed lifetimes by almost an order of magnitude. Since the spectral overlap did describe the qualitative trend it was suggested that the source of the discrepancy is the electronic coupling term [20]. It has been pointed out that the carotenoid molecule may contribute to the electronic coupling between B800 and B850 (see [4] and references therein). Alternatively, the nondiagonal and/or diagonal [21] electron phonon coupling may facilitate efficient excitation transfer to optically forbidden exciton levels. In the spirit of the same ideas a modified Förster theory adapted for transfer to the collective exciton states with spectral inhomogeneity has been used for describing B800 to B850 transfer, apparently leading to quantitative agreement between theory and experiment [22].

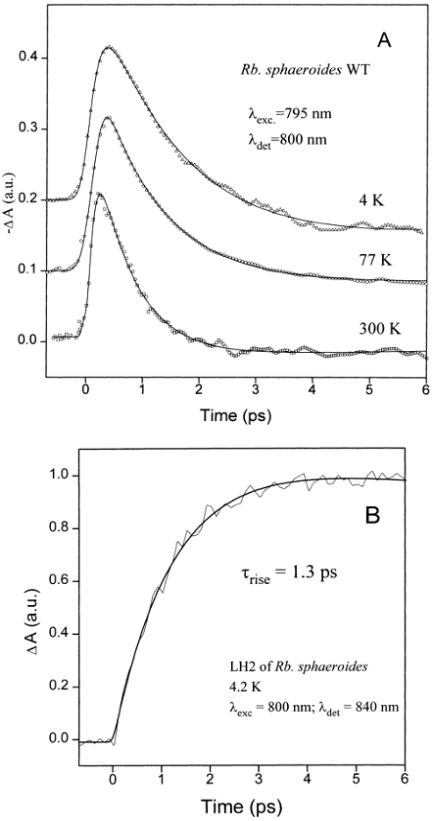

Figure 4. Transient absorption kinetics illustrating energy transfer from B800 to B850 in LH2. B800 is excited by a femtosecond pulse at 800 nm and the energy transfer is monitored in (a) as the decay of B800 excited state population, and in (b) as the corresponding rise of B850 population. The transfer becomes somewhat slower at low temperature.

1.6. EFFICIENT ANTENNA – RC COUPLING: LONG DISTANCE ENERGY TRANSFER VS. SHORT DISTANCE CHARGE TRANSFER

The last step in excitation transfer is transfer from the antenna to the special pair of the RC (energy trapping). Already early studies indicated that the trapping by the RC is slow [23]. The rate of antenna to RC transfer was first determined by Timpmann et al. [24] to be 30–40 ps, i.e. demonstrating that the final antenna-RC energy transfer step is the slowest and rate limiting step in the overall energy converting process. The trapping of excitation energy by the photosynthetic RC has often been discussed in terms of a trap-limited or diffusion-limited process, implying that the rate limiting process is charge separation in the RC, or the energy diffusion process through the antenna, respectively. The realization that the antenna to reaction center energy transfer step is rate limiting, was termed transfer-to-trap-limited [2, 24]. The structure of the purple bacterial LH1–RC complex (Fig 1a) explains the result – the distance between the RC and the LH1 BChls is the longest distance, which by virtue of the strong distance dependence (sixth power) of the energy transfer rate will be the slowest step. The functional importance of this large LH1–RC distance is that it prevents photo-oxidation of antenna BChls, and concomitant excited state quenching in the antenna, by the oxidized special pair of the reaction center.

An issue sometimes raised in literature is the role of collective excited states, excitons, in photosynthetic light-harvesting. Formation of collective excited states through inter-chromophore interaction leads to increased dipole strength of the collective state as compared to the monomeric chromophore. Energy transfer involving collective excited states will therefore be faster than energy transfer involving monomeric pigments under otherwise identical conditions. Since the last energy transfer step to the RC is the slowest, this step is most influenced by collective excitations. Thus, the overall trapping and thereby efficiency of photosynthesis is significantly improved by exciton formation in LH1.

Characteristic times of the different energy transfer steps discussed above are highlighted in the figure of the purple bacterial photosynthetic unit in Fig. 1a. Energy transfer between neighboring BChl molecules within the LH1 or LH2 pigment–protein complexes occurs on the ~0.1–1 ps time scale, whereas transfer between these complexes takes ~5 ps. The final energy transfer step from the LH1 ring to the special pair in the reaction center is characterized by the slowest energy transfer, ~35 ps. This results in efficient transfer of energy from any point in the network of antenna pigments to the reaction center, such that energy is stored in the RC within 50–100 ps after light absorption with an overall quantum efficiency approaching unity. Other pigment systems of other photosynthetic organisms, despite being composed of different pigments and having very different organization, show similar time scales of the energy transfer processes [2, 25–29].

1.7. STORING THE ENERGY OF LIGHT – PHOTOSYNTHETIC CHARGE SEPARATION

As already discussed above, excitation energy captured by the antenna is transferred to the pigments of the reaction center where a sequence of ultrafast electron transfer steps convert the excited state energy in the antenna to a transmembrane potential. The core

of the RC is made up of two homologous membrane proteins, called L and M, while a third polypeptide, H, covers the cytosolic surface [30]. Both L and M possess five membrane-crossing helices forming a cage around the four BChls, two bacteriopheophytins and two quinones non-covalently bound to the RC (Fig. 5). With respect to both the proteins and the cofactors, the RC shows a remarkable C2-symmetry with the symmetry axis running through the middle of the centrally located "special pair" (P) of BChl molecules and the non-heme iron. The pigments are arranged in two branches labelled A and B, but surprisingly, electron transfer occurs only along the A (or "active") branch. Following excitation of the special pair (transfer of excitation energy from the antenna), charge separation occurs within a few picoseconds to yield the oxidized special pair, P^+, and a reduced bacteriopheophytin, H_A^-. The electron then hops to a quinone molecule, Q_A, in about 200 ps, and on to a second quinone Q_B in 100 μs. P^+ is restored to neutrality by electron transfer from a cytochrome. This sequence of reactions is repeated after the absorption of a second photon, and then the doubly reduced Q_B molecule leaves the RC as Q_BH_2 and an electrochemical gradient has been created across the photosynthetic membrane in which the RC is positioned.

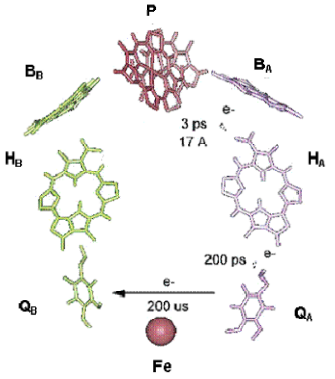

Figure 5. Structure of the bacterial reaction center, showing the cofactors. P – special pair; B_A and B_B – accessory monomeric chlorophylls; H_A and H_B – pheophytins; Q_A and Q_B – quinines.

2. The Artificial Way

2.1. NANOSTRUCTURED MATERIALS FOR SOLAR ELECTRICITY

Green plant photosynthesis converts water and carbon dioxide into a fuel, carbohydrates, with the help of the energy of light. Vast research efforts are exercised in the search and development of artificial systems carrying out the same task, i.e. convert sunlight into a fuel of some kind. The materials considered for this mission range from inorganic metal oxides and semiconductors to complex molecular systems more or less mimicking the photosynthetic machinery [see e.g. [31]]. The fuel to be produced in such artificial systems is generally less complex than the products of photosynthesis and small molecules like molecular hydrogen or methanol.

As discussed above, the first light driven steps of photosynthesis is conversion of excited states of antenna molecules and reaction centers into energy rich electrons. The basic antenna-reaction center concept for efficient light harvesting and charge separation could therefore be employed in molecular materials for solar cells. The Grätzel solar cell [32–34] and plastic solar cells based on the so called bulk heterojunction (BHJ) concept [35–37] utilize this principle. In the Grätzel solar cell, dye molecules attached to a nanostructured metal oxide film plays the role of the light harvesting antenna and the metal oxide nanoparticles can be seen as the equivalent to the photosynthetic reaction center, storing and transporting electrons. In a BHJ plastic solar cell it is the conjugated polymer that harvests the light and fullerene molecules now play the role of the reaction center. Despite these obvious similarities there are important differences between the primary photosynthetic processes and those in the two solar cell materials mentioned. In a Grätzel solar cell charge separation occurs between the sensitizer dyes and the metal oxide nanoparticle, as an electron is injected from the photoexcited dye molecule into the nanoparticle. Thus, if we view the sensitizer molecules as an antenna, charge separation involves the antenna molecules and the hole left behind electron injection into the metal oxide nanoparticle is located in the antenna. This never happens in a functioning photosynthetic pigment system, because if it would, it would cause efficient quenching of antenna excitations due to the very efficient energy transfer in a photosynthetic antenna system. In a Grätzel cell this is not a problem because energy transfer between sensitizers is generally not extremely fast, and re-reduction of the oxidized dye is fast because of efficient shuttling of charge by a redox electrolyte. Similarly, for the BHJ plastic solar cell charge separation occurs between the conjugated polymer (antenna) and a fullerene electron acceptor. A further difference here is that the polymer also has the function of charge transport (the holes) in the solar cell; the fullerenes transport the electrons.

For any solar energy converting system based on the antenna-reaction center concept several processes should be considered that may contribute to the overall conversion efficiency of a material and device, namely

- Light absorption
- Energy transfer in the light harvesting material
- Charge generation
- Charge separation and formation of mobile charges
- Charge recombination
- Charge transport and extraction

In what follows, after a short description of the overall function, we will discuss these processes for the two solar cell materials mentioned above, nanostructured dye sensitized metal oxides of Grätzel solar cells and BHJ polymer/fullerene blends of plastic solar cells.

2.2. NANOSTRUCTURED DYE SENSITIZED METAL OXIDES OF GRÄTZEL SOLAR CELLS

Sensitized wide band-gap semiconductors have since long been considered as materials for photovoltaics. However, not until the discovery by Grätzel and co-workers [32], that a material with high conversion efficiency could be produced by sensitising a nanostructured thin film of a wide band-gap semiconductor, real progress towards a competitive solar cell device was taken. A so-called dye-sensitized solar cell (DSC) typically consists of a thin (~1 μm) TiO_2 film of nanometer-sized (~10 nm) particles sintered together for electrical contact. This thin film is deposited on a conducting glass (ITO) electrode and brought in electrical contact with a counter electrode via an electrolyte (Fig. 6). Light energy conversion in such a solar cell starts when light is absorbed by the sensitising dye and electrons are injected from the excited state of the dye into the conduction band of the semiconductor. Electrons then migrate between semiconductor particles until they reach the back contact and the external circuit, where they can perform work. Finally, electrons are lead back to a redox couple (often I^-/I_3^-), which regenerates the oxidized dye back to the neutral ground state and the dye can absorb another photon and start a new conversion cycle.

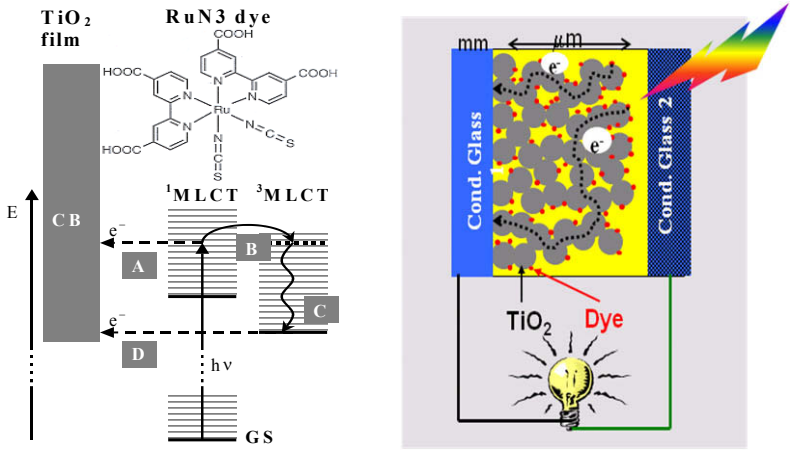

Figure 6. (Left) Schematic model for two-state electron injection and structure of RuN3. Following MLCT excitation (at 530 nm) of the RuN3-sensitized TiO_2 film an electron is promoted from a mixed ruthenium NCS state to an excited π^* state of the dcbpy-ligand and injected into the conduction band (CB) of the semiconductor. GS: ground state of RuN3. Channel A: electron injection from the non-thermalized, singlet ^{1}MLCT excited state. Channel B and C: ISC followed by internal vibrational relaxation in the triplet ^{3}MLCT excited state. Channel D: electron injection from the thermalized, triplet ^{3}MLCT excited state. (Right) Schematic representation of a dye sensitized solar cell with its thin film of TiO_2 nanoparticles (gray circles) sensitized by molecules (red dots). Photoexcitation of the dye results in electron transport through the nanostructured metal oxide film.

High efficiency of the electron injection step and a low yield of electron recombination between electrons in the semiconductor conduction band and oxidized dye are essential for an efficient material. The electron injection efficiency can be optimised by ensuring very fast injection, much faster than all competing processes deactivating the excited state of the sensitizer. The fraction of injected electrons that recombine with the oxidized dye may be influenced in several different ways. One possibility is to choose sensitizer and redox couple in such a way that their electrochemical properties maximize the ratio of rates for oxidized dye reduction by the redox couple and electron recombination from the semiconductor. Another possibility is to decrease the rate of back-electron transfer from the semiconductor to the oxidized dye, by increasing the distance between the semiconductor and sensitizer [38]. The key primary electron transfer processes in a DSC material are illustrated in the energy diagram of Fig. 6. Design of sensitizers to control dye-semiconductor binding and distances of electron transfer often leads to counter intuitive results because of the multitude of factors controlling the binding. Still another approach that has been explored, is to use a secondary electron donor attached to the sensitizer and hence move the positive hole on the sensitizer further away from the semiconductor surface [39]. An exhaustive and recent review of most aspects of the DSC can be found in [40]. The most efficient DSC so far constructed has an overall light-to-electricity conversion efficiency of ~11% [32, 34] and relies on TiO_2 anatase for the semiconductor and a transition metal complex $(Ru(dcbpy)_2(NCS)_2$ (dcbpy = 4,4′-dicarboxylate-2,2′-bipyridine, RuN3 for short) as sensitizer.

2.3. PLASTIC SOLAR CELLS BASED ON THE BULK HETEROJUNCTION CONCEPT

Organic conjugated polymers are remarkable in the sense that they may be designed for the dual functions of light-generation and light-energy conversion. The first function relies on the fact that these materials are electroluminescent, *i.e.* upon leading electric current through the material, electron and holes recombine to form light emitting excited states. The second function rests on the property of polymer excited states formed by light absorption to dissociate into electrons and positive holes. Conjugated polymer-based solar cells are promising alternatives to inorganic semiconductor photovoltaic devices. Since the initial step in the photovoltaic action of polymeric solar cells is exciton dissociation leading to charge pairs, their performance has been found to improve considerably in the presence of an electron acceptor (e.g., a C60 derivative) [41, 42]. Early devices from this combination of materials gave low power conversion efficiencies because of low interfacial contact area between the donor and acceptor. A major breakthrough in this direction was achieved by blending the polymer and a soluble fullerene derivative such that the two components form an interpenetrating network on the nanometer scale (the bulk heterojunction, BHJ) [37, 41]. A schematic structure of a BHJ solar cell is shown in Fig. 7. Polymer/fullerene bulk heterojunction solar cells have now been demonstrated to achieve a power conversion efficiency of 6% under AM 1.5 conditions [43].

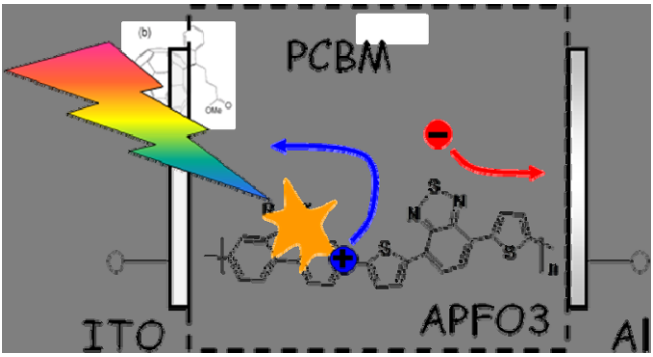

Figure 7. Schematic structure of a bulk heterojunction plastic solar cell. A thin (~100 nm) film of the active conjugated polymer-fullerene material is placed between electrodes. Light absorption by the polymer results in charge generation and transport of mobile charges; electrons in the fullerene phase and holes in the polymer phase.

We have applied various forms of transient laser spectroscopy to obtain detailed mechanistic understanding of the light induced processes underlying the photon to current conversion processes in these materials, with the aim to gain knowledge that could be used to further improve efficiency. We have studied a low band-gap polyfluorene/fullerene BHJ material (APFO3/PCBM) [44, 45] and obtained detailed knowledge about charge generation and separation, as well as charge recombination and charge transport, all important processes for the function of a solar cell. Detailed information about the excited state and charge dynamics for several different APFO3/PCBM blends from 30 fs to 50 μs was obtained by combining the results of transient kinetics measured with a femtosecond spectrometer and a nanosecond flash photolysis setup [45] (Figs. 8 and 9). In this way, the complete life cycle of light induced excitations, from the initial excitation of the polymer to disappearance of the charges, was monitored in an unbroken chain of events. The kinetic traces in Fig. 8 for all three studied blends at low excitation flux (~10^{13} ph/cm^2 per pulse) show three main features: (i) an initial ultrafast decay (~200 fs) of the transient absorption followed by (ii) a picosecond rise (~30 ps), and finally (iii) a second decay on the ~30-ns time scale (Fig. 8). Since charge carrier dynamics in polymer/fullerene-based devices has been shown to be dependent on the concentration of the carriers, we also examined the effect of incident light intensity on the transient absorption dynamics in the blends. Figure 9 shows the intensity dependence of the kinetics for the 1:1 APFO3/PCBM blend with the excitation intensity varied over almost two orders of magnitude. At the two lowest intensities (<6.6 × 10^{13} ph/cm^2 per pulse), the kinetics are intensity-independent within experimental error. We note that, at 20 ns, about 50% of the initial signal has decayed and very small amplitude extends into the microsecond time region. Above ~1 × 10^{14} ph/cm^2 per pulse, the kinetics becomes strongly intensity-dependent, with an increasingly faster decay at higher light intensities. Measurements of several different blend ratios with APFO3:PCBM stoichiometries varying from 99:1 to 1:4 by weight, and careful kinetic analysis of the data [44, 45] lead to the reaction scheme shown in Fig. 10. Following photoexcitation of the APFO3 polymer charge generation (process 1 in Fig. 10) occurs within ~200 fs by

the very fast decay of the transient absorption signal in Fig. 8. This very fast charge generation is virtually the same down to a PCBM concentration of 20%, but even at a PCBM concentration of only 5% the excited state of the polymer is quenched within 10 ps by electron transfer to the fullerene. The rise of the transient absorption kinetics with a time constant of ~30 ps (Fig. 8) represents formation of mobile charges (process 2 in Fig. 10) and the final slow decay on the ~30 ns time scale represents recombination of electrons in the fullerene and holes on the polymer. The fact that this recombination time is obtained at the lowest excitation intensities and is independent of intensity shows that it is first order, or geminate, recombination. At higher excitation intensity (Fig. 9) the kinetics becomes strongly intensity dependent as a consequence of non-geminate second order recombination. At solar light intensities, which are significantly lower than the lowest excitation intensity used in the experiment, only first order recombination plays a role.

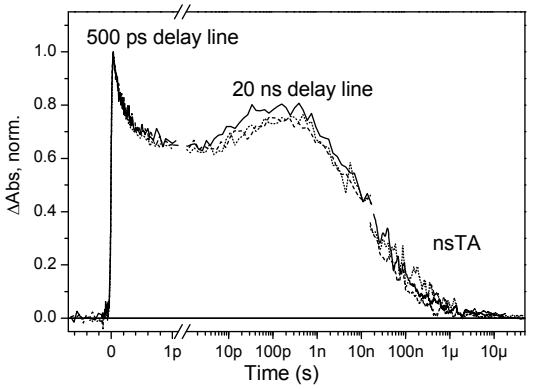

Figure 8. TA kinetics over the entire timescale for different APFO3:C60PCBM blends at low fluence (~10^{13} ph/cm^2 per pulse): 1:1 blend – solid; 1:3 blend - dashed, and 1:4 blend – dotted line. The ns kinetics were smoothed, scaled, and the early parts of them were truncated for clarity of presentation.

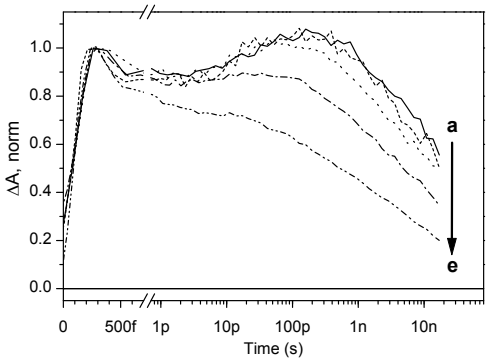

Figure 9. Intensity dependence of the TA kinetics for the 1:1 blend of APFO3:C60PCBM at various incident photon fluences (ph/cm^2 per pulse): (a) 2.3×10^{13}, (b) 6.6×10^{13}. (c) 1.1×10^{14}, (d) 2.3×10^{14}, (e) 8.0×10^{14}.

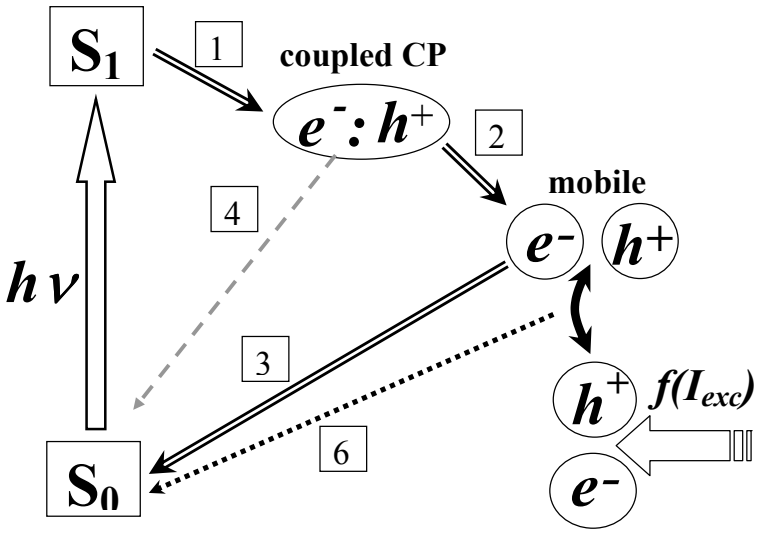

Figure 10. Processes occurring subsequent to light absorption in APFO3:C60PCBM blends.

Many different polymer/fullerene blends have been examined for solar cell application, but only a relatively small number have been found to give good conversion efficiency. Of these only few have been studied in some detail with respect to their light induced excited state processes and charge dynamics. Although similarities and common features certainly can be distinguished there is not yet a general picture of which are the important steps of the light-to-current conversion and their mechanisms. Much more work remains to reach this point and it is also likely that some materials are sufficiently different that processes are qualitatively different.

Acknowledgements This work was supported by the Swedish Energy Administration, The Swedish Research Council, The Wallenberg Foundation, the Swedish Foundation for Strategic Research and the Swedish Institute (Guest Scholarship Programme). The US department of Energy (DE-FG02-01ER15256), Czech Science Foundation (202/09/P099), Academy of Sciences of the Czech Republic (A100100902 and MEXT, Japan (Grant-in-aid 19350068) are also acknowledged for their support.

References

1. R. vanGrondelle, *Biochimica Et Biophysica Acta*, 1985, **811**, 147–195.
2. R. vanGrondelle, J. P. Dekker, T. Gillbro, and V. Sundstrom, *Biochimica Et Biophysica Acta-Bioenergetics*, 1994, **1187**, 1–65.
3. T. Pullerits and V. Sundstrom, *Accounts of Chemical Research*, 1996, **29**, 381–389.

4. V. Sundstrom, T. Pullerits, and R. van Grondelle, *Journal of Physical Chemistry B*, 1999, **103**, 2327–2346.
5. A. W. Roszak, T. D. Howard, J. Southall, A. T. Gardiner, C. J. Law, N. W. Isaacs, and R. J. Cogdell, *Science*, 2003, **302**, 1969–1972.
6. G. Mcdermott, S. M. Prince, A. A. Freer, A. M. Hawthornthwaitelawless, M. Z. Papiz, R. J. Cogdell, and N. W. Isaacs, *Nature*, 1995, **374**, 517–521.
7. E. Gantt, *Annual Review of Plant Physiology and Plant Molecular Biology*, 1981, **32**, 327–347.
8. J. M. Olson, *Biochimica Et Biophysica Acta*, 1980, **594**, 33–51.
9. R. E. Fenna and B. W. Matthews, *Nature*, 1975, **258**, 573–577.
10. P. Jordan, P. Fromme, H. T. Witt, O. Klukas, W. Saenger, and N. Krauss, *Nature*, 2001, **411**, 909–917.
11. A. Zouni, H. T. Witt, J. Kern, P. Fromme, N. Krauss, W. Saenger, and P. Orth, *Nature*, 2001, **409**, 739–743.
12. K. N. Ferreira, T. M. Iverson, K. Maghlaoui, J. Barber, and S. Iwata, *Science*, 2004, **303**, 1831–1838.
13. T. Forster, *Naturwissenschaften*, 1946, **33**, 166–175.
14. V. Sundstrom, R. vanGrondelle, H. Bergstrom, E. Akesson, and T. Gillbro, *Biochimica Et Biophysica Acta*, 1986, **851**, 431–446.
15. A. Schubert, A. Stenstam, W. J. D. Beenken, J. L. Herek, R. Cogdell, T. Pullerits, and V. Sundstrom, *Biophysical Journal*, 2004, **86**, 2363–2373.
16. S. Hess, M. Chachisvilis, K. Timpmann, M. R. Jones, G. J. S. Fowler, C. N. Hunter, and V. Sundstrom, *Proceedings of the National Academy of Science of the United States of America*, 1995, **92**, 12333–12337.
17. V. Nagarajan and W. W. Parson, *Biochemistry*, 1997, **36**, 2300–2306.
18. A. Freiberg, V. I. Godik, T. Pullerits, and K. Timpman, *Biochimica Et Biophysica Acta*, 1989, **973**, 93–104.
19. N. J. Fraser, P. J. Dominy, B. Ucker, I. Simonin, H. Scheer, and R. J. Cogdell, *Biochemistry*, 1999, **38**, 9684–9692.
20. J. L. Herek, N. J. Fraser, T. Pullerits, P. Martinsson, T. Polivka, H. Scheer, R. J. Cogdell, and V. Sundstrom, *Biophysical Journal*, 2000, **78**, 2590–2596.
21. H. Sumi, *Journal of Physical Chemistry B*, 1999, **103**, 252–260.
22. G. D. Scholes and G. R. Fleming, *Journal of Physical Chemistry B*, 2000, **104**, 1854–1868.
23. K. J. Visscher, H. Bergstrom, V. Sundstrom, C. N. Hunter, and R. vanGrondelle, *Photosynthesis Research*, 1989, **22**, 211–217.
24. K. Timpmann, F. G. Zhang, A. Freiberg, and V. Sundstrom, *Biochimica Et Biophysica Acta*, 1993, **1183**, 185–193.
25. H. van Amerongen and R. van Grondelle, *Journal of Physical Chemistry B*, 2001, **105**, 604–617.
26. R. van Grondelle and V. I. Novoderezhkin, *Physical Chemistry Chemical Physics*, 2006, **8**, 793–807.
27. R. Croce, M. G. Muller, R. Bassi, and A. R. Holzwarth, *Biophysical Journal*, 2003, **84**, 2508–2516.
28. N. V. Karapetyan, A. R. Holzwarth, and M. Rogner, *Febs Letters*, 1999, **460**, 395400.
29. R. Croce, D. Dorra, A. R. Holzwarth, and R. C. Jennings, *Biochemistry*, 2000, **39**, 6341–6348.
30. J. Deisenhofer, O. Epp, K. Miki, R. Huber, and H. Michel, *Nature*, 1985, **318**, 618–624.
31. A. Magnuson, M. Anderlund, O. Johansson, P. Lindblad, R. Lomoth, S. Ott, K. Stensjo, S. Styring, T. Polivka, and V. Sundstrom, L. Hammarstrom, *Accounts of Chemical Research*, 2009, **42**, 1899–1909.
32. B. Oregan and M. Gratzel, *Nature*, 1991, **353**, 737–740.
33. A. Hagfeldt and M. Gratzel, *Chemical Reviews*, 1995, **95**, 49–68.

34. A. Hagfeldt and M. Gratzel, *Accounts of Chemical Research*, 2000, **33**, 269–277.
35. G. Yu, J. Gao, J. C. Hummelen, F. Wudl, and A. J. Heeger, *Science*, 1995, **270**, 1789–1791.
36. C. J. Brabec, N. S. Sariciftci, and J. C. Hummelen, *Advanced Functional Materials*, 2001, **11**, 15–26.
37. C. J. Brabec, G. Zerza, G. Cerullo, S. De Silvestri, S. Luzzati, J. C. Hummelen, and S. Sariciftci, *Chemical Physics Letters*, 2001, **340**, 232–236.
38. B. Burfeindt, C. Zimmermann, S. Ramakrishna, T. Hannappel, B. Meissner, W. Storck, and F. Willig, *Zeitschrift Fur Physikalische Chemie-International Journal of Research in Physical Chemistry and Chemical Physics*, 1999, **212**, 67–75.
39. R. Ghanem, Y. H. Xu, J. Pan, T. Hoffmann, J. Andersson, T. Polivka, T. Pascher, S. Styring, L. C. Sun, and V. Sundstrom, *Inorganic Chemistry*, 2002, **41**, 6258–6266.
40. S. Ardo and G. J. Meyer, *Chemical Society Reviews*, 2009, **38**, 115–164.
41. N. S. Sariciftci, L. Smilowitz, A. J. Heeger, and F. Wudl, *Science*, 1992, **258**, 1474–1476.
42. K. M. Coakley and M. D. McGehee, *Chemistry of Materials*, 2004, **16**, 4533–4542.
43. K. Kim, J. Liu, M. A. G. Namboothiry, and D. L. Carroll, *Applied Physics Letters*, 2007, **90**. 163511.
44. S. De, T. Kesti, M. Maiti, F. Zhang, O. Inganas, A. Yartsev, T. Pascher, and V. Sundstrom, *Chemical Physics*, 2008, **350**, 14–22.
45. S. De, T. Pascher, M. Maiti, K. G. Jespersen, T. Kesti, F. L. Zhang, O. Inganas, A. Yartsev, and V. Sundstrom, *Journal of the American Chemical Society*, 2007, **129**, 8466–8472.

WHISPERING GALLERY MODE BIOSENSOR:

Fulfilling the Promise of Single Virus Detection without Labels

S. ARNOLD*, S.I. SHOPOVA
MicroParticle PhotoPhysics Laboratory (MP3L)
Polytechnic Institute of NYU, Brooklyn, NY 11201

1. Introduction

None of civilization's socio-political catastrophes (e.g. world wars) have caused an equivalent destructive effect on the world's population as biological pandemics [1]. Exponentially growing pathogens are difficult to contain and eliminate unless they can be detected early on. Some years ago, one of us (S.A.) reflected on this problem as a friend was dying from a viral infection. His friend's diagnosis came too late; real-time methods for testing for the virus were not available. Fast and early detection on site of an outbreak requires biosensors where ideally individual viral particles produce a quantitative signal. A decision was made to direct the MicroParticle PhotoPhysics Lab toward finding a solution. Our approach was to sense bio-particles using the high sensitivity afforded by the perturbation that an adsorbed molecule has on high Q (10^7) optical resonances of a microparticle [2]. In particular, bio-particle adsorption was sensed from the associated shift in resonance frequency [3, 4]. Through all the eons of evolution, nature has evolved bio-nano-probes that specifically grab onto protein, DNA and foreign invaders through physio-chemical interactions. Following nature, our approach was to use these bio-nano-probes as surface-bound recognition elements and the microparticle to transduce (report) the interaction [5]. We seek to identify the whole virus by tranducing the immobilization that takes place when a coat protein on its surface interacts with a complementary antibody anchored to the microparticle surface. We set a goal to record binding steps of individual virions that can exceed the experimental noise level [6]. Although field effect techniques using nano-fibers have demonstrated single virion sensing in the past [7], reactive Whispering Gallery Mode (WGM) biosensing adds a new dimensions to what can be learned: the measured wavelength shift enables one to identify the virion size and mass. In the process of working on single particle detection we discovered that light confined in a WGM can manipulate a nanoparticle's motion and substantially enhance the rate at which these particles are sensed. This effect dimensionally reduces the transport process by forming a carousel of particles that "hunt" for anti-bodies where the sensitivity is greatest (WGM Carousel) [8].

* S. Arnold, MicroParticle PhotoPhysics Laboratory (MP3L), Polytechnic Institute of NYU, Brooklyn, NY 11201, e-mail: arnold@photon.polu.edu, sarnold935@aol.com

B. Di Bartolo and J. Collins (eds.), *Biophotonics: Spectroscopy, Imaging, Sensing, and Manipulation*,
DOI 10.1007/978-90-481-9977-8_11, © Springer Science+Business Media B.V. 2011

2. Resonant Sensors-General Considerations

Each and every oscillator, whether a mass on a spring, a violin string, the thorax of a cricket or a Fabry–Perot cavity has the common property of resonance. If they are driven by a harmonic source, the square of the oscillator's amplitude $|A|^2$ (i.e., energy) will demonstrate a Lorentzian-shaped frequency response with maximum at ω_r and linewidth γ (Fig. 1).

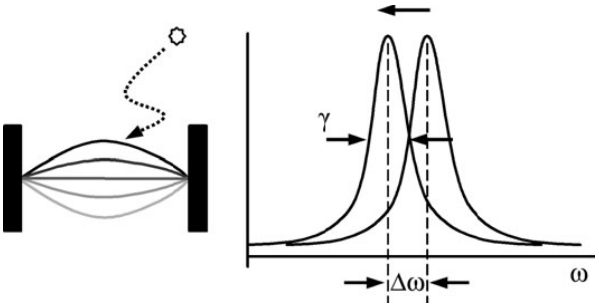

Figure 1. The frequency response of an oscillator before and after a perturbation.

At the same time they can be sensitive to perturbations. Allowing dust to fall on a violin string causes its tone to be reduced by $|\Delta\omega|$. One can imagine putting bio-nano-probes on the violin string in order to detect specific dust (e.g. anthrax spore). However, one is apt to find in a world awash with noise that the frequency shift may not be sufficient for real time detection. The principal difficulty is in measuring a frequency shift much smaller than the linewidth (Fig. 1). We will characterize this competition by a ''measurement acuity factor'', $F = |\Delta\omega|_{min}/\gamma$ where $|\Delta\omega|_{min}$ is the smallest measurable frequency shift. Clearly, smaller F is better, but more difficult to achieve. One thing is certain: for a given F the minimum frequency shift that can be measured is proportional to the line width, so that the fractional minimum shift $|\Delta\omega|_{min}/\omega_r = F\gamma/\omega_r$. Whereas F and ω_r are controlled principally by the non-dissipative physics of the oscillator and the bandwidth of the detection system, γ is principally controlled by dissipation. To reduce the minimum measurable shift, one can reduce dissipation. By convention we will represent the linewidth-to-frequency ratio by $1/Q$, where Q is the so-called Quality factor; $\gamma/\omega_r = 1/Q$. With this definition

$$\left|\Delta\omega\right|_{\min} / \omega_r = F / Q \,. \tag{1}$$

The larger Q, the smaller the dissipation and the smaller the dust particle that can be detected. Since a mechanical system like a violin string agitates the fluid around it, it is a far from an ideal sensor; dissipation is assured. By the same token, a Fabry–Perot cavity with metalized mirrors has dissipation due to Ohmic losses on reflection. The least dissipative reflection in this regard is Total Internal Reflection (TIR), in which light propagating in a medium with refractive index n_1 is reflected at a sufficient angle θ

from a medium with a lower refractive index n_2. TIR is, in principle, without loss. Light that bounces off the interior surface of a sphere while executing a polygonal orbit has this appeal.

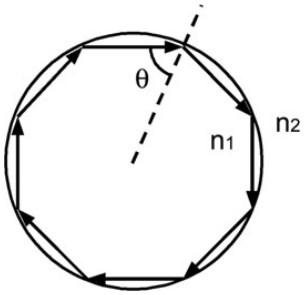

Figure 2. WGM within a dielectric microsphere.

Such an orbit [Fig. 2, with $\theta > \sin^{-1}(n_2/n_1)$] is known as a Whispering Gallery Mode (WGM).

The WGM in Fig. 2 has no apparent loss. This implies an infinite Q. However, it is well known that Q has limits. The largest Q for a WGM mode currently measured in a silica microsphere is ~10^{10} [9]. Clearly, Fig. 2 is misleading, light does not have stationary states in a dielectric. Photons orbiting in the polygon are only partially trapped. They can ‘‘tunnel’’ into free space modes. In what follows we are providing a more complete description of a WGM and the shift of its resonant frequency due to a local perturbation associated with adsorption of a single nanoparticle.

3. Theory of Reactive Sensing

Molecules that approach the surface of a microsphere in which photons are confined within a WGM are not without interactaction even though it appears from Fig. 2 that the mode is stealth as seen from the outside. They enter an evanescent field that rapidly decays spatially. This oscillating field polarizes molecules, and as a consequence causes a frequency shift of the mode. Fields due to photons are polarized due to the photon’s spin. If a microsphere is in a single photon resonant state of energy $\hbar\omega$, it will have an associated semiclassical field $\boldsymbol{E}(r,t) = \mathrm{Re}[\boldsymbol{E}_0(r)\, e^{i\omega t}]$. With a bio-particle outside the sphere at position $\mathbf{r}_j$, an interaction will occur; the bio-particle will be polarized and develop an oscillating dipole moment in excess of the displaced solvent, $\Delta\boldsymbol{p}(t) = \mathrm{Re}[\Delta\boldsymbol{p}_0\, e^{i\omega t}]$. The time-averaged energy required to polarize the bio-particle serves as the perturbation that shifts the photon energy of the resonant state by [10]

$$\hbar\,\Delta\omega = -\frac{1}{2}\left\langle \Delta\boldsymbol{p}(t)\bullet\boldsymbol{E}_0(r_j,t)\right\rangle_t = -\frac{1}{4}\mathrm{Re}[\boldsymbol{E}_0(r_j)^*\bullet\Delta\underset{\sim}{\alpha}_j\bullet\boldsymbol{E}_0(r_j)], \tag{2}$$

where $\Delta\underline{\underline{\alpha}}$ is the bio-particle's excess polarizability tensor. By dividing this energy shift by the energy of the mode

$$\hbar\omega_r = (1/2)\int \varepsilon(r)\, \boldsymbol{E}_0(r)^* \bullet \boldsymbol{E}_0(r)\, dV \tag{3}$$

we arrive at a useful expression for the shift associated with a single bio-particle interaction,

$$\left(\frac{\Delta\omega}{\omega_r}\right)_j = -\frac{\mathrm{Re}[\boldsymbol{E}_0(r_j)^* \bullet \Delta\underline{\underline{\alpha}}_j \bullet \boldsymbol{E}_0(r_j)]}{2\int \varepsilon(r)\, \boldsymbol{E}_0(r)^* \bullet \boldsymbol{E}_0(r)\, dV} \tag{4}$$

where $\varepsilon(r)$ is the dielectric function within the microparticle and in its surroundings (absent the bio-particle). By simply switching from a real to imaginary operator in Eq. (4) one may also obtain an expression for the change in the linewidth $\Delta\gamma$ of the resonant mode due to molecular absorption,

$$\left(\frac{\Delta\gamma}{\omega_r}\right)_j = \frac{\mathrm{Im}[\boldsymbol{E}_0(r_j)^* \bullet \Delta\underline{\underline{\alpha}}_j \bullet \boldsymbol{E}_0(r_j)]}{2\int \varepsilon(r)\, \boldsymbol{E}_0(r)^* \bullet \boldsymbol{E}_0(r)\, dV} \tag{5}$$

For our experiments, $\Delta\underline{\underline{\alpha}}$ can be assumed to have no imaginary part, since experiments will be carried out at low enough energies to avoid absorption and scattering by protein or DNA. Consequently our prmary probe to interation is Eq. (4).

So long as one uses photon energies well below excited electronic states, water-soluble proteins have dielectric properties that deviate less than 1% from one to another. In addition they also share very similar mass densities. On this basis the trace of the polarizability tensor is proportional to the volume of the protein [11], and to the mass. This allows the Whispering Gallery Mode Biosensor (WGMB) to enjoy a distinct advantage. The resonance shift contributed by a protein contains molecular weight and size information. This is distinct from sensing schemes that use labels or detection involving protein charge [7, 12]. Another distinct advantage is contained within the form of the interaction.

Since the shift is proportional to $\boldsymbol{E}_0(r_j)^* \bullet \Delta\underline{\underline{\alpha}}_j \bullet \boldsymbol{E}_0(r_j)$, a non-spherical protein molecule when adsorbed on a surface will show a different shift for a field polarized perpendicular to the interface (TM polarization) than for the parallel case (TE polarization). This approach has recently been used for determining the orientation of the protein Bovine Serum Albumin (BSA) on a silica microsphere in biological buffer [13].

However, many viruses that infect our cells are nearly spherical. For example HIV, HPV, and HSV are icosahedral. This is fortunate since the excess polarizability tensor for such a shape is essentially diagonal with identical elements (i.e. isotropic), and the basic interaction between the field and the bio-particle at r_j in Eq. (4) may be written as

$$\boldsymbol{E}_0(r_j)^* \bullet \Delta\underline{\underline{\alpha}}_j \bullet \boldsymbol{E}_0(r_j) = \Delta\alpha_j \ \boldsymbol{E}_0(r_j)^* \bullet \boldsymbol{E}_0(r_j) \tag{6}$$

On this basis the shift due to a single bio-particle perturbation is

$$\left(\frac{\Delta\omega}{\omega_r}\right)_j = -\frac{\Delta\alpha_j \ \boldsymbol{E}_0(r_j) \bullet \boldsymbol{E}_0(r_j)^*}{2\int \varepsilon(r)\, \boldsymbol{E}_0(r)^* \bullet \boldsymbol{E}_0(r)\ dV} \tag{7}$$

The shift caused by a large number of bio-particles is most easily computed by assuming that the field at a particular bio-particle is not influenced by the contributions from its neighbors [14], so that Eq. (7) can be summed over a number density $\rho(\mathbf{r})$,

$$\left(\frac{\Delta\omega}{\omega_r}\right) = -\frac{\int \rho(r)\, \Delta\alpha(r)\ \boldsymbol{E}_0(r) \bullet \boldsymbol{E}_0(r)^*\, dV}{2\int \varepsilon(r)\, \boldsymbol{E}_0(r)^* \bullet \boldsymbol{E}_0(r)\ dV} \tag{8}$$

By taking a more condensed view (i.e. $\rho(r) \gg \lambda^{-3}$), the factor $\rho(r)\Delta\alpha(r)\boldsymbol{E}_0(r)$ within the integrand in Eq. (8) may be replaced by $\Delta\varepsilon(r)\ \boldsymbol{E}_{in}(r)$ where $\Delta\varepsilon(r)$ and $\boldsymbol{E}_{in}(r)$ are the excess permittivity and the "true" local field at r respectively. With this Maxwellian approach, a truly continuum equation for the frequency shift perturbation evolves

$$\left(\frac{\Delta\omega}{\omega_r}\right) = -\frac{\int \Delta\varepsilon(r)\ \boldsymbol{E}_{in}(r) \bullet \boldsymbol{E}_0(r)^*\, dV}{2\int \varepsilon(r)\, \boldsymbol{E}_0(r)^* \bullet \boldsymbol{E}_0(r)\ dV} \tag{9}$$

This is a familiar result obtained from traditional perturbation theory for dielectric particles within metallic cavities [15] and near dielectric cavities [16]. Our approach of starting from a molecular property is somewhat non-traditional, however it leaves us with several useful results for perturbations that are discrete (Eq. (4)) or continuous (Eq. (9)).

Equation (9) may be applied to analyte molecules in solution as well as those adsorbed. The former, which is normally referred to as refractive index sensing, is of little interest to our current investigation.

Up to this point our theoretical description has had little to do with a microsphere resonator. We can apply the description equally well to WGM resonators having cylindrical or toroidal geometries, or to photonic crystal cavities.

For comparison with the experiments to follow we will now concentrate on virus and on the use of a spherical WGM cavity. For virus of radius a less than the characteristic evanescent intensity length L_e, Eq. (7) is more straight forward than Eq. (9). The field polarizing the virus may be considered to be the field at the resonator surface times the evanescent attenuation factor $exp(-\xi/L_e)$ associated with the separation between the center of the virus and the resonators surface (i.e. $\xi = r_j - R$). The mode which will give the largest frequency shift is the one with the smallest mode volume. For a spherical resonator this mode is the one for which the azimuthal and orbital quantum numbers are equal (i.e. $m = l$). It is easily excited

with a tapered optical fiber, and its field amplitude $\boldsymbol{E}_0$ is obtained from a solution of the vector Helmholtz equation which handly separates into the product of a spherical Bessel function and a vector spherical harmonic, $\boldsymbol{E}_0 = A_{\text{in}} j_l(n_s k_0 r)\hat{\boldsymbol{L}} Y_{ll}$, where n_s is the sphere's refractive index and k_0 is the propagation constant in vacuum. With all of these considerations Eq. (7) becomes

$$\left(\frac{\Delta\omega}{\omega_r}\right)_j \approx -\frac{\Delta\alpha_j \left[j_l(n_s k_0 R)\right]^2 \left|\hat{\boldsymbol{L}} Y_{ll}\right|^2 e^{-(r_j - R)/L}}{2\varepsilon_s \int \left[j_l(n_s k_0 r)\right]^2 r^2 dr \int \left|\hat{\boldsymbol{L}} Y_{ll}\right|^2 \sin(\theta) d\theta d\phi}, \tag{10}$$

where we have evaluated the energy in the denominator of Eq. (7) by only including the field within the interior of the sphere, since this corresponds to more than 95% of the total energy.

Some more simplifications are now in order: For $l \gg 1, \left|\hat{\boldsymbol{L}} Y_{ll}\right|^2 \propto \left|Y_{ll}\right|^2$.[17] In addition, the spherical harmonic is normalized with respect to solid angle, $\oint \left|Y_{ll}\right|^2 d\Omega = 1$, which reduces Eq. (10) to:

$$\left(\frac{\Delta\omega}{\omega_r}\right)_j \approx -\frac{\Delta\alpha_j \left[j_l(n_s k_0 R)\right]^2 \left|Y_{ll}\right|^2 e^{-(r_j - R)/L}}{2\varepsilon_s \int \left[j_l(n_s k_0 r)\right]^2 r^2 dr}. \tag{11}$$

On resonance, the integral in the denominator of Eq. (11) may be asymptotically $(2\pi R/\lambda \gg 1)$ related to the surface value of j_l^2 through

$$\int_0^R [j_l(n_s k_0 r)]^2 r^2 dr \cong \frac{R^3}{2} [j_l(n_s k_0 R)]^2 \frac{n_s^2 - n_m^2}{n_s^2} \tag{12}$$

where n_m is the refractive index of the surrounding medium [18]. By combining Eq. (11) with Eq. (12), the shift due to a single bio-particle appears,

$$\left(\frac{\Delta\omega}{\omega_r}\right)_j \approx -\frac{\Delta\alpha_j \left|Y_{ll}(\hat{r}_j)\right|^2 e^{-(r_j - R)/L}}{\varepsilon_0 R^3 \left(n_s^2 - n_m^2\right)} \tag{13}$$

where ε_0 is the permittivity of free space $(\varepsilon_0 = \varepsilon_s / n_s)^2$, and the unit position vector $\hat{r}_j$ is used to denote the angular orientation at which the spherical harmonic is evaluated. This result does not depend on the resonance order, but possesses a strong dependence on polar angle and microsphere radius. In particular, the spherical harmonic in Eq. (13) has a square modulus that peaks at $(\theta = 90^o)$, producing a "band" of sensitivity around

the equator (Fig. 3). With Eq. (13) in hand it is now possible to estimate the limit of detection (LOD).

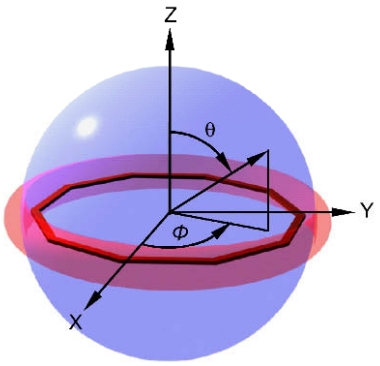

Figure 3. Depiction of the intensity associated with an equatorial mode $(l = m)$.

We will first concentrate on this equatorial region since particles adhering to this region produce the largest possible shift. For a small number of virus particles N we will assume that each particle produces an equivalent shift. To estimate the smallest detectable number N_{LOD} we allow $|\Delta\omega|$ in Eq. (13) to be equal to $|\Delta\omega|_{\min}$ in Eq. (1);

$$N_{LOD} \approx \frac{R^3 \left(n_s^{\,2} - n_m^{\,2}\right) F}{(\Delta\alpha/\varepsilon_0)\left|Y_{ll}(\pi/2)\right|^2 Q\, e^{-a/L_e}} \tag{14}$$

N_{LOD} is controlled by a number of factors. Since purified silica is readily available (i.e. optical fiber) and easily shaped, we choose silica for the microsphere. We assume the virus to be blood borne, so the medium will be essentially aqueous. F is fixed by the measurement system and fluctuation theory, however we find that a 10 Hz bandwidth can be achieved with F = 1/50, and we will use this number in subsequent calculations. Microsphere size plays a critical role. It explicitly affects the R^3 factor in the numerator, and implicitly affects the $\left|Y_{ll}(\pi/2)\right|^2 Q$ factor in the denominator. At a fixed wavelength the spherical harmonic factor increases with l, and therefore increases with R. For large l , $\left|Y_{ll}(\pi/2)\right|^2 \sim R^{1/2}$~, so $R^3/\left|Y_{ll}(\pi/2)\right|^2 \sim R^{5/2}$. As for Q, the story is more complicated. Q is a measure of the rate at which a mode's energy decays (i.e. $\gamma = \omega/Q$). The paths for decay are numerous including loss rates due to intrinsic leakage associated with diffractive "tunneling" through the curved surface (ω/Q_{int}), absorption (ω/Q_{abs}), Raman scattering (ω/Q_{Raman}) and Raleigh scattering ($\omega/Q_{Raleigh}$), including surface roughness); $(\omega/Q) = \omega/Q_{\text{int}} + \omega/Q_{abs} + \omega/Q_{Raman} + \omega/Q_{Raleigh}$. Surface scattering is expected to limit the ultimate Q for a large silica sphere in vacuum (~10^{12}) [19]. For our experiments in aqueous buffer

solution, Q for spheres with radii from 20 to 200 μm is limited to values orders of magnitude below the ultimate vacuum value due to loss of dielectric contrast (i.e. increased tunneling) and absorption;

$$\frac{1}{Q} \approx \frac{1}{Q_{\text{int}}} + \frac{1}{Q_{abs}} \tag{15}$$

As R increases above 20 μm, both tunneling and absorption decrease, causing $1/Q$ to decrease faster than $R^{-5/2}$. As a result N_{LOD} decreases with increasing R. But tunneling decreases much more rapidly than absorption causing it to have a minority influence as the size further increases. This causes N_{LOD} to begin to increase. A theoretical plot for N_{LOD} for HIV virus particles as a function of the silica sphere radius for two wavelength regions, 1,300 and 780 nm is shown in Fig. 4.

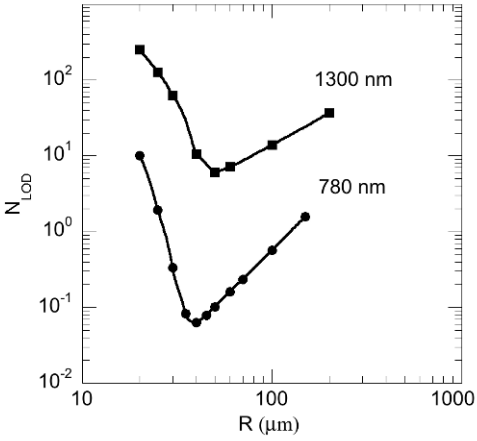

Figure 4. Smallest theoretical detectable number of HIV virus particles adsorbed on the equatorial rim of a homogeneous silica WGMB as a function of microsphere radius R for F = 1/50, and wavelength near 1,300 or 780 nm.

The substantially smaller N_{LOD} values in the 780 nm region are due to considerably smaller absorption by water at this wavelength. At either wavelength we predict very high sensitivity, with N_{LOD} dipping below one tenth at 780 nm for a microsphere approximately 40 μm in radius. Our calculations are essentially saying that it may be possible to detect virus one tenth the mass of HIV.

Figure 4 was constructed from an estimate of the HIV polarizability. Although the excess polarizability of HIV has not been measured it is not difficult to estimate $\Delta\alpha$ from the virus' mass. Viruses are principally composed of protein and protein has the convenient property of raising the refractive index of an aqueous solution by

nearly the same amount for the same mass concentration; the differential refractive index of protein in an aqueous buffer $dn/dc \approx 0.18$ cm^3/g (visible) [20]. Tobacco mosaic virus (TMV) is one of the few examples for which dn/dc has been measured and the correspondence with protein verified ($\lambda = 488$ nm) [21]. Although dispersion is projected to lower dn/dc by 0.006 between 780 and 1,300 nm [22], we have neglected this difference and used the visible value for our calculations. The excess polarizability is related to dn/dc and the molecular mass m through

$$\frac{\Delta\alpha}{\varepsilon_0} = 2n_m \frac{dn}{dc} m \,. \tag{16}$$

HIV is a fusion virus with a lipid bilayer surrounding its capsid. From the density and average size of the viral particle (110 nm) we estimate its mass to be 8×10^{-16} g, and $\Delta\alpha/\varepsilon_0$ from Eq. (16) to be 4×10^{-4} μm^3.

Although we will capture virus particles from a fluid flow, we are currently not at the point of having them deposit only at the micro-sphere equator. Instead the entire spherical surface will be functionalized. Here the more relevant question is the theoretical limit of detection associated with surface mass density, $\sigma_{m,LOD}$, which is derived by adding individual frequency shifts (Eq. (13)) from bio-particles placed at random positions on the surface and setting this overall shift to the minimum measurable shift (Eq. (1)). Before calculating $\sigma_{m,LOD}$ we will first obtain the shift due to a uniform layer of bio-particles.

The frequency shift due to a random layer of bioparticles is found by summing Eq. (13) over random position coordinates on the microsphere surface. This discrete sum may be made continuous by defining a number of adsorbates per unit solid angle $dN/d\Omega = \sigma 4\pi R^2/4\pi$, and integrating over solid angle,

$$\frac{|\Delta\omega|}{\omega_r} = \frac{\Delta\alpha \;\; \sigma e^{-a/L_e}}{\varepsilon_0 \left(n_s^{\,2} - n_m^{\,2}\right) R} \tag{17}$$

We can now calculate the limit of detection for surface mass density by setting $\sigma = \sigma_{m,LOD}/m$ in Eq. (17). The results for 760 and 1,300 nm are shown in Fig. 5. It should be noted that we have indicated the typical baseline sensitivity levels for other label free sensing techniques in Fig. 5. Interestingly the sensitivity for the WGMB at 1,300 nm for a relatively large microsphere (200 μm) is potentially better than the typical baseline sensitivity for the Quartz Crystal Microbalance (QCM), SPR [23], or micro-cantilevers (MC) [24], and the minimum on the 780 nm curve beats the best of these by more than two orders of magnitude.

In what follows we will describe our experimental approach, and present our results on specific virus sensing ans single particle and virus detection.

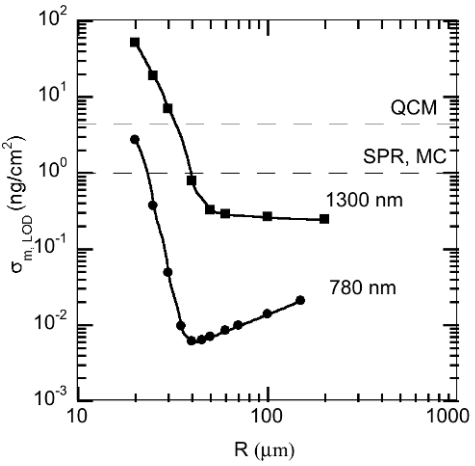

Figure 5. Smallest theoretical detectable uniform mass density on a silica WGMB as a function of microsphere radius R for F = 1/50, and wavelength near 1,300 or 780 nm.

4. Experimental Approach

The WGM resonator was originally formed from silica by rotating the end of a bare telecommunication fiber in an oxygen–propane micro-flame. The end of the glass softens and flows into a spheroidal shape. These spheroids are oblate with an eccentricity ~6% and equatorial radii near 200 μm. The resonator is driven by evanescently coupling at its equator to a tapered optical fiber waveguide. Excitation of a micro-spheroid mode is signaled by a dip in the transmission through the fiber [25]. The resolution in our experiments is controlled by the linewidth of a Distributed Feedback Laser (DFB, < 0.00001 nm). Movement of the resonance dip tracks the perturbation in the frequency/wavelength of a resonance by using a five point parabolic fit. Frequency/wavelength positions are recorded every 200 ms as a "dip trace". For a resonance having a Q~10^6, the fluctuations in the base line of the dip trace have an rms value as small as 0.00002 nm for a time period of 5 s. In what follows we will present our experimental results for specific detection with discrimination between similar viruses. These experiments and the theoretical investigations further helped us to achieve single nanoparticle and single virion detection.

4.1. SPECIFIC ADSORPTION EXPERIMENTS

Specific sensing was tested through the difference in desorption rates asociated with different virus on a surface functionalized with antibody. This was done by utilizing a microfluidic flow system that incorporates the microsphere and a tapered optical fiber. Our specific sensing system is shown in Fig. 6.

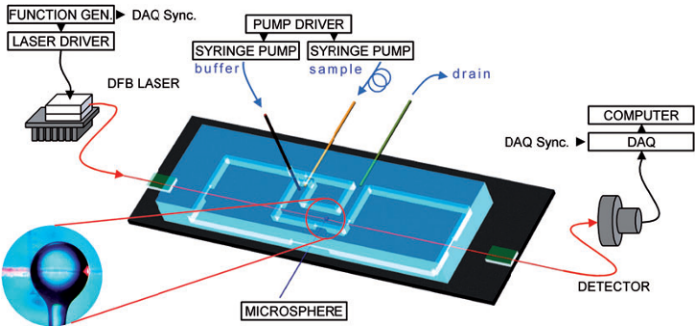

Figure 6. Microfluidic system for sensing.

It consists of a tapered fiber bound to a glass slide as a foundation. Below this foundation is a thermoelectric stage, and above it is a polymer cap (PDMS) with multiple entry points. The microfluidic channel has a total volume of 100 μL. A fluidic system was designed to handle the various solutions used in our experiments. It consists of two syringe pumps that are directed by a custom LabVIEW program. One pump is dedicated to the buffer used for washing in between each sample injection. The other is the sample pump that pushes the contents of a 700 μL teflon sample loop into the fluidic channel. The loop is washed with buffer between each sample injection, insuring that the syringe is free of cross-sample contamination. The surface was modified for specific virus detection as anti-MS2 (in PBS, pH 7.4, Tetracore) antibodies were covalently linked to the microsphere using amine–carboxyl coupling chemistry [5].

In order to discriminate between different virus we designed a cycling scheme which included another E.coli virus, Phix174, as a negative control. Phix174 is a DNA virus of icosahedral shape and has a mass and diameter of 6.2×10^6 Da [26] and 28.4 nm, respectively. Its coat proteins contain epitopes different from MS2 virus, and therefore should not exhibit specific binding to our anchored anti-MS2. As a first step 500 μL of MS2 phage at a final concentration of 2.5 pM was flowed through the microfluidic channel, and then the pump was turned off. MS2 was allowed to bind to surface for 5 min. The microsphere resonators radii, used in these experiments, were 200 μm and the wavelenght of WGM excitation was 1,312 nm. We observed that all resonant dips shifted to longer wavelengths indicating interaction between the modified surface and virus. Just after, PBS was flowed into the channel for 10 min and there was no evidence of desorption. At higher concentration (5 pM) however, we observed a resonance frequency shift towards smaller wavelength, indicating that weakly bound virus was present on our surface. The residual surface bound MS2 after this wash was calculated (from Eq. (17) soled for σ) to be $\sigma_v = 9 \times 10^9$ cm^{-2} which is far less than the maximum density for random sequential adsorption, even though there are an average of five antibodies within an MS2 footprint. We conclude that only a small fraction of the antibodies are viable for specific adsorption. After a surface regeneration step the microsphere was ready for reuse with another virus (e.g. the control Phix174). Phix174 was injected into the cell at 5 pM and allowed to bind as above. After injection the

frequency shifted toward longer wavelength, reaching equilibrium before the pump was turned off. After PBS was pumped into the channel for 100 s the wavelength dropped toward the baseline, indicating that Phix174 was nonspecifically bound to the surface. Figure 7 clearly shows that the WGMB technique can discriminate between the nonspecific binding by Phix174 and specific binding by MS2. The experiments were repeated several times with similar results.

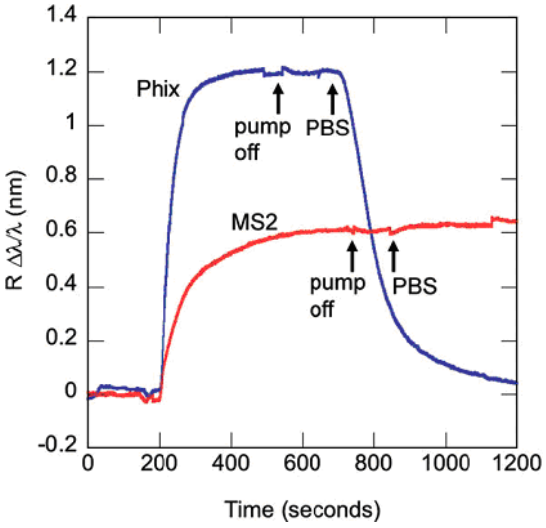

Figure 7. Comparison between Phix174 and MS2 experiments on the same sphere.

By using perturbation ideas from microparticle photophysics, combined with biochemical surface functionalization and microfluidics, we have found a means for specifically sensing virus. However we did not observe single particle steps. In what follows we show that principle reason was the large mode volume associate with our microspheres, and the relatively small masses of MS2 and Phix-174 in comparison with human viruses such as HIV or InfluenzaA.

4.2. SINGLE PARTICLE NONSPECIFIC ADSORPTION EXPERIMENTS

As the theoretical resoning presented in part 3 suggested WGM resonances are perturbed towards longer wavelength as particles with polarizability in excess to that of water adsorb to a microsphere cavity. Individual binding events should ideally produce discrete steps in a time-trace of the wavelength shift. The previous experiment did not take advantage of the signal enhancement which could be produced by reducing the cavity dimensions (i.e. radius, Fig. 4). Consequently to probe for single binding events we required more localized heating to produce smaller spheres. Microspheres were fabricated from tapered optical fiber tips that are melted in a focused 10 W CO_2 laser which allowed us to produce silica microspheres with radii

between 30 and 50 μm. At first the microsphere was immered in a suspension of relativly large polystyrene particles (PS) with radius a = 250 nm (Fig. 8). The PS particles are diluted in phosphate buffer (PBS) to final concentrations ~10–50 fM.

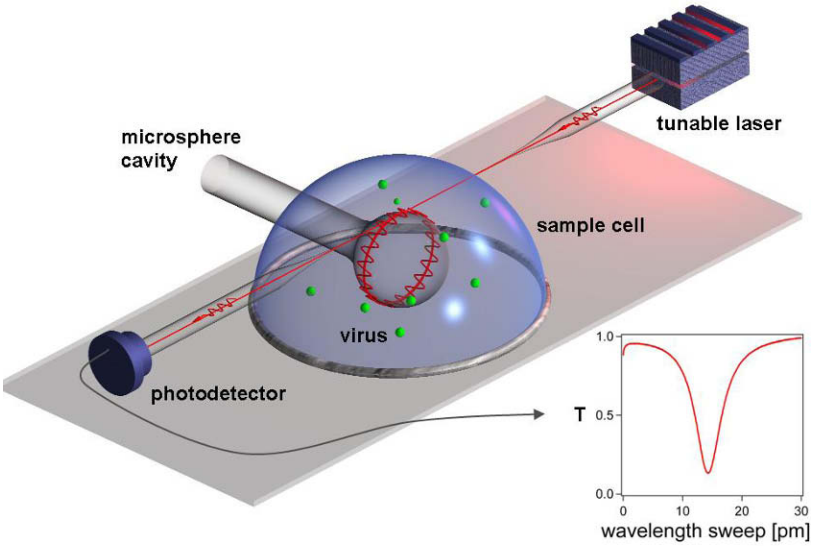

Figure 8. Excitation of an equatorial WGM of a microsphere by evanescent coupling to a guided wave in a tapered optical fiber. Resonance positions are detected as dips in the transmitted light T at particular laser wavelengths.

Figure 8 (inset) shows the typical transmission spectrum for a WGM excited in silica microsphere (here radius R ~ 50 μm) immersed in aqueous solution. The linewidth $\delta\lambda \sim 5$ pm, as determined from the full width at half-maximum, corresponds to a Q-factor $Q = \lambda/\delta\lambda \sim 2.6 \times 10^5$, primarily limited by overtone vibrational absorption of water in the near infrared [27]. Immediately after fabrication, the microsphere-on-a-stem is mounted on the sample cell and immersed in PBS solution. A small box encloses the sample cell to limit air flow and stabilize the ambient humidity level. A transmission spectrum is acquired every ~20 ms, and the resonance wavelength is determined from a parabolic minimum fit to the Lorentzian-line, typically with precision ~1% of the linewidth. The dip-trace is displayed as fractional shift in wavelength $\Delta\lambda/\lambda$. Figure 9 shows a trace of $\Delta\lambda/\lambda$ for a = 250 nm PS particles interacting with a microsphere with $R \sim 45$ μm. Steps of various heights are clearly visible against the background cavity noise indicating adsorption of individual PS particles. With the ability to detect discrete steps and identify optimal step height within a dip trace for a given nanoparticle radius, we can now direct our attention toward measuring the dependence of the optimal shift signal on the microsphere curvature.

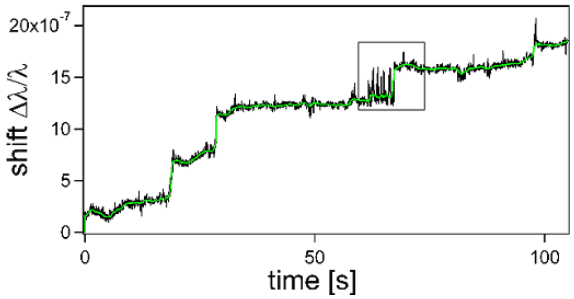

Figure 9. Dip-trace for a = 250 nm PS particles interacting with a microsphere with $R \sim 45$ μm.

We experiment with different-sized microspheres (R = 44 μm – 105 μm) and plot maximum step heights versus curvature (i.e. 1/R, Fig. 10). Interestingly, we find a strong dependence of the fractional wavelength shift on the cavity radius, scaling as $R^{-2.67}$. This is in good agreement with electromagnetic theory associated with reactive WGM sensing (reactive sensing principle RSP), discussed in part 3 predicting a maximum step heights in proportion to $R^{-2.5}$ for a single binding event. The largest step heights are predicted for protein particles binding to the equator, whereas a *~1/R* dependence [10] is expected for a shift due to a random surface density [4]. The small discrepancy in the exponent (–2.67 vs –2.5) in our PS particle experiments may be explained by an increase in the evanescent interaction caused by a slight lengthening in the evanescent field depth L as the microsphere size is decreased, and is associated with large particles adsorbed for which $a/L \sim 1$. For particles that are small compared with the evanescent field depth, such as protein or InfA virus, our optimal wavelength shifts are consistent with the reactive theory, but the weak signal associated with these smaller particles prohibits us from acquiring data over a wide range of microsphere sizes.

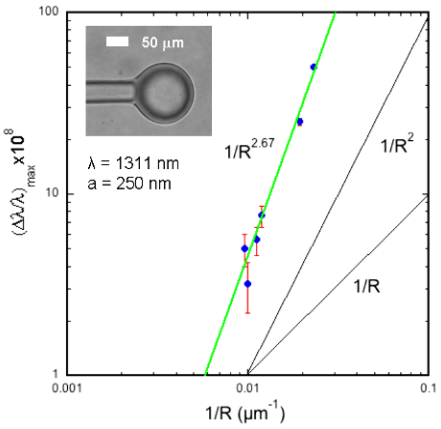

Figure 10. Maximum step height versus microsphere curvature for polystyrene particles with radius a = 250 nm.

Having identified a means for enhancing the shift magnitude by reducing microcavity size, we set out to optimize the microsphere system for the detection of single InfA virions. InfA virions have an average radius $a \sim 50$ nm [28], and a refractive index below that of PS. Although our microcavity fabrication method would allow us to take further advantage of the large curvature enhancement of the wavelength shift signal by forming smaller cavities, the success of this approach is limited: further reduction of cavity size also increases cavity leakage (Fig. 4) so that any gain in sensitivity due to shift enhancement is offset by a broadening of the resonance linewidth. Instead, we find that further increase in sensitivity is possible if we additionally scale down the wavelength λ. A wavelength shorter than 1,311 nm is also favorable due to less absorption in water. Following this approach, we use DFB laser with $\lambda \sim 763$ nm and excite a WGM with $Q \sim 6.4 \times 10^5$ in $R = 39$ μm microspheres. We inject InfA virions at concentration of ~10 fM directly into a PBS filled sample cell, since the virions are known to adsorb to silica [29]. The dip-trace of the resonance wavelength $\Delta\lambda_{InfA}/\lambda$ in Fig. 11 reveals clear steps associated with binding of single viral particles. The signal-to-noise ratio ($\Delta\lambda_{InfA}/\Delta\lambda_{noise} \sim 3$) can be further improved upon by signal processing schemes such as Median filtering; the solid line in Fig. 11 shows a Median filter of rank 3.

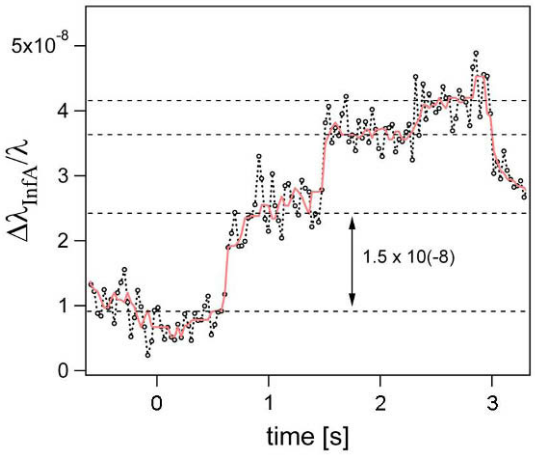

Figure 11. Shift signal for InfA. The data was acquired for a microsphere with R = 39 μm, and a DFB laser having a nominal wavelength of 763 nm.

High sensitivity measurements of individual virus particles are made possible by reducing modal volume, a principle that should also apply to other WGM cavity geometries, [30] as well as other non-WGM micro-cavities (e.g. photonic crystals with "defects").

Equation (13) provides a clear statement with respect to the dependence of the wavelength shift on microsphere curvature, and our polystyrene experiments agree well with respect to the exponent. Further evidence for the reactive mechanism results by comparing the nominal radii of the particles used in our experiments with the radii

arrived from the maximum measured wavelength shifts. Equation (13) may be inverted to obtain the virion radius a_v from a measurement of the maximum shift [6].

$$a_v \cong \frac{a_0}{1-\frac{a_0}{3L}}, \tag{18}$$

where $L \approx (\lambda/4\pi)(n_s^2 - n_m^2)^{-1/2}$ is the evanescent length and a_0 is:

$$a_0 \cong R^{5/6}\frac{\lambda_r^{1/6}}{D^{1/3}}\left(\frac{\Delta\lambda_r}{\lambda_r}\right)^{1/3}_{\max}, \tag{19}$$

where $D = 2n_m^2\,(2n_s)^{1/2}(n_{np}^2 - n_m^2)/(n_s^2 - n_m^2)(n_{np}^2 + 2n_m^2)$ is a dielectric factor, and n_s, n_m, and n_{np} are the refractive indices of the microsphere (1.45), aqueous medium (1.33), and nanoparticle (1.5 for virus and 1.59 for polystyrene; D = 1.50 and 2.26 respectively). These results are summarized in Table 1:

TABLE 1. A comparison of the particle size calculated from the wavelength shift with the expected size

Particle, radius	Wavelength λ (nm)	Cavity radius R (μm)	Max.expt.step $(\Delta\lambda/\lambda)_{max}$	Radius from Eq. 19, a (nm)
PS, 250 nm, σ < 5	1,311	44	5×10^{-7}	211
PS, 100 nm, σ < 5%	763	30	2.2×10^{-7}	100
InfA, SEM[a] 45–55 nm	763	39	1.5×10^{-8}	47

[a] Scanning Electron Microscope

We note that our measurements agree well with Eq. (19) for a < 250 nm. We also would like to point out that the estimate of radius is a lower limit since only few particles bind directly on the equator. The mass m_v of the InfA virion can now be evaluated from its volume times its density to be 5.2×10^{-16} g, in agreement with results for InfA's molecular weight found from the sedimentation in density gradients based on a statistical number of viruses (~3×10^8 g/mol).[31]

Prior to the single steps for the nanoparticles in Fig. 9 we occasionally observe fluctuations with amplitudes approaching the height of the adsorption step. These fluctuations occur over a period much larger than the time to freely diffuse though the evanescent length L_e. This phenomenon led us to question whether interfacial and optical forces might be forming a trap near the surface. Indeed this was the case and the physical interpretation of these fluctuations revealed the trapping potential and the nanoparticle size. This potential is responsible for increased transport of target nanoparticles to the sensing volume. In what follows we will describe and analyze what has become known as the Carousel Trap.

4.3. WGM CAROUSEL BIOSENSOR

Nanoparticles suspended in an aqueous environment normally appear to be in Brownian motion. However, we observe in the vicinity of a bare silica microsphere (radius $R \approx 50$ μm) excited into a circulating WGM (quality factor $Q \sim 10^6$), nanoparticles as small as 140 nm radius (a) are trapped for hundreds of seconds in orbit within the sensing volume with driving light power $P \approx 50$ μW. As shown in Fig. 12a, these nanoparticles appear to circumnavigate in the direction that light takes within the WGM. The nanoparticle concentration was ≈ 1 fM in D_2O (D_2O was used to minimize absorption loss in the infrared).

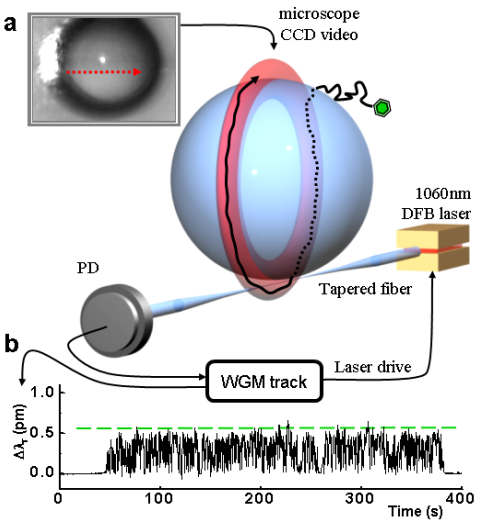

Figure 12. WGM-Carousel-Trap. (a) WGM excited in a microsphere (radius R = 53 μm) with Q = 1.2 × 10^6 by a 1,060 nm tunable laser using fiber-evanescent-coupling. The resonance wavelength is tracked from a dip in the transmitted light (PD). An elastic scattering image shows a polystyrene particle (radius a = 375 nm) trapped and circumnavigating at 2.6 μm/s using a drive power of 32 μW. (b) A particle is sensed through resonance wavelength fluctuations $\Delta\lambda_r$ that identify its size/mass. These fluctuations are recorded from before the particle enters the Carousel-trap until after it escapes ≈ 6 min later.

Fractional fluctuations in the resonance wavelength from the background level $\Delta\lambda_r/\lambda_r$ are clearly due to perturbations in the WGM as the result of nanoparticle's interaction with the microcavity, and are equal at each instant to the ratio of the energy polarizing the particle W_p to the energy in the cavity W_c [10],

$$\Delta\lambda_r/\lambda_r = W_p/W_c \tag{20}$$

The shift $\Delta\lambda_r$ is therefore independent of the power driving the resonator but is proportional in a dipole approximation to the ratio of the intensity at the nanoparticle's center r_c to the energy in the mode; $\Delta\lambda_r(r_c) \propto E_0^2(r_c)\Big/\left\langle \varepsilon(r)E_0^2(r)\right\rangle$, where E_0 is the electric field amplitude and $\varepsilon(r)$ is the modal permittivity. For the lowest order angular wave excited in our experiments the intensity function is symmetrical about the equator with a Gaussian-like shape, and falls off at "latitudes" on either side with a characteristic width $w \approx 6$ μm. In contrast, in the radial direction the intensity falls off as the square of a spherical Hankel function which is well approximated by a decaying exponentially with a much shorter "evanescent length" $L \approx 150$ nm. Images of the particle's orbit show it traveling along the equator with a root mean square transverse displacement to either side of <1.5 μm. The time to diffuse over this distance for our typical nanoparticle is several seconds, whereas the observed fluctuations in $\Delta\lambda_r$ occur much faster: over a time scale associated with diffusion through a length ~100 nm. Consequently, these fluctuations are due to changes in the interfacial separation h between the nanoparticle's surface and the surface of the microsphere, with the maximum fluctuation occurring at $h \approx 0$ (i.e. green line in Fig. 12b). Translating other wavelength shift levels into h values is critical to our analysis. Fortunately, this translation is easily implemented. Based on the RSP [10] the wavelength shift for the nanoparticle's center at $h + a$ to that on the surface is

$$\frac{\Delta\lambda_r(h+a)}{\Delta\lambda_r(a)} = \frac{\exp[-(h+a)/L]}{\exp[-a/L]} = \exp[-h/L]. \tag{21}$$

Equation (21) enables wavelength shift statistics to be transformed into separation statistics. The results are particularly revealing. Figure 13 shows the separation histogram taken on a nanoparticle (a = 140 nm) that circumnavigated a microsphere for just over two orbits.

A pronounced maximum is seen at $h \cong 35\,\text{nm}$ from the sensing surface. The peak is indicative of a surface repulsion that becomes more evident by translating these separation statistics into a potential curve using equilibrium statistical mechanics.

Under the assumption of thermal equilibrium the Boltzmann distribution relates the potential $U(h)$ to the probability density $p(h)$; $U(h) = -k_B T \ln[p(h)/p(h_{ref})]$, where h_{ref} is a reference separation for which $U(h_{ref}) = 0$. Figure 12b shows the result. The particle is clearly trapped in a radial potential well with its minimum 35 nm from the surface as it is driven to orbit by the WGM's tangential momentum flux. These potential points were fit by a sum of two exponentials: a short-range repulsive interaction $U_s/k_BT = 6.2\exp\left[-h/(17.6\text{ nm})\right]$, and a long-range attractive interaction $U_p/k_BT = -8.0\exp\left[-h/(142.7\text{ nm})\right]$. The latter supports our hypothesis that the particle's motion is principally radial; its characteristic length of 143 nm is close to the evanescent length in the radial direction (146 nm). The attractive force arising from this potential is similar to the gradient force in optical tweezer experiments, for which the potential in the equatorial plane is expected to be the negative of the polarization energy,

$U_p(h) \approx -(\alpha_{ex}/4)E_0^2(a)\exp(-h/L)$ where α_{ex} is the nanoparticle's polarizability. Indeed, a series of experiments show that the value of this "polarization potential" at the surface $U_p(0)$ is proportional to the power P entering the mode. The gradient force is aided in keeping the particle on an equatorial track by a transverse phase-gradient contribution.[32] The positive potential U_s is independent of power, and appears to be due to repulsion between ionized silanol groups on the bare silica surface (pH = 7), and the negatively charged polystyrene nanoparticle (the particles used were slightly sulfonated). The characteristic length of U_s is close to the Debye length λ_D arrived at from the measured conductivity of our medium, [33] $\lambda_D \approx 20$ nm, assuming monovalent ions. By varying the ionic conductivity of the solution one can effectively change the range of U_s. In contrast, U_p is independent of ionic conductivity and reaches much deeper into the solution. In effect the combined potential forms a "sink-hole" that draws particles toward the optimal region in the sensing volume.

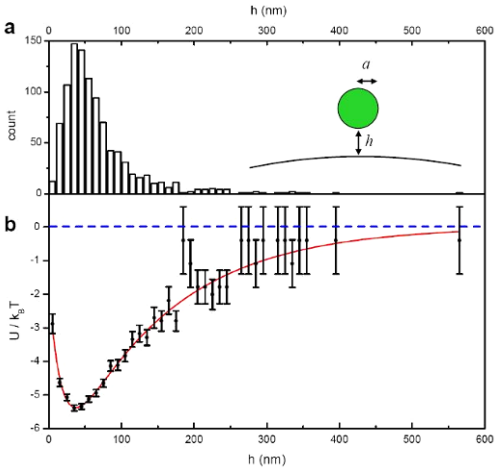

Figure 13. Separation histogram and trapping potential. (a) separation histogram collected from a single tapping event of a polystyrene (PS) particle (from mean radius <*a*> =140 nm hydrosol). The WGM with $Q = 7.3 \times 10^5$ was excited with $P = 233$ μW at $\lambda \approx 1{,}060$ nm in a microsphere with $R = 44$ μm. The statistics were comprised of 1,000 points. (b) Potential plot arrived at from the histogram in (a). These points are fit to a sum of two potentials (in red).

Carousel trapping is expected to enhance binding rate detection in the following manner: The enhanced transport increases accumulation of particles in the sensing volume, and forced re-visitations by a particle to the surface increases the probability for finding a binding site. To measure the enhancement of the transport rates we compared the case of pure diffusion driven particles by operating at an arbitrarily low polarization potential $|U_p(0)|_d \approx 0.01\ k_BT$ to the case where the polarization potential was near the threshold for escape, $|U_p(0)|_e \approx 1 k_BT$. These experiments were carried out for particles with $a = 250$ nm and for a concentration of 6 fM. In each case we counted the number of visitations to the sensing volume by registering the number of wavelength shift pulses exceeding $0.25(\Delta\lambda_r)_{\max}$. For $|U_p(0)|_d$ we detected only one visitation to the

sensing volume in 1 h. However for $|U_p(0)|_e$, 49 visitations ~1 s in duration were detected in 1 h. As the potential was increased to $|U_p(0)| > 5k_BT$, particles were strongly trapped in the Carousel, and accumulation of multiple particles over time became unavoidable. With $|U_p(0)|$ above $2k_BT$ trapping of a single particle for several minutes became highly probable, which allowed us to observe the delimited fluctuation. This limit, where the particle temporarily "touches" the surface, $(\Delta\lambda_r)_{max}$ provides a means for the determination of the particle size/mass.

The maximum wavelength shift signal $(\Delta\lambda_r)_{max}$ registered for a given laser-resonator combination appears to depend only on the size and dielectric properties of the orbiting nanoparticle. This signal occurs when the particle encounters the greatest evanescent field. As the drive power is raised more of these events occur, but the largest have the same limiting value. Theory was constructed early on that related this wavelength shift to the particle's polarizability and size by using the RSP, [10, 16] but its confirmation has only come recently with the observation and measurement of single wavelength shift steps in non-specific binding experiments [6]. However, these steps were random in size, associated with particles adsorbing at different latitudes on the sphere's surface where the sensing response can vary over orders of magnitude. In the Carousel mechanism, the particles are attracted to the equator, and therefore produce uniform response in the delimited fluctuation. This allows a nanoparticle to be sized without the need for binding. This clearly opens the door for a nanoparticle size/mass spectrometer in solution. The translation from a size to a mass spectrum requires knowledge of mass density. With a microsphere for which R = 40 μm and $Q \approx 10^7$ individual bioparticles having a mass of HIV (600 ag, $a \approx$ 50 nm) should be easily sizable with $P \approx$ 50 μW at $\lambda \approx$ 780 nm. For a power of 2 mW using the same resonator a smaller virus with a = 15 nm (mass ≈ 15 ag, e.g. Poliovirus) is within reach.

Finally we return to the subject of binding. A particle caught in a Carousel orbit is in a pre-binding state which is easily converted to a binding state by reducing the range of the electrostatic repulsion and thereby allowing the optical force to pull a nanoparticle to the surface where the intrinsic van der Waal attraction can take hold. Decreasing the range of the electrostatic repulsion is accomplished by increasing the conductivity of the solution. Two separate experiments were performed on individual particles caught in Carousels for which the solution conductivities differed by an order of magnitude. The experiment at higher conductivity clearly shows the separation between the nanoparticle and the surface to be substantially reduced. An analysis of these separation statistics gave a repulsive potential for the low conductivity case corresponding to 0.5 mM NaCl of $U_s / k_BT = 6.2\exp\left[-h/(17.6\text{ nm})\right]$, whereas in the higher conductivity case corresponding to 5 mM NaCl $U_s / k_BT = 4.9\exp\left[-h/(6.1\text{ nm})\right]$. The reduction in the range of the repulsive potential by a factor of 2.9 is close to the expected reduction in the Debye length. The later is known to be inversely proportional to the square root of the salt ionic strength, thereby causing a reduction in range by a factor of 3.2 [33]. By adding 20 mM of NaCl to our D_2O solution its conductivity was increased ×40. Nanoparticles (a = 375 nm) were trapped in the Carousel and quickly bound to the surface. Figure 14a shows the first three binding events registered as uniform steps in $\Delta\lambda_r$. Although spatially random particle adsorption leads to a distribution of step heights which vary by more than an order of magnitude [6], the

constancy of the step heights in Fig. 14a shows that the equator can be spatially isolated for binding. Such characteristics were also demonstrated with smaller nanoparticles (a = 140 nm). Figure 14b shows an experiment in which several of these particles bind to the Carousel surface from a 10 fM solution over a period of 20 min.

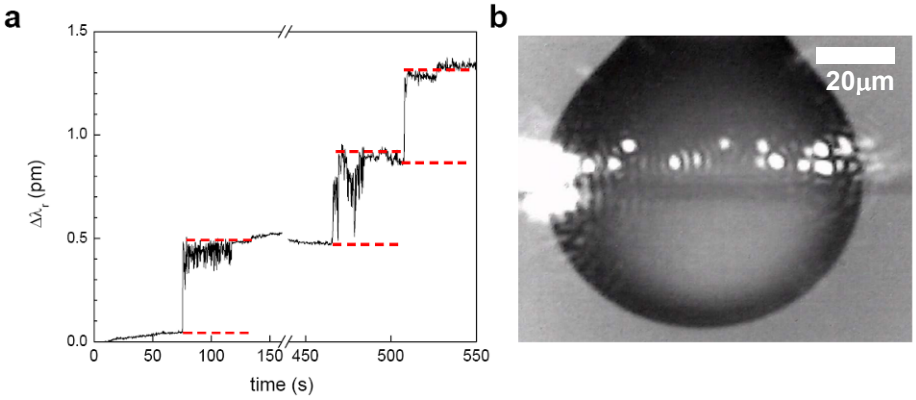

Figure 14. (a) First three binding steps of nanoparticles (a = 375 nm) on a microsphere with R = 45 μm and P = 150 μW, Q = 2×10^5, Note the uniformity in step height. Red dash separation is set to 0.45 pm. (b) Image of a = 140 nm particles trapped and bound in the Carousel orbit, R = 39 μm.

In this case, there were two parallel paths, corresponding to a mode for which quantum number $m = l - 1$, indicating that the Carousel effect exists for higher order angular modes as well. Recently a similar optical trapping mechanism was reported to further benefit from a self-induced-back-action [34].

5. Conclusions

By using perturbation ideas from microparticle photophysics, combined with biochemical surface functionalization and microfluidics, we have found a means for specifically sensing virus. The axial symmetry associated with a slightly perturbed sphere allows for simple analytical equations that connect up wavelength shifts with the polarizability and surface density of adsorbed virus. We have shown that adsorption of individual nanoparticles produce discrete changes in resonance frequency/wavelength of a WGM. Signal enhancement was achieved by reducing the size of microspherical cavities. Detection of individual InfA virions in aqueous buffer was then demonstrated directly from steps in the wavelength shift signal. Both the virus size and mass are identified from maximum step height associated with binding near the equator.

Finally, the WGM Carousel provides a mechanism for enhanced transport of bio-nanoparticles in the sensing volume. We clearly see that detection rates are not limited by diffusion, and can be increased by ~×100. In addition we discover that the new light-force mechanism provides a sensitive means for sizing individual particles and detecting their interactions with the sensor's surface. The effects produced by Carousel trapping should be difficult to avoid for viral sized nanopartices such as HIV or Influenza A,

since the power needed to form the Carousel is <200 μW. Analytical and experimental studies show that our low trapping power is due to resonant build up within the spherical microcavity structure. In addition, by controlling the ionic strength and the optical trapping power, the particles are shown to bind preferentially within the Carousel. All of this provides optical WGM sensors with a distinct advantage not afforded to non-optical devices since the attractive potential reaches out into a solution and draws nanoparticles to the optimal sensing region unabated by ionic screening.

Acknowledgments Steve Arnold thanks Rino DiBartolo for his kind invitation to lecture at this school and the National Science Foundation grant CBET 0933531 for the financial support.

References

1. Ewald, P. W. (2002) *The Next Fifty Years*, Vintage Books, New York.
2. Serpenguzel, A., Arnold, S. & Griffel, G. (1995) Excitation of Resonances of Microspheres on an Optical-Fiber, *Optics Letters* **20,** 654–656.
3. Arnold, S. (2001) Microspheres, photonic atoms and the physics of nothing, *American Scientist* **89,** 414–421.
4. Vollmer, F., Braun, D., Libchaber, A., Khoshsima, M., Teraoka, I. & Arnold, S. (2002) Protein detection by optical shift of a resonant microcavity, *Applied Physics Letters* **80,** 4057–4059.
5. Arnold, S., Ramjit, R., Keng, D., Kolchenko, V. & Teraoka, I. (2008) MicroParticle photophysics illuminates viral bio-sensing, *Faraday Discussions* **137,** 65–83.
6. Vollmer, F., Arnold, S. & Keng, D. (2008) Single Virus Detection from the Reactive Shift of a Whispering-Gallery Mode, *Proceedings of the National Academy of Sciences of the United States of America* **105,** 20701–20704.
7. Patolsky, F., Zheng, G. F., Hayden, O., Lakadamyali, M., Zhuang, X. W. & Lieber, C. M. (2004) Electrical detection of single viruses, *Proceedings of the National Academy of Sciences of the United States of America* **101,** 14017–14022.
8. Arnold, S., Keng, D., Shopova, S. I., Holler, S., Zurawsky, W. & Vollmer, F. (2009) Whispering gallery mode carousel - a photonic mechanism for enhanced nanoparticle detection in biosensing, *Optics Express* **17,** 6230–6238.
9. Gorodetsky, M. L., Savchenkov, A. A. & Ilchenko, V. S. (1996) Ultimate Q of optical microsphere resonators, *Optics Letters* **21,** 453–455.
10. Arnold, S., Khoshsima, M., Teraoka, I., Holler, S. & Vollmer, F. (2003) Shift of whispering-gallery modes in microspheres by protein adsorption, *Optics Letters* **28,** 272–274.
11. Frolich, F. (1958) *Theory of Dielectrics*, Oxford University Press, London.
12. Wang, W. U., Chen, C., Lin, K. H., Fang, Y. & Lieber, C. M. (2005) Label-free detection of small-molecule-protein interactions by using nanowire nanosensors, *Proceedings of the National Academy of Sciences of the United States of America* **102,** 3208–3212.
13. Noto, M., Keng, D., Teraoka, I. & Arnold, S. (2007) Detection of protein orientation on the silica microsphere surface using transverse electric/transverse magnetic whispering gallery modes, *Biophysical Journal* **92,** 4466–4472.
14. Teraoka, I. & Arnold, S. (2007) Dielectric property of particles at interface in random sequential adsorption and its application to whispering gallery mode resonance-shift sensors, *Journal of Applied Physics* **101,** 023505.

15. Harrington, R. P. (2001) *Time-Harmonic Electromagnetic Fields*, Wiley-IEEE Press.
16. Teraoka, I. & Arnold, S. (2006) Theory of resonance shifts in TE and TM whispering gallery modes by nonradial perturbations for sensing applications, *Journal of the Optical Society of America B-Optical Physics* **23,** 1381–1389.
17. Jackson, J. D. (1962) *Classical Electrodynamics*, Wiley, New York.
18. Khoshsima, M. (2004) Perturbation of Whispering Gallery Modes in Microspheres by Protein Adsorption: Theory and Experiment, PhD thesis in Physics Polytechnic University, New York.
19. Gorodetsky, M. L., Pryamikov, A. D. & Ilchenko, V. S. (2000) Rayleigh scattering in high-Q microspheres, *Journal of the Optical Society of America B-Optical Physics* **17,** 1051–1057.
20. Armstrong, S. H., Budka, M. J. E., Morrison, K. C. & Hasson, M. (1947) Preparation and Properties of Serum and Plasma Proteins . XII The Refractive Properties of the Proteins of Human Plasma and Certain Purified Fractions, *Journal of the American Chemical Society* **69,** 1747–1753.
21. Coles, H. J., Jennings, B. R. & Morris, V. J. (1975) Refractive-Index Increment Measurement for Bacterial Suspensions, *Physics in Medicine and Biology* **20,** 310–313.
22. Alupoaei, C. E., Olivares, J. A. & Garcia-Rubio, L. H. (2004) Quantitative spectroscopy analysis of prokaryotic cells: vegetative cells and spores, *Biosensors & Bioelectronics* **19,** 893–903.
23. Karlsson, R. & Stahlberg, R. (1995) Surface-Plasmon Resonance Detection and Multispot Sensing for Direct Monitoring of Interactions Involving Low-Molecular-Weight Analytes and for Determination of Low Affinities, *Analytical Biochemistry* **228,** 274–280.
24. Burg, T. P. & Manalis, S. R. (2003) Suspended microchannel resonators for biomolecular detection, *Applied Physics Letters* **83,** 2698–2700.
25. Griffel, G., Arnold, S., Taskent, D., Serpenguzel, A., Connolly, J. & Morris, N. (1996) Morphology-dependent resonances of a microsphere-optical fiber system, *Optics Letters* **21,** 695–697.
26. Burgess, A. B. (1969) Studies on Proteins of Phix174 .2. Protein Composition of Phix Coat, *Proceedings of the National Academy of Sciences of the United States of America* **64,** 613.
27. Collot, L., Lefevreseguin, V., Brune, M., Raimond, J. M. & Haroche, S. (1993) Very High-Q Whispering-Gallery Mode Resonances Observed on Fused-Silica Microspheres, *Europhysics Letters* **23,** 327–334.
28. Lamb, R. A. & Krug, R. M. (2001) *Fundamental Virology*, Lippincott Williams & Wilkins, Philadelphia.
29. Bresler, S. E., Bespalova, G. I., Kolikov, V. M., Zhdanov, S. P., Koromaldi, E. V., Luzyanina, T. Y. & Reikh, L. Y. (1975) Purification of Influenza-Viruses on Wide-Pore Glass Columns, *Acta Virologica* **19,** 190–196.
30. Vollmer, F. & Arnold, S. (2008) Whispering-gallery-mode biosensing: label-free detection down to single molecules, *Nature Methods* **5,** 591–596.
31. Reimer, C. B., Baker, R. S., Newlin, T. E. & Havens, M. L. (1966) Influenza Virus Purification with Zonal Ultracentrifuge, *Science* **152,** 1379–&.
32. Roichman, Y., Sun, B., Roichman, Y., Amato-Grill, J. & Grier, D. G. (2008) Optical forces arising from phase gradients, *Physical Review Letters* **100,** 013602.
33. Izraelachvili, J. N. (1987) *Intermolecular And Surfaces Forces*, Academic Press, Inc., San Diego, CA.
34. Juan, M. L., Gordon, R., Pang, Y., Eftekhari, F. & Quidant, R. (2009) Self-induced back-action optical trapping of dielectric nanoparticles, *Nature Physics* **advance online publication,** doi.org/10.1038/nphys1422.

TWO-PHOTON ABSORPTION AND APPLICATIONS TO BIOLOGICAL SYSTEMS

J. COLLINS*
Department of Physics and Astronomy
Wheaton College
Norton, MA 02766 USA

Abstract Fluorescent ions and molecules are important probes for the investigation of biological systems. To initiate the fluorescence, such ions and molecules are usually excited by absorption of a single photon. It is often advantageous, however, to excite the molecule using two or more photons. In this article we examine the multiphoton absorption process, and discuss of the advantages and disadvantages it offers for the investigation of biological systems. The main point of this article is to review the basic physics of two-photon absorption process. We also define the two-photon absorption cross section and discuss how it is measured. Finally, the advantages of two photon absorption are discussed and some applications to biological systems are presented.

1. Introduction to Two-Photon Absorption

The excitation of a molecule into an excited state involves the transfer of energy from some external system to the molecule. Perhaps the most common means of excitation is via the absorption of a single photon. As laser technology continues to develop toward shorter pulse widths and higher peak powers, two-photon absorption (TPA) has become an increasingly important tool in the investigation of a wide variety of materials. Our first task here is to clarify what is meant by two-photon absorption.

One process by which two photons are absorbed by a molecule is through the stepwise process shown in Fig. 1a. In this process, the first photon is absorbed, exciting the molecule from the initial state (i) to an intermediate state (j). The second photon brings the molecule from the intermediate state to the final energy state (f). We note that the intermediate state is a real electronic state of the molecule.

A second way that two-photon absorption occurs is shown in Fig. 1b. In this process, the two photons are absorbed, " simultaneously" [1]. Whether the absorption of the two photons is really simultaneous will be discussed in Section 2, as will the nature of the intermediate state (not shown in Fig. 2. Conservation of energy, of course, must apply: that is, $\hbar\omega_1 + \hbar\omega_2 = E_f - E_i$.

* J. Collins, Department of Physics and Astronomy, Wheaton College, Norton, MA 02766 USA, jcollins@wheatonma.edu

B. Di Bartolo and J. Collins (eds.), *Biophotonics: Spectroscopy, Imaging, Sensing, and Manipulation*, 261
DOI 10.1007/978-90-481-9977-8_12, © Springer Science+Business Media B.V. 2011

The process shown in Fig. 1b is the focus of this article. As we shall see, the advantages that this two-photon absorption process offers rests, in a large part, on the fact that the probability per unit time for TPA is proportional to the square of the intensity of the photon field.

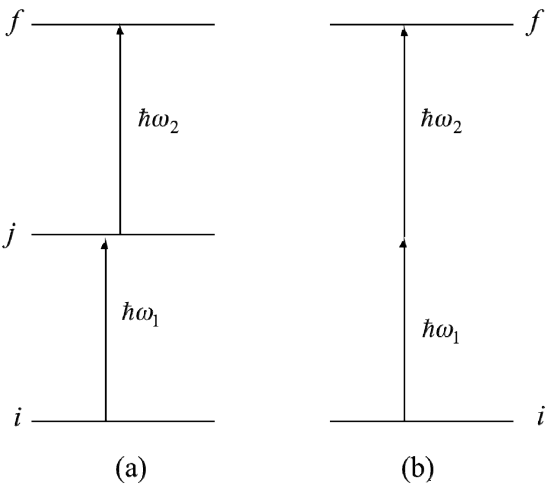

Figure 1. Energy level diagrams showing the absorption of two photons by (a) a sequential process involving a real intermediate state and (b) a "simultaneous" process via a virtual intermediate state.

2. Theory of Two-Photon Absorption

2.1. CLASSICAL TREATMENT

The interaction of radiation with matter is guided by the relationship between the polarization of the material and the applied electric field. For a process that requires only a single interaction, that is where the polarizability is independent of the applied field, the equation is linear in the applied field and is given by

$$\vec{P} = \chi \vec{E} \tag{1}$$

where χ is the electric susceptibility and $\vec{E}$ is the applied field. For a field consisting of light of frequency ω and polarization $\vec{\varepsilon}$, then the electric field is given by

$$\vec{E} = E_0 \vec{\varepsilon} \left(e^{i\omega t} + e^{i\omega t} \right) \tag{2}$$

In the quasi-classical picture of the optical interaction of a photon with matter, the absorption rate of a single photon by an atomic system is due to the imaginary part of

the susceptibility. That is, the susceptibility contains within it the matrix elements that govern the absorption process [e.g. 2, 3]. The susceptibility is a function of ω and the direction of polarization, but is independent of E_0 for the single-photon absorption, and other linear processes.

A classical treatment of multi-photon process requires consideration of the nonlinear contributions to the polarization. A more general form of (1) is

$$\vec{P} = \chi^{(1)}\vec{E} + \chi^{(2)}\vec{E}^2 + \chi^{(3)}\vec{E}^3 + \chi^{(4)}\vec{E}^4 + \chi^{(5)}\vec{E}^5 + \ldots \,. \tag{3}$$

For two-photon absorption in materials having inversion symmetry, such as atoms and some molecules, one must consider only terms in the odd powers of the electric field.

Let us assume that we have such a material, and that we allow it to interact with two laser beams having frequencies ω_1 and ω_2. The electric field is

$$\vec{E}(t) = \vec{E}_1\ e^{i\omega_1 t} + \vec{E}_1\ e^{-i\omega_1 t} + \vec{E}_2\ e^{i\omega_2 t} + \vec{E}_2\ e^{-i\omega_2 t} \,. \tag{4}$$

Inserting (4) into (3) leads to a polarization that is quite complicated: for the various combinations of the field components there is a specific χ that depends on ω_1 or ω_2 or both. Because we are interested only in showing a term representative of two-photon absorption, we make the following simplifications.

1. We assume that conservation of energy requires photons of both frequencies participate in the absorption process (i.e. $\hbar\omega_1 + \hbar\omega_2 = E_f - E_i$). Thus we retain only those terms containing both laser fields.
2. Following Loudon [2], we exclude all terms greater than $\chi^{(3)}$.
3. We reduce the number of term further by considering only those terms that oscillate according to $e^{-i\omega_1 t}$.

The resulting polarization is

$$\vec{P}(\omega_1) = \chi^{(1)}(\omega_1)\left(\vec{E}\ e^{-i\omega_1 t}\right) + 6\chi^{(3)}(-\omega_1, -\omega_2, \omega_2)\,E_2{}^2\vec{E}_1\ e^{-i\omega_1 t} \,. \tag{5}$$

The strength of the electric field of beam 2 is related to the time averaged intensity of the beam according to

$$E_2{}^2 = \frac{\omega_2}{2\varepsilon_0 c^2 k_2}\langle I_2\rangle_{ave} \,. \tag{6}$$

Combining (5) and (6) we obtain

$$\vec{P}(\omega_1) = \left[\chi^{(1)}(\omega_1) + \left(\frac{\omega_2}{2\varepsilon_0 c^2 k_2}\right)6\chi^{(3)}(-\omega_1, -\omega_2, \omega_2)\langle I_2\rangle_{ave}\right]E_1\ e^{-i\omega_1 t} \,. \tag{7}$$

Equation (7) is written in the exact same form as (1). The polarization now contains the linear term $\chi^{(1)}(\omega_1)$ and a term that is proportional to the intensity of beam 2.

As the imaginary part of $\chi^{(1)}$ is responsible for one-photon absorption, two-photon absorption is determined by the imaginary part of $\chi^{(3)}$. Because $\chi^{(3)}$ is multiplied by a term proportional to the intensity of one of the laser beams, the two-photon absorption coefficient is dependent on the intensity of the beam.

2.2. QUANTUM MECHANICAL TREATMENT OF TWO-PHOTON ABSORPTION

A quantum mechanical treatment of two-photon absorption was first given by Maria Goeppert-Mayer in 1931 [4], though the first confirmed observation of two-photon absorption did not occur until 1961, following the invention of the laser [5]. Here, we describe the two-photon absorption process using a perturbation approach.

The combined system of an atom or molecule and a radiation field is described by the following Hamiltonian:

$$H = H' + H_R + \frac{1}{2m}\sum_i \left(\vec{p}_i + (e/c)\vec{A}_i\right)^2 \tag{8}$$

where the following assignments are made.

H': This contains atomic contributions to the energy, such as the central field potential, the spin-orbit interaction, the electron-electron interaction, and other smaller interactions. Note that it does not include the kinetic energies of the unperturbed electrons.

H_R: This is the energy of the radiation field in the absence of the atom.

$\frac{1}{2m}\sum_i \left(\vec{p}_i + (e/c)\vec{A}_i\right)^2$: This is the kinetic energy of the electrons in the presence of the field. It contains the kinetic energy of the electrons in the unperturbed atom and the interaction energy between the atom and the field.

In a perturbative treatment, it is necessary to know precisely the interaction Hamiltonian. Thus, our first goal is to rewrite the kinetic energy term so as to separate out the interaction energy.

Expanding $\left(\vec{p}_i + (e/c)\vec{A}_i\right)^2$, we get

$$\left(\vec{p}_i + (e/c)\vec{A}_i\right)^2 = \vec{p}_i \bullet \vec{p}_i + (e/c)\vec{p}_i \bullet \vec{A}_i + (e/c)\vec{A}_i \bullet \vec{p}_i + (e/c)^2 \vec{A}_i \bullet \vec{A}_i \,. \tag{9}$$

We further note the following.

$$\begin{aligned} \left(\vec{p}_i \bullet \vec{A}_i\right)\psi &= \left(\vec{p}_i\psi\right) \bullet \vec{A}_i + \vec{p}_i \bullet \left(\vec{A}_i\psi\right) \\ &= -i\hbar\left[\left(\vec{\nabla}_i\psi\right) \bullet \vec{A}_i + \left(\vec{\nabla}_i \bullet \vec{A}_i\right)\psi\right] \end{aligned} \tag{10}$$

In the Coulomb gauge, $\vec{\nabla} \bullet \vec{A} = 0$, so that Eq. (10) can be rewritten as

$$\begin{aligned}\left(\vec{p}_i \bullet \vec{A}_i\right)\psi &= -i\hbar\left[\left(\vec{\nabla}\psi\right)_i \bullet \vec{A}_i\right] \\ &= -i\hbar\left[\vec{A}_i \bullet \left(\vec{\nabla}\psi\right)_i\right] = \left(\vec{A}_i \bullet \vec{p}_i\right)\psi\end{aligned} \tag{11}$$

Combining (11), (9), and (8), the full Hamiltonian of the system becomes

$$H = H_R + H' + \frac{1}{2m}\sum_i p_i^2 + \left(2e/c\right)\vec{p}_i \bullet \vec{A}_i + \left(e/c\right)^2 \vec{A}_i \bullet \vec{A}_i \tag{12}$$

In this equation the term $\frac{1}{2m}\sum_i p_i^2$ is the kinetic energy of the electrons of the unperturbed atom. This term may be combined with H' to give the full Hamiltonian of the unperturbed atom, H_{atom}. The Hamiltonian of the entire system can the be written

$$H = H_R + H_{atom} + \sum_i \left(e/mc\right)\vec{A}_i \bullet \vec{p}_i + \left(e^2/2mc^2\right)\vec{A}_i \bullet \vec{A}_i \tag{13}$$

The last two terms represent the interaction energy between the atom and the field.

We will find it convenient to treat the two terms interaction terms in (13) separately, and rewrite the full Hamiltonian as follows:

$$H = H_R + H_{atom} + H_1 + H_2 \tag{14}$$

where, the interaction terms H_1 and H_2, are given by

$$H_1 = \sum_i \left(e/mc\right)\vec{p}_i \bullet \vec{A} \tag{15}$$

$$H_2 = \sum_i \left(e^2/2mc^2\right)\vec{A} \bullet \vec{A} \tag{16}$$

Since $\vec{A}$ represents the vector potential of the electromagnetic field, H_1 depends linearly on the strength of the field and H_2 has a quadratic dependence on the field strength.

The Hamiltonian of the radiation field, when quantized, is written:

$$H_R = \sum_\lambda \sum_\varepsilon \hbar\omega_\lambda \left(a_\lambda^{\varepsilon +} a_\lambda^\varepsilon + \frac{1}{2}\right). \tag{17}$$

The a_λ^ε and $a_\lambda^{\varepsilon +}$ are the photon annihilation and creation, respectively, where λ is the wavelength of the radiation and ε the polarization. The eigenfunctions and eigenvalues of H_R are given by

$$\psi_{n_1^{\varepsilon_1} n_1^{\varepsilon_2} n_2^{\varepsilon_1} \ldots} = \prod_{\lambda,\varepsilon} \left| n_\lambda^\varepsilon \right\rangle \tag{18}$$

$$E_{n_1^{\varepsilon_1} n_1^{\varepsilon_2} n_2^{\varepsilon_1} \ldots} = \sum_\lambda \sum_\varepsilon \hbar \omega_\lambda \left(n_\lambda^\varepsilon + \frac{1}{2} \right) \tag{19}$$

where the sums are over all photon frequencies and polarizations, and n_λ^ε represents the density of photons in a mode having wavelength λ and polarization ε.

The vector potential associated with such a mode is

$$\vec{A}_\lambda^\varepsilon \left(\vec{r}, t \right) = \left(\frac{hc^2}{\omega_\lambda V} \right)^{1/2} \vec{\pi}_\lambda^\varepsilon \left(a_\lambda^\varepsilon e^{i\left(\vec{k}_\lambda \bullet \vec{r} - \omega_\lambda t \right)} + a_\lambda^{\varepsilon +} e^{-i\left(\vec{k}_\lambda \bullet \vec{r} - \omega_\lambda t \right)} \right) \tag{20}$$

For two laser beams with frequencies ω_1 and ω_2 and polarizations $\vec{\varepsilon}_1$ and $\vec{\varepsilon}_2$, we can make the following assignments:

State function of the field: $$\left| \psi^R \right\rangle = \left| n_1^{\varepsilon_1} \right\rangle \left| n_2^{\varepsilon_2} \right\rangle = \left| n_1^{\varepsilon_1} n_2^{\varepsilon_2} \right\rangle \tag{21}$$

Energy in the field: $$E_{n_1^{\varepsilon_1} n_2^{\varepsilon_2}} = \hbar \omega_1 \left(n_1^{\varepsilon_1} + \frac{1}{2} \right) + \hbar \omega_2 \left(n_2^{\varepsilon_2} + \frac{1}{2} \right) \tag{22}$$

Vector potential of the field:

$$\left(\frac{hc^2}{V} \right)^{1/2} \left[\frac{\vec{\varepsilon}_1}{\sqrt{\omega_1}} \left(a_1^{\varepsilon_1} e^{i\left(\vec{k}_1 \bullet \vec{r}_i - \omega_1 t \right)} + a_1^{\varepsilon_1 +} e^{-i\left(\vec{k}_1 \bullet \vec{r}_i - \omega_1 t \right)} \right) + \frac{\vec{\varepsilon}_2}{\sqrt{\omega_2}} \left(a_2^{\varepsilon_2} e^{i\left(\vec{k}_2 \bullet \vec{r}_i - \omega_2 t \right)} + a_2^{\varepsilon_2 +} e^{-i\left(\vec{k}_2 \bullet \vec{r}_i - \omega_2 t \right)} \right) \right] \tag{23}$$

The creation and annihilation operators act on the states of the radiation field in the usual manner:

$$a_1^{\varepsilon_1} \left| n_1^{\varepsilon_1} n_2^{\varepsilon_2} \right\rangle = \sqrt{n_1^{\varepsilon_1}} \left| n_1^{\varepsilon_1} - 1 \; n_2^{\varepsilon_2} \right\rangle \quad \text{and} \tag{24}$$

$$a_1^{\varepsilon_1 +} \left| n_1^{\varepsilon_1} n_2^{\varepsilon_2} \right\rangle = \sqrt{n_1^{\varepsilon_1} + 1} \left| n_1^{\varepsilon_1} + 1 \; n_2^{\varepsilon_2} \right\rangle . \tag{25}$$

The laser fields present a time-dependent (non-adiabatic) interaction, which can cause a transition of the atomic/molecular system from one electronic state to another. In a perturbative treatment, these transition probabilities are governed by the following matrix elements.

First order perturbation terms: $$\left\langle \psi_f^e \psi_f^R \left| H_1 \right| \psi_i^e \psi_i^R \right\rangle \tag{26}$$

$$\left\langle \psi_f^e \psi_f^R \left| H_2 \right| \psi_i^e \psi_i^R \right\rangle \tag{27}$$

Second order perturbation terms: $\left\langle \psi_f^e \psi_f^R \left| H_1 \right| \psi_j^e \psi_j^R \right\rangle \left\langle \psi_j^e \psi_j^R \left| H_1 \right| \psi_i^e \psi_i^R \right\rangle$ (28)

$\left\langle \psi_f^e \psi_f^R \left| H_2 \right| \psi_j^e \psi_j^R \right\rangle \left\langle \psi_j^e \psi_j^R \left| H_2 \right| \psi_i^e \psi_i^R \right\rangle$ (29)

The $\left| \psi^e \right\rangle$ in these terms is the eigenvectors of H_{atom}. The first order matrix element involving H_1 is responsible for one-photon processes (e.g. absorption). Because H_2 contains terms with the vector potential to the second power, this will lead to two-photon processes. The second order term with matrix element containing H_1 also give rise to second-order processes. Finally, the second order term with matrix elements containing H_2 will result in fourth order processes. Since our focus is on two photon absorption, the terms (26) and (29) will be ignored.

2.2.1. First Order Perturbation Treatment of H_2

We first examine the first order term containing H_2. When two laser fields are present, H_2 has the form

$$\begin{aligned} H_2 &= \left({}^2e/2mc^2 \right) \vec{A} \bullet \vec{A} \\ &= \frac{e^2}{2m} \frac{h}{V} \sum_i \left[\frac{\vec{\pi}_1^{\varepsilon_1}}{\sqrt{\omega_1}} \left(a_1^{\varepsilon_1} e^{i\left(\vec{k}_1 \bullet \vec{r}_i - \omega_1 t\right)} + a_1^{\varepsilon_1 +} e^{-i\left(\vec{k}_1 \bullet \vec{r}_i - \omega_1 t\right)} \right) + \frac{\vec{\pi}_2^{\varepsilon_2}}{\sqrt{\omega_2}} \left(a_2^{\varepsilon_2} e^{i\left(\vec{k}_2 \bullet \vec{r}_i - \omega_2 t\right)} + a_2^{\varepsilon_2 +} e^{-i\left(\vec{k}_2 \bullet \vec{r}_i - \omega_2 t\right)} \right) \right] \\ &\quad \bullet \left[\frac{\vec{\pi}_1^{\varepsilon_1}}{\sqrt{\omega_1}} \left(a_1^{\varepsilon_1} e^{i\left(\vec{k}_1 \bullet \vec{r}_i - \omega_1 t\right)} + a_1^{\varepsilon_1 +} e^{-i\left(\vec{k}_1 \bullet \vec{r}_i - \omega_1 t\right)} \right) + \frac{\vec{\pi}_2^{\varepsilon_2}}{\sqrt{\omega_2}} \left(a_2^{\varepsilon_2} e^{i\left(\vec{k}_2 \bullet \vec{r}_i - \omega_2 t\right)} + a_2^{\varepsilon_2 +} e^{-i\left(\vec{k}_2 \bullet \vec{r}_i - \omega_2 t\right)} \right) \right] \end{aligned} \quad (30)$$

Neglecting the exponentials and the constants, H_2 contains 16 terms having the following forms:

$$\begin{aligned} &\vec{\varepsilon}_1 \bullet \vec{\varepsilon}_1 \left({a_1}^2 + a_1 a_1^+ + a_1^+ a_1 + a_1^+ a_1^+ \right) \\ &\vec{\varepsilon}_1 \bullet \vec{\varepsilon}_2 \left(a_1 a_2 + a_1 a_2^+ + a_1^+ a_2 + a_1^+ a_2^+ \right) \\ &\vec{\varepsilon}_2 \bullet \vec{\varepsilon}_1 \left(a_2 a_1 + a_2 a_1^+ + a_2^+ a_1 + a_2^+ a_1^+ \right) \\ &\vec{\varepsilon}_2 \bullet \vec{\varepsilon}_2 \left({a_2}^2 + a_2 a_2^+ + a_2^+ a_2 + a_2^+ a_2^+ \right) \end{aligned} \quad (31)$$

Since a is an annihilation operator and a^+ is a creation operator, it can be concluded that in each of the above parentheses, the first term corresponds the two-photon absorption, the last term to two-photon emission, and the middle terms to photon scattering.

Retaining only those terms relevant to two-photon absorption

$$H_2^{abs} = \frac{e^2}{2m} \frac{h}{V} \sum_i \frac{1}{\omega_1} {a_1}^2 e^{2i\left(\vec{k}_1 \bullet \vec{r}_i - \omega_1 t\right)} + \frac{1}{\omega_2} {a_2}^2 e^{-2i\left(\vec{k}_2 \bullet \vec{r}_i - \omega_2 t\right)} + \frac{2\vec{\varepsilon}_1 \bullet \vec{\varepsilon}_2}{\sqrt{\omega_1 \omega_2}} a_1 a_2 e^{i\left(\left(\vec{k}_1 + \vec{k}_2\right) \bullet \vec{r}_i - \left(\omega_1 + \omega_2\right) t\right)} \quad (32)$$

When H_2^{abs} is placed between the initial and final unperturbed wavefunctions in (27), terms of the following kind emerge.

$$\left\langle \psi_f^e \left| e^{-i\left((\vec{k}_1+\vec{k}_2)\bullet\vec{r}_i\right)} \right| \psi_i^e \right\rangle = \left\langle \psi_f^e \left| 1 + i\left(\vec{k}_1+\vec{k}_2\right)\bullet\vec{r}_i - \frac{1}{2}\left[\left(\vec{k}_1+\vec{k}_2\right)\bullet\vec{r}_i\right]^2 + \ldots \right| \psi_i^e \right\rangle \quad (33)$$

The first term on the right of (33) is zero, since the initial and final wavefunctions are orthogonal. Under the assumption that the wavelength of the radiation is much larger than the size of the atom or molecule, i.e. $\vec{k}_{1,2}\bullet\vec{r}_i << 1$, then we may retain only terms in the first order of $\vec{k}_{1,2}\bullet\vec{r}_i$, and the matrix element in (33) can be approximated by

$$\left\langle \psi_f^e \left| e^{-i\left((\vec{k}_1+\vec{k}_2)\bullet\vec{r}_i\right)} \right| \psi_i^e \right\rangle \approx \left\langle \psi_f^e \left| i\left(\vec{k}_1+\vec{k}_2\right)\bullet\vec{r}_i \right| \psi_i^e \right\rangle \quad (34)$$

We note that since $\vec{r}$ is an odd operator, if the wavefunctions of the atomic/molecular system are of definite parity, the final and initial wavefunctions must be of opposite parity in order to give an non-zero contribution.

In addition to the terms involving the atomic wavefunctions, there are also terms from (27) that involve the eigenvectors of the radiation field.

$$\left\langle \psi_f^R \left| \frac{a_1^{\dagger 2}}{\omega_1} + \frac{a_2^{\dagger 2}}{\omega_2} + \vec{\varepsilon}_1\bullet\vec{\varepsilon}_2 \frac{a_1 a_2}{\sqrt{\omega_1\omega_2}} \right| \psi_i^R \right\rangle \quad (35)$$

If we assume that absorption must involve photons of frequencies ω_1 and ω_2 ($\hbar\omega_1 + \hbar\omega_2 = E_f - E_i$), the first two terms in the operator of (35) will give zero contribution. The third term in the operator will contribute, and is maximum when the directions of polarization of the two laser fields are identical.

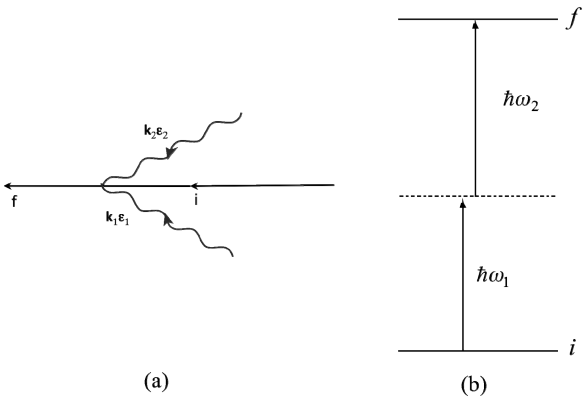

Figure 2. (a) A Feynman diagram and (b) an energy level diagram of two-photon absorption due to H_2. The intermediate virtual state is represented by the dashed line.

Thus, we can conclude that first order matrix elements of H_2 will only connect electronic wavefunctions that do not have the same parity. The probability of the process occurring is proportional to $\left(\vec{k}_1 + \vec{k}_2\right) \bullet \vec{r}_i$ and to the cosine of the angle between the directions of polarization of the two laser beams. In this first-order treatment, there is no term representing an intermediate state, though an intermediate "virtual" state is often portrayed. Diagrams of this process are shown in Fig. 2.

2.2.2. Second Order Perturbation Treatment of H_1

The first order interaction H_1 taken to the second order in the perturbation leads to terms similar to the following

$$\left\langle \psi_f \left| H_1 \right| \psi_i \right\rangle = \frac{\left\langle \psi_f^e \psi_f^R \left| H_1 \right| \psi_j^e \psi_j^R \right\rangle \left\langle \psi_j^e \psi_j^R \left| H_1 \right| \psi_i^e \psi_i^R \right\rangle}{E_i - E_j} \tag{36}$$

where H_1 is

$$\begin{aligned} H_1 &= \sum_i (e/mc) \vec{p}_i \bullet \vec{A} \\ &= \frac{e}{m} \sum_i \left(\frac{h}{V}\right)^{1/2} \vec{p}_i \bullet \left[\frac{\vec{\varepsilon}_1}{\sqrt{\omega_1}} \left(a_1 e^{i\left(\vec{k}_1 \bullet \vec{r}_i - \omega_1 t\right)} + a_1^{+} e^{-i\left(\vec{k}_1 \bullet \vec{r}_i - \omega_1 t\right)} \right) + \frac{\vec{\varepsilon}_2}{\sqrt{\omega_2}} \left(a_2 e^{i\left(\vec{k}_2 \bullet \vec{r}_i - \omega_2 t\right)} + a_2^{+} e^{-i\left(\vec{k}_2 \bullet \vec{r}_i - \omega_2 t\right)} \right) \right] \end{aligned} \tag{37}$$

Inserting (37) into (36)l leads to matrix elements of the form

$$\left\langle \psi_j^e,\ \psi_j^R \left| \vec{p} \bullet \vec{\varepsilon}_l \left(e^{i\vec{k}_l \bullet \vec{r}} \right) a_l \right| \psi_i^e,\ \psi_i^R \right\rangle . \tag{38}$$

We may expand the exponential in (38):

$$e^{i\vec{k}_l \bullet \vec{r}} = 1 + i\vec{k}_l \bullet \vec{r} + ... \tag{39}$$

At optical frequencies $\vec{k}_l \bullet \vec{r} << 1$, so that $e^{i\vec{k}_l \bullet \vec{r}} \approx 1$. This is the dipole approximation. Equation (38) then takes the form:

$$\left\langle \psi_j^e,\ \psi_j^R \left| \vec{p} \bullet \vec{\varepsilon}_l a_l \right| \psi_i^e,\ \psi_i^R \right\rangle = \vec{\varepsilon}_l \bullet \left\langle \psi_j^e \left| \vec{p} \right| \psi_i^e \right\rangle \left\langle \psi_j^R \left| a_l \right| \psi_i^R \right\rangle \tag{40}$$

This may be further simplified by noting that in the absence of the field, $\vec{p}$ is the momentum of the electron, and so can be written in terms of the following commutator:

$$\vec{p} = m\frac{d\vec{r}}{dt} = m\frac{i}{\hbar}\left[H_{atom},\ \vec{r}\right] \tag{41}$$

Using this definition of $\vec{p}$ the first matrix element on the right side of (40) becomes

$$\begin{aligned}\left\langle \psi_f^e \left| \vec{p} \right| \psi_i^e \right\rangle &= m\frac{i}{\hbar}\left\langle \psi_j^e \left| \left[H_{atom},\, \vec{r} \right] \right| \psi_i^e \right\rangle \\ &= m\frac{i}{\hbar}\left\langle \psi_j^e \left| H_{atom}\vec{r} \right| \psi_i^e \right\rangle - m\frac{i}{\hbar}\left\langle \psi_f^e \left| \vec{r} H_{atom} \right| \psi_i^e \right\rangle \\ &= m\frac{i}{\hbar}\left(E_j - E_i \right)\left\langle \psi_j^e \left| \vec{r} \right| \psi_i^e \right\rangle \\ &= im\omega_{ji}\left\langle \psi_j^e \left| \vec{r} \right| \psi_i^e \right\rangle \end{aligned} \tag{42}$$

Combining (37), (39), and (42), the matrix element of H_1 between the initial state i and the intermediate state j of the system (atom + field) is:

$$\begin{aligned}\left\langle \psi_j^e \psi_j^R \left| H_1 \right| \psi_i^e \psi_i^R \right\rangle = -i\left(\frac{h}{V}\right)^{1/2} \omega_{ji} \sum_l \Bigg[&\frac{1}{\sqrt{\omega_1}}\left\langle \psi_j^e \left| e\vec{r}_l \bullet \vec{\varepsilon}_1 \right| \psi_i^e \right\rangle \left\langle \psi_j^R \left| a_1 + a_1^{+} \right| \psi_i^R \right\rangle + \\ &\frac{1}{\sqrt{\omega_2}}\left\langle \psi_j^e \left| e\vec{r}_l \bullet \vec{\varepsilon}_2 \right| \psi_i^e \right\rangle \left\langle \psi_j^R \left| a_2 + a_2^{+} \right| \psi_i^R \right\rangle \Bigg] \end{aligned} \tag{43}$$

To find matrix element representing the second order contribution of H_1, we use (43) and a similar matrix element connecting the intermediate and final states, and insert them into the numerator of (36). The result is

$$\begin{aligned}\left\langle \psi_f \left| H_1 \right| \psi_i \right\rangle &= \left\langle \psi_f^e \psi_f^R \left| H_1 \right| \psi_j^e \psi_j^R \right\rangle \left\langle \psi_j^e \psi_j^R \left| H_1 \right| \psi_i^e \psi_i^R \right\rangle \\ &= -\frac{h}{V} \sum_l \sum_{j,j'} \left\langle \psi_f^e \psi_f^R \left| \frac{\vec{r}_l \bullet \vec{\varepsilon}_1}{\sqrt{\omega_1}}\left(a_1 + a_1^{+} \right) + \frac{\vec{r}_l \bullet \vec{\varepsilon}_2}{\sqrt{\omega_2}}\left(a_2 + a_2^{+} \right) \right| \psi_j^e \psi_{j'}^R \right\rangle \\ &\quad \times \left\langle \psi_j^e \psi_{j'}^R \left| \frac{\vec{r}_l \bullet \vec{\varepsilon}_1}{\sqrt{\omega_1}}\left(a_1 + a_1^{+} \right) + \frac{\vec{r}_l \bullet \vec{\varepsilon}_2}{\sqrt{\omega_2}}\left(a_2 + a_2^{+} \right) \right| \psi_i^e \psi_i^R \right\rangle \end{aligned} \tag{44}$$

The sums are over all electrons and all intermediate states of the atom/molecule and the field. Each term in the sum on the right of (44) contains 16 combinations of the raising and lowering operators. As with the case of H_2 to the first order, eight of those combinations result in photon scattering, four in two-photon emission, and four in two-photon absorption.

Neglecting the sum over the electrons, simplifying the notation, and removing some of the constants, we see that the two-photon transition probability is governed by the following:

$$\mathrm{M}_{if} = \sum_j \frac{\left\langle f \left| e\vec{r} \bullet \vec{\varepsilon}_2 \right| j \right\rangle \left\langle j \left| e\vec{r} \bullet \vec{\varepsilon}_1 \right| i \right\rangle}{\omega_{ij} - \omega_1} + \frac{\left\langle f \left| e\vec{r} \bullet \vec{\varepsilon}_1 \right| j \right\rangle \left\langle j \left| e\vec{r} \bullet \vec{\varepsilon}_2 \right| i \right\rangle}{\omega_{ij} - \omega_2} \tag{45}$$

In this second order treatment, the transition occurs in two steps: first from the initial state i to an intermediate state j, and second from the intermediate state j to the

final state *f*. The denominator in (45) affects the strength of the transition: the further the intermediate state is from resonance with the photon field, the weaker the transition. Feynman diagrams and energy level diagrams of this process are shown in Fig. 3. Note that in the figure that the intermediate state has been placed above the final state.

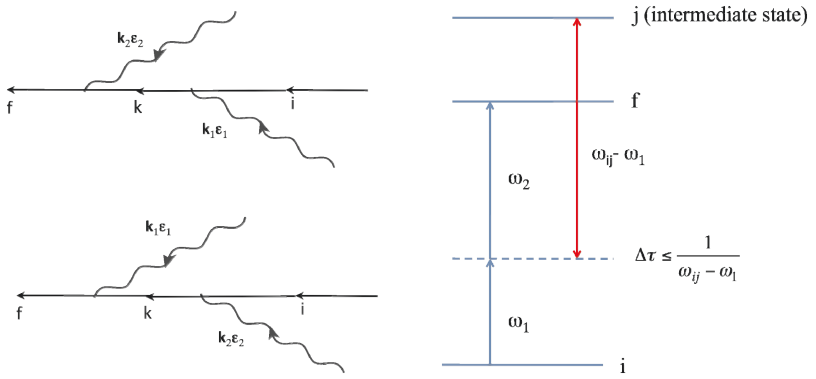

Figure 3. (a) Feynman diagrams and (b) energy level diagram of two photon absorption. As shown in (b) the energy difference between the first absorbed photon (ω_1) and the intermediate state mediating the transition is $\hbar\left(\omega_{ij}-\omega_1\right)$. When this energy corresponds to optical tansitions, the lifetime will be in the order of 10^{-14} s.

2.2.3. Comments on the Intermediate Virtual State

Let us look more closely at the intermediate state. A matrix element of H_I between the initial state *i* and the intermediate state *j* is the product of a matrix element involving the states of the field and one involving the electronic states of the atom/molecule.

$$\left\langle \psi_j^e \left| er_l \bullet \vec{\varepsilon} \right| \psi_i^e \right\rangle \left\langle \psi_j^R \left| a \right| \psi_i^R \right\rangle \tag{46}$$

The intermediate photon state is the initial state of the field with the number of photons reduced by one. The intermediate electronic state is a real state of the atomic system. For all free atoms and for many molecules, the electronic states are of definite parity. In such a system, because $\vec{r}$ is an odd operator, a non-zero matrix element requires that the intermediate electronic state must have parity opposite that initial electronic state.

We may say the following regarding the second order perturbation contribution of the operator H_I to the two-photon absorption process.

1. The intermediate state is a direct product of a real state of the unperturbed atomic system and a real state of the unperturbed radiation field.
2. The electronic transition from the initial state to the intermediate state need not be resonant with the available photons. Typically, in fact, the photon energy is much

less than the energy of the transition, requiring energy to be "borrowed" from another source – e.g. the zero field.

3. This energy mismatch, determines, through the uncertainty relation, the "lifetime" of the intermediate state. That is, $(\Delta\tau)_j = 1/(\omega_{ij} - \omega_1)$. Because this lifetime is usually short, the state is referred to as a virtual state, and the transition a virtual one.
4. The selection rules for the transition are determined by the nature of the electronic wavefunctions.
5. Figure 1b is somewhat misleading, in that it shows no intermediate state. In fact, there is a real intermediate state, which often has energy above that of the final state, as shown in Fig. 2b.
6. It was mentioned in Section 1 that in two-photon absorption the photons are absorbed simultaneously. Whether this is precisely true is debatable. What is true is that the lifetime of the intermediate state is typically very short, and that the second photon must be absorbed during this time.

In the case of two-photon absorption driven by the first order contribution of H_2, the atom absorbs both photons "simultaneously". Nonetheless, it is meaningful to talk about an intermediate state. The following can be said about this intermediate state.

1. It has an energy position between the initial and final states of the atomic system.
2. The intermediate state is an eigenstate of the combined system (atom + field), sometimes referred to as the dressed atom.
3. Because this state only exists when the laser field in turned on, the relevant "lifetime" of the level is constrained by the width of the laser pulse. Even if the inherent lifetime of such a state is long, that state can never remain occupied longer than a time on the order of the width of the pulse.

2.3. EXAMPLE: TWO-PHOTON ABSORPTION IN ETHYLENE

To demonstrate the selection rules for two-photon absorption as given in (45), let us consider the case of ethylene. The molecular formula of ethylene is C_2H_4, and it has D_{2h} symmetry, as shown in Fig. 4. The electronic states are labeled according to the irreducible representations of the point group D_{2h}, and are divided into even and odd states:

even: A_g B_{1g} B_{2g} B_{3g}
odd: A_u B_{1u} B_{2u} B_{3u}

Note that all states are of definite parity.

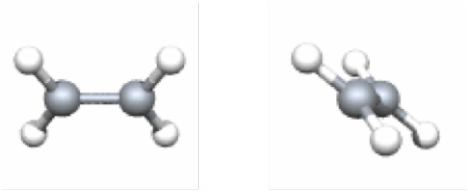

Figure 4. Two views of the ethylene molecule.

Recall that an even state is one in which the wavefunction does not change sign under the operation of inversion (x→–x, y→–y, z→–z), while an odd state changes sign. To visualize these states, envision a plane that cuts the molecule through the middle of each atom. The top and bottom sides of that plane can then be represented as rectangles, with the wavefunction in different sections of the rectangles having a definite positive or negative value. This highly simplified visualization of the various states are thus shown in Fig. 5. (Similar representations have been presented in reference [6]).

The two-photon absorption rate, governed by (45), contains matrix elements of the form:

$$\left\langle f \left| e\vec{r} \bullet \vec{\varepsilon}_2 \right| j \right\rangle \left\langle j \left| e\vec{r} \bullet \vec{\varepsilon}_1 \right| i \right\rangle \tag{47}$$

Because all the electronic states of ethylene are of definite parity, then the matrix element on the right in (47) is non-zero only if the intermediate state has parity opposite that of the initial state. Likewise for the matrix element on the left in (47): a non-zero result requires that the intermediate state has parity opposite that of the final state. Thus one immediately sees that the allowed two-photon transitions are allowed only between states having the same parity, and that the transition is mediated by a state of opposite parity. For ethylene, the ground state is A_g. This means that a two-photon transition is only "allowed" to any of the other even states.

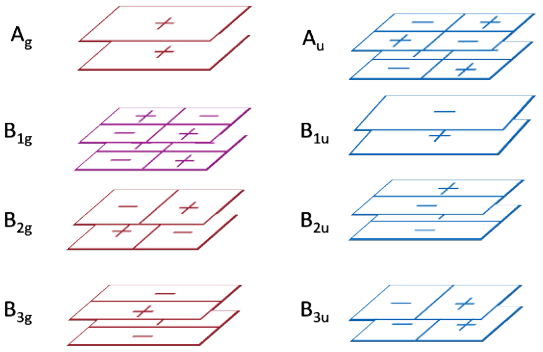

Figure 5. Visualization of the electronic states of ethylene showing the parity of each state: even states on the left and odd on the right.

Polarization selection rules are also contained in (47). Since $e\vec{r}$ is the induced dipole moment on the molecule, the term $\vec{r} \bullet \vec{\varepsilon}$ means that the transition rate is maximum when the induced dipole moment is in the same direction as the polarization of the absorbed photon. An example of this is shown in Fig. 6 In this figure, going from the A_g state (as oriented) to the intermediate B_{1u} requires a photon polarized in the z-direction, and going from the B_{1u} to the final B_{3g} state requires a photon polarized in the y-direction.

We may broaden this example more by asking: "Which of the odd states may act as an intermediate state for a two-photon transition from A_g to B_{3g}?". The results are shown pictorially in Fig. 7. In this figure, one can see that the top transition is forbidden. There is no single photon that can cause the charge distribution in the initial (A_g) wavefunction to that of the intermediate (A_u) wavefunction. The bottom-most transition is also forbidden: an x-polarized photon could cause the A_g to B_{3u} transition, but there is no photon that can cause the B_{3u} to B_{3g} transition. The middle two transitions, $A_g \rightarrow B_{1u} \rightarrow B_{3g}$ and $A_g \rightarrow B_{2u} \rightarrow B_{3g}$, are allowed, with photon polarizations as indicated.

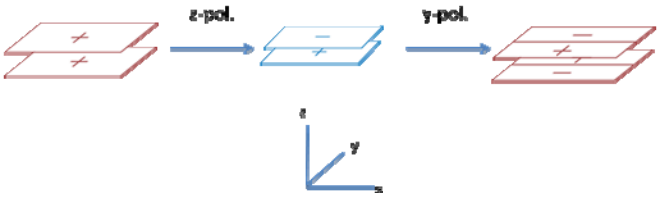

Figure 6. Two-photon transition from the A_g state to the B_{3g} state of ethylene via the B_{1u} state. The polarization of the photon responsible for each transition is shown.

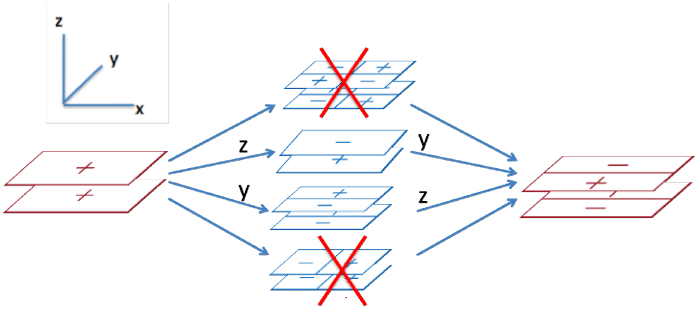

Figure 7. A_g to B_{3g} two-photon transitions through various odd intermediate states. Transitions with the intermediate state crossed-out are forbidden: there is no photon that will connect that intermediate state to either the initial state or the final state, or both. The polarizations of the allowed transitions are also shown.

3. Measuring the Two-Photon Absorption Cross Section

3.1. ONE-PHOTON ABSORPTION MEASUREMENTS

Measuring the absorption cross section for one-photon absorption is familiar to most readers. The absorption of a photon by an infinitesimally thin slice of a sample, in Fig. 8a, is proportional to the intensity of the incoming light. When a single species is responsible for the absorption, the amount absorbed, dI, is governed by the equation.

$$dI = -\sigma n I dx \tag{48}$$

In this equation n is the concentration (cm^{-3}) of absorbers and σ is the absorption cross section (cm^2). The solution to (48) gives the intensity as a function of the sample thickness x (Fig. 8b).

$$I(x) = I_0 e^{-\sigma n x} \tag{49}$$

This result, known as Beer's law, can be written in terms of the transmission, T.

$$T = \frac{I(x)}{I_0} = e^{-\sigma n x} \tag{50}$$

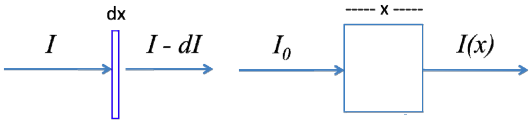

Figure 8. (a) Absorption by a sample of (a) infinitesimal thickness and of (b) finite thickness.

3.2. TWO-PHOTON ABSORPTION MEASUREMENTS

Two-photon absorption behaves differently because the probability that a two-photon process occurs is proportional to the square of the intensity of the incoming light. So, in analogy with (48), the amount absorbed via a two photon process by an infinitesimally thin sample is

$$dI = -\sigma_2 n I^2 dx \tag{51}$$

where σ_2 is the two-photon absorption cross section. The solution (51) is

$$I(x) = \frac{I_0}{1 + \sigma_2 n x I_0} \tag{52}$$

Rewriting (52) in terms of the transmission gives

$$T = \frac{I(x)}{I_0} = \frac{1}{1 + \sigma_2 n x I_0} \tag{53}$$

Thus, the fraction of the incoming light transmitted by the sample depends not only on the sample thickness, but also on the initial intensity of the light beam. This is very different than single photon absorption, where T depended only on the sample thickness.

The same reasoning can be used for N-photon absorption. Namely:

$$dI = -\sigma_N n I^N dx \tag{54}$$

where σ_N is the two-photon absorption cross section. The intensity and the fraction of energy transmitted as a function of sample thickness are

$$I(x) = \frac{I_0}{1 + \sigma_N n x {I_0}^{N-1}} \tag{55}$$

$$T = \frac{I(x)}{I_0} = \frac{1}{1 + \sigma n x {I_0}^{N-1}} \ . \tag{56}$$

This dependence on the initial intensity is problematic from an experimentalist's point of view. There are several reasons for this difficulty. Among others, we note the following two.

(1) Detectors (e.g. photomultipliers) have responses that vary widely with wavelength, and calibration of these, though possible, is no small task.
(2) The light sources used in two photon absorption are generally pulsed lasers whose beam is focused on the sample. There is, therefore, no single number that corresponds to the intensity of the beam – the intensity varies across the beam width in both space and time. It is possible to know how the beam varies, but one needs a great amount of control over both the beam profile and its temporal behavior to obtain a reliable estimate of an absorption cross section. This is further complicated by the fact that, unlike traditional lamps, lasers are not as readily tunable over a wide spectral range.

To circumvent problem (1) above, one may take advantage of the fact that the fluorescence efficiency of most dyes is independent of the wavelength of the existing light. That is, an occupied excited state retains no memory of how it became occupied. One example of how fluorescence can be used to measure the two-photon absorption cross section is shown in Fig. 9. This method is known as the z-scan method. In this experiment, a collimated laser beam is focused down to its beam waist and allowed to expand out, and is then recollimated. A thin sample containing a fluorescent center is moved along the z-axis, along with a detector, which detects the florescence over the range of z. The results in the figure show the difference for a one-photon and a two-photon absorption process.

Let us examine the process more closely. The intensity of the photoluminescence (I_{PL}) coming out of the material is proportional to the amount energy absorbed and the quantum efficiency of the fluorescent level (η_{PL}). Since the amount of energy absorbed is proportional to the change in intensity of the beam ($I(x) - I_0$), then using (53) we find that the intensity of the detected photoluminescence from the sample to be

$$I_{PL} = A \frac{\sigma_2 n x {I_0}^2}{1 + \sigma_2 n x I_0} \eta_{PL} . \tag{57}$$

In this equation A is a factor having to do with the geometry of the experimental set up and with the type of detector used. For a thin sample, we may make the approximation that $\sigma_2 n x I_0 << 1$. Equation (57) becomes

$$I_{PL} \approx A\sigma_2 nx I_0^2 \eta_{PL} \tag{58}$$

That is, the fluorescence signal is proportional to the square of the beam intensity. The results shown in Fig. 9 are now clear. For two-photon absorption as the beam becomes more focused, the intensity of the beam changes, and the fluorescence follows those changes. For a one-photon process, the fluorescence signal depends only on the total energy in the beam, which is independent of z.

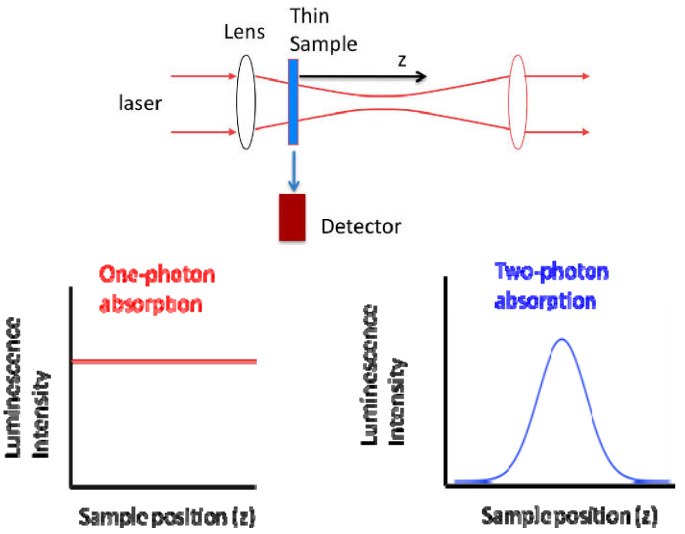

Figure 9. The z-scan method of measuring absorption by using detection of fluorescence. The graphs show the result of moving the sample along the beam while detecting fluorescence resulting from one- and two-photon absorption in the sample.

This z-scan method requires the following conditions.

(1) The sample thickness must be much smaller than the beam's waist length.
(2) The laser beam is well characterized spatially and at all values of z.
(3) High energy pump pulses and high concentration of TPA absorbers are necessary to obtain reasonable accuracy.
(4) One scan is required per wavelength.
(5) A reference sample is required so that the quantum efficiency of the molecule can be ascertained.
(6) Other effects such as scattering, excited state absorption, or higher order absorption processes can create artifacts in the signal.
(7) The geometrical factor A in Eq. (58) can be challenging to obtain.

Other methods of determining the two-photon absorption cross sections using fluorescence have been used. One such method is to compare the fluorescence signals resulting from one-photon absorption and the two-photon absorption measurements carried out under exactly the same carried out under the same experimental conditions,

except for the beam intensity. The reader is referred to the work of Markarov et al., who claim to have estimated the cross section of various dyes to within 10% [7].

It is not necessary to use fluorescence to measure the two-photon absorption cross section. For example, one may use the z-scan method with a detector opposite the source to measure the transmitted light. A schematic of this experimental set-up is shown in Fig. 10. Such a measurement has all of the concerns of the previously described z-scan experiment, except that no reference sample is required and the geometric factor does not come into play.

The detection issues are somewhat different than in absorption mode. For measuring transmission over a wide wavelength span, the detector response with wavelength must be known. Also, the intensity of the light hitting the detector will generally be large, and so care must be taken to ensure that the detector operates in a linear regime.

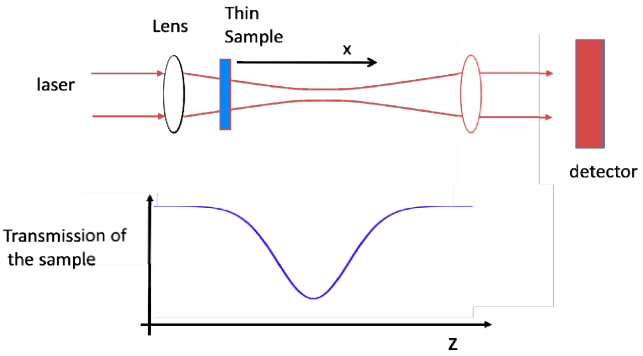

Figure 10. The z-scan method by detecting transmission through the sample.

3.3. UNITS OF THE MULTIPHOTON ABSORPTION CROSSECTION

To examine the units of the two-photon absorption cross section, let us recognize that the term $\sigma_2 nxI_0$ in the denominator of (57) must be unitless. If we assume that, for a given wavelength, the intensity has the units photons/cm^2 s, then the units of σ_2 are

$$[\sigma_2]=\left[\frac{1}{nxI_0}\right]=\left(\text{cm}^3\right)\left(\text{cm}^{-1}\right)\left(\frac{\text{cm}^2\text{ - sec}}{\text{photon}}\right)=\frac{\text{cm}^4\text{ - sec}}{\text{photon}} \tag{59}$$

The standard unit of the two-photon absorption cross section is the GM (Goeppert–Mayer), where 1 GM = 10^{-50} cm^4-s/photon. Typical values of σ_2 run from 0.1 to several hundred GM.

For multiphoton absorption processes involving N photons, the term $\sigma_N nxI_0^{N-1}$ is unitless, so that the units of σ_N are

$$[\sigma_N]=\left[\frac{1}{nxI_0}\right]=\left(\text{cm}^3\right)\left(\text{cm}^{-1}\right)\left(\frac{\text{cm}^2\text{ - sec}}{\text{photon}}\right)^{\text{N}}=\frac{\text{cm}^{2\text{N}+2}\text{ - sec}^{\text{N}}}{\text{photon}^{\text{N}}} \tag{60}$$

Note that the ratio of the cross section for a N-photon process to that of an (N – 1)-photon process is 1 GM. Thus, very roughly speaking, if a typical cross sections for a two photon process in 10^{-50} cm^4-s/photon, then for a three photon process the cross section will be on the order of 10^{-100} $(cm^4\text{-s/photon})^2$, and so on.

3.4. LASER CONSIDERATIONS

In order to measure the two-photon absorption cross section, it is necessary to have a measureable amount of absorption in the sample. Let us assume that the sample is thin so that the absorbance is low, i.e. the assumption described by (58) is reasonable. Under such circumstances, the fraction of photons absorbed by a sample of length Δx is

$$\frac{\Delta I}{I_0} \approx -\sigma_2 n I_0 \Delta x \tag{61}$$

Because the fraction absorbed energy is proportional to the intensity of the beam, then it is reasonable to ask "What beam intensity is necessary to measure the absorption cross section?". Let us suppose that, for the experiment shown in Fig. 10, a reliable signal measureable signal requires that the fraction of absorbed photons be at least 10^{-4}. For a concentration of absorbers 10^{-5} mol/cm^3, a sample thickness of 1 mm, and an absorption cross section of 10 GM, then the necessary intensity of the beam necessary

$$I = \left(-\frac{\Delta I}{I}\right)\left(\frac{1}{\sigma n \Delta x}\right) \approx 10^{27}\,\frac{photons}{cm^2 - \sec} \tag{62}$$

Given the speed of light as 3×10^{10} cm/s, the intensity above corresponds to ~10^{17} photons/cm^3.

What kind of light source is necessary to produce this intensity? Practically speaking, the only sources able to produce such intensities, especially in a small wavelength range, are lasers. If we assume that the laser beam can be focused to 10 μm (spot size ~10^{-6} cm^2), then you need the laser to produce 10^{21} photons/s. For a Q-switched Nd:YAG laser (λ = 1,064 nm) with a pulse width of 10 ns, this corresponds to ~10 μJ per pulse. For an ultrafast Ti-sapphire laser (λ = 800 nm) and a pulse width of 100 fs, then each pulse must have an energy ~0.1 nJ.

4. Applications to Biological Systems

4.1. WHY MULTI-PHOTON ABSORPTION?

For the study of biological systems using optical techniques, it is often necessary to excite either the biological system directly or a biological marker, such as an organic dye molecule. There are several reasons why multi-photon absorption is preferred over single-photon absorption as a means of exciting a molecule. They are as follows.

1. Some “forbidden” transitions become allowed.
2. Higher spatial resolution.
3. Less photodegradation.
4. Better able to measure anisotropy.
5. Reduced scattering.
6. Depth-profiled 3D imaging.
7. Access to higher excitation energies.

In this section, we make some simple observations on how the items listed above are relevant to the investigation of biological systems.

4.2. RECOGNIZING MULTIPHOTON ABSORPTION

Excitation of organic molecules (fluorescent dyes and many bio-molecules) are often strongest in the blue and UV regions of the spectrum. Their absorption spectra are characterized by broad bands allowing for excitation over a wide range of wavelengths. Following absorption, the molecules fluoresce in either the visible or near infrared. The emission spectrum is, however, independent of the means of excitation. That is, whether the molecule is excited via a single photon or multiple photons, the emission spectrum is typically unchanged. Thus, one is generally unable to distinguish from the emission spectrum whether one or more photons were used to excite the sample.

In order to determine the number of photons involved in the excitation process, one takes advantage of Eq. (55) and the fact that the fluorescence is proportional to the number of molecules being excited. Under these conditions, the energy of the luminescence from the sample is proportional to the N^{th} power of the beam intensity. A plot of the log(fluorescence signal) versus the log(beam intensity) gives a line, whose slope gives information of the number of photons involved in the transition. A slope is 1 indicates single photon absorption, a slope 2 means two-photon absorption, etc. It is not uncommon to have more than one type of absorption process occurring at the same time. In such a case, the line will have a non-integer slope or the line may not even approximate a straight line, so that the concept of a single slope cannot be applied. Decomposing such lines to discern how much of each type of process is present is not generally useful, since one is not aware of the absorption cross sections for the different order processes. The presence of higher order scattering processes may also complicate the situation. Some examples of two photon fluorescence of dyes can be found in references [9, 10].

4.3. ANISOTROPY MEASUREMENTS USING MULTIPHOTON ABSORPTION

Molecules in solutions and in biological systems take on different orientations, and depending on their surroundings, these molecules will rotate in time about one or more axes. The molecular rotation rates depend on the viscosity of the surrounding medium and the size of the molecule. Interactions between the molecule and its surroundings may also lead to flexing of the molecule, which are often associated with the creation or breaking of certain bonds. Naturally, these interactions are of great interest. It is

possible to gain information on the molecular motion using fluorescence spectroscopic techniques so long as the lifetime of the fluorescence is on the order of (or even exceeds) the time scale over which the interactions cause some deformation or reorientation of the molecule. In many cases, this condition is satisfied, since rotations and flexing of molecules in viscous media typical of biological systems occur on the nanosecond time scale, which is similar to the fluorescence lifetime. One method employed for such investigations is fluorescence anisotropy. The reader is referred to Lakowicz [1] and Birch [10] for further discussion of this topic.

The method takes advantage of the fact that transitions in absorption and emission often follow polarization selection rules. Let us first discuss the detection of fluorescence from a molecule with a transition dipole oriented at an angle θ with respect to the z-axis. The intensity of a radiating dipole so oriented will have components of the electric field both parallel and perpendicular to the z-axis, and the intensity of the emission for these polarizations depend on the angle θ as follows:

$$I_{\parallel} \propto \cos^2\theta\ , \qquad \mathrm{I}_{\perp} \propto \sin^2\theta$$

Of course, the intensity of an observed signal will also depend on the number of molecules oriented at that angle θ. Defining a function $f(\theta)$ that represents the probability of a molecule being oriented at an angle θ with respect to the z-axis, the fractional intensity of the fluorescence parallel and perpendicular to the polarization direction (the z-axis in our case) are

$$I_{\parallel} = \int_0^{\pi/2} f(\theta)\cos^2\theta\, d\theta \quad \text{and} \quad I_{\perp} = \int_0^{\pi/2} f(\theta)\sin^2\theta\, d\theta. \tag{63}$$

The anisotropy, represented by *r*, becomes

$$r = \frac{I_{\parallel} - I_{\perp}}{I_{\parallel} + 2I_{\perp}} = \frac{3\left\langle \cos^2\theta \right\rangle - 1}{2} \tag{64}$$

where the brackets $\langle\ \rangle$ represent a weighted average with according to the weighting function $f(\theta)$. That is,

$$\left\langle \cos^2\theta \right\rangle = \frac{\int_0^{\pi/2} f(\theta)\cos^2\theta\, d\theta}{\int_0^{\pi/2} f(\theta)\, d\theta} \tag{65}$$

The maximum anisotropy depends on $f(\theta)$, which in turn depends on whether one excites the molecule with a single photon or with multiple photons. Let us first discuss the case of excitation using one photon.

Suppose the sample is excited with incident light polarized along the z-axis, and that the transition dipole moment connecting the ground and excited state is oriented also along the z-axis (as was the case in the previous paragraph). In this case, molecules which have their moments oriented along the z-axis will be preferentially excited. In a one-photon process, the matrix element driving the transition depends $e\vec{r}\cdot\vec{\varepsilon}$, where $e\vec{r}$ is the dipole moment operator and $\vec{\varepsilon}$ is the unit vector in the direction of polarization. Thus, the probability of excitation (which depends of the square of the matrix element) of a particular molecule is proportional to $\cos^2\theta$, where θ is the angle that the dipole moment of the molecule makes with the z-axis. Also, since the likelihood that the molecule is oriented between and angle θ and $\theta + d\theta$ is $\sin\theta\, d\theta$, then the number of excited molecules for one-photon absorption is

$$f_1(\theta) = \cos^2\theta \sin\theta\, d\theta \tag{66}$$

In this situation,

$$I_{\|} = \int_0^{\pi/2} \cos^4\theta \sin\theta\, d\theta \quad \text{and} \quad I_{\perp} = \int_0^{\pi/2} \cos^2\theta \sin^3\theta\, d\theta. \tag{67}$$

Using (67), (65) and (64) , we gat an anisotropy of 0.4.

Now consider two-photon absorption in the case of collinear polarizations of the absorption and fluorescence dipole moments. When the absorption and the fluorescence dipole moments are at an angle β with respect to one another, the anisotropy reduces to:

$$r = \left(\frac{2}{5}\right)\frac{3\langle\cos^2\beta\rangle - 1}{2} \tag{68}$$

For two-photon absorption the weighting function in (65) also changes. Let us consider the simplest case first – that of a single excitation beam with the emission and each of the two transitions are all polarized in the same direction. Because there are two transitions that occur in absorption, and each matrix element carries a $\cos\theta$ dependence, then

$$f_2(\theta) = \cos^4\theta \sin\theta\, d\theta \tag{69}$$

and the maximum anisotropy, using (69) and (68) is 0.57.

The situation becomes more complicated when we allow for the following for the relative directions of the dipole moments to vary from one another. If the first transition (ground to intermediate state) has a dipole moment in the z-direction and the second transition (intermediate to final state) has a dipole in the y-direction, and that the fluorescence is also polarized in the z-direction, then the number of excited molecules between an angle θ and $\theta + d\theta$ is given by

$$f_{2'}(\theta) = \pi \cos^2\theta \sin^3\theta\, d\theta \tag{70}$$

where the factor of π is a result of integrating over the azimuthal angle ϕ. In this case, the maximum value for r is 0.14. This is a drastic reduction from the previous case where all the transitions were collinear (r = 0.57), and from the case of one photon absorption (r = 0.4).

Even for these relatively simple cases, it is clear that the maximum anisotropy has a strong dependence on the number of photons involved in the excitation process and on the relative polarizations between the transitions in excitation and in emission. Unless one is aware of the polarizations of all these transitions, it should not be expected that multi-photon excitation will offer any advantage of one-photon excitation.

4.4. MULTIPHOTON MICROSCOPY

Since the development of femtosecond lasers based on the Ti-sapphire crystals, the use of multiphoton microscopy has become commonplace [e.g. 11–14]. The femtosecond system is highly desirable because it is relatively easy to generate high intensity pulses, thereby increasing the probability of inducing multiphonon absorption. The Ti-sapphire system is desirable because it is tunable in the wavelength range from roughly 700–1,000 nm, which matches well the region of the spectrum that tissue is most transparent to optical radiation. Images that result from the multiphoton microscopy are better resolved than those resulting from single photon absorption and also are able to be taken deeper into the biological sample. The final goal of this article is to briefly describe why these two characteristics are possible using multiphoton microscopy.

First consider the wavelength of the Ti-sapphire laser. Its emission wavelength is favorable for the following reasons.

1. The fact that the Ti-sapphire laser emits in a region where tissue is most transparent allows the laser light to penetrate deeper into the sample.
2. Because it wavelength is longer than that of visible light, Mie scattering is smaller. Thus there a fewer losses, which also increases the penetration depth and reduces noise due to scattering.
3. Single photon fluorescence microscopy often uses UV photons, which can cause damage to tissue. The near infrared radiation of the T-sapphire laser causes much less damage, in spite of the higher intensities.

Multiphoton absorption also allows for tighter focusing, and thereby higher resolutions. Figure 11 shows the general idea. Assuming a Gaussian shaped beam cross section, the intensity of the beam varies with the distance from the center of the beam, *r*, according to

$$I = Ne^{-r^2/2a^2} \tag{71}$$

where N is a constant proportional to the peak intensity. This is represented in Fig. 11 by the broader Gaussian. In single photon absorption microscopy, excitation is proportional to the intensity, and the excitation density of at the focal point goes as Eq. (71). Since multiphoton absorption goes as the square of the intensity, the beam width will go according to

$$I^2 = N'e^{-2r^2/2a^2} = N'e^{-r^2/a^2} \tag{72}$$

This has beam width that is smaller than that given in (71) by a factor of $\sqrt{2}$. In two photon absorption, the hence the excitation region will be smaller by a factor of $\sqrt{2}$. This advantage becomes even more significant for three-, four-, and five-photon absorption.

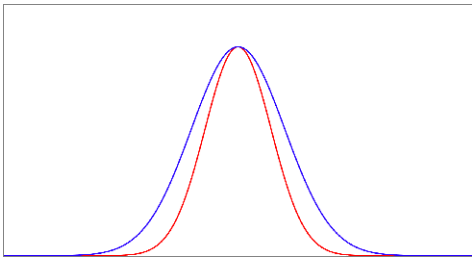

Figure 11. The shape of the intensity of light in a beam (broader Gaussian) and of the square of the intensity of the same beam (narrower Gaussian).

Of course, one must also consider the fact that the longer wavelength of the Ti-sapphire emission is more difficult to focus tightly. The focusing limit is proportional to the wavelength, so that the increased resolution due the squaring of the beam intensity of offset by the longer wavelength of the T-sapphire laser compared to visible or UV excitation.

Though in the above argument we discussed the beam at its focal point, the same reasoning applies to the beam at any position along the direction of propagation. Above and below the focal plane, two photon absorption will be less that one phonon absorption. The same argument was made in section where the z-scan method was described. Thus, the excitation of the sample occurs very close to the focal plane, with very little absorption (or fluorescence) above of below the plane. This results in a depth resolution much smaller than in single photon fluorescence microscopy, and consequently much clearer images.

References

1. Lakowicz, J.R., Principles of Fluorescence Spectroscopy, 3rd ed., (Springer, New York, 2006).
2. Loudon, R., *Quantum Theory of Light*, 2nd ed., (Oxford, Clarendon Press, New York, 1973).
3. Ashfold, N.M.R. and Prince, J.D., Multiphoton processes in molecular gases, Contemp. Phys. 29 (2), 125–157 (1988).
4. Goeppert-Mayer, M., Uber Elementarakte mit zwei Quantensprungen, *Ann. Phys.* **9**, 273–295 (1931).
5. Kaiser, W. and Garrett, C.G.B., Two-photon excitation in CaF_2:Eu^{2+}, *Phys. Rev. Lett.* **7**, 229–232 (1961).

6. Wirth, M.J., Koskelo, A., and Sanders, M.J., Molecular spectroscopy and symmetry, *Appl Spectrosc.* **35** (1), 14–21 (1981).
7. Makarov, N.S., Drobizhev, M., and Rebane, A., Two-photon absorption standards in the 550–1600 nm excitation wavelength range, *Optics Express* **16** (6), 4029–4047 (2008).
8. Mikalai Kruka, M., Karotkib, A., Drobizhev, M., Kuzmitskya, V., Gaela, V., and Aleksander Rebane, A., Two-photon absorption of tetraphenylporphin free base, *J. Luminesc*. 105, 45–55 (2003).
9. Tkaczyk, E. R., Tkaczyk, A. H., Mauring, K., Ye, J. Y., Baker, J. R., Jr., and Norris, T. B., Control of Two-photon Fluorescence of Common Dyes and Conjugated Dyes, *J Fluoresc*. **19**, 517–532 (2009). doi: 10.1007/s10895-008-0441-z
10. Birch, D., Multiphoton excited fluorescence spectroscopy of biomolecular systems, *Spectrochimica Acta* **A 57,** 2313–2336 (2001).
11. Dong Li, Wei Zheng, and Jianan Y., Two-photon autofluorescence microscopy of multicolor excitation, *Optics Lett.* **34**, 2 (2009).
12. Helmchen, F. and Denk, W., Deep Tissue Two-photon microscopy, *Nature Methods* **2** (12), 932–940 (2005).
13. Skala, M.C., Squirrell, J.M., Vrotsos, K.M., Eickhoff, J.C., Gendron-Fitzpatrick, A., Eliceiri, K.W., and Ramanujam, N., Multiphoton microscopy of endogenous fluorescence differentiates normal, precancerous, and cancerous squamous epithelial tissues, *Cancer Res*. **65** (4) (2005).
14. Mayevsky, A. and Rogatsky, G.R., Mitochondrial function in vivo evaluated by NADH fluorescence: from animal models to human studies, *Am. J. Physiol. Cell Physiol.* **292**, C615–C640 (2007).

TERAHERTZ SPECTROSCOPY OF BIOLOGICAL SYSTEMS

J.W. BOWEN*
School of Systems Engineering
University of Reading
Whiteknights, Reading
RG6 6AY, United Kingdom

Abstract Following recent developments in instrumentation, the terahertz part of the electromagnetic spectrum, lying between the microwave and infrared regions, now offers considerable potential for the study of the structure, dynamics and function of biological systems. The energies involved in many key biological processes lie in the terahertz frequency range, such as protein conformational changes and the collective motion of DNA base pairs along the hydrogen-bonded backbone. Terahertz spectroscopy is also a very sensitive probe of water in biological systems.

This chapter will consider the terahertz spectroscopy of biological systems at three levels of increasing scale and complexity: the macromolecular, cellular and organism levels. Relevant instrumentation and spectroscopic techniques will be introduced, and biomedical applications, such as label-free detection of DNA mutations and non-invasive biopsy to distinguish between normal and cancerous tissue, will be described. The particular challenges involved in carrying out terahertz spectroscopy of biological systems will be considered, together with some possible future directions.

1. Introduction

The terahertz range covers frequencies between 100 GHz and 10 THz, corresponding to wavelengths from 3 mm down to 30 μm. In the past, terahertz spectroscopy has been challenging, particularly due to the lack of convenient sources of terahertz radiation. However, recent technological advances have enabled the development of terahertz systems having unprecedented levels of sensitivity and sub-picosecond time resolution. Later sections of this chapter will show how spectroscopy in this range can provide a unique window on the structure and behaviour of biological systems. Prior to this, it will be helpful to consider the operation of a basic terahertz time-domain spectroscopy (TDS) system.

Terahertz TDS relies on ultrafast pulsed lasers for both the generation and coherent detection of broadband terahertz radiation. Systems are typically based around Ti:sapphire lasers emitting pulses of near-infrared (NIR) radiation with pulse widths of a few tens of femtoseconds. Such pulses contain frequency components spanning a bandwidth of several THz but are centred on an infrared wavelength of around 800 nm (equivalent to

* J.W. Bowen, School of Systems Engineering, University of Reading, Whiteknights, Reading, RG6 6AY, United Kingdom, e-mail: j.bowen@reading.ac.uk

B. Di Bartolo and J. Collins (eds.), *Biophotonics: Spectroscopy, Imaging, Sensing, and Manipulation*,
DOI 10.1007/978-90-481-9977-8_13,

a frequency of 375 THz). To be useful for terahertz spectroscopy, this output wavelength has to be shifted into the terahertz range whilst retaining as much of the bandwidth as possible. There are two broad approaches to achieving this: photoconductive generation and optoelectronic generation.

Photoconductive generation makes use of a metallised antenna structure photolithographically defined on the surface of an electrically insulating substrate. The antenna may be a simple planar dipole-like structure, with the two arms of the dipole connected to a dc bias supply. Underlying the gap between the dipole arms is a patch of semiconductor material, typically radiation damaged silicon on a sapphire substrate. With no illumination from the laser, the semiconductor region is non-conducting and no current flows through the antenna. However, when a pulse from the laser falls on the semiconductor, photocarriers are generated and current flows through the antenna. The current persists until the photo-excited electrons relax back to the semiconductor valence band after the laser pulse has subsided. As a consequence of the current flow, a terahertz beam is radiated from the antenna with a pulse width rather longer than the laser pulse width; typically a few 100 fs. The resulting terahertz pulse typically has a bandwidth spanning 0.1–3 THz.

In optoelectronic generation, the Ti:sapphire laser pulse is incident on a material with a non-linear second order susceptibility, such as a crystal of ZnTe. The non-linearity results in difference frequency generation between the different frequency components in the input laser pulse. The beam emerging from the crystal is therefore composed of these difference frequencies, and can span a bandwidth from 0.1 to 35 THz. However, the level of phase matching that can be achieved between the incident and emerging beams can limit the output frequency range and impose structure on the output spectrum. Attention has to paid to the crystallographic orientation to achieve maximum efficiency.

Gated detection of the terahertz beam can, again, be accomplished in two ways. Photoconductive detection employs an antenna structure similar to that used for photoconductive generation. A terahertz signal can only be detected when the semiconductor region is illuminated by an NIR pulse from the ultrafast laser. If this is the case, an incident terahertz signal will drive a current in the antenna. For a train of terahertz pulses, the resulting average current can be measured using conventional electronics. Varying the delay between the terahertz pulse and the NIR gating, or probe, pulse enables the shape of the terahertz pulse to be recorded.

In electro-optic detection, the terahertz pulse is incident co-linearly with the NIR probe pulse on a crystal (e.g. ZnTe) that exhibits the linear Pockels effect. If no terahertz pulse were present, an incident linearly polarized NIR beam would emerge from the crystal with a circular polarization. If a terahertz pulse is incident, the NIR birefringence of the crystal changes via the linear Pockels effect and the NIR probe beam emerges with an elliptical polarization. The degree of ellipticity depends on the terahertz field amplitude. A quarter-wave plate and Wollaston prism can be used to resolve the emergent NIR beam into orthogonal linear polarization components, which can be detected with a pair of balanced photodetectors. The terahertz field amplitude is directly proportional to the difference between the NIR intensities detected by the photodetectors. Again, the delay between the terahertz pulse and NIR probe pulse can be changed to record the shape of the terahertz pulse in the time domain.

A typical layout for a terahertz TDS system is illustrated in Fig. 1. The beam from the ultrafast laser is split into a pump beam, to drive the terahertz generator, and a probe beam to gate the terahertz detector. A scanning optical delay line is used to vary the relative time of arrival of the terahertz and probe pulses at the detector, thereby allowing the detected terahertz pulse shape to be mapped out. A pair of off-axis mirrors focuses the terahertz beam to a beam-waist at the sample, while a second pair of mirrors is used to deliver the transmitted terahertz beam to the detector. The terahertz time domain signal recorded by scanning the delay line contains information on both amplitude and phase transmission through the sample. Fourier transformation yields the transmission spectrum of the sample, with a spectral resolution that is inversely proportional to the recorded length of the time domain waveform (i.e. the maximum delay between the pump and probe pulses). Although a transmission system is shown, the optics can be rearranged to measure the reflected spectrum from the sample at a small oblique incidence angle. Raster scanning the sample through the terahertz beam, or arranging for the beam to be scanned across the sample, enables an image to be built up. Each pixel in such an image contains full spectral information. Signatures in the time domain can be related to discrete reflections within the sample and be used to provide depth information and 3D imaging.

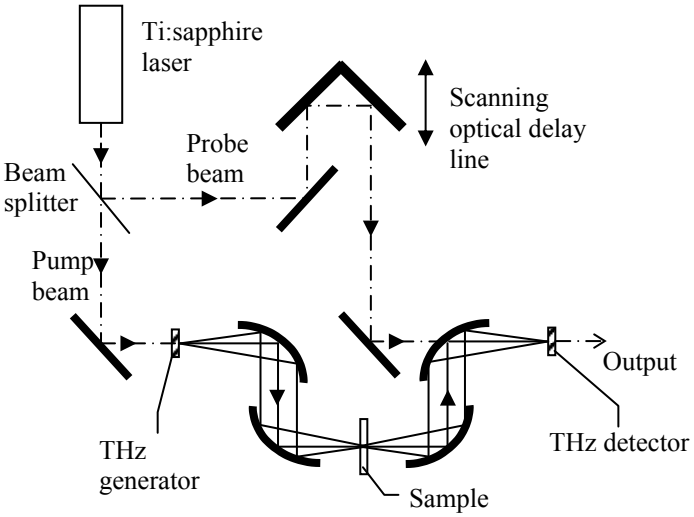

Figure 1. Terahertz time-domain spectroscopy system.

2. Terahertz Spectroscopy at the Molecular Level

Energies corresponding to molecular rotations, hydrogen bonding stretches and torsions, bond vibrations and crystalline phonon transitions lie within the terahertz range. All of these can give rise to distinct spectral signatures. Water in particular plays an important role in biological systems, with a network of water molecules surrounding and influencing

the dynamical behaviour of biomolecules, such as proteins. The water network is held together with hydrogen bonds, each water molecule bonding with three or four other water molecules at any given time. [1] However, each water molecule can undergo a variety of stretching, bending, librational and rotational modes on a sub-picosecond timescale, so that the hydrogen bonds between the water molecules are continually broken and reformed. Once a hydrogen bond is broken, translation and rotation of the molecule can lead to it forming bonds with new water molecules, with diffusion occurring on the picosecond timescale. Therefore the water network is in a constant state of flux. As the dynamical behaviour takes place on picosecond and sub-picosecond timescales, the corresponding frequencies lie in the terahertz range. However, this continual fluctuation and lack of long-range order gives rise to a spectrum that is devoid of sharp features at terahertz frequencies. The net effect is that liquid water is a strong absorber of terahertz radiation, the absorption coefficient rising almost linearly from about 125 cm^{-1} at 0.25 THz to around 350 cm^{-1} near 2 THz [2]. This makes terahertz spectroscopy an exquisitely sensitive probe of water in biological systems.

Many biomolecules, such as proteins, are complicated structures made up of large numbers of atoms. In this case, terahertz spectroscopy probes the collective vibrational modes of the whole molecule. Different molecules vibrate in different ways, giving rise to characteristic spectral signatures. Moreover, these large macromolecules can fold into different conformational states, which affect their biological function. Different conformations of the same molecule will have different collective vibrational modes and different spectral signatures in the terahertz range. However, biological systems operate in a hydrated state and so, in order to study the functional behaviour of biomolecules in something approaching their natural environment, it is necessary to ensure that they are sufficiently hydrated. This leads to two approaches to studying the terahertz spectra of biomolecules:

1. In the hydrated state the spectra are broad and featureless due to the lack of long-range order and continual fluctuation of the water network, but provide important information on the dynamical behaviour and conformational state of biomolecules.
2. In a polycrystalline state, the increased order enables the detection of discrete spectral fingerprints that identify different biomolecules. While this does not allow a direct measurement of the dynamical behaviour of the molecules, it may provide a useful input to modelling the underlying vibrational modes. We will consider this approach first.

2.1. FINGERPRINT SPECTRA

Early measurements of the spectra of biomolecules at terahertz frequencies were carried out on samples in the form of pellets pressed out of a mixture of the biomolecule in lyophilized (i.e. freeze-dried) polycrystalline powder form with a transparent host material, such as polyethylene. The absorption coefficient and refractive index can be determined with comparison to reference spectra of pellets of the pure host material. This yielded promising results – for example, Fischer et al. published a series of spectra of DNA nucleobases and nucleosides showing discrete spectral features [3]. However, for many molecules the spectral resolution of this technique is limited by inhomogeneous broadening of the spectral features due to the disordered nature of the sample.

Recently, significant improvements in linewidth have been demonstrated by using a technique known as waveguide THz-TDS [4]. The set-up is illustrated in Fig. 2. Instead of a pellet, the sample is in the form of an ordered polycrystalline film deposited on one plate of a parallel plate metal waveguide. The film can be prepared using techniques such as drop-casting or sublimation. The sub-wavelength size of the gap in the waveguide ensures TEM mode dispersion-free propagation. The terahertz beam in a standard THz-TDS transmission system is coupled into and out of the waveguide using cylindrical silicon lenses. The planar ordering of the film strongly reduces the inhomogeneous broadening, which can be further improved by cooling the waveguide assembly to 77 K in a liquid nitrogen cryostat. Using this technique Laman et al. [4] have published sharply defined fingerprint spectra for the nucleobase thymine, the nucleoside adenosine, the deoxynucleoside deoxycytidine, the sugar D-glucose, and the amino acids tryptophan, glycine and L-alanine. The authors intend to apply the technique to larger biomolecules in the future.

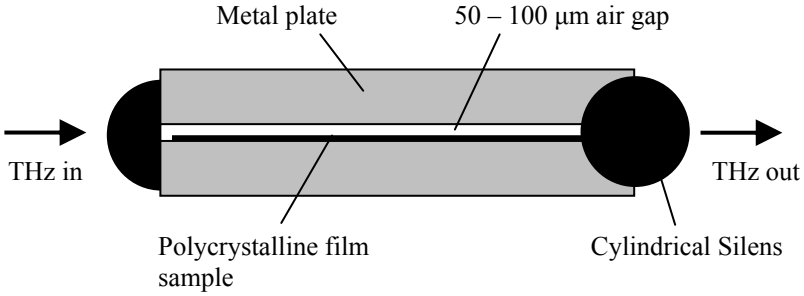

Figure 2. Waveguide THz-TDS set-up.

2.2. SOLVATION DYNAMICS

It has already been mentioned that hydrated biomolecules have broad, featureless spectra in the terahertz range. However, terahertz spectroscopy of biomolecules in solution can provide dynamical information about the molecule and its interaction with its solvent which is unobtainable through any other means. Recent work in this area has indicated that biomolecules influence the dynamics of the surrounding water network to a much greater distance from the molecule than had previously been thought. It has been shown that proteins can slow down the fluctuations in the water hydrogen bond network out to a distance of at least 10 Å [1]. In the case of the lambda repressor protein $\lambda^*_{6\text{-}85}$, this distance exceeds 20 Å. These distances are much greater than the static hydration radius probed using techniques such as nuclear magnetic resonance and neutron scattering. Within this dynamical hydration shell, the water dynamics are distinct from those of bulk water and give rise to a distinct terahertz absorbance. As the distance between molecules in living cells is only about 20–30 Å, the collective protein–water dynamics can result in a new medium in which very little bulk water is present. These results have profound implications for understanding biological function.

Biomolecule solvation dynamics can be explored by measuring the concentration dependence of the terahertz absorption of the biomolecule in an aqueous buffer solution. At first glance, the results can seem surprising. For low concentrations of the biomolecule, the absorbance tends to be greater than that for the buffer solution alone. This is known as the "terahertz excess". As the concentration is increased, the absorbance reaches a peak and then falls until, for sufficiently high concentrations, it is below that of the pure buffer solution. This is known as the "terahertz defect". This behaviour can only be explained by the presence of "biological" or "hydration" water, with terahertz response different to bulk water.

Consider a single biomolecule added to a terahertz-transparent container of fixed volume completely filled with bulk water. The molecule will take up some space and so displace some of the water from the container. As the molecule is likely to have a lower absorption than water in the terahertz range, the overall absorption of the contents of the container would be expected to be reduced. Taken on its own, this would constitute a terahertz defect. However, if the molecule is surrounded by a dynamical hydration shell of water with modified physical properties, which has higher terahertz absorption, the overall absorption can increase. This contributes to a terahertz excess. As the presence of the biomolecule slows the fluctuations in the surrounding water network, the frequency of peak absorption shifts, resulting in increased terahertz absorption by the hydration water. Whether the overall effect is a terahertz excess or terahertz defect depends on the volume of bulk water displaced by the molecule relative to that of its surrounding dynamical hydration shell, as well as the relative terahertz absorptions of the molecule and the hydration water. It transpires that for a single biomolecule the contribution from the hydration water outweighs that due to displacement, leading to a terahertz excess. If we steadily add more biomolecules, each will be surrounded by a dynamical hydration shell and the overall volume of bulk water modified to become hydration water will begin to increase. As a result, the terahertz absorption will increase with the concentration of biomolecules. If we continue adding biomolecules, eventually a concentration will be reached where, on average, the dynamical hydration shells begin to touch each other, at which point all of the bulk water will have been converted to hydration water. If the concentration is increased beyond this point, the dynamical hydration shells will overlap. As all of the bulk water has already been converted to hydration water, the only effect of adding further biomolecules will be to displace an increasing amount of this water, resulting in a reduction in terahertz absorption. For a sufficiently high concentration, the overall absorption can fall below that of pure bulk water, giving an overall terahertz defect. This simple model fits the measured data well in the case of smaller biomolecules, such as sugars. Larger biomolecules, such as proteins, show a more complicated concentration dependence with the absorption falling off more rapidly at higher concentrations [5]. It is thought that this may be due to the hydration water influenced by two or more protein molecules having a different dynamical behaviour to that around a single protein molecule. Nevertheless, even in this case, the model fits the experimental data well for concentrations up to the absorption peak and can be used to estimate the radius of the dynamical hydration shell.

Leitner et al. [1] have used this technique to measure the size of the dynamical hydration shell around saccharide molecules. They found that the shell radius is: 3.7 ± 0.9 Å, containing about 50 water molecules, for glucose; 5.7 ± 0.4 Å, or 150 water molecules,

for lactose; and 6.5 ± 0.9 Å, or 190 water molecules, for trehalose. It is known that plants that can survive extreme drought conditions produce sugars for protection. This process, known as anhydrobiosis, seems to have a stabilising effect on proteins and cell membranes and is now used for storage of vaccines in a dried state. The terahertz measurements suggest that the sugars slow the hydration dynamics, leading to reduced biological activity of the proteins.

Further measurements of this sort on protein solutions [6] have indicated that the influence on water dynamics is much less for partially unfolded proteins than for the wild type. However, large changes are seen for site specific mutants. From transient fluorescence spectroscopy it is known that the protein ubiquitin takes around 1 s to fold to its native state. However, the terahertz response is around 100 times faster, suggesting that the solvent has undergone major rearrangement long before the protein has settled into its native shape [7]. This has lead to speculation that protein surfaces may have evolved to dynamically restructure their solvents [1].

2.3. CONFORMATIONAL CHANGE

Conformational change of proteins plays an important role in many biological processes. Because it modifies both the collective vibrational modes of the protein and its influence on the dynamics of the surrounding water network, changes occur to the terahertz absorption spectrum. Therefore, terahertz spectroscopy may prove useful in understanding protein dynamics and monitoring conformational changes.

The transmembrane protein bacteriorhodopsin, found in the archaebacteria *Halobacterium salinarum*, which lives in high salinity environments, undergoes a series of conformational changes in response to light. The net effect is the transfer of a proton from the cytoplasmic to the extracellular face of the membrane. It is a key step in enabling the organism to generate energy through photosynthesis. Conformational change in bacteriorhodopsin is convenient for spectroscopic study because one of its intermediate states (state M) can be prolonged indefinitely by cooling below 233 K. Whitmire et al. [8] measured the terahertz absorbance of 200 μm thick hydrated films of bacteriorhodopsin. A distinct increase in the absorbance of wild-type bacteriorhodopsin, cooled below 233 K, was seen when the sample was illuminated with white light. Monitoring the UV/visible absorption was used to confirm that this corresponded to a change in conformation. Similar measurements on D96N mutant bacteriorhodopsin showed no change on illumination.

An increase in terahertz absorption has also been seen on illumination of photo-active yellow protein with 450 nm light [9]. In this case, the protein was suspended in physiological buffer solution and the measurements were carried out at room temperature. The change in absorbance corresponds with a change in conformation of the protein from the pG ground state to the pB photo-intermediate state.

2.4. LIGHT-INDUCED TERAHERTZ RADIATION

Terahertz radiation can be used to explore light-induced biological processes at an even more direct and fundamental level than observing the associated conformational changes. As a result of illuminating a biological sample with an ultrafast pump pulse of appropriate

wavelength light, terahertz radiation is emitted due to the fundamental primary charge translocation phenomena. Groma et al. [10] have explored the terahertz emission from the light-induced sudden polarization of the retinal chromophore in bacteriorhodopsin. They used the pump-probe set-up illustrated in Fig. 3 to record the time-domain terahertz emission from both the wild-type and acid blue forms of bacteriorhodopsin. They found that their results were best modelled by a correlated sequence of electron and proton transfer.

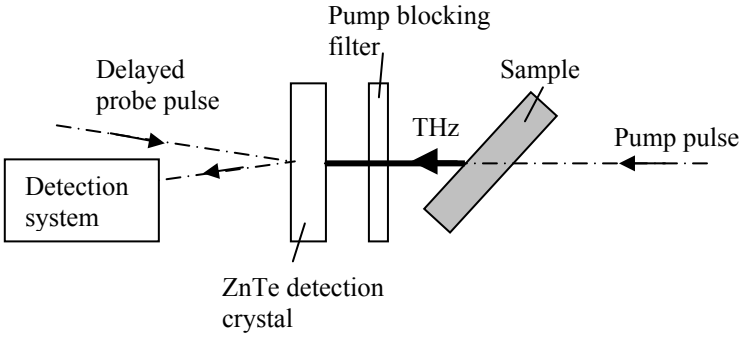

Figure 3. Set-up for light-induced terahertz radiation from biological sample.

2.5. LABEL-FREE DNA SEQUENCING

Distinct differences are seen between the terahertz complex optical constants of hybridized and denatured DNA, with both the refractive index and absorption coefficient of hybridized DNA being higher than those of denatured DNA [11]. This has been exploited to enable label-free DNA sequencing with femtomolar sensitivity levels and single-base mutation detection capability. Unlike current DNA sequencing techniques, there is no need to label with fluorescent chromophores. This avoids the costly additional preparatory labeling step which can introduce modifications in DNA strand conformation, lowering the precision of gene detection. Label degradation, labeling yield fluctuations, fluorescence efficiency site dependence and fluorophore quenching are also avoided.

The procedure involves denaturing the DNA to be tested, so that it is separated into single strands. This denatured DNA is then mixed with short single-stranded DNA molecules (oligos) with a single-base mutation, and allowed to rehybridize. The oligos act as probes, attaching to the long single-stranded DNA wherever there is a complementary single-base mutation and blocking the rehybridization of pairs of long strands showing the mutation. The non-mutated long strands rehybridize to form long double-stranded DNA. The mutated long strands with probe oligos attached have a refractive index and absorption coefficient close to those of denatured DNA. Therefore, the overall effective terahertz optical constants of the DNA sample will lie somewhere between those for hybridized and denatured DNA, and are related to the relative proportion of DNA showing the single-base mutation. Different single-base mutations can be tested for by using oligos with different mutations.

In order to improve the sensitivity of the technique for small amounts of DNA, the sample is placed on a terahertz transmission line resonator structure. A recent version of this type of terahertz biochip consists of a parallel plate waveguide with integrated photoconductive terahertz generator and detector [12]. The upper plate of the waveguide is removable and has a series of corrugations across it forming a resonator. This plate can be functionalized with probe oligos to which the DNA to be tested can be added. The resulting optical constants of the DNA sample modify the resonant frequency and allow the concentration of mutated DNA to be determined. Once used, the functionalized upper plate of the waveguide can be discarded and replaced with a new one, enabling the integrated terahertz generator and detector to be re-used.

2.6. BIOAFFINITY SENSORS

Some work has been carried out towards the development of terahertz bioaffinity sensors aimed at high-throughput applications, such as medical diagnosis and allergy testing based on antigen-antibody reactions. Ogawa et al. [13] have demonstrated label-free detection of the protein streptavidin using terahertz imaging. They used a polyvinylidene difluoride membrane with an array of dots consisting of biotin molecules immobilized on its surface using polytheylene glycol or polytheylene glycol methyl. Different concentrations of streptavidin (which binds to biotin) were applied to the biotin array, and the membrane was sandwiched between a mirror and a silicon plate. This whole sandwich structure was then imaged in a terahertz TDS reflection imaging system. Fabry–Perot interference within the sandwich structure is sensitive to the refractive index of the streptavidin and the resulting fringes in the frequency domain are shifted dependent on the streptavidin concentration. By forming an image at a frequency for which the reflection change with streptavidin concentration is maximized, it was found that 1.6×10^{-5} M (27 ng mm^{-2}) of streptavidin could be detected. This was markedly better than 8×10^{-5} M streptavidin detected with fluorescent label imaging.

3. Terahertz Spectroscopy at the Cellular Level

Cells are complex assemblages of many molecules – each molecule has collective vibrational modes and associated hydration water dynamics which contribute to the terahertz spectra of the cell. Terahertz spectroscopy can be used to differentiate between cells and to sense changes in cells. It is also not unreasonable to assume that terahertz radiation that is absorbed may modify cellular function. These aspects are considered in this section.

3.1. DIFFERENTIATION BETWEEN BACTERIAL SPORES

Terahertz spectroscopy between 0.5 and 1.5 THz has shown that refractive index in this range can be used to differentiate between bacterial spores of *Bacillus subtilis* and *Bacillus thuringiensis* [14]. On the other hand, the absorption coefficient proved to be not specific enough to allow discrimination. The measurements were carried out on pellet samples

formed from a mixture of the bacterial spores with high density polyethylene. The refractive index of the spores was recovered using a Maxwell–Garnett effective medium model. This work is of interest for the detection of bacterial spores, such as anthrax, in security applications, as many packing materials are relatively transparent to terahertz radiation.

3.2. SENSING CHANGES IN LIVING CELL MONOLAYERS

The extreme sensitivity of terahertz spectroscopy to water can be exploited to sense nano-scale changes in living cell monolayers. By rapidly switching the sample in and out of the beam and using lock-in detection, the difference between the transmission of a thin film and its blank substrate can be measured with a signal-to-noise ratio higher than conventional THz-TDS. A signal-to-noise ratio of around 20,000:1 can be achieved by using this technique, which is known as terahertz differential time domain spectroscopy (THz-DTDS) [15]. The absorption coefficient of water at room temperature is around 200 cm^{-1} at 1 THz and so the amplitude change caused by 1 nm of liquid water is of the order of 10^{-5}. Therefore, THz-DTDS is capable of sensing a 1 nm thickness difference of liquid water.

In [15], Liu et al. present the results of experiments carried out on living monolayers of bovine lung microvessel endothelial cells. They treated the cells with vascular endothelial growth factor (VEGF) which induces flattening and retraction of cells within the monolayer. They compared their results with phase contrast microscopy and electrical cell-substrate impedance sensing (ECIS). Three hours after treatment with VEGF, they could see a 29% difference in terahertz transmission between treated and untreated cells, but could not detect any change using optical phase contrast microscopy. After 24 h there was a visible difference with phase contrast microscopy and a 43% difference in terahertz transmission. The terahertz measurements agreed well with changes detected with ECIS. However, THz DTDS can sense subtle changes in cell thickness and changes in cell architecture, unlike ECIS which can only detect changes that affect inter-cell spacing. Therefore, THz DTDS can be used to measure minute changes in cell monolayers. Used in conjunction with optical microscopy or ECIS, it may be useful for measuring cell growth, cell volume and morphology changes over time.

3.3. NEAR-FIELD IMAGING OF NEURONS

In common with molecules, ions in solution can influence the dynamical behaviour of surrounding water atoms, leading to a concentration dependent terahertz absorbance. Ionic concentrations play a crucial role in neural signal transduction along axons. Axons are tubular structures with distinct intracellular and extracellular ionic concentrations. Flow of potassium ions out of the axon through the cell membrane, together with flow of sodium ions into the axon can establish an action potential or nerve impulse across the membrane. Disruption of these concentrations can modify the functioning of the neuron. Potassium (K^+) ions in solution, which are usually in the majority inside an axon, show a higher terahertz absorbance than sodium (Na^+) ions. Therefore, it is possible to use this ionic contrast to image neurons at terahertz frequencies and monitor the axonal water flux [16].

As axons are of small diameter, near-field imaging techniques have to be used to achieve the necessary sub-wavelength resolution. In [16], Masson et al. focus the beam in a terahertz transmission TDS system onto a sub-wavelength aperture placed just in front of the sample to be imaged. Aperture sizes from 100 to 200 μm were used. Radiation transmitted through the aperture and sample was collected with a second lens and focused onto the terahertz detector. The delay between the pump and probe pulses from the ultrafast laser were kept constant and the sample mechanically scanned relative to the aperture to build up an image. The samples were earthworm axons from 50 to 100 μm in diameter, which remain alive for at least 10 h after dissection.

Results are presented in [16] which explore how the image contrast depends on ionic concentration. As well as a 3D image of an axon, image cross-sections are presented which show the changes in ionic concentration and morphology induced by the toxic effect of a sodium-channel activator and by temperature changes. Variations as small as 10 μM of ion concentration and 20 fl of water volume were detected.

3.4. EFFECTS OF TERAHERTZ RADIATION ON CELL GROWTH RATES

Despite the fact that terahertz radiation is non-ionising, there has been continued speculation since the 1970s that low levels of terahertz radiation may influence biological processes such as cell division. More recently, irradiation of the yeast *Saccharomyces cerevisiae* with continuous wave radiation at 341 GHz indicated enhanced growth rates at early stages of exposure [17]. These experiments were carried out on yeast microcolonies growing on agar plates. The power density was 57.8 μW mm^{-1}. Other frequencies in the 192–341 GHz range resulted in no change. Similar effects were seen by Grundler and co-workers in the 1970s–1990s at frequencies around 40 GHz [18, 19]. Other irradiation effects reported recently include an increase in genomic instability in human lymphocytes [20], and morphological and membrane potential changes in neurons [21]. Apart from obvious safety concerns, understanding effects of this sort may shed light on biological processes and lead to new biomedical application areas.

4. Terahertz Spectroscopy at the Organism Level

4.1. PLANT WATER CONTENT

The sensitivity of terahertz to the presence of water makes it an excellent non-contact, non-destructive probe of water content in plants. The quantification of water content and the onset of water stress is of interest to plant physiologists. Measurements relating leaf transmittance to water loss of drying leaves and negative water potential are presented in [22].

4.2. MEDICAL IMAGING

Terahertz imaging shows potential as a new imaging modality for a number of medical applications. Unlike X-rays, it is non-ionising and so potentially safer, and each pixel contains spectral information which may be used to identify different tissue types,

diseased regions etc. However, it is not clear what the image contrast mechanisms are, although they tend to be related to water content. For example tumours tend to have a higher water content and lower lipid concentration than normal tissue [23]. Terahertz absorption of water is much higher than that of lipid and is probably a major contributor to differences in terahertz reflection from tumours and normal tissue. However, dehydrated specimens have also shown tissue contrast between normal regions and tumours, and so increased cell density and the presence of certain proteins may also have a role to play. Examples of terahertz medical imaging include: imaging of teeth and tooth decay [24]; imaging of the skin cancer, basal cell carcinoma [25]; imaging of breast cancer [23]; and imaging of colon cancer [26]. Cancer imaging shows good agreement with histopathology and gives hope for the development of non-invasive biopsy techniques, whereby the full extent of the tumour can be determined by terahertz imaging prior to carrying out any surgical procedure to remove tissue. This would remove the need for repeated surgery, which is sometimes currently necessary because not all of the tumour has been removed in first instance.

The terahertz images can be constructed from a spatial map of a wide range of different imaging parameters. For example, pulse height, pulse width and time delay can all be used. Another parameter that has been used is the time post-pulse (TPP), which is equal to the ratio of the electric field amplitude at some time after the pulse minimum to the electric field amplitude at the minimum [25]. The time at which the electric field is sampled after the pulse minimum can be adjusted to maximize the image contrast. An alternative imaging parameter is the ratio of the maximum to minimum pulse amplitudes across the image area [23].

One drawback with terahertz medical imaging is the limited penetration depth into body tissues due to the high water content. At 0.5 THz, the penetration depth into skin for one commercially available terahertz imaging system (TeraView TPI Imaga) is around 0.5 mm [2]. The penetration depth into fatty tissue (typical of breast tissue) is much higher, at around 6.5 mm. Nevertheless, a high proportion of cancers lie in the outer regions of organs and Ashworth et al. [27] have demonstrated an interoperative terahertz probe that can be used during surgery to indicate the extent of a tumour.

In an attempt to increase the terahertz contrast of cancer cells, Oh et al. [28] have demonstrated the use of gold nano-rods as nanoparticle contrast agents. They have presented results for gold nano-rods bound to live epidermoid carcinoma A431 cells in solution. NIR laser radiation gives rise to surface plasmon polaritons, inducing a water temperature increase. The terahertz refractive index of the water increases as a consequence, giving rise to a terahertz reflection change. As well as increased contrast, there is scope for micrometre spatial resolution by focusing and direction of the NIR laser illumination.

Another potential application is in burn wound assessment. Burned skin has lower water concentration, giving a lower effective terahertz refractive index and therefore is less reflective [29]. A halo effect in terahertz images indicates the extent of the damaged tissue. An added advantage is that terahertz radiation can penetrate through medical dressings and so there is no need to remove a dressing to make an assessment.

4.3. PHARMACEUTICALS

Another important medical application of terahertz spectroscopy and imaging is in the development and testing of pharmaceutical products. It is possible to distinguish between different polymorphs [30] and hydrate forms [31] of drugs. This is of importance both for the therapeutic behaviour of the drug, for quality assurance during in manufacture, and legally to identify counterfeit drugs. Terahertz imaging can also be used to measure the coating thickness and dissolution performance in sustained release tablets [32].

4.4. IMAGING AND SPECTRAL ARTEFACTS

One complication associated with terahertz imaging and spectroscopy of inhomogeneous samples, as typically encountered in medical imaging applications, is the introduction of image and spectral artefacts. Indeed, some artefacts due to distortion of the terahertz beam by the sample can even occur in samples consisting of homogeneous parallel-sided slabs of material. Thus far, there has been little recognition in the terahertz community that the images and spectra recorded with time-domain imaging systems are dependent on the design of the system and the form of the beam as well as the properties of the object being imaged.

In terahertz systems, the terahertz beam is typically only a few wavelengths or tens of wavelengths across. This lateral confinement leads to the beam diffractively spreading as it propagates. In a typical imaging system, the sample is placed at a tightly focused beam-waist in order to gain high spatial resolution, but this tends to magnify the diffractive spreading and the associated artefacts.

For the purposes of analyzing the artefacts introduced as the beam passes through or is reflected from the sample, it is simplest to model the beam as a superposition of plane waves travelling in all possible directions [33]. Each plane wave has associated with it a complex amplitude. The full set of these amplitude weighting factors for all of the plane waves travelling at different angles is known as the beam's angular spectrum. As the beam propagates, the plane waves go in and out of phase with each other giving rise to the changing form and diffractive spreading of the beam. The amplitude and phase of the electric field at any point in the beam can be determined by summing the plane waves at that point, taking account of their relative phases (i.e. by integrating the phase-shifted angular spectrum of plane waves over all angles). Therefore, the angular spectrum describes the whole beam throughout the region of space in which it exists. It is necessary to retain a full vectorial model of the beam, which can be done by representing it as two superimposed independently propagating beams of differing polarization, each described by its own angular spectrum of plane waves. The complex amplitudes of each angular spectrum can be determined from two-dimensional Fourier transformation of the beam profile in a designated "source" plane. The theorems of Fourier Optics can be used to determine the transformations of the angular spectrum as the beam propagates through a train of focusing elements.

Once the angular spectrum of plane waves has been determined, the interaction of the beam with the sample can be considered in terms of the interaction of each plane wave with the sample, as governed by the Fresnel equations.

Using this approach, it is found that, even with a homogeneous plane-parallel sample, the emergent beam profile is distorted so that it loses any axial symmetry and cross-polarized components are generated [34]. These effects prove to be much more significant for the short pulses of terahertz radiation used in THz-TDS than in continuous wave systems [35]. This is a consequence of the effects being washed-out in continuous wave systems due to multiple reflections within the sample.

Distortion of the beam and cross-polarization generation both lead to a reduction in the signal coupled to the detection system and an over estimation of the sample's absorption coefficient. They can also result in an error in the recorded phase. These effects are frequency dependent, with the distortion more severe at low frequencies and detection often more efficient at high frequencies.

In determining the optical constants of a sample, it has been usual to assume that the incident beam can be treated as a normal incidence plane wave and that the sample does not distort the beam. In fact, this can be a rather poor approximation if the sample is placed at a tightly focused beam waist and errors in the optical constants can result [34].

A more complicated situation occurs in the case of non-homogeneous samples. In the case of a boundary between two different materials that bisects the beam, part of the beam will travel through one material and part through the other. This results in distinct phase-cancellation features that appear as dips at specific frequencies in the transmission or reflection spectrum, due to destructive interference between the two regions of the spatially coherent beam [36]. Dark lines due to this effect can be seen in some terahertz images presented at specific frequencies.

However, there is potential for this phase cancellation effect to give improved edge detection and sub-wavelength resolution of edges. The strength of the phase cancellation feature depends on the relative location of the material boundary with respect to the beam. With continuous wave radiation at 94 GHz, it has proven possible to exploit this to determine the edge location to better than 1/50 of the wavelength and 1/158 of the beam waist size [37]. Similar results should be possible at higher terahertz frequencies and with time domain systems, opening up the possibility of sub-wavelength edge resolution at large stand-off distances and with improved signal-to-noise ratio compared to near-field microscopy techniques.

5. Conclusions

As we have seen, terahertz spectroscopy is a powerful new tool for studying the structure and behaviour of a wide range of biological systems, from the molecular to the organism level. It is a particularly sensitive probe of the dynamics of biomolecules and their surrounding water networks on the picosecond and sub-picosecond timeframe, and may lead to greater understanding of biological function at the molecular level. Much of this work has only recently begun, and there is much still left to do, particularly in understanding the interaction of terahertz radiation with biological systems at the cellular level. At the organism level, terahertz techniques offer the promise of a new medical imaging modality, capable of distinguishing cancerous from normal tissue. The information is likely to be complementary to that obtained using other imaging modalities. However, this work would benefit from the development of wideband flexible terahertz endoscopes capable of delivering the radiation inside the body in order

to overcome the limited penetration depth. There is scope to develop tomographic techniques for 3D imaging of body tissues, but further work needs to be done to understand image contrast mechanisms, to identify and remove image and spectral artefacts, and to capitalize on the potential for improved spatial resolution.

References

1. Leitner, D.M., Gruebele, M. and Havenith, M. (2008) Solvation dynamics of biomolecules: modeling and terahertz experiments, *HFSP Journal* **2**, 314–323.
2. Pickwell, E. and Wallace, V.P. (2006) Biomedical applications of terahertz technology, *J. Phys. D: Appl. Phys.* **39**, R301–R310.
3. Fischer, B.M., Walther, M. and Uhd Jepsen, P. (2002) Far-infrared vibrational modes of DNA components studied by terahertz time-domain spectroscopy, *Phys. Med. Biol.* **47**, 3807–3814.
4. Laman, N., Sree Harsha, S., Grischkowsky, D. and Melinger, J.S. (2008) High-resolution waveguide THz spectroscopy of biological molecules, *Biophys. J.* **94**, 1010–1020.
5. Born, B., Kim, S.J., Ebbinghaus, S., Gruebele, M. and Havenith, M. (2009) The terahertz dance of water with the proteins: the effect of protein flexibility on the dynamical hydration shell of ubiquitin, *Faraday Discuss.* **141**, 161–173.
6. Ebbinghaus, S., Kim, S.J., Heyden, M., Yu, X., Gruebele, M., Leitner, D.M. and Havenith, M. (2008) Protein sequence- and pH-dependent hydration probed by terahertz spectroscopy, *J. Am. Chem. Soc.* **130**, 2374–2375.
7. Kim, S.J., Born, B., Havenith, M. and Gruebele, M. (2008) Real-time detection of protein-water dynamics upon protein folding by terahertz absorption spectroscopy, *Angew. Chem. Int. Ed.* **47**, 6486–6489.
8. Whitmire, S.E., Wolpert, D., Markelz, A.G., Hillebrecht, J.R., Galan, J. and Birge, R.R. (2003) Protein flexibility and conformational state: a comparison of collective vibrational modes of wild-type and D96N bacteriorhodopsin, *Biophys. J.* **85**, 1269–1277.
9. Castro-Camus, E. and Johnston, M.B. (2008) Conformational changes of photoactive yellow protein monitored by terahertz spectroscopy, *Chem. Phys. Lett.* **455**, 289–292.
10. Groma, G.I., Hebling, J., Kozma, I.Z., Váró, G., Hauer, J., Kuhl, J. and Riedle, E. (2008) Terahertz radiation from bacteriorhodopsin reveals correlated primary electron and proton transfer processes, *PNAS* **105**, 6888–6893.
11. Haring Bolivar, P., Nagel, M., Richter, F., Brucherseifer, M., Kurz, H., Bosserhoff, A. and Büttner, R. (2004) Label-free THz sensing of genetic sequences: towards 'THz biochips', *Phil. Trans. R. Soc. Lond.* A **362**, 323–335.
12. Nagel, M., Först, M. and Kurz, H. (2006) THz biosensing devices: fundamentals and technology, *J. Phys.: Condens. Matter.* **18**, S601–S618.
13. Ogawa, Y., Hayashi, S., Oikawa, M., Otani, C. and Kawase, K. (2008) Interference terahertz label-free imaging for protein detection on a membrane, *Opt. Expr.* **16**, 22083–22089.
14. Maleck-Rassoul, R., Garet, F. and Fromentin, P. (2008) Study of two sporulated bacillus species by THz time domain spectroscopy, *EOS Annual Meeting*, Paris, 852.
15. Liu, H.-B., Plopper, G., Earley, S., Chen, Y., Ferguson, B. and Zhang, X.-C. (2007) Sensing minute changes in biological cell monolayers with THz differential time-domain spectroscopy, *Biosens. Bioelect.* **22**, 1075–1080.
16. Masson, J.-B., Sauviat, M.-P., Martin, J.-L. and Gallot, G. (2006) Ionic contrast terahertz near-field imaging of axonal water fluxes, *PNAS* **103**, 4808–4812.

17. Hadjiloucas, S., Chahal, M.S. and Bowen, J.W. (2002) Preliminary results on the non-thermal effects of 200–350 GHz radiation on the growth rate of *S. cerevisiae* cells in microcolonies, *Phys. Med. Biol.* **47**, 3831–3839.
18. Grundler, W., Kaiser, F. and Frohlich, H. (1977) Resonant growth rate response of yeast cells irradiated by weak microwaves, *Phys. Lett.* A **62**, 463–466.
19. Grundler, W. (1992) Intensity and frequency dependent effects of microwaves on cell growth rates, *Bioelectrochem. Bioenerg.* **27**, 361–365.
20. Korenstein-Ilan, A., Barbul, A., Hasin, P., Eliran, A., Gover, A., Korenstein, R. (2008) Terahertz radiation increases genomic instability in human lymphocytes, *Radiat. Res.* **170**, 224–234.
21. Olshevskaya, J.S., Ratushnyak, A.S., Petrov, A.K., Kozlov, A.S. and Zapara, T.A. (2008) Effect of terahertz electromagnetic waves on neurons systems, *IEEE Region 8 SIBIRCON 2008,* 210–211.
22. Hadjiloucas, S., Karatzas, L.S. and Bowen, J.W. (1999) Measurements of leaf water content using terahertz radiation, *IEEE Trans. Microwave Theory Tech.* **47**, 142–149.
23. Fitzgerald, A.J., Wallace, V.P., Jimenez-Linan, M., Bobrow, L., Pye, R.J., Purushotham, A.D. and Arnone, D. (2006) Terahertz pulsed imaging of human breast tumors, *Radiology* **239**, 533–540.
24. 24. Crawley, D., Longbottom,C., Wallace, V.P., Cole, B., Arnone, D.D. and Pepper, M. (2003) Three-dimensional terahertz pulse imaging of dental tissue, *J. Biomed. Opt* **8**, 303–307.
25. Woodward, R.M., Wallace, V.P., Pye, R.J., Cole, B.E., Arnone, D., Linfield, E.H., and Pepper, M. (2003) Terahertz pulse imaging of *ex vivo* basal cell carcinoma, *J. Investigat. Dermatol.* **120**, 72–78.
26. Reese, G., Reid, C., Goldin, R., Tran-Dang, M.-A.., Fitzgerald, A., Tekkis, P., and Wallace, V.P (2008) Using terahertz pulsed imaging (TPI) to identify colonic pathology, *33rd International Conference on Infrared, Millimeter and Terahertz Waves,* Pasadena, 532.
27. Ashworth, P.C., O'Kelly, P., Purushotham, A.D., Pinder, S.E., Kontos, M., Pepper, M., and Wallace, V.P (2008) An intra-operative THz probe for use during the surgical removal of breast tumors, *33rd International Conference on Infrared, Millimeter and Terahertz Waves,* Pasadena, 767–769.
28. Oh, S.J., Kang, J., Maeng, I., Suh, J.-S., Huh, Y.,-M., Haam, S. and Son, J.-H. (2009) Nanoparticle-enabled terahertz imaging for cancer diagnosis, *Opt. Expr.* **17**, 3469–3475.
29. Taylor, Z.D., Singh, R.S., Culjat, M.O., Suen, J.Y., Grundfest, W.S., Lee, H. and Brown, E.R. (2008) Reflective terahertz imaging of porcine skin burns, *Opt. Lett.* **33**, 1258–1260.
30. Taday, P.F., Bradley, I.V., Arnone, D.D., and Pepper, M. (2003) Using terahertz pulse spectroscopy to study the crystalline structure of a drug: a case study of the polymorphs of ranitidine hydrochloride, *J. Pharm. Sci.* **92**, 831–838.
31. Zeitler, J.A., Kogermann, K., Rantanen, J., Rades, T., Taday, P.F., Pepper, M., Aaltonen, J. and Strachan, C.J. (2007) Drug hydrate systems and dehydration processes studied by terahertz pulsed spectroscopy, *Int. J. Pharm.* **334**, 78–84.
32. Ho, L., Müller, R., Gordon, K.C., Kleinebudde, P., Pepper, M., Rades, T., Shen, Y., Taday, P.F. and Zeitler, J.A. (2008) Applications of terahertz pulsed imaging to sustained-release tablet film coating quality assessment and dissolution performance, *J. Control. Release*, **127**, 79–87.
33. Martin, D.H. and Bowen, J.W. (1993) Long-wave optics, *IEEE Trans. Microw Theory Tech* **41**, 1676–1690.
34. Bowen, J.W., Walker, G.C., Hadjiloucas S. and Berry, E.A. (2004) The consequences of diffractively spreading beams in ultrafast THz spectroscopy, *Joint 29th International Conference on Infrared and Millimeter Waves and 12th International Conference on Terahertz Electronics*, Karlsruhe, 551–552.

35. Bowen, J.W., Walker G.C. and Hadjiloucas S. (2007) Sample-induced beam distortions in terahertz time domain spectroscopy and imaging systems, *Joint 32nd International Conference on Infrared and Millimetre Waves and 15th International Conference on Terahertz Electronics*, Cardiff, 208–209.
36. Walker, G.C., Bowen. J.W., Zafiropoulos, A., Hadlington, T., Hadjiloucas, S. and Chamberlain J.M. (2007) Quantification of boundary definition using pulsed terahertz radiation for wedged geometries, *Joint 32nd International Conference on Infrared and Millimetre Waves and 15th International Conference on Terahertz Electronics*, Cardiff, 512–513.
37. Bowen, J.W., Walker, G.C., Alozie, D. and Hadjiloucas, S. (2008) Achieving sub-wavelength spatial resolution in terahertz imaging by exploiting phase cancellation effects, *EOS Annual Meeting*, Paris, 997.

LASER-PRODUCED PLASMAS FOR BIO-PHOTONICS

PAOLO DI LAZZARO*
ENEA Research Center of Frascati
P.O. Box 65, 00044 Frascati (Italy)

1. Introduction

Laser-produced plasmas (LPP) are laboratory-scale, table-top and high-brightness sources of partially coherent radiation that can be tuned between the extreme ultraviolet and the hard X-rays.

A few LPP emission wavelengths have important applications in bio-photonics. As an example, LPP emitting in the so called "water window" (spectral range $\lambda = 4.4$ nm–2.3 nm) allowed the world first X-ray scanning microscopy and contact microscopy, the latter being able to perform *in vivo* molecules imaging with 50-nm spatial resolution.

Another important application of LPP is the radiobiology. In fact, LPP emitting at $\lambda \sim 1$ nm can deliver high dose rate of over 1 Gy/shot or 100 Gy/s to biological cells. This huge and instantaneous X-ray dose is due to the brightness of the LPP source and to the short penetration depth of 1-nm X-rays. Remarkable results have been obtained in the measurements of cell survival and DNA repair kinetics.

This paper summarizes my lecture at the International School of Atomic and Molecular Spectroscopy, 26th Course: Bio-Photonics: Spectroscopy, Imaging, Sensing and Manipulation, NATO ASI 983377 (Erice, July 2–17, 2009) and it consists of a "back to basics" description of principles of Lasers and of Laser-produced-plasmas, and of a second part focusing the attention to X-ray microscopy imaging and to radiobiology, including some basic principles of the interaction of soft X-rays with organic matter.

2. Back to Basic Principles of Lasers

Basically, a laser consists of three components: the active medium (gas, liquid or solid), the energy source that creates population inversion into the active medium, the optical resonator (two mirrors at least) that enhances the stimulated emission mechanism, selects the spatial and spectral characteristics of the Laser beam and couples out part of the generated laser light. The choice of the pump energy source depends on the active medium: electric discharges are suitable for gaseous media, flashlamps for both liquid and solid media, other external Lasers are suitable for all media provided the pumping Laser wavelength is absorbed by the active medium.

* Paolo Di Lazzaro, ENEA Research Center of Frascati, P.O. Box 65, 00044 Frascati (Italy), e-mail: paolo.dilazzaro@enea.it

B. Di Bartolo and J. Collins (eds.), *Biophotonics: Spectroscopy, Imaging, Sensing, and Manipulation*, 305
DOI 10.1007/978-90-481-9977-8_14, © Springer Science+Business Media B.V. 2011

In the Erice lecture we have described how the optical resonator provides selective feedback, showing that the Laser starts to oscillate only when the mirrors feedback is larger than losses, that is

$$R_1 R_2 e^{(g-\alpha)2\ell} > 1 , \tag{1}$$

where R_1 and R_2 are the reflectivity of the two resonator mirrors, g is the gain for unit length of the active medium, α is a coefficient representing all the losses for unit length different than those of the mirrors (i.e. active medium absorption, geometrical losses, absorbing intracavity elements), and ℓ is the length of the active medium.

The optical resonator allows propagation of those electromagnetic fields that reproduce themselves upon reflections between mirrors. These particular field configurations respectively are the Transverse Electromagnetic Modes (TEM) and the longitudinal electromagnetic modes of a resonator. Lasers are multimode oscillators, because a large number of longitudinal resonator modes fall within the bandwidth of the active medium Laser transition, and a large number of transverse resonator modes can fill the cross-section of the active medium. As a consequence, the spatial distribution of the energy of the Laser beam is made by the addition of many different transverse modes oscillating into the resonator. This means that the spatial characteristics of the beam (divergence, diameter, energy distribution) mainly depends on the transverse modes selected by the resonator. Whereas spectral characteristics (line-width, coherence length) are governed by longitudinal modes. Longitudinal modes differ from one another only in their oscillation frequency; TEMs differ each other not only in the oscillation frequency, but also in the field distribution in a plane transverse to the direction of propagation. Corresponding to a given TEM, there are longitudinal modes that have the same field distribution but a different frequency.

2.1. TRANSVERSE ELECTROMAGNETIC MODES

Depending on the active medium geometry and/or on the intracavity apertures, transverse modes can be described by Hermite polynomials and Laguerre polynomials, respectively for rectangular and cylindrical coordinates. [1] Transverse Electromagnetic Modes are designated by TEM_{mn} where integers m, n are the orders of the Laguerre (Hermite) polynomial, corresponding to the number of zeros (nodes) in different directions. The size W_{mn} of the TEM_{mn} scales with the mode number according to the law:

$$W_{mn} = W_{00} [(2m+1)(2n+1)]^{1/2} . \tag{2}$$

Figure 1 shows the calculated pattern of Laguerre and Hermite polynomials.

A number of applications (including LPP) require a Laser beam that does not spread during propagation and/or a Laser power density as large as possible: in these cases, we need to select a low-order transverse mode, preferably the lowest fundamental TEM_{00} mode. This is because the smaller the order of the transverse mode, the smaller the divergence, and hence the higher the brightness and the power density of the beam. In fact the diameter of the Laser beam in the focal plane of a lens can be approximated as:

$$2w = F\left(K\frac{\lambda}{D}\right) \times (2m + n + 1) \quad (3)$$

where F is the focal length of the lens, K is a coefficient ranging from 2.44 (plane wave beam) to 1.27 (pure gaussian beam), λ is the Laser wavelength and D is the beam diameter on the lens. From Eqs. (2) and (3) we know that the lower the orders of the TEM, the smaller the spot and the higher the power density.

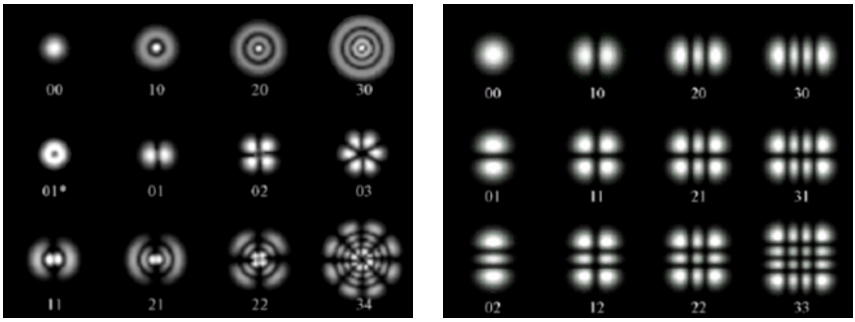

Figure 1. Calculated pattern of TEMs in cylindrical (left) and rectangular (right) coordinates. Numbers below each pattern are the m and n order of the Laguerre (left) and Hermite (right) polynomials.

In general, many applications require a high brightness (power/unit area/solid angle) rather than a large emitted power. In particular, we will show that Laser-produced plasmas performance are improved by high-brightness, high focusability laser beams.

There are many different techniques to select the TEM_{00}. The simplest one is an intracavity aperture having the same diameter of the mode to be selected. This shall restrict the cross section area of the oscillating radiation, stopping the modes having a larger-than-aperture spatial extent. Unfortunately, this simple technique is not convenient because usually the diameter $2W_{00}$ of the lowest order mode is much smaller than the commonly available sections of the Laser active medium, thus only a small fraction of the stored energy can be extracted from the active medium. As an example, we have shown that for a typical Nd–YAG Laser (λ = 1,06 μm, rod diameter D = 0.63 cm loading a resonator with mirror curvature radii $r_1 = r_2 = 100$ cm and resonator length L = 100 cm) only a fraction 3.6% of the emitted power will be available.

A solution came from the unstable resonator (UR) proposed by Siegman [2]. In its simplest configuration, the UR is made by two totally reflecting mirrors arranged as shown in Fig. 2, which allow a telescopic expansion of the TEM_{00} beam size to match the active medium size [3]. The UR selects low-orders transverse modes with a good filling of the active medium, and the next higher order modes can be suppressed by a careful design of the cavity. The UR near-field intensity profile may have a hole on axis due to the shadow of the convex mirror, as shown in Fig. 2, unless intracavity polarization output coupling devices are used. This hole will no longer appear in the far field (focal plane) where the beam pattern has a central lobe surrounded by side lobes or diffraction rings of decreasing amplitude [4].

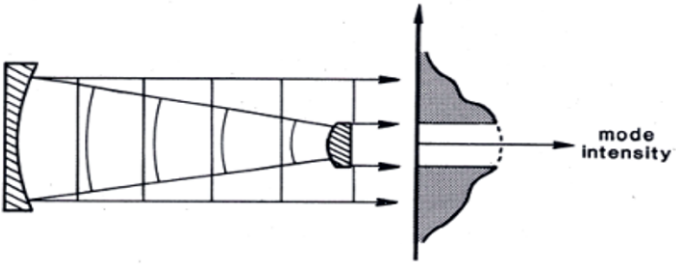

Figure 2. Schematic of a positive branch unstable resonator, made by two totally reflecting mirrors. The small convex mirror (having a diameter d) provides a selective feedback to the smaller order modes close to the optical axis and acts also as output coupler.

2.2. DESIGNING AN UNSTABLE RESONATOR

The design of an UR is quite a complex issue [5, 6]. Nevertheless, a simplified, geometrical approach allows didactic exercises whose results are not too far from those achieved by a rigorous integral calculation.

The main UR parameter is the magnification M, defined as

$$M = \frac{D}{d} = -\frac{f_1}{f_2} > 1, \tag{4}$$

where d is the diameter of the output coupler of the UR (see Fig. 2), $f_1 = r_1/2$ and $f_2 = r_2/2$ are the focal lengths of the concave and of the convex mirror in Fig. 2, respectively.

Usually URs have a high output coupling (or low equivalent reflectivity of the output mirror). The equivalent reflectivity γ^2 of the output mirror (assuming a circular symmetry) can be approximated by

$$\gamma^2 \approx M^{-2(1+n)} \tag{5}$$

where n is the radial order of the mode. According to Eq. (5), the lowest transverse mode (n = 0) is easily selected as it experiences the largest reflectivity (internal feedback transmittance).

In order to fully exploit the mode selection capability of URs, the time necessary to achieve the TEM_{00} must be shorter than the Laser gain duration above-threshold. In other words, the steady-state establishment of the mode structure must be faster than the round trips time that is available to select the transverse mode. This is of primary importance when designing an UR for short-pulse Lasers. According to [7], the number of round trips necessary to achieve the lowest order mode, thus generating laser pulses having the diffraction-limited divergence, is given by:

$$\kappa \approx 1 + \frac{\ln N_f}{\ln M} \tag{6}$$

where $N_f \approx d^2/L\lambda$ is the Fresnel number of the unfolded resonator.

As an example, let's reduce to practice Eqs. (4)–(6) designing the optimum UR for a pulsed Laser with an active medium volume D × D × ℓ = 3 cm × 3 cm × 50 cm emitting at λ = 308 nm with a net gain peak value $g_{max} = 0.07\ cm^{-1}$ and a gain duration ΔT = 150 ns. For practical reasons, the resonator length L must be longer than 100 cm and shorter than 200 cm.

For a proper design of the optimum UR we need the net gain duration Δt, that is the above-threshold gain duration, which is a function of losses $(1 - \gamma^2)$ and of g_{max}. To estimate Δt, let us approximate the shape of the gain vs. time by a parabolic function. As this parabola crosses the abscissa (time axis) at $t_1 = 0$ and $t_2 = \Delta T = 150$ ns, knowing g_{max} as the vertex value we can write the time evolution of the gain as

$$g(t) = bt - at^2 \tag{7}$$

where $a = g_{max}/t_{max}^2$, $b = 2g_{max} / t_{max}$ and $t_{max} = \Delta T/2$ is the time corresponding to g_{max}.

Mixing Eqs. (1) and (5) we have

$$\gamma^2 e^{(g-\alpha)2\ell} \geq 1 \tag{8}$$

When M = 9, Eq. (5) gives $\gamma^2 \approx 0.012$, and Eq. (8) gives the threshold condition $(g - \alpha) \geq \ln (M)/\ell = 0.0439\ cm^{-1}$. This threshold line crosses Eq. (7) in two points t_3 and t_4 giving a net gain duration $\Delta t \approx (t_4 - t_3) = 80$ ns. Analogously, for M = 8 we have $(g - \alpha) \geq \ln (M)/\ell = 0.0416\ cm^{-1}$ and Δt ≈ 90 ns. When M = 7, $(g - \alpha) \geq \ln (M)/\ell = 0.0389\ cm^{-1}$ and Δt ≈ 100 ns.

Note that for M = 7, Δt ≈ 2/3 of ΔT, so that it is not convenient considering a lower M. Moreover, as a rule of thumb the maximum delay τ for the laser onset should be smaller than ΔT/2. So let us consider the choice M = 7 that guarantees $\Delta t > \Delta T/2 > \tau$ and smaller losses compared to M = 8 and M = 9 (see Eq. (5)). Note that M = 7 is also adequate to discriminate the fundamental from higher order transverse modes, being, e.g., $\gamma^2_{n=1} \approx 10^{-4}$ (see Eq. (5)).

From Eq. (4) the condition for the expanding TEM_{00} to match the active medium cross section is $d = D/M = 0.43$ cm, and we can choose, for example, $f_1 = 175$ cm and $f_2 = -25$ cm, so that the confocal condition to have a collimated output beam is $L = f_1 + f_2 = 150$ cm. Then, Eq. (6) gives κ = 2.9.

As a check, in order to achieve the diffraction limited performance, the delay τ between the onset of fluorescence and the laser threshold must be much larger than the time necessary to achieve the lowest order mode. That is, the cavity length L must satisfy the condition:

$$\frac{2L}{c} \times \kappa << \tau$$

In our UR in fact $\Delta T/2 > \tau$ is about 2.6 times larger than the time necessary to achieve the lowest order mode.

We can conclude the exercise summarizing the results: the optimum UR for the considered Laser has a magnification M = 7, the concave mirror has a diameter D = 3 cm and curvature radius $2f_1 = 350$ cm, the convex mirror has diameter $d = 0.43$ cm and curvature radius $2f_2 = -50$ cm, being the mirrors separated by a distance L = 150 cm. This positive branch UR is able to select the lowest transverse order mode in 29 ns, that is in less than three round trips.

3. Laser-Produced Plasmas

Let us consider a high-power Laser pulse focused onto a very small spot (see Eq. (3)) on a suitable target material in a vacuum chamber. This pulse instantaneously heats the target spot area hence producing a high-temperature plasma (i.e., a cloud of electrons, ions, neutral particles) above the target surface. The plasma expands in vacuum, ions recombine thus emitting pulsed radiation having a broad wavelength spectrum, including extreme ultraviolet and soft X-rays. As an example, Fig. 3 shows a plasma generated by focusing 30 ns pulses from a XeCl excimer laser onto a thin copper tape target in a vacuum chamber, at ENEA Frascati.

Laser plasma sources are point-like (their size is smaller than the Laser-spot heating the target, typically less than 100 μm) and the performance of the plasma radiation is a function of the Laser pulse (wavelength λ, intensity I_ℓ, duration Δt) and of the target (atomic number Z, density). Namely, I_ℓ determines the plasma temperature, λ is inversely proportional to both the electron density n and the critical density n_c where most laser radiation is absorbed. Moreover, the heavier the target (high Z) the larger the conversion efficiency η laser-to-plasma, while Δt determines the spatial shape of the expanding plasma.

Although comprehensive theoretical LPP models are quite complex and CPU-time-consuming [8, 9], when dealing with $Z > 50$ and $I_\ell < 10^{12}$ W/cm^2 the plasma can be approximated as a thick black-body emitter. Then, we can deduce the total radiative intensity emitted by the plasma as

$$I_x = \eta\, I_\ell = \sigma T^4 , \tag{9}$$

where σ is the Stefan Boltzmann constant and η is the Laser-to-plasma conversion efficiency. Using the Wien's law

$$\lambda_x \text{ (at max } I_x) = 250 \times (kT)^{-1} , \tag{10}$$

where λ_x is expressed in nm and kT in eV, it is possible to assess the position of the wavelength band of the maximum spectral intensity of the plasma radiation. For

example, when $I_\ell = 10^{11}$ W/cm^2 and $\eta = 30\%$, Eq. (9) gives a radiative plasma temperature $T \approx 3 \times 10^5$ K, corresponding to kT = 23 eV, and Eq. (10) gives $\lambda_x \approx 11$ nm. The radiative temperature T characterizes to some extent the radiation properties of the plasma source.

Obviously, LPP may differ from a black-body, as LPP spectra show line radiation and the conversion efficiency η may depend on the target, especially in the case of low-Z materials. The interested reader may refer to excellent textbooks for a comprehensive description of ns-to-ps LPP [10].

Shorter Laser pulses in the fs range that can be tightly focused to reach intensities in excess of 10^{20} W/cm^2 generate relativistic LPP, which emit beams of highly energetic electrons, protons and ions [11]. These relativistic plasmas are beyond the scope of this paper, and are not discussed here.

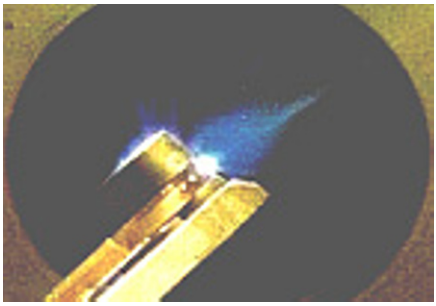

Figure 3. LPP developed at ENEA Frascati. The hot, 30-μm diameter plasma at about one million degrees Celsius ejects the drop-shaped plasma plume containing the ablated copper ions that recombine in the residual 10^{-3} mbar air in the vacuum chamber to emit a broadband radiation, including the blue light visible in the photo.

4. Laser Plasmas for X-ray Microscopy

Biologists use optical microscopes to observe the behavior of living specimens, with a poor detail resolution due to the diffraction limit of light wavelength used to illuminate the sample and to form the image. A sub-nanometer resolution can be achieved by electron microscopes that allow a detailed inspection of dehydrated and stained cell structure. A compromise between the optical and the electron microscope resolution is given by the soft X-ray microscope. It is based on a unique spectral region between the oxygen K-edge at 2.3 nm and the carbon K-edge at 4.4 nm, called "water window", where the carbon-containing proteins show a much larger absorption than the oxygen-containing water, see Fig. 4, thus allowing a high-contrast image when irradiating the living specimen in its natural water-nutrient environment, as shown in Fig. 5.

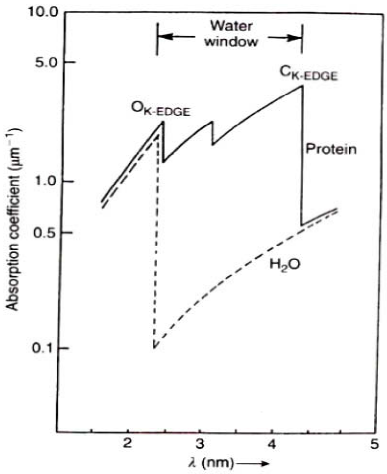

Figure 4. Absorption coefficient of water and carbon-based proteins in the "water window" spectral region.

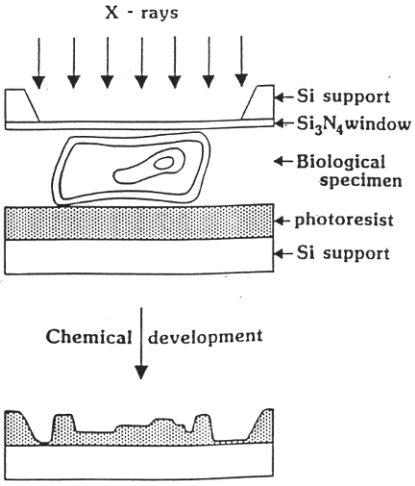

Figure 5. Contact X-ray microscopy concept. The living specimen in its water-nutrient environment is sandwiched between a transparent window and the photoresist. After irradiation, the photoresist is chemically developed to remove the parts reached by the plasma radiation, which correspond to the water-reach specimen regions, see Fig. 4. Finally, the resulting replica of the carbon-density distribution of the original specimen (a sort of high-resolution 3-D carbon map) can be imaged by an Atomic-Force Microscope.

4.1. ADVANTAGES, DRAWBACKS AND RESOLUTION LIMIT OF THE X-RAY CONTACT MICROSCOPY

The main attraction of the contact X-ray microscopy schematized in Figs. 4 and 5 is the imaging of specimens while they are still leaving. In fact, if the exposure is sufficiently short (i.e. in the sub-microsecond range) the image can be recorded before any structural damage occurs, even though the X-ray dose is ultimately fatal. Additional advantages are on the one hand the possibility to obtain a quantitative density profile of the carbon content of the biological specimen that is not easy to achieve using electron microscopes, on the other hand the image map record on the photoresist can be iteratively performed. That is, we can first image the specimen after a short chemical development, thus gaining information on the specimen surface, then we can repeat the development and image again, and so on, till the most deep carbon structure has been imaged. The main drawback of this technique is the lengthy resist processing and imaging.

The resolution limit of the contact X-ray microscopy technique is determined by two main factors: the penumbra blurring effect and the statistical fluctuation of photons. Let's analyze separately these effects.

Penumbra blurring. A simple exercise shows that the penumbra of a sample illuminated by a source of diameter D at a distance d_1 being the sample at a proximity distance d_2 from a recording screen is given by

$$\delta_{pb} = D \times \frac{d_2}{d_1} \tag{11}$$

Typical values for contact X-ray microscopy using a LPP are in the following ranges: D ≈ (30–50) μm; d_1 ≈ (5–10) mm; d_2 ≈ (2–8) μm. As a consequence, penumbra blurring is in the range (6–80) nm.

Statistical fluctuation of photons. Assuming a Poisson distribution of the photon number incident on the sample [12], the fluctuation of N photon is ± √N. Then, referring to Fig. 6, in order to discriminate between the images of the photon erosion effect on the photoresist area covered by the specimen and on the surrounding region, photons passing through the specimen must be much larger (say, a factor 4 larger) than the photons fluctuation, that is

$$N - N_a \approx N(1 - e^{-\alpha S}) \geq 4\sqrt{N}, \tag{12}$$

where N_a is the number of photons absorbed by the specimen and S is the diameter of the spherical-like specimen. Due to the relatively small absorption coefficient α we can use the Taylor expansion and Eq. (12) can be simplified as $N - N_a \approx N\alpha S \geq 4\sqrt{N}$. As a consequence, the number of photons N must be large enough to satisfy the condition

$$N \geq \left(\frac{4}{\alpha S}\right)^2. \tag{13}$$

The number of photons impinging on the specimen of Fig. 6 can be written as

$$N \approx \frac{\pi F}{4h\nu} S^2 \tag{14}$$

where F is the photon fluence (energy for unit surface) and hν is the energy of the single photon. Mixing Eqs. (13) and (14) we obtain the limit of the spatial resolution δ_{sf} that corresponds to the minimum cell diameter detectable:

$$\delta_{sf} \approx S \geq 2{,}12 \left(\frac{h\nu}{F\alpha^2} \right)^{1/4} \tag{15}$$

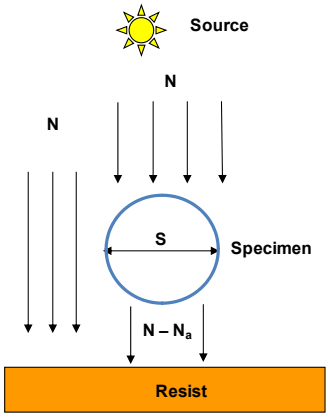

Figure 6. Schematic of the contact X-ray microscopy limit of resolution due to the statistical fluctuation of photons.

Once fixed both the photon energy hν in the water window spectral region (see Fig. 4) and the specimen with a given absorption coefficient α, Eq. (15) suggests that an increment of the photon fluence F can improve the resolution limit due to the statistical fluctuation of photons. This can be achieved either increasing the LPP emitted energy or by reducing the distance d_1 source–cell. In the latter case, however, the limit of resolution due to penumbral blurring becomes worst, see Eq. (11). When looking for a compromise between δ_{pb} (Eq. 11) and δ_{sf} (Eq. 15) the following LPP parameters can be used: D = 30 μm, $d_1 \approx 6$ mm, $d_2 \approx 3$ μm, F = 10 mJ/cm^2, hν ≈ 310 eV. In this way, the total resolution limit is $\delta_{TOT} \approx \sqrt{(\delta_{pb})^2 + (\delta_{sf})^2} = 52$ nm. Figure 7 shows a typical contact X-ray microscopy image of living and hydrated bacteria Leptolyngbya [13, 14].

In the Erice lecture we also discussed the use of fluorescent materials (like, e.g., LiF) as high-spatial resolution and high dynamic image-storing device for X-ray contact microscopy of not hydrated biological specimens [15].

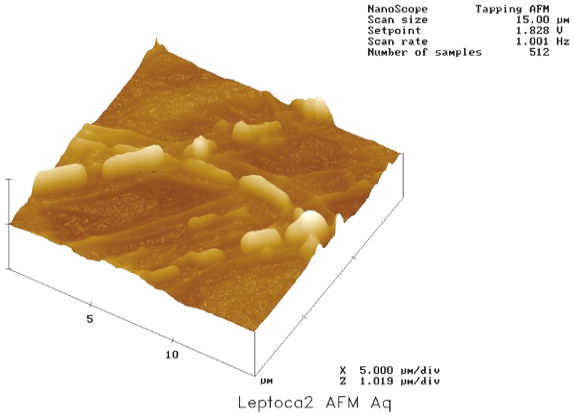

Figure 7. Atomic force microscope imaging of contact X-ray microscopy of *in vivo* bacteria Leptolyngbia. Horizontal scale is in µm.

5. Laser Plasmas for Radiobiology

When a soft X-ray photon of energy $h\nu << 10^4$ eV interacts with an atom, the absorption process is dominated by the photoelectric effect [16]. That is, the atom absorbs the photon and ejects one of its inner shell electrons, called "photoelectron". Then, the vacancy created in the inner shell can be filled by an electronic transition from an outer shell that is preferably accompanied by the emission of fluorescence radiation (when the atomic number of the material is $Z > 40$) or by Auger electrons (when $Z < 20$) as the atom returns to a lower energy state. Finally, Auger electrons and photoelectrons deposit energy in the surrounding material.

As both Auger electrons and photoelectrons generated by soft X-ray photons have energies in the range of a few hundred eV, they are absorbed by low-Z materials (including biological specimens) in a very short depth range, of the order of few nanometers [17]. As a consequence, each soft X-ray photons absorbed via photoelectric effect delivers its energy in a very small volume of biological specimens, allowing deposit of a huge energy density and dose. Let's estimate this dose value.

Assuming the soft X-ray absorption A in a specimen having a thickness x and an absorption coefficient µ is described by the conventional Beer–Lambert law: $A = 1 - e^{-\mu x}$, when $\mu x << 1$ we obtain

$$\mu \approx \frac{dA}{dx}. \tag{16}$$

The X-ray dose D absorbed by the specimen is the energy E absorbed for unit specimen mass m, that is

$$D = \frac{dE}{dm} = \frac{dE}{\rho dV} \approx \frac{FdA}{\rho dx} \approx \frac{F\mu}{\rho} \tag{17}$$

where ρ is the density of the specimen, F is the X-ray fluence (energy for unit area) at the surface of the specimen, and we used Eq. (16) in the last equivalence.

Let us consider the case of V79 chinese hamster fibroblasts cells irradiated by 1.5 keV photons (1 keV = 10^3 eV). In this case, $\mu/\rho \approx 2\times10^3$ cm^2/g. Then, according to Eq. (17), $D/F \approx 2$ Gy cm^2/μJ. That is, for each μJ/cm^2 impinging on the V79 cell the dose delivered at the specimen surface is of the order of 2 Gy, corresponding to 2 J/kg. Figure 8 shows the experimental surviving fraction of a monolayer of V79 mammalian cells as a function of the dose delivered by multiple soft X-rays pulses at 1.5 keV. For comparison, are also reported the V79 surviving fractions after irradiations with hard X-rays and α-particles, respectively.

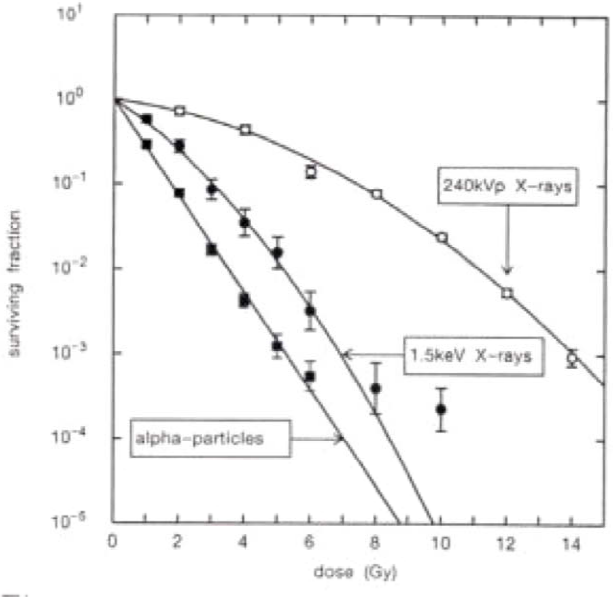

Figure 8. The fraction of V79 hamster cells surviving as a function of the dose delivered by 1.5 keV X-rays, 3.8 MeV α-particles and 250 keV X-rays. The error bars are ± one standard error of the mean (From [19]).

Figure 8 shows that for a fixed dose value, the cellular damaging effect of soft X-rays emitted by LPP is substantially higher than hard X-rays and a bit smaller than α-particles, confirming the ionizing radiations damage is proportional to the so called "Linear Energy Transfer" (LET, usually expressed in keV/μm) that represents the ionization density of a given radiation. In addition, Fig. 8 demonstrates that only the high-LET α-particle data follow a simple exponential function, while hard-X-ray data (and to a smaller extent soft- X-ray data) show a "shoulder" probably due to dose-dependent

repair of sub-lethal damage. High LET radiations produce damage that is less repairable, hence no shoulder and an increased effectiveness for unit dose.

As the damage inside cells is determined by photoelectrons and Auger electrons, a quite broad soft X-ray spectral range 0.3–1.6 keV is effective at killing cells, although the biological effectiveness of soft X-rays increases as the spectral energy is reduced (and LET increased).

5.1. DNA DAMAGE

The deoxyribonucleic acid (DNA) is the key macromolecule of living organisms. It is located in the cell nucleus and carries the genetic code of each organism. The study of radiation damage to the DNA of mammalian cells and the response of the DNA repair mechanisms are of great importance for assessing the exposure risks in the environment to natural radiation and for estimating the benefit-to-risk ratio of medical radiotherapy with ionizing radiation.

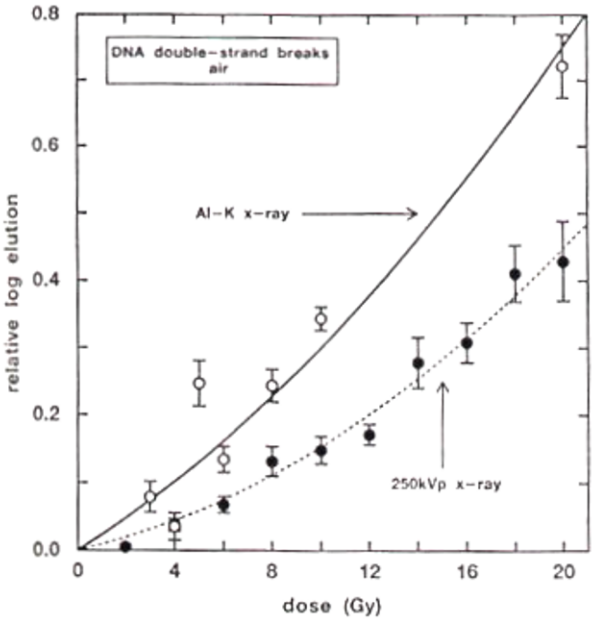

Figure 9. The induction of DNA double strand breaks as a function of the dose delivered by 1.5 keV X-rays, and 250 keV X-rays. Relative log elution is a quantity proportional to the number of breaks induced (From [19]).

Ionizing radiations can induce a broad range of damage within DNA. Among possible DNA lesions, the most effective to generate permanent biological effects (cell killing, chromosome aberrations, loss of genetic materials) is the “double-strand break” (dsb) where both strands of the DNA double-helix are broken within a few base-pairs of each

other. Figure 9 shows the relative number of dsb produced versus the radiation dose of soft X-rays pulses at 1.5 keV or 250 kV hard X-rays.

The increased efficiency of DNA dsb induction of soft X-rays with respect to 250 kV X-rays (see Fig. 9) correlates with their increased efficiency at killing cells. Clearly, the majority of DNA damage induced is of little biological relevance since even 2 Gy of soft X-rays has only a 60% probability of damaging a cell (see Fig. 8). This may be due to the DNA repair capability at low doses. In alternative, the lower than expected lethality of ionizing radiations can be explained assuming that only a fraction of the DNA is critically sensitive to radiation damage.

6. Concluding Remarks

The selection of TEM_{00} by using unstable resonators can substantially improve the focussability of the Laser beams.

Laser Produced Plasmas (LPP) are generated by focusing high-power Laser pulses onto a suitable target material in a vacuum chamber. The brightness (energy for unit area for unit time for unit solid angle) of LPP radiation is improved by using tightly focused laser pulses.

Water-window LPP emission allows *in vivo* imaging of internal structures of molecules with 50-nm spatial resolution. The resolution is mainly limited by the size of the LPP and by the radiation energy density on the photoresist that stores the image. In practice, the use of unstable resonators (that guarantees the smallest Laser spot size in the focal plane of a given lens and as a consequence the smallest size of LPP) drastically improves the resolution of LPP *in vivo* imaging of biological molecules.

The high brightness of LPP radiation sources and the low penetration depth in biological cells of the 1 keV radiation allow a high dose rate delivered to biological specimen of over 1 Gy/shot. A very large total dose can be delivered by consecutve pulses in a short time: as an example, a commercial 100-Hz excimer Laser can deliver up to 100 Gy/s. This dose can act at DNA level because biological cells absorb radiation around 1 keV by photoelectric effect, which produces photoelectrons and Auger electrons that deliver instantaneously a huge dose in a few nanometers.

References

1. Koechner W. (1976) *Solid-State Laser Engineering.* Springer Verlag, New York Inc. Chapter 5.
2. Siegman A.E. (1965) Unstable optical resonators for laser applications. *Proc. IEEE* **53,** 277–287.
3. Siegman A.E. (1986) *Lasers.* University Science Books. Stanford University, Stanford, CA, Chapter 22.
4. Mahan A.I., Bitterli C.V. and Cannon S.M. (1964) Far-field diffraction patterns of single and multiple apertures bounded by arcs and radii of concentric circles. *J. Opt. Soc. Am.* **54,** 721–732.
5. Ananev Yu. (1992) *Laser Resonators and the Beam Divergence Problem.* Adam Hilger, Bristol, PA.

6. Di Lazzaro P., Bollanti S., Murra D. and Zheng C.E. (2001) Improved beam quality excimer lasers: a filtering resonator study. *Filtering Resonators*, S.K. Dixit Ed. Nova Science Publisher, Huntington, New York, Chapter 5.
7. Zemskov K.I., Isaev A., Kazaryan M., Petrash G. and Rautian S. (1975) Use of unstable resonators in achieving the diffraction divergence of the radiation emitted from high-gain pulsed lasers. *Sov. J. Quant. Electron*. **4,** 474–477.
8. Vergunova A., Magunov A., Dyakin V., Faenov A., Pikuz T., Batani D., Flora F., Di Lazzaro P., et al. (1997) Features of plasma produced by excimer laser at low intensities. *Physica Scripta* **55**, 483–490.
9. Fournier K., Faenov A., Pikuz T., Skobelev I., Flora F., Bollanti S., Di Lazzaro P., Murra D., et al. (2003) Rydberg transitions in the spectra of near-neon-like Cu and Zn ions in different laser-produced plasmas: observations and modeling. *J. Quant. Spectrosc. Radiat. Transfer* **81**, 167–182.
10. See e.g., Turcu I.C.E. and Dance J.B. (1999) *X-Rays from Laser Plasmas: Generation and Applications.* Wiley, New York.
11. See e.g., Galy J., Hamilton D.J. and Normand C. (2009) High-intensity lasers as radiation sources. *Eur. Phys. J. Special Topics* **175**, 147–152.
12. Loudon R. (2003) *The Quantum Theory of Light,* Third Edition*.* Oxford University Press, Oxford, Chapter 5.
13. Albertano P., Reale L., Palladino L., Reale A., Cotton R., Bollanti S., Di Lazzaro P., Flora F., et al. (1997) X-ray contact microscopy using an excimer plasma source with different target materials and laser pulse duration. *J. Microsc.* **187**, 96–103.
14. Bollanti S., Albertano P., Belli M., Di Lazzaro P., Faenov A., Flora F., Giordano G., Grilli A., et al. (1998) Soft X-ray plasma source for atmospheric pressure microscopy, radiobiology and other applications. *Il Nuovo Cimento* D **20**, 1685–1696.
15. Baldacchini G., Bollanti S., Bonfigli F., Di Lazzaro P., Faenov A., Flora F, Marolo T., Montereali R., et al. (2004) Point defects in Lithium Fluoride by EUV and soft X-rays exposure for X-ray microscopy and optical applications. *IEEE J.Selected Topics Quant El*. **10**, 1435–1445.
16. See e.g., Segre E. (1965) *Nuclei and Particles.* W.A. Benjamin Inc., New York.
17. Pianetta P. (1986) Low-energy electron ranges in matter. *X-ray data booklet* D. Vaughan Ed. Lawrence Berkeley Laboratory, Berkeley, CA, Chapter 3.
18. Folkard M. (1992) Radiation damage to cells by ultrasoft X-rays. *X-ray microscopy III*, A. Michette, G. Morrison, C. Buckley Eds. Springer Verlag, Berlin, pp. 306–312.

REAL-TIME SPECTROSCOPY OF SOLID-STATE RANDOM LASERS

J. FERNÁNDEZ*, S. GARCÍA-REVILLA, R. BALDA
Dpto. Física Aplicada I, Escuela Superior de Ingenieros, Alda. Urquijo s/n 48013 Bilbao, Spain
Centro Física de Materiales CSIC-UPV/EHU and Donostia International Physics Center, Apartado 1072, 20080 San Sebastian, Spain

Abstract Random lasers are the simplest sources of stimulated emission without a cavity, with the feedback provided by disorder-induced scattering in a gain medium. Since the first experimental observation of a lasing-like emission in a dye solution with scatterers took place, the incorporation of dye molecules into a solid host has attracted much interest in the development of new random lasers. Random laser action is demonstrated in two kinds of powder samples containing rhodamine 6G (Rh6G) doped SiO_2 nanoparticles which are either directly dispersed within pure silica particles or embedded in a silica gel matrix which is subsequently ground. Both organic–inorganic hybrid materials present different laser thresholds and emission features which are systematically studied and compared. The dependence of the emission kinetics, emission spectrum, random laser threshold and slope efficiency on the dye doped nanoparticles concentration is investigated in both cases. The laser-like emission dynamics can be accurately described by a light diffusive propagation model. The device behavior is close to a conventional ultrafast Q-switched laser, which is an interesting fact aimed to further applications.

1. Introduction

Light amplification in locally inhomogeneous dielectric materials is a fascinating topic that gathers fundamental aspects of both classical and quantum optics together. In 1967, Letokhov theoretically predicted the possibility of generating laser-like emission starting from scattering particles with negative absorption, the so-called *random* or *powder laser*, in which the feedback mechanism is provided by disordered-induced light scattering due to the spatial inhomogeneity of the medium [1]. Since then lasing in random media has become a subject of intense theoretical and experimental studies due to its important scientific and technological implications. To date, mirror-less laser emission has been successfully observed in a wide range of scattering systems including colloidal dye solutions, crystal powders, ceramics, organic composites or biological

* J. Fernández, Dpto. Física Aplicada I, Escuela Superior de Ingenieros, Alda. Urquijo s/n 48013 Bilbao, Spain, Centro Física de Materiales CSIC-UPV/EHU and Donostia International Physics Center, Apartado 1072, 20080 San Sebastian, Spain, e-mail: joaquin.fernandez@ehu.es,

B. Di Bartolo and J. Collins (eds.), *Biophotonics: Spectroscopy, Imaging, Sensing, and Manipulation*, 321
DOI 10.1007/978-90-481-9977-8_15, © Springer Science+Business Media B.V. 2011

tissues (see Refs. [2–4] and references therein). The nature and morphology of each amplifying disordered medium determine their specific feedback mechanism [2, 3] and random laser behavior, making it difficult to study all the previously mentioned systems with a unique theoretical treatment. Therefore, many theoretical analyses and numerical simulations have been constructed trying to understand the physical mechanisms behind general signatures of the random laser action such as an overall narrowing of the emission spectrum (with the eventual presence of narrow spikes), a threshold behavior, and an output pulse shortening [5–10]. In addition, much care is needed when comparing results from different random laser experiments because they can be influenced by experimental conditions such as the boundaries imposed by the sample holder, the way in which the sample is excited or light emission collected [11, 12]. An overview of the latest results and theories concerning random lasers can be found in a recent publication by Wiersma [4].

Within the class of dye random lasers, laser dyes are used to provide the optical gain amplification whereas the scattering typically comes from a suspension of particles in a dye solution [13–15]. Nevertheless, the search for novel and efficient random laser materials has motivated to follow a different approach in order to achieve random lasing in a dye system. In particular, we present here recent experimental results of laser-like action in two kinds of powder samples where the rhodamine 6G (Rh6G) dye is embedded in porous silica nanoparticles [16–18]. In these new proposed solid-state systems, the Rh6G–SiO_2 nanoparticles are either directly dispersed within undoped silica particles (dispersed powder samples, DP samples) or incorporated into a bulk silica gel matrix which is subsequently ground (ground powder samples, GP samples). Compared with other random media, the advantages of these dye-doped powders samples are its solid-state nature, quenched disorder, high laser-like emission efficiency, and the possibility to be functionalized for various applications in the field of biosensors or biotracers.

The laser radiation generated in both powder materials is described as random lasing with non-resonant feedback. This type of lasing is normally observed in scattering media in which the transport mean-free path is much longer than the wavelength. As it was stated in [19], a ‘stochastic resonator’ in the form of scattering medium constitutes a system with a large number of modes, which are strongly coupled by scattering and which have large radiation losses. The large radiation losses and the strong interaction of the modes lead to a complete overlap of their frequency spectra. The concept of ‘mode’ loses here its usual meaning and the spectrum becomes continuum. If the number of interacting ‘modes’ is sufficiently large, the feedback becomes non-resonant. In many random laser powders, the wave propagation can be described by the classical diffusion theory [6, 20]. In particular, it can be applied to our GP samples since their mean particle size provides transport mean-free-paths which are much larger than the wavelength but much smaller than the sample thickness [16, 17]. By comparing the theoretical predictions with the experimental results of a GP sample, we conclude that a simplified rate equation-diffusion model is able to successfully describe the emission dynamics of such kind of disordered active media. Furthermore, the temporal analysis of the light emitted above threshold clearly suggests a behavior which is similar to a laser device working in a Q-switch-like regime. Moreover, as in conventional lasers, the most important properties of a random laser are the lasing threshold and the efficiency.

Therefore, the spectroscopic properties of the GP and DP samples as a function of the dye-doped nanoparticles concentration have been investigated in order to reduce the onset of laser-like action and to optimize the random laser output under short pump pulse excitation. In addition, we explore if the incorporation of additional TiO_2 scatterers to our dye-doped silica powders could enhance the random laser performance. The analysis of the results shows that the smallest onset of laser-like emission and the highest slope efficiency occur in a ground silica gel sample doped with a 4 wt% of Rh6G–SiO_2 nanoparticles [18].

2. Theoretical Background

2.1. MEAN-FREE-PATHS

In order to understand the operation regime of the random laser powders, a detailed characterization of light propagation in the scattering material is needed. Particularly, the estimation of the mean-fee-path lengths involved in the scattering and absorption processes is very important to analyze their behavior. The relevant length scales which describe the scattering process in random media are the scattering mean-free-path l_s, defined as the average distance between two successive scattering events, and the transport mean-free-path l_t, defined as the average distance the light travels before its direction of propagation is randomized [21]. In a steady state regime, l_s and l_t are given by:

$$l_s = \frac{1}{\rho\sigma_s} \qquad l_t = \frac{1}{\rho\sigma_t} \tag{1}$$

where σ_s and σ_t are the scattering and transport scattering cross-section, respectively, and ρ is the number density of scatterers.

On the other hand, the inelastic mean-free-path, l_i, and the diffusive absorption length, l_{abs}, describe the photon propagation in random absorbing systems. The former is the length of the light path in which the intensity is reduced to 1/e of its initial value due to absorption, whereas the latter is defined as the average distance between the beginning and the end points of paths of length, l_i. They are given as:

$$l_i = \frac{1}{\rho\sigma_a} \qquad l_{abs} = \sqrt{\frac{l_t l_i}{3}} \tag{2}$$

where σ_a is the absorption cross-section. Finally l^* is the extinction mean-free-path defined as:

$$l^* = \left(\frac{1}{l_i} + \frac{1}{l_s}\right)^{-1} \tag{3}$$

Note that these definitions make sense in the diffusion approximation, when the random media are far from the localization condition, i.e., $kl_s >> 1$.

2.2. DIFFUSION THEORY

Light propagation through optically dense random systems, where the transport mean-free-path l_t is much longer than the emission wavelength but smaller than the scattering sample thickness ($\lambda << l_t << L$), is commonly described by the model of light diffusion. The essential approximation underlying the diffusion theory is that after going through a large number of scattering events, the phases of the scattered waves are randomized so that any interference effect in the medium can be neglected. As a result, only the light intensity needs to be considered in the description of light propagation [21]. This approximation has been conscientiously tested and its validity has been proven for the description of light transport [22, 23]. Moreover, since the pioneering work of Letokhov in 1968 [19], it has been successfully used to analyze the behavior of several random lasers [5, 6, 24–26].

In the present work, we have performed theoretical calculations on light diffusion with amplification in order to describe the random laser operation of one powder sample, in particular, of the GP of a bulk silica gel containing 2 wt% Rh6G-SiO_2 nanoparticles where random laser action was firstly observed [16]. The average particle size of this disordered active media provides mean-free-paths which are much larger than the wavelength (l_t = 9.5 μm at 656 nm) and, consequently, the condition for the diffusion approximation is satisfied. The propagation of the pumped and the emitted photons through the sample can be therefore described by two diffusion equations: one for every kind of photons. The volume densities of both kinds of photons are coupled by a rate equation corresponding to the inversion of population of the dye molecules. For simplicity we have considered a plane wave incident along the z direction upon a slab sample with dimensions x and y much larger than the z-dimension. Under this hypothesis the general diffusion equation reduces to the one-dimensional case (the z-direction) and the evolution of the system is described in our model by three differential coupled equations:

$$\frac{\partial W_p(z,t)}{\partial t} = D_p \frac{\partial^2 W_p(z,t)}{\partial z^2} - \frac{D_p}{l_{abs}^2} W_p(z,t) + p(z,t) \tag{4}$$

$$\frac{\partial W_e(z,t)}{\partial t} = D_e \frac{\partial^2 W_e(z,t)}{\partial z^2} + f\,\mathrm{v}\sigma_{em} N(z,t) W_e(z,t) + \beta \frac{N(z,t)}{\tau_s} \tag{5}$$

$$\frac{\partial N(z,t)}{\partial t} = f\,\mathrm{v}K_{abs} W_p(z,t) - f\,\mathrm{v}\sigma_{em} N(z,t) W_e(z,t) - \frac{N(z,t)}{\tau_s} \tag{6}$$

where $W_{p,e}(z,t)$ are the pump and emission light densities, $N(z,t)$ is the density of the dye molecules in the excited state, $\mathrm{v} = \dfrac{c}{n_{eff}}$ is the light speed in the medium with n_{eff} the

effective refractive index, σ_{em} is the stimulated emission cross-section, τ_s is the excited state lifetime, K_{abs} is the absorption coefficient of the material at the pump wavelength, and l_{abs} is the diffusive absorption length previously defined. $D = \frac{\mathrm{v} l_t}{3}$ is the light diffusion coefficient that replaces the cavity loss coefficient of a conventional laser. We have distinguished the diffusion coefficients for pump and emitted radiation, D_p and D_e, respectively. β is the fraction of spontaneous emission contributing to the laser process. The volume fraction occupied by the scatters, f, has been included into the equations to take into account the effective part of the light density which penetrates inside the particles. This effect is not considered in most of the laser equations under the diffusion approximation given in the literature [6, 26, 27] but it must be regarded in order to explain the dependence of random laser threshold and efficiency on volume filling factor [28]. The source of diffuse radiation, $p(z,t)$, is a Gaussian pulse incoming the sample in the z direction which is extinguished (scattered and absorbed) along the scattering path:

$$p(z,t) = \frac{j_0}{l_s}\frac{\sqrt{\ln 2}}{\sqrt{\pi}\Delta}\exp(-\frac{z}{l^*})\exp\left(-\left(\frac{(t - t_{peak} - z/\mathrm{v})}{\Delta}\right)^2 \ln 2\right) \tag{7}$$

Here, j_0 is the incident light intensity, t_{peak} is the time at which the pump pulse is maximum at the sample surface and Δ is its length half width at half maximum.

For a slab geometry in the x–y plane, the boundary conditions are:

$$W_p(-l_e^0,t) = W_p(L + l_e^L,t) = W_e(-l_e^0,t) = W_e(L + l_e^L,t) = N(z,0) = 0 \tag{8}$$

where the extrapolation lengths are given by:

$$l_e^0 = \frac{2}{3}(\frac{1+r_0}{1-r_0}) \times l_t \quad \text{and} \quad l_e^L = \frac{2}{3}(\frac{1+r_L}{1-r_L}) \times l_t \tag{9}$$

with r_0 and r_L the internal reflectivities at the front ($z = 0$) and rear ($z = L$) surface.

As the emitted photons are collected along the backward direction of the incident pump beam, the time evolution of the emitted light predicted by this model is $\vec{F}_e(t) = -D_e \frac{\partial W_e(z,t)}{\partial z}\vec{z}$ evaluated at the front sample surface ($z = 0$). Consequently, the theoretical pulse shortening can be calculated from the reduction of the full width at half maximum (FWHM) of the temporal profiles when increasing the pump pulse energies. The lasing threshold can be also estimated by plotting the integrated intensity of the output pulses versus the pump pulse energy. Above the threshold, a linear dependence is obtained. Therefore, the intersection of the straight line with the abscissa axis provides the theoretical lasing threshold.

3. Experimental

3.1. SYNTHESIS AND CHARACTERIZATION OF THE POWDER LASER SAMPLES

Two kinds of powder laser samples were prepared via the sol-gel method containing different concentrations of Rh6G doped silica nanoparticles and TiO_2 scatterers. In the first stage the Rh6G–SiO_2 nanoparticles (~10 nm) were synthesized. Then, the fluorescent nanoparticles and the TiO_2 scatterers were either embedded in a silica matrix to obtain doped silica gels which were subsequently ground (GP samples), or dispersed within pure silica nanoparticles (DP samples).

The fluorescent nanoparticles were prepared by dissolving rhodamine 6G in ethanol (6.6×10^{-3} M) and the subsequent addition of tetraethoxysilane (TEOS) to obtain a Rh6G/TEOS ratio of 0.022. The solution was stirred prior to the addition of 1M ammonia solution (ammonia/Si = 0.174). The resulting mixture was vigorously stirred for 1 h, and then 10 mL of 0.269 M TEOS in ethanol solution were added to 17 mL of the previously prepared solution, followed by the addition of 3.8 mL of 0.206 M ammonia solution. The solution was allowed to hydrolyze under vigorous stirring and then stabilized for the precipitation of the Rh6G doped SiO_2 nanoparticles. After separation from the supernatant liquid and drying, the dye-doped particles were ready for the next step of the procedure.

For the preparation of the doped silica gels, the corresponding amount of Rh6G-SiO_2 nanoparticles and TiO_2 nanoparticles were dispersed in ormosil sols to form the fluorescent particles doped hybrid gels with and without TiO_2 scatterers (~15 nm). Note that the homogeneity of the silica gel samples cannot be preserved by doping with larger TiO_2 nanoparticles. The doped silica gels were finally dried at 50°C for 2 weeks. In order to obtain GP samples, a mixer mill was employed. The polydispersity of the measured ground powders was evaluated from SEM (scanning electron microscope) photographs. As an example, Fig. 1 shows the photograph of the GP of a bulk silica gel containing 2wt% Rh6G-SiO_2 nanoparticles and the corresponding particle size histogram. By fitting it to a log-normal function, an average powder size of 3 ± 1.2 μm was obtained. Similar average particle sizes are estimated for all the studied GP samples.

In the DP samples, different concentrations of Rh6G doped silica nanoparticles were mixed with undoped SiO_2. SEM photographs of the dispersed powders reveal an average particle size of 92 nm. In some of these samples different concentrations of TiO_2 particles (~405 nm) were also added.

All the powder laser samples were compacted in a quartz cell for handling ease and optical characterization. The volume filling factor of the powder materials was calculated by measuring sample volume and weight.

Thickness dependence of diffuse transmittance was evaluated in the GP of the silica gel containing 2wt% Rh6G–SiO_2 nanoparticles in order to experimentally determine the corresponding transport mean-free-path (l_t). The absolute diffuse transmittance spectra of the GP with less than 500 μm sample thickness were measured in a Cary 5 spectrometer with an integrated sphere assembly. The transmission measurements of those samples

with a larger thickness (up to 2.5 mm) were acquired by using a narrow-angle arrangement. In this case, a diode laser at 656 nm was used as the excitation source and the transmitted light was detected by means of a photomultiplier connected to a lock-in amplifier. Following the method outlined in Refs. [29, 30], the estimated value of l_t was 9.5 ± 0.5 μm for a wavelength of 656 nm.

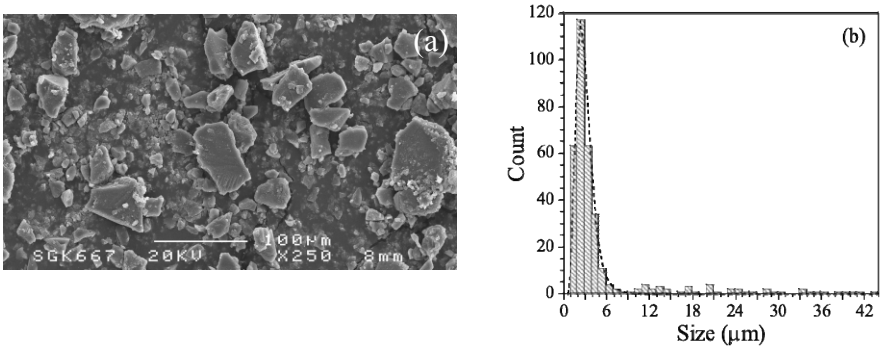

Figure 1. (a) Scanning electron microscope photograph of the GP of a bulk silica gel containing 2wt% Rh6G-SiO_2 nanoparticles. (b) Particle size histogram of the grains. The dashed line corresponds to the log-normal fit from which an average particle size of 3 ± 1.2 μm is calculated.

3.2. EXPERIMENTAL TECHNIQUES

The spectral and temporal measurements were performed at room temperature by using the frequency doubled output (532 nm) of a 10 Hz, Q-switched Nd: YAG laser as the excitation source. The pump pulse duration was 40 ps. The laser excitation energy was controlled by using a pair of polarizers and measured with an energy meter. The powder samples were compacted in a 6 mm high cylindrical cuvette with no front cell window. This sample holder has a diameter size larger than the incident laser spot (6 mm and ~2 mm, respectively). The emission from the front face of the sample was collected with an optical fiber by use of two lenses. This geometry, also used to perform temporal measurements, is particularly useful to avoid reflection effects of the pump and emitted radiation in the cuvette walls. A long-pass filter was used to remove light at the pump frequency.

In the spectral measurements, the emitted light was dispersed by a 0.5 m imaging spectrograph and recorded by a gated intensified CCD camera (see Fig. 2). This camera allows time-resolved detection of luminescence with exposure times down to 200 ps and variable delays after excitation. Time reference was provided by a fast photodiode which monitored a small fraction of the incident laser beam.

The excited state decays were recorded by coupling the optical fiber with a fast phototodiode connected to a 13 GHz bandwidth digital oscilloscope. In this case, the temporal response was limited by the 100 ps detector resolution. It is worth mentioning that both time-resolved spectral and temporal studies were performed in single shot measurements.

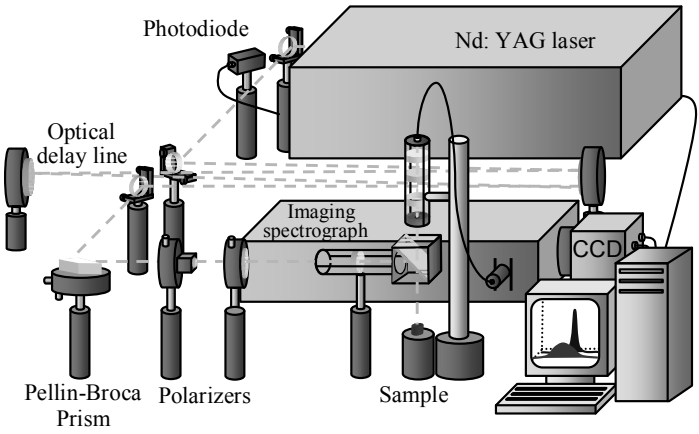

Figure 2. Experimental set-up for time-resolved spectroscopy measurements.

4. Results and Discussion of a Dye-Ddoped Silica Gel Powder

The laser-like effects of the GP of a bulk silica gel containing 2wt% Rh6G-SiO_2 nanoparticles was initially investigated. The concentration of Rh6G in the particles was in this case 3.1wt%. An experimental survey around the spectral and temporal characteristics of its random laser emission followed by a theoretical comparison with the temporal results obtained with a light diffusive propagation model are detailed below.

4.1. EXPERIMENTAL RESULTS

Figure 3a exhibits the normalized emission spectra obtained in the GP of a silica gel containing 2wt% Rh6G-SiO_2 nanoparticles at 19, 25, 37, and 748 μJ/pulse. At the lowest excitation energy the emission spectrum shows the typical broad fluorescence band of Rh6G centered at 616 nm (point line in Fig. 3a). However, as the pump energy is increased the linewidth is reduced due to the rise of a gain-narrowed peak centered at 598 nm which reveals the appearance of laser-like emission. At sufficiently high energies, only the gain-narrowed peak survives whereas the broad tails of the photoluminescence are completely suppressed (see thick full line of Fig. 3a). Figure 3b shows the effective linewidth ($\Delta\lambda_{eff} = \int \frac{I(\lambda)d\lambda}{I_{\max}}$) collapse from 51.8 to 10.8 nm. This result confirms that the GP acts as an efficient enough light scatter in the spectral range of the Rh6G optical gain. Note that the corresponding bulk dye doped silica gel is transparent at daylight so it is necessary to obtain GP out of it to give the scattering effect required for random lasing. The experimental data shown in Fig. 3b indicates that the laser threshold of this sample (defined as the energy value above which a suddenly drop of the spectral linewidth is observed) is around 24 μJ/pulse.

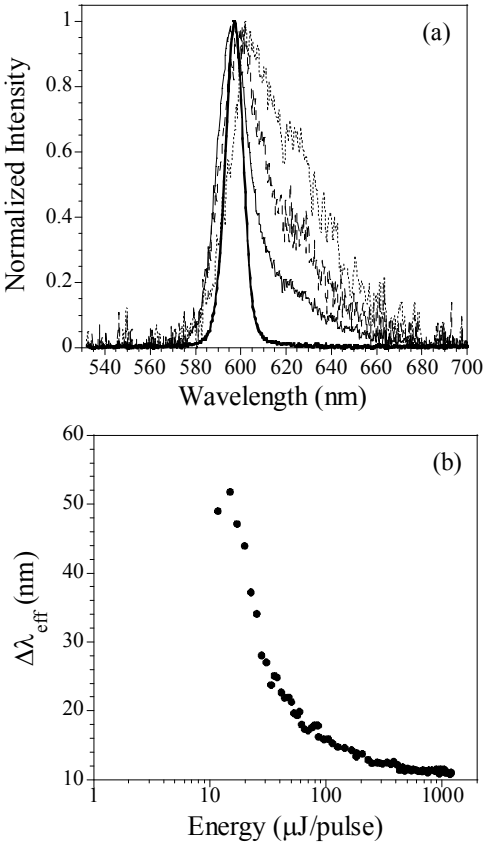

Figure 3. (a) Normalized emission spectra of the GP of a bulk silica gel containing 2wt% Rh6G-SiO_2 nanoparticles obtained at 19 μJ/pulse (point line), 25 μJ/pulse (dashed line), 37 μJ/pulse (thin full line) and 748 μJ/pulse (thick full line). (b) Pump energy dependence of the corresponding emission linewidths.

Time-resolved spectroscopy measurements were also carried out around the onset of the laser-like action. It is worthy to notice that this is the only experimental technique which allows us to separate the narrow laser-like contribution to the emission spectrum from the spontaneous emission present when exciting around the threshold. It therefore provides a detailed insight into the emission dynamics of the random laser sample based on the different characteristic time scales involved in both processes. As an example, Fig. 4a shows the emission spectra of the GP of a silica gel containing 2wt% Rh6G-SiO_2 nanoparticles measured after excitation with 27.8 μJ single shot pulses, by using a 200 ps gate width, and delays of 0, 0.5, 0.75 and 1.3 ns. This figure evidences the different emission bandshapes obtained at variable delays. Stimulated emission, which in this case has a maximum net gain in a narrow spectral region around 598 nm, appears at the shortest time exposure and delays (see the two upper curves in Fig. 4a). At time delays longer than 0.5 ns, a broader and weaker emission band is observed, exhibiting

the dominant photoluminescence contribution to the emission spectrum (see the two lower curves in Fig. 4a). Figure 4b thus shows the enhancement of the effective emission linewidth found as time delay is increased. On the other hand, the spontaneous emission of this sample is completely suppressed above a time delay of 1.8 ns. This result agrees well with the Rh6G lifetime measured at low excitation energies (1.65 ns) in the GP sample.

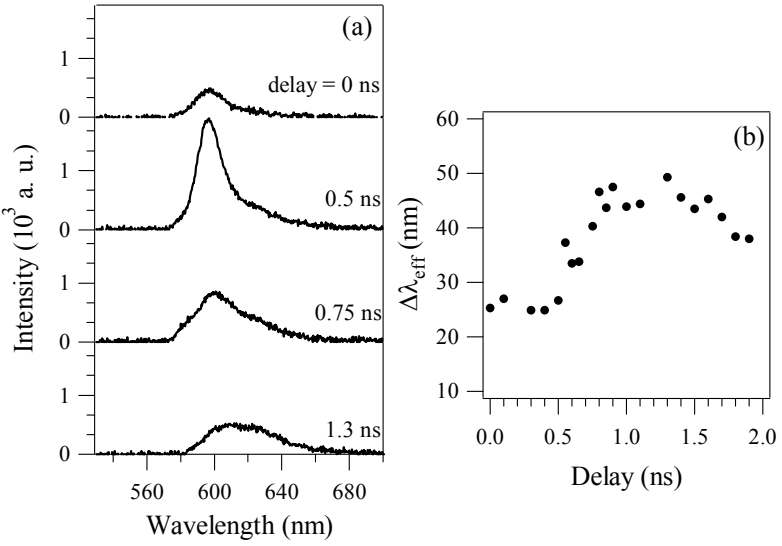

Figure 4. (a) Emission spectra of the GP of a bulk silica gel containing 2wt% Rh6G-SiO_2 nanoparticles obtained at variable delays after excitation with 27.8 μJ/pulse energy. The exposure time was 200 ps. (b) Linewidths obtained at 27.8 μJ/pulse energy as a function of the time delay in this sample.

Figure 5a shows the normalized emission decays of Rh6G measured at 15.7, 19 and 169 μJ/pulse in the GP of a silica gel containing 2wt% Rh6G-SiO_2 nanoparticles. Note that the wavy structure of these curves is due to the typical response of the fast photodiode used in the experimental set-up. At the lowest excitation energies the output pulse duration is limited by the lifetime of the Rh6G dye in this sample (1.65 ns) (see point line of Fig. 5a). However, a marked shortening of the output pulse is observed when increasing the pump energy (see Fig. 5a and b). In particular, the FWHM of the time profile was reduced down to around 100 ps above the lasing threshold (see Fig. 5b). This is the actual time resolution of the detector we used to perform this set of measurements, so our real temporal width might be much narrower. As a matter of fact, studies on liquid dye and polymer sheet random lasers have given emission pulses as short as 50 ps [31] or even less [14, 24].

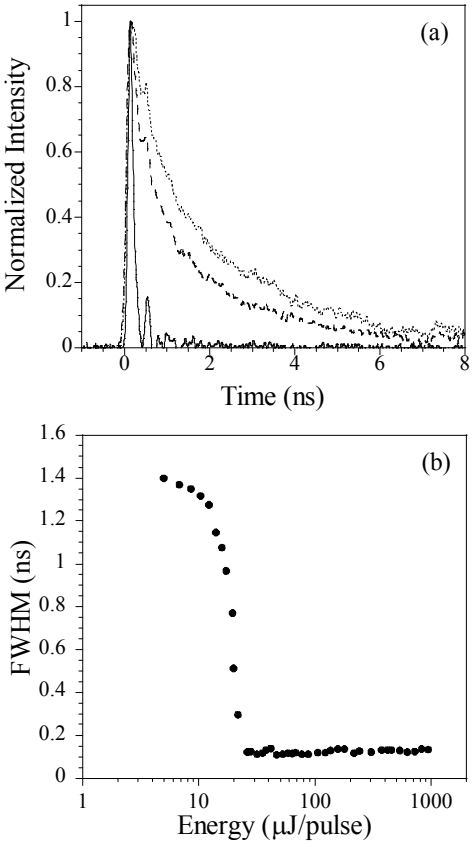

Figure 5. (a) Normalized temporal profiles of the GP of a bulk silica gel containing 2% Rh6G-SiO_2 nanoparticles obtained at 15.7 μJ/pulse (point line), 19 μJ/pulse (dashed line) and 169 μJ/pulse (thin full line). (b) FWHM of the corresponding time profiles as a function of the pump energy.

4.2. MODELING

We have performed theoretical calculations to study the laser-like emission dynamics of the previously explored GP sample by using the laser model described in section 2. The set of coupled nonlinear partial differential equations (Eqs. (4–6)) has been numerically solved by the Crank–Nicholson finite difference method (Δz = 0.05 μm, Δt = 10 ps). The input values for the calculation are the material parameters: $\sigma_{em} = 2.5 \times 10^{-16}$ cm^2, τ_s = 1.65 ns, K_{abs} (532 nm) = 148.5 cm^{-1}, n_{eff} = 1.16, f = 0.43 and t_{peak} = 120 ps and Δ = 20 ps. The effective refractive index has been calculated by using the Maxwell–Garnet theory. The mean-free-paths at the required wavelengths (λ_p = 532 nm and λ_e = 598 nm) have been calculated by using the Mie theory for spheres in the independent-scatter approximation with a diameter equal to the averaged mean particle size (ϕ = 3 μm). In spite of the fact that this material can be closely-packed, the effect of the spatial

correlations on the scattering and absorption processes can be neglected [29]. The obtained values for the mean-free-paths are: $l_s = 2$ μm, $l_t = 8.9$ μm, $l_{abs} = 21.6$ μm, $l^* = 2.0$ μm at 532 nm, and $l_t = 9$ μm at 598 nm. The value for l_t calculated from this theory at 656 nm agrees with the one experimentally obtained from the dependence on the sample thickness of the diffuse transmittance. This proves the Mie theory is reliable in order to predict the mean-free-paths in our scattering medium. The average internal reflectivities of the sample have been estimated from the Fresnel reflection coefficients by using the effective refractive index of the random system [29,30] ($r_0 = 0.24$ and $r_L = 0.3$).

Figure 6a compares the excited-state populations and the temporal profiles of the emitted light obtained by using this laser model at 0.15, 60.8, 85.2, and 185.5 μJ/pulse. These curves have been normalized for the sake of comparison. In addition, this plot shows the theoretical pulse shortening predicted by our model as the excitation energy is increased. In fact, the FWHM of the output pulse is reduced from 1.31 ns to 12 ps (see Fig. 6b). This result can be reliably used to determine the threshold energy where narrowing takes place [27, 31], leading to a theoretical threshold of 24 μJ/pulse. It is worthy to notice that although the experimental pulse width is limited by the actual time resolution of the detector, and, therefore a larger experimental pulse duration is obtained at high energies, the theoretical and experimental FWHM collapse around the same energy value (compare Figs. 5b and 6b).

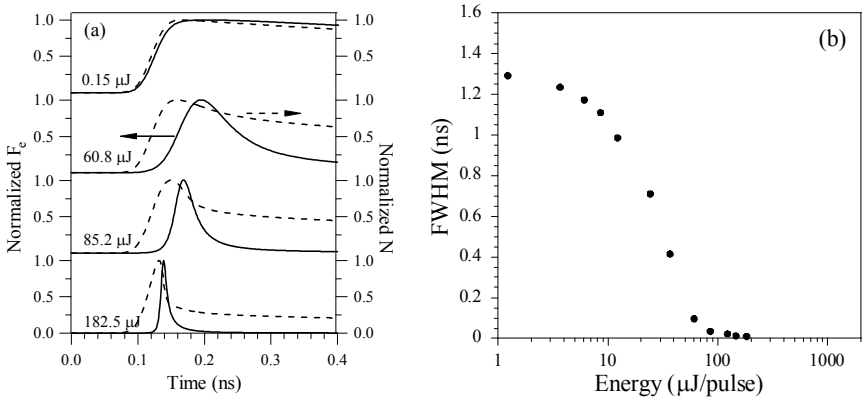

Figure 6. (a) Normalized time profiles (F_e, solid lines) and excited-state populations (N, dashed line) calculated for $\beta = 0.5$ at 0.15, 60.8, 85.2 and 182.5 μJ/pulse by using the laser model described in section 2.2 (b) FWHM of the simulated time profiles as a function of the pump pulse energy.

On the other hand, the build-up of the laser-like emitted pulse can be interpreted in the framework of ordinary Q-switch laser theory account taken of the formal similarity between our "laser equations" (see section 2.2) and the ones proposed by Florescu and John [23]. Moreover, following Ref. [23], our equations can be reduced to the basic Q-switch laser equations $\frac{dW_e}{dt} = v\sigma_{em} N W_e - \gamma_c W_e$, $\frac{dN}{dt} \approx -2v\sigma_{em} W_e N$ during the pulse build-up time [32]. Here, N is the population difference density, and γ_c the "cavity"

decay rate which is related to the diffusion coefficient by $\gamma_c \equiv D_e / l_z^2$, where $l_z \cong 3l_{abs}$ [26, 33]. A "cavity" decay time $\tau_c = 1/\gamma_c$ of 5.5 ps is thus obtained for our system. This value is close to the one given by the Q-switch theory, 6.4 ps, obtained from the time-dependence of N around the threshold and the output pulse width [32].

Figure 7 shows the integrated intensity of the output pulses measured as a function of the excitation energy in the GP sample (dots). The dashed line represents the linear fit to the experimental data which provides a laser threshold around 24 μJ/pulse. This value agrees well with the theoretical estimation given above. The solid curve represents the theoretically calculated input-output curve obtained from numerical integrations of the temporal profiles for $\beta = 0.5$. Note that it perfectly follows the experimental behavior of the GP (dots).

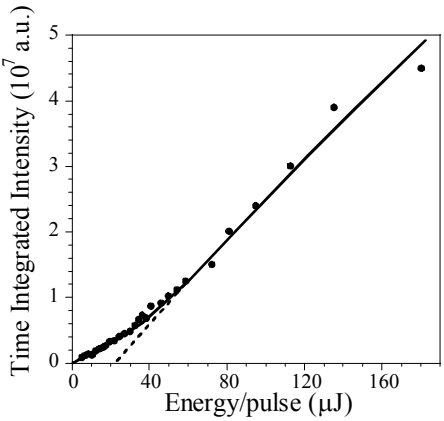

Figure 7. (a) Integrated intensity of the output pulses obtained as a function of the pump pulse energy in the GP of a bulk silica gel containing 2% Rh6G-SiO_2 nanoparticles. The solid line represent the simulated data for $\beta = 0.5$. A laser threshold of 24 μJ/pulse is estimated from the linear fit (dashed line) of the experimental data (dots).

5. Effect of the Dye-Doped Nanoparticle Concentration and of Additional Passive Scatterers on the Random Laser Action

The dependence of the random laser threshold and of the slope efficiency on the Rh6G doped SiO_2 nanoparticles concentration is investigated in the GP and DP samples by using the same experimental conditions. It is worthy mentioning that the concentration of the Rh6G dye in the fluorescent nanoparticles employed to prepare the powders studied in this section was 0.75wt%. TiO_2 particles were also incorporated in some samples in order to explore the effects of additional passive scatterers on their random laser phenomenon.

5.1. GROUND POWDER SAMPLES

We have performed spectral and temporal measurements in the GP of different silica gels containing 0.1, 1, 2, 3, 4, and 5wt% Rh6G-SiO_2 nanoparticles in order to investigate if the laser threshold energy could be minimized and the random laser output could be optimized. Figure 8a compares the spectral narrowing of these samples as a function of the pump pulse energy. As it can be clearly seen, a similar behavior is obtained regardless the dye-doped nanoparticles concentration, only a slightly larger laser threshold is found in the GP containing 0.1wt% Rh6G–SiO_2 nanoparticles. This is the less efficient sample as can be observed in Fig. 8b. In this figure, the integrated intensity of the corresponding emission spectra is plotted as a function of the pump pulse energy. In contrast, the GP of the silica gel containing 4wt% Rh6G–SiO_2 nanoparticles has the largest slope efficiency.

Figure 8c shows the temporal shortening obtained as a function of the excitation energy in the same set of GP of silica gel samples. In agreement with the spectral results, a slightly larger laser threshold is found in the sample containing 0.1wt% Rh6G–SiO_2 nanoparticles.

This plot also exhibits the different output pulse FWHM at low excitation energies. It is worthy mentioning the enhancement of the lifetime value when increasing the fluorescent nanoparticles concentration from 0.1wt% (τ = 4.6 ns) to 2wt% (τ = 6.2 ns) and the subsequent lifetime quenching obtained when the amount of Rh6G–SiO_2 nanoparticle is further increased up to 5wt% (τ = 5 ns). This behavior could be qualitatively explained by the presence of two competing phenomena such as the re-absorption and the formation of dye aggregates. In the first case, an increase of the lifetime is expected owing to the radiation trapping effect. On the contrary, the presence of dye aggregates could be the source for the lifetime quenching found when using 5 wt% Rh6G–SiO_2 nanoparticles. Note that the formation of dye aggregates is expected to be a gradual process as the concentration of the fluorescent nanoparticles increases. Their effect could thus become the dominant lifetime contribution at high concentrations.

It is also remarkable the different emission features described in section 4 for a GP sample containing 2wt% Rh6G–SiO_2 and those presented in this section for another containing the same amount of fluorescent nanoparticles (compare Figs. 3b and 5b with triangles of Fig. 8). In particular, a lower Rh6G lifetime value and a larger laser threshold energy was found in the firstly studied powder sample where the actual Rh6G concentration in the nanoparticles was higher (3 and 0.75wt%, respectively) and the pump laser beam was focused into a smaller spot size (2 and 2.8 mm, respectively). Note that the formation of Rh6G aggregates due to the larger dye concentration could account for the lifetime quenching found in such case. Moreover, one has to bear in mind that on decreasing the pump beam diameter, the threshold shifts to larger energies as it has been previously reported in the literature [27].

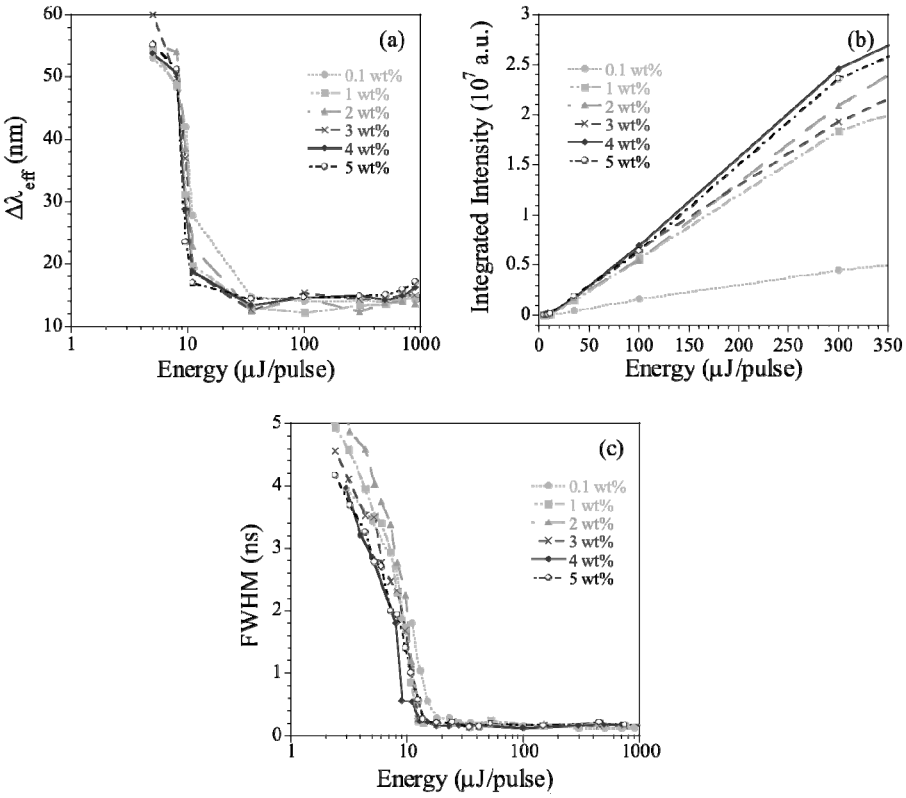

Figure 8. (a) Pump energy dependence of the effective emission linewidth obtained in the GP of different silica gels containing 0.1wt% (dots), 1wt% (squares), 2wt% (triangles), 3wt% (crosses), 4wt% (diamonds), and 5wt% (circles) Rh6G-SiO_2 nanoparticles. (b) Integrated intensity of the emission spectra as a function of the pump pulse energy. (c) FWHM of the time profiles obtained in the mentioned GP samples as a function of the pump pulse energy.

In order to investigate the possible influence of passive scatterers in the random laser threshold of GP samples, we have studied the emission spectra and kinetics of powders of different silica gels containing 4wt% Rh6G-SiO_2 nanoparticles and 0, 0.1, and 0.8wt% TiO_2 nanoparticles. These nanoparticles were to be small enough (~15 nm) to preserve the homogeneity of the gels. Nevertheless, the introduction of such small TiO_2 scatterers does not lead to a significant change in the emission features or in the onset of laser-like action. In particular, regardless the TiO_2 concentration, the spectral

narrowing (data not shown) and the output pulse shortening (Fig. 9) occur in all of them around the same energy value (~8.5 μJ/pulse). This evidences that the scattering effect of of these passive dispersors is not enough to reduce the random laser threshold. However, the significant reduction of the FWHM found at low excitation energies when increasing the TiO_2 concentration reflects the lifetime quenching from 5 ns (in the GP sample without TiO_2 dispersors) till 3.2 ns (in the GP sample with 0.8wt% TiO_2 scatterers). This suggests the presence of additional non-radiative de-activation channels when the TiO_2 nanoparticles are embedded in the silica matrix.

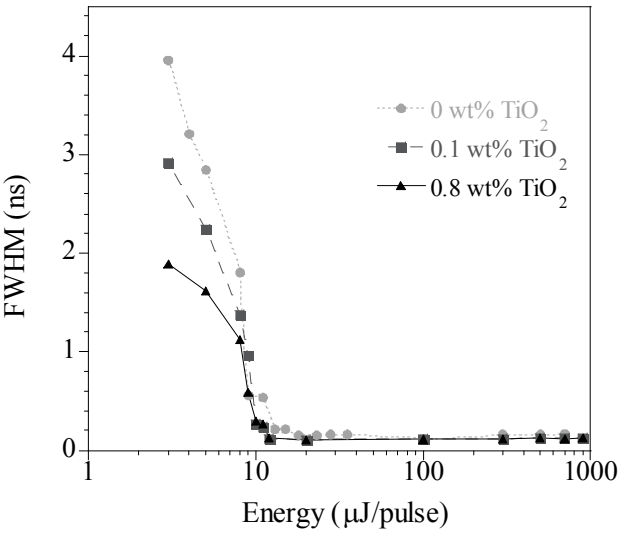

Figure 9. FWHM of the temporal profiles obtained as a function of the pump pulse energy in the GP of different silica gels containing 4wt% Rh6G-SiO_2 nanoparticles and 0wt% (dots), 0.1wt% (squares) and 0.8wt% (triangles) TiO_2 dispersors.

5.2. DISPERSED POWDER SAMPLES

Different Rh6G–SiO_2 nanoparticles concentrations were also tried to study their effect in the optical properties of the DP samples. Figure 10a shows the pump energy dependence of the effective emission linewidth of 2, 4, 6, and 8wt% Rh6G–SiO_2 nanoparticles dispersed in silica powder. From these experimental data a laser threshold around 40 μJ/pulse is inferred in the four cases. This spectral narrowing demonstrates that no embedding medium for the Rh6G–SiO_2 nanoparticles is required to achieve random lasing. Nevertheless, it is clear from the comparison between Figs. 8a and 10a that the DP samples have a laser threshold around four times larger than the GP samples.

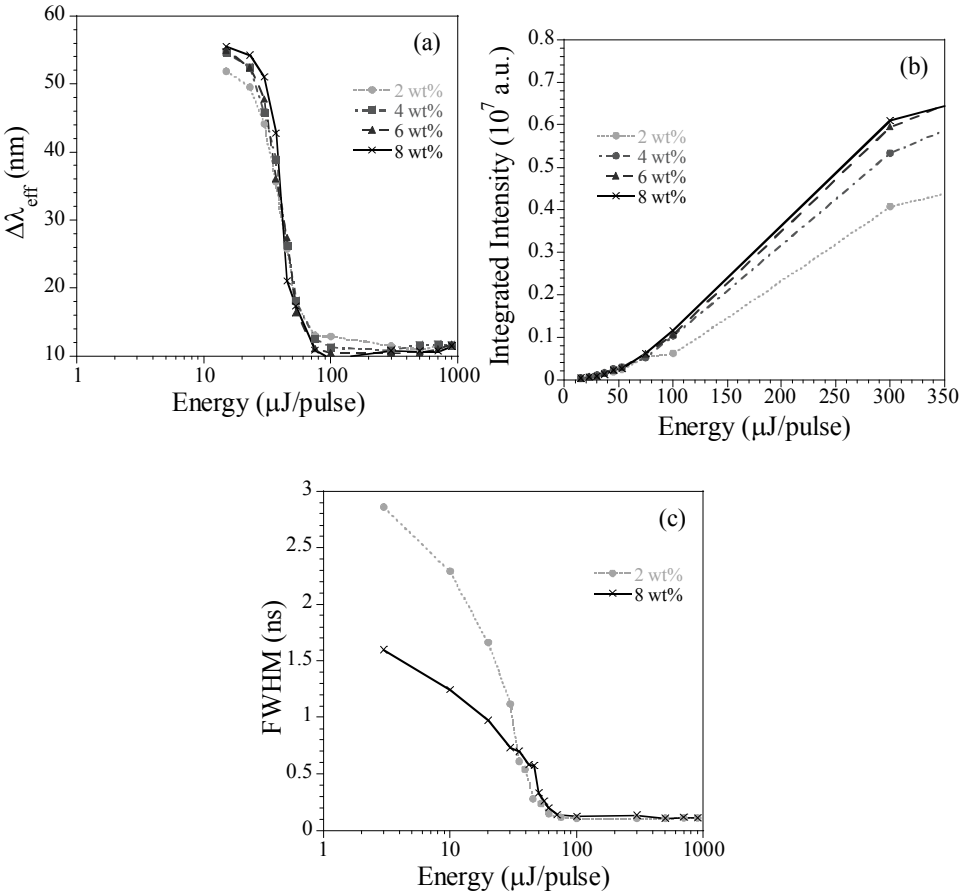

Figure 10. (a) Pump energy dependence of the effective emission linewidth obtained in 2wt% (dots), 4wt% (squares), 6wt% (triangles), and 8wt% (crosses) Rh6G–SiO_2 nanoparticles dispersed in silica powder. (b) Integrated intensity of the emission spectra as a function of the pump pulse energy. (c) FWHM of the time profiles obtained in the DP samples containing 2wt% (dots) and 8wt% (crosses) Rh6G-SiO_2 nanoparticles as a function of the pump pulse energy.

On the other hand, the increase of the fluorescent nanoparticles concentration dispersed within undoped silica nanoparticles does not remarkably improve the laser threshold either. It yields only an enhancement of the slope efficiency as can be seen in Fig. 10b where their spectrally integrated emission intensity is plotted as a function of the pump pulse energy. Figure 10c compares the pulse shortening found when increasing the pump pulse energy in the DP samples containing 2 and 8wt% fluorescent nanoparticles. As it is suggested in this figure, the increase of fluorescent nanoparticles leads to a reduction of the Rh6G lifetime value from 4 ns for the sample containing

2wt% of Rh6G doped nanoparticles to 2.9 ns for the one with a concentration of 8wt%. Moreover, the former sample seems to have a slightly smaller laser threshold.

On the other hand, Fig. 11 compares the laser-like emission spectra found at 900 μJ/pulse in the GP and DP samples both containing 2wt% of the same Rh6G–SiO_2 nanoparticles. As it is shown, they have different spectral position and spectrum bandshape. The emission peak of the GP sample is broader and is red-shifted around 23 nm. Moreover, the Rh6G lifetime of the DP sample is 4 ns whereas the lifetime of the GP sample is 6.2 ns. These experimental results seem to indicate a larger contribution of the re-absorption phenomena in the GP samples. Note that although both samples contain the same dye doped nanoparticles concentration, it is rather possible that the actual Rh6G concentration be higher in the GP samples. A dye leakage is expected in the final preparation step of the DP samples due to the method employed for the dispersion in solution of the pure SiO_2 particles and the fluorescent nanoparticles.

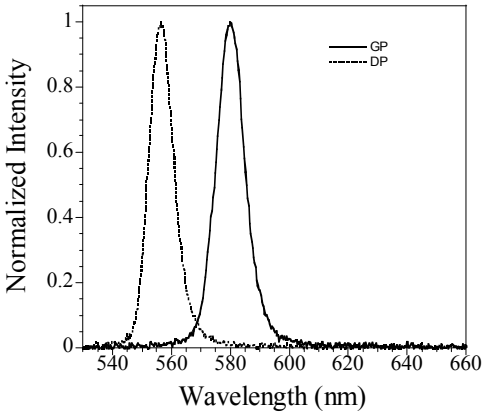

Figure 11. (a) Normalized emission spectra of the GP (full line) and DP (dashed line) samples both containing 2wt% Rh6G–SiO_2 nanoparticles obtained at 900 μJ/pulse.

To explore a possible enhancement of random laser emission in DP samples we have also tested DP samples in which passive scatterers were added. In this case, larger TiO_2 particles (~405 nm) were employed in order to increase the light scattering effect. Figure 12a shows the effective emission linewidth of 4wt% Rh6G–SiO_2 nanoparticles dispersed in silica powder with 0.7, 1.4, 2.8, and 7.1wt% TiO_2 dispersors as a function of the pump energy. This plot reveals the slightly smaller laser threshold of the powder sample containing 7.1wt% TiO_2 scatterers. Nevertheless, as evidenced in Fig. 12b where the pump energy dependence of their spectrally integrated intensity is plotted, this sample has the smallest slope efficiency. Moreover, a parallel behavior is obtained in the time domain. Figure 12c shows the FWHM of the time profiles obtained in the DP samples containing 0.7 and 7.1wt% TiO_2 scatterers as a function of the pump pulse energy. This plot exhibits the reduction of the laser threshold energy, from 40 to 27 μJ/pulse, when increasing the TiO_2 concentration. Nevertheless, it is worthy to remark that the latter laser threshold value is still around three times larger than the one found in GP samples.

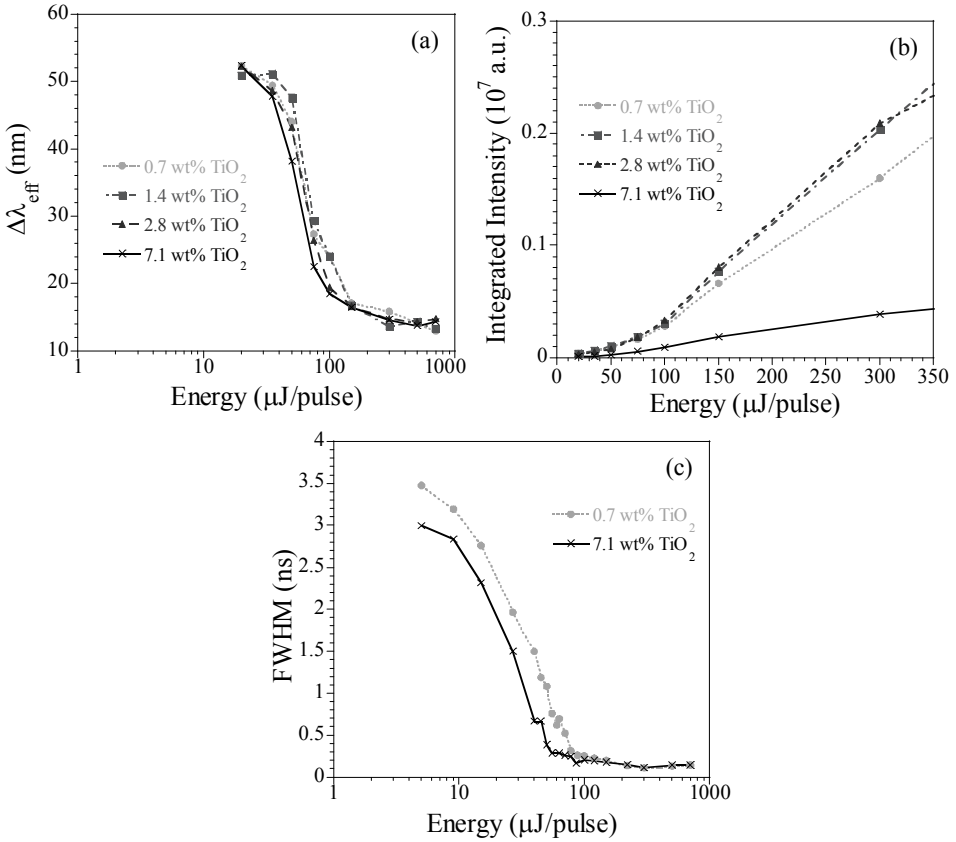

Figure 12. (a) Pump energy dependence of the effective emission linewidth obtained in 4wt% Rh6G-SiO_2 nanoparticles dispersed in silica powder with 0.7wt% (dots), 1.4wt% (squares), 2.8wt% (triangles), and 7.1wt% (crosses) TiO_2 scatterers (~ 405 nm). (b) Integrated intensity of the emission spectra as a function of the pump pulse energy. (c) FWHM of the time profiles obtained in the DP samples containing 0.7wt% (dots) and 7.1wt% (crosses) TiO_2 as a function of the pump pulse energy.

From the experimental data presented so far, we have demonstrated that the GP samples behave, even without the need of passive scatterers, as more efficient systems to achieve random lasing. They therefore seem to be the most attractive ones for potential future application so the study of their susceptibility to optical damage under VIS laser pulse irradiation becomes crucial. As an example, Fig. 13 shows the integrated emission intensity of the GP sample containing 2wt% Rh6G-SiO_2 nanoparticles when pumping with 35μJ/pulse (i.e. above the threshold), as a function of the irradiation time. After 8h, it almost does not change which is a clear evidence of the good photostability of this kind of powder laser materials.

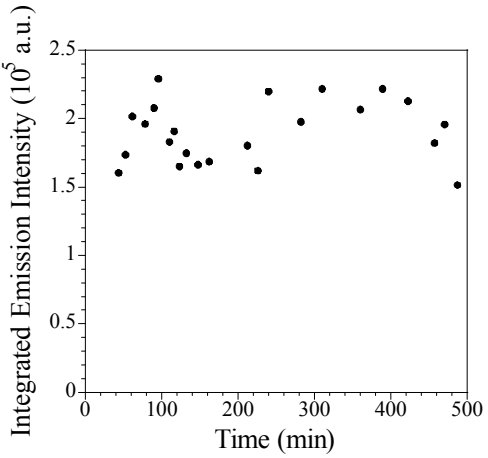

Figure 13. Irradiation time dependence of the integrated emission intensity of the GP containing 2wt% Rh6G–SiO_2 nanoparticles after exciting at 532 nm with 35 μJ/pulse.

6. Conclusions

We have observed and characterized random laser-like effects such as spectral narrowing, emission intensity increase and pulse shortening in two different kinds of silica based powder samples. Both were synthesized by the sol-gel technique and contain different amount of Rh6G doped SiO_2 nanoparticles and TiO_2 scatterers. Note that in the studied powder laser samples they were either dispersed within pure silica particles (DP samples) or embedded in a silica gel matrix which is subsequently ground (GP samples). We have also demonstrated that within diffusive conditions of light propagation, a laser model with the feedback provided by the powder is able to describe the observed random laser behavior. In particular, we have found both good qualitative and quantitative agreements for the pulse duration collapse and laser threshold of the GP sample containing 2wt% Rh6G–SiO_2 nanoparticles chosen as an example. The behavior of this system is close to a classical Q-switched laser under ultrashort pumping. In addition, the ultrafast spectroscopies performed to find the optimal powder composition for random laser operation demonstrate that the laser threshold value is just slightly modified when increasing the concentration of the fluorescent nanoparticles whereas it increases their slope efficiency. On the other hand the incorporation of small TiO_2 particle (~15 nm) in the GP samples has no influence on their laser threshold. Nevertheless, the dispersion of larger TiO_2 particles (~405 nm) within the dye-doped silica powders slightly improves the laser threshold but decreases their slope efficiency. The comparison between the emission features of both kinds of powders reveals that lower thresholds for laser-like emission are achieved in the GP samples, even in the absence of passive scatterers. As we have mentioned in section 5.2, the different preparation procedures between GP and DP samples could allow for an actual larger Rh6G concentration in GP samples which could favor an enhancement of the optical gain required for random lasing. Moreover, the different average particle size between GP and DP samples (~3 μm and 92 nm,

respectively) could influence the multiple scattering efficiency and therefore the onset of laser-like emission. Note that the GP sample with a dye-doped concentration of 4wt% is the one with the smallest onset of laser-like action (around 8.5μJ/pulse) and is the most efficient random laser emitter. The good photoestability of the GP samples has been also proven under VIS laser pulse irradiation by exciting above the threshold.

We believe that our findings could be of much interest in the understanding of results obtained from other solid-state random lasers as well as the development of new systems operating within the diffusive approximation. Moreover, the low laser-like threshold found in the GP based samples opens a challenging field of new applications such as biosensors or biotracers based on these dye-doped nanoparticles.

Acknowledgments This work was supported by the Spanish Government MEC under Projects No. MAT2008-05921/MAT, MAT2008-00010/NAN, Consolider SAUUL CSD2007-00013, and Basque Country Government (IT-331-07). S. G.-R acknowledges financial support from the Spanish MEC under the "Juan de la Cierva" program.

Theoretical model and simulations would not have become possible without the help of Dr. M.A. Illarramendi. We also thank the group of Prof. David Levy from the Institute of Materials Science in Madrid (Spain) for providing the high quality dye-doped samples used in this work, and Dr. M. Al-Saleh for sample preparation.

References

1. Letokhov, V. S. (1967) Stimulated emission of an ensemble of scattering particles with negative absorption, *JETP Lett.* **5**, 212–215.
2. Cao, H. (2003) Lasing in random media, *Waves Random Media* **13**, R1–R39.
3. Noginov, M. A. (2005) *Solid-State Random Lasers*, Springer, Berlin.
4. Wiersma, D. S. (2008) The physics and applications of random lasers, *Nat. Phys.* **4**, 359–367.
5. John, S., and Pang, G. (1996) Theory of lasing in a multiple-scattering medium, *Phys. Rev. A* **54**, 3642–3652.
6. Wiersma, D. S., and Lagendijk, A. (1996) Light diffusion with gain and random lasers, *Phys. Rev. E* **54**, 4256–4265.
7. Jiang, X., and Soukoulis, C. M. (2000) Time dependent theory for random lasers, *Phys. Rev. Lett.* **85**, 70–73.
8. Burin, A. L., Ratner, M. A., Cao, H., and Chang, R. P. H. (2001) Model for a random laser, *Phys. Rev. Lett.* **87**, 215503.
9. Mujumdar, S., Turck, V., Torre, R., and Wiersma, D. S. (2007) Chaotic behavior of a random laser with static disorder, *Phys. Rev. A* **76**, 033807.
10. Türeci, H. E. (2008) Strong interactions in multimode random lasers, *Science* **320**, 643–646.
11. van der Molen, K. L., Mosk, A. P., and Lagendijk, A. (2007) Quantitative analysis of several random lasers, *Opt. Commun.* **278**, 110–113.
12. Ferjani, S., Barna, V., De Luca, A., Versace, C., and Strangi, G. (2008) Random lasing in freely suspended dye-doped nematic liquid crystals, *Opt. Lett.* **33**, 557–559.
13. Lawandy, N. M., Balachandran, R. M., Gomes, A. S. L., and Sauvain, E. (1994) Laser action in strongly scattering media, *Nature* **368**, 436–438.

14. Sha, W. L., Liu, C. H., and Alfano, R. R. (1994) Spectral and temporal measurements of laser action of Rhodamine 640 dye in strongly scattering media, *Opt. Lett.* **19**, 1922–1924.
15. Noginov, M. A., Caulfield, H. J., Noginova, N. E., and Venkateswarlu, P. (1995) Line narrowing in the dye solution with scattering centers, *Opt. Commun.* **118**, 430–437.
16. García-Revilla, S., Fernández, J., Illarramendi, M. A., García-Ramiro, B., Balda, R., Cui, H., Zayat, M., and Levy, D. (2008) Ultrafast random laser emission in a dye-doped silica gel powder, *Opt. Express* **16**, 12251–12263.
17. García-Revilla, S., Fernández, J., Balda, R., Zayat, M., and Levy, D. (2009) Real-time spectroscopy of novel solid-state random lasers, *Proc. SPIE* **7212**, K1–K11.
18. García-Revilla, S., Zayat, M., Balda, R., Al-Saleh, M., Levy, D., and Fernández, J. (2009) Low threshold random lasing in dye-doped silica nano powders, *Opt. Express* **17**, 13202–13215.
19. Letokhov, V. S. (1968) Generation of light by a scattering medium with negative resonance absorption, *Sov. Phys. JETP* **26**, 835–840.
20. Wiersma, D. S., Albada, M. P. v., and Lagendijk, A. (1995) Coherent backscattering of light from amplifying random media, *Phys. Rev. Lett.* **75**, 1739–1742.
21. Ishimaru, A. (1997) *Wave propagation and scattering in random media*, IEEE Press and Oxford University Press, New York
22. Genack, A. Z. (1987) Optical transmission in disordered media, *Phys. Rev. Lett.* **58**, 2043–2046.
23. Florescu, L., and John, S. (2004) Lasing in a random amplifying medium: Spatiotemporal characteristics and nonadiabatic atomic dynamics, *Phys. Rev. E* **70**, 036607.
24. Siddique, M., Alfano, R. R., Berger, G. A., Kempe, M., and Genack, A. Z. (1996) Time-resolved studies of stimulated emission from colloidal dye solutions, *Opt. Lett.* **21**, 450–452.
25. Berger, G. A., Kempe, M., and Genack, A. Z. (1997) Dynamics of stimulated emission from random media, *Phys. Rev. E* **56**, 6118–6122.
26. van Soest, G., Poelwijk, F. J., Sprik, R., and Lagendijk, A. (2001) Dynamics of a random laser above threshold, *Phys. Rev. Lett.* **86**, 1522–1525.
27. van Soest, G. (2001) *Thesis: Experiments on Random Lasers*, University of Amsterdam, Amsterdam.
28. García-Ramiro, B., Aramburu, I., Illarramendi, M. A., Fernández, J., and Balda, R. (2009) Study of lasing threshold and efficiency in laser crystal powders, *Eur. Phys. J. D* **52**, 195–198.
29. García-Ramiro, B., Illarramendi, M. A., Aramburu, I., Fernández, J., Balda, R., and Al-Saleh, M. (2007) Light propagation in optical crystal powders: effects of particle size and volume filling factor, *J. Phys.: Condens. Matter* **19**, 456213.
30. Illarramendi, M. A., Aramburu, I., Fernández, J., Balda, R., Williams, S. N., Adegoke, J. A., and Noginov, M. A. (2007) Characterization of light scattering in translucent ceramics, *J. Opt. Soc. Am. B* **24**, 43–48.
31. Zacharakis, G., Heliotis, G., Filippidis, G., Anglos, D., and Papazoglou, T. G. (1999) Investigation of the laserlike behavior of polymeric scattering gain media under subpicosecond laser excitation, *Appl. Opt.* **38**, 6087–6092.
32. Siegman, A. E. (1986) *Lasers*, University Science Books, Mill Valley, California.
33. Balachandran, R. M., and Lawandy, N. M. (1997) Theory of laser action in scattering gain media, *Opt. Lett.* **22**, 319–321.

INTERDISCIPLINARY LECTURE

NEUTRINOS IN PARTICLE PHYSICS AND ASTROPHYSICS

G. COSTA*
Dipartimento di Fisica "G. Galilei", Università di Padova
Istituto Nazionale di Fisica Nucleare, Sezione di Padova
Via Marzolo 8, 35131 Padova, Italy

Abstract Neutrinos, first introduced for theoretical reasons, were discovered long ago, but their main properties have been established rather recently, especially by analyzing the so-called atmospheric and solar neutrinos. Now we know that there are three kinds of neutrinos that, in their propagation, get mixed among themselves through the mechanism of oscillations. In this paper we discuss this phenomenon and the main features of neutrinos; we mention also the neutrinos emitted by supernovae and the relic neutrinos. Neutrino telescopes represent a useful tool for investigating new phenomena both in particle physics and in astrophysics.

1. Introduction

Neutrinos have already a long history and I will summarize here the main steps of this long and exciting path. They enter the field of physics in 1930; it was Wolfang Pauli who, in a famous letter addressed to the participants in a conference on radioactivity in Tubingen, suggested the existence of a spin-1/2 neutral particle with zero (or very tiny) mass to save the conservation of energy and angular momentum in the β-decays of atomic nuclei (A, Z):

$$(A, Z) \rightarrow (A, Z+1) + e^{-} + \bar{\nu}_e . \quad (1)$$

He called this particle neutron, but the true *neutron* was discovered by James Chadwick in 1932, and the Pauli particle was renamed *neutrino* by Enrico Fermi who, in 1933, formulated the first theory of weak interaction [1]. It is a four-fermion contact interaction, which applies, in particular, to the neutron decay:

$$n \rightarrow p + e^{-} + \bar{\nu}_e . \quad (2)$$

We have introduced the present notation ν_e which distinguishes the electron neutrinos from other two kinds of neutrinos with a different *flavor*. The symbol $\bar{\nu}_e$ indicates the *antineutrino*; it is a firmly established fact that, for each particle there is a

* G. Costa, Dipartimento di Fisica "G. Galilei", Università di Padova, Istituto Nazionale di Fisica Nucleare, Sezione di Padova, Via Marzolo 8, 35131 Padova, Italy, e-mail: giovanni.costa@pd.infn.it

B. Di Bartolo and J. Collins (eds.), *Biophotonics: Spectroscopy, Imaging, Sensing, and Manipulation*, 345
DOI 10.1007/978-90-481-9977-8_16,

corresponding *antiparticle* with the same properties but opposite electric charge and opposite additive quantum numbers.

It took several years to get experimental evidence of the existence of the electron neutrino. It was discovered in 1956 by Frederick Reines, Clide Cowan and collaborators [2], who made use of the antineutrinos $\bar{\nu}_e$ emitted by a nuclear reactor (at Savannah River, North Carolina) to produce and confirm the occurrence of the inverse β-decay process:

$$\bar{\nu}_e + \mathrm{p} \rightarrow \mathrm{n} + \mathrm{e}^+ . \tag{3}$$

The second kind of neutrinos was discovered in 1962 [3]; it was the *muon neutrino* ν_μ which appears in the reactions

$$\pi^+ \rightarrow \mu^+ + \nu_\mu \tag{4}$$

$$\nu_\mu + \mathrm{n} \rightarrow \mathrm{p} + \mu^- . \tag{5}$$

In 1975 Martin Pearl *et al.* at SLAC [4] discovered the *tauon*, a particle similar to (but much heavier than) the electron and the muon; this fact suggested the existence of a third neutrino flavor: ν_τ detected 25 years later at Fermi Laboratory, Illinois [5].

An intense flux of neutrinos is emitted by the Sun (they are called *solar neutrinos*), generated by nuclear reactions in its interior; neutrinos are produced also in the upper layers of the atmosphere (they are called *atmospheric neutrinos*). In 1968 Raymond Davies jr. *et al.* [6] measured the flux of the solar neutrinos and found a *deficit* with respect to the theoretical estimates. Also the flux of atmospheric neutrino resulted to be less than what expected [7]. In the following we discuss the *atmospheric neutrino anomaly* and the *solar neutrino problem* and their solutions. The solutions to these problems rely on the hypothesis of *neutrino oscillations*, so that it is convenient to discuss first the mechanism of neutrino oscillations. Finally we shall briefly consider the neutrinos emitted by supernovae and the so-called relic neutrinos.

2. Neutrino Oscillations

Neutrino oscillations (between neutrinos and antineutrinos) were proposed originally by Pontecorvo [8], when only electron neutrinos were known. Later, it became clear that the relevant oscillations occur among neutrinos with different flavors. The general case has to deal with three flavors; there are three kinds of neutrinos ν_e, ν_μ, ν_τ coupled respectively to electrons, muons and tauons. In Table 1 we list the three neutrinos together with their charged partners; all together they are called *leptons*: they participate in the weak interactions and, obviously, the charged ones also in electromagnetic interactions.

TABLE 1. Leptons

Flavor	Charge (Q/e)	Mass (MeV/c^2)
Electron e	−1	0.511
e-neutrino ν_e	0	$<2 \times 10^{-6}$
Muon μ	−1	105.66
μ-neutrino ν_μ	0	< 0.17
Tau τ	−1	1,776.8
τ-neutrino ν_τ	0	<24

It turned out that neutrinos of different flavors do not have definite masses, but they are linear combinations of three mass eigenstates ν_1, ν_2, ν_3 … Flavor neutrino states and mass eigenstates are related by a 3 × 3 unitary mixing matrix U:

$$\begin{pmatrix} \nu_e \\ \nu_\mu \\ \nu_\tau \end{pmatrix} = \mathrm{U} \begin{pmatrix} \nu_1 \\ \nu_2 \\ \nu_3 \end{pmatrix} \tag{6}$$

The matrix U contains three angles and a phase [9] and it can be written in the following way:

$$\mathrm{U}= \begin{pmatrix} 1 & 0 & 0 \\ 0 & c_{23} & s_{23} \\ 0 & -s_{23} & c_{23} \end{pmatrix} \begin{pmatrix} c_{13} & 0 & -s_{13}e^{-\gamma} \\ 0 & 1 & 0 \\ -s_{13}e^{-i\gamma} & 0 & c_{13} \end{pmatrix} \begin{pmatrix} c_{12} & s_{12} & 0 \\ -s_{12} & c_{12} & 0 \\ 0 & 0 & 1 \end{pmatrix} \tag{7}$$

where we have made use of the notation: c = cos θ, s = sin θ.

As a matter of fact, atmospheric and solar neutrinos can be analyzed separately. Then a two flavor mixing is sufficient and we limit ourselves here to this case. Specifically, we consider the mixing between ν_e and ν_μ, that is the case of solar neutrinos, so that we can write

$$\begin{aligned} \nu_e &= \cos\theta_{12}\,\nu_1 + \sin\theta_{12}\,\nu_2 \\ \nu_\mu &= -\sin\theta_{12}\,\nu_1 + \cos\theta_{12}\,\nu_2. \end{aligned} \tag{8}$$

The mass eigenstates ν_1 and ν_2 propagate as plane wave solutions, which (in the system of natural units ħ = c = 1) are expressed by

$$|\nu_i(t)> = \exp\{-i\,(E_i\,t - p_i\,x)\}\,|\nu_i(0)> \approx \exp\{-i\,(m_i^2\,L / 2E_i)\}\,|\nu_i(0)>, \tag{9}$$

where E_i, p_i and m_i are the energy, linear momentum and mass of ν_i (i=1,2) and L≈ ct = t; in the last expression, we made use of the approximation: $p_i >> m_i$, $p_i \approx E_i$, $E_i \approx E + m_i^2/2E$. Then one can write

$$|\nu_e(L)> \approx \cos\theta_{12} \exp\{-i\,(m_1^2\ L/2E)\}|\nu_1(0)> + \sin\theta_{12} \exp\{-i\,(m_2^2\ L/2E)\}|\nu_2\ (0)> , \quad (10)$$

from which one can obtain the probability of the transition $\nu_e \rightarrow \nu_\mu$

$$P(\nu_e \rightarrow \nu_\mu) = |<\nu_\mu \mid \nu_e(L)>|^2 \approx \sin^2 2\theta_{12} \sin^2(\Delta m_{12}^2\ L / 4E) , \quad (11)$$

where $\Delta m_{12}^2 = m_1^2 - m_2^2$. A useful form is obtained by expressing L in Km and E in GeV:

$$P(\nu_e \rightarrow \nu_\mu) \approx \sin^2 2\theta_{12} \sin^2\{1.27\,\Delta m_{12}^2\ L/\ 4E\} . \quad (12)$$

One realizes that the probability oscillates as a wave in time or, correspondingly, along the propagation distance L.

The above relations can be applied also to the case of the atmospheric neutrinos, in which the mixing occurs between ν_μ and ν_τ, replacing θ_{12} and Δm_{12} by θ_{23} and Δm_{23}.

3. Atmospheric Neutrinos

The so-called atmospheric neutrinos are produced in the hadronic showers created by interactions of cosmic rays, which consist mainly of protons and light atomic nuclei. The main source of these neutrinos are the π-mesons, through the reactions:

$$\begin{aligned} \pi^+ &\rightarrow \mu^+ + \nu_\mu \\ \mu^+ &\rightarrow e^+ + \bar{\nu}_\mu + \nu_e \end{aligned} \quad (13)$$

and similarly for π^- and μ^-. The ratio between muon and electron neutrinos is expected to be approximately

$$R = N(\nu_\mu + \bar{\nu}_\mu) / N(\nu_e + \bar{\nu}_e) \approx 2, \quad (14)$$

while the experimental value is less than 30% of this figure [7].

In 1998, at the International Neutrino Conference in Takayama, Japan, new results on atmospheric neutrinos were presented [10]: they were obtained at Super-Kamiokande, a large neutrino underground observatory, with a huge detector containing 50,000t of pure water surrounded by 10,000 photomultipliers. The neutrinos were detected through the charge current reactions

$$\nu_e\ (\nu_\mu) + N \rightarrow e^-\ (\mu^-) + N' \quad (15)$$

where N, N' stand for two nucleons (p, n), and similarly for the antineutrinos $\bar{\nu}_e$ ($\bar{\nu}_\mu$). From the analysis of these events, one can determine the energy and direction of the incoming neutrinos.

The results can be summarized in the following way:

1) The ν_μ neutrino data present a deficit and an anomalous zenith angle distribution.
2) The ν_e neutrino data present no deficit and no anomalous behavior; they have a flat zenith angular distribution.

The solution of the problem is based on the hypothesis of *neutrinos oscillation*, which we discussed in the previous section. From a detailed analysis of the data, one can draw the following conclusions:

1) The ν_e neutrinos do not change flavor and they indicate no sign of oscillation.
2) The ν_μ neutrinos do not transform themselves into ν_e
3) The ν_μ neutrinos are assumed to oscillate transforming into ν_τ. The charged lepton τ cannot be detected, since its mass is very high, and it cannot be produced because the energy of the reaction is not high enough.

In analogy with Eq. (11), the $\nu_\mu \rightarrow \nu_\tau$ transition probability is

$$P(\nu_\mu \rightarrow \nu_\tau) = |< \nu_\tau \mid \nu_\mu (L) >|^2 \approx \sin^2 2\theta_{23} \sin^2 (\Delta m_{23}^2 L / 4E) , \qquad (16)$$

while the *survival* probability of ν_μ is given by

$$P(\nu_\mu \rightarrow \nu_\mu) = |< \nu_\mu \mid \nu_\mu (L) >|^2 = 1 - P(\nu_\mu \rightarrow \nu_\tau) . \qquad (17)$$

What can be observed is the ν_μ disappearance; the number of ν_μ events varies with the energy, but the crucial feature is given by the zenith angle distribution: the number is maximum for the *downward* ν_μ that enter the detector from above, and it decreases for the *upward* ν_μ coming from below. The interpretation is based on the following fact: the downward neutrinos have crossed the atmosphere from a height of about 1,520 km, while the upward neutrinos have crossed the Earth (twice the Earth radius $r_E \approx 6{,}400$ km). Intermediate situations occur for other directions, and consequently for values of L in the interval $h < L < 2\, r_E$. It happens that, while the disappearance probability is practically zero for $L \approx h$, it increases and then oscillates for $L \gg h$. The fit of the data gives the following values for the two parameters in Eq. (16):

$$\Delta m_{23}^2 \approx 2.4 \times 10^{-3}\ \text{eV}^2 \quad \text{and} \quad \theta \approx 42^0 . \qquad (18)$$

This interpretation has been confirmed by other experiments, in particular by K2K [11]. This experiment does not detect the atmospheric neutrinos, but the events produced by an artificial ν_μ beam, sent from the Japanese KEK laboratory to the SuperKamiocande detector (the average neutrino energy is $E \approx 1.3$ GeV and $L \approx 250$ km).

Other kinds of experiments on ν_μ oscillations are running (for a more complete lists see ref. [12]). In particular , MINOS (Main Injector Neutrino Oscillation Search) is a *long-baseline* neutrino experiment which makes use of two detectors: one at Fermilab at the source of the neutrinos and the another at 450 miles away, in the Soudan mine, in Minnesota. The aim is to obtain further information on $\nu_\mu \rightarrow \nu_\tau$. Another important experiment is OPERA: a ν_μ beam is produced at the SPS (Super Proton Synchrotron)

accelerator at CERN and a large detector is placed in the laboratory under the Gran Sasso mountain, in Italy, 730 km away (a distance very close to that of MINOS). The main aim is to produce and detect the τ-lepton:

$$\nu_\mu \rightarrow \nu_\tau \qquad \text{and} \qquad \nu_\tau + n \rightarrow \tau^- + p. \tag{19}$$

4. Solar Neutrinos

In the core of the Sun, the fusion of hydrogen into helium takes place through several intermediate nuclear reactions with production of neutrinos (their energies range from 0.3 to 20 MeV). The results can be summarized by

$$4\,p + 2\,e^- = {}^4He + 2\,\nu_e\ . \tag{20}$$

The total flux of electron–neutrinos from the Sun on the Earth can be estimated with accuracy from the Solar Standard Model, elaborated especially by John Bacall and collaborators at Princeton [13]: flux $\approx 6.5 \times 10^{10}$ neutrinos /cm^{2}s (compare with the photon flux: 3.8×10^{17}/cm^{2}s).

The first observation by Davies [6] was obtained making use of a radiochemical method: in a chlorine-based detector, solar neutrinos are captured by ^{37}Cl atoms and converted into argon ^{37}Ar; from the amount of argon he could deduce the flux of neutrinos. Many experiments where realized in USA, in Japan and in Europe with different methods [12]: they measured flux significantly smaller than what predicted, and this is the content of the so-called *solar neutrino deficit*.

As already said, the solution of the problem is the flavor neutrino oscillations, as it was clearly confirmed by the results obtained in the years 2001–2002 by SNO (Sudbury Neutrino Observatory, Canada) [14]. SNO is an underground laboratory (at the depth of 2 km) with a heavy water Cherenkov (1,000t) detector. They were able to observe three different kind of reactions (x = e, μ, τ):

$$\begin{aligned} &\nu_e + d \rightarrow p + p + e^- && \text{(CC)} \\ &\nu_x + d \rightarrow p + n + \nu_x && \text{(NC)} \\ &\nu_x + e^- \rightarrow \nu_x + e^- && \text{(ES)} \end{aligned} \tag{21}$$

The charged current reaction (CC) occurs only for ν_e , so that it measures the electron neutrino flux on the detector; the neutral current reaction (NC) is equally sensitive to all flavor neutrinos and this is the situation also for the elastic scattering (ES). The analysis of all the results provides not only the amount of the ν_e flux, but also of the flux of all kinds of neutrinos. On one hand, the ν_e flux is much lower than the total flux of neutrinos, which agrees with the neutrino flux predicted by the Standard Solar Model. On the other hand, the deficit of electron neutrino flux is consistent with the hypothesis of oscillations (mainly $\nu_e \rightarrow \nu_\mu$).

Also in the case of solar neutrinos, it is sufficient to consider two-flavor mixing ($\nu_e \rightarrow \nu_\mu$). The transition probability $P(\nu_e \rightarrow \nu_\mu)$ is given in Eq. (11), and the fit gives

$$\Delta m_{12}^2 \approx 7.7 \times 10^{-5}\ \text{eV}^2 \quad \text{and} \quad \theta_{12} \approx 35^0 . \tag{22}$$

The results from KamLAND (Kamioka Liquid Scintillator Anti-Neutrino Detector) confirmed SNO results and showed explicitly the electron antineutrino oscillations [15]. The detector (one Kton liquid scintillator) is placed in the Kamioka mine, surrounded by a few nuclear power plants (at distances around 170 km); the reactors provide $\overline{\nu}_e$ beams. A convenient choice was done for the energy E and the distance L, so that it was possible to detect the effect of oscillation and observe the first dip in the survival probability.

A global fit was performed of both atmospheric and solar neutrinos with the 3×3 mixing matrix given in Eq. (7); the following values have been obtained for the mixing angles and the squared mass differences:

$$\begin{aligned} \Delta m_{12}^2 &= (7.67 \pm 0.35) \times 10^{-5}\ \text{eV}^2 \quad ; \quad \sin^2\theta_{12} = 0.312 \pm 0.037 \\ \Delta m_{23}^2 &= (2.39 \pm 0.24) \times 10^{-3}\ \text{eV}^2 \quad ; \quad \sin^2\theta_{23} = 0.466 \pm 0.0118 \\ \sin^2\theta_{13} &= 0.012 \pm 0.013 \quad ; \quad \theta_{13} < 10.3^0\ (2\sigma). \end{aligned} \tag{23}$$

The small value of θ_{13} justifies the separate two-flavor analyses of the atmospheric and solar neutrinos.

5. The Problem of Neutrino Mass

From the expressions of the transition probabilities, Eqs. (11) and (16), one sees that the occurrence of oscillations implies that neutrinos (at least two of them) have non vanishing mass. However, as shown in the previous sections, the experiments on oscillations provide only the square mass difference; the values of the masses are not determined and not even the sign of Δm^2 is known (two neutrinos are almost degenerate in mass, but the mass *hierarchy*, i.e. whether the third neutrino is lighter or heavier than the two others is not yet known).

Several experiments, since a long time, have been looking for the determination of the mass of the electron neutrino ν_e. The method is based on the analysis of the β-decay of tritium [17]:

$$^3\text{H (nnp)} \rightarrow {}^3\text{He (npp)} + e^- + \nu_e . \tag{24}$$

The present upper bound (from the tail of the energy spectrum) is:

$$m(\nu_e) < 2.2\ \text{eV}/c^2 . \tag{25}$$

KATRIN (Karlsruhe Tritium Neutrino experiment) is designed to measure the electron neutrino mass with a sensitivity of 0.2 eV/c^2 [18].

From the theoretical point of view, it is important to understand why the neutrino mass is so small in comparison with the masses of the charged leptons:

$$m(\nu_e) / m(e) < 4 \times 10^{-6}. \tag{26}$$

First we make a technical remark. In the Standard Model (SM) of elementary particles (see e.g. ref. [19]), spin ½ fermions are described by *right-handed* and *left-handed* spinors, which correspond to positive and negative *helicities*. The neutrino helicity was determined in a famous experiment in 1958, based on the analysis of angular momentum conservation in the reactions [20]

$$e^- + {}^{152}Eu \rightarrow {}^{152}Sm^* + \nu_e \rightarrow {}^{152}Sm + \gamma\,, \tag{27}$$

and then we know that neutrino are only left-handed (ν_L) and anti-neutrinos right-handed (ν_R). With appropriate modifications, which go beyond the SM, one can have different models able to give non vanishing mass to the neutrinos.

In the Standard Model, the neutrino, which is strictly massless, has only one helicity (left-handed), while all the other particles have both helicities. A normal mass term appears as a scalar term L_D in Lagrangian; it is the so-called *Dirac mass* term and it requires the presence of both helicities (ψ is a spinor, solution of the Dirac equation):

$$L_D = m_D(\overline{\psi}_L\psi_R + \overline{\psi}_R\psi_L) \tag{28}$$

A Dirac mass term is not possible for neutrinos, since they have only left-handed helicity (unless very heavy, undetected, right-handed neutrinos are introduced), but oscillations indicate that $m_\nu \neq 0$. A possible solution is provided by the peculiar feature of the neutrino: it is *neutral* (no electric charge, no magnetic moment). According to the hypothesis formulated by Ettore Majorana, neutrino and antineutrino can be the *same particle* (which is not possible for any other fermion), and one can have a *Majorana mass* term in which ν_L is coupled to ν_R This hypothesis violates the so-called *lepton number* conservation, and this can happen going beyond the Standard Model. However, one faces also the problem of explaining why the neutrino masses are much smaller than the masses of all the other elementary particles. Theoretical models have been proposed and they provide possible explanations [21]. However, a discussion on this subject is outside the scope of the present paper.

6. Neutrinos from Supernovae and Relic Neutrinos

On February 24, 1987 a supernova (SN 1987A) appeared in the sky of Southern Hemisphere (in the Large Magellanic Cloud) and it was observed in Chile and New Zealand. Few hours before the first light signal, neutrino bursts were detected in several laboratories (Kamiokande in Japan, IMB in USA and Baksan in Russia) [22].

It was the first time in which neutrinos coming from outside the solar system were observed. Unfortunately only a few, rather small, detectors were available at that time, and a small number of neutrino events was observed. However, those events were important because the neutrino detection from supernovae gave rise to a new astronomy, with *neutrino telescopes*. Instead of using light, gamma-rays and cosmic rays, the new astronomy makes use of neutrinos, which can propagate without being absorbed by interstellar medium or deviated by magnetic fields. Neutrinos interact very weakly, but they can give information about remote sources: neutron stars, black holes and active galactic nuclei.

The mechanism of the explosion of a supernova is not very well understood. During the collapse, intense fluxes of neutrinos are emitted, produced by the processes

$$\begin{aligned} e^- + p &\rightarrow n + \nu_e \\ e^+ + n &\rightarrow p + \bar{\nu}_e \quad . \end{aligned} \tag{29}$$

In the *core* collapse, density (10^{17} kg/m^3) and temperature (10^{11}K) are extremely high; a neutron star (or a black hole) is formed and almost all the thermal energy is released in a few seconds in the form of neutrinos.

Neutrino detection requires apparatus of huge dimensions. In the future, on the occasion of the appearance of another supernova, they will be able to get enough data and to clarify all the steps of the mechanism of the explosion.

We quote here a few neutrino telescopes, taking data or in construction [23]. The AMANDA telescope, situated at the South Pole, measures very high energy neutrinos and is taking data on atmospheric neutrinos and cosmic ray particles. Neutrinos interact with atomic nuclei in ice and produce charged leptons of the same flavor, e.g. charged μ-leptons. The μ's emit light (Cherenkov radiation), which is detected by photomultipliers; direction and energy of neutrinos can be determined. IceCube is another neutrino telescope in construction at the South Pole; it has the dimensions of a cubic kilometer. It will be also a powerful tool for searching new particles, such as the constituents of dark matter. Underwater neutrino telescopes are planned in the Mediterranean sea: ANTARES, in construction at about 40km from the French coast, near Toulon; NEMO (Neutrino Mediterranean Observatory), planned at about 70km from Capo Passero, Sicily, at a depth of 3,350m.

Finally, we would like to mention the *relic neutrinos*. The interest in relic neutrinos is related to the fact that, through them, one could get some information on the history of the primordial Universe and its evolution according to Big Band Model.

In 1964 the two astronomers Arno Penzias and Robert Wilson discovered the cosmic microwave background radiation (CMB), signal of a remote epoch (about 380,000 years after Big Bang). Before the formation of stars and galaxies, the Universe was much smaller and hotter: filled with a uniform hot plasma (electrons, protons, photons, etc.). Photons could not propagate and the Universe was opaque. As the Universe expanded, temperature went down, electrons and protons combined to form hydrogen atoms ($T \approx$ 3,000K). The Universe became transparent and photons began to propagate freely; what is observed to-day is the remnant of this radiation: CMB at $T \approx 2.7$K. Precise measurements of the spectrum of CMB performed by COBE (Cosmic Background

Explorer, NASA satellite) [24], showed that CMB is isotropic and its spectrum is that of black body at 2.7K. In 2003 the results of a second NASA mission, WMAP (Wilkinson Microwave Anisotropy Probe) showed very small fluctuations and anisotropy [25] in the temperature distribution of CMB, which indicate density fluctuations in the primordial Universe giving rise to galaxy formation (due to gravitational attraction).

Neutrinos from Big Bang are expected as the most abundant particles, after the photons. Unlike the relic photons, *relic neutrinos* have not been observed so far. The Cosmic Neutrino Background (CνB) would be the oldest relic (within 10s after Big Bang) and should give important information about leptogenesis, baryogenesis and nucleosynthesis. The problem of relic neutrino search is open; the detection of relic neutrinos was proposed [26] through their interactions with ultra-high energy neutrinos produced by astrophysical sources.

7. Conclusions

The progress in neutrino physics has been very slow; the idea of this peculiar particle was formulated in 1930 and its existence was established in 1956. During many years there was no significant progress in the understanding of the neutrino properties; a few problems became evident (atmospheric neutrino anomaly, solar neutrino deficit), but it took several years to reach a satisfactory solution.

In the last 10 years important new experiments allowed to discover unknown properties: different kinds of neutrinos (three flavors), neutrino mixing, neutrino oscillations and the fact that neutrinos have non-vanishing mass.

In conclusion, notwithstanding the big experimental and theoretical progress, few important questions are still open.

We do not know the nature of the neutrino mass and the values of the three masses. There are theoretical models and experiments are going on.

The problem of CP violation in the neutrino sector has not been investigated from the experimental point of view. We note that, with three flavor neutrinos, the mixing matrix contains a phase which would be responsible for CP violation, and this feature could be essential for the baryogenesis, i.e. the process which, in the evolution of the Universe after the Big Bang, gave rise to matter overwhelming antimatter.

It would be important to detect the relic neutrinos, because they could give further information in cosmology.

New experiments and new searches will continue with bigger and bigger detectors; the use of neutrino telescopes will provide important results both in astrophysics and in cosmology. Also new physics from accelerators (from the Large Hadron Collider at CERN) will open hopefully new ways to further progress in neutrino physics and astrophysics.

References

1. Fermi, E. (1934) Tentativo di una teoria dei raggi β, *Nuovo Cim.* **XI**, 1–19.
2. Cowan,C., Reines, F., Harrison, F.B., Kruse, H.W. and McGuire, A.D. (1956) Detection of the free neutrino: a confirmation, *Science* **124**, 103–104.
3. Dunby, G. et al. (1962) Observation of high-energy neutrino reactions and the existence of two kinds of neutrinos, *Phys. Rev. Lett*. **9**, 36–44.
4. Pearl, M.L. *et al*. (1975) Evidence for anomalous lepton production in e^+ - e^- annihilation, *Phys. Rev. Lett.* **35**, 1489–1492.
5. Kodama, K. et al. (2008) Final tau-neutrino results from the DONuT experiment, *Phys.Rev.* **D78**, 052002 (1–37).
6. Davis, R. (1964) Solar neutrinos. II.Experimental, *Phys. Rev. Lett.* **12,** 303–305.
7. Hirata, K.S. *et al*. (1988) Experimental study of the atmospheric neutrino flux, *Phys*. *Lett.* **B205**, 416–420.
8. B.Pontecorvo (1957) Inverse beta processes and non conservation of lepton charge, *Zh. Eksp. Teor. Fiz*. **34**, 247, *Sov. Phys. JETP* **7**, 172–173.
9. Maki, Z., M.Nakagawa, M. and Sakata, S. (1962) Remarks on the unified model of elementary particles, *Prog. Theor. Phys.* **28**, 870–880.
10. Kajita, T. (1999) Atmospheric neutrino results from Super-Kamiokande and Kamiokande – Evidence for ν_μ oscillations, *Neutrino Physics and Astrophysics, Proceedings of the XVIII International Conference on Neutrino Physics and Astrophysics*, ed. By Y. Suzuki and Y. Totsuka, Elsevier, Amsterdam, 123–132.
11. Ann, M.H. (2006) Measurement of neutrino oscillations by the K2K experiment, *Phys.Rev*. **D74**, 072003 (1–39).
12. Strumia, A. and Vissani, F. (2008) Neutrino masses and mixing and…, *arXiv.org/abs/hep-ph/069* 6054 (1–219).
13. J.N. Bahcall, J.N, Basu,S and Pinsonneault, M.H.(2001) Solar models: Current epoch and time dependences, neutrinos, and helioseismological properties. *Astrophys. J.* **555**, 990–1012.
14. McDonald, A.B. (2000) First Neutrino Observations from the Sudbury Neutrino Observatory, *Neutrino 2000*, *Proceedings of the XIXth International Conference on Neutrino Physics and Astrophysics, Sudbury*, ed. by J. Law, R.W. Ollerhead and J.J. Simpson, North Holland, 21–28.
15. Eguchi, K. *et al*. (2003) First results from KamLAND: Evidence for reactor antineutrino disappearance, *Phys. Rev. Lett.* **90**, 021802 (1–6).
16. Fogli, G.L., Lisi, E., Marrone, A., Palazzo, A. and Rotunno, A.M. (2008) Neutrino masses and mixing, *Nucl. Phys. Proc. Suppl.* **188**, 27–30.
17. Otten, E.W. and Weinheimer, C. (2008) Neutrino mass from tritium beta decay, *Rept. Prog. Phys.* **71** 086201.
18. Bonn, J. (2008) The Karlsruhe tritium neutrino mass experiment KATRIN *AIP*, *Conf. Proc.* **972**, 404–411.
19. Costa, G. (1997) Unification of the fundamental interactions: problems and perspectives, *Spectroscopy and Dynamics of Collective Excitations in Solids*, ed. by B. Di Bartolo, Plenum Press, New York, 581–597.
20. Goldhaber, M., Grodzins, L. and Sunyar, A.W. (1958) Helicity of neutrinos, *Phys. Rev.* **109**, 1015–1017.
21. Feruglio, F., Hagedorn, C., Yin Lin and Merlo, L. (2008) Theory of the neutrino mass, *Fourth International Workshop on Neutrino Oscillations in Venice*, ed. by M.Baldo-Ceolin, Papergraf, Padova, 29–43.
22. Fogli, G.L., Lisi, E.,Mirizzi, A. and Montanino, D. (2007) Supernova neutrino observation twenty years after SN1987A: status and perspectives, *Nuovo Cim.* **122B**, 573–578.

23. DeYoung, T. (IceCube collaboration) (2009) Recent results from IceCube and AMANDA, *arXi/astro-phv*:0910.3644.
24. Wright, E.L. (2003) COBE observation of the cosmic infrared background, *New. Astron. Rev.* **48**, 465–468.
25. Smoot, G.F. (2007) Nobel Lecture: Cosmic microwave background radiation anisotropies: their discoveries and utilization, *Rev. Mod. Phys.***79**, 1349–1379.
26. Gelmini, G.B. (2005) Prospect for relic neutrino searches, Nobel Symposium 2004: Neutrino Physics, *Phys. Scripta* **T121**, 131–136.

SHORT SEMINARS

PERSISTENT HOLE BURNING INDUCED BY RESONANT ENERGY MIGRATION

MIA MILOS, ANDREAS HAUSER
Département de chimie physique, Université de Genève
30 quai Ernest-Ansermet, CH-1211 Genève 4, Switzerland

Abstract Excitation energy migration is an important phenomenon at high concentration of luminescent chromophores. In the three-dimensional network $[Ru(bpy)_3][NaCr(ox)_3]$ it is possible to unambiguously identify three different mechanisms for energy migration within the R_1 line of the $^4A_2 \rightarrow {}^2E$ transition of Cr^{3+} [1]. In addition to the common temperature dependant phonon-assisted process, a resonant process between the zero-field split components of the $^4A_2$ ground state leading to a multi-line pattern in a Fluorescence Line Narrowing spectrum and a quasi-resonant process within the same component leading to fast spectral diffusion can be identified at very low temperature. On the other hand, in $NaMgAl_{1-x}Cr_x(ox)_3{\cdot}9H_2O/D_2O$, x = 0.1% it is possible to efficiently

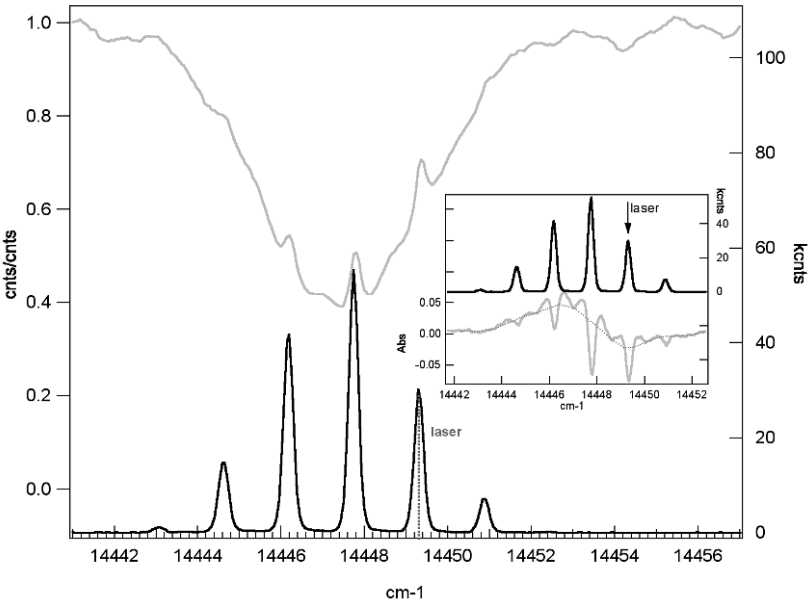

Figure 1. Fluorescence line narrowing spectrum (—) and transmission spectrum after prolonged laser irradiation (—) of the R_1 line in $NaMgAl_{1-x}Cr_x(ox)_3{\cdot}9H_2O/D_2O$, x = 30%, at 4.2 K. Inset: Fluorescence line narrowing spectrum (—) and difference in transmission spectrum before and after irradiation into the R_1 line at 4.2 K.

B. Di Bartolo and J. Collins (eds.), *Biophotonics: Spectroscopy, Imaging, Sensing, and Manipulation*, 359
DOI 10.1007/978-90-481-9977-8_17, © Springer Science+Business Media B.V. 2011

burn persistent spectral holes within the $^4A_2 \rightarrow {}^2E$ absorption bands of Cr^{3+} based on a novel hole burning mechanism involving flips of non-coordinated water molecules [2]. Here, we showed that in an optimized sample of the latter compound with x = 0.3, it is possible to observe both phenomena, that is, resonant excitation energy migration and persistent spectral hole burning (see Fig. 1). In addition to the usual resonant hole and side holes spaced by the ground-state zero-field splitting, persistent spectral holes are also burnt by resonant energy migration.

1. M. Milos, S. Kairouani, S. Rabaste, A. Hauser, *Coord. Chem. Rev*. 252 (2008) 254.
2. M.L. Lewis, H. Riesen, *J. Phys. Chem. A* 106 (2002) 8039.

THE BIOPHOTONICS GROUP @ "NAPLES-1" UNIVERSITY

CARLO ALTUCCI
Department of Physics, University of Naples "Federico II", Naples Italy
CNISM – Consorzio Nazionale Interuniversitario per le Scienze Fisiche della Materia, Unità di Napoli

Abstract Recent advances in Biophotonics at the University of Naples "Federico II" were presented. In particular, the project "Development of Laser-Based Technologies and Prototype Instruments for Genome-Wide Chromatin ImmunoPrecipitation Analyses" (ATLAS), fully funded by the EU within the seventh FP, was briefly illustrated. Further applications of ultrashort UV laser pulses to induce interactions between proteins we also reported.

B. Di Bartolo and J. Collins (eds.), *Biophotonics: Spectroscopy, Imaging, Sensing, and Manipulation*,
DOI 10.1007/978-90-481-9977-8_18,

SPECTROSCOPY OF INDIVIDUAL "ARTIFICIAL ATOMS"

MARTIN HUSNIK[1], NILS FETH[1,2], MICHAEL KÖNIG[3], JENS NIEGEMANN[3], KURT BUSCH[2,3], STEFAN LINDEN[1,2], MARTIN WEGENER[1,2]

[1]*Institut für Angewandte Physik, Universität Karlsruhe (TH), 76131 Karlsruhe, Germany*

[2]*Institut für Nanotechnologie, Forschungszentrum Karlsruhe in der Helmholtz-Gemeinschaft, 76021 Karlsruhe, Germany*

[3]*Institut für Theoretische Festkörperphysik, Universität Karlsruhe (TH), 76131 Karlsruhe, Germany*

Abstract Metamaterials exhibiting a magnetic response at optical wavelengths have recently attracted much attention [1]. The magnetic response depends on both the design of the individual building blocks ("artificial atoms") and on electromagnetic coupling effects between them. Thus for future developments, investigation of the individual "artificial atoms" is crucial.

Here, we presented absolute extinction cross-section spectra of individual split-ring resonators (SRR) measured by means of a spatial modulation technique [2, 3]. The extinction cross-section at the fundamental magnetic resonance is found to be eight times the geometrical area covered by the SRR. The experimental results are in excellent agreement with microscopic calculations and can be understood by a simple electric circuit model.

1. V. M. Shalaev et al., Nat. Photon. 1, 41 (2007).
2. A. Arbouet et al., Phys. Rev. Lett. 93, 127401 (2004).
3. M. Husnik et al., Nat. Photon. 2, 614 (2008).

B. Di Bartolo and J. Collins (eds.), *Biophotonics: Spectroscopy, Imaging, Sensing, and Manipulation*,
DOI 10.1007/978-90-481-9977-8_19,

SPONTANEOUS LIGHT EMISSION FROM ALIVE COTTON CELL-HAIR

A.A. PAIZIEV*, V.A. KRAKHMLEV
Institute of Electronics Uzbek Academy of Science
Tashkent, Uzbekistan

Abstract At present work light emission was observed from apex of alive cotton cell-hair (*Tashkent-1, 108-F G. hirsutum L., C-6030, C-6524 G. barbadense L. and Turfan gusa G. herbaccum)* at difference developmental stages. To visualize light emission a replica-print method has been used to see not visible UV light. The alive cotton cell-fibers from fresh cotton boll has been detached and emerged into polymer emulsion (polymethylmethacrylate, gelatin, polyvinylpyrrolidone). After long time exposition (12h) cotton cell-fibers has been detached and produced replica on polymer substrate has been investigated under convenient optical microscope. In result we observed directed spur near apex of cell. We suppose that this spur is result polymer molecules destruction in area of light emission from end point of cotton cell.

It was shown that at early developmental stage cotton initiation and elongation there is no luminescence from cell. But at the next elongation period (10 day post anthesis DPA) we observed luminescence from many of the cells under microscope. Comparison with cellulose deposition and fiber elongation dynamic shows that maximal luminescence intensity corresponds to maximal rate of cell elongation and cellulose deposition (20–30 DPA). It means that cotton fiber luminescence is connected with physiological processes cotton fiber growth and development.

* A.A. Paiziev, Institute of Electronics Uzbek Academy of Science, Tashkent, Uzbekistan, e-mail: adxam_payziev@rambler.ru

B. Di Bartolo and J. Collins (eds.), *Biophotonics: Spectroscopy, Imaging, Sensing, and Manipulation*, 365
DOI 10.1007/978-90-481-9977-8_20, © Springer Science+Business Media B.V. 2011

MESOSCOPIC SPECTRAL MODULATION OF LIGHT TRANSMITTED BY A SUBWAVELENGTH APERTURE

M. RÄHN, M. PÄRS, V. PALM, V. HIZHNYAKOV, L. DOLGOV
Institute of Physics, University of Tartu
Riia 142, 51014 Tartu, Estonia

Abstract We are currently studying the transmission of light through a tapered metal-coated optical fiber with a subwavelength aperture (SWA). The problem under investigation is the effect of SWA on the spectrum of the transmitted light. According to our experimental findings, one can observe, under certain conditions, a remarkable modulation of the spectrum of the transmitted light. The effect has a mesoscopic origin: the modulation takes place if the number of transmitted light modes is small but exceeds unity, which indicates the phase shifts between different modes. One possible source of such phase shift could be the different propagation speed for different modes in the fiber, but this effect should be small. In our opinion, the origin of the phase shifts is in the (different for different modes) slowdown of the light near the tip with SWA due to the interaction of propagating modes with surface plasmons of the metal coating of the fiber. One can expect that the interaction strength depend on the actual shape of the light field in the mode, which results in different modes getting different delays before passing through the tip. In case of sufficiently small SWA diameter only few modes can pass through the tapered fiber region [1], and their delay differences can cause an observable modulation of the transmitted light spectrum. In case of larger diameters many light modes can pass out, and no significant spectral modulation can be observed due to the effect of averaging. An observable modulation also disappears for SWA diameters as small as 100 nm, because in this case only one (the fundamental) light mode passes out [1].

1. L. Novotny and C. Hafner, Phys. Rev. E., **50** (1994) 4094.

B. Di Bartolo and J. Collins (eds.), *Biophotonics: Spectroscopy, Imaging, Sensing, and Manipulation*,
DOI 10.1007/978-90-481-9977-8_21,

OPTICAL AND VIBRATIONAL CHARACTERIZATION OF NANOSTRUCTURED SEMICONDUCTOR MATERIALS

IVAN KARBOVNYK*
Department of Electronics, Ivan Franko National University of Lviv, Lviv, Ukraine

Abstract There are several technologically relevant semiconductors that through the years were in the focus of an extensive research. Among these one can outline aluminum nitride (AlN) – chemically inert, thermally stable and having excellent mechanical properties wide band gap III–V semiconductor and silicon carbide (SiC) – a promising semiconductor for high-temperature applications, able to withstand high radiation loads and existing in several polytypes which, in turn, have own specific unique properties. A leap in the nanotechnology opened the way towards creating various semiconductor nanostructures like nanorods, nanobelts, nanowires etc. with even more fascinating features than the bulk materials. For example, a particularly interesting possibility is the obtaining of an adjustable emission from a nanostructured semiconductor by changing the size/diameter of nanowires. In this manner LEDs covering the entire visible range can be created.

This report dealt with some recent results obtained in the study of aluminum nitride and silicon carbide 1D nanostructures – nanotubes and nanowires. Details of the experimental techniques were discussed. The luminescence properties of the investigated nanomaterials were compared to those of commercially available reference samples.

* Ivan Karbovnyk, Department of Electronics, Ivan Franko National University of Lviv, Lviv, Ukraine, e-mail: ivan_karbovnyck@yahoo.com

B. Di Bartolo and J. Collins (eds.), *Biophotonics: Spectroscopy, Imaging, Sensing, and Manipulation*, 369
DOI 10.1007/978-90-481-9977-8_22, © Springer Science+Business Media B.V. 2011

DEFECTS IN THE ATP2B2 GENE CAUSING HEREDITARY HEARING AND BALANCE LOSS IN MICE AND HUMANS: A BIOPHYSICAL STUDY OF NORMAL AND MUTATED PMCA2 PUMP FUNCTION

MARIO BORTOLOZZI*, Ph.D.
Venetian Institute of Molecular Medicine (VIMM), Padua, Italy; Department of Physics "Galileo Galilei", University of Padua, Padua, Italy

Abstract Ca^{2+} acts as a fundamental signal transduction element in the inner ear, delivering information about sound acceleration and gravity through a small number of mechano-transduction channels in the hair cell stereocilia as far as to the ribbon synapse, where it drives neurotransmission. The genetic approach is proving fundamental in unravelling the molecular basis of these important biological functions. In particular, ablation or missense mutations of the PMCA2 Ca^{2+}-pump of stereocilia cause deafness and loss of balance. To investigate the physiological significance of these genetic defects, we used a combination of confocal fluorescence microscopy and cytosolic Ca^{2+} photo-liberation. The study of Ca^{2+}-extrusion in hair cells from neonatal mice inner ear permitted us to show that Ca^{2+} extrusion was compromised by various degrees in PMCA2 knockout mice as well as in the mutant *deafwaddler* and *Oblivion* mice. We suggest that the consequent reduced endolymphatic Ca^{2+} concentration can trouble the finely tuned control mechanisms of signal transduction, eventually resulting in hair cell death.

* Mario Bortolozzi, Venetian Institute of Molecular Medicine (VIMM), Padua, Italy; Department of Physics "Galileo Galiler", University of Padua, Padua, Italy, e-mail: mario.bortolozzi@gmail.com

B. Di Bartolo and J. Collins (eds.), *Biophotonics: Spectroscopy, Imaging, Sensing, and Manipulation*, 371
DOI 10.1007/978-90-481-9977-8_23, © Springer Science+Business Media B.V. 2011

ON THE WAY TO STUDY THE UPTAKE MECHANISMS OF CELL PENETRATING PEPTOIDS BY SINGLE-MOLECULE METHODS

BIRGIT RUDAT*[1,2,3], SIDONIE VOLLRATH[1,3], ESTHER BIRTALAN[1,3], HANS-JÜRGEN EISLER[2,3], ULI LEMMER[2,3], STEFAN BRÄSE[1,3]

[1] *Institute of Organic Chemistry, University of Karlsruhe (TH), 76131 Karlsruhe*

[2] *Light Technology Institute, University of Karlsruhe (TH), 76131 Karlsruhe*

[3] *Karlsruhe Institute of Technology, 76131 Karlsruhe, Germany*

Abstract It is well known that peptoids with cationic side chains have the ability to enhance the bioavailability and the cellular uptake of targets, such as fluorescent dyes [1, 2]. Because of this and their stability against protease degradation they are interesting molecules for drug delivery systems.

However, the internalization mechanisms of such transporters are still unresolved. Thus we plan to use single-molecule fluorescence microscopy to get a better understanding for those mechanisms. As we label our peptoids on solid phase it is necessary to find fluorophores which are suitable for single-molecule studies and are additionally not influenced by the synthetic steps. Here we presented our studies on an Atto532 labeled polyamine peptoid. We immobilized the Atto dye itself as well as the transporter molecules in nanomolar concentrations in Poly(methyl methacrylate) (PMMA) matrices. By scanning the samples and detecting the fluorescence signal with avalanche photodiodes we were able to image single dye and peptoid molecules. We also recorded the fluorescence intensity time traces for several molecules. The mean survival times are 2.0 s for the dye and 1.8 s for the peptoid respectively. These experiments show that the properties of the dye don't seem to be influenced either by the synthetic steps or by the peptoid itself.

1. P. A. Wender, D. J. Mitchell, K. Pattabiraman, E. T. Pelkey, L. Steinman, J. B. Rothbard, *PNAS* **2000**, *79*, 13003–13008.
2. T. Schröder, K. Schmitz, N. Niemeier, T. S. Balaban, H. F. Krug, U. Schepers, S. Bräse, *Bioconj. Chem.* **2007**, *18*, 342–354.

* Birgit Rudat, Institute of Organic Chemistry, University of Karlsruhe (TH), 76131 Karlsruhe, e-mail: birgit.rudat@kit.edu

B. Di Bartolo and J. Collins (eds.), *Biophotonics: Spectroscopy, Imaging, Sensing, and Manipulation*, DOI 10.1007/978-90-481-9977-8_24, © Springer Science+Business Media B.V. 2011

HYBRID SOLAR CELLS

JONAS CONRADT
Universitaet Karlsrhue, Institut fuer Angewandte Physik
Wolfgang-Gaede-Strasse 1
76131 Karlsruhe, Germany

Abstract Hybrid solar cells represent a promising (cost-efficient) alternative to pure Hybrid inorganic solar cells. We presented dye-sensitized solar cells (DSSC) and polymer solar cells, which are based on a zinc oxide (ZnO) electrode. Our work focuses on the morphology of the ZnO electrode and its impact on the photovoltaic performance of the solar cell. In addition, novel self-assembling (porphyrin) dyes are tested as sensitizer within DSSCs.

B. Di Bartolo and J. Collins (eds.), *Biophotonics: Spectroscopy, Imaging, Sensing, and Manipulation*,
DOI 10.1007/978-90-481-9977-8_25,

BIO-ELECTROMAGNETICS: MICROWAVE RADAR SYSTEM FOR BREAST CANCER DETECTION

MACIEJ KLEMM
Electromagnetics Group
Centre for Communications Research
University of Bristol
Bristol, BS8 1UB, UK

Abstract In this talk we presented the microwave radar system developed for breast cancer imaging. During the past decade there has been a growing interest in application of microwave frequencies, between 3 and 10 GHz, to the medical imaging. Breast cancer imaging has been of the particular interest. Currently there are two main streams in microwave breast imaging: (a) microwave tomography, (b) radar-based imaging. Both approaches rely on a difference in the electrical properties of normal and malignant breast tissues.

At the University of Bristol, we have focused our research efforts on the design of the ultra-wideband (UWB) radar-based imaging system for breast cancer detection. Our UWB radar system uses a hemi-spherical real aperture antenna array and a realistic 3D spherical breast phantom model, with electrical properties similar to real breast tissues. Our experimental system was built in such way that it can be used directly with real breast cancer patients.

In this talk the development of this world's first operational breast imaging radar was presented. Design details shown in the presentation covered: UWB antenna design, full-wave electromagnetic modelling and signal processing. We showed some first prototypes, as well as the latest, fully operational system which has recently been used in the clinical trial in Frenchay Hospital in Bristol.

B. Di Bartolo and J. Collins (eds.), *Biophotonics: Spectroscopy, Imaging, Sensing, and Manipulation*,
DOI 10.1007/978-90-481-9977-8_26,

NANOCRYSTAL QUANTUM DOTS FOR QUANTUM INFORMATION PROCESSING

BRAD LITTLETON
Department of Physics
King's College London
Strand WC2R 2L, UK

Abstract Nanocrystal quantum dots (NC's) are routinely used in biophotonics as chromophores to bind to specific proteins and structures. Emission from NC's is due to a quantum confined exciton, and so is strongly dependent on the size of the crystal and local electric fields. In the absence of thermal phonons, the exciton is a decent approximation to an atomic-like transition with a large oscillator strength, and the NC's themselves are relatively robust and easy to manipulate. These properties make them attractive in fields outside of biophotonics, for example, as an "artificial atom" system for quantum information processing and cavity-QED experiments. Of course, there are also drawbacks, and colloidal NC's are subject to undesirable dissipative processes, as well as blinking, bleaching, and spectral diffusion. In this talk I went through some experimental studies of CdSe NC's, which indicate that later generations of these materials show less coupling to dissipative processes, and appear to be at the point where they will be useful for simple QIP devices.

B. Di Bartolo and J. Collins (eds.), *Biophotonics: Spectroscopy, Imaging, Sensing, and Manipulation*,
DOI 10.1007/978-90-481-9977-8_27, © Springer Science+Business Media B.V. 2011

SOLVATION DYNAMICS USING ULTRAFAST X-RAY ABSORPTION SPECTROSCOPY

M. REINHARD[1], F.A. LIMA[1,2], A. EL NAHHAS[1], C. MILNE[1,2], V.T. PHAM[1], R. VAN DER VEEN[1,2] , D.C.V. AMARASINGHE[1,2], S.L. JOHNSON[2], P. BEAUD[2], D. GROLIMUND[2], C.N. BORCA[2], R. ABELA[2], G. INGOLD[2], C. BRESSLER[1], M. CHERGUI[1]

[1]*Laboratory of Ultrafast Spectroscopy*
Institute of Chemical Sciences and Engineering
Swiss Federal Institute of Technology - EPFL, 1015 Lausanne, Switzerland

[2]*Swiss Light Source, Paul-Scherrer Institute, 5232 Villigen, Switzerland*

Abstract Solvation dynamics aims to incorporate the active role of the solvent in chemical and biochemical reactions and its relevance stems from the fact that most of chemistry and biology takes place in liquids. A full description of the electronic and molecular changes associated with these reactions includes time-resolved structural information, which can be obtained using transient X-ray absorption spectroscopy.

Carrying out optical pump and X-ray probe experiments using a synchrotron X-ray source involves the drawback that time resolution is limited by the shortest achievable particle bunch length and therefore lies in the picosecond time domain. However, it can be considerably improved applying the slicing scheme where a femtosecond laser pulse is co-propagated with an electron bunch such that the energy of the electrons within the spatially overlapping region will be modulated due to their interaction with the laser field. Suitable X-ray optics subsequently allows for the extraction of femtosecond X-ray pulses but on the other hand roughly the same factor gained in X-ray pulse duration is lost in flux, which increases the integration time significantly.

A feasibility study for a particular system should include a realistic estimation of the expected integration time. This can be done by calculating the signal to noise ratio $S/\Delta S$ in dependence of the total number of necessary X-ray photons which in turn can be related to the integration time. Neglecting any pump-pulse-induced solvent or counter-ion excitation the transient signal can be written in a simple form and its noise can be estimated applying error propagation on $S(I^{p}; I^{unp})$ where the errors on the pumped and unpumped intensity values can be determined in the shot-noise limit. The sample specific influence on the integration time shows up in the fraction of molecules that can be excited during the pump process.

B. Di Bartolo and J. Collins (eds.), *Biophotonics: Spectroscopy, Imaging, Sensing, and Manipulation*, 381
DOI 10.1007/978-90-481-9977-8_28, © Springer Science+Business Media B.V. 2011

DEVELOPMENT OF OPTICAL BIOSENSORS ON BASIS OF MICRO-DISK RESONATORS

TORSTEN BECK
Institut fur Angewandte Physik, Universität Karlsruhe
Wolfgang-Gaede-Strasse 1
76131 Karlsrhue, Germany

Abstract Optical Wispering Gallery Modes in micro-cavities with toroidal shape offer small mode volumes and high Quality-Factors. The shift of the mode frequencies when biological substances are attached to the resonators surface allows detection down to singles molecules. For the parallel detection of different types of bio-molecules, each resonator has to be functionalized for specific molecules. The goal of our project is the development of a device for label-free, parallel detection of biomolecules.

B. Di Bartolo and J. Collins (eds.), *Biophotonics: Spectroscopy, Imaging, Sensing, and Manipulation*,
DOI 10.1007/978-90-481-9977-8_29,

MULTIPLE TRAP OPTICAL TWEEZERS FOR LIVE CELL FORCE MEASUREMENTS

MELANIE SCHWINGE, MARTIN BASTMEYER
Zoologisches Institut I, Cell and Neurobiology,
Universität Karlsruhe (TH), 76131
Karlsruhe, Germany

Abstract Since their invention in 1986 by A. Ashkin, optical tweezers have become increasingly valuable tools for research in the biological and physical sciences. Using a focused beam of light to trap and move matter, optical tweezers offer convenient access to processes at the mesoscopic scale. Due to the non-invasiveness of this technique, optical tweezers have found a broad range of applications not only in physics and chemistry but also in cell biology.

Large arrays of optical tweezers can be used to organize microscopic particles into complex structures, to sort them intelligently, and to manipulate delicate materials like living cells or enzyme complexes. We use an experimental design which is based on an acousto-optical deflection system (AOD) which allows the independent steering and intensity modulation of an incoming laser beam. A large number of spatiotemporally modulated optical traps is created by beam time sharing with a high switching rate induced by the AOD. To adopt the laser tweezers system to conditions necessary for force measurements in biological samples the setup is equipped with epifluorescence optics and a live cell imaging chamber.

Cells exert forces onto their growth substrate during spreading and migration. In addition, they can measure the rigidity of their growth substrate and consequently the elastic properties of the substrate influence cell behavior. Cells apply intracellular forces to newly formed contact sites. These forces range between 2 pN for initial receptor–ligand interactions to 5 nN for fully developed focal contacts, whereas an optical tweezers can exert forces exceeding 100 pN.

To understand how cell behavior is dictated by the architecture of their environment, we expose cells to flexible patterned substrates, obtained with the laser tweezers. The patterning is realized with protein coated beads in the (sub-) micrometer range that are held in position by sets of time shared optical traps generated by the laser tweezers. The concentration of proteins in the cell's environment is mimicked by the spacing between the functionalized beads and the substrate rigidity is varied by applying different trap stiffness to the beads.

To manipulate cell adhesion with laser tweezers we covalently couple polystyrol beads with proteins, functional protein domains, or bioactive peptides. The beads are then placed on the apical surface of adherent cells to mimic new contact sites and the cell response is recorded. Additionally, functionalized beads are placed at the tips of

B. Di Bartolo and J. Collins (eds.), *Biophotonics: Spectroscopy, Imaging, Sensing, and Manipulation*, 385
DOI 10.1007/978-90-481-9977-8_30,

filopodia, which are spike-like extensions from the cell body, to measure the traction forces a cell can generate.

The cell adhesion forces can be measured in relation to the geometry of contact sites by monitoring small lateral displacements of the functionalized beads out of the laser focus. For small displacements, the distance between the equilibrium bead position and the actual bead position is linearly related to the force applied by the cell.

HETERODYNE INTERFEROMETRIC POLARIZATION-SENSITIVE COHERENT ANTI-STOKES RAMAN SCATTERING (HIP-CARS) SPECTROSCOPY

E.T. GARBACIK*, M. JURNA, C. OTTO, J.L. HEREK, H.L. OFFERHAUS
OPTICAL Sciences group, Biophysical Engineering, University of Twente, Enschede, The Netherlands

Abstract Coherent anti-Stokes Raman scattering, better known as CARS, is a powerful and versatile spectroscopic and microscopic technique, with many advantages over traditional Raman and fluorescence methods. It is immune to autofluorescence, does not require labeling, and returns molecules to their ground states, which reduces sample heating. However, CARS suffers from two negative traits compared to Raman and fluorescence measurements. First, a non-resonant background is frequently more intense than the resonant contributions in a sample. Second, CARS signals are orders of magnitude weaker than Stokes Raman lines, rendering the detection of small concentrations of weakly-resonant molecules difficult. Our current research focuses on these two problems in particular: inherent polarization-sensitivity of CARS allows isolation and rejection of the non-resonant component of CARS, though at the cost of a significant reduction in resonant signal1; heterodyning techniques provide simultaneous enhancement of CARS signals and rejection of the non-resonant background, but require explicit knowledge of the phase relations in the CARS process2. Using a home-built optical parametric oscillator3 we have developed a method that exploits both heterodyning and polarization sensitivity that offers resonant-only enhancement of CARS signals without and specific knowledge of the phases. This "HIP-CARS" procedure significantly simplifies the detection elements of the system and provides for future development of fast, resonant-only CARS imaging.

1. J-X. Cheng, L.D. Book, X. S. Xie. Polarization coherent anti-Stokes Raman scattering microscopy. Optics Letters, **26** (2001), 1341–1343.
2. M. Jurna, J.P. Korterik, C. Otto, and H.L. Offerhaus. Shot noise limited heterodyne detection of CARS signals. Optics Express, **15** (2007), 15207–15213.
3. P.F. Chimento, M. Jurna, H.S.P. Bouwmans, E.T. Garbacik, L. Hartsuiker, C. Otto, J.L. Herek, and H.L. Offerhaus. High-resolution narrowband CARS spectroscopy in the spectral fingerprint region. Journal of Raman Spectroscopy, **40** (2009), 1229–1233.

* E.T. Garbacik, OPTICAL Sciences group, Biophysical Engineering, University of Twente, Enschede, The Netherlands, e.t.garbacik@student.utwente.nl — http://www.opticalsciences.nl

B. Di Bartolo and J. Collins (eds.), *Biophotonics: Spectroscopy, Imaging, Sensing, and Manipulation*,
DOI 10.1007/978-90-481-9977-8_31, © Springer Science+Business Media B.V. 2011

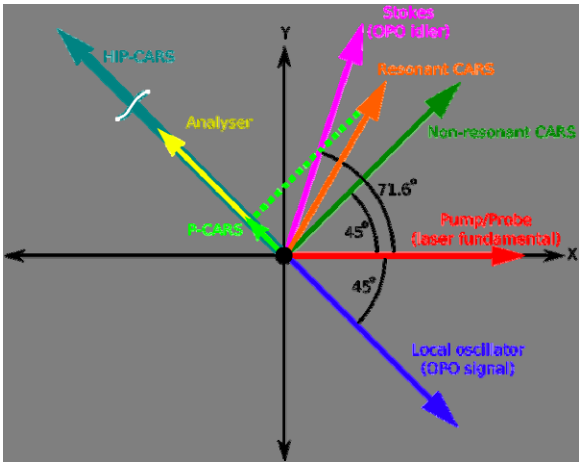

Figure 1. Diagram showing the polarizations of the various beam components used and generated in HIP-CARS. Note that a HIP-CARS "beam" is not actually created; the vector above simply indicates that it is an enhancement of the P-CARS signal.

FROM CURVED SPACE TO OPTICAL CLOAKING

TOLGA ERGIN[1], NICOLAS STENGER[1], JONATHAN MUELLER[1], JAD HALIMEH[1], MARTIN WEGENER[1,2]
[1]*Institut für Angewandte Physik, Universität Karlsruhe, 76131 Karlsruhe, Germany*
[2]*Institut für Nanotechnologie, Forschungszentrum Karlsruhe in der Helmholtz-Gemeinschaft, 76021, Karlsruhe, Germany*

Abstract Transformation optics is a powerful approach to manipulate the propagation of electromagnetic waves [1]. Here, the curvature of space is mimicked by an anisotropic metamaterial, which is described by effective medium theory [2, 3]. An interesting application of such metamaterials is optical cloaking. The metamaterial will prevent that light interact with the cloacked object and in the same time will leave the electromagnetic wave unperturbed. We present the basics of transformation optics and two examples of cloaking devices. This talk will be illustrated with full-wave finite element simulations of feasible cloak designs in homogeneous medium approximation as well as in full geometry.

1. U. Leonhardt, Science 312, 1777 (2006).
2. J.B. Pendry, *et al.,* Science 312, 1780 (2006).
3. W. Cai, *et al.,* Nature Photonics 1, 224 (2007).

B. Di Bartolo and J. Collins (eds.), *Biophotonics: Spectroscopy, Imaging, Sensing, and Manipulation*,
DOI 10.1007/978-90-481-9977-8_32,

POSTER PRESENTATIONS

(ZN,CU)O PHOTOCATALYTIC MATERIAL AND $ZNGA_2O_4$: EU^{3+} PHOSPHORS:

Tailoring Structure–Property Relationships

LAURA BOVO[1]*, LIDIA ARMELAO[2], MARCO BETTINELLI[3], EUGENIO TONDELLO[1]

[1]*Dipartimento Scienze Chimiche, Università di Padova, via Marzolo 1 35131 Padova, INSTM,*

[2]*CNR, ISTM, INSTM, Dipartimento di Scienze Chimiche, Università di Padova, via Marzolo 1 35131 Padova*

[3]*Lab. Chimica dello Stato Solido, DB, Università di Verona, INSTM, Strada Le Grazie 15 37134 Verona*

Abstract Zinc oxide, an important II–IV semiconductor with direct band gap (3.2 eV [1]) and large exciton binding energy (60 meV [1]), has become one of the most attractive materials in research due to its wide application ranging from optoelectronic [2], (photo)catalysis [3] and devices for optic [4] or biology [5] together with its peculiar properties of good stability, bio-compatibility and non-toxicity. The control over the size and morphology of nanometer micrometer-sized ZnO crystals represents a great challenge for the design of novel functional devices. Doping with selective elements (generally transition metal ions), also offers an effective method to adjust the electrical, magnetic and optical properties of zinc oxide.

In terms of practical photocatalytic applications the ability to fabricate ZnO nanosystems with defined morphology and high surface-to-volume ratio under soft processing conditions is highly desirable. Our project is concerned with sol-gel and hydrothermal synthesis of undoped and Cu-doped zinc oxide nanosystems (powders or layers) to prepare novel photocatalytic materials. The systems have been characterized by complementary techniques, providing important information on their composition, structure, morphology and optical properties.

Moreover, ZnO is a suitable host material for doping with luminescence centers: in this sense, lanthanide-doped ZnO nanocrystals may represent a novel class of light-emitting materials in which the optical properties of the single units are combined to enhance the performance of the resulting materials. It is also possible to tailor the doping of host ZnO with III group metals (Ga, Al or In) to improve the properties of the final materials. In this, the oxide structure is modified thus allowing a higher lanthanide doping level and, at the same time, to have an efficient energy-transfer from the matrix to the emitting centers. $ZnGa_2O_4$ is a binary compound oxide material which crystallizes in the spinel structure. It has an energy gap of about 5.0 eV, and under excitation with

* Laura Bovo, Dipartimento Scienze Chimiche, Università di Padova, via Marzolo 1 35131 Padova, INSTM, e-mail: laura.bovo@unipd.it

B. Di Bartolo and J. Collins (eds.), *Biophotonics: Spectroscopy, Imaging, Sensing, and Manipulation*, DOI 10.1007/978-90-481-9977-8_33, © Springer Science+Business Media B.V. 2011

ultraviolet light emits blue light due to transitions via a self-activation center. In addition, $ZnGa_2O_4$ is a promising transparent conducting oxide material, particularly when transparency through violet to near UV region is desired [6, 7]. In this work we reported the sol-gel and hydrothermal synthesis of undoped and Eu-doped $ZnGa_2O_4$ nanopowder to study the effect on emission properties as a function of different synthetic strategies.

References

1. S. Sakthivel et al. *Sol. Energy Mater.Sol. Cell* **77** (2003) 65.
2. J.C. Johnson et al. *Phys. Chem. B* **105** (2001) 11387.
3. (**a**) M.R. Hoffman et al. *Chem. Rev.* **95** (1995) 69 **(b)** O. Legrini et al. *Chem Rev.* 93 (1993) 671.
4. (**a**) N. Saito et al. *Adv. Mater.* **14** (2002) 418 **(b)** J. Liquianga et al. *Solar Energy Mater. Solar Cells* **90** (2006) 1773.
5. A. Dorfan et al. *Langmuir* **22** (2006) 4890.
6. Liang Xu et al. *Crystal Growth Des.* **7** (4) (2007) 810.
7. Masanori Hirano *J. Mater. Chem.* **10** (2000) 469.

INTEGRATED WAVEGUIDE PROBES AS ALTERNATIVES TO FIBER-OPTIC PROBES FOR BACKSCATTERING AND FLUORESCENCE MEASUREMENTS

NUR ISMAIL, FEI SUN, FEHMI CIVITCI, KERSTIN WÖRHOFF, RENÉ M. DE RIDDER, MARKUS POLLNAU, ALFRED DRIESSEN
Integrated Optical MicroSystems group (IOMS), University of Twente 7500 AE Enschede, The Netherlands

Abstract Integrated optical probes for detecting backscattered light (i.e. in Raman spectroscopy) show desirable characteristics when compared to conventional fiber probes despite the fact that the latter generally present better collection efficiencies. The major advantages of integrated probes are the reduced size; reduced background noise due to scattering in the probe because of reduced propagation length; potential for monolithic integration with filters, spectrometers and detectors; very small collection volumes, providing high spatial resolution; and polarization maintenance. In our work we demonstrated that in a practically relevant case where scattered light needs to be collected from a thin layer at the samples surface, integrated probes have better collection efficiency than fiber probes do.

We modeled a multimode integrated waveguide probe by adapting an analytical model that had been developed by Schwab et al. (1984) for fiber probes. The improvements that we introduced in the model account for arbitrary waveguide geometries and the low number of discrete modes present in an integrated waveguide compared to the quasi-continuum of modes in a typical multimode fiber. Using this model we compared the collection efficiencies of both integrated and fiber probes in case of the probes being placed in contact with the sample and for different distances between the excitation and collection waveguides. We found that the efficiency of the integrated probe is higher for scattering layer thicknesses smaller than ~100 mm.

In order to validate our model we fabricated multi-waveguide integrated probes having rectangular cross-sections in silicon oxynitride. The probes were used to measure fluorescence from a ruby rod that was excited through one probe channel, while fluorescent light was collected by the other probe channels. The measurements confirmed the validity of our probe model.

B. Di Bartolo and J. Collins (eds.), *Biophotonics: Spectroscopy, Imaging, Sensing, and Manipulation*, 395
DOI 10.1007/978-90-481-9977-8_34,

Our model, only applies to the case in which the single scattering approximation holds. In the more general case of multiple scattering it is convenient to use a Monte Carlo based approach to model light propagation in the sample. To investigate the collection of backscattered light from highly scattering media we developed a Monte Carlo code following the implementation steps described in the work of Wang et al. (1995). We also presented our experimental results on the measurement of backscattered light from a water suspension of latex spheres which we used for the validation of the Monte Carlo model.

CHARACTERIZATION OF NANOPOROUS CERAMIC MATERIALS USING COMBINED XRD, XPS AND PAL SPECTROSCOPY

HALYNA KLYM*
Institute of Materials of SRC "Carat"
202, Stryjska str., 79031, Lviv, Ukraine

Abstract Some functional nanoporous materials such as dielectric magnesium aluminate $MgAl_2O_4$ ceramics with spinel structure are widely used for environment humidity sensors. It is established that functionality of these humidity-sensitive ceramics depends on their microstructural peculiarities concerning mainly of phase composition. This work is aimed to investigate a microstructure of sintered nanoporous magnesium aluminate materials using combined X-ray diffractometry (XRD), high-resolution X-ray photoelectron spectroscopy (XPS) and positron annihilation (PAL) methods.

The studied ceramics were sintered in a special regime with maximal temperatures from 1,100°C to 1,400°C during 2 h. The initial powders of Al_2O_3 and MgO were used as starting components within conventional ceramics technology route.

The XRD results showed that ceramics sintered at 1,100–1,200°C contained mainly the spinel phase and additional MgO and Al_2O_3 phases. In contrast, the ceramics sintered at 1,300–1,400°C contained only the MgO phase. These conclusions agree well with XPS data, where a core-level O 1s spectrum deconvoluting on two independent peaks corresponds to main spinel and additional phases (MgO and/or Al_2O_3).

The PAL results showed that more perfect ceramic microstructure representing mainly in small amount of additional phases reflects more considerable changes in the positron trapping parameters such as mean and defect-free bulk positron lifetimes.

Thus, the combined using of XPS, XRD and PAL spectroscopy is a quite informative tool to study phase interactions in nanoporous spinel-type ceramic materials caused by their technological modification owing to sintering temperature.

* Halyna Klym, Institute of Materials of SRC "Carat", 202, Stryjska str., 79031, Lviv, Ukraine, e-mail: klymha@yahoo.com

B. Di Bartolo and J. Collins (eds.), *Biophotonics: Spectroscopy, Imaging, Sensing, and Manipulation*,
DOI 10.1007/978-90-481-9977-8_35, © Springer Science+Business Media B.V. 2011

FEMTOSECOND LASER SURGERY: FROM THE TISSUE TO THE CELLS

V. NUZZO[1], D. NEEDLEMAN[1], J. BRUGUES[1], E. MAZUR[1], K. PLAMANN[2], F. APTEL[3], M. SAVOLDELLI[3], J.-M. LEGEAIS[3]
[1]*School of Engineering and Applied Sciences, Harvard University, 9 Oxford Street, Cambridge, MA 02138*
[2]*Laboratoire d'Optique Appliquée, ENSTA-Ecole Polytechnique-CNRS, UMR 7639, chemin de la Hunière, 91761 Palaiseau cedex, France*
[3]*Laboratoire Biotechnologie et Œil, Hotel Dieu de Paris, Université Paris V, 1, Place du Parvis Notre Dame, 75181 PARIS cedex 04*

Abstract In the last decade, femtosecond laser applications in the biology and medicine have largely developed. The ultrashort laser has proved to be a strongly accurate and selective cutting tool, by depositing energy in a very confined volume with minimum collateral effects.

Corneal Surgery

The objective of the research work, carried out at the Laboratoire d'Optique Appliquée, in collaboration with the Hospital Hôtel Dieu de Paris, has been to study the femtosecond laser–tissue interaction in order to define optimal conditions for performing keratoplasty of pathological corneas by femtosecond laser.

The femtosecond laser has recently been introduced for substituting traditional mechanical instruments for corneal transplant or keratoplasty, which consists in replacing a pathological cornea of a patient with a healthy cornea from a donor. Approximately 100,000 procedures are performed per year worldwide. Leading indications for keratoplasty involve opacification of corneal tissue due to a dysfunction of the endothelial cells. The cornea becomes permeable and loses its transparency. The oedema degree increases progressively and if not interrupted by transplantation can cause total opacification of the cornea and a drastic decrease of the visual acuity. Traditional techniques for keratoplasty present a high risk of rejection, insufficient visual recovery and/or a risk of failure because technically delicate. In this context, femtosecond lasers represent a safe, accurate, and reliable surgical tool. However, clinical systems commercially available are very successful in cutting transparent corneal tissue (donor) but present technical limitations when inducing dissection in pathological corneas (receiver). Moreover, the laser parameters are chosen qualitatively, possibly inducing secondary effects.

At the interface between the physics and the ophthalmology, this research work has allowed assessing the potential and the limitations of the present clinical systems. It has

B. Di Bartolo and J. Collins (eds.), *Biophotonics: Spectroscopy, Imaging, Sensing, and Manipulation*, 399
DOI 10.1007/978-90-481-9977-8_36, © Springer Science+Business Media B.V. 2011

brought solutions for optimizing the laser–tissue interaction, also indicating directions for the development of a further high performing system.

Spindle Surgery

Modern biology understanding is based on a dissection approach by which structures are investigated by removing part of it and by studying the effect of the removal on the structure.

In our project at Harvard University, we aim to use femtosecond pulses to ablate intracellular organelles, more specifically, cell spindles composed of microtubules. Spindles are strongly involved in cell division, as microtubules emerging from two opposite poles in the cells segregate chromosomes by attaching to them in cell division and pulling away the two sister chromatids of each chromosome right before duplication. The spindle is a non-equilibrium steady-state structure and by selectively ablating microtubules, our purpose is to study the dynamics of reorganization of the spindle and to quantify the forces involved. Preliminary time-lapse imaging has shown relaxation of microtubule following the laser cut of one pole.

FLUORESCENCE SPECTROSCOPY OF CRYSTALLINE CONFORMATIONAL CHANGES UNDER UV-RADIATION

NADEZHDA ZHDANOVA, EUGENE A. SHIRSHIN
Quantum Electronics Division, Faculty of Physics, M.V. Lomonosov Moscow State University, Moscow, Russia

Abstract Cataract eye illness represents itself a great problem – about 60% of people over 60 overcome eyesight difficulties due to it. A complex investigation of cataract must be performed and some novel methods for diagnostics, control and treatment are to be developed. It has been discovered that one of the reasons that lead to cataract is absorption of UV radiation by eye lens. The proposed mechanism of cataract formation includes two stages: absorption of UV quanta by crystallins (eye lens proteins), conformational changes of cristallins and their consequent aggregation.

The kinetics of UV-aggregation of lens proteins was experimentally studied by the means of light scattering. It has been shown that the aggregation process can be described by the system of differential equations and the rates of changes on second range were determined.

However, such experiments do not explain the nature of aggregation – it is not clear what happens to crystallins under UV radiation. In order to investigate aggregation processes on molecular level and to monitor molecular phohtophysical parameters one needs to apply fluorescent spectroscopy.

We propose a novel method of aggregation diagnostics based on the application of laser fluorimetry complimentary with the conventional methods – polarization spectroscopy, FRET-spectroscopy etc. This method includes the determination of singlet-singlet annihilation rate in crystalline complexes. It is expected that its application to eye lens proteins will help to understand the origins of aggregation.

B. Di Bartolo and J. Collins (eds.), *Biophotonics: Spectroscopy, Imaging, Sensing, and Manipulation*,
DOI 10.1007/978-90-481-9977-8_37, © Springer Science+Business Media B.V. 2011

INCORPORATION OF AXIALLY SUBSTITUTED MONOPHTALOCYANINES OF ZIRCONIUM, HAFNIUM AND SELECTED LANTHANIDES IN MONOLITHIC SILICA BLOCKS AND THEIR OPTICAL PROPERTIES

Y. GERASYMCHUK[1], L. TOMACHYNSKI[2], I. TRETYAKOVA[2], ST. RADZKI[3], J. LEGENDZIEWICZ[1]
[1]*Faculty of Chemistry, Wroclaw University, 14 F. Joliot-Curie, 50-383 Wroclaw, Poland*
[2]*V. I. Vernadskii Institute of General and Inorganic Chemistry, 32/34 Palladin Ave., 03-680 Kiev, Ukraine*
[3]*Faculty of Chemistry, Maria Curie-Sklodowska University, 2 M.Curie-Sklodowska sq., 20-031 Lublin, Poland*

Abstract The monolithic silica gels with incorporated phthalocyanine complexes of metals is the good model system for investigations on phthalocyanine based laser, optical waveguides, for searching of photovoltaic effects of phthalocyanine complexes, for investigations on cytostatic activity of this complexes in photodynamic therapy of cancer and as biosensors. The difficulty of obtaining of phthalocyanine dotted transparent monolithic silica gels without chemical changes of phthalocyanine ring and with retaining of stability of metal-phthalocyanine complexes in conditions of gel-formation reactions caused, that most of articles about silica gels, dotted by phthalocyanines are concentrate on metal phthalocyanine complexes with lateral substitutors in phthalocyanine ring (such as aluminum or zinc tetrasulfophthalocyanine), or on sandwich type compounds, in case of phthalocyanato lanthanide complexes. The monolithic transparent silica gel blocks dotted with axially substituted monophtalocyanine complexes of Zr (IV), Hf(IV), Er(III), Tm(III) and Yb (III) were obtained. Stability of complexes in gels on different stages of gel formation was provided by absorption spectra. The influence of silica matrix to absorption and emission spectra of metal monophthalocyanine complexes was investigated in comparison with spectra of these complexes in solid and DMSO solutions.

B. Di Bartolo and J. Collins (eds.), *Biophotonics: Spectroscopy, Imaging, Sensing, and Manipulation*, 403
DOI 10.1007/978-90-481-9977-8_38,

DESIGN OF THE UNEQUAL MULTILAYER STRUCTURES FOR THE SELECTIVE OPTICAL FILTERS

IRYNA YAREMCHUK*
Department of Photonics, Lviv Polytechnic National University, 12 S. Bandera str., 79013 Lviv, Ukraine

Abstract This work is devoted to the design of the unequal multilayer structures for the selective optical filters. The new constructions of filters are designated for the infrared region of the spectrum. There are band pass filters that includes structure with three-layer periods and structure with the metallic thin film; the narrowband filters that includes five layers only and band pass filters of type "layer with the high refractive index – interference mirror – layer with the high refractive index".

The concept of pointer function which can be used for prognostication the region of high transmission (reflection) in band pass multilayered periodic interference filters without the thorough analysis of such structures is entered.

Analytical connection is determined between the thickness and refractive index of materials for the design of filter, which includes of interference mirror and limited layers with the high index of refraction.

Certain rules and connections are denoted between structural properties of the multilayer systems and their optical characteristics (transmission, reflection and absorption). Influence of losses is researched in the layers of thin-film structures on their optical characteristics.

* Iryna Yaremchuk, Department of Photonics, Lviv Polytechnic National University, 12 S. Bandera str., 79013 Lviv, Ukraine, e-mail: yaremchuk@polynet.lviv.ua

B. Di Bartolo and J. Collins (eds.), *Biophotonics: Spectroscopy, Imaging, Sensing, and Manipulation*, 405
DOI 10.1007/978-90-481-9977-8_39, © Springer Science+Business Media B.V. 2011

OPTICAL PROPERTIES, MORPHOLOGY AND LONG TIME DEGRADATION OF ALQ3 THIN FILMS

P. CHIACCHIARETTA[1], G. BALDACCHINI[1],
T. BALDACCHINI[2], F. BONFIGLI[1], R.B. PODE[3],
R.M. MONTEREALI[1], M.A. VINCENTI[1]
[1] *ENEA, Advanced Technologies and New Materials Dep., C: R. Frascati, 00044 Frascati, (Rome) Italy*
[2] *Newport Corporation, Technology and Application Center, Irvine, California 92606, USA*
[3] *Department of Physics, Kyung Hee University, Seoul 130-701, South Korea*

Abstract The photoluminescence (PL) of Alq3 thin films decays in time because physical and chemical degradation processes start to take place soon after their evaporation. The time evolution is very complex and dependent on the environmental conditions. Moreover, also thermal treatments strongly influence the decay. In order to understand the behaviour from the microscopic point of view, systematic measurements of the optical properties were performed on several thin films of Alq3. Their monitoring was carried out for about 50,000h, and mostly emission properties were measured. Lately, we found that the PL time evolution can be described as the sum of four exponential decays which possess vastly different amplitudes, constant times and spectral features. This phenomenological approach was called the Four Components Model (FCM). Preliminary results in a particular film are substantially in agreement with the FCM, but other films are still being analyzed in details, with some interesting novelties. It is worthwhile to note that the FCM not only describes the optical properties of the Alq3 films, but is deeply connected with their molecular structure, and then with the OLEDs properties.

B. Di Bartolo and J. Collins (eds.), *Biophotonics: Spectroscopy, Imaging, Sensing, and Manipulation*, 407
DOI 10.1007/978-90-481-9977-8_40,

TRIPLET–TRIPLET ENERGY TRANSFER IN NANODIMENSIONAL MOLECULAR LAYERS

E.V. SELIVERSTOVA*, N.KH. IBRAYEV,
A.K. AIMUKHANOV
Karaganda State University, Department of Physics, Karaganda, Kazakhstan

Abstract The triplet–triplet (T-T) energy transfer is one of the fundamental problems in condensed state physics. From exchange-resonant nature of T-T energy transfer it follows that the efficiency of energy transfer must depend on the separation and mutual orientation of the energy donor and acceptor. To investigate experimentally the influence of the orientational and separation factors on the efficiency of intermolecular energy transfer, we took advantage of the Langmuir–Blodgett (LB) technology which allowed donor-acceptor systems to be formed with predicted separation and mutual orientation of molecules.

In the present work results of research of the interlayer T-T energy transfer from aromatic hydrocarbons molecules to molecules of dyes in LB films are adduced.

The anthracene and 1.2-benz(a)anthracene molecules (1.2-BA) were chosen as triplet energy donors, the Nile red and heptadecyl ether rhodamine B molecules served as triplet energy acceptors. Molecular structures "anthracene-nile red" and "1.2-BA-rhodamine B" were synthesized by LB technology on quartz substrates. Spectral and kinetic characteristic of samples were measured using an automated facility with registration on the photon counting regime.

Absorption and fluorescence spectra of investigated structures have very weak degree of overlapping that excludes a probability of singlet-singlet energy transfer from anthracene to Nile red molecules. Fluorescent spectra not overlaps that allows to identify theirs separately.

Delayed luminescence spectra of heterostructure "anthracene–Nile red" were observed. Excitation was realized in absorption band of the donor. The measurements were spent at sample temperature T = 90K for exclusion of quenching processes by uncontrollable impurity and defects. The luminescence spectrum consists of the annihilation delayed fluorescence band of monomers (λ_{max} = 420 nm) and excimers (λ_{max}= 500, 530nm) of anthracene, and luminescence band at λ_{max} = 650nm, that spectroscopically coinciding with a fluorescence band of Nile red. The increase of the dye concentration in the monolayer leads to quenching of energy donor luminescence. Delayed luminescence spectra of "1.2-BA–rodamine B" pair LB film also were observed. The observed spectrum of sensitized luminescence coincides with band of

* E.V. Seliverstova, Karaganda State University, Department of Physics, Karaganda, Kazakhstan, e-mail: evgeshka_silver@mail.ru, nibraev@ksu.kz

B. Di Bartolo and J. Collins (eds.), *Biophotonics: Spectroscopy, Imaging, Sensing, and Manipulation*, 409
DOI 10.1007/978-90-481-9977-8_41, © Springer Science+Business Media B.V. 2011

dyes fluorescence then the given luminescence should be carried to its annihilation delayed fluorescence (ADF).

Curves of luminescence decay of 1.2-BA at different rhodamine B concentrations in LB film are observed**.** Fluorescence duration of energy donor decreases with the increasing of number of acceptor molecules. Analogous data have been received for pair "anthracene–Nile red".

It has been shown that decay kinetics of ADF of aromatic LB films is described by combination of power and exponential functions. The received curves it is well described by power dependence of kind $I_{ADF} \sim t^{-n}$. The power index changes from 0.2 to 0.5 at the given acceptor concentrations. Similar data have been received and for pair "1.2-BA-rhodamine B".

To investigate experimentally the influence of the separation factors on the efficiency of T-T energy transfer the influence of distance between donor and acceptor layers at the luminescence quenching of the acceptor were studied. Maximal quenching of the donor triplet states is observed at intimate contact of donor layer and the acceptor molecules layer**.** The increase of the distance leads to decrease of energy transfer efficiency.

The temperature influence on energy transfer between 1.2-BA and rhodamine B molecules was investigated at the range from room temperature to 90 K. It has been found that intensity of ADF of donor LB films has prominent maximum at T = 170K. The received temperature influence of ADF is associated with the inhomogeneous broadening of triplet levels of donor molecules. The maximum of donor luminescent intensity at the presence of acceptor molecules is observed at the same temperature.

THE INFLUENCE OF DRIVING FORCE ON FORMATION AND GEMINATE RECOMBINATION OF CHARGES IN ALTERNATING POLYFLUORENE COPOLYMER/FULLERENE BLENDS

TOMAS ÖSTERMAN*, TORBJÖRN PASCHER, ARKADY YARTSEV, VILLY SUNDSTRÖM
Department of Chemical Physics, Lund University, Box 124, 22100 Lund, Sweden

Abstract Conjugated polymer/fullerene-based solar cells are, due to their potential flexibility, cost efficiency and low weight, interesting as future alternatives to today's silicon cells [1]. In these cells, both the dissociation of the polymer exciton into extractable charges, i.e. charges that are free and mobile, and the recombination of the free charges are expected to be crucial in order to obtain high light-to-charge conversion efficiencies. The exciton dissociation is believed to strongly depend upon the driving force [2] while the driving force dependence of the recombination has not been thoroughly investigated. Therefore, we have studied the charge formation and recombination in blends of alternating polyfluorene copolymers (APFO polymers) and PCBM with different driving force. By varying the polymer in the blends, a driving force range of 0.05–0.77 eV has been covered.

The formation of charges that are free and mobile, and thus believed to be extractable in solar cell devices, in APFO/PCBM blends has been shown to occur in two steps. First, the excitons very efficiently dissociate into bound charges with a time constant of ~200 fs [3], and then the bound charges are converted into free and mobile charges with a time constant of ~30 ps [4]. In order to resolve these processes, we have performed ultrafast transient absorption. The results give further support for the present two-step model and show that some driving force is needed for the dissociation of the exciton to be efficient but that the driving force does not seem to determine the rate of exciton dissociation.

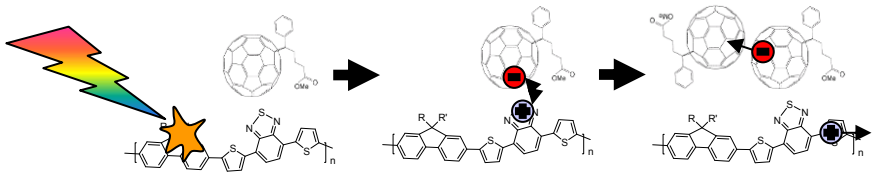

* Tomas Österman, Department of Chemical Physics, Lund University, Box 124, 22100 Lund, Sweden, e-mail: Tomas.Osterman@chemphys.lu.se

B. Di Bartolo and J. Collins (eds.), *Biophotonics: Spectroscopy, Imaging, Sensing, and Manipulation*, DOI 10.1007/978-90-481-9977-8_42, © Springer Science+Business Media B.V. 2011

The recombination of free charges is believed to compete with charge extraction and is therefore likely to significantly affect the amount of extractable charges [5]. Studies of APFO/PCBM blends have shown that charges recombine quite fast (~30 ns) under solar illumination conditions although only geminate charge recombination is present at these intensities [4]. We have studied the driving force dependence of the charge recombination by performing transient absorption measurements with low pump intensities. The results show no clear dependence on driving force for the geminate recombination process. More factors, such as morphology and charge mobility, are needed to explain the observations.

(SUB)PICOSECOND DYNAMICS IN MGDNA COMPLEXES UPON LOWERING THE PH: A RAMAN MICROSPECTROSCOPIC STUDY

CRISTINA M. MUNTEAN, IOAN BRATU
National Institute of Research & Development for Isotopic and Molecular Technologies, P.O. 5, Box 700, R-400293 Cluj-Napoca, Romania

Abstract Spontaneous Raman scattering can be used to study the fast dynamics of molecules. This paper presents a confocal Raman microspectroscopic study into the vibrational half bandwidths of molecular subgroups in calf-thymus DNA, upon lowering the pH, and in the presence of Mg^{2+} ions.

Low pH-induced melting of double helical structure in calf-thymus DNA results for some vibrations in smaller global relaxation times, and larger bandwidths, respectively, as a consequence of the increased interaction of the base moieties with the solvent molecules. This behaviour is most evident for the bands at 1,377, 1,488, 1,580cm^{-1} and partially confirmed for the adenine band near 728cm^{-1}. For this last band, the global relaxation time increases at 1.04 ps for the pH value 3.45, before starting to decrease. The vibrational energy transfer processes are the most rapid for the adenine 728cm^{-1} vibration around the pH 2.82 (global relaxation time 0.82 ps), for the vibration near 1,377cm^{-1} at pH 3.45 (global relaxation time 0.34 ps), for the guanine band around 1,488cm^{-1} at pH 3.1 (global relaxation time 0.65 ps) and for the band around 1,580cm^{-1} at pH 3.45 (global relaxation time 0.37 ps) [1]. Upon lowering the pH under these values, the global relaxation times increase at the highest values for the bands at 1,377, 1,488, and 1,580cm^{-1} and this slower dynamics is probably due to the aggregation and sedimentation of calf thymus DNA complexes, in association with acidic melting of the double helix. An increase of the global relaxation time is also observed upon DNA protonation at very low pH for the adenine vibration at 728cm^{-1}, but the respective values are not so high as compared to those of the bases bands [1].

Apart from the data above, the global relaxation time of the band near 1,094 cm^{-1} of the DNA backbone PO_2^- symmetric stretching vibration, has a tendency to decrease upon decreasing the pH. The fastest dynamics was observed for this band at pH 2.1 (global relaxation time 0.39 ps) and this is opposite with the behaviour of the relaxation processes characterizing the DNA bases bands at 1,377, 1,488, and 1,580cm^{-1}. In this study the Raman band parameters of the cytosine ring breathing mode near 785 cm^{-1} did not show a definite behavior [1].

B. Di Bartolo and J. Collins (eds.), *Biophotonics: Spectroscopy, Imaging, Sensing, and Manipulation*, 413
DOI 10.1007/978-90-481-9977-8_43, © Springer Science+Business Media B.V. 2011

ONE- AND TWO-PHOTON PUMPED DFB LASER BASED ON SEMICONDUCTOR QUANTUM DOTS EMBEDDED IN A SOL-GEL MATRIX

I. FORTUNATI[1], S. GARDIN[1], F. TODESCATO[1], R. SIGNORINI[1], R. BOZIO[1], J.J. JASIENIAK[2], A. MARTUCCI[3], G. DELLA GIUSTINA[3], G. BRUSATIN[3], M. GUGLIELMI[3], M. PRASCIOLU[4], F. ROMANATO[5]

[1]*Dipartimento di Scienze Chimiche e U.R. INSTM, Università di Padova, Via Marzolo 1, I-35131 Padova, Italy*

[2]*CSIRO Division of Molecular and Health Technologies Ian Wark Laboratory, Bayview Avenue, Clayton 3168, Australia*

[3]*Dipartimento di Ingegneria Meccanica, Settore Materiali e U.R. INSTM, Università di Padova, via Marzolo 9, I-35131 Padova, Italy*

[4]*CNR-INFM Laboratorio nazionale TASC, S.S. 14 km 163,5, I-34012 Basovizza, Trieste, Italy*

[5]*Dipartimento di Fisica, Università di Padova, Via Marzolo 8, I-35131 Padova, Italy*

Abstract In the last years inorganic semiconductor (CdSe and CdS) quantum dots (QDs) have received great attention for their important optical properties: the design of DFB devices, based on QDs as active optical material, leads to the realization of compact laser systems.

QDs are characterized by 3D-nanoscale dimensions (R < 10 nm), corresponding to a strong confinement effect, well defined when their dimensions are comparable or below the exciton Bohr radius. In particular, the great possibility to tune the emission wavelength, together with their high fluorescence quantum efficiency and their photostability, can be exploited in photonic and optoelectronic technological applications, like DFB realization.

When QDs are pumped into high-energy excited states, the population inversion and the build-up of optical gain take place, allowing the Amplified Spontaneous Emission (ASE) process. The competition between radiative and nonradiative processes crucially affects the QDs optical gain, which is only possible if the relaxation down to the ground state is faster than the Auger process. In QDs, nonradiative carrier losses are dominated by surface trapping and multiparticle Auger relaxation. It is therefore important to strictly control the surface quality of the semiconductor nanocrystals. To this end, we performed a careful study to investigate the best QDs surface quality to allow the inclusion in sol-gel matrices, characterized by high optical gain and photostability.

In this work the interactions between the CdSe–ZnS quantum dots and different sol-gel matrices were investigated and characterized by one- and two-photon excitation, in a

B. Di Bartolo and J. Collins (eds.), *Biophotonics: Spectroscopy, Imaging, Sensing, and Manipulation*, DOI 10.1007/978-90-481-9977-8_44,

femtosecond regime. The QDs doped matrices show high stability both under one- and two-photon irradiation.

Preliminary DFB devices, based on calculated parameters, have been realized by imprinting, performed with a 1D master on an epoxy/GeO_2 hybrid sol-gel film, and by e-beam lithography, realizing 2D gratings on GPTMS/Germanium tetraethoxide hybrid matrix. The resulting samples possess respectively a 1 cm^2 area, with a first order grating, and a 100 × 100 μm area, with second order gratings. We reported the first performance tests showing good and promising results.

NATO ASI 983377
BIOPHOTONICS
Spectroscopy, Imaging, Sensing and Manipulation

LIST OF PARTICIPANTS

1. Carlo Altucci
Dipartimento di Scienze Fisiche
Università di Napoli "Federico II"
Via Cintia, 26 Ed. 6
80126 Napoli, Italy
altucci@na.infn.it
Areas of Interest: high-order harmonic generation, attoseond physics, biophotonics

2. Jose Isidro Alvelo
George Mason University
National Center for Biodefense
Fairfax, VA 22030, USA
jose.alvelo@live.com
Areas of Interest: biophotonics, nanomagnetics, systems biology, tissue engineering, brain-machine interface

3. Steve Arnold
Brooklyn Polytechnic University – 6 Metroteck Center
Brooklyn, NY 11201, USA
Tel.: (1) 718 260-3296; 917 568-6549
arnold@photon.poly.edu,sarnold935@aol.com
Areas of Interest: whispering gallery ode biosensing, microparticle photophysics, nano-optics, biooptics, biophotonics, molecular electromagnetism

B. Di Bartolo and J. Collins (eds.), *Biophotonics: Spectroscopy, Imaging, Sensing, and Manipulation*,
DOI 10.1007/978-90-481-9977-8_45, © Springer Science+Business Media B.V. 2011

4. Rolindes Balda
Departamento de Fisica Applicada I- Escuela Tecnica Superior de
Ingenieros Industriales Y de Telecomunicacion-Universidad del Pais Vasco
Alda, Urquio, S/N49013 Bilbao, Spain
Tel.: (34)-94 601 40 52; Fax: (34) 94 601 41 78
wupbacrr@bi.ehu.es
Areas of Interest: luminescent materials,
rare-earth and transition metal ion doped crystals and glasses,
solid state laser materials

5. Torsten Beck
Universitaet Karlsrhue
Insitut fuer Angewandte Physik
Group Prof. Dr. H. Kalt
Wolfgang-Gaede-Strasse 1
76131 Karlsrhue, Germany
torsten.beck@kit.edu

6. Mario Bortolozzi
University of Padova and
Venetian Institute of Molecular Medicine (VIMM),
Via G. Orus 2, 35129 Padova, Italy
Tel.:/Fax: +39 049 7923247/250
mario.bortolozzi@unipd.it
Areas of Interest: genetic deafness, second messenger molecular dynamics,
fluorescence confocal microscopy,
Ca^{2+} dynamics numerical simulations

7. Georges Boulon
Université Claude Bernard- Lyon I
Laboratoire de Physico-Chimie de Materiaux Luminescents, Bât. 205
F-69622 Villeurbanne Cedex, France
Tel.: (33) 47 244-8271; Fax.: (33) 7 243-1130
georges.boulon@pcml.univ-lyon1.fr

8. Laura Bovo
Dipartimento di Chimica
Università di Padova
Via Marzolo, 1
1- 35131 Padova, Italy
laura.bovo@unipd.it
Areas of Interest: synthesis and characterization of based oxide materials,
applications to photonics, photocatalysis and biosensing

9. John W. Bowen
School of Systems Engineering
The University of Reading
Reading RG6 6AY, UK
Tel: (44) (0)118 378 6702; Fax.: +44(0)118 378 8220
j.bowen@reading.ac.uk
Areas of Interest: terahertz systems,
micromachining, coherent control

10. Majed Chergui
Laboratoire de Spectroscopie Ultrarapide (LSU)
Institut des Sciences et Ingénierie Chimiques (ISIC)
Faculté des Sciences de Base (FSB), BSP
Ecole Polytechnique Fédérale de Lausanne (EPFL)
CH-1015 Lausanne-Dorigny, Switzerland
Tel.: (41) 21 693 0457 or 0447; Fax.: (41) 21 693 0422
Majed.Chergui@epfl.ch

11. Piero Chiacchiaretta
Via Aldo Moro, 114
66020 San Giovanni Teatino (Chieti), Italy
piero.chiacchiaretta@gmail.com
Areas of Interest: OLED, biosensing, SQUID, neuroscience

12. John Collins
Department of Physics
Wheaton College
Norton, MA, USA
Tel.: 39 617 3320371
jcollins@wheatonma.edu
Areas of Interest: spectroscopy of rare earth
and transition metal ions in solids, laser and phosphor materials

13. Jonas Conradt
Universitaet Karlsrhue
Institut fuer Angewandte Physik
Group Prof. Dr. H. Kalt
Wolfgang-Gaede-Strasse 1
76131 Karlsruhe, Germany
Jonas.Conradt@aph.uni-karlsruhe.de
Areas of Interest: time-resolved spectroscopy,
energy transfer, photovoltaics, ZnO

14. Giovanni Costa
Dipartimento di Fisica
Università degli Studii
35128 Padova, Italy
Tel.: 39 (049) 827-7131
costa@pd.inf

15. Johannes F. de Boer
Department of Physics-VU University
De Boelelaan 1081
1081 HV Amsterdam, The Netherlands
Phone: +31-20-5987972
Email: jfdeboer@few.vu.nl
Areas of Interest: biomedical optics, diagnosis of disease, tissue optics, techniques

16. Baldassare Di Bartolo (Co-Director of the Institute)
Department of Physics, Boston College
Chestnut Hill, MA 02167, USA
Tel.: (1) 617 552-3601; home (1) 781 483-3993
Fax.: (1) 617 552-8478
dibartob@bc.edu, rinodiba@comcast.net
Areas of Interest: laser theory, fluorescence spectroscopy

17. Paolo Di Lazzaro
ENEA FIM FIS-ACC – Excimer Laser Lab
via E. Fermi 45, 00044 Frascati, Italy
Tel: (39) 06 9400 5722; Fax: (39) 06 9400 5334
dilazzaro@frascati.enea.it

18. Joaquin Fernandez
Applied Physics Department I
Escuela Superior de Ingenieros
University of the Basque Country
Alda. de Urquijo s/n
48013 Bilbao, Spain
Tf.: 34-94 601 40 52; Fax.: 34- 94 601 41 78
wupferoj@bi.ehu.es

19. Ottavio Forte
Department of Physics
Boston College
Chestnut Hill, MA 02467, USA
forteo@bc.edu

20. Erik Thomas Garbacik
Optical Sciences Group
University of Twente, Hogekamp T-10
7500 AE Enschede, The Netherlands
e.t.garbacik@student.utwente.nl
Areas of Interest: CARS, non-linear spectroscopy and microscopy, optical parametric oscillators

21. Juriy Gerasymchuk
Faculty of Chemistry
Wroclaw University
F. Joliot-Curie St. 14
Wroclaw, Poland
juretz@interia.pl
Areas of Interest: spectroscopy of metal complexes of polyphrine and phthalocyanine, sol-gel technology, photodynamic therapy of cancer, macrocycle agent for PDT

22. Alexander Heisterkamp
Biophotonics Group
Department of Biomedical Optics
Hollerithallee 8
D-30419 Hannover, Germany
Tel.: ++49 511 2788-484; Fax.: ++49 511 2788-100
E-mail: a.heisterkamp@lzh.de
Internet: www.biophotonics.uni-hannover.de | www.lzh.de

23. Stefan W. Hell
Max Planck Institute for Biophysical Chemistry
Gottingen 37077, Germany
Tel.:(49) (0)551 201 2501; Fax.: +49 (0)551 201 2505
shell@gwdg.de

24. Martin Husnik
Institut für Angewandte Physik
Universität Karlsruhe (TH)
76131 Karlsruhe, Germany
Tel.: +49-721-608 7481; Fax: +49-721-608 8480
martin.husnik@physik.uni-karlsruhe.de
Areas of Interest: spectroscopy of indivdual nanoparticles, nano-photonics, metamaterials, biophotonics

25. Yingyot Infahsaeng
Chemical Physics
PO Box 124 SE-22100
Lund University, Sweden

Tel.: +46 076 268 1299
Yingyot.Infahsaeng@chemphys.lu.se
Areas of Interest: functional organic solar cells, ultrafast spectroscopy, charge transfer and transport

26. Nur Ismail
Integrated Optical MicroSystems group (IOMS)
University of Twente
Faculty of Elektrotechniek, Wiskunde en Informatica (EWI)
P.O. Box 217
7500 AE Enschede, The Netherlands
Tel.: + 31 53 489 5417; Fax.: + 31 53 489 3343
n.ismail@ewi.utwente.nl
Areas of Interest: biophotonics, integrated optics, spectroscopy

27. Heinz Kalt
Institut für Angewandte Physik der Universität
W. Gaede Str.1
D 76131 Karlsruhe, Germany
Tel.: +49-(0)721 608 3402
Heinz.Kalt@Physik.Uni-Karlsruhe.de

28. Ivan Karbovnyk
National University of Lviv
Department of Electronics
107 Tarnavskogo str, 79017
Lviv, Ukraine
Ph. 38 032 2394224
ivan_karbovnyck@yahoo.com
Areas of Interest: optical and IR spectroscopy, fractal structures, electrical and optical properties of nanoparticles (experiment and modeling), use of LabVIEW in experiments

29. Maciej Klemm
Electromagnetics Group
Centre for Communications Research
University of Bristol
Bristol, BS8 1UB, UK
Tel.: +44 117 331 5160
m.klemm@bristol.ac.uk
Areas of Interest: biophotonics, plasmonics, nano-antennas, biosensors, bio-electromagnetics

30. Halyna Klym
Lviv Scientific Research Institute of Materials of SRC “Carat”
202, Stryjska str.
Lviv, UA-79031, UKRAINE
klymha@yahoo.com
Areas of Interest: characterization of nanostructured materials,
XRD, XPS, PALS, biosensors, humidity and temperature sensors,

31. Brad Littleton
Department of Physics
King’s College London
Strand WC2R 2LS, UK
Tel.:+44 207 848 1531; Fax: +44 207 848 2420
bradley.littleton@kcl.ac.uk
Areas of Interest: optical proteomics, CARS microspectroscopy

32. Koit Mauring
Institute of Physics
University of Tartu
42 RIIA
Tartu, Estonia 51014
Tel.: +372 7374737
mauring@fi.tartu.ee

33. Tiina Mauring
Eye Clinic
University of Tartu
Tartu, Estonia
Tel.: +372 7313762
tiina.mauring@klinikum.ee

34. Eric Mazur
School of Engineering and Applied Sciences
Harvard University – Pierce Hall 225
Cambridge, MA 02138, USA
Tel.: (1) 617 495-8729; Fax.: (1) 617 495-1229 or 9837
http://mazur-www.harvard.edu
mazur@physics.harvard.edu
Areas of Interest: nanophotonics, biophotonics,
femtosecond laser - materials interaction

35. Mia Milos
Département de Chimie Physique
Université de Genève
36 quai Ernest-Ansermet
CH-1211 Genève 4, Switzerland
mia.milos@unige.ch
Areas of Interest: photophysical and photochemical
properties of transition metal coordination compounds

36. Cristina M. Muntean
National Institute for Research and Development of Isotopic and Molecular
Technologies,
R-400293 Cluj-Napoca, P. O. 5, Box 700, Romania
Tel.: 40-264-584037 or 585027; Fax: 40-264-420042
E-mail: cmuntean@itim-cj.ro
Areas of Interest: spectroscopy of biological molecules,
nanobiophotonics, DNA structural transitions and dynamics

37. Valeria Nuzzo
Mazur Group
School of Engineering and Applied Sciences
Harvard University
Cambridge, MA 02138, USA
vnuzzo@seas.harvard.edu
Areas of Interest: biophotonics, laser-matter interactions
and applications, microscopy

38. Ahmad Odeh
Laboratoire de Spectroscopie Ultrarapide (LSU)
Institut des Sciences et Ingénierie Chimiques (ISIC)
FSB – BSP
CH – 1015 Lausanne, Switzerland
Tél : (+41) 21 693 0452; Fax: (+41) 21 693 0422
ahmad.odeh@epfl.ch
Areas of Interest: nanophotonics, ultrafast spectroscopy,
non-linear laser techniques

39. Stefano Orlando,
CNR - IMIP (Potenza Branch)
Zona Inustriale di Tito Scalo
85050 Tito Scalo (PZ), Italy
stefano.orlando@imip.cnr.it
Areas of Interest: laser–matter interactions, emission spectroscopy,
thin film deposition (PLD)

40. Tomas Österman
Chemical Physics
Lund University
P.O. Box 124
SE-22100 Lund, Sweden
Tomas.Osterman@chemphys.lu.se
Areas of Interest: conjugated polymers, ultrafast spectroscopy, solar energy

41. Adkhamjon Paiziev
Institut of Electronics Uzbek
Academy of Sciences Tashkent
100125 Academgorodok
Durmon Yoli 33, Uzbekistan
Tel.: (998-71) 2470701; Fax.: (998-71) 2628767
adxam_payziev@rambler.ru
Areas of Interest: optical microscopy, biophotonics, materials science, X-ray imaging, positron physics

42. Paras Prasad
Institute for Lasers, Photonics and Biophotonics
The State University of New York, University of Buffalo
Buffalo, NY 14260-3000, USA
Tel.: (1) 716 645-4148; Fax.: (1) 716 645-6945
pnprasad@acsu.buffalo.edu
Areas of Interest: nanophotonics, biophotonics, solar energy conversion, metamaterials

43. Mihkel Rähn
Institute of Physics
University of Tartu
Riia 142, Tartu, Estonia
Tel: +372 55994767
Mihkel.rahn@ut.ee
Areas of Interest: single molecule emission investigations and applications

44. Marco Reinhard
Ecole Polytechnique Fédérale de Lausanne
Laboratoire de Spectroscopie Ultrarapide
Insititut de Sciences et Ingénieriè Chimique
FSB-BSP
CH-1015 Lausanne, Switzerland
marco.reinhard@epfl.ch
Areas of Interest: Ultrafast dynamics of biosystems

45. Brigit Rudat
Institute of organic Chemistry and Light Technology Institute
University of Karlsrhue
76131 Karlsrhue, Germany
Tel.: +49 721 608 7118
birgit.rudat@kit.edu
Areas of Interest: single-molecule spectroscopy, fluorescence correlation spectroscopy, biophotonics, penetrating molecules/drug delivery

46. Petra Schwille
Biotechnologisches Zentrum der TU Dresden
Tatzberg 47-51
01307 Dresden, Germany
Tel. (49) (0)351-463-40329; Fax: (49)-(0)351-463-40342
petra.schwille@biotec.tu-dresden.de
Areas of Interest: single-molecule microscopy and spectroscopy, FCS, two-photon microscopy, membrane and cell biophysics,microfluidics, synthetic biology

47. Melanie Schwingel
Universität Karlsruhe (TH)
Zoologisches Institut I
Haid-und-Neu-Str. 9
D-76131 Karlsruhe, Germany
Tel: +49 721-608-8172; Fax: +49 721-608 4848
Email: melanie.schwingel@bio.uka.de
Areas of Interest: biophotonics, optical manipulation, biosensing, nano-optics

48. Evgeniya Seliverstova
Karaganda State University
Molecular Nanophotonics Institute
Karaganda, Kazakhstan
evgeshka_silver@mail.ru
Areas of Interest: photophysical properties of nanodimensional objects, nanophotonics, energy transfer in thin films

49. Eugene A. Shirshin
Quantum Electronics Division
Faculty of Physics
M.V. Lomonosov Moscow State University
119991, Leninskye Gory, 1,
Moscow, Russia
eshirshin@mail.ru
Areas of Interest: FRET-sensors, luminescence enhancement in local fields, biophotonics

50. Nicolas Stenger
Institut für Angewandte Physik- Universität Karlsruhe
76131 Karlsruhe, Germany
Tel.: +49 (0) 721 608 7327
nicolas.stenger@physik.uni-karlsruhe.de
Areas of Interest: direct laser lithography,
transformation optics, nanophotonics, metamaterials

51. Villy Sundström
Chemical Physics-Chemical Center
Lund University – Box 124
S-22100 Lund, Sweden
Tel.: (46) 46-2224690; Fax.: (46) 46-222411
Villy.sundstrom@chemphys.lu.se

52. Demet Tatar
Istanbul Technical University
Materials Science and Engineering
Kadın Mektebi Sokak 10/3 Rumeli Hisari
Istanbul 34470, Turkey
Tel.: (+90) 532 353 3028
demettatar@yahoo.com
Areas of Interest: glass and glass ceramics, XRD,
Raman spectroscopy, lasing glasses, production of nanoparticles

53. Philip Tinnefeld
Angewandte Physik – Biophysik
Ludwig-Maximilians-Universität
Amalienstr. 54
80799 München
Tel: +49 89 2180 1438; Fax: +49 89 2180 2050
Philip.Tinnefeld@lmu.de
Areas of Interest: single-molecule fluorescence,
photophysics and photochemistry, DNA nanotechnology,
single molecule FRET, biomolecular interactions and dynamics

54. Francesco Todescato
Dipartimento di Scienze Chimiche
Università di Padova
Via Marzolo 1
35131 Padova, Italy
Tel: +39 049 8275726
francesco.todescato@unipd.it
Areas of Interest: nanoplasmonics, organic photovoltaics,
SERS, DFB lasing, quantum dots, nanolithography

55. Raffaele Velotta
Dipartimento di Scienze Fisiche
Università di Napoli “Federico II”
Via Cintia, 26 Ed. 6
80126 Napoli, Italy
Tel. +39 081 676148 (office); +39 081 676319 (lab.); Fax.: +39 081 676346
rvelotta@unina.it
http://people.na.infn.it/velotta/
http://www.docenti.unina.it/raffaele.velotta
Areas of Interest: molecular alignment, high order harmonics, biophotonics

56. Alexander Voitovich (Co-Director of the Institute)
Academy of Sciences of Belarus
Institute of Physics
Pr. Nezalejnosci 68
220072 Minsk, Belarus
Voitovich@imaph.bas-net.by; avoitovich@gmail.com
Areas of Interest: nonophotonics, luminescence, non-linear dynamics

57. Frank Vollmer
Rowland Institute at Harvard
Cambridge, MA, USA
Tel.: (1) 617 497 4681
Fax: (1) 617 497 4627
Vollmer@rowland.harvard.edu
Areas of Interest: photonic biosensing, nanophotonics, experimental biophysics

58. Martin Wegener
Institut für Angewandte Physik- Universität Karlsruhe
D-76128 Karlsruhe, Germany
Tel.: (49) 721 608-3400; Fax.: (49) 721 607- 593
martin.wegener@physik.uni-karlsruhe.de
Areas of Interest: nanophotonics, plasmonics, metamaterials

59. Jean-Pierre Wolf
Université de Gèneve
Biophotonics Group
Gèneve, Switzerland
Tel.: (41) 22 37965 94
jean-pierre.wolf@physics.unige.ch

60. Iryna Yaremchuk
PhD degree Techniques
Department of Photonics
Lviv Polytechnic National University
12, Bandera str., UA-79013, Lviv, Ukraine
yaremchuk@polynet.lviv.ua
Areas of Interest: nanophotonics, nanoparticles, plasmonics, biosensors, periodic structures

61. Nadezhda Zhdanova
Quantum Electronics Division
Faculty of Physics
M.V. Lomonosov Moscow State University
119991, Leninskye Gory, 1
Moscow, Russia
nadezda1989@gmail.com
Areas of Interest: fluorescence spectroscopy of proteins

INDEX

B. Di Bartolo and J. Collins (eds.), *Biophotonics: Spectroscopy, Imaging, Sensing, and Manipulation*,
DOI 10.1007/978-90-481-9977-8, © Springer Science+Business Media B.V. 2011